List of Contributors

H. M. Al-Hashimi, *Department of Chemistry & Biophysics Research Division, University of Michigan, Ann Arbor, MI 48109-1055, USA*

I. Ando, *Department of Chemistry and Materials Science, International Research Center of Macromolecular Science, Tokyo Institute of Technology, Ookayama, Meguro-ku, Tokyo, Japan*

V. Barone, *Physics Department, School of Sciences, University of Buenos Aires and CONICET, Ciudad Universitaria, P. 1, (1428) Buenos Aires, Argentina*

R. H. Contreras, *Physics Department, School of Sciences, University of Buenos Aires and CONICET, Ciudad Universitaria, P. 1, (1428) Buenos Aires, Argentina*

J. C. Facelli, *Center for High Performance Computing, University of Utah, 155 South 1452 East RM 405 Salt Lake City, UT 84112-0190, USA*

D. Gudat, *Institut für Anorganische Chemie der Universität Stuttgart, Pfaffenwaldring 55, 70550 Stuttgart, Germany*

E. Katoh, *Department of Biochemistry, National Institute of Agrobiological Sciences, Kannondai, Tsukuba, Ibaraki, Japan*

S. Kuroki, *Department of Chemistry and Materials Science, International Research Center of Macromolecular Science, Tokyo Institute of Technology, Ookayama, Meguro-ku, Tokyo, Japan*

K. Murata, *Department of Chemistry and Materials Science, International Research Center of Macromolecular Science, Tokyo Institute of Technology, Ookayama, Meguro-ku, Tokyo, Japan*

J. E. Peralta, *Department of Chemistry, Rice University, Houston, TX 77005-1892, USA*

W. P. Power, *Department of Chemistry, University of Waterloo, Waterloo, ON N2L 3G1, Canada*

J. R. Tolman, *Department of Chemistry, Johns Hopkins University, 3400 N. Charles St., Baltimore, MD 21218, USA*

Preface

Applications of NMR are well established in all areas of science and new ones are being regularly reported. Annual Reports on NMR reflect developments in all areas of science. Contained within Volume 51 of this series are reviews from five different areas of interest.

'A Study of Conformational Stability of Polypeptide Blends by Solid State NMR Spectroscopy' is contributed by K. Murata, S. Kuroki, E. Katoh and I. Ando, D. Gudat reports on 'Applications of Heteronuclear X/Y-Correlation Spectroscopy in Organometallic and Organoelement Chemistry: Recent Developments', 'NMR Studies of Biomolecular Dynamics and Structural Plasticity using Residual Dipolar Couplings' is reviewed by J. R. Tolman and H. M. Al-Hashimi, R. H. Contreras, V. Barone, J. C. Facelli and J. E. Peralta cover 'Advances in Theoretical and Physical Aspects of Spin–Spin Coupling Constants' and 'High Resolution Magic Angle Spinning-Applications to Solid Phase Synthetic Systems and other Semi-Solids' is reviewed by W. P. Power.

Expressions of gratitude go to all of these reporters and to the production staff at Elsevier for their generous cooperation in the realisation of this volume.

Contents

A Study of Conformational Stability of Polypeptide Blends by Solid State NMR Spectroscopy
K. MURATA, S. KUROKI, E. KATOH and I. ANDO

Applications of Heteronuclear X/Y-Correlation Spectroscopy in Organometallic and Organoelement Chemistry: Recent Developments
DIETRICH GUDAT

NMR Studies of Biomolecular Dynamics and Structural Plasticity Using Residual Dipolar Couplings
JOEL R. TOLMAN and HASHIM M. AL-HASHIMI

Advances in Theoretical and Physical Aspects of Spin–Spin Coupling Constants

RUBÁN H. CONTRERAS, VERÓNICA BARONE, JULIO C. FACELLI, and JUAN E. PERALTA

High Resolution Magic Angle Spinning – Applications to Solid Phase Synthetic Systems and Other Semi-Solids

WILLIAM P. POWER

A Study of Conformational Stability of Polypeptide Blends by Solid-State NMR Spectroscopy

K. MURATA[1], S. KUROKI[1], E. KATOH[2] and I. ANDO[1]

[1]*Department of Chemistry and Materials Science, International Research Center of Macromolecular Science, Tokyo Institute of Technology, Ookayama, Meguro-ku, Tokyo, Japan*
[2]*Department of Biochemistry, National Institute of Agrobiological Sciences, Kannondai, Tsukuba, Ibaraki, Japan*

In polypeptide blends, the balance of intra- and intermolecular hydrogen bond interactions in two kinds of polypeptide chains play an important role for the conformational stability and the blend miscibility. The observation of the ^{13}C NMR chemical shifts and relaxation times, and the two-dimensional

NMR spectrum leads to a deep understanding of the conformational stability and the miscibility. In this chapter, the most recent research works are introduced.

1. INTRODUCTION

Synthetic homopolypeptides consist of a repeated sequence of an amino acid. Although the structures of the homopolypeptides are not as complicated as those of proteins, homopolypeptides take some specified conformations such as the α-helix, β-sheet, etc., which appear in proteins. These conformational properties of homopolypeptides are shown in Table 1. The individual conformations are transformed into other conformations under certain conditions such as temperature and quenching.[1–7] For example, the main chain of poly (β-benzyl L-aspartate) takes on a right-handed $\alpha(\alpha_R)$-helix form within the temperature range from room temperature to 117°C and is transformed to the left-handed $\alpha(\alpha_L)$-helix form, the ω-helix form and the β-sheet form at temperatures above 117°C. On the other hand, copolymers of L-alanine (Ala) and glycine (Gly) [(Ala, Gly)$_n$] take the right-handed α-helix, β-sheet and the 3$_1$-helix forms in the solid state as obtained by changing the mixture ratio or by solvent treatment.[8–11] A scheme of conformational generation of polypeptides, copolypeptides and proteins is shown in Fig. 1.

These transformations arise from the energetical stability caused by intramolecular or intermolecular hydrogen bond (HB) interactions. Thus, by the balance of intramolecular and intermolecular HB interactions in polypeptide blends, it is expected that the strength of intermolecular interaction in the blends is different from those in homopolypeptides then new conformations can be formed by intermolecular HB interactions that do not exist originally in homopolypeptides. There are many studies on intermolecular HB interactions in homopolypeptides and copolypeptides in the solid state, but to the best of our knowledge there is little study on intermolecular HB interactions in polypeptide blends except for our previous studies.

In order to understand the conformations or conformational changes of homopolypeptides and copolypeptides, solid-state NMR is a very useful method. After the first NMR experiment for obtaining high-resolution spectra of solids was carried out with the high-speed magic angle spinning (MAS) method,[12] the cross polarization (CP) procedure [13] was developed by Hartmann and Hahn.[14] On the basis of these methods a CP/MAS technique that combines MAS and CP has been conventionally used to obtain high-resolution solid-state NMR spectra.[15,16] In the solid-state, the NMR chemical shift is often characteristic of a specified conformation because of the highly restricted molecular motion. For example, it has been elucidated

Table 1. Preferred conformations of homopolypeptides in the solid-state

Amino acid residue		Conformation[a]		
		1	2	
Glycine		β-Sheet (PG-I)	3_1-Helix (PG-II)	Hydrophobic side chain Hydrophobic interaction
Alanine		α-Helix	β-sheet	Oligomers are β-sheet Hydrophobic side chain Hydrophobic interaction
Valine		β-Sheet		Hydrophobic side chain Hydrophobic interaction
Leucine		α-Helix		Hydrophobic side chain Hydrophobic interaction
Isoleucine		β-Sheet		Hydrophobic side chain Hydrophobic interaction
Serine		β-Sheet		Hydroxylic side chains of hydrogen bonding
Threonine		β-Sheet		Hydroxylic side chains of hydrogen bonding
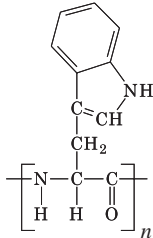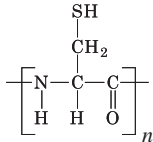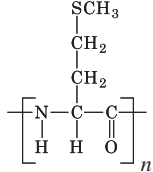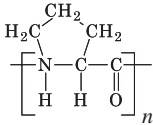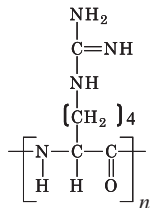
(*Continued*)

Table 1.   Continued

Amino acid residue	Conformation[a]		
	1	2	
Aspartic acid[b]	α-Helix		Hydrophilic side chain
Glutamic acid[b]	α-Helix	(β-Sheet)	Hydrophilic side chain Salts Ca, Sr, Ba are β-sheet
Lysine[c]	α-Helix	β-Sheet	Hydrophilic side chain Salts, HPO_4 are β-sheet, Also Product from high pH, high temperature is β-sheet
Histidine	α-Helix		This residue is capable of hydrogen bonding and of other interaction.
Phenylalanine	α-Helix		Hydrophobic side chain Hydrophobic interaction
Tyrosine	β-Sheet		Hydroxylic side chains of hydrogen bonding

(*Continued*)

Table 1. Continued

Amino acid residue	Conformation[a]		
	1	2	
Tryptophan	α-Helix		Hydrophobic side chain
Cysteine	β-Sheet		
Methionine	α-Helix		
Proline	pP-II	pP-I	Hydrophobic side chain
Arginine	α-Helix		Hydrophilic side chain

[a] All β-sheet form are antiparallel.

[b] Polyaspartic acid and polyglutamic acid in the solid state are in the neutral carboxyl form. The conformational influence in solution at neutral pH where the side chain is ionized is one of α-helix disruption.

[c] Polylysine in the solid state is normally in the form of the HBr salt. The charged residue in solution at neutral pH would have an α-helix disruptive influence.
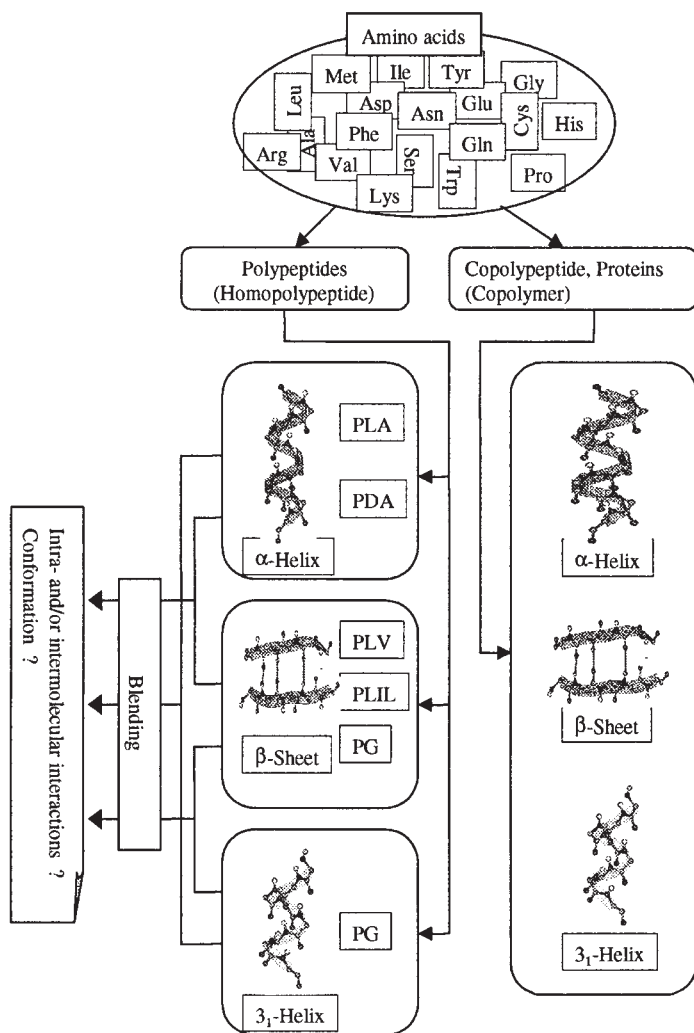
Fig. 1. A scheme of conformational generation of polypeptides, copolypeptides and proteins.

that the ^{13}C NMR chemical shifts of a number of polypeptides and proteins in the solid state, as determined by the CP/MAS method, are significantly displaced, depending on their particular conformations such as α-helix, 3_1-helix or β-sheet.[17–31]

However, relaxation times can be used as well as the chemical shifts to provide information on the dynamics. Especially, the spin-lattice relaxation time in the rotating frame of ^{1}H (^{1}H $T_{1\rho}$) is very sensitive to the

domain size of individual polymers in polymer blends through the spin diffusion process and thus can be used to study the miscibility of polymer blends. Since the efficiency of spin diffusion is governed by dipole–dipole interactions, knowledge of the rate of spin diffusion among proton spins of individual polymers in polymer blends would provide useful information about domain sizes in the region of 1.7–5.5 nm.[32–54] Recently, the two-dimensional (2D) ^{13}C–^{1}H heteronuclear correlations (HETCOR) NMR method by using the frequency-switched Lee–Goldberg (FSLG) ^{1}H decoupling sequence[55] at high MAS rates has been developed, in order to provide intermolecular and spatial distance information. The HETCOR spectrum often has multiple proton cross peaks for each carbon, and these cross peaks can be extremely helpful for assigning the spectrum. Thus, this method can also be used to characterize the structure of polymers in solids.[56–71]

From such a background, some kinds of polypeptide blend samples have been studied by solid state NMR.[27,72–74] Especially, detailed information for four kinds of blend samples such as poly(L-alanine) (PLA)/poly(L-valine) (PLV), PLA/poly(L-isoleucine) (PLIL), poly(D-alanine) (PDA)/PLV and polyglycine (PG)/PLV blends, have been reported. Here, let us describe some reasons why PLA/PLV, PDA/PLV, PLA/PLIL and PG/PLV blends are interesting systems. PLA and PDA in the solid-state can take the α-helix and β-sheet forms due to intra- and intermolecular HBs, respectively. PG in the solid-state can take the 3_1-helix (PG-II) and β-sheet (PG-I) forms due to intra- and intermolecular HBs, respectively. However, PLIL and PLV in the solid state can predominantly take the β-sheet form as the stable conformation. For this reason, it is interesting to know whether an isolated α-helix or 3_1-helix form polypeptide surrounded by a major polypeptide in the β-sheet form can take the helical conformation, or not, due to the balance between intramolecular and intermolecular hydrogen bonds. In addition, we would like to know whether a polypeptide in the β-sheet form surrounded by a major polypeptide in the α-helix or 3_1-helix form can take the β-sheet form.

By using their blended systems, such a conformational change may provide some useful knowledge about the conformational stability due to the balance of intermolecular HB interactions between helical form polypeptides and sheet form polypeptides, and also due to the balance of intra- and intermolecular HB interactions. The balance of intra- and intermolecular HB interactions would also play an important role for the conformational stability.

Some kinds of polypeptide blend samples (PLA/PLV, PLA/PLIL, PG/PLV and PDA/PLV) have been treated with different blend conditions, and their miscibility has been investigated by the observation of ^{13}C NMR chemical shifts and ^{1}H T_1 data.[17–27] Furthermore, we need more detailed information about the miscibility of the polypeptides to understand the polypeptide blend by using further sophisticated NMR methodology. Thus, 2D FSLG ^{13}C–^{1}H HETCOR NMR is useful to elucidate intermolecular HB interactions between two kinds of polypeptide chains and their miscibility.

In this review, therefore, we describe mainly our work on the study of the conformational stability and miscibility of some kinds of polypeptide blend samples obtained by ^{13}C CP/MAS NMR, ^{1}H $T_{1\rho}$ and 2D FSLG ^{13}C–^{1}H HETCOR NMR experiments.

2. POLYPEPTIDE BLEND PREPARATIONS

Poly (L-alanine) (molecular weight (Mw): 23,600) in the right-handed α-helix (α(α_R)-helix) form, poly (D-alanine) (Mw: 3000) in the left-handed α-helix (α(α_L)-helix) form, poly (L-valine) (Mw: 1700 ∼ 1900) in the β-sheet form, poly (L-isoleucine) (Mw: 8500) in the β-sheet form and polyglycine (Mw: 1000) in the β-sheet form (PG-I) are employed. Polyglycine in the 3_1-helix (PG-II) form is obtained by precipitation from an aqueous lithium bromide (LiBr) solution of PG in the β-sheet (PG-I) form.[8–11] Poly (L-alanine) with molecular weight of 1000 ∼ 5000 is a mixture of the β-sheet and α-helix forms because PLA with low molecular weight component and high molecular weight component takes the β-sheet form and α-helix form, respectively.[17] The conformations of these polypeptides are recognized by ^{13}C CP/MAS NMR.[11,17–31] The preferred conformations of these homopolypeptides are shown in Table 2.

It is well known that a synthetic polypeptide can be dissolved in a solvent such as chloroform in which the α-helical conformation and its behaviour may be examined upon the addition of a strong hydrogen bonding solvent (random coil solvent) such as dichloroacetic acid (DCA) and/or trifluoroacetic acid (TFA).[75–77] Further, Saito *et al.* have reported that poly (L-isoleucine) and poly (L-leucine) can be changed to a random coil structure in TFA solution with a few drops of concentrated sulphuric acid (H_2SO_4).[17] From these results, the relative strength of hydrogen bonding is as follows: DCA < DCA/TFA mixture < TFA < TFA with a few drops of conc. H_2SO_4. In order to obtain the blend homopolypeptides, it may be a most important point whether homopolypeptide dissolved in a random coil solvent takes the random coiled structure or not. In this review, four kinds of random coiled solvents have been shown (*Methods* 1–4).

On the other hand, the 'deposition' process is also important to prepare blend samples. A mixture of homopolypeptide solutions in which they take a random coiled structure are added into a poor solvent. For polypeptides, water is a poor solvent in general. If the hydration rate is different for each polypeptides, they form their preferred secondary structures by themselves and then do not blend with each other. On the basis of this assumption, in order to make the hydration at the same time, the solution is added to alkaline water. In this review, two kinds of quieting solvents such as water and alkaline water have been used. (*Methods* 1–4 and *Method* 5). *Method* 1: Helical polypeptide and β-sheet polypeptide are dissolved in DCA and agitated

Table 2. Preferred conformations of homopolypeptides used in this review

Polypeptides		Molecular weight	Conformation
 Polyglycine (PG)		1000 DP(VIS)18	3_1-Helix
Poly(L-alanine) PLA		23,600 DP(VIS)333	α_R-Helix
Poly(D-alanine) PDA		3000 DIP(VIS)42	α_L-Helix
Poly(L-valine) PLV		1700~1900 DP(VIS)18	β-Sheet
Poly(L-isoleucine) PLIL		8500 DP(VIS)75	β-Sheet

at room temperature. *Method* 2: The helical polypeptide and β-sheet polypeptide with a mixture ratio of 50/50 (wt/wt%) are dissolved in a mixture of DCA and TFA with a ratio of 1:1. solution. The solution is added to water at room temperature and the precipitated mixture sample is washed by water and dried under vacuum at temperatures from 308 to 318 K. *Method* 3: The helical polypeptide and β-sheet polypeptide with a mixture ratio of 50/50 (wt/wt%) are dissolved in TFA. The solution is added to water at room temperature and the precipitated mixture sample is washed by water and dried under vacuum at temperatures from 308 to 318 K, respectively. *Method* 4: Helical polypeptide and β-sheet polypeptide are dissolved in TFA with a 2.0 wt/wt% amount of H_2SO_4. Next, a mixture of helical polypeptide and β-sheet polypeptide with various ratios of 80/20, 50/50 and 20/80 (wt/wt%) are dissolved in TFA with a 2.0 wt/wt% amount of H_2SO_4. The solution is added to water at room temperature and then the precipitated mixture sample is washed with water and dried under vacuum at temperatures from 308 to 318 K. *Method* 5: Helical polypeptide and β-sheet polypeptide are dissolved in TFA with a 2.0 wt/wt% amount of H_2SO_4. Next, a mixture
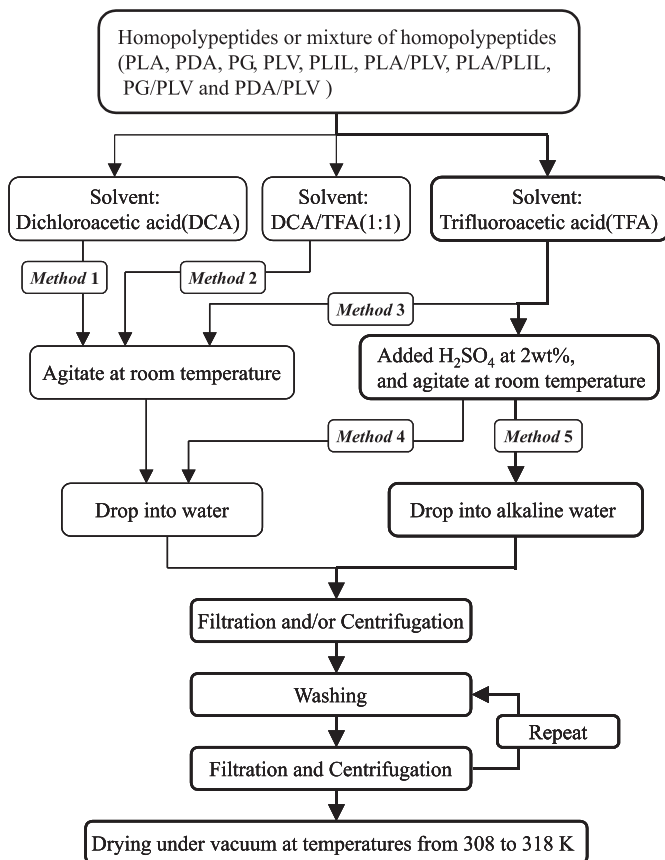
Fig. 2. Sample preparation pathway for obtaining polypeptide blends.

of helical polypeptide and β-sheet polypeptide with various ratios of 80/20, 50/50 and 20/80 (wt/wt%) are dissolved in TFA with a 2.0 wt/wt% amount of H_2SO_4. The solution is added to alkaline water at room temperature and then the precipitated mixture sample is washed by water and dried under vacuum at temperatures from 308 to 318 K, respectively. These sample preparation pathways are summarized in Fig. 2.

3. ^{13}C CP/MAS NMR SPECTRAL ANALYSIS AND CONFORMATIONAL CHARACTERIZATION OF HOMOPOLYPEPTIDES AND THEIR BLENDS

In order to understand the conformations or conformational changes of homopolypeptides and copolypeptides, solid-state ^{13}C NMR is a very useful

method. NMR experiments for obtaining high-resolution spectra of solids are carried out with a combination of the high-speed magic angle spinning (MAS) method[12] and cross polarization (CP).[13] The CP/MAS technique has been conventionally used to obtain high-resolution solid state NMR spectra.[15,16] In solids, the NMR chemical shift is often characteristic of a specified conformation because of the highly restricted molecular motion.

As an NMR methodology for elucidating conformational stability in the polypeptide blends, the conformation-dependent ^{13}C NMR chemical shift for polypeptides in the solid state has been reported.[27,72,73] It has been elucidated that the ^{13}C NMR chemical shifts of a number of polypeptides in the solid state, as determined by the ^{13}C CP/MAS method, are significantly displaced, depending on their particular conformations such as α-helix, 3_1-helix or β-sheet form.[11,17–31]

3.1. PLA/PLV blends

In order to elucidate the conformational characterization of PLA/PLV blend samples obtained by using the four methods as mentioned above, solid-state ^{13}C NMR measurements are made on the blend samples.

The observed ^{13}C CP/MAS NMR spectra of pure PLA and pure PLV are shown in Fig. 3 (a) and (d), respectively. The assignments of these spectra are straightforwardly made by using reference data of polypeptides with the α-helix and β-sheet forms reported previously.[21,22,26] The ^{13}C chemical shift values of these polypeptide samples are listed together with reference data of PLA and PLV with the right-handed α-helix form and the β-sheet form in Table 3. The three intense peaks at 177.0, 53.2, and 15.8 ppm which appear in the spectrum of pure PLA (Fig. 3 (a)) can be assigned to the C=O, Cα and Cβ carbons, respectively. From these ^{13}C chemical shift values, it is found that PLA takes the right-handed α-helix form. There are no peaks which come from the β-sheet form. On the other hand, in the spectrum of PLV (Fig. 3 (d)), the four intense peaks appear at 172.4, 58.9, 33.2 and 19.2 ppm and can be assigned to the C=O, Cα, Cβ and Cγ carbon, respectively. From these ^{13}C chemical shift values, it is found that PLV takes the β-sheet form. There are no peaks which come from the α-helix.

Next, the observed ^{13}C CP/MAS NMR spectra for the PLA/PLV (50/50) blend samples obtained by *Methods* 2 and 3, are shown in Fig. 3 (b) and (c), respectively. From these ^{13}C chemical shift values, the seven most intense peaks appear at about 177, 172, 59, 53, 33, 19 and 16 ppm and can be assigned to the PLA in the C=O (177), Cα (53) and Cβ (16) carbon, respectively, and PLV in the C=O (172), Cα (59), Cβ (33) and Cγ (19) carbon, respectively. From the above results, it is possible to realize that a mixture of PLA and PLV obtained by *Methods* 2 and 3 are not miscible.
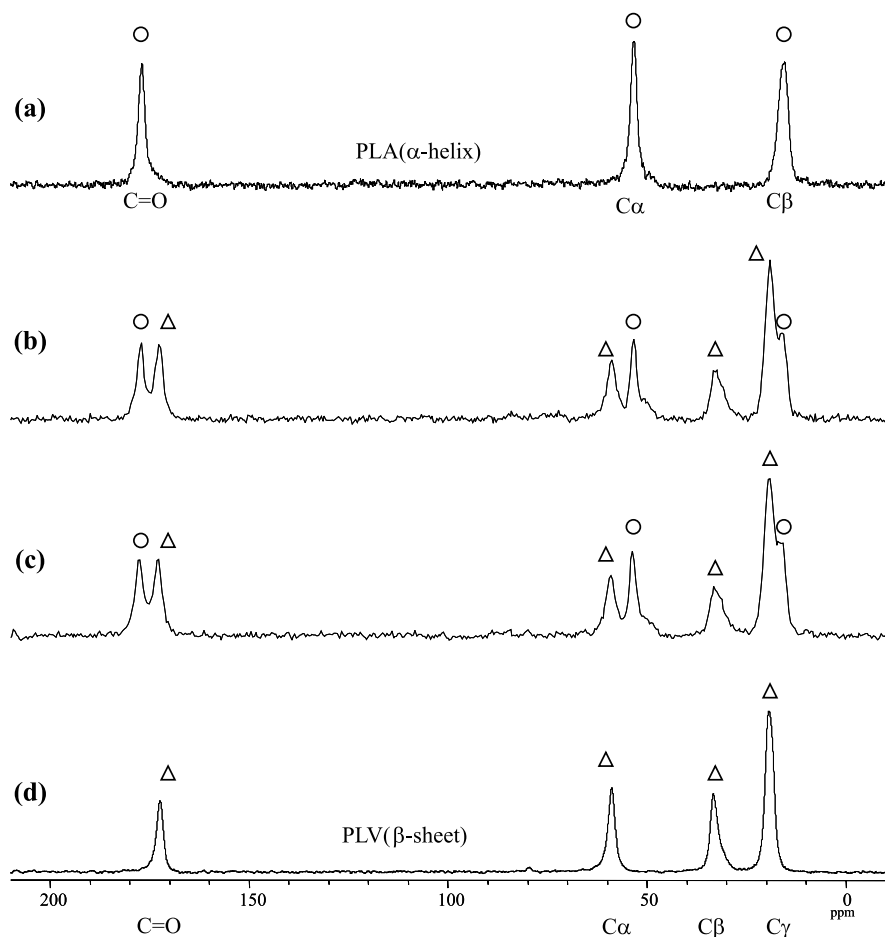
Fig. 3. ^{13}C CP/MAS NMR spectra of PLA ($\bigcirc$), PLV ($\triangle$) and PLA/PLV mixture samples. (a) pure PLA (α-helix), (b) prepared by adding mixture of PLA/PLV (50/50) DCA/TFA (1:1) solution to water (*Method* 2), (c) prepared by adding mixture of PLA/PLV (50/50) TFA solution to water (*Method* 3), and (d) pure PLV (β-sheet).

Furthermore, the observed ^{13}C CP/MAS NMR spectra of PLA, PLV and PLA/PLV blend samples obtained by *Method* 4, with various mixture ratios, are shown in Fig. 4. The assignments of these spectra are made using reference data reported previously.[21,22,26] The ^{13}C chemical shift values of these polypeptide samples are listed together with reference data in Table 4. In the spectrum of PLA (Fig. 4a) we can assign peaks to the C=O, Cα and Cβ carbons, respectively. From the ^{13}C chemical shift values, it is found that PLA takes the right-handed α-helix form. On the other hand, in the spectrum of PLV (Fig. 4e) we can assign peaks to the C=O, Cα, Cβ and Cγ carbons,

Table 3. Observed solid-state ^{13}C chemical shifts of pure PLA, pure PLV and PLA/PLV blend samples obtained by *Methods* 2 and 3

Polypeptide sample	^{13}C Chemical shift (ppm)				Conformation
	C=O	Cα	Cβ	Cγ	
PLA	176.7	53.2	16.0		α-Helix[a]
	172.5	49.5	20.7		β-Sheet[a]
PLV	174.9	65.5	28.7	20.9/19.0	α-Helix[a]
	172.3	58.6	32.9	19.0	β-Sheet[a]
Pure PLA	177.0	53.2	15.8		PLA α-helix
PLA/PLV[b] (50/50)	177.0	53.2	15.8		PLA α-helix
	172.3	58.6	33.2	19.0	PLV β-Sheet
PLA/PLV[c] (50/50)	176.9	53.2	15.9		PLA α-helix
	172.2	58.5	32.8	18.9	PLV β-Sheet
Pure PLV	172.4	58.9	33.2	19.2	PLV β-Sheet

[a] Refs. 21, 22, 26.
[b] PLA/PLV (50/50) blend sample obtained by *Method* 2.
[c] PLA/PLV (50/50) blend sample obtained by *Method* 3.

respectively. From these ^{13}C chemical shift values, it is found that PLV takes the β-sheet form. Next, the observed ^{13}C CP/MAS NMR spectra of PLA/PLV blend samples, with various mixture ratios (20/80, 50/50 and 80/20 wt/wt%), are shown in Figs. 4 (b)–(d). From these spectra, it can be recognized that there is no new conformation. This means that PLA and PLV are not miscible.

On the other hand, the observed ^{13}C CP/MAS NMR spectra of PLA, PLV, and the PLA/PLV blend samples with mixture ratios of 80/20, 50/50 and 20/80 (wt/wt%) obtained by *Method* 5, are shown in Fig. 5. In these spectra, homopolypeptides of PLA (α-helix) and PLV (β-sheet) are treated using the same conditions as the mixture of the PLA/PLV blend samples. The assignments of these spectra are straightforwardly made by using reference data of polypeptides with the α-helix and β-sheet forms reported previously.[21,22,26] The ^{13}C chemical shift values of these polypeptide samples are listed together with reference data of PLA and PLV with the right-handed α-helix form and the β-sheet form in Table 5. The three intense peaks at 176.7, 53.2, and 16.0 ppm which appear in the spectra of PLA (Fig. 5 (a)) can be assigned to the C=O, Cα and Cβ carbons, respectively. From these ^{13}C chemical shift values, it is found that the PLA used in this work takes the right-handed α-helix form. There are no peaks which come from the β-sheet form. On the other hand, in the spectrum of PLV (Fig. 5 (e)), the four intense peaks appear at 172.3, 58.6, 32.9 and 19.0 ppm and can be assigned to the C=O, Cα, Cβ and Cγ carbon, respectively. From these ^{13}C chemical shift values, it is found that PLV takes the β-sheet form. There are no peaks which come from the α-helix.
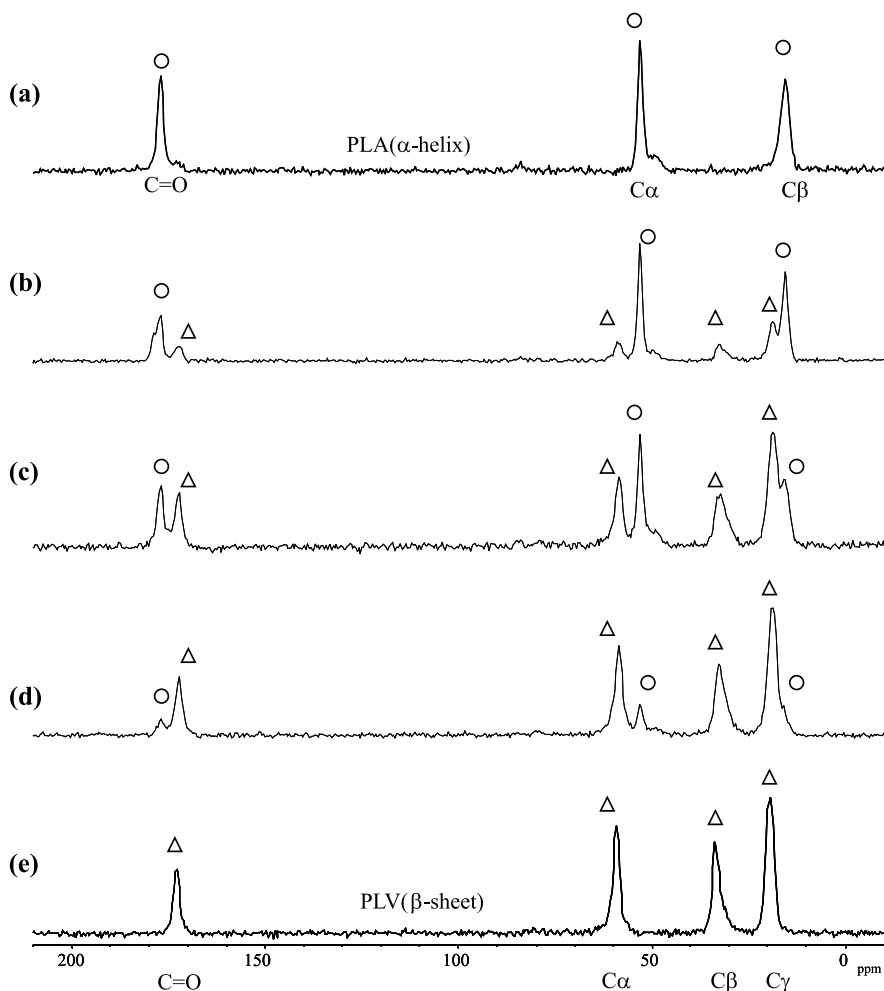
Fig. 4. ^{13}C CP/MAS NMR spectra of PLA (○), PLV (△) and PLA/PLV blend samples which were prepared by adding their TFA solutions with 2.0 wt/wt% amount of H_2SO_4 to water (*Method* 4). Homopolpeptides of PLA (α-helix) and PLV (β-sheet) are prepared using same condition as PLA/PLV (80/20, 50/50, 20/80) blend samples. (a) PLA, (b) PLA/PLV (80/20), (c) PLA/PLV (50/50), (d) PLA/PLV (20/80) and (e) PLV.

Next, the observed ^{13}C CP/MAS NMR spectra for the PLA/PLV blend samples with various ratios of 80/20, 50/50, and 20/80 (wt/wt%) obtained by *Method* 5 are shown in Fig. 5 (b)–(d), respectively. In these ^{13}C CP/MAS spectra a new peak for the Cα carbon of PLA appears clearly at 49.1–49.6 ppm. This peak can be assigned to the Cα carbon of PLA with the β-sheet form by using the reference data as shown in Table 5.

Table 4.   Observed solid-state ^{13}C chemical shifts of PLA, PLV and PLA/PLV blend samples obtained by *Method* 4

Polypeptide sample	^{13}C Chemical shift (ppm)				Conformation
	C = O	Cα	Cβ	Cγ	
PLA	176.7	53.2	16.0		α-Helix[a]
	172.5	49.5	20.7		β-Sheet[a]
PLV	174.9	65.5	28.7	20.9/19.0	α-Helix[a]
	172.3	58.6	32.9	19.0	β-Sheet[a]
PLA[b]	176.8	53.2	15.8		PLA α-helix
PLA/PLV (80/20)	176.9	53.1	15.6		PLA α-helix
	172.2	58.9	32.7	18.9	PLV β-Sheet
PLA/PLV (50/50)	176.8	53.2	15.7		PLA α-helix
	172.0	58.6	32.4	18.9	PLV β-Sheet
PLA/PLV (20/80)	176.7	53.1	16.0		PLA α-helix
	172.1	58.7	32.8	19.0	PLV β-Sheet
PLV[b]	172.0	58.6	32.8	19.0	PLV β-Sheet

[a] Refs. 21, 22, 26.
[b] Homopolypeptides of PLA (α-helix) and PLV (β-sheet) are prepared using same condition as PLA/PLV (20/80, 50/50, 80/20) blend samples.

In order to clarify in detail the appearance of this new peak, the carbonyl carbon region and the Cα, Cβ and Cγ carbon region in the spectrum of the PLA/PLV blend, with a mixture ratio of 50/50, were expanded as shown in Fig. 6. By computer-fitting the observed spectrum was decomposed to a sum of Lorentzian lines, and then the components of the α-helix and β-sheet forms for PLA and PLV were determined.

If we look at the spectra carefully, another new peak of the Cβ carbon of PLA appears at about 21.1 ppm, in addition to an intense peak assigned to the α-helix form (16.0 ppm), and can be assigned to the β-sheet form (21.1 ppm) by using reference data. These results show that the α-helix form of PLA in the PLA/PLV blend samples are partially transformed to the β-sheet form.

It is very significant to state that if only PLA is treated by TFA–alkaline water (*Method* 5), then PLA does not change its conformation. Nevertheless, when PLA/PLV blend samples prepared by the same treatment are used then, the β-sheet form is formed. The origin of the formation of the β-sheet form in PLA comes from the existence of PLV. Therefore, it can be said that the β-sheet form of PLA in the PLA/PLV blends is incorporated into the PLV with the β-sheet form and then takes the β-sheet form by forming intermolecular interactions with PLV. Another component of PLA remains in the α-helix form, and the β-sheet form of the PLA chains intermolecular interactions with PLV chains is much more stable than the α-helix form of the PLA chains themselves. Thus, the generation of same conformations of PLA in PLA/PLV blends may be closely associated with
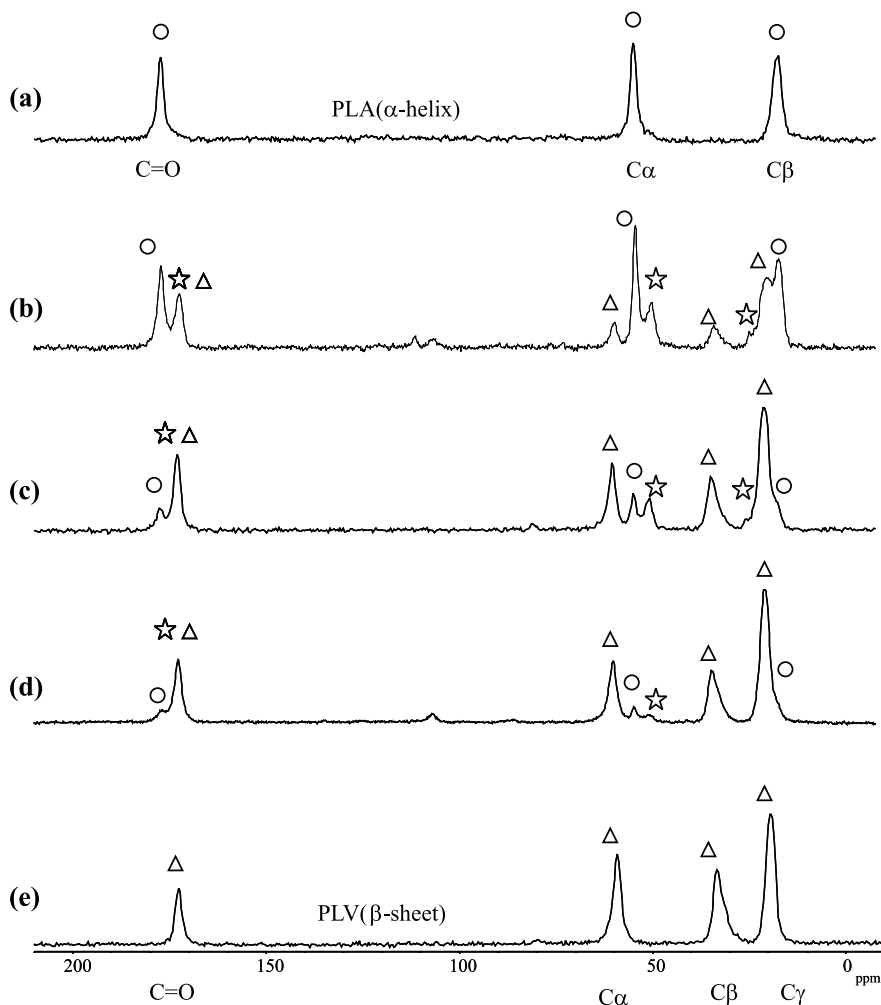
Fig. 5. ^{13}C CP/MAS NMR spectra of PLA (○), PLV (△) and PLA/PLV blend samples which were prepared by adding their TFA solutions with a 2.0 wt/wt% amount of H_2SO_4 to alkaline water (*Method* 5). Homopolypeptides of PLA (α-helix) and PLV (β-sheet) are prepared using same condition as PLA/PLV (80/20, 50/50, 20/80) blend samples. The symbols of star(☆) show the new signals that were produced by this blend condition. (a) PLA, (b) PLA/PLV (80/20), (c) PLA/PLV (50/50), (d) PLA/PLV (20/80) and (e) PLV.

changes in the strength of intermolecular interactions between polypeptides, which comes from rapid environmental changes which occur by adding the TFA solution of PLA/PLV blends with a 2.0 wt/wt% of H_2SO_4 to alkaline water. These results are similar to those as reported previously[78] where the

Table 5. Observed solid-state ^{13}C chemical shifts of PLA, PLV and PLA/PLV blend samples obtained by *Method* 5

| Polypeptide sample	^{13}C Chemical shift (ppm)				Conformation
	C＝O	Cα	Cβ	Cγ	
PLA	176.7	53.2	16.0		α-Helix[a]
	172.5	49.5	20.7		β-Sheet[a]
PLV	174.9	65.5	28.7	20.9/19.0	α-Helix[a]
	172.3	58.6	32.9	19.0	β-Sheet[a]
PLA[b]	176.9	53.2	15.5		PLA α-helix
PLA/PLV	176.8	53.2	16.2		PLA α-helix
(80/20)	172.2	49.1	20.0		PLA β-Sheet
	c	58.6	33.0	18.6	PLV β-Sheet
PLA/PLV	176.7	53.2	16.0		PLA α-helix
(50/50)	c	49.2	21.1		PLA β-Sheet
	172.2	58.6	33.0	19.2	PLV β-Sheet
PLA/PLV	176.9	53.2	16.2		PLA α-helix
(20/80)	c	49.6	21.0		PLA β-Sheet
	172.2	58.7	33.0	19.1	PLV β-Sheet
PLV[b]	172.0	58.6	32.8	19.0	PLV β-Sheet

[a] Refs. 21, 22, 26.
[b] Homopolypeptides of PLA (α-helix) and PLV (β-sheet) are prepared using same condition as PLA/PLV (20/80, 50/50, 80/20) blend samples.
[c] Not determined because of the overlap of the minor peak with the major peak.

conformation of the minor L-alanine residue component in the major β-benzyl L-aspartate residue component in the copolypeptides depends on the conformation of the major β-benzyl L-aspartate residue component. When the L-alanine residues are hydrogen-bonded with the β-benzyl L-aspartate residues with the β-sheet form, the L-alanine residues are incorporated into the β-sheet form.

3.2. PLA/PLIL blends

The observed ^{13}C CP/MAS NMR spectra of PLA, PLIL and the PLA/PLIL (20/80, 50/50 and 80/20 wt/wt%) blend samples, prepared by adding a TFA solution with a 2.0 wt/wt% amount of H$_2$SO$_4$ to alkaline water (*Method* 5), are shown in Fig. 7. In the spectra, homopolypeptides of PLA (α-helix) and PLIL (β-sheet) are treated using the same condition as for the mixture of PLA/PLIL blend samples. The assignments of these spectra are made by the above mentioned method. The ^{13}C chemical shift values of these poly-peptide samples are listed together with the reference data of PLA in the right-handed α-helix form and the β-sheet form, and PLIL in the β-sheet form in Table 6.[21,22,26] The reference ^{13}C chemical shift data were used
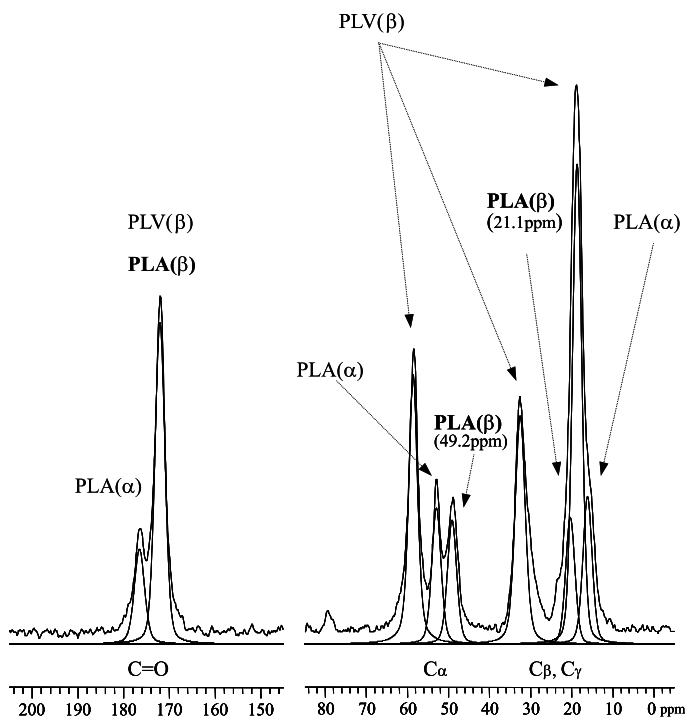
Fig. 6. Expanded ^{13}C CP/MAS NMR spectra for the carbonyl-carbon region and for the Cα, Cβ and Cγ carbons region of PLA/PLV (50/50) blend sample.

for conformational characterization as shown below. The three intense peaks at 176.9, 53.3 and 15.5 ppm which appear in the spectrum of PLA (Fig. 7a) can be assigned to the C=O, Cα and Cβ carbons, respectively. From these ^{13}C chemical shift values, it is found that the PLA used in this work takes the α-helix form. There are no peaks which come from the β-sheet form. On the other hand, in the spectrum of PLIL (Fig. 7e), the six intense peaks appear at 172.0, 58.1, 39.6, 25.9/15.0 and 12.3 ppm and can be assigned to the C=O, Cα, Cβ, Cγ/Cγ and Cδ carbons, respectively. From these ^{13}C chemical shift values, it is found that PLIL takes the β-sheet form.

The observed ^{13}C CP/MAS NMR spectra for PLA/PLIL blend samples with a mixture ratio of 80/20, 50/50 and 20/80 (wt/wt%) are shown in Fig. 7 (b)–(d). In the ^{13}C CP/MAS spectra, there is a new peak for the Cα carbon of PLA which appear clearly at 48.9–49.2 ppm. This peak can be assigned to the Cα carbon of PLA in the β-sheet form. In order to clarify in detail the appearance of this new peak, the C=O carbon region and the Cα, Cβ, Cγ and Cδ regions in the spectrum of the PLA/PLIL blend with a mixture ratio of 50/50 (wt/wt%), were expanded as shown in Fig. 8.
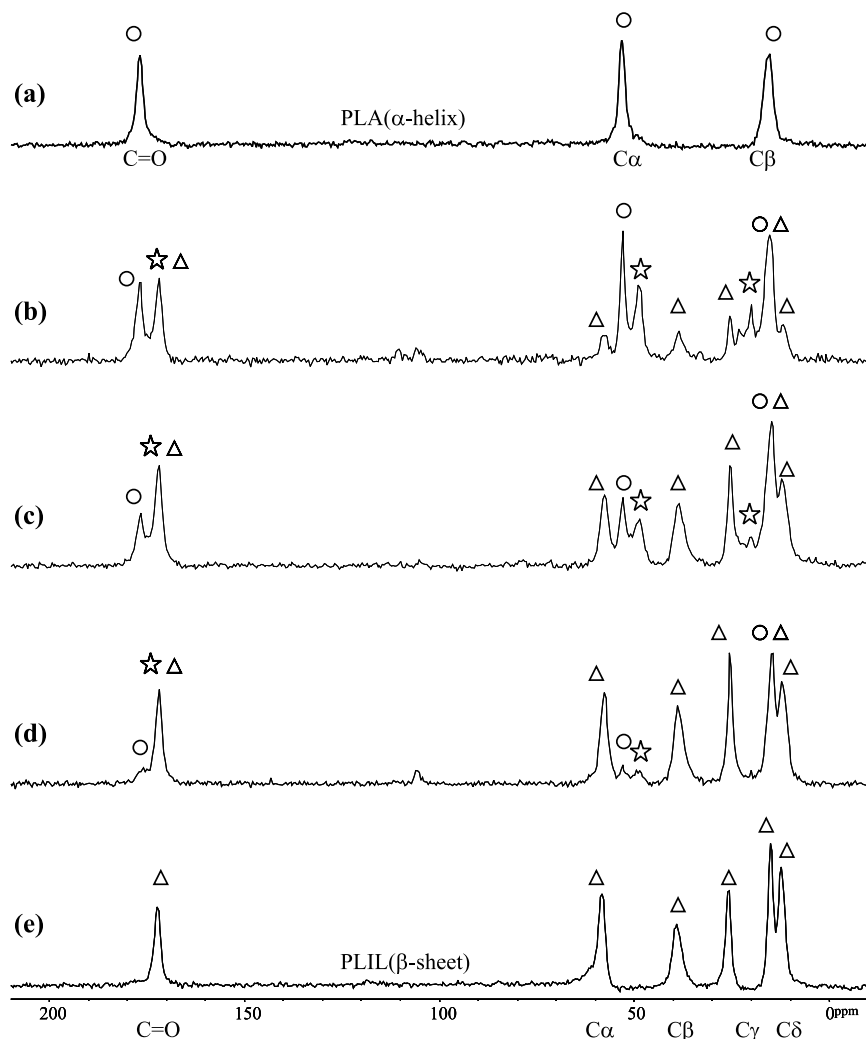
Fig. 7. ^{13}C CP/MAS NMR spectra of PLA (○), PLIL (△) and PLA/PLIL blend samples which were prepared by adding their TFA solutions with a 2.0 wt/wt% amount of H$_2$SO$_4$ to alkaline water (*Method* 5). Homopolypeptides of PLA (α-helix) and PLIL (β-sheet) are prepared using same condition as PLA/PLIL (80/20, 50/50, 20/80) blend samples. The symbols of star (☆) show the new signals that were produced by this blend condition. (a) PLA, (b) PLA/PLIL (80/20), (c) PLA/PLIL (50/50), (d) PLA/PLIL (20/80) and (e) PLIL.

By computer-fitting the observed spectrum was decomposed to a sum of Lorentzian lineshapes, and then the fractions of the α-helix and β-sheet forms for PLA and PLIL were determined. The PLA/PLIL blend sample with a mixture ratio of 50/50 (wt/wt%) corresponds to the molar mixture ratio

Table 6. Observed solid-state ^{13}C chemical shifts of PLA, PLIL and PLA/PLIL blend sample obtained by *Method* 5

| Polypeptide sample	^{13}C Chemical shift (ppm)					Conformation
	C=O	Cα	Cβ	Cγ	Cδ	
PLA	176.7	53.2	16.0			α-Helix[a]
PLA	172.4	49.4	20.7			β-Sheet[a]
PLIL	172.0	58.0	38.6	25.9/15.0	12.0	β-Sheet[a]
PLA[b]	176.9	53.2	15.5			PLA α-helix
PLA/PLIL	176.7	53.2	15.5			PLA α-helix
(80/20)	172.1	49.2	20.3			PLA β-Sheet
	c	58.1	38.8	25.7/c	12.2	PLIL β-Sheet
PLA/PLIL	176.7	53.2	c			PLA α-helix
(50/50)	c	49.1	20.5			PLA β-Sheet
	172.1	58.0	38.7	25.6/15.0	12.3	PLIL β-Sheet
PLA/PLIL	176.7	53.2	c			PLA α-helix
(20/80)	c	48.9	20.3			PLA β-Sheet
	172.1	58.0	39.6	25.7/15.0	12.3	PLIL β-Sheet
PLIL[b]	172.0	58.1	39.6	25.9/15.0	12.3	PLIL β-Sheet

[a] Refs. 21, 22, 26.
[b] Homopolypeptides of PLA (α-helix) and PLIL (β-sheet) are prepared using same condition as PLA/PLIL (20/80, 50/50, 80/20) blend samples.
[c] Not determined because of the overlap of the minor peak with the major peak.

of 1.60. The determined (α-helix form + β-sheet form) peak intensity for the Cα carbons of PLA(f_{PLA}) is much larger than that for the Cα carbons of PLIL in the β-sheet form(f_{PLIL}). Then, the ratio of f_{PLA}/ f_{PLIL} is about 1.61. This is very close to a theoretical prediction of 1.60. This means that the fractions of the α-helix form and the β-sheet form can be estimated by ^{13}C CP/MAS NMR. Another new peak for the Cβ carbon of PLA appears at about 20.5 ppm, in addition to an intense peak assigned to the α-helix form (16.0 ppm), and this can be assigned to the β-sheet form (20.5 ppm). These results show that the α-helix form of PLA in PLA/PLIL blends is partially transformed to the β-sheet form.

On the other hand, the observed ^{13}C CP/MAS NMR spectra of the PLA, PLIL and PLA/PLIL (80/20, 50/50 and 20/80 wt/wt%) mixture samples are treated by adding a TFA solution with a 2.0 wt/wt% amount of H_2SO_4 to water (*Method* 4), together with those of PLA and PLIL are shown in Fig. 9. In the spectra, homopolypeptides of PLA (α-helix) and PLIL (β-sheet) are treated using the same conditions as for PLA/PLIL (80/20, 50/50 and 20/80 wt/wt%) mixture samples, respectively.

From these spectra, it can be recognized that no new conformation, such as those obtained by blending PLA and PLIL, is formed. This means that PLA and PLIL are completely separate from each other.
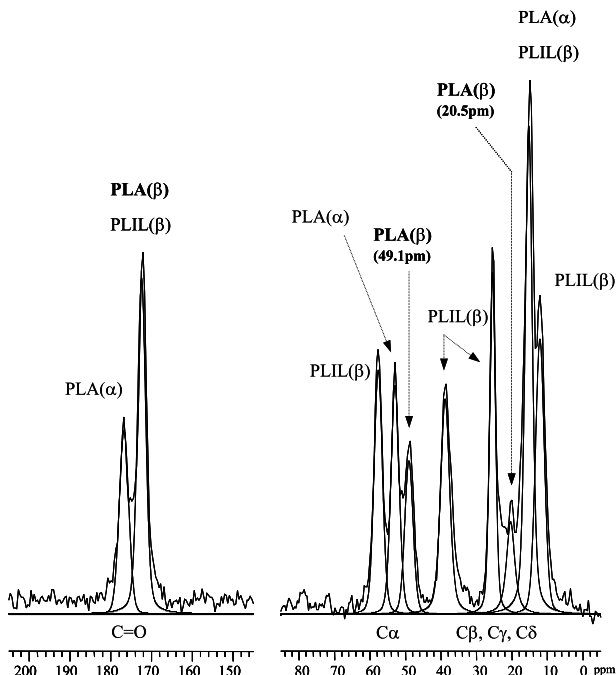
Fig. 8. Expanded ^{13}C CP/MAS NMR spectra for the carbonyl carbon region and for the Cα, Cβ, Cγ and Cδ carbons region of PLA/PLIL (50/50) blend sample.

3.3. PG/PLV blends

The observed ^{13}C CP/MAS NMR spectra of PG, PLV and the PG/PLV (20/80, 50/50 and 80/20 wt/wt%) blend samples as prepared by adding a TFA solution with a 2.0 wt/wt% amount of H_2SO_4 to alkaline water (*Method* 5) are shown in Fig. 10. In the ^{13}C CP/MAS NMR spectra, homopolypeptides of PG (3_1-helix) and PLV (β-sheet) are prepared using the same conditions as for PG/PLV blend samples. The assignments of these spectra were made by the above-mentioned method. The ^{13}C chemical shift values of these blend samples are listed together with those for PG in the 3_1-helix form (PG-II) and the β-sheet form (PG-I), and PLV in the β-sheet form in Table 7.[21,22,26] The two intense peaks at 172.9 and 42.9 ppm, which appear in the spectrum of PG (Fig. 10 a) can be assigned to the C=O and Cα carbons. From these ^{13}C chemical shift values, it is found that the PG used in this work takes the 3_1-helix form. There are no peaks which come from the β-sheet form. On the other hand, in the spectrum of PLV (Fig. 10 e), the four intense peaks appear at 172.0, 58.6, 32.8 and 19.0 ppm and can be assigned to the C=O, Cα, Cβ and Cγ carbons, respectively. From these ^{13}C chemical shift values, it is found that PLV takes the β-sheet form.

The observed ^{13}C CP/MAS NMR spectrum for the PG/PLV (50/50) blend sample is shown in Fig. 10 (c). In the ^{13}C CP/MAS spectrum, a new
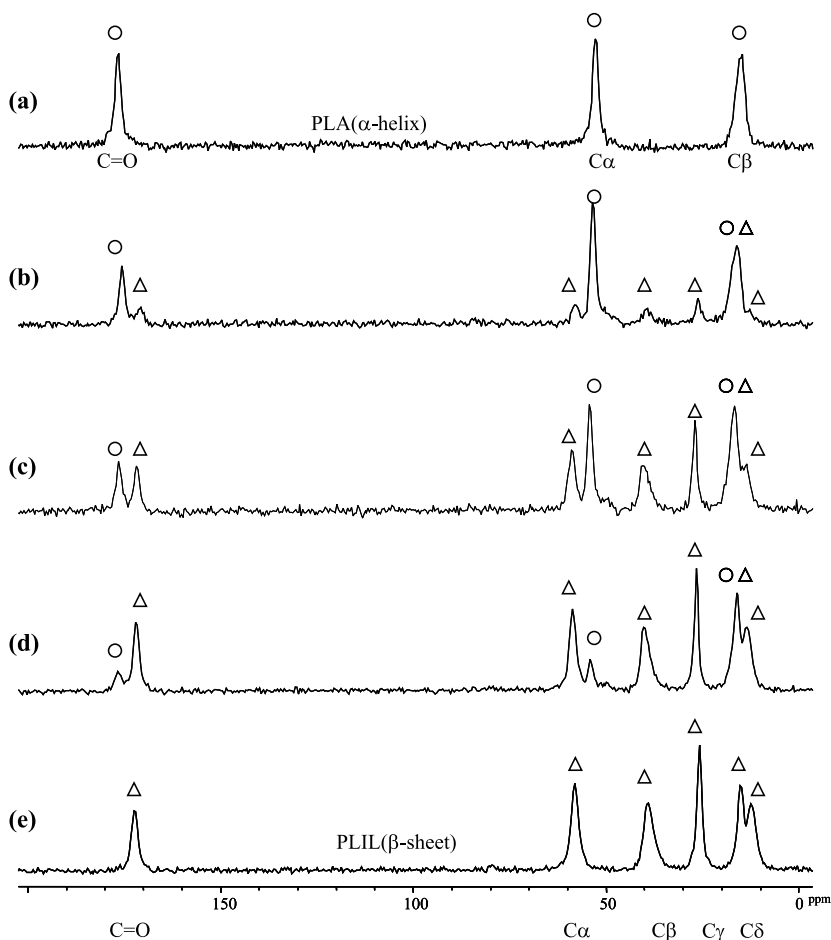
Fig. 9. ^{13}C CP/MAS NMR spectra of PLA ($\bigcirc$), PLIL ($\triangle$) and PLA/PLIL blend samples which were prepared by adding their TFA solutions with a 2.0 wt/wt% amount of H_2SO_4 to water (*Method* 4). Homopolypeptides of PLA (α-helix) and PLIL (β-sheet) are prepared using same condition as PLA/PLIL (80/20, 50/50, 20/80) blend samples. (a) PLA, (b) PLA/PLIL (80/20), (c) PLA/PLIL (50/50), (d) PLA/PLIL (20/80) and (e) PLIL.

peak for the C=O carbon appears clearly at 169.5–169.9 ppm. This peak can be assigned to the C=O carbon of PG in the β-sheet form as seen from Table 7. In order to clarify in detail the appearance of this new peak, the carbonyl-carbon region and the Cα, Cβ and Cγ carbon regions in the spectrum of the PG/PLV blend, with a mixture ratio of 50/50 (wt/wt%), were expanded as shown in Fig. 11. By computer-fitting the observed spectrum was decomposed, and then the fractions of the 3_1-helix and β-sheet forms for PG and PLV were determined.
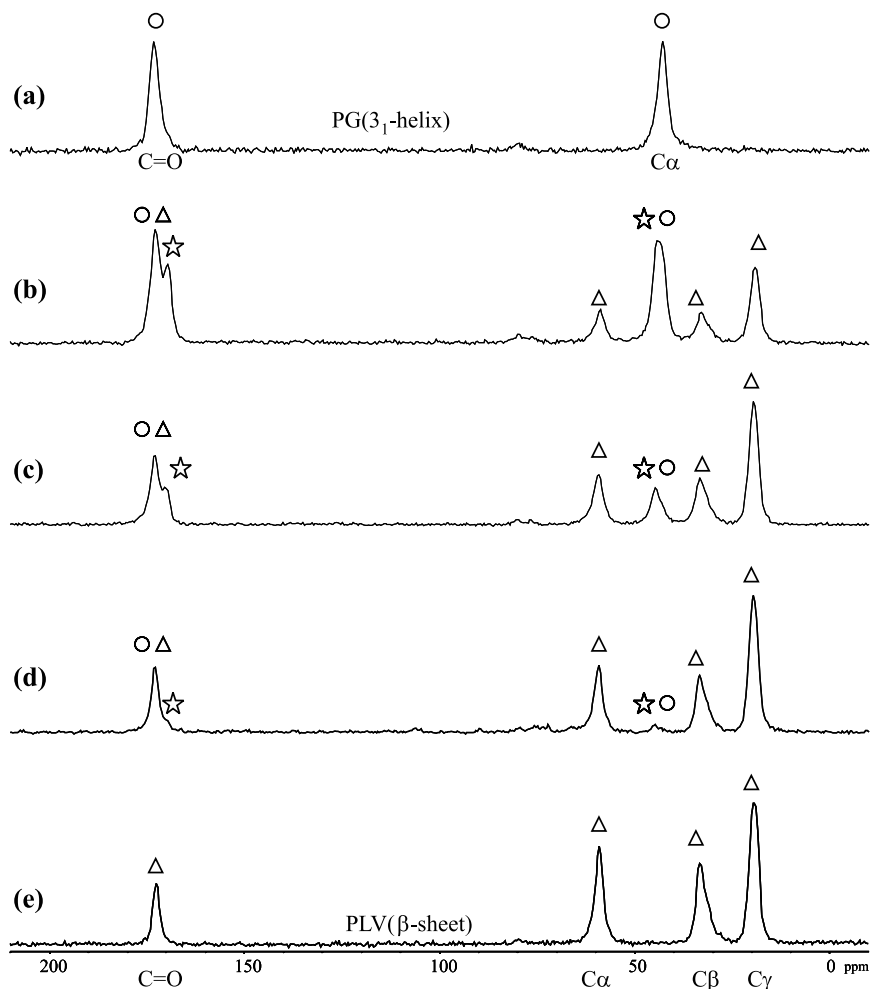
Fig. 10. ^{13}C CP/MAS NMR spectra of PG ($\bigcirc$), PLV ($\triangle$) and PG/PLV blend samples which were prepared by adding their TFA solutions with a 2.0 wt/wt% amount of H_2SO_4 to alkaline water (*Method* 5). Homopolypeptides of PG (3_1-helix) and PLV (β-sheet) are prepared using same condition as PG/PLV (80/20, 50/50, 20/80) blend samples. The symbols of star ($\star$) show the new signals that were produced by this blend condition. (a) PG, (b) PG/PLV (80/20), (c) PG/PLV (50/50), (d) PG/PLV (20/80) and (e) PLV.

Another new peak of the Cα carbon of PG appears at about 44.3 ppm in addition to a small peak assigned to the 3_1-helix form (42.6 ppm), and can be assigned to the β-sheet form (44.3 ppm). These results show that the 3_1-helix form of PG in the PG/PLV blends is almost transformed to the β-sheet form.

Table 7. Observed solid-state ^{13}C chemical shifts of PG, PLV and PG/PLV blend samples obtained by *Method* 5

Polypeptide sample	^{13}C Chemical shift (ppm)				Conformation
	C=O	Cα	Cβ	Cγ	
PG	172.9	42.6			3_1-Helix[a]
PG	169.0	44.3			β-Sheet[a]
PLV	172.3	58.6	32.9	19.0	β-Sheet[a]
PG[b]	172.9	42.9			PG 3_1-helix
PG/PLV	172.5	42.8			PG 3_1-helix
(80/20)	169.5	44.0			PG β-Sheet
	c	58.6	32.7	19.1	PLV β-Sheet
PG/PLV	*c*	42.8			PG 3_1-helix
(50/50)	169.5	44.3			PG β-Sheet
	172.2	58.9	32.9	19.0	PLV β-Sheet
PG/PLV	*c*	42.8			PG 3_1-helix
(20/80)	169.9	44.5			PG β-Sheet
	172.2	58.8	33.0	19.0	PLV β-Sheet
PLV[b]	172.0	58.6	32.8	19.0	PLV β-Sheet

[a] Refs. 21, 22, 26.
[b] Homopolypeptides of PG (3_1-helix) and PLV (β-sheet) are prepared using same condition as PG/PLV (20/80, 50/50, 80/20) blend samples.
[c] Not determined because of the overlap of the minor peak with the major peak.

3.4. PDA/PLV blends

The observed ^{13}C CP/MAS NMR spectra of PDA, PLV and the PDA/PLV (50/50 wt/wt%) blend sample are prepared by adding a TFA solution with a 2.0 wt/wt% amount of H_2SO_4 to alkaline water (*Method* 5) are shown in Fig. 12. In the spectra, homopolypeptides of PDA (α-helix) and PLV (β-sheet) are prepared using the same conditions as for PDA/PLV (50/50 wt/wt%) blend sample. The assignments of these spectra are made by the above-mentioned method. The ^{13}C chemical shift values of these polypeptide samples are listed in Table 8, together with the reference data of PDA in the α-helix form, PLA in the β-sheet form and PLV in the β-sheet form.[21,22,26] Very small β-sheet C=O and Cα peaks appear at ca. 172 and 49 ppm, respectively, as a broad shoulder of an intense α-helix peak. Therefore, it is difficult to obtain the exact chemical shift values of the PDA β-sheet form. However, the chemical shift values of the PLA β-sheet form may be the same as those of PDA. The three intense peaks at 176.6, 53.3 and 15.7 ppm which appear in the spectrum of PDA (Fig. 12 (a)) can be assigned to the C=O, Cα and Cβ carbons, respectively.

From these ^{13}C chemical shift values, it is found that the PDA used in this work takes the α-helix form. On the other hand, in the spectrum of PLV (Fig. 12 c), the four intense peaks appear at 172.2, 58.9, 32.9 and
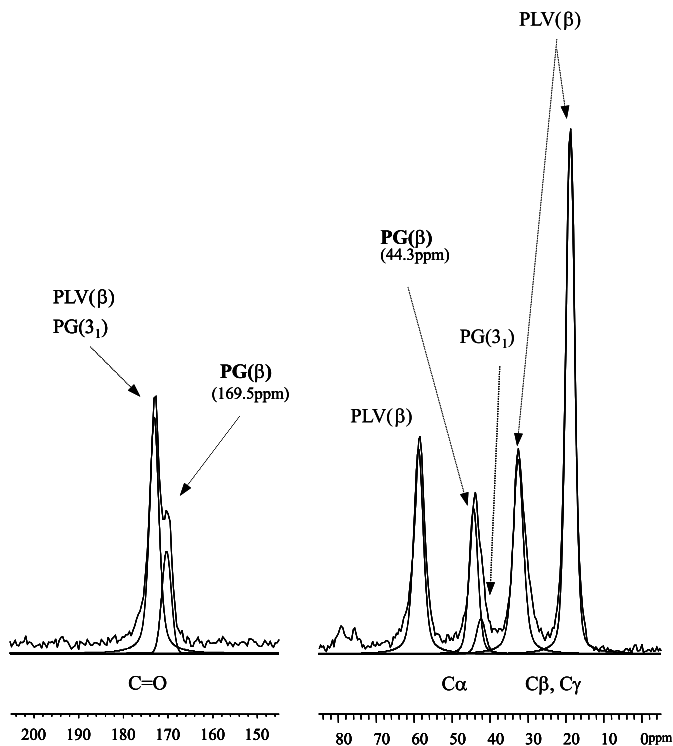
Fig. 11. Expanded ^{13}C CP/MAS NMR spectra for the carbonyl-carbon region and for the Cα, Cβ and Cγ carbons region of PG/PLV (50/50) blend sample.

19.0 ppm, and can be assigned to the C=O, Cα, Cβ and Cγ carbons, respectively. From these ^{13}C chemical shift values, it is found that PLV takes the β-sheet form.

We are concerned with the conformational characterization of a PDA/PLV blend sample. The observed ^{13}C CP/MAS NMR spectrum for the PDA/PLV (50/50) blend sample is shown in Fig. 12 (b). In the ^{13}C CP/MAS spectrum, a new peak for the Cα carbon of PDA appears clearly at 48.9 ppm. This peak can be assigned to the Cα carbon of PDA in the β-sheet form. In order to clarify in detail the appearance of this new peak, the carbonyl-carbon region and the Cα, Cβ and Cγ carbon regions in the spectrum of the PDA/PLV (50/50) blend sample were expanded as shown in Fig. 13. By computer-fitting the observed spectrum was decomposed, and then the fractions of the α-helix and β-sheet forms for PDA and PLV were determined. Another new peak of the Cβ carbon of PDA appears at about 20.9 ppm, in addition to an intense peak assigned to the α-helix form (15.7 ppm), and this can be assigned to the β-sheet form (20.9 ppm). These results show that the α-helix form of PDA in the PDA/PLV blends is partially transformed.
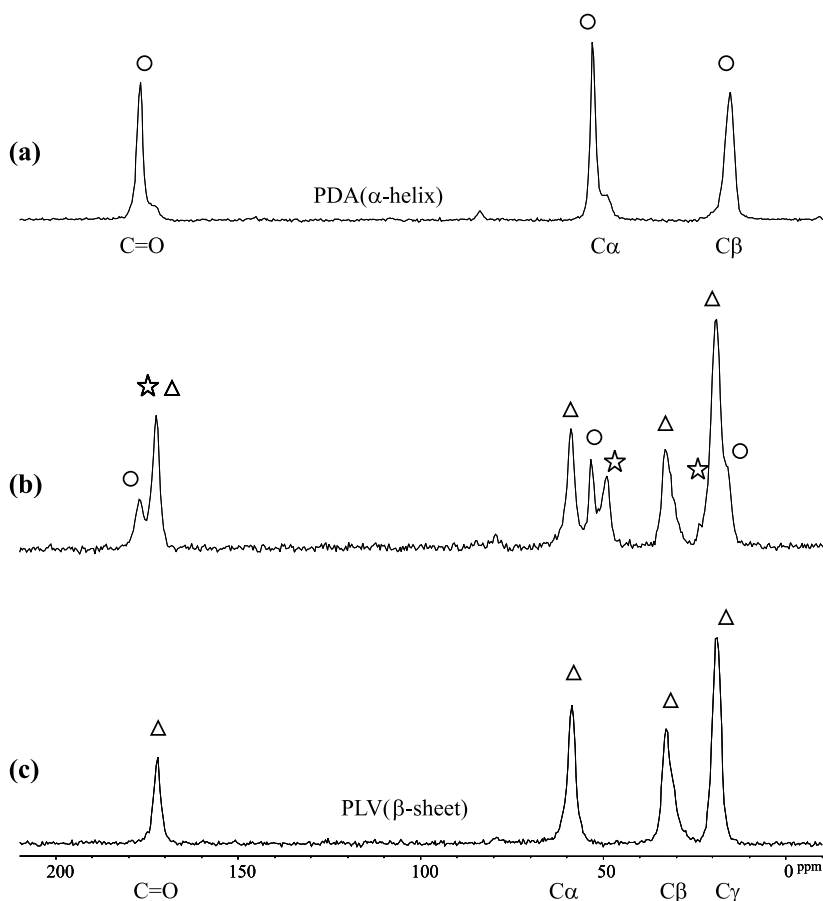
Fig. 12. ^{13}C CP/MAS NMR spectra of PDA (○), PLV (△) and PDA/PLV blend samples which were prepared by adding their TFA solutions with a 2.0 wt/wt% amount of H_2SO_4 to alkaline water (*Method* 5). Homopolypeptides of PDA (α-helix) and PLV (β-sheet) are prepared using same condition as PDA/PLV (50/50) blend samples. The symbols of star (☆) show the new signals that were produced by this blend condition. (a) PDA, (b) PDA/PLV (50/50) and (c) PLV.

From the above results, it is very significant to realize that the homopolypeptides of PLA, PDA and PG in the helix form do not form the β-sheet form used by the TFA-alkaline treatment (*Method* 5) for preparing blend samples. However the conformation of their blend samples, prepared by the TFA-alkaline treatment (*Method* 5), is changed from the α-helix or 3_1-helix form to the β-sheet form. Further, it can be said that the β-sheet form of PLA, PDA and PG in the blend polymers is incorporated into PLIL and PLV in the β-sheet form. It then takes the β-sheet form by forming hydrogen bonds with PLIL and PLV, and the other components of PLA, PDA and PG take the

Table 8. Observed solid-state ^{13}C chemical shifts of PDA, PLV and PDA/PLV blend samples obtained by *Method* 5

| Polypeptide sample	^{13}C Chemical shift (ppm)				Conformation
	C=O	Cα	Cβ	Cγ	
PDA[a]	176.8	53.1	15.7		α-Helix[b]
PLA	172.4	49.4	20.7		β-Sheet[b]
PLV	172.3	58.6	32.9	19.0	β-Sheet[b]
PDA[c]	176.6	53.3	15.7		PDA α-helix
PDA/PLV	176.8	53.1	15.9		PDA α-helix
(50/50)	d	48.9	20.9		PDA β-Sheet
	172.2	58.6	32.7	19.0	PLV β-Sheet
PLV[c]	172.2	58.9	32.9	19.0	PLV β-Sheet

[a] Very small β-sheet C=O and Cα peaks appear at ca. 172 and 49 ppm, respectively, as a broad shoulder of an intense α-helix peak. Therefore, it is difficult to obtain the exact chemical shift values of the PDA β-sheet form. As the chemical shift values of PDA β-sheet form, the chemical shift values of PLA β-sheet form are showm instead of PDA as references data.

[b] Refs. 21, 22, 26.

[c] Homopolypeptides of PDA (α-helix) and PLV (β-sheet) are prepared using same condition as PDA/PLV (50/50) blend sample.

[d] Not determined because of the overlap of the minor peak with the major peak.

helix form. Thus, we can say that the generation of the conformation of PLA, PDA and PG in PLA/PLV, PLA/PLIL, PDA/PLV and PG/PLV blends may be closely associated with changes in the strength of intermolecular interactions between the polypeptides.

Such a conclusive consideration is certainly speculative. Nevertheless, it may be acceptable because of the detailed analysis of the experimental data. When each of the PLA, PDA, PG, PLIL and PLV samples was treated under the same conditions as in the individual cases of their blends as described above, the structure of polypeptides after its treatment did not change from the original structure as seen from the ^{13}C CP/MAS NMR experiments. On the other hand, the structure of blended polypeptides after the treatment changes significantly. Therefore, it can be said that such a change comes from intermolecular interactions.

4. $^{1}HT_{1\rho}$ S OF HOMOPOLYPEPTIDES AND THEIR BLEND COMPATIBILITY

As an NMR methodology for elucidating miscibility in the PLA/PLV, PLA/PLIL, PDA/PLV and PG/PLV blends, the proton spin–lattice relaxation times in the rotating frame ($^{1}HT_{1\rho}$) for homopolypeptides and their blends in the solid state have been used. The $^{1}HT_{1\rho}$ value is very sensitive to the
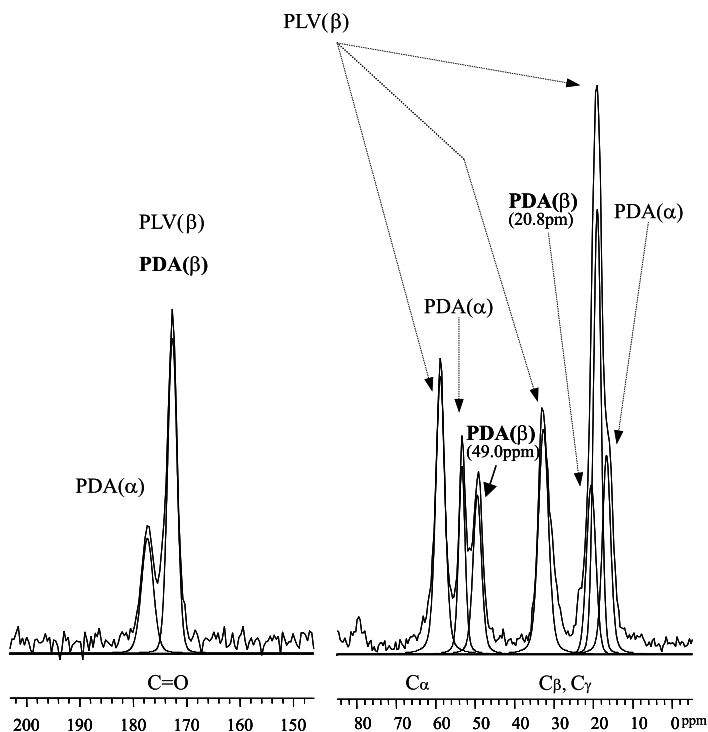
Fig. 13. Expanded ^{13}C CP/MAS NMR spectra for the carbonyl-carbon region and for the Cα, Cβ and Cγ carbons region of PDA/PLV (50/50) blend sample.

domain size of individual polymers in polymer blends through the spin diffusion process and thus can be used to study the miscibility of polymer blends as shown above. Since the efficiency of spin diffusion is governed by dipole–dipole interactions, knowledge of the rate of spin diffusion among proton spins of individual polymers in polymer blends would provide useful information about domain sizes in the region of 1.7–5.5 nm.[54,79–82]

Thus, more detailed information about the miscibility of PLA/PLV (50/50), PLA/PLIL (50/50), PG/PLV (50/50) and PDA/PLV (50/50) blend samples can be obtained by the $^1\text{H}T_{1\rho}$ experiments. The ^{13}C CP/MAS NMR spectra of PLA/PLV (50/50), PLA/PLIL (50/50), PG/PLV (50/50) and PDA/PLV (50/50) blend samples are measured as a function of ^{1}H spin-locking time, τ, at 0.01–10 ms. The intensities of the individual peaks decrease with an increase in τ. The semi-log plot of the peak intensities for the individual carbons of the blend samples, against τ, becomes a straight line, and from its slope the $^1\text{H}T_{1\rho}$ value is obtained. From the $^1\text{H}T_{1\rho}$ values, we can get information on the relationship between individual homopolypeptide chains in the polypeptide blend samples.

4.1. $^1H T_{1\rho}$ experiments on polypeptide blends

A nuclear spin system achieves thermal equilibrium by exchanging energy with its surrounding medium or the lattice which is governed by the NMR relaxation rate. The lattice consists of all degrees of freedom associated with the physical system of interest such as a polymer blend system. Experimentally there are three kinds of relaxation times such as T_1, spin–lattice or longitudinal relaxation time (ns–μs timescale), T_2, spin–spin or transverse relaxation time: (ms–s) and $T_{1\rho}$, spin–lattice relaxation time in the rotating frame (μs–ms).[83] T_1 is sensitive to molecular motion on the MHz timescale, T_2 is sensitive to the slow molecular motions and $T_{1\rho}$ is related to the spin-locking field (kHz timescale).

Since macroscopic properties of polymer blends are influenced by the degree of blending between component polymers,[84,85] it is important to know the size and morphological information of the domains in a blend. Miscibility is a term based on thermodynamics, and a miscible state means a homogeneous single phase on a molecular level. In practice, the miscibility depends on how closely we look at the blend; if the domain size is smaller than the characteristic space scale of a particular observation, the blend appears to be miscible/homogeneous. A blend which is homogeneous for a certain observation is often found to be heterogeneous by another observation with a smaller scale of observation.

In solids, the different ^1H relaxation rates of respective spins are averaged by a mechanism called spin diffusion. Spin diffusion is the equilibration process of non-equilibrium polarizations of spins at different local sites through the mutual exchange of magnetization. Since the efficiency of spin diffusion is governed by the strength of a dipole–dipole interaction, the domain size of a blend can be estimated by analyzing the spin-diffusion rates among component polymers.

A schematic illustration of how the relaxation process (T_1 or $T_{1\rho}$) for ^1H spins in a blend of polymers A and B proceeds with spin diffusion (SD) is shown in Fig. 14. Here, we assume that (1) the ^1H spins are divided into two species: species A for polymer A and species B for polymer B, and (2) both A and B are characterized by their common relaxation times T_A and T_B, respectively. Suppose T_A is much shorter than T_B, and the whole spins are inverted by a π pulse. If spin diffusion between component polymers is slow, the spin system may reach a situation where all of the ^1H spins of polymer A are fully relaxed or 'up', while those of polymer B are still 'down' (Fig. 14 (**1**)). Spin diffusion tries to average this polarization gradient created by different T values, that is, to flip down the half of the ^1H spins in polymer B (Fig. 14 (**2**)). The down spins of polymer A quickly flip up to create a polarization gradient again due to the short T of polymer A (Fig. 14 (**3**)), and again spin diffusion tries to average it, and so on. After all, both spin species eventually reach thermal equilibrium. When spin diffusion is much
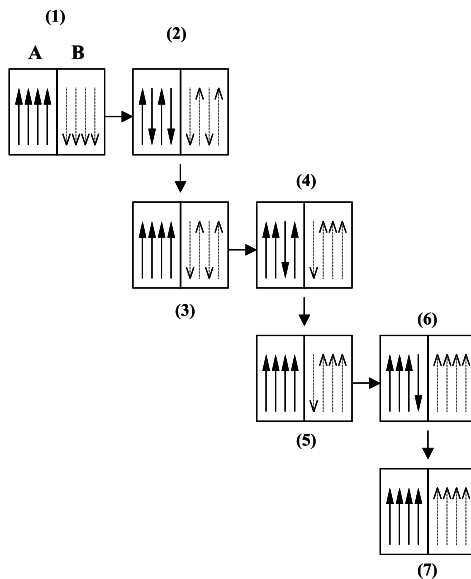
Fig. 14. A scheme of the spin–lattice relaxation process together with spin diffusion. A and B are two kind of spins in the component polymers A and B. Its assumed that T_1 of A is much shorter than that of B.

faster than the relaxation rates, any polarization gradient created is quickly averaged, and both spins relax at a common rate. However, when spin diffusion is very slow, the polarization gradient is not averaged, and both spins relax with their respective relaxation rates. Then, the question arises as to how fast should the spin diffusion be to achieve a common rate, or how slow to keep different rates?

The equations describing the dynamics of magnetization in the two-spin species may be given as follows:[32]

$$\frac{d}{dt}\begin{pmatrix} M_A \\ M_B \end{pmatrix} = \begin{pmatrix} -\xi_A & f_A K_C \\ f_B K_C & -\xi_B \end{pmatrix}\begin{pmatrix} M_A \\ M_B \end{pmatrix} \tag{1}$$

$$\xi_A = K_A + f_B K_C, \qquad \xi_B = K_B + f_A K_C, \tag{2}$$

where M_i, f_i and K_i ($i = A$ and B) denote the magnetization, proton molar fraction and the intrinsic relaxation rate, respectively. K_C is the spin-diffusion (cross-relaxation) rate between A and B.

From numerical calculations using these equations, it can be shown that when the spin-diffusion rate is at least 10 times faster than the K values, the apparent relaxation decays for both M_A and M_B become practically identical and can be expressed by a single exponential with a common relaxation rate. In this fast spin-diffusion case, the apparent relaxation rate

K_{ave} may be given as a ^{1}H mole weighted average of the intrinsic rates of component polymers as[86,87]

$$K_{ave} = f_A K_A + f_B K_B \tag{3}$$

In evaluating Equation (3), one may use the relaxation rate of the pure polymer A for K_A ($= 1/T_A$) and that of B for K_B ($= 1/T_B$), provided that blending does not alter molecular motion.

When the spin-diffusion rate is comparable to the K values, the relaxation decay curves become non-single exponential, and when the spin-diffusion rate is less than 10% of the K values, the relaxation decay curve can be described by a single exponential with an intrinsic relaxation rate.

From these semi-quantitative estimations, one can regard that, if the observed T_1 values for the component polymers are the same, the size of the domain is small enough for spin diffusion to average the polarization gradient among spins A and B created by the different intrinsic relaxation rates. Then, the question arises as to how small the size of the domains should be to realize fast spin diffusion? The maximum diffusive path length r by spin diffusion in three-dimensions for a time T may be given as[88,89]

$$r^2 = 6DT \tag{4}$$

where D is the spin-diffusion constant. Note that the factor 6 in Equation (4) may be different if one starts from a different model such as diffusion from a 1D lamellar morphology (in this case, the factor becomes 4/3),[90,91] 1D and 2D point sources (in these cases, the factor becomes 2 and 4, respectively). Fortunately, however, such differences depending on the model chosen are not serious when one deduces domain size from the magnetic relaxation experiments. The typical D values are in the range of $10^{-15}-10^{-16}$ m^2 s^{-1}.[44,87,91–93] By putting $D = 5 \times 10^{-16}$ m^{2}s^{-1}, we obtain $r = 17$–55 nm for T_1 values of 0.1–1 s, and $r = 1.7$–5.5 nm for $T_{1\rho}$ values of 1–10 ms. In other words, if the domain size is smaller than 17 nm, spin diffusion can effectively average any polarization gradient created due to T_1 values which differ by a few seconds. To phrase it differently, when one observes the same T_1 values for both component polymers, one can regard the blend as homogeneous on a scale of 17–55 nm. Similar criteria hold for $T_{1\rho}$ experiments on a scale of 1.7–5.5 nm.

By using high-resolution ^{13}C solid-state NMR, it is possible to observe the ^{1}H relaxation curve of each component polymer individually via well-resolved ^{13}C peaks. Due to the ease of T_1 and $T_{1\rho}$ experiments, these criteria are frequently used to establish the length-scale over which the blend is homogeneously mixed. Various factors affecting miscibility,[34,38,41,45,46,51–53] such as molecular weight,[37,42,43] side-chain difference,[33,35,36,94] number of monomer units in the copolymer[40] and tacticity,[95] have been investigated.
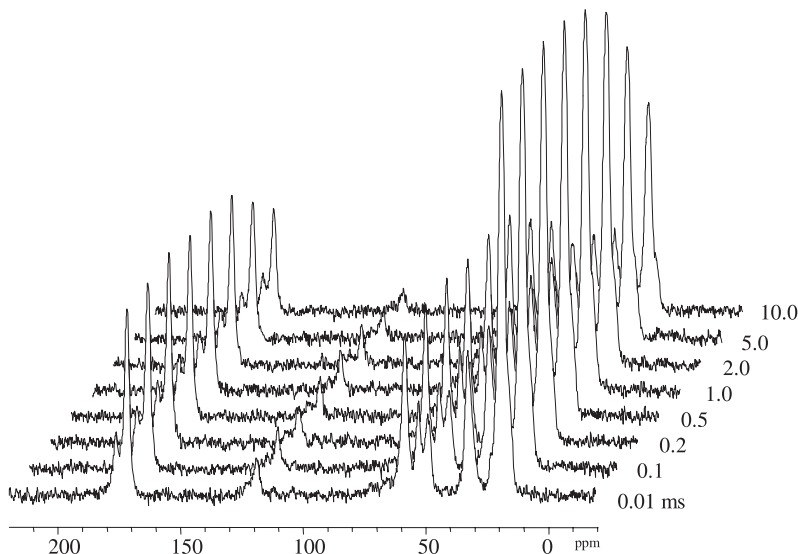
Fig. 15. Typical ^{13}C CP/MAS NMR spectra of a PLA/PLV (50/50) blend as prepared by adding the TFA solution with a 2.0 wt/wt% amount of H_2SO_4 to alkaline water (*Method* 5) are shown a function of proton spin-locking time τ.

4.2. PLA/PLV (50/50) blend

Typical ^{13}C CP/MAS NMR spectra of the PLA/PLV (50/50) blend are shown as a function of proton spin-locking time, τ, in Fig. 15. The intensities of the individual peaks decrease with an increase in τ. The semi-log plots of the peak intensities for the individual carbons of PLA and PLV in the blend against τ are a straight line and from its slope the $^1H T_{1\rho}$ value is obtained. As a typical example, it is convenient to show the semi-log plot of the peak intensity of the PLA Cα against the spin-locking time τ in the $^1H T_{1\rho}$ experiments on pure PLA with the α-helix form and PLA with the α-helix form in the PLA/PLV (50/50) blend in Fig. 16 (a). It is clear that there are significant differences between the two slopes of the semi-log plots for pure PLA with the α-helix form and for PLA in the PLA/PLV (50/50) blend. The experimental errors are within $\pm 5\%$. From these plots, the $^1H T_{1\rho}$ values of 22 and 16 ms are calculated, respectively. Similarly, the $^1H T_{1\rho}$ values for pure PLA and PLV in the PLA/PLV (50/50) samples can be obtained. All of the $^1H\ T_{1\rho}$ values of pure PLA, pure PLV, and the PLA/PLV (50/50) samples are shown in Table 9. The $^1H\ T_{1\rho}$ values of the shoulder peaks in the PLA Cβ carbon region of the PLA/PLV (50/50) blend are determined by computer-fitting the spectra obtained at various proton spin-locking times.
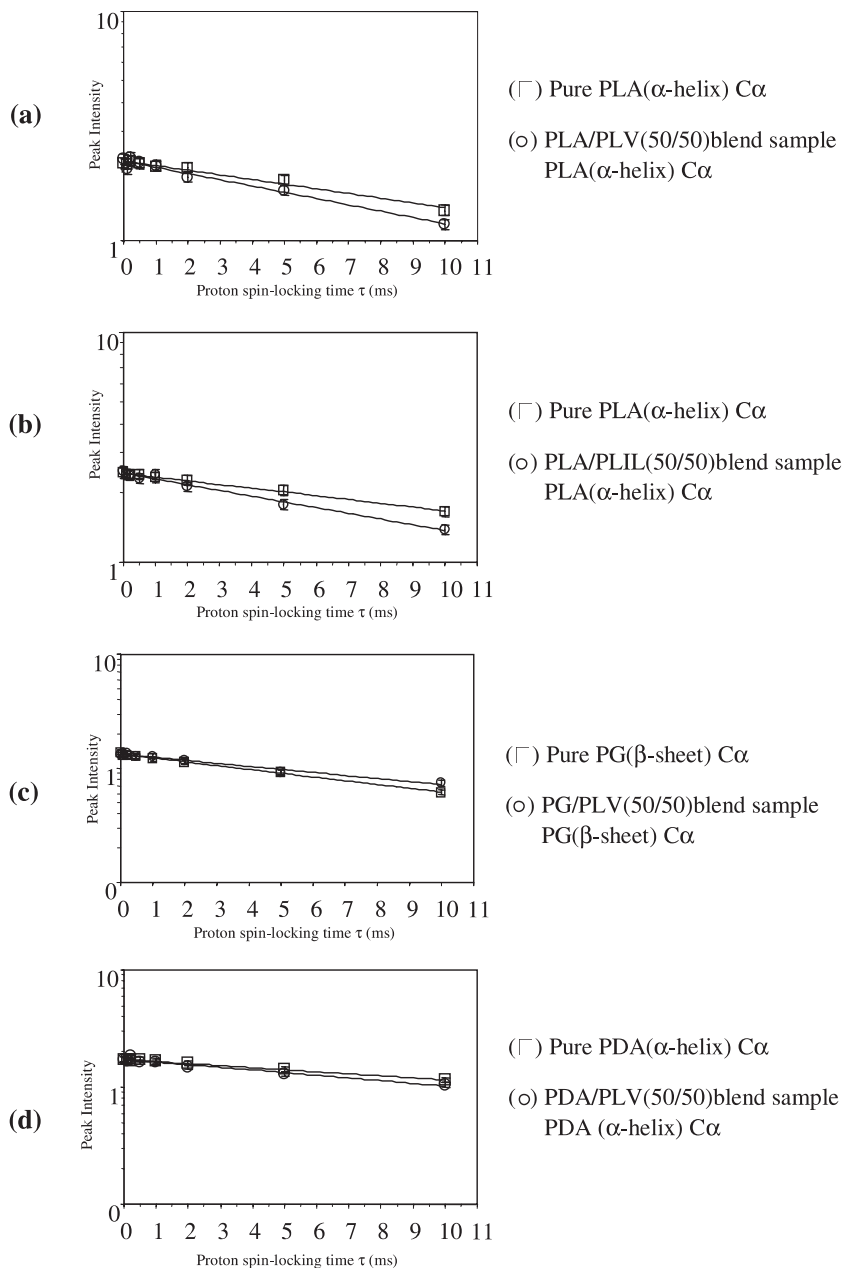
Fig. 16. Typical semi-log plots of the peak intensities for the pure homopoly-peptides and blend samples against the proton spin-locking time τ. (a) PLA/PLV (50/50), (b) PLA/PLIL (50/50), (c) PG/PLV (50/50) and (d) PDA/PLV (50/50).

Table 9.   Determined $^1H\ T_{1\rho}$ values of PLA, PLV and PLA/PLV (50/50) blend samples obtained by *Methods* 4 and *Methods* 5

Polypeptide sample	$^1H\ T_{1\rho}$ (ms)				Conformation
	C=O	Cα	Cβ	Cγ	
PLA	24	22	22		α-Helix
	19	16	14		β-Sheet
PLV	15	14	15	15	β-Sheet
PLA/PLV[a] (50/50)	21	23	14		PLA α-helix
	14	16	18	19	PLV β-sheet
PLA/PLV[b] (50/50)	19	16	13		PLA α-helix
	16	19	*c*		PLA β-sheet
	16	17	16	15	PLV β-sheet

[a] TFA solution of PLA/PLV (50/50) with a 2.0 wt/wt% of H_2SO_4 to water *Method* 4.
[b] TFA solution of PLA/PLV (50/50) with a 2.0 wt/wt% of H_2SO_4 to alkaline water *Method* 5.
[c] Not determined because of the overlap of the minor Cβ (β-sheet) peak with the major Cγ (PLV) peak by computer fitting.

The $^1H\ T_{1\rho}$ values determined from the Cα, Cβ and C=O carbon signals of pure PLA with the α-helix form are 22, 22 and 24 ms, respectively, and those of the PLA (mixture of the β-sheet and α-helix forms, 1:1) with the β-sheet form are 16, 14 and 19 ms, respectively. On the other hand, the $^1H\ T_{1\rho}$ values determined from the Cα, Cβ, Cγ and C=O of pure PLV with the β-sheet form are 14, 15, 15 and 15 ms, respectively. The $^1H\ T_{1\rho}$ values for PLA with the β-sheet form are somewhat longer than those for PLV with the β-sheet form. However, the $^1H\ T_{1\rho}$ values for PLA in the α-helix form are much larger than those for PLA and PLV in the β-sheet form. In the PLA/PLV (50/50) blend, the $^1H\ T_{1\rho}$ values determined from the Cα, Cβ and Cγ of PLV in the β-sheet form are 17, 16 and 15 ms, respectively, and are thus slightly larger than those for pure PLV. The $^1H\ T_{1\rho}$ values determined from the Cα and Cβ of PLA in the α-helix form, are 16 and 13 ms, respectively, and for the Cα carbon of PLA in the β-sheet form it is 19 ms. The $^1H\ T_{1\rho}$ values for the α-helix form thus decrease. Hence, these ^1H $T_{1\rho}$ values are very close to each other. This shows that proton spin diffusion between the PLAs in the α-helix and β-sheet forms and PLV in the β-sheet form occurs on the $^1H\ T_{1\rho}$ time scale.

4.3. PLA/PLIL (50/50) blend

It is clear that there are significant differences between the two slopes of the semi-log plots for the Cα carbon of pure PLA with the α-helix form and the Cα carbon of PLA (α-helix form) in the PLA/PLIL (50/50) blend sample

Table 10. Determined ^{1}H $T_{1\rho}$ values of PLA, PLIL and PLA/PLIL (50/50) blend samples obtained by *Methods 5*

Polypeptide sample	^{1}H $T_{1\rho}$ (ms)					Conformation
	C=O	Cα	Cβ	Cγ	Cδ	
PLA	27	27	26			α-helix
PLA	21	19	20			β-sheet
PLIL	11	11	11	12/11	11	β-sheet
PLA/PLIL (50/50)	16	17	*a*			PLA α-helix
	b	17	19			PLA β-sheet
	12	14	13	14/14	14	PLIL β-sheet

^{a} Not determined because of the overlap of the minor Cβ (PLA: α-helix) peak with the major Cδ (PLIL: β-sheet) peak by computer fitting.

^{b} Not determined because of the overlap of the minor C=O (PLA: β-sheet) peak with the major C=O (PLIL: β-sheet) peak by computer fitting.

(Fig. 16 (b)), and the experimental error is within $\pm 5\%$. From these plots, the ^{1}H $T_{1\rho}$ values of 27 and 17 ms for these samples can be calculated, respectively. Similarly, the significant ^{1}H $T_{1\rho}$ values for PLA and PLIL in the PLA/PLIL (50/50) samples can be obtained. All of the ^{1}H $T_{1\rho}$ values of PLA, PLIL and the PLA/PLIL (50/50) blend samples are shown in Table 10. The ^{1}H $T_{1\rho}$ values for the Cβ and the C=O carbons of the PLA/PLIL (50/50) blend indicated by *a* and *b* in Table 10, could not be determined because of the overlap of the minor Cβ (PLA: α-helix) peak with the major Cγ (PLIL) peak and the minor C=O (PLA: β-sheet) peak with the major C=O (PLIL) peak as determined by computer-fitting.

The ^{1}H $T_{1\rho}$ values determined from the Cα, Cβ and C=O carbon signals of pure PLA in the α-helix form are 27, 26 and 27 ms, respectively, and those of the PLA (mixture of the β-sheet and α-helix forms, 1:1) with the β-sheet form are 19, 20 and 21 ms, respectively. However, the ^{1}H $T_{1\rho}$ values determined from the Cα, Cβ, Cγ, Cδ and C=O carbons of pure PLIL in the β-sheet form are 11, 11, 12/11, 11 and 11 ms, respectively. The ^{1}H $T_{1\rho}$ values for PLA in the β-sheet form are larger than those for PLIL in the β-sheet form. However, the ^{1}H $T_{1\rho}$ values for PLA in the α-helix form are much larger than those for PLA and PLIL in the β-sheet form. In the PLA/PLIL (50/50) blend, the ^{1}H $T_{1\rho}$ values determined from the Cα, Cβ, Cγ, Cδ and C=O of PLIL in the β-sheet form are 14, 13, 14/14, 14 and 12 ms, respectively, and are thus slightly larger than those for pure PLIL. The ^{1}H $T_{1\rho}$ values determined from the Cα and Cβ carbons of PLA in the β-sheet form are 17 and 19 ms, respectively, and the Cα of PLA in the α-helix form is 17 ms. Hence, these ^{1}H $T_{1\rho}$ values are very close to each other. This shows that proton spin diffusion between the PLAs in the

Table 11.   Determined ^{1}H $T_{1\rho}$ values of PG, PLV and PG/PLV (50/50) blend samples obtained by *Method 5*

Polypeptide sample	^{1}H $T_{1\rho}$ (ms)				Conformation
	C=O	Cα	Cβ	Cγ	
PG	17	18			3_1-Helix
PG	13	13			β-sheet
PLV	19	19	18	18	β-sheet
PG/PLV (50/50)	*a*	15			PG 3_1-Helix
	16	16			PG β-sheet
	13	14	14	12	PLV β-sheet

^{a} Not determined because of the overlap of the minor C=O (PG: 3_1-helix) peak with the major C=O (PLV: β-sheet) peak by computer fitting.

α-helix and β-sheet forms and PLIL in the β-sheet form occurs on the ^{1}H $T_{1\rho}$ time scale.

4.4. PG/PLV (50/50) blend

From Fig. 16 (c), it can be seen that ^{1}H $T_{1\rho}$ values of the Cα of pure PG in the β-sheet form and the Cα of PG in the β-sheet form in the PG/PLV (50/50) blend sample are 13 and 16 ms, respectively. Similarly, the significant ^{1}H $T_{1\rho}$ values for PG and PLV in the PG/PLV (50/50) blend sample can be obtained. All of the determined ^{1}H $T_{1\rho}$ values of PGs, PLV and PG/PLV (50/50) blend samples are shown in Table 11, where the ^{1}H $T_{1\rho}$ value for the C=O carbon of PG/PLV (50/50) indicated by *a* (in Table 11) could not be determined because of the overlap of the minor C=O (PG: 3_1-helix) peak with the major C=O (PLV: β-sheet) peak as determined by computer-fitting.

The ^{1}H $T_{1\rho}$ values determined from the Cα and C=O signals of pure PG in the β-sheet form are 13 and 13 ms, respectively, and those for pure PG in the 3_1-helix form are 18 and 17 ms, respectively. On the other hand, the ^{1}H $T_{1\rho}$ values determined from the Cα, Cβ, Cγ and C=O of pure PLV in the β-sheet form are 19, 18, 18 and 19 ms, respectively. The ^{1}H $T_{1\rho}$ values for PG in the 3_1-helix form are larger than those of PG in the β-sheet form, and are somewhat smaller than those of PLV in the β-sheet form. In the PG/PLV (50/50) blend, the ^{1}H $T_{1\rho}$ values determined from the Cα, Cβ and Cγ of PLV in the β-sheet form are 14, 14 and 12 ms, respectively, and are smaller than those for pure PLV. The ^{1}H $T_{1\rho}$ value determined from the Cα of PG in the 3_1-helix form is 15 ms, and that from the Cα of PG in the β-sheet form is 16 ms. These values are approximately equal to each other. This shows that proton spin diffusion,

Table 12. Determined ^{1}H $T_{1\rho}$ values of PDA, PLV and PDA/PLV (50/50) blend samples obtained by *Method 5*

Polypeptide sample	^{1}H $T_{1\rho}$ (ms)				Conformation
	C=O	Cα	Cβ	Cγ	
PDA	26	25	26		α-Helix
PLA[a]	21	19	20		β-sheet
PLV	19	19	18	18	β-sheet
PDA/PLV (50/50)	17	20	19		PDA α-Helix
	b	18	17		PDA β-sheet
	18	16	16	16	PLV β-sheet

[a] As the ^{1}H $T_{1\rho}$ values of PDA β-sheet form have not been reported, the ^{1}H $T_{1\rho}$ values of PLA β-sheet form have been shown instead of PDA.

[b] Not determined because of the overlap of the minor C=O (PDA: β-sheet) peak with the major C=O (PLV: β-sheet) peak by computer fitting.

between the PGs in the 3_1-helix and β-sheet forms and PLV in the β-sheet form, occurs on the ^{1}H $T_{1\rho}$ time scale.

4.5. PDA/PLV (50/50) blend

As shown in Fig. 16 (d), it is clear that there are significant differences between the two slopes of the semi-log plots for the Cα of pure PDA in the α-helix form and the Cα of PDA in the α-helix form in the PDA/PLV (50/50) blend. From these slopes, the ^{1}H $T_{1\rho}$ values of 25 and 20 ms can be calculated, respectively. Similarly, the significant ^{1}H $T_{1\rho}$ values for PDA and PLV in the PDA/PLV (50/50) blend sample can be obtained. All of the determined ^{1}H $T_{1\rho}$ values of the PDA, PLV and PDA/PLV (50/50) blend samples are shown in Table 12, where the ^{1}H $T_{1\rho}$ value of the C=O of PDA/PLV (50/50) indicated by *b* (in Table 12) could not be determined because of the overlap of the minor C=O (PDA: β-sheet) peak with the major C=O (PLV) peak as determined by computer-fitting. The ^{1}H $T_{1\rho}$ values of the PDA β-sheet form are not known. However, the ^{1}H $T_{1\rho}$ values of the PLA β-sheet form may be the same as those of PDA.

The ^{1}H $T_{1\rho}$ values determined from the Cα, Cβ and C=O signals of pure PDA in the α-helix form are 25, 26 and 26 ms, respectively, and those of the PLA (mixture of the β-sheet and α-helix forms, 1:1) in the β-sheet form are 19, 20 and 21 ms, respectively. However, the ^{1}H $T_{1\rho}$ values determined from the Cα, Cβ, Cγ and C=O of pure PLV in the β-sheet form are 19, 18, 18 and 19 ms, respectively. The ^{1}H $T_{1\rho}$ values for PLV with the β-sheet form and PLA in the β-sheet form are very close to each other. However, the

^{1}H $T_{1\rho}$ values for PDA in the α-helix form are larger than those for PLA and PLV in the β-sheet form. In the PDA/PLV (50/50) blend, the ^{1}H $T_{1\rho}$ values determined from the Cα, Cβ and Cγ of PLV in the β-sheet form are 16, 16 and 16 ms, respectively, and are thus slightly smaller than those for pure PLV. The ^{1}H $T_{1\rho}$ values determined from the Cα and Cβ of PDA in the α-helix form are 20 and 19 ms, respectively, and for the Cα and Cβ of PDA in the β-sheet form are 18 and 17 ms, respectively. These ^{1}H $T_{1\rho}$ values are approximately equal to each other. This shows that proton spin diffusion between the PDAs in the α-helix and β-sheet forms and PLV in the β-sheet form occurs on the ^{1}H $T_{1\rho}$ time scale.

4.6. The domain size of blends

In all of the polypeptide blend samples obtained by *Method* 5, the proton spin diffusion between each homopolypeptide occurs on the ^{1}H $T_{1\rho}$ time scale.

The maximum effective diffusion distance was obtained from these ^{1}H $T_{1\rho}$ values. The maximum effective diffusion distance L of the proton spin diffusion is expressed by the following equation (5) from equation (4),

$$L = (6D_{spin}t)^{1/2} \qquad (5)$$

In this work ^{1}H $T_{1\rho}$ is used for t. Although the value of D_{spin} may somewhat depend on the different proton densities in the blend systems, the average D_{spin} has been used in the analysis of polymer blend systems. In general, in the $T_{1\rho}$ experiments on polymer blends 10^{-12} cm^2/s, as the averaged value, has been used for determining qualitatively or semi-quantitatively the domain size of the blend systems.[44,87,91–93] By substituting the ^{1}H $T_{1\rho}$ values averaged over all of the protons for PLA/PLV (50/50), PLA/PLIL (50/50), PG/PLV (50/50) and the PDA/PLV (50/50) blend samples into equation (5), we can approximately estimate L to be about 3 nm as the domain size (in Table 13). This shows that the domain size of the individual polypeptides in the blend is not so large, and they are miscible at the molecular level. It can be said that this equation should be used for qualitative or semi-quantitative discussions of the miscibility of polymer blends as suggested by many reports.[27,32,34,38,39,41,45–47,49,51–53,94,96]

We note that PLA with the β-sheet form in the PLA/PLV blends is incorporated into PLV in the β-sheet form and then takes the β-sheet form by making intermolecular interactions with PLV. However, the other component of PLA takes the α-helix form. In addition, proton spin diffusion between the PLAs in the α-helix and β-sheet forms and PLV in the β-sheet form occurs on the ^{1}H $T_{1\rho}$ time scale and so PLA and PLV are miscible at the molecular level with a domain size of about 3 nm. The other

Table 13. Averaged ^{1}H $T_{1\rho}$ values and maximum effective diffusion distance (L) of polypeptide blend samples

Blend sample	^{1}H $T_{1\rho}$ (ms)[a]	L(nm)
PLA/PLV(50/50)	16	3.1
PDA/PLV(50/50)	18	3.3
PG/PLV(50/50)	15	3.0
PLA/PLIL(50/50)	16	3.1

[a] The ^{1}H $T_{1\rho}$ value averaged over all of the protons.

three kinds of PLA/PLIL, PG/PLV and PDA/PLV blend samples, are also miscible at the molecular level with a domain size of about 3 nm.

5. TWO-DIMENSIONAL ^{13}C–^{1}H HETCOR SPECTRAL ANALYSIS AND STRUCTURAL CHARACTERIZATION OF POLYPEPTIDES BLENDS

It is very important to obtain more detailed information about the relationship between the character and miscibility of polypeptide blends. For example, the PG/PLV (50/50) blend sample, the preferred conformation of the PLV is he β-sheet which exists in the PG/PLV (50/50) blend sample. On the other hand, the 3_1-helix form of PG in PG/PLV blends is almost transformed to the β-sheet form in the PG/PLV blend sample. We have been expecting two kinds of hydrogen bonding interactions with the β-sheet. One is a β-sheet conformation of intermolecular HB interactions between the PG and PG, and another is a β-sheet conformation of intermolecular HB interactions between the PG and PLV. It is important to discuss the blend mechanism. The relationships between the starting materials, the preferred conformations and the new HB interactions are shown in Fig. 17.

Thus, it is useful to get more detailed information about the miscibility of polypeptides and to understand the polypeptide blend by using further sophisticated NMR methodology.

Recently, the two-dimensional ^{13}C–^{1}H heteronuclear correlation (HETCOR) NMR method, using the frequency-switched Lee–Goldberg (FSLG) ^{1}H decoupling sequence[55] at high MAS rates, has been developed, in order to provide intermolecular and spatial distance information. The HETCOR spectrum often has multiple proton cross peaks for each carbon, and these cross peaks can be extremely helpful for assigning the spectrum. Thus, this method can be used to characterize the structure of polymers in solids.[55–71]

Thus, in this section, we aim to introduce the 2D FSLG ^{13}C–^{1}H HETCOR NMR[55] spectrum of a PG/PLV (50/50) blend sample and to elucidate the intermolecular HB interactions between PG and PLV chains.
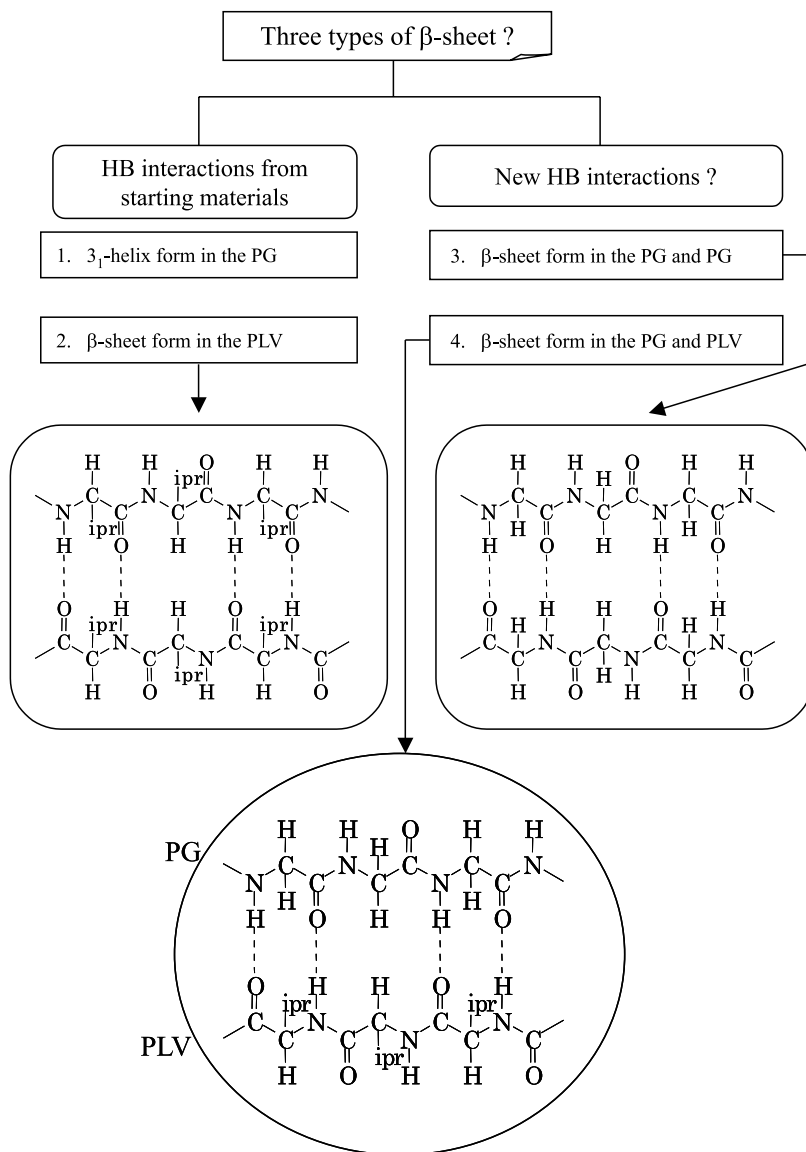
Fig. 17.   The relationship between starting materials, preferred conformations and new conformations for PG/PLV (50/50) blend sample.

Further, a molecular model for the anti-parallel β-sheet conformation of PG and PLV have been calculated using the X-PLOR 3.1 program, and we have measured carbon–proton distances from the modeled structure.

5.1. Frequency-switched Lee–Goldburg (FSLG) ^{13}C–^{1}H heteronuclear correlation (HETCOR) experiments

Solid-state NMR spectroscopy has been extensively used to investigate biological systems such as polypeptides and proteins, with most studies focusing on the well resolved ^{13}C or ^{15}N spectra. The resolution of solid state ^{1}H NMR spectra is poor due to very strong dipolar–dipolar couplings between protons which results in extremely broad lines. The information available from ^{1}H NMR could be very useful for studying ionizable groups involved in hydrogen bonding or proton transfer reactions. Several methods have been developed to increase the resolution and decrease the line width of ^{1}H NMR spectra. The line narrowing in the proton dimension is generally achieved by application of combined rotation and multiple pulse spectroscopy (CRAMPS) techniques to suppress the strong homonuclear dipolar interactions between the abundant protons.[57,58,60,68,97–103] However, in a high-speed MAS NMR study of, for instance, biological systems, the use of multiple-pulse techniques to study the proton chemical-shift dispersion is limited for several reasons. First, the application of multiple-pulse techniques usually requires cycle times that are short compared to the rotor period. This effectively puts a restriction on the spinning speeds that can be used in practise and the efficacy of the MAS averaging. It also limits the possibilities for application of CRAMPS techniques in high-field MAS, where high spinning speeds will be required to obtain sufficient resolution in multi-dimensional spectra. For instance, the pulse sequence WAHUHA-4, which has the shortest cycle time, performs well only at moderately high spinning rates. More-elaborate CRAMPS sequences require longer cycle times, and the possibility for application in high-speed MAS will be even less favourable. In addition, biological MAS NMR studies must be often performed at low temperature, which makes the use of tuned-up multiple-pulse sequences impractical.

However, the measurement of a ^{13}C–^{1}H heteronuclear intermolecular distance is potentially an important tool in the structure determination of solids,[56–71] since it can provide restraints that can be used for structure refinement by modeling. Information about the inter-nuclear distance between two spins can be deduced from the strength of the ^{13}C–^{1}H heteronuclear dipolar interaction. For a static sample, the dipolar interaction between the two spins of a heteronuclear spin-pair yields a symmetric Pake doublet,[104] in which the separation between the two maxima provides a direct measure for the heteronuclear dipolar coupling strength. MAS, however, averages the heteronuclear dipolar interactions and gives rise to a pattern of spinning sidebands, with the relative intensities of the spinning sidebands determined by both the dipolar interaction and the chemical shift.[105]

A useful approach to solve these problems is solid-state two-dimensional (2D) ^{13}C–^{1}H heteronuclear correlation (HETCOR) spectroscopy.

2D HETCOR can enhance ^{1}H resolution. Moreover, it can separate the dipolar interaction from the chemical shift interactions of each nucleus; one dimension is correlated with the dipolar coupling to neighbouring spins in the second dimension.[62,105–112] The first HETCOR experiments were proposed by Caravatti *et al.*[56,57] and were later modified by Burum and Bielecki,[58] who designed the first method which produced well-resolved lines with little experimental difficulty. This experiment uses a BLEW-12 windowless homonuclear proton decoupling sequence with simultaneous BR-24 decoupling of ^{1}H from ^{13}C, which provides pure ^{1}H chemical shift evolution. Mixing is achieved by a WIN-24 sequence which selectively transfers magnetization from a ^{1}H to a strongly coupled ^{13}C. This method provides well-resolved correlation maps in a straightforward manner. However, a severe limitation of the sequence is the use of a homonuclear decoupling sequence with long cycle times. These impose a limit on the maximum usable MAS spin rate since the rotation period must be long compared to the sequence cycle time. In practice a 5 kHz spin rate is the upper limit even for high RF power levels and short pulses. This is obviously a problem at high magnetic field strengths, where spinning rates of more than 10 kHz are required in order to sufficiently separate spinning sidebands from the spectral range of interest. However, with the availability of high-performance CP/MAS equipment for field strengths much higher than 7 T, it is very desirable to make use of the much higher proton shift dispersion at high fields.

For the above reasons, a new pulse sequence[55] has been developed which can operate at a very high spinning rate (limited only by the applicability of cross polarization) and is extremely simple and reliable in setup and reproducibility. Suppression of proton homonuclear dipolar interactions and observation of proton chemical shift evolution is achieved by a frequency-switched Lee–Goldberg sequence (FSLG), which has an inherently short cycle time since it consists of only two pulses with 2π flip angles.[113] These pulses can be applied at high spin rates without simultaneous decoupling of protons from the X-spin. Therefore, at high RF power levels, the rate is typically 10 μs, which is short compared to the MAS period, and may be used with less risk of RF breakthrough in the probe. Modern NMR spectrometers enable rapid coherent switching of both frequency and phase of the RF during a pulse, and the FSLG sequence is relatively straightforward to implement. Since the only parameters that need to be adjusted are the offset frequency Δ_{LG} and the duration of the successive frequency intervals τ, the sequence is robust and can easily be readjusted if necessary. Mixing is achieved with a simple Hartmann-Hahn contact, in order to select for correlations via strong heteronuclear dipolar couplings and to avoid cross peaks due to spin diffusion in the proton reservoir.

We introduce the use of solid-state 2D FSLG ^{13}C–^{1}H HETCOR experiments for correlating intermolecular interactions in miscible, hydrogen bonded polypeptide blends in this section. The pulse sequence that is used
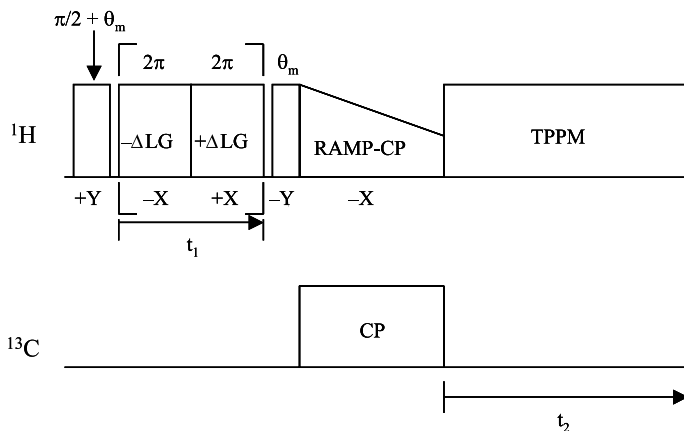
Fig. 18. The pulse sequence for measuring the 2D heteronuclear correlation NMR spectrum with frequency-switched Lee-Goldburg irradiation during the evolution.

in this section is depicted in Fig. 18. The sequence starts with a $(\pi/2 + \theta_m)_y$ pulse on the protons, directly followed by a train of frequency- and phase-switched LG pulses in the xz plane. After the evolution period, the proton magnetization is turned back by a single magic angle y pulse, which will turn any component perpendicular to the LG pulse back into the xy plane, and which will bring the spin-locked component along the LG-pulse back to the z axis. The resulting ^{1}H magnetization after variable contact times is transferred to the ^{13}C spins by CP. Although the high speed MAS is needed to obtain a narrowed proton resonance, the Hartmann-Hahn matching and corresponding efficiency of CP magnetization transfer is very sensitive to *rf* power instabilities at high MAS frequencies. In this pulse sequence (Fig. 18), ramped-amplitude CP (RAMP-CP)[114] is used for protons to restore a broader matching profile. Further, to obtain high resolution ^{1}H NMR spectra, two pulse phase-modulation (TPPM) decoupling is also used during the acquisition time.

5.2. Structural modelling of PG and PLV with the anti-parallel β-sheet form

The structural modeling of PG and PLV with the anti-parallel β-sheet form is carried out by the hybrid distance geometry-dynamic simulated annealing method[115] as contained in the X-PLOR 3.1 program.[116] For structural calculations, the proton–proton distance restraints and the torsion angle restraints ($\phi = -139°$ and $\psi = 135°$) are derived from reference data by Wüthrich *et al.*[117] Hydrogen-bond distance restraints are used for the N and O atoms (2.7–3.3 Å) in the secondary structure.[118–120] The reference data of intra- and intermolecular proton–proton distances are shown in Fig. 19.
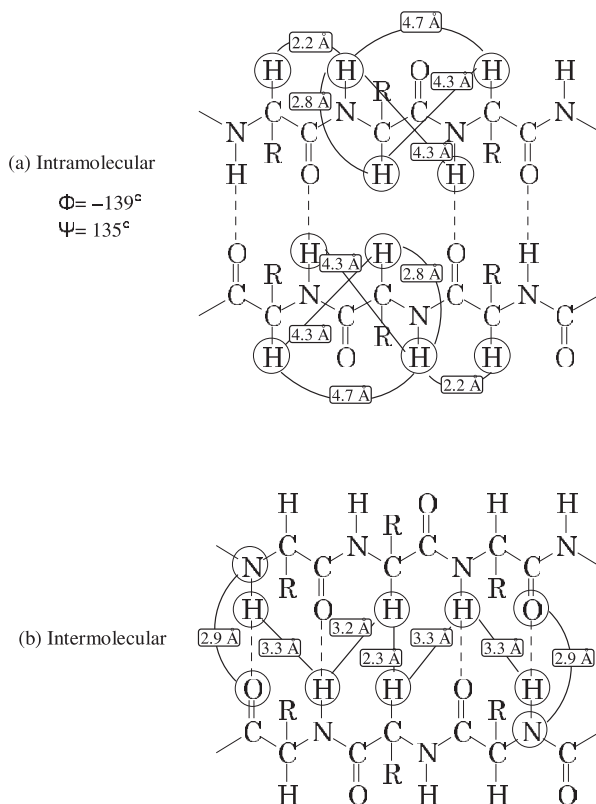
Fig. 19.   Intra- (a) and intermolecular (b) proton–proton distances in regular, non-twisted antiparallel β-sheet.

A final set of 10 lowest-energy structures are selected from 30 calculated results, where the structures with distance and dihedral angle > 0.5 Å and 5°, respectively, are omitted. The average coordinates of the ensembles of the preferable 10 structure candidates are subjected to 500 cycles of Powell restrained energy minimization to improve non-bonded contacts. The modelling structure was embodied by RasMol.[121] (Fig. 20). The intra- and inter-nuclear distances of the antiparallel β-sheet conformation for PG/PLV have been measured by using the Insight II program, and they are shown in Table 14.

5.3. ^{13}C–^{1}H HETCOR spectral analysis and structural characterization

The HETCOR spectrum often has multiple proton cross peaks for each carbon, and these cross peaks can be extremely helpful for assigning the spectrum. Thus, this method can be used to characterize the structure of polymers in solids.[55–71]
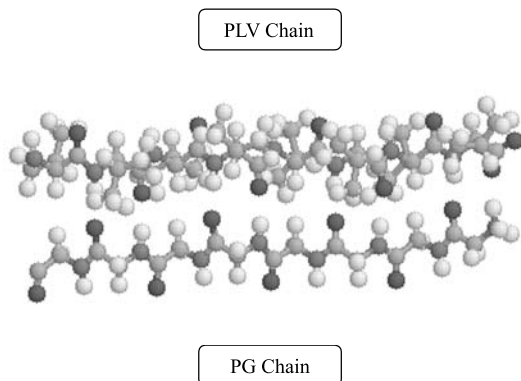
Fig. 20. The molecular model of antiparallel β-sheet confirmation for PG/PLV obtained by X-PLOR 3.1.

Table 14. The calculated carbon–proton distances for antiparallel β-sheet for the PG–PG, PLV–PLV and PG–PLV

	Distances (Å)			
	Intramolecular		Intermolecular	
	PG–PG	PLV–PLV	PG–PLV	PLV–PG
Cα–Hα	1.08	1.08	3.09–3.30	3.17–3.34
Cα–Hβ	–	2.15	4.30–6.04	–
Cα–Hγ	–	2.53–3.39	3.32–6.65	–
Cα–HN	2.15	2.15	3.93–4.23	4.00–4.23
Cβ–Hα	–	2.15	–	3.90–6.54
Cβ–Hγ	–	2.15	–	–
Cβ–HN	–	2.89	–	4.12–5.04
Cγ–Hα	–	2.68–3.43	–	3.56–6.32
Cγ–Hβ	–	2.15	–	–
Cγ–HN	–	2.67–3.64	–	3.21–6.20
C=O–Hα	2.15	2.15	3.80–4.00	3.72–4.01
C=O–Hβ	–	2.62–2.72	4.34–6.70	–
C=O–Hγ	–	2.39–4.15	3.27–7.10	–
C=O–HN	1.98	1.98	3.17	3.17

A two-dimensional (2D) FSLG ^{13}C–^{1}H HETCOR spectrum with a short contact time (0.2 ms) of a PG/PLV (50/50) blend is shown in Fig. 21. The horizontal axis (F2) corresponds to the ^{13}C (chemical shift range: 3 to +182 ppm), and the vertical axis (F1) corresponds to the ^{1}H (chemical shift range: −1 to +12 ppm). A one-dimensional (1D) ^{13}C CP/MAS spectrum for the horizontal (^{13}C) axis is shown at the top of this Figure. In the
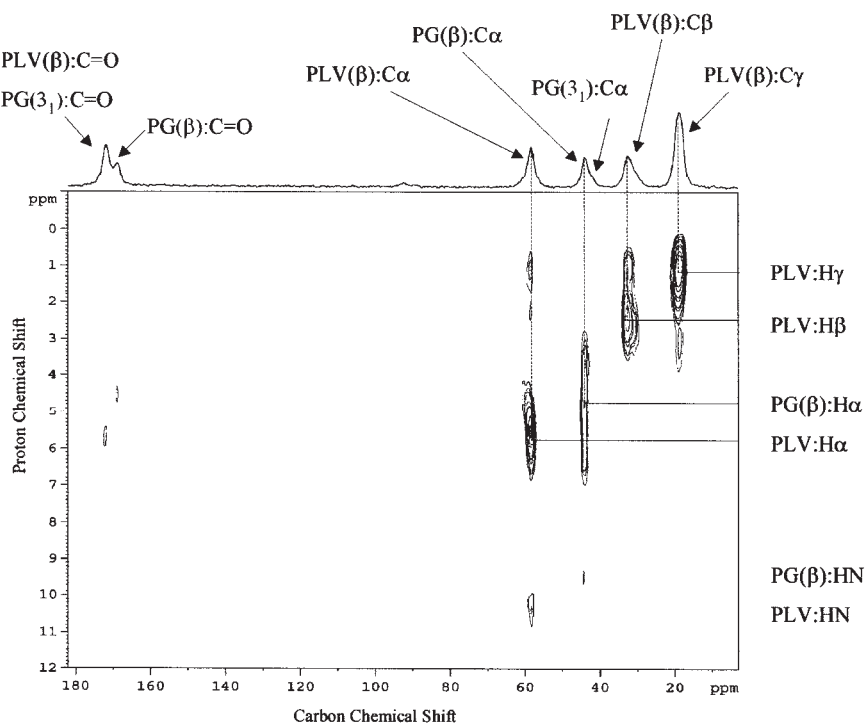
Fig. 21. The 2D FSLG ^{13}C–^{1}H HETCOR spectra of PG/PLV (50/50) blend sample with contact time of 0.2 ms.

spectrum, the intense correlations arise from the dipolar coupling between the carbons and their directly-bonded protons. The corresponding signals for the Cα and Hα (Cα–Hα) dipolar coupling in PG (β-sheet) and for the Cα–Hα, Cβ–Hβ and Cγ–Hγ dipolar couplings in PLV appear. Further, other weak correlation peaks are observed for the Cα–Hγ, Cβ–Hγ, Cα–NH and C=O–Hα dipolar couplings in PLV, and for the Cα–NH and C=O–Hα dipolar couplings in PG (β-sheet).

In the ^{1}H spectrum, the peaks at 9.3 and 4.7 ppm can be assigned to the NH and Hα protons of PG in the β-sheet form, respectively, and further peaks at 10.3, 5.6, 2.3 and 1.1 ppm to the NH, Hα, Hβ and Hγ protons of PLV in the β-sheet form, respectively. The ^{1}H peaks for PG in the 3_1-helix form are not assigned by the FSLG HETCOR method with a contact time of 0.2 ms because the 3_1-helix form in PG is the minor component. The FSLG ^{13}C–^{1}H HETCOR spectrum with a contact time of 0.5 ms (Fig. 22) shows the correlation signal between the Cα and the Hα of PG in the 3_1-helix form, and the ^{1}H chemical shift of the Hα is 4.3 ppm. Each of the ^{1}H signals have sufficiently large chemical shift differences to permit analysis of the corresponding correlation signals.
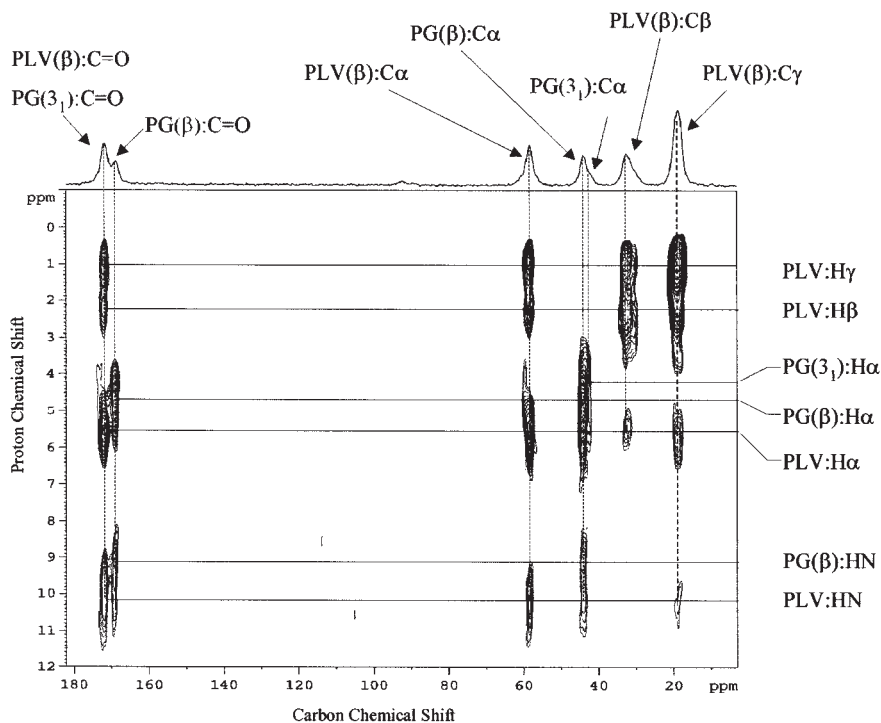
Fig. 22.   The 2D FSLG ^{13}C–^{1}H HETCOR spectra of PG/PLV (50/50) blend sample with contact time of 0.5 ms.

Further, correlation signals for the C=O–NH, C=O–Hβ, C=O–Hγ and Cγ–Hα dipolar couplings in PLV, and for the C=O–NH dipolar coupling in PG with the β-sheet form are observed. In addition, it is very significant to note that the intermolecular correlation signals for the PG(β-sheet) Cα–PLV(β-sheet)Hα, PG(β-sheet)Cα–PLV(β-sheet)NH, PG(β-sheet)C=O–PLV(β-sheet)Hα and PG(β-sheet)C=O–PLV(β-sheet)NH dipolar couplings are observed.

However, the 2D FSLG ^{13}C–^{1}H HETCOR spectrum with a long contact time of 1.5 ms (Fig. 23) shows a significant and new signal. In order to clarify the appearance of this new signal, the carbonyl carbon signal region and the Cα, Cβ and Cγ signal regions in the HETCOR, spectrum with a contact time of 1.5 ms, are expanded as shown in Fig. 24. The new correlation signal appears between the Cγ of PLV (β-sheet) at 19 ppm and the Hα of PG (β-sheet) at 4.7 ppm as shown by the arrow in Fig. 24.

In order to get more detailed information, ^{1}H slice projection of the Hα (4.7 ppm) and NH (9.3 ppm) of PG (β-sheet), Hγ (1.1 ppm) and Hβ (2.3 ppm) protons of PLV (β-sheet), and that of the Hα (5.7 ppm) and NH (10.3 ppm) of PLV (β-sheet) are shown in Figs. 25–27, respectively.
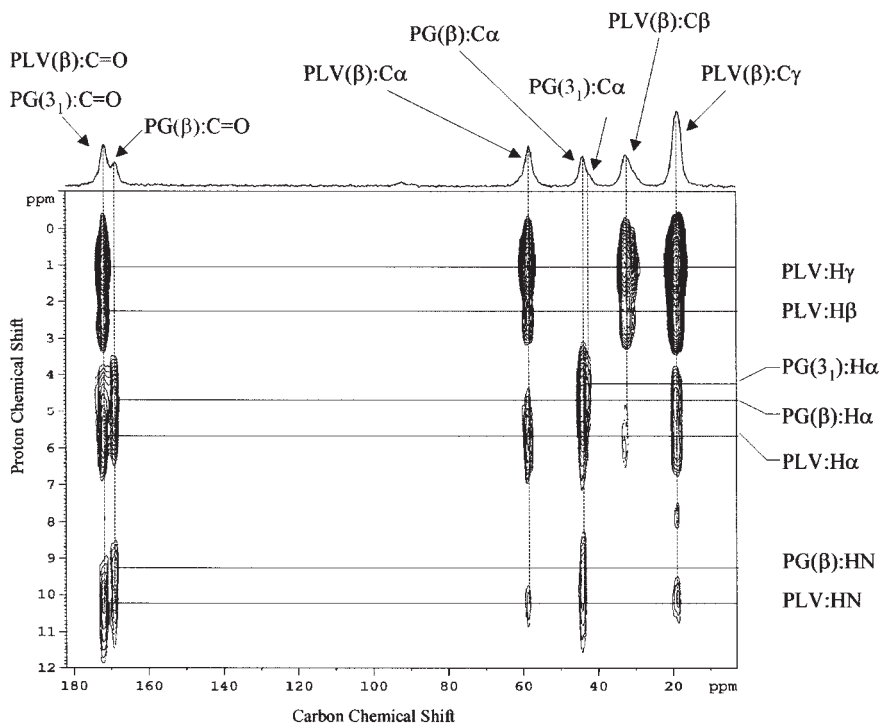
Fig. 23.   The 2D FSLG ^{13}C–^{1}H HETCOR spectra of PG/PLV (50/50) blend sample with contact time of 1.5 ms.

From these spectra, intermolecular correlations are shown more clearly. For example, the slice spectra of the Hα for PG (β-sheet) show the intermolecular correlations with the C=O, Cα and side chains of PLV (β-sheet), and also the sliced spectra of the Hα for PLV (β-sheet) show the intermolecular correlations with the C=O and Cα of PG (β-sheet). Similarly, the sliced spectra of the NH for PG (β-sheet) show the intermolecular correlations with the C=O, Cα and side chains of PLV (β-sheet), and those of the NH of PLV (β-sheet) show the intermolecular correlations with the C=O and Cα of PG (β-sheet).

In order to clarify the relationship between cross peaks and carbon–proton inter-atomic distances, molecular model for the anti-parallel β-sheet conformation of PG and PLV have been calculated using reference data (Wüthrich, *et al.*)[117] by the X-PLOR 3.1 program, and we measured the carbon–proton distances from the modeled structure (Table 14). The distances between the carbons and their directly bonded protons are ca. 1.1 Å and their signals can be observed in the FSLG ^{13}C–^{1}H HETCOR spectrum with contact time of 0.2 ms. Further, in the FSLG ^{13}C–^{1}H HETCOR spectrum with a contact time of 0.5 ms the signals corresponding
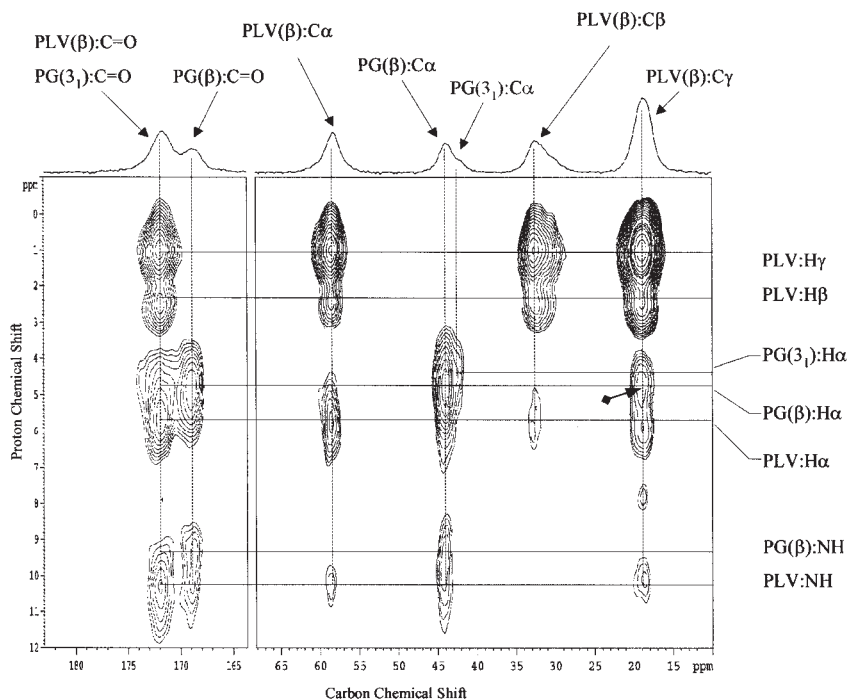
Fig. 24. Expanded 2D FSLG ^{13}C–^{1}H HETCOR spectra for the carbonyl carbon region and for the Cα, Cβ and Cγ carbons region of PG/PLV (50/50) blend sample with contact time of 1.5 ms.

to another intramolecular carbon–proton distance, which is less than 3 Å, are observed.

The correlation signals between PG and PLV corresponding to an intermolecular distance less than 4 Å are observed in the FSLG ^{13}C–^{1}H HETCOR spectra with a contact time of 0.5 ms. Further, the correlation signals between PG (Hα) and the side chain of PLV (Cγ) are observed only in the FSLG ^{13}C–^{1}H HETCOR spectra with a long contact time of 1.5 ms. For the modeled structure, the intermolecular distance between PG (Hα) and the side chain of PLV (Cγ) are obtained to be in the 3.56–6.32 Å range.

These intermolecular correlation peaks mean that intermolecular cross polarization (CP) occurs between the carbon and proton of intermolecular – interacting polypeptides in blend. There may be two pathways for the observed intermolecular CP. One is that a direct transfer from proton to carbon exists, and another is that a change in the magnetization by spin diffusion (homonuclear Hartmann–Hahn transfer) exists. It is thought that the former is much more efficient than the latter because the former comes from only one magnetization transfer process, but the latter comes from two

(a) PG (β-sheet): Hα
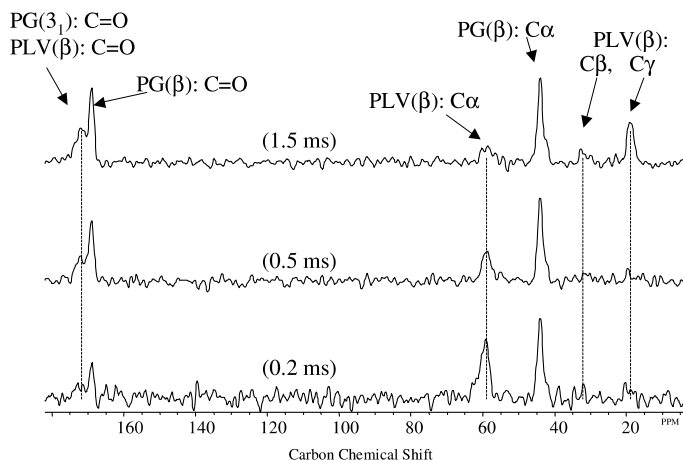
(b) PG (β-sheet): HN
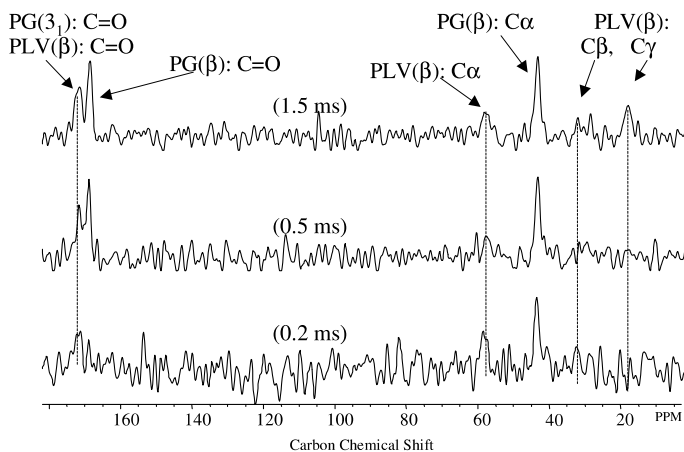
Fig. 25. One-dimensional slices along the horizontal axis of the 2D FSLG ^{13}C–^{1}H HETCOR spectra taken at (a) 4.7 ppm (PG (β) : Hα) and (b) 9.3 ppm (PG (β) : HN) on the ^{1}H chemical shift axis. The contact time used in this experiment: 1.5, 0.5 and 0.2 ms.

magnetization transfer processes. Further, it can be said that as the FSLG ^{13}C–^{1}H HETCOR pulse program is used in this experiment, the intermolecular correlations through strong heteronuclear dipolar couplings are mainly observed and thus the appearance of cross peaks due to spin diffusion in the proton reservoir is avoided. From the above experimental results,

(a) PLV (β-sheet): Hγ

(b) PLV (β-sheet): Hβ
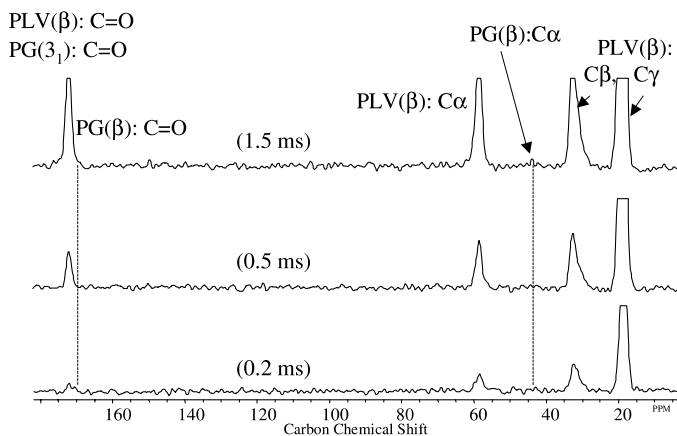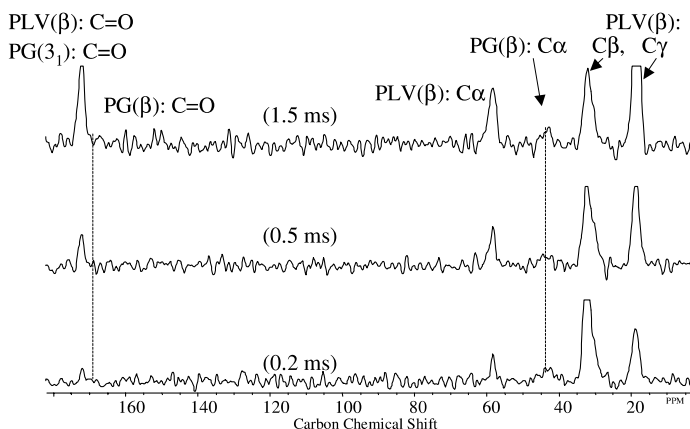
Fig. 26. One-dimensional slices along the horizontal axis of the 2D FSLG ^{13}C–^{1}H HETCOR spectra taken at (a) 1.1 ppm (PLV (β) : Hγ) and (b) 2.3 ppm (PLV (β) : Hβ) on the ^{1}H chemical shift axis. The contact time used in this experiment: 1.5, 0.5 and 0.2 ms.

it can be concluded that the backbones of the two kinds of PG (β-sheet) and PLV (β-sheet) are very close to each other and thus they are highly miscible at the molecular level.

However, side chain protons of PLV (β-sheet), especially the Hγ, have a very weak intermolecular correlation with the carbons of PG (β-sheet).

(a) PLV (β-sheet): Hα
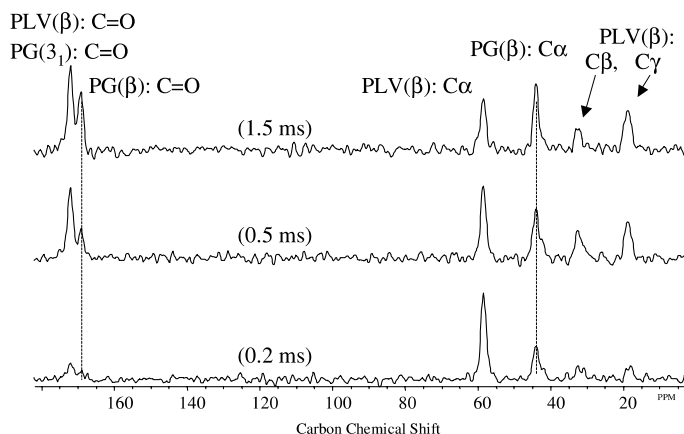
(b) PLV (β-sheet): HN
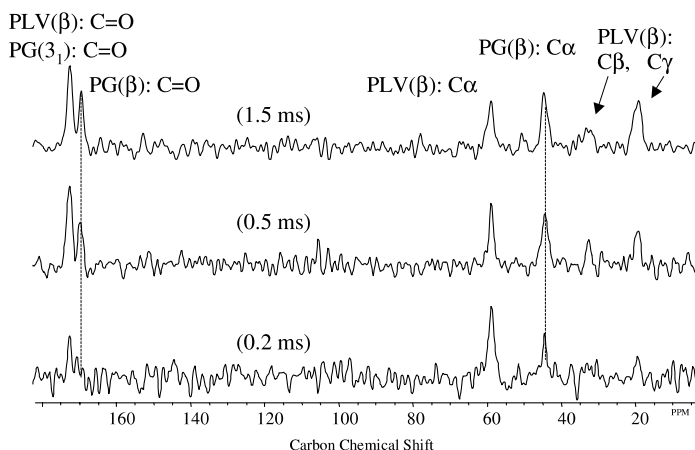
Fig. 27.   One-dimensional slices along the horizontal axis of the 2D FSLG ^{13}C–^{1}H HETCOR spectra taken at (a) 5.6 ppm (PLV (β) : Hα) and (b) 10.3 ppm (PLV (β) : HN) on the ^{1}H chemical shift axis. The contact time used in this experiment: 1.5, 0.5 and 0.2 ms.

The molecular modeling shows that side chain protons are not so far from each other, as the distances of PLV(β-sheet)Hγ–PG(β-sheet)Cα and PLV(β-sheet)Hγ–PG(β-sheet)C=O are in the 3.32–6.65 and 3.27–7.10 Å ranges, respectively. It is caused by rapid rotational motion of the methyl group of PLV.

Table 15. Observed 2D FSLG ^{13}C–^{1}H HETCOR correlation peaks of PG/PLV (50/50) blend sample and calculated carbon–proton distances for antiparallel β-sheet for the PG–PLV

Polypeptides	Calculated carbon–proton distances (Å)		Contact time (ms)		
			0.2	0.5	1.5
PG–PG	Cα–Hα	1.08	◉	◉	◉
	Cα–HN	2.15	△	◉	◉
	C=O–Hα	2.15	△	◉	◉
	C=O–HN	1.98		◉	◉
PLV–PLV	Cα–Hα	1.08	◉	◉	◉
	Cα–Hβ	2.15	△	◉	◉
	Cα–Hγ	2.53–3.39	△	◉	◉
	Cα–HN	2.15	△	◉	◉
	Cβ–Hα	2.15		○	○
	Cβ–Hβ	1.08	◉	◉	◉
	Cβ–Hγ	2.15	◉	◉	◉
	Cβ–HN	2.89			
	Cγ–Hα	2.68–3.43		◉	◉
	Cγ–Hβ	2.15	△	◉	◉
	Cγ–Hγ	1.08	◉	◉	◉
	Cγ–HN	2.67–3.64		△	○
	C=O–Hα	2.15	△	◉	◉
	C=O–Hβ	2.62–2.72		◉	◉
	C=O–Hγ	2.39–4.15		◉	◉
	C=O–HN	1.98		◉	◉
PG–PLV	Cα–Hα	3.09–3.30		◉	◉
	Cα–Hβ	4.03–6.04			
	Cα–Hγ	3.32–6.65			
	Cα–HN	3.93–4.23		◉	◉
	C=O–Hα	3.80–4.00		○	○
	C=O–Hβ	4.34–6.70			
	C=O–Hγ	3.27–7.10			
	C=O–HN	3.17		○	○
PLV–PG	Cα–Hα	3.17–3.34		△	△
	Cα–HN	4.00–4.23			
	Cβ–Hα	3.90–6.54			
	Cβ–HN	4.12–5.04			
	Cγ–Hα	3.56–6.32			◉
	Cγ–HN	3.21–6.20			
	C=O–Hα	3.72–4.01		△	△
	C=O–HN	3.17		△	△
			~2.15 Å	~4.23 Å	~6.32 Å

◉ = strong peak intensity; ○ = moderate peak intensity; △ = weak peak intensity.

The relationship between intra- and intermolecular correlation signals from the 2D FSLG ^{13}C–^1H HETCOR spectra and carbon–proton distances from the modeled structure is shown in Table 15.

The CP experiments on polymer blend systems, using a mixture of two polymers in which one is deuterated and another is protonated, have been carried out in order to elucidate their miscibility. This information is given by whether protons in the protonated polymer are cross-polarized to deuterons of the other deuterated polymer or not.[36,122–126] These studies show that effective ^1H–^{13}C CP transfer may be limited to about 10 Å. In the present FSLG ^{13}C–^1H HETCOR experiments, spin diffusion in protons can be avoided to a certain extent. From the above experimental results, it is found that PG with the β-sheet form and PLV with the β-sheet form are blended with each other on the scale below 10 Å.

The miscibility scale of PG/PLV (50/50) has been shown to be about 3 nm by the ^1H $T_{1\rho}$ experiments.[72,73] These values are consistent with each other because the value of 2–3 nm is the upper-limit of the domain size.[54] Thus, it can be said that the 2D FSLG ^{13}C–^1H HETCOR experiments do not conflict with the ^1H $T_{1\rho}$ experiments reported previously. These results show that the PG and PLV chains in the blend are sufficiently close to each other to make intermolecular hydrogen bonds.

6. CONCLUSIONS

From these results, it can be said that the helix and β-sheet forms of PLA, PG or PDA in the blend samples are incorporated into the PLIL or PLV in the β-sheet form and then takes the β-sheet form by forming hydrogen bonds with the β-sheet form of PLIL or PLV. This means that polypeptide chains, by changing from the helix form to the β-sheet form are hydrogen-bonded with β-sheet type polypeptide chains which are energetically more stable than the helix form of the polypeptide chains hydrogen-bonded by themselves.

Finally, it is concluded that solid state high resolution NMR spectroscopy (^{13}C CP/MAS, ^1H $T_{1\rho}$ and 2D FSLG ^{13}C–^1H HETCOR) is a very useful methodology for elucidating the conformational stability and miscibility of polypeptide blends.

REFERENCES

1. E. M. Bradbury, A. R. Downie, E. A. Lliott and W. E. Hanby, *Proc. Roy. Soc. London Ser.*, 1960, **259**, 110.
2. R. H. Karson, K. S. Norland, G. D. Fasman and E. R. Bluot, *J. Am. Chem. Soc.*, 1960, **82**, 2268.
3. B. R. Malcom, *Biopolymers*, 1970, **9**, 911.
4. H. Kyotani and H. Kanetsuna, *J. Polym. Sci., Polym. Phys.*, 1972, **10**, 1931.

5. H. Saito, R. Tabeta, I. Ando, T. Ozaki and A. Shoji, *Chem. Lett.*, 1983, 1437.
6. M. Okabe, T. Yamanobe, T. Komoto, J. Watanabe and I. Ando, *J. Mol. Structure*, 1989, **213**, 213.
7. T. Akieda, H. Mimura, S. Kuroki, H. Kurosu and I. Ando, *Macromolecules*, 1992, **25**, 5794.
8. J. C. Andries, J. M. Anderson and A. G. Walton, *Biopolymers*, 1971, **10**, 1049.
9. H. Saito, T. Tabeta, A. Shoji, T. Ozaki, I. Ando and T. Miyata, *Biopolymers*, 1984, **23**, 2279.
10. H. Saito, T. Tabeta, T. Asakura, Y. Iwanaga, A. Shoji, T. Ozaki and I. Ando, *Macromolecules*, 1984, **17**, 1405.
11. S. Ando, T. Yamanobe, I. Ando, A. Shoji, T. Ozaki, T. Tabeta and H. Saito, *J. Am. Chem. Soc.*, 1985, **107**, 7648.
12. E. R. Andrew, A. Bradbury and R. G. Eades, *Nature*, 1959, **183**, 1802.
13. A. Pines, M. G. Gibby and J. S. Waugh, *J. Chem. Phys.*, 1973, **59**, 569.
14. S. R. Hartmann and E. L. Hahn, *Phys. Rev.*, 1962, **128**, 2042.
15. J. Schaefer and E. O. Stejskal, *J. Am. Chem. Soc.*, 1976, **98**, 1031.
16. R. A. Komoloski, ed., *High Resolution NMR of Synthetic Polymers in Bulk*, VCH, Deerfield Beach, FL, 1986.
17. H. Saito, R. Tabeta, A. Shoji, T. Ozaki and I. Ando, *Macromolecules*, 1983, **16**, 1050.
18. I. Ando, H. Saito, R. Tabeta, A. Shoji and T. Ozaki, *Macromolecules*, 1984, **17**, 457.
19. A. Shoji, T. Ozaki, H. Saito, R. Tabeta and I. Ando, *Macromolecules*, 1984, **17**, 1472.
20. H. Saito, R. Tabeta, A. Shoji, I. Ando and T. Asakura, *Magnetic Resonance in Biology and Medicine*, G. Govil, C. L. Khetrapal, and A. Saran, eds., Tata McGraw-Hill, New Delhi. India, 1985, 195.
21. H. Saito and I. Ando, *Ann. Rep. NMR Spectrosc.*, 1989, **21**, 210.
22. I. Ando, T. Yamanobe and N. Asakawa, *Prog. NMR Spectrosc.*, 1990, **22**, 349.
23. S. Tuzi, S. Sakamaki and I. Ando, *J. Mol. Structure*, 1990, **221**, 289.
24. A. Shoji, S. Ando, S. Kuroki, I. Ando and G. A. Webb, *Ann. Rep. NMR Spectrosc.*, 1993, **26**, 55.
25. N. Asakawa, T. Kameda, S. Kuroki, H. Kurosu, S. Ando, I. Ando and A. Shoji, *Ann. Rep. NMR Spectrosc.*, 1998, **35**, 55.
26. I. Ando and T. Asakura, eds., *Solid State NMR of Polymers*, Elsevier Science, Amsterdam, 1998, 819.
27. J. Nakano, S. Kuroki, I. Ando, T. Kameda, H. Kurosu, T. Ozaki and A. Shoji, *Biopolymers*, 2000, **54**, 81.
28. T. Taki, S. Yamashita, M. Satoh, A. Shibata, T. Yamashita, R. Tabeta and H. Saito, *Chem. Lett.*, 1981, 1803.
29. D.-K. Lee and A. Ramamoorthy, *J. Phys. Chem. B*, 1999, **103**, 271.
30. Y. Wei, D.-K. Lee and A. Ramamoorthy, *J. Am. Chem. Soc.*, 2001, **123**, 6118.
31. T. Kameda and T. Asakura, *Ann. Rep. NMR Spectrosc.*, 2002, **46**, 101.
32. E. O. Stejskal, J. Schaefer, M. D. Sefcik and R. A. Mckay, *Macromolecules*, 1981, **14**, 275.
33. L. C. Dickinson, H. Yang, C. W. Chu, R. S. Stein and J. C. W. Chien, *Macromolecules*, 1987, **20**, 1757.
34. C. W. Chu, L. C. Dickinson and J. C. W. Chien, *Polymer Bull.*, 1988, **19**, 265.
35. J. F. Parmer, L. C. Dickinson, J. C. W. Chien and R. S. Porter, *Macromolecules*, 1989, **22**, 1078.
36. X. Zhang, A. Natansohn and A. Eisenberg, *Macromolecules*, 1990, **23**, 412.
37. C. Marco, J. G. Fatou, M. A. Gomez, H. Tanaka and A. E. Tonelli, *Macromolecules*, 1990, **23**, 2183.
38. C. W. Chu, L. C. Dickinson and J. C. W. Chien, *J. Appl. Polym. Scil.*, 1990, **41**, 2311.
39. B. Mohanty, J. Watanabe, I. Ando and K. Sato, *Macromolecules*, 1990, **23**, 4908.
40. L. Jong, E. M. Pearce, T. K. Kwei and L. C. Dickinson, *Macromolecules*, 1990, **23**, 5071.
41. J.-F. Masson and R. St. J. Manley, *Macromolecules*, 1992, **25**, 589.
42. C. Brosseau, A. Guillermo and J. P. Cohen-Addad, *Polymer*, 1992, **33**, 2076.
43. C. Brosseau, A. Guillermo and J. P. Cohen-Addad, *Macromolecules*, 1992, **25**, 4535.

44. J. Gluss, K. Schmidt-Rohr and H. W. Spiess, *Acta. Polymer*, 1993, **44**, 1.
45. S. Schantz and N. Ljungqvist, *Macromolecules*, 1993, **26**, 6517.
46. T. K. Kwei, Y. K. Dai, X. Lu and R. A. Weiss, *Macromolecules*, 1993, **26**, 6583.
47. A. Asano, K. Takegoshi and K. Hikichi, *Polymer*, 1994, **35**, 5630.
48. D. E. Demco, A. Johansson and J. Tegenfeldt, *Solid State Nucl. Magn. Reson.*, 1995, **4**, 13.
49. T. Miyoshi, K. Takegoshi and K. Hikichi, *Polymer*, 1996, **37**, 11.
50. D. L. VanderHart and G. B. McFadden, *Solid State Nucl. Magn. Reson.*, 1996, **7**, 45.
51. S.-Y. Kwak and N. Nakajima, *Macromolecules*, 1996, **29**, 3521.
52. S.-Y. Kwak, J.-J. Kim and U. K. Kim, *Macromolecules*, 1996, **29**, 3560.
53. M. Guo, *Macromolecules*, 1997, **30**, 1234.
54. A. Asano and K. Takegoshi, *Solid State NMR of Polymers.*, Chapter 10, I. Ando and T. Asakura, eds., Elsevier Science, Amsterdam, 1998, p. 351.
55. B.-J. Van Rossum, H. Forester and H. J. M. de Groot, *J. Mag. Reson.*, 1997, **124**, 516.
56. P. Caravatti, G. Bodenhausen and R. R. Ernst, *Chem. Phys. Lett.*, 1982, **89**, 363.
57. P. Caravatti, L. Braunschweiler and R. R. Ernst, *Chem. Phys. Lett.*, 1983, **100**, 305.
58. D. P. Burum and A. Bielecki, *J. Magn., Reson.*, 1991, **94**, 645.
59. A. Bielecki, D. P. Burum, D. M. Rice and F. E. Karasz, *Macromolecules*, 1991, **24**, 4820.
60. C. E. Bronnimann, C. F. Ridenour, D. R. Kinney and G. E. Maciel, *J. Magn. Reson.*, 1992, **97**, 522.
61. S. Kaplan, *Macromolecules*, 1993, **26**, 1060.
62. C. H. Wu, A. Ramamoorthy and S. J. Opella, *J. Magn. Reson.*, 1994, **109A**, 270.
63. K. Takegoshi and K. Hikichi, *Polymer J.*, 1994, **26**, 1377.
64. J. L. White and P. A. Mirau, *Macromolecules*, 1994, **27**, 1648.
65. S. Li, D. M. Rice and F. E. Karasz, *Macromolecules*, 1994, **27**, 2211.
66. S. Li, D. M. Rice and F. E. Karasz, *Macromolecules*, 1994, **27**, 6527.
67. P. A. Mirau and J. L. White, *Magn. Reson. Chem.*, 1994, **32**, S23.
68. Z. Gu, C. F. Ridenour, C. E. Bronnimann, T. Iwashita and A. McDermott, *J. Am. Chem. Soc.*, 1996, **118**, 822.
69. J. J. Balbach, Y. Ishii, O. N. Antzutkin, R. D. Leapman, N. W. Rizzo, F. Dyda, J. Reed and R. Tycko, *Biochemistry*, 2000, **39**, 13748.
70. B.-J. van Rossum, C. P. de Groot, V. Ladizhansky, S. Vega and H. J. M. de Groot, *J. Am. Chem. Soc.*, 2000, **122**, 3465.
71. B.-J. van Rossum, E. A. M. Schulten, J. Raap, H. Oschkinat and H. J. M. de Groot, *J. Magn. Reson.*, 2002, **155**, 1.
72. K. Murata, S. Kuroki, H. Kimura and I. Ando, *Biopolymers*, 2002, **64**, 26.
73. K. Murata, S. Kuroki and I. Ando, *Polymer*, 2002, **43**, 6871.
74. K. Murata, H. Kono, E. Katoh, S. Kuroki and I. Ando, *Polymer*, 2003, **44**, 4021.
75. E. R. Blout, P. Doty and J. T. Yang, *J. Am. Chem. Soc.*, 1957, **79**, 749.
76. M. Galvin, J., Jr., Hermans and H. A. Scheraga, *J. Am. Chem. Soc.*, 1959, **81**, 5048.
77. G. D. Fasman, *Poly-α-Amino Acid*, Chapter 11, Marcel Dekker, Inc., New York, 1967.
78. S. Tuzi, T. Komoto, I. Ando, H. Saito, A. Shoji and T. Ozaki, *Biopolymers*, 1987, **26**, 1983.
79. X. Zhang, K. Takegoshi and K. Hikichi, *Polymer J.*, 1991, **23**, 87.
80. P. Tang, J. A. Reimer and M. M. Denn, *Macromolecules*, 1993, **26**, 4269.
81. M. Guo, *TRIP*, 1996, **4**, 238.
82. S. Schantz, *Macromolecules*, 1997, **30**, 1419.
83. R. K. Harris, *State of the art for solids,* Chemistry in Britain, 1993, 601.
84. D. R. Paul and S. Newmann, eds., *Polymer Blends,* Vol. 1, Academic Press, New York, 1979, 353.
85. O. Olabisi, L. M. Robeson and M. T. Shaw, *Polymer-Polymer Miscibility*, Academic Press, New York, 1979.
86. D. C. Douglass and V. J. McBrierty, *Macromolecules*, 1978, **11**, 766.
87. V. J. McBrierty, D. C. Douglass and T. K. Kwei, *Macromolecules*, 1978, **11**, 1265.

88. B. Albert, R. Jerome, P. Teyssie, G. Smyth and V. J. McBrierty, *Macromolecules*, 1984, **17**, 2552.
89. B. Albert, R. Jerome, P. Teyssie, G. Smyth, N. G. Boyle and V. J. McBrierty, *Macromolecules*, 1985, **18**, 388.
90. D. L. VanderHert, *Macromol. Chem.* Macromol. Symp., 1990, **34**, 125.
91. J. R. Havens and D. L. VanderHert, *Macromolecules*, 1985, **18**, 1663.
92. R. A. Assink, *Macromolecules*, 1978, **11**, 1233.
93. D. C. Douglass and G. P. Jones, *J. Chem. Phys.*, 1966, **45**, 956.
94. Z. Gao, A. Molnar, F. G. Morin and A. Eisenberg, *Macromolecules*, 1992, **25**, 6460.
95. L. Jong, E. M. Pearce and T. K. Kwei, *Polymer*, 1993, **34**, 48.
96. A. Asano, K. Takegoshi and K. Hikichi, *Polym. J.*, 1992, **24**, 555.
97. J. E. Roberts, S. Vega and R. G. Griffin, *J. Am. Chem. Soc.*, 1984, **106**, 2506.
98. J. S. Waugh, L. M. Hubr and U. Haeberlen, *Phys. Rev. Lett.*, 1968, **20**, 180.
99. P. Mansfield, *J. Phys.*, 1971, **C4**, 1444.
100. W.-K. Rhim, D. D. Elleman, L. B. Schreiber and R. W. Vaughan, *J. Chem. Phys.*, 1974, **60**, 4595.
101. W.-K. Rhim, D. D. Elleman and R. W. Vaughan, *J. Chem. Phys.*, 1973, **59**, 3740.
102. D. P. Burum and W. K. Rhim, *J. Chem. Phys.*, 1979, **71**, 944.
103. D. P. Burum, M. Linder and R. R. Ernst, *J. Magn. Reson.*, 1981, **44**, 173.
104. G. E. Pake, *J. Chem. Phys.*, 1948, **16**, 327.
105. J. E. Roberts, G. S. Harbison, M. G. Munowitz, J. Herzfeld and R. G. Greffin, *J. Am. Chem. Soc.*, 1987, **109**, 4163.
106. M. G. Munowitz, R. G. Griffin, G. Bodenhausen and T. H. Huang, *J. Am. Chem. Soc.*, 1981, **103**, 2529.
107. M. G. Munowitz and R. G. Griffin, *J. Chem. Phys.*, 1982, **76**, 2848.
108. M. G. Munowitz, W. P. Aue and R. G. Griffin, *J. Chem. Phys.*, 1982, **77**, 1686.
109. M. G. Munowitz and R. G. Griffin, *J. Chem. Phys.*, 1983, **78**, 613.
110. A. C. Kolbert, H. J. M. de Groot, M. H. Levitt, M. G. Munowitz, J. E. Roberts, G. S. Harbison, J. Herzfeld and R. G. Griffin, *Multinuclear Magnetic Resonance in Liquids and Solids-Chemical Applications*, Kluwer Academic Publishers, The Netherlands, 1990, 339.
111. A. C. Kolbert, H. J. M. de Groot and R. G. Griffin, *J. Magn. Reson.*, 1989, **85**, 60.
112. A. Ramamoorthy and S. J. Opella, *Solid State Nucl. Magn. Reson.*, 1995, **4**, 387.
113. A. Bielecki, A. C. Kolbert, H. J. M. de Groot, R. G. Griffin and M. H. Levitt, *Adv. Magn. Reson.*, 1990, **14**, 111.
114. O. B. Peersen, X. Wu, I. Kustanovitch and S. O. Smith, *J. Magn. Reson.*, 1993, **104**, 334.
115. M. Nilges, A. M. Gronenborn, A. T. Brunger and G. M. Clore, *Protein Eng.*, 1988, **2**, 27.
116. A. T. Brunger, *X-PLOR Mannual Version 3.1*, 1993.
117. K. Wüthrich, M. Billeter and W. Braun, *J. Mol. Biol.*, 1984, **180**, 715.
118. S. Kuroki, N. Asakawa, S. Ando, I. Ando, A. Shoji and T. Ozaki, *J. Mol. Structure*, 1991, **245**, 69.
119. S. Kuroki, A. Takahashi, I. Ando, A. Shoji and T. Ozaki, *J. Mol. Structure*, 1994, **323**, 197.
120. K. Tsuchiya, A. Takahashi, N. Takeda, N. Asakawa, S. Kuroki, I. Ando, A. Shoji and T. Ozaki, *J. Mol. Structure*, 1995, **350**, 233.
121. R. A. Sayle and E. J. Milner-White, *Trends Biochem. Sci.*, 1995, **20**, 374.
122. J. Schaefer, M. D. Sefcik, E. O. Stejskal and R. A. McKay, *Macromolecules*, 1981, **14**, 188.
123. J. F. Parmer, L. C. Dickinson, J. C. W. Chien and R. S. Porter, *Macromolecules*, 1987, **20**, 2308.
124. G. C. Gobbi, R. Silvestri, T. P. Russell, J. R. Lyerla, W. W. Fleming and T. Nishi, *J. Polymer. Sci., C, Polymer. Lett.*, 1987, **25**, 61.
125. M. Guo and H. G. Zachmann, *Polymer*, 1993, **34**, 2503.
126. C. M. Roland, J. B. Miller and K. J. McGrath, *Macromolecules*, 1993, **26**, 4967.

Applications of Heteronuclear X/Y-Correlation Spectroscopy in Organometallic and Organoelement Chemistry: Recent Developments

DIETRICH GUDAT

Institut für Anorganische Chemie der Universität Stuttgart, Pfaffenwaldring 55, 70550 Stuttgart, Germany; E-mail: gudat@iac.uni-stuttgart.de

An overview in the application of solution NMR methods involving X/Y correlation between two heteronuclei for the characterisation of organometallic and organoelement compounds is given. The focus is both on recent methodical advances and the exploration of new applications for these techniques. Technical improvements under discussion include in particular the introduction of pulsed field gradient-assisted experiments and of two- and three-dimensional pulse schemes for indirect observation of X/Y correlations through ^{1}H. Current uses of these methods concentrate on the indirect observation of low-γ nuclei with low receptivity, and on the structure elucidation of molecular and polymeric organometallic substrates of increasing degrees of complexity. The examples presented illustrate in particular the application of X/Y correlation spectroscopy in transition metal NMR spectroscopy and for spectral assignment and structure elucidation of organoelement compounds, highlighting the prospect of these methods in modern branches of chemistry such as catalysis studies and organometallic polymer chemistry.

1. INTRODUCTION

Multi-dimensional NMR spectroscopy[1] has in the last few decades developed into an extremely versatile and powerful analytic tool for the constitution of molecular materials of all kinds. The strongpoint – in particular the potential to unravel crowded spectral regions by dispersing NMR signals in more than one-dimension and, furthermore, to map the mutual interactions in a network of coupled nuclei which simplifies the assignment of chemical bond patterns – makes these methods particularly useful for the analysis of large molecules. Consequently, the application of multidimensional NMR to the characterisation of biopolymers has contributed considerably to the recent development of structural biochemistry and biology and, vice versa, the continuing interest in these fields has also promoted the methodological and instrumental development of NMR spectroscopy.

Apart from all of this, multi-dimensional NMR finds considerable and still growing applications in more traditional areas of chemistry. Even if most organometallic and coordination compounds are smaller in size and exhibit simpler spectra than biopolymers, they are composed of a large pool of building blocks whose spectroscopic characteristics are less well known or unknown at all, and the bond connectivity patterns are much more diverse and intricate. Consequently, NMR spectra of organometallic and coordination compounds are less predictable, and multi-dimensional techniques are in many cases indispensable as analytical tools when structural assignments derived from the analysis of one-dimensional NMR spectra remain ambiguous or even incomplete.

In principle, multidimensional NMR experiments can be grouped according to the type of coupling interaction that is responsible for the correlation between nuclear spins, and according to the types of nuclei involved. In liquids, correlations arise generally from dipolar interactions such as NOE, or from J-couplings that are transmitted via the electrons in chemical bonds. The discrimination between homonuclear and heteronuclear experiments involving only one or several nuclides, respectively, is – apart from technical aspects – of importance as heteronuclear correlations offer the further asset of measuring NMR parameters of nuclei with low gyromagnetic ratio δ/γ at enhanced sensitivity. For experiments involving coherence transfer via J-couplings, the signal-to-noise ratio (S/N) is, with neglect of relaxation effects, expressed by the well known relation[2] $S/N \propto \gamma_{exc} \times \gamma_{det}^{3/2}$ where γ_{exc} and γ_{det} denote the gyromagnetic ratios of the excited and detected nucleus, respectively. Thus, for an XY spin system with $\gamma_X > \gamma_Y$, an INEPT or DEPT experiment with initial excitation of X and detection of Y after a single coherence transfer yields an increase of S/N by a factor γ_X/γ_Y with respect to a standard one pulse experiment on the Y-nucleus. The largest amplification is achievable in multi-dimensional 'inverse' or 'indirect' NMR spectroscopy where the nucleus Y is characterised indirectly through its satellites in the X-spectrum. These

experiments start and finish with X-magnetisation and involve two coherence transfer steps, from X to Y and back to X, to give an overall gain in S/N of $(\gamma_X/\gamma_Y)^{5/2}$.

The use of ^1H as source and receptor nucleus X in inverse experiments is particularly advantageous because of obvious reasons: protons are available in many organic and biological as well inorganic and organometallic samples, yield the highest signal enhancement as their gyromagnetic ratio is larger than that of all other nuclei except ^3H, and allow fast pulse repetition rates due to their short T_1 relaxation times. Proton detected inverse spectroscopy has now routinely been implemented for almost any spin-half nucleus.[1–5] Correlations with quadrupolar nuclei are in principle also feasible, but may suffer substantial reductions in the amplitudes of correlation signals induced by rapid transversal relaxation of the quadrupolar nucleus.[2]

Correlations involving two different heteronuclei X,Y[5–9,11] appear on one hand inferior to ^1H-detected inverse spectroscopy as, owing to a smaller gyromagnetic ratio of γ_X as compared to $\gamma_{^1H}$, the expected gains in S/N are smaller. On the other hand, however, these experiments are appealing as they allow one to detect directly the pattern of metal-ligand bonding interactions in metal complexes, or the connectivity between chemically significant heteroatoms in the molecular skeleton of organoelement compounds, and may thus yield more detailed structural information which finally justifies the higher initial effort. Furthermore, X/Y correlated spectroscopy allows for the characterisation of inorganic compounds which lack through-bond communication between protons and heteronuclei in cases where protons are absent, $^nJ_{X,H}$ couplings vanish, or the coherence transfer via small long-range couplings becomes ineffective due to relaxation induced magnetisation losses. The latter situation occurs frequently in transition metal complexes or in main group compounds where chemically reactive heteronuclei in the centre of the molecule need to be protected by bulky substituents and are thus separated by long bond paths from protons on the surface of the molecule.

Even though the widespread use of X/Y correlated spectroscopy was long restricted by the limited availability of spectrometers which were capable of carrying out experiments with irradiation of two different heteronuclei, the potential of these methods was recognised even in the era of cw-spectroscopy when, in the beginning of the 1970s, Mc Farlane and co-workers used $^{19}F\{^{31}P\}$ and $^{19}F\{^{183}W\}$-INDOR schemes for indirect recording of ^{31}P and ^{183}W chemical shifts of the reaction products of tungsten hexafluoride with trimethyl phosphite.[10] The methodology changed with the introduction of FT-spectrometers, with INDOR having been largely superseded by inverse detected two-dimensional spectroscopy, but the application of X/Y correlations continued to receive attention by a small, but steadily increasing group of researchers until today. During recent years, the introduction of multidimensional triple-resonance pulse schemes as key experiments for the structure determinations of proteins and nucleotides[1] has made appropriately

equipped spectrometers more readily available, and opens the way for a more widespread and routine utilisation of triple-resonance experiments in research in inorganic and organometallic chemistry.

Considering that the literature on the development of experimental methods and important fields of application of X/Y correlations in inorganic, organoelement and organometallic chemistry up to 1997 has been covered in earlier reviews,[11] we will focus here on recent improvements of experimental techniques and novel applications for compound characterisation. Despite the recently increasing interest in the application of X/Y correlation spectroscopy in solids,[12,13] this review will cover only solution NMR techniques. Likewise, a survey of specialised triple-resonance NMR experiments devoted to the characterisation of bio-molecules, and their application, is considered beyond the scope of this article.

2. METHODS

In contrast to applications in structural biology where X/Y correlations are nowadays normally executed as ^{1}H detected, three-dimensional experiments because of sensitivity reasons,[14] many studies on inorganic or organometallic compounds are still performed as two-dimensional experiments with direct detection of one heteronucleus and under ^{1}H-decoupling. As compared to these two categories, one-dimensional polarisation transfer methods such as (semi) selective X/Y-INEPT or INDOR-type techniques, which had in the past been shown to be particularly useful for the characterisation of substrates with only one or two heteronuclei,[11] have recently received less attention.[15] NOE-based correlations, which are frequently employed for the structure elucidation of bio-molecules, remain rare, and apart from an earlier report of a ^{13}C/^{6}Li HOESY experiment,[16] have not been further investigated.

Consequently, the remainder of this section will be used to outline further developments and refinements of pulse schemes for two- and three-dimensional X/Y and ^{1}H/X/Y correlations via scalar couplings. Special hardware considerations for triple-resonance experiments and practical aspects such as pulse calibration and relaxation measurements have been discussed in some detail in an earlier review[11] and will not be repeated. Referencing of the chemical shifts of the X and Y nuclei in heteronuclear correlations should be carried out according to the convention recently recommended by IUPAC.[17] Following this protocol, the chemical shift $\delta(X)$ of a heteronucleus X is now referenced by means of a standard reference frequency $\Xi(X)$ with respect to the ^{1}H signal of TMS according to equation (1), with values of $\Xi(X)$ being available for almost all NMR active isotopes of s-, p-, and d-block elements.[17]

$$\delta(X)(\text{ppm}) = 10^6 \times (\nu_{\text{obs}}/\nu_{\text{TMS}}) \times 100/\Xi(X) - 1 \qquad (1)$$

For the description of correlation experiments throughout this review, the following conventions will be used: The detected nucleus in a two- or three-dimensional experiment is written first and is followed by the other nuclei involved in any of the coherence transfer steps of an n-dimensional experiment separated by slashes. Notation in parentheses ( ) denotes an intermediate nucleus in a relayed correlation experiment; this nucleus is actively involved in the coherence transfer sequence but its chemical shift is not sampled in a separate time domain. Notation in { } denotes additional nuclei that are not involved in the coherence transfer but decoupled during acquisition (usually ^{1}H).

2.1. Two-dimensional correlation experiments with detection of a heteronucleus

Even though the choice of the observed nucleus in a two-dimensional X/Y correlation experiment is less obvious than in the case of ^{1}H/X experiments,[11] there seems to be an ongoing trend to the utilisation of 'inverse' pulse schemes that operate with initial excitation and detection of the nucleus of higher gyromagnetic ratio. Nonetheless, conventional HETCOR experiments involving a single polarisation transfer from the nucleus with higher to the one with lower gyromagnetic ratio, and detection of the latter, keep being in use,[18] and in a special case even a 'reverse' ^{13}C/^{119}Sn HMQC experiment operating with excitation and detection of the low-γ nucleus, ^{13}C, was reported.[19]

In general, inverse two-dimensional X/Y correlations involving two spin-1/2 nuclei – which have attracted by far the greatest deal of attention – are carried out by adapting the standard pulse sequences based on single quantum (HSQC) or multiple quantum coherence transfer (HMQC, HMBC) that are commonly employed in ^{1}H/X correlation spectroscopy for X/Y coherence transfer and additional ^{1}H decoupling. A detailed analysis of these basic sequences is found elsewhere,[1] and their adaptation to the use in X/Y correlation spectroscopy has been discussed earlier[11] and need not be repeated. Recent methodological developments of X/Y correlation experiments were mainly directed towards three goals, viz. the incorporation of pulsed field gradients[20] for the selection of desired coherence pathways, the optimisation of coherence transfer amplitudes in the presence of a wide range of coupling constants, and the optimisation of experiments for the indirect detection of groups of several Y-nuclei, e.g., in XY_{n} spin systems.

Reports on the application of pulsed field gradient (PFG) assisted pulse schemes for two-dimensional X/Y correlation spectroscopy focused mainly on the adaptation of HSQC sequences which seemed to perform better than HMQC experiments under these conditions.[21] Although the generalisation of standard pulse sequences for ^{1}H/^{13}C correlation spectroscopy should in principle be straightforward, large spectral ranges and short relaxation
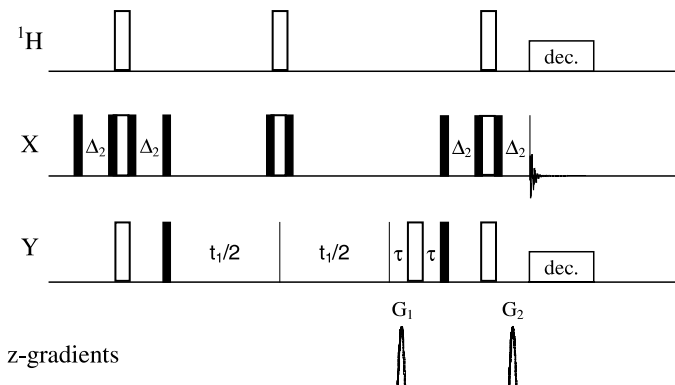
Fig. 1. Pulse sequence for the X/Y{^{1}H} PFG-HSQC experiment as employed for ^{19}F/^{13}C correlation spectroscopy in Ref. 21. 90° and 180° hard pulses are denoted by solid and open bars, respectively; groups of two solid and one open bars denote $90°_\phi - 180°_{\phi+90} - 90°_\phi$ pulse sandwiches that serve as composite 180° pulses. Δ_2 are delays of length $1/(2\,J_{X,Y})$, and τ is a short delay of the same length as the gradient pulse (typically ≈ 1 ms). Phase cycles are as in the standard HSQC experiment, and the ratio of gradient pulse strengths is set to G2/G1 $= \gamma_Y/\gamma_X$. Decoupling is employed using WALTZ-16 (^{1}H) and GARP (Y) pulse trains.

times of many heteronuclei may require special modifications. An example is the adaptation of the PFG-HSQC experiment[22] for ^{19}F/^{13}C correlation by Assemat and Rinaldi[21] to give the pulse scheme shown in Fig. 1 (X $= ^{19}$F, Y $= ^{13}$C). The original sequence was modified to introduce composite pulses in the X-transmitter channel to reduce offset effects, and decoupling of ^{1}H was accomplished by a gated decoupling scheme involving the application of a WALTZ composite pulse decoupling during acquisition and additional $\pi(^1$H)-refocusing pulses to remove $J_{C,H}$ couplings during the mixing and evolution periods. The coherence selection is accomplished by the pair of pulsed field gradients G$_1$ (which is inserted into a τ–π(Y)–τ spin-echo building block in order to avoid the need for large first order phase corrections of the resulting 2D-spectrum) and G$_2$.

   To understand the principle of the coherence selection by the pulsed field gradients, one must consider that the effect of a z-gradient on a coherence is represented in the frame of the product operator formalism[23] as a phase shift $\phi = \mathrm{G} \cdot \sum p_i \gamma_i$ on a spin operator where G denotes the gradient strength (which may be expressed as a product of the gradient amplitude, gradient duration, and a shape factor), and p_i and γ_i the coherence order and gyromagnetic ratio of the nuclear spin i involved in the coherence.[20] The selection of a certain coherence pathway is based on the effect that a proper combination of gradients refocuses signals from desired pathways to give an overall phase shift of zero, while all undesired signals acquire finite phase shifts and thus remain spoiled. Considering that the gradients G$_1$ and G$_2$ are
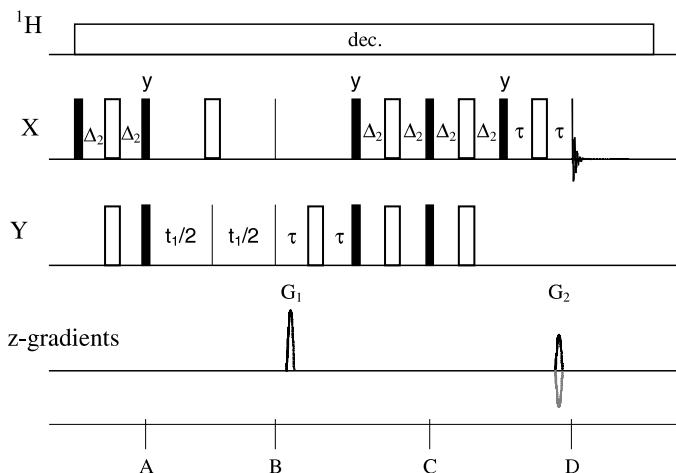
Fig. 2. Pulse scheme for the gradient-selected, sensitivity-enhanced X/Y se-HSQC experiment as employed for $^{31}P/^{15}N$ correlation spectroscopy in Ref. 25. 90° and 180° hard pulses are denoted by solid and open bars, respectively. Δ_2 are delays of length $1/(4 J_{X,Y})$, and τ is a short delay of the same length as the gradient pulse (typically $\approx$ 1 ms). Pulse phases are x, unless specified. The ratio of gradient pulse strengths is set to $G_2/G_1 = \gamma_Y/\gamma_X$, and quadrature detection in F_1 is achieved by recording every transient twice and changing the sign of G_2 in the second scan.

applied when the coherences $\mathbf{Y}^+\mathbf{X}_z$ and $\mathbf{Y}_z\mathbf{X}^-$ are active (for the discussion of coherence pathway selection it is convenient to replace the Cartesian operators $\mathbf{I}_x$ and $\mathbf{I}_y$ by the raising and lowering operators $\mathbf{I}^+ = \mathbf{I}_x + i\mathbf{I}_y$ and $\mathbf{I}^- = \mathbf{I}_x - i\mathbf{I}_y$[20,23]), the final gradient induced phase shift ϕ vanishes only if $\phi = \gamma_X\, G_1 - \gamma_Y\, G_2 = 0$, i.e., when $G_2 = \gamma_Y/\gamma_X \cdot G_1$.[20]

A further variation of an X/Y-HSQC experiment which combines the use of PFGs for coherence selection with sensitivity enhanced (se) HSQC polarisation transfer[24] was designed by Carbajo *et al.*[25] for the indirect observation of ^{15}N NMR spectra of phosphazenes through ^{31}P and is illustrated in Fig. 2 (X = ^{31}P, Y = ^{15}N). The sequence differs from the HSQC-type experiment of Fig. 1 by the continuous application of cpd-decoupling instead of a gated decoupling scheme, and by the extension of the INEPT-back-transfer from Y- to X-spins by a second set of mixing and refocusing pulses. The pulse scheme yields in-phase X-magnetisation which is recorded without Y-decoupling during t_2 to be able to determine the magnitude of $J_{X,Y}$. The coherence selection by the pair of matched pulsed field gradients G_1 and G_2, where $G_2 = \gamma_Y/\gamma_X \cdot G1$ (both of which are in this case embedded in a spin-echo building block) operates as discussed previously. Quadrature detection in the $F1$ dimension is achieved by the echo/anti-echo scheme by recording each t_1-increment twice and changing the sign of the second gradient in the second cycle. The same pulse sequence can be turned into a one-dimensional sequence for the measurement

of isotope-edited X-spectra by using a fixed evolution time t_1 tuned to the magnitude of $J_{X,Y}$.[25]

The principle of the sensitivity improvement in the INEPT back-transfer sequence has been explained by means of a product operator analysis.[26] The initial excitation of X-nuclei and the first INEPT transfer to Y generate, as in a normal HSQC experiment, heteronuclear antiphase magnetisation which is represented by an operator $-2\mathbf{X_z Y_y}$ (point A, Fig. 2). This term evolves then solely under the influence of the chemical shift of Y to yield at the end of $t1$ a state $2\mathbf{X_z Y_y} \cdot \cos(\omega_Y\, t_1) - 2\mathbf{X_z Y_x} \sin(\omega_Y\, t_1)$ which represents the sum of two orthogonal components of heteronuclear antiphase magnetisation (point B, Fig. 2). For a two-spin system consisting of a pair of X- and Y-nuclei, the reverse INEPT sequence transforms this state to yield $\mathbf{X_y} \cdot \cos(\omega_Y. t_1) - 2\mathbf{X_x Y_x} \sin(\omega_Y. t_1)$. At this point (C, Fig. 2) where the signal acquisition in a normal HSQC experiment begins, only the first term contributes to the observable signal while the second one represents multiple-quantum coherences that are unobservable during t_2. In contrast, further evolution during the remainder of the sensitivity improved pulse sequence gives (at point D) $-\mathbf{X_x} \cdot \cos(\omega_Y. t_1) + \mathbf{X_y} \cdot \sin(\omega_Y. t_1)$ where now both terms describe orthogonal components of observable in-phase X-spin magnetisation. Combination of both contributions into a single pure-phase correlation signal by appropriate phase handling results under neglect of imperfection and relaxation effects in a theoretical enhancement of the S/N-ratio by a factor of $(2)^{1/2}$. Further analysis shows, however, that the extended pulse sequence does not provide increased sensitivity for $X_n Y$ spin systems with more than one X-nucleus since here, as in standard HSQC, only one-half of the initial I-spin polarisation remains observable under all conditions.[26]

Comparison of the results of the one-dimensional gradient supported $^{31}P/^{15}N\{^1H\}$-se-HSQC experiment with phase-cycled HSQC and HMQC experiments gave relative S/N-ratios of 0.75:0.92:1 which was, under consideration of the suppression of one of the two possible coherence transfer pathways by the field gradients and the longer duration of the pulse sequence, interpreted in terms of a very good performance.[25] The main benefits of the PFG-es-HSQC sequence were seen, however, in the excellent level of artefact suppression which allowed one to observe correlations via very small couplings even in cases where the active isotopomer is present in low natural abundance and its lines are normally obscured by residual parent signals (Fig. 3).

An approach to observe long-range correlations between different heteronuclei over a large range of magnitudes of $^nJ_{X,Y}$ was suggested by Russell et al.[27] who used the principle of accordion optimisation[28,29] in a modified IMPEACH-MBC[30] pulse scheme, shown in Fig. 4, to observe $^{19}F/^{15}N$ correlations arising from $^nJ_{F,N}$ ($n = 2, 3$) in isomeric fluoropyridines. The experiment differs from a standard HMBC scheme by splitting the fixed mixing delay after the first excitation pulse in HMBC into a spin-echo sequence d/2-180°(Y)-d/2 and a variable accordion delay, vd. The spin-echo element
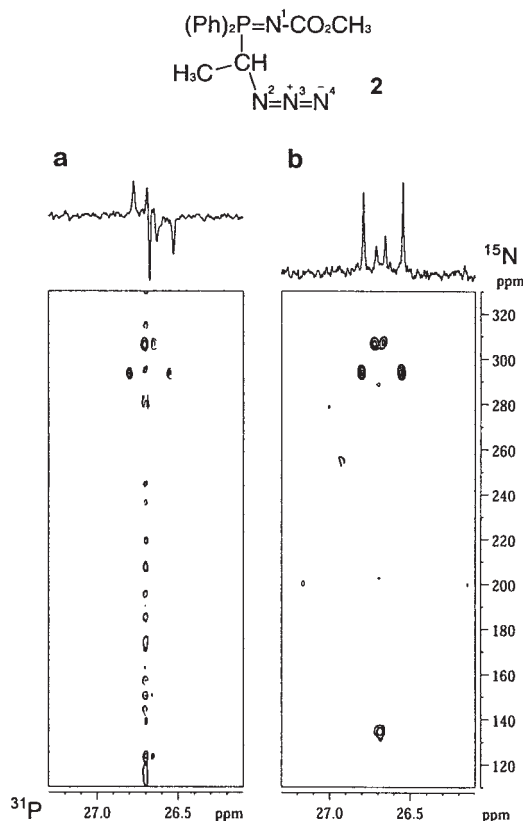
Fig. 3. Sections of two-dimensional ^{31}P/^{15}N{^{1}H} correlation spectra of the azido-substituted monophosphazene derivative shown. The 2D spectra were recorded by using a conventional ^{31}P/^{15}N HMQC pulse scheme with phase-cycling (left), and the gradient-enhanced enhanced sensitivity HSQC pulse sequence of Fig. 2 (right). The one-dimensional spectra on top of the 2D-maps were acquired with the 1D-versions of both pulse sequences. The right spectrum is distinguished by a substantially lower artefact level and displays an additional clearly visible correlation of the ^{31}P with nitrogen atom N^3. Reproduced from Ref. 25 by permission of Elsevier Ltd.

represents a delay whose length is incremented together with t_1 while the accordion delay is concurrently decremented. As components of heteronuclear long-range magnetisation are refocused during d/2 and sampled during vd, the defocusing delay during the whole two-dimensional experiment varies to allow coherence transfer over a range of heteronuclear couplings extending from $J_{min} = 1/(2\ vd_{max})$ to $J_{max} = 1/(2\ vd_{min})$.[27–30] Coherence selection and suppression of parent signals is achieved by a combination of phase-cycling and application of the matched pulsed field gradients G_1 and $G_2 = 2G_1\ \gamma_Y/\gamma_X$; the magnitude of the bipolar gradients G_s can be set to any arbitrary
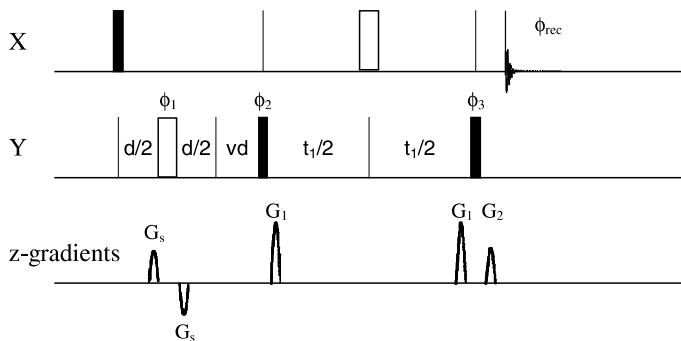
Fig. 4. Modified X/Y IMPEACH-MBC pulse sequence used for ^{19}F/^{15}N shift correlation according to Ref. 27. The notation of 90° and 180° pulses is as before. The $(d/2 - 180°(Y) - d/2)$ element represents a variable delay that is incremented concurrently with the decrementation of the accordion delay vd. Pulse phases are x, unless specified: $\phi_1 = -x$; $\phi_2 = x, -x$; $\phi_3 = x, x, -x, -x$; $\phi_{rec} = x, -x, -x, x$. The bipolar gradients G_s flanking the 180°(Y) pulse can be set to arbitrary power levels, and the relative strengths of the coherence selection gradients G_1 and G_2 are determined by $G_2/G_1 = 2 \ \gamma_Y/\gamma_X$.

power level. Even if the pulse scheme shown was used without ^{1}H decoupling, composite pulse decoupling of protons is obviously accomplishable without any problem provided that one has the availability of a dedicated probe and filter set.

The application of this pulse sequence results in two-dimensional NMR-spectra whose cross peaks show an apparent doublet splitting centred about the chemical shift of the Y-nucleus along F_1 (Fig. 5) which arises from an amplitude modulation of the multiple quantum transfer efficiency. The magnitude of this apparent 'doublet', J_{obs}, is a function of the accordion delay, $vd_{max} - vd_{min}$, the maximum acquisition time, t_{1max}, and the actual heteronuclear coupling constant, $J_{X,Y}$, according to $J_{obs} = J_{X,Y} (vd_{max} - vd_{min})/t1_{max}$.[27] Accordingly, the splitting becomes perceptible only when large $J_{X,Y}$ couplings are sampled, and its size is scaled if the maximum evolution time t_{1max} used in digitising the F_1 frequency domain is increased, or the accordion range is decreased close to a sufficiently narrow window around the actual coupling constant. For most applications the overlap of components of different of these doublets in $F1$ was considered as not problematic.[27]

Indirect detection of the spin-1/2 Y-nuclei of XY_n (or X_mY_n) spin systems is of importance for studying the structures of multinuclear metal complexes and clusters which contain an insensitive (i.e., low-γ) metal nucleus in high natural abundance, or of organometallic aggregates with isotope enriched metal or ligand atoms. Typical examples are represented by metal complexes containing e.g., ^{89}Y (100%), $^{107/109}$Ag (51.8/48.2%), ^{103}Rh (100%), or ^{195}Pt (33.8 %), and by organometallic aggregates containing isotope labelled (e.g., >98% ^{6}Li, ^{15}N, ^{13}C) metal or ligand atoms. Standard indirect detection
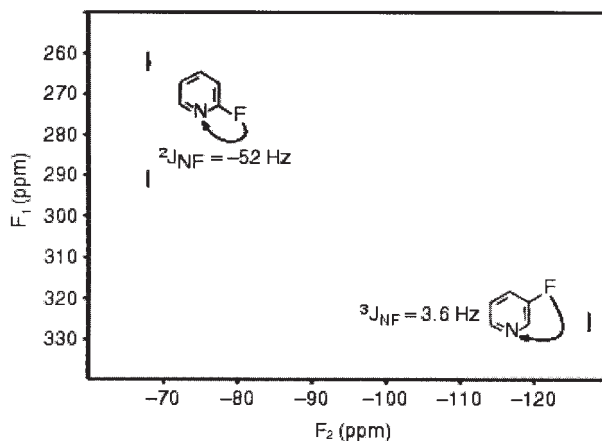
Fig. 5. ^{19}F/^{15}N IMPEACH MBC spectrum of a mixture of 2- and 3-fluoropyridine. The accordion optimisation range was varied from 4 to 50 Hz; the F_1 frequency domain was digitised using 64 increments of the evolution time, t_1. The F_1 'doublet' splitting for the 2-fluoropyridine correlation of $J_{obs} = 728$ Hz (see text) is clearly visible while the smaller one for the 3-fluoropyridine correlation is no longer resolved. Reproduced from Ref. 27 by permission of J. Wiley & Sons.

schemes such as HSQC and HMQC were predominantly designed and optimised for the indirect detection of rare spins such as ^{13}C or ^{15}N whose low natural abundance ensures that only single quantum transitions of the Y-spin are important. In metal clusters and labelled compounds, however, the detected nucleus may couple with several Y-spins at the same time, and multiple quantum transitions of the whole assembly of Y-spins must now be considered. Although the consequences of this effect are in principle understood[31] and the use of the HMQC experiment for the indirect detection of X_mY_n spin systems with several spin-1/2[31] and spin-1 nuclei[32] has been demonstrated, its application is not straightforward but requires special consideration.

Two recent studies focused on a more general analysis of the problem of indirect detection of XY_n spin systems (Y = spin-1/2 nucleus) using the product operator formalism, and on the appropriate optimisation of HMQC and HSQC pulse schemes to perform this task. In their analysis of the effect of a ^{13}C/^{103}Rh-HMQC pulse sequence on the signals of face bridging carbonyls in a rhodium cluster with couplings to three rhodium atoms Heaton et al.[33] showed that the excitation of multiple quantum coherences yields a state whose spin operator is composed of a sum of four terms referred to as zero- one-, two- and three-rhodium spin coherences, respectively. While magnetisation arising from the zero- and two-rhodium spin coherences is suppressed by the standard HMQC phase cycle, the remaining components survive and give rise to observable cross peaks. Of these, however, only the contribution from the

single-rhodium quantum transitions leads to a 'correct' correlation at the true rhodium chemical shift while the triple-rhodium quantum peaks occur at positions that are linear combinations of the chemical shifts of all three metal nuclei involved. Importantly, the magnitude of the 'correct' cross peak reaches a maximum at a defocusing delay of $\sim 1/(5\ J_{Rh,C})$ and equals zero at the conventional defocusing delay of $1/(2\ J_{Rh,C})$ when the three-rhodium spin coherences are at their peak. Accordingly, a HMQC spectrum recorded with a 'conventional' mixing delay of $1/(2\ J_{Rh,C})$ is dominated by the unexpected three-rhodium spin coherences (Fig. 6a), while the expected cross peaks are observable (albeit with an intensity that is nearly a factor of 10 weaker as compared to a XY two-spin system) when the shorter 'unconventional' mixing delay of $1/(5\ J_{Rh,C})$ is used (Fig. 6b).[33]

   The results of Heaton *et al.* were recently confirmed by Xiang *et al.*[34] who were further able to show that the intensity of the desired single-Y quantum peak in an X/Y-HMQC experiment on a general XY_n spin system composed of spin-1/2 nuclei is highest at a mixing time of $d^{opt} = 1/(\pi\ J_{X,Y})\ \text{arccot}(n-1)^{1/2}$ and that the relative strength of this signal vs. the unwanted triple-Y quantum peak can be described (for $n \geq 3$) by the ratio $^1Y_n/^3Y_n = 4\ \tan^{-4}(\pi\ J_{X,Y}\ d)$ which reduces to $^1Y_n/^3Y_n = 4\ (n-1)^2$ when $d = d^{opt}$. The listing of the values for the optimum delay d^{opt}, the relative intensity of the single-Y quantum correlation signal, and the ratio $^1Y_n/^3Y_n$ for XY_n-spin systems containing one–five Y-nuclei in Table 1 confirms that at the optimum condition the unwanted signal is in all cases satisfactorily reduced, but this correlation may become dominant if d is increased significantly above d^{opt}. The above considerations are as well valid for X_mY_n spin systems if X is a spin-1/2 or -1 nucleus and the homonuclear coupling between X-nuclei can be ignored, and the same optimum value for the mixing time as in an HMQC experiment applies as well for HSQC experiments.[34] Furthermore, it should be noted that Nanz and von Philipsborn had previously likewise suggested a value of $1/(4\ J_{X,Y})$ instead of $1/(2\ J_{X,Y})$ as the optimum mixing time in HMQC-type experiments for the inverse detection of pairs of spin-1/2 nuclei in X_mY_2 spin systems,[31] and of single spin-1 nuclei in X_mY spin systems,[32] respectively.

2.2. Proton-detected correlation experiments

The task of generating a display of heteronuclear X/Y-connectivities with optimum sensitivity can in principle be performed by recording a three-dimensional proton detected shift correlation in which the chemical shifts of both heteronuclei X and Y are each sampled in a separate indirect dimension. Three-dimensional fourier transformation of the data then generates a cube which is defined by three orthogonal axes representing the chemical shifts of the three nuclei ^1H, X, Y, and the desired two-dimensional X/Y-correlation is readily obtained as a two-dimensional projection parallel to the axis
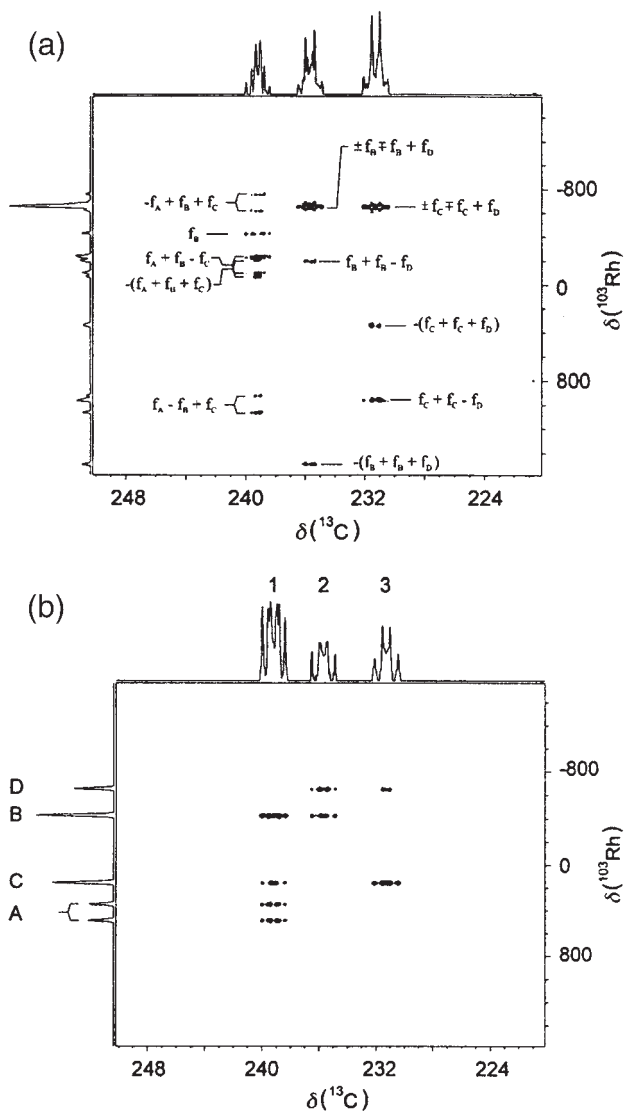
Fig. 6. Expansion of the inverse detected $^{13}C/^{103}Rh$ HMQC NMR spectra of $[Rh_6(CO)_{15}(P\{4\text{-}F\text{-}C_6H_4\}_3)]$ and one-dimensional projections showing the region of the bridging carbonyls. The spectra were obtained with defocusing delays of 17.9 ms ($\approx 1/(2\ J_{Rh,C})$, a) and 7.14 ms ($\approx 1/(5\ J_{Rh,C})$, b), respectively. The expected correlations at the 'true' ^{103}Rh chemical shifts are clearly visible in the bottom spectrum, but are very weak or entirely absent in the top spectrum which displays correlations due to three-rhodium spin coherences as the dominant signals. Reproduced from Ref. 33 by permission of The Royal Chemical Society.

Table 1. Optimum mixing times τ_m for HMQC-type experiments, and absolute intensities ^1Y_n and relative intensities $^1Y_n/^3Y_n$ of single- and triple-Y quantum peaks at the mixing time τ_m for XY_n spin systems; data from Ref. 34

	n				
	1	2	3	4	5
τ_m	$1/2J_{X,Y}$	$1/4J_{X,Y}$	$1/5.1J_{X,Y}$	$1/6J_{X,Y}$	$1/6.8J_{X,Y}$
^1Y_n	1	0.25	0.148	0.106	0.082
$^1Y_n/^3Y_n$			16	36	64

representing the chemical shift of the detected nucleus, ^{1}H (Fig. 7a). Even if this approach to indirect detection of a heteronuclear X/Y-correlation is straightforward, sampling of the complete data cube requires normally a considerable amount of measurement time, and digitising one (or even both) indirect dimensions with high spectral resolution may easily become prohibitive. Regarding, however, that many organometallic or coordination compounds contain only one or two transition metal or heteroatoms of one kind, say Y, the whole information of the three-dimensional data matrix is contained in one or two 2D-slices, and the acquisition time can be greatly reduced if only these relevant cross-sections rather than the whole cube are sampled. One approach to achieve this relies on a back transformation of the three-dimensional experiment by replacing a hard excitation pulse on Y by a frequency-selective 'soft' pulse that excites only a single Y-resonance, and then recording a small set of two-dimensional spectra with fixed mixing times rather than an array of spectra with incremented evolution times.[35] Using this approach, only a few selected H/X-slices of the whole 3D-cube are recorded whose projections on the X/Y-plane contain one-dimensional cross sections of the total X/Y-correlation map that include all connectivities of the X-nuclei to one given Y-nucleus (Fig. 7b). In practice, both approaches have been used for the measurement of indirectly detected X/Y-correlation spectra, and will be discussed in the following two sections.

2.2.1. Three-dimensional ^{1}H/X/Y-correlations

Three-dimensional ^{1}H-detected correlation experiments[1] have so far mainly been applied to the structural characterisation of biological or synthetic polymers whose one-dimensional spectra contain a large number of over-lapping signals of closely similar building blocks that can only be successfully resolved by spectral dispersion in three dimensions. Particular applications devoted to the structure elucidation of heteroatom-doped polymers were elaborated in the first place by the group of Rinaldi.[36–39] Although these experiments were initially designed to characterise structural elements in the backbones of polymers that are composed of a linear carbon chain with some terminal or intermittent phosphorus, tin, or silicon atoms (Fig. 8), they
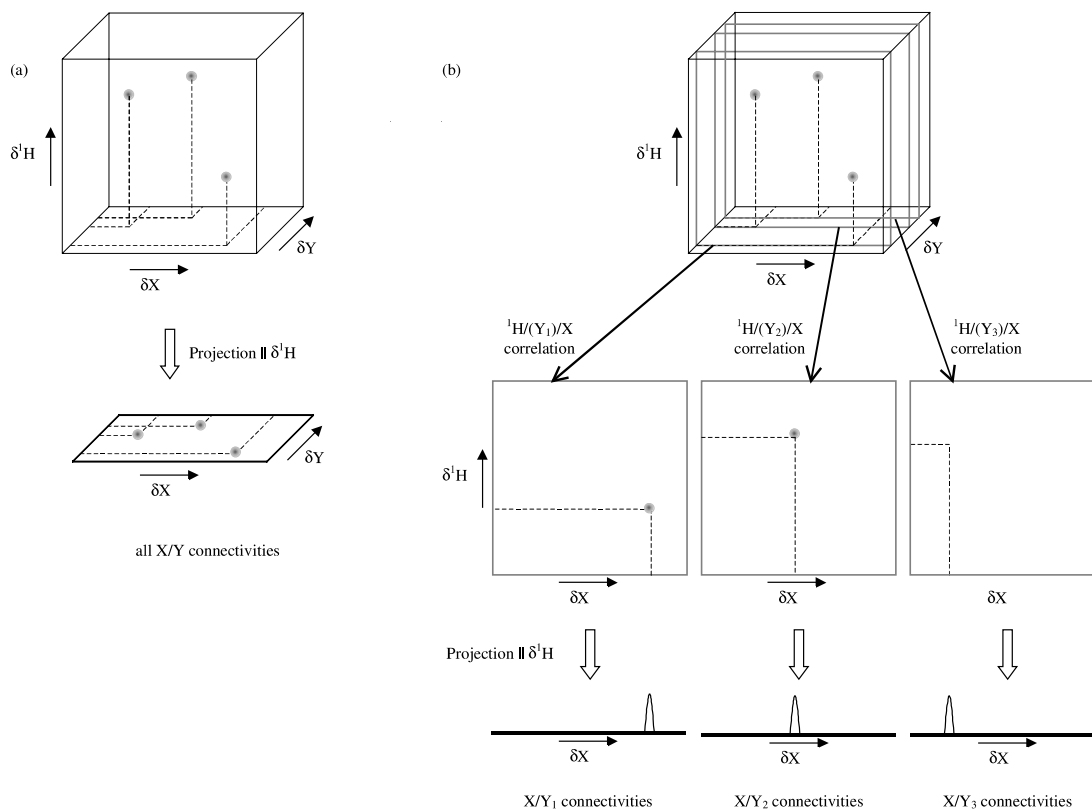
Fig. 7. Schematic representation showing how X/Y correlation maps can be obtained either from the appropriate 2D projection of a three-dimensional ^{1}H/X/Y correlation spectrum (a), or alternatively from a sequence of two-dimensional ^{1}H/Y correlations acquired with relayed ^{1}H/(Y)/X coherence transfer via a selected Y-nucleus as relay.
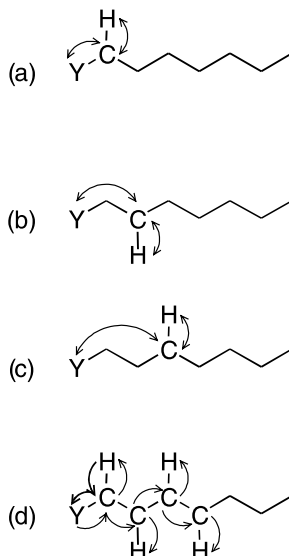
Fig. 8. Schematic representation of heteroatom-containing structural elements in polymers that are disposed for characterisation by ^{1}H/X/Y triple resonance experiments where X $=$ ^{13}C and Y $=$ ^{19}F, ^{31}P, ^{29}Si, ^{119}Sn, with possible coherence transfer pathways being indicated by single and double headed arrows.[36–39] Selective observation of the correlations of the building blocks in (a)–(c) requires experiments involving 'out-and-back' coherence transfer via $^1J_{C,H}/^1J_{C,X}$ (a), $^1J_{C,H}/^2J_{C,X}$ (b), or $^1J_{C,H}/^3J_{C,X}$ (c), whereas the simultaneous observation of all correlation signals originating from a chain of an isotope labelled sample (d) is feasible by means of a HC$^\alpha$(Y)-CC-TOCSY sequence.[39]

are in principle much more generally applicable in the field of organometallic and coordination chemistry and will thus be discussed here.

The experimental schemes described in detail in this section date back to a pulse sequence first introduced by Marino *et al.*[40] for the characterisation of oligonucleotides which uses an 'out-and-back' coherence transfer involving two sequences of double INEPT steps to correlate the chemical shifts of a mutually coupled ^{1}H/X/Y spin-triple. This approach appears recently to be preferred to pulse sequences based on HNCA-type experiments[41] that use a combination of HSQC and HMQC polarisation transfer steps. Two basic implementations of the single-quantum experiment (which has been dubbed HCAP if applied to correlations between the H$^\alpha$, C$^\alpha$ and P atoms in substructures as shown in Fig. 8a with X $=$ ^{31}P[39]) this uses pulsed field gradients for coherence selection are illustrated in Fig. 9.[36,42] Both experiments share the same coherence transfer pathway with the earlier phase-cycled version,[40] involving ^{1}H/X/Y coherence transfer via two consecutive INEPT steps, evolution of δY during t_1, INEPT back-transfer to X and evolution of δX during t_2, and finally a further INEPT back-transfer and detection of
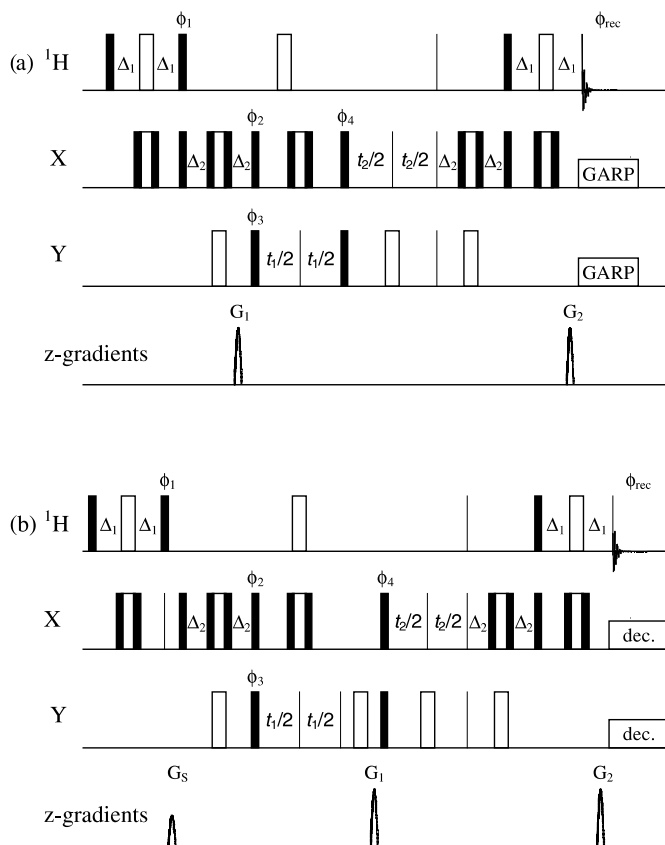
Fig. 9. Pulse sequences for three-dimensional ^{1}H/X/Y correlation experiment using consecutive HSQC transfer steps and pulsed field gradients for coherence selection of ^{1}H/X spin pairs (a)[36] or ^{1}H/Y spin pairs (b),[42] respectively. The notation of 90° and 180° pulses is as before. Delays Δ_1 and Δ_2 are of length $1/(4\,J_{H,X})$ and $1/(4\,J_{X,Y})$, respectively. The relative strengths of the coherence selection gradients G_1 and G_2 are determined by $G_2/G_1 = \gamma_H/\gamma_X$ in a) and $G_2/G_1 = \gamma_H/\gamma_Y$ in b), respectively; the spoil gradient in b) may be set to arbitrary strength. Basic phase cycling is as follows: $\phi_1 = \phi_2 = y$; $\phi_3 = x, -x$; $\phi_4 = y, y, -y, -y$; $\phi_{rec} = x, -x, -x, x$; ϕ_3 and ϕ_4 are incremented during t_1 and t_2 according to the States method.[36] ^{1}H/^{13}C/^{29}Si correlation spectra with pulse sequence b) have been acquired by using an extended phase cycle with $\phi_2 = (x)_4, (y)_4, (-x)_4, (-y)_4$.[42]

^{1}H magnetisation during acquisition. The implementation shown employs decoupling of both X and Y nuclei during acquisition which can be accomplished by means of a GARP sequence, but other variants using adiabatic decoupling schemes or single-channel decoupling of X only have also been presented.

The most significant difference between the two experimental variants includes the positioning of the PFGs which are in the first case (Fig. 9a) set to select signals precessing at the X resonance frequency during G_1 and at the ^{1}H resonance frequency during G_2, and in the second case (Fig. 9b) to select signals which precess at the Y resonance frequency during G_1 and at the ^{1}H-resonance frequency during G_2, respectively. It is easily seen that the gradient filter in the first sequence passes all components arising from ^{1}H/X spin-pairs, regardless of whether the spins are further coupled to a Y-nucleus or not, and that selection of ^{1}H/X/Y spin-triples requires additional support from phase cycling. In contrast, as the coherence selection between the Y- and ^{1}H-nuclei in the sequence of Fig. 9b picks up only those coherence components which have previously passed the relayed ^{1}H/X/Y coherence transfer, the selection of the desired signals needs much less help from phase-cycling, and this implementation gives in practice much better suppression of undesired signals.[39] Consequently, the pulse sequence of Fig. 9a, which has become somewhat out of use recently, should be tolerable in cases where Y is an abundant nucleus (e.g., in ^{1}H/^{13}C/^{31}P correlations) and the requirements for the suppression of the signals of ^{1}H/X spin-pairs with respect to ^{1}H/X/Y spin-triples are less stringent, while the sequence of Fig. 9b is certainly much more suitable for applications such as ^{1}H/^{13}C/^{29}Si correlations where both heteronuclei are rare.

Recent modifications of the sequence of Fig. 9b include several constant time (CT) variants one of which is depicted in Fig. 10a, and the implementation of TOCSY-elements (Fig. 10b) to accomplish scrambling of the magnetisation between several X-nuclei and be able to detect selectively e.g., the signals originating from a chain of several CH_n groups in the vicinity of a heteronuclear spin label (Fig. 8b).[38,39] The version of the single-quantum CT-^{1}H/X/Y experiment[38] (dubbed CT-HCAP if designed for the detection of triples of adjacent H–C–P nuclei) is characterised by the use of a constant time evolution period CT to encode X chemical shifts resembles very much the original experiment of Marino et al.[40] The constant time evolution during $CT = 1/(2\ J_{X,X})$ is required to eliminate the effects of homonuclear $J_{X,X}$ couplings during $t2$ which may lead to undesired additional modulation of correlation signals if samples with several magnetically active X-nuclei such as uniformly ^{13}C-labelled materials are studied (the same argument applies if phosphorus-containing materials with several mutually coupled phosphorus atoms are studied and the X-channel is tuned to ^{31}P). The pulse sequence shown contains four PFGs two of which (G_2 and G_4) are used for coherence selection between ^{1}H- and Y-nuclei and must be calibrated to a relative level of $G_1/G_2 = \gamma_Y/\gamma_H$; furthermore, the sign of G_2 is reversed every other scan for n/p-type peak selection. The remaining two gradients G_1 and G_3 serve as spoil gradients to eliminate undesired transversal magnetisation and further reduce the artefact level in the resulting spectrum; in principle, these gradients may be set to arbitrary levels or even be omitted.
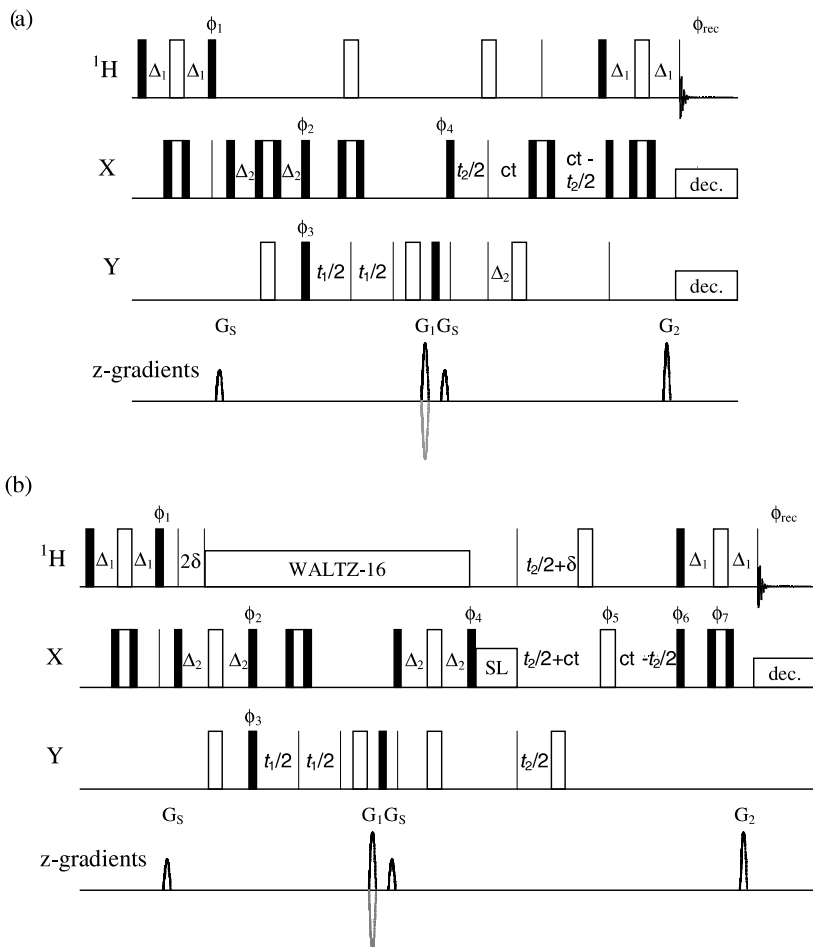
Fig. 10. Variants [38,39] of pulse schemes for three-dimensional ^{1}H/X/Y correlation experiment with consecutive HSQC transfer steps using (a) constant time evolution during t_2 and (b) an additional X,X-TOCSY transfer to spread magnetisation over a system of mutually coupled X-spins. The notation of 90° and 180° pulses is as before. Delays Δ_1 and Δ_2 are of length $1/(4\,J_{H,X})$ and $1/(4\,J_{X,Y})$, respectively, $2\delta \le 1/(2\,J_{X,H})$, and the constant time delay is set to ct $= 1/(2\,J_{X,X})$ in systems with several coupled X-spins. The relative strengths of the coherence selection gradients G_1 and G_2 are determined by $G_2/G_1 = \gamma_H/\gamma_Y$; the remaining gradients were used to purge undesired magnetisation and may be set to arbitrary length. Both sequences were employed with the same basic phase cycle as in Fig. 9, and phase sensitive data sets were acquired by incrementing ϕ_4 according to the States method during t_2 and switching the sign of G_1 in order to achieve echo/anti-echo coherence selection during t_1.[39] An extended phase-cycling scheme for the H(CA)P-CC-TOCSY sequence of (b) involved the following phase shifts: $\phi_1 = y, -y$; $\phi_2 = x, -x$; $\phi_3 = x, x, -x, -x$; $\phi_4 = (x)_4, (-x)_4$; $\phi_5 = (x)_4$, $(y)_4, (-x)_4, (-y)_4$; $\phi_6 = x$; $\phi_7 = \phi_{rec} = (x)_4, (-x)_4$; phase sensitive data sets were acquired by incrementing ϕ_6 according to the States method during t_2 and switching the sign of G_1 in order to achieve echo/anti-echo coherence selection during t_1.[38]

In contrast to the previous three-dimensional pulse sequences which employ an 'out-and-back' coherence transfer scheme where the same proton is initially excited and detected, the variant shown in Fig. 10b uses a TOCSY-sequence to spread coherences over a spin-system of mutually coupled X-nuclei and finally picks up the observable magnetisation, after a last back-transfer, from different proton signals as were initially excited.[38,39] The initial part of this H(Xa)Y-XX-TOCSY sequence (which was originally implemented for $X = {}^{13}C$ and $Y = {}^{31}P$[38,39]) uses, as before, two consecutive INEPT steps to generate heteronuclear double antiphase magnetisation described by an operator $^1\mathbf{H_zX_zY_x}$. As the magnetisation will finally not be transferred back to the proton from where it originated, the evolution of heteronuclear $J_{X,H}$ coupling during the sequence cannot simply be refocused by the application of $\pi(^1H)$ pulses in the middle of the evolution periods t_1 and t_2, but is eliminated by the application of ^1H decoupling after a refocusing delay 2δ after the first INEPT transfer to X. The $^1\mathbf{H_zX_zY_x}$ double antiphase magnetisation is allowed to evolve during $t1$, phase encoded by a pulsed field gradient, and shifted back by a further INEPT step to yield heteronuclear antiphase magnetisation $^1\mathbf{H_zX_y}$. At this point, a spin-lock pulse distributes the magnetisation over the whole system of mutually coupled X-nuclei. A constant evolution period $(CT = 1/(2 J_{X,X}))$ is used to encode the X chemical shift during t_2, and magnetisation is finally transferred back to ^1H for detection. As before, the pair of matched gradients G2 and G4 provide for coherence selection between the ^1H- and Y-nuclei while G1 and G3 represent additional spoil gradients which serve for a further reduction of the artefact level.

The application of the pulse sequence of Fig. 10b to a sample containing several structural elements of the type shown in Fig. 8a–c (where Y may e.g., denote a heteroatom such as ^{31}P or ^{29}Si, and X the ^{13}C-nuclei of the backbone under conditions of uniform ^{13}C-labelling) gives rise to a three-dimensional spectrum whose H/X planes, taken at the chemical shift of an individual Y-atom, represent a two-dimensional correlation of all X signals coupled with the selected Y-atom. Recognising that there are circumstances when the Y signals of different fragments in a sample are not very well resolved, Rinaldi et al. suggested a modification of the pulse sequence which places the t_1 chemical shift evolution period to encode the X chemical shift before the application of the spin lock, making the experiment a three-dimensional $HX^\alpha(Y)$-XX-TOCSY experiment where the Y nuclei are merely used as a relay in the coherence transfer pathway.[39] Considering that the coherence transfer efficiency in the CT-experiments of Fig. 10 depends on the matching between the constant time delay and $J_{X,X}$ it is expected that the experiments behave particularly well for samples with several mutually coupled X-nuclei and a narrow distribution of $J_{X,X}$ (which for example is fulfilled for ^{13}C-labelled materials with the structural elements in Fig. 8d) but might
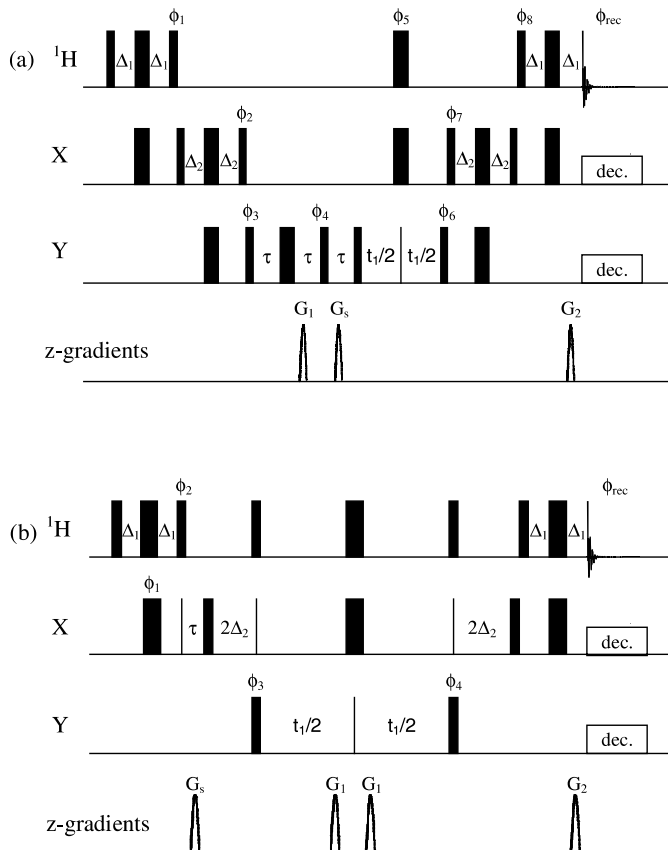
Fig. 11. Pulse sequences for ^{31}P-relayed ^{1}H/(X)/Y correlation via double INEPT (a) or INEPT/HMQC coherence transfer (b).[43] Filled and open bars represent 90° and 180° pulses. Delays were set to $\Delta_1 = 1/(4\ J_{X,H})$ and $\Delta_2 = 1/(4\ J_{X,Y})$, respectively, and τ was chosen as short as possible still to allow gradient recovery. Heteronuclear GARP decoupling was applied to X or both X and Y during acquisition. Pulse and receiver phase cycles and gradient strengths were as follows: a) $\phi_1 = \phi_2 = \phi_7 = \phi_8 = y$; $\phi_3 = (y)_2,\ (-y)_2$; $\phi_4 = -y$; $\phi_5 = (x)_4,\ (-x)_4$; $\phi_6 = x,\ -x$ (incremented after each scan according to the TPPI scheme); $\phi_{rec} = x,\ -x,\ -x,\ x$; $G_2 = G_1 \cdot \gamma(Y)/\gamma(H)$. b) $\phi_1 = x_4,\ -x_4$; $\phi_2 = y$; $\phi_3 = x,\ -x$; $\phi_4 = (x)_2,\ (-x)_2$; $\phi_{rec} = x,\ -x,\ -x,\ x$; $G_2 = G_1 \cdot 2\gamma(X)/\gamma(H)$.

show low-intensity cross peaks or even missing correlations for samples with a large spread of $J_{X,X}$ values.

2.2.2. Two-dimensional ^{1}H/Y-correlations with relayed coherence transfer

As mentioned already, indirect detection of the Y-signals of compounds that contain a structural fragment of the type shown in Fig. 8a but exhibit

only a single (or a few) X-atoms may not require to sample the whole three-dimensional data matrix, while conducting a triple-resonance experiment may still be inevitable, e.g., if the direct $J_{Y,H}$ coupling is zero and recording a simple heteronuclear H/Y correlation remains thus unfeasible. A situation of this type is frequently encountered in metal complexes or organoelement compounds with bulky substituents where long bond paths between peripheral protons and the metal or heteroatom of interest suppress any direct $J_{Y,H}$ couplings, whereas $J_{X,H}$ and $J_{Y,X}$ couplings to a common intermediate heteroatom are still observable. Two experimental schemes for ^{1}H-detected two-dimensional ^{1}H/Y correlations with relayed ^{1}H $\rightarrow$ X/X $\rightarrow$ Y coherence transfer which were originally suggested for the analysis of phosphorus compounds (X $=$ P)[43] but should be more generally applicable, are shown in Fig. 11.

The first sequence shown in Fig. 11a[43] differs from the three-dimensional version shown in Fig. 9b essentially by replacing the former evolution period $t2$ which served to sample the chemical shift of the Y nuclei by a fixed delay tuned to $1/(2\ J_{X,Y})$, and further by replacing the unselective excitation and refocusing pulses in the X-channel by low power rectangular or shaped (Gaussian) pulses to achieve the selective irradiation of a specifically chosen relay nucleus X. The desired magnetisation is selected by the application of a pair of matched pulsed field gradients G_1 and G_2, and any unwanted magnetisation is further suppressed by an additional spoil gradient G_s. Phase sensitive quadrature detection in F_1 is achieved by phase-cycling according to the States-TPPI method. The application of heteronuclear decoupling during acquisition on one or both channels is straightforward, but the elimination of active $J_{X,H}$ and $J_{X,Y}$ couplings in F_1 by the π-pulses to ^{1}H and X in the middle of t_1 requires some further consideration. If both the $\pi/2$- and π-pulses on X are selective, only couplings to the *excited* X nucleus are refocused while the remaining ones may lead to signal broadening or splitting in F_1. 'Broadband decoupling' may in principle be achieved by unselective π-pulses, however, this requires all X chemical shifts to be in the excitation range of the refocusing pulse and decoupling may become unfeasible if the range of X chemical shifts is too large. In order to prevent a reduction of cross peak intensities by pulse imperfections at large off-resonance frequencies, it was suggested to employ *selective* refocusing of active $J_{X,Y}$ couplings and consider splitting by passive couplings as a source of additional structural information.[43] A similar implementation of a two-dimensional ^{1}H/X/Y correlation with relayed coherence transfer, that differs from the experiment of Fig. 11a mainly by the use of an echo/anti-echo scheme for coherence selection, was also recently reported by Koch *et al.*[44]

A remaining limitation of the pulse sequence shown – the restriction of the accessible spectral range of Y nuclei which results as a consequence of the need to apply π-pulses to the Y-channel – is circumvented by the sequence shown in Fig. 11b[43] which uses INEPT for the ^{1}H/X and a HMQC scheme for the
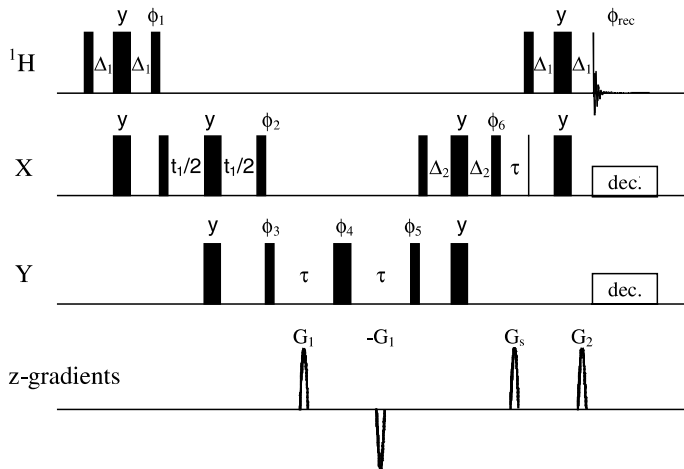
Fig. 12. Pulse sequence for ^{1}H detected determination of $J_{X,P}$ couplings.[43] Pulses and delays are as in Fig. 11. Heteronuclear GARP decoupling was applied to ^{31}P or both ^{31}P and X during acquisition. Pulse and receiver phase cycles and gradient strengths were as follows: $\phi_1 = \phi_2 = \phi_6 = y$; $\phi_3 = (x)_4, (-x)_4$; $\phi_4 = x, y, -x, -y$; $\phi_5 = (x)_8, (-x)_8$; $\phi_{rec} = (x, -x)_2, (-x, x)_4, (x, -x)_2$; $G_2 = G_1 \cdot \gamma(Y)/\gamma(H)$.

X/Y coherence transfer steps as in the original HNCA experiment.[41] As in the previous case, X nuclei are selectively irradiated by low power rectangular or shaped pulses, and coherence selection is accomplished by the matched pulsed field gradients G_1, G_2 and further assisted by a spoil gradient G_s. Owing to the need to avoid π-pulses in the X-channel, the spectra are processed in magnitude mode in the F_1 dimension.

All ^{1}H-detected two- and three-dimensional experiments described so far allow in principle (i.e., neglecting relaxation[9,11]) indirect detection of het- eronuclei with superior sensitivity than X-detected indirect X/Y-correlations, but fall short of determining the magnitude of $J_{X,Y}$. To achieve this, a ^{1}H-detected $J_{X,P}$-resolved experiment was proposed[43] (Fig. 12) which is in essence an adaptation of the PDIJ-technique described by Nanz et al. for the indirect determination of homonuclear $J_{C,C}$ couplings.[45] The experiment begins likewise with an initial INEPT step to generate $\mathbf{H_z X_x}$ antiphase magnetisation which evolves into $\mathbf{H_z X_y Y_z}$ double-antiphase magnetisation during t_1. The sine-modulated term is then converted into $\mathbf{H_z X_z Y_y}$ coherence by a pair of $\pi/2$-pulses on X and Y, and finally detected after a double INEPT back-transfer to ^{1}H. Coherence selection was achieved by the matched PFGs G1 and G2 and assisted by the spoil gradient G_s. Similar to the PDIJ experiment,[45] the desired coherences are modulated with $\sin(\pi\,J_{PX}\,t_1)$ during t_1 whereas the orthogonal component modulated by $\cos(\pi\,J_{PX}\,t_1)$ does not pass through the filters provided by the gradients and phase cycles. Consequently, the real part of the FID in t_1 contains no signal. In order to improve the
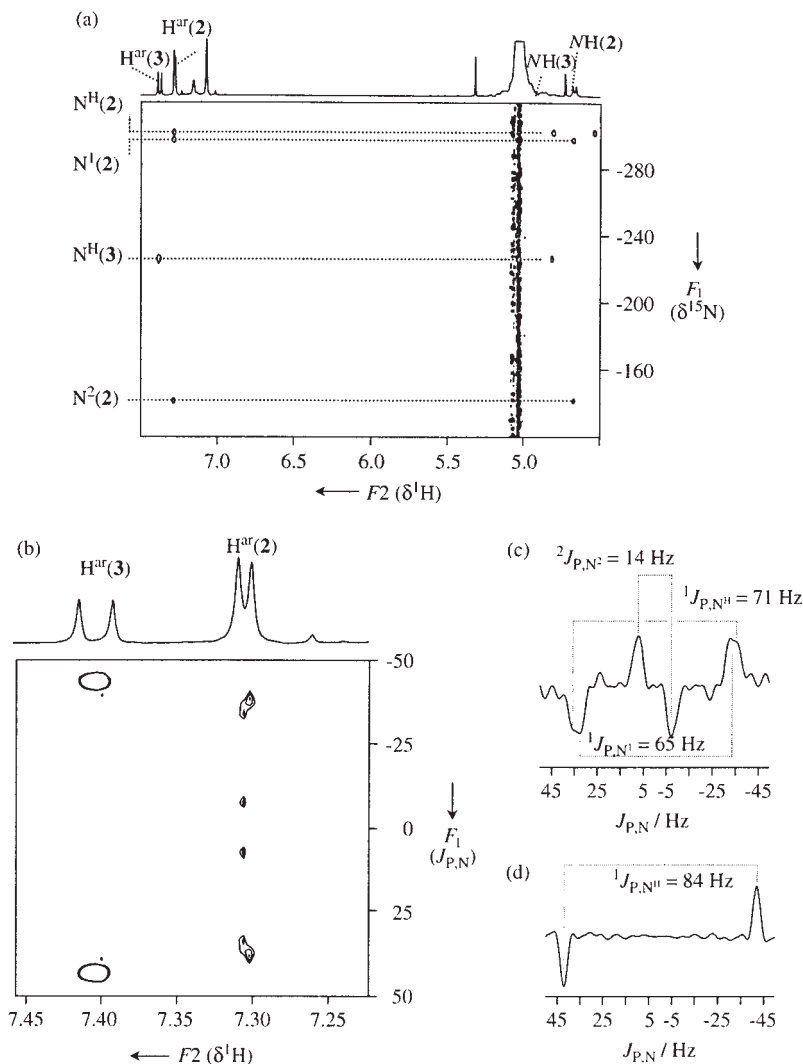
Fig. 13. (a) $^1H/(^{31}P)/^{15}N$ correlation of a mixture of Mes*P($=NH)=NMes*$ (compd. **2**, Mes* = 2,4,6-tri-t-butylphenyl) and Mes*P(NHMes*)-$N^1=N^2=N^3$ (compd. **3**) with correlations involving the NH and aromatic protons in the P-Mes* substituents. The spectrum was obtained with the pulse sequence shown in Fig. 11a. The t_1 noise around $\delta^1H = 5.1$ is due to a solvent signal (CH_2Cl_2) which is $\sim 4*10^5$ times more intense than that of the ^{15}N-satellites of the NH-resonance of **3**. (b) Expansion of a ^1H-detected 2D-$J_{P,N}$-resolved spectrum of the same mixture with correlations of the aromatic protons in the P-Mes*-substituents as obtained with the pulse sequence shown in Fig. 12. F_1 cross-sections of the 2D-spectrum at the chemical shifts of the aromatic protons of **2** and **3** are given in (c) and (d), respectively, and reveal the presence of one (2) and three (3) resolved $J_{P,N}$ couplings. Reproduced from Ref. 43 by permission of John Wiley & Sons.

signal-to-noise ratio, the same scheme to measure only the imaginary part of the FID in t_1 as in the original PDIJ sequence[45] was applied.

The pulse sequence described was employed to correlate ^{1}H chemical shifts with heteronuclear $J_{P,Y}$ couplings, and the result appears as a J-resolved spectrum that displays ^{1}H chemical shifts in F_2 and the magnitudes of all $J_{P,Y}$ couplings to a specific ^{31}P nucleus coupled to the appropriate proton – which is again selectable by appropriate soft pulses – in F_1 (Fig. 13). Assignment of couplings to specific heteronuclear coupling partners is unfeasible, but can in principle be achieved with a doubly selective variant of the experiment employing frequency-selective excitation to both heteronuclei.[43]

2.2.3. One-dimensional ^{1}H/X/Y-correlations

The idea of back transformation of a three-dimensional NMR experiment involving heteronuclear ^{1}H/X/Y 'out-and-back' coherence transfer can in principle be carried to the extreme by fixing the mixing time in both indirect domains. Even if one-dimensional experiments of this kind fall short of providing any information on heteronuclear chemical shifts, they may still serve to obtain isotope-filtered ^{1}H NMR spectra. A potential application of this technique is the detection of appropriately labelled metabolites in metabolism studies, and a one dimensional variant of the double INEPT ^{1}H/X/Y sequence has in fact been applied to pharmacokinetics studies of doubly ^{13}C, ^{15}N labelled metabolites.[46] Even if the pulse scheme relied exclusively on phase-cycling for coherence selection, a suppression of matrix signals by a factor of $\sim 10^4$ proved feasible, and it is easily conceivable that the performance can still be improved by the application of pulsed field gradients.

2.3. Comparison of experiments

The design of pulse sequences with inverse detection and the incorporation of pulsed field gradients has during recent years revolutionised the technical development of NMR spectroscopy, and ^{1}H-detected ^{1}H/X/Y correlations are now widely used as the standard technique for the analysis of intramolecular connectivities between different heteronuclei X and Y in biochemical samples. Quite a different situation prevails, however, in the fields of organometallic and coordination chemistry. Even though here the indirect observation of the NMR signals of one (or more) heteronuclei through a scalar coupled detector nucleus gains likewise increasing importance over techniques employing X/Y polarisation transfer and direct observation of a low-γ nucleus, much work still relies on the application of X- rather than ^{1}H-detected methods, and phase-cycling schemes keep in use beside PFG-based techniques for coherence selection. The reason for this methodical variety is easily understood if one compares the diverse needs of

such differing analytical tasks as the constitutional characterisation of organometallic polymers on the one hand, and the measurement of the metal NMR spectra of organometallic or inorganic coordination compounds on the other.

Polymeric substrates are frequently composed of a number of chemically closely similar repeat units that give rise to crowded spectra with many closely spaced and partially overlapping signals in narrow regions. Signal dispersion in three or more spectral dimensions may under these conditions be the only way to resolve individual resonances and establish coupling pathways which constitutes a prerequisite for the successful analysis of the back-bone sequence or the stereochemistry of a polymer. In addition, the application of PFG-based techniques for coherence selection is often essential to achieve a sufficient level of suppression of unwanted signals that permits one to detect signals of rare isotopes in natural abundance, or provides for a secure assignment of weak but diagnostically highly relevant signals originating from the end-groups of the polymer chain. The need to meet both demands simultaneously is in principle resolved by the application of ^{1}H-detected three-dimensional ^{1}H/X/Y correlation techniques. Due to many inherent similarities of the tasks to characterise the structures of organometallic polymers and bio-macromolecules, many pulse schemes from biological experiments have thus successfully been adapted to the NMR analysis of synthetic organometallic polymers,[38,39,47] and an evaluation of the applicability of a suite of two- and three-dimensional pulse schemes has lead to the development of a protocol which can be used to characterise the structures of organometallic polymers and other heteroatom-containing molecular materials in much the same way that multiple combinations of 3D NMR experiments have been used in biological structure elucidation.[39]

In contrast, many inorganic and organometallic coordination compounds exhibit much smaller molecular structures and simpler spectra which make time-consuming three-dimensional experiments for the indirect detection of low-γ metal nuclei obsolete. Many of the complexes studied recently exhibit spectroscopically easily detectable ^{19}F or ^{31}P nuclei directly in the metal coordination sphere, and metal NMR spectra are thus in principle available in a straightforward manner from two-dimensional inverse experiments operating either with detection of ^{1}H or X (X = ^{19}F, ^{31}P). ^{1}H-detected heteronuclear correlations are often substantially deteriorated due to relaxation during the long delay times that are needed to accomplish polarisation transfer via small $^nJ_{Y,H}$ long-range couplings, and due to interference between homonuclear $J_{H,H}$ and heteronuclear $J_{X,H}$ couplings that may render the excitation of heteronuclear multiple quantum coherences inefficient. For example, it has been shown that the practical sensitivity advantage of ^{1}H- vs. ^{31}P-detection in the indirect observation of ^{183}W NMR spectra of some tungsten carbene complexes was less than a factor of

2, as compared to the theoretical value of $(\gamma_H/\gamma_P)^{5/2} = 9.6$.[48] Consequently, X/Y correlations via large $^1J_{X,Y}$ couplings may not only be competitive or even preferable from the point of sensitivity, but may still remain applicable even if $^nJ_{Y,H}$ long-range couplings vanish totally. Furthermore, as the observation of metal satellites in the X-spectrum is frequently facilitated by a large magnitude of $^1J_{X,Y}$ which prevents overlap of parent and satellite lines, and by high isotopic abundance of metal nuclei, the use of PFG's for the suppression of parent lines and the reduction of artefacts becomes less important and the older schemes based on coherence selection by phase-cycling suffice.

With regard to the wealth of pulse schemes for X/Y and three- or two-dimensional ^1H/X/Y correlation experiments, some consideration has to be given to the selection of the best suited method for a certain application. For two-dimensional X/Y-correlations, inverse detection schemes with observation of the nucleus with the higher gyromagnetic ratio now appear in most cases to be preferred over HETCOR experiments with a single X/Y-polarisation transfer step. As has been outlined previously,[11] HMQC gives superior suppression of artefacts and is generally preferred over HSQC pulse schemes. Additional broadening of cross-peaks in HMQC spectra due to the presence of homonuclear spin couplings is considered of little importance for the A_nX spin systems of many metal complexes, or for ^{13}C/Y correlations where both nuclei are isotopically diluted. In cases where relaxation-induced decay of coherences is critical (i.e., as in the indirect observation of rapidly relaxing quadrupolar nuclei or spin-1/2 nuclei that experience rapid relaxation of the second kind mediated by coupling to a quadrupolar nucleus) the best results are generally obtained with the shortest and simplest pulse schemes available, and phase-cycled HMQC schemes without refocusing and decoupling during acquisition were under these circumstances frequently found to be the best choice.[11]

A notable exception from the rule of observing the isotope with higher Larmor frequency in a HMQC experiment was reported by Lycka et al.[19] who used a 'reverse' pulse scheme for the measurement of a ^{13}C/^{119}Sn correlation of an organotin compound. Detection of the ^{13}C nuclei was in this case preferred since (a) it allowed one to maintain a sufficient digital resolution in the indirect domain with a lower number of t_1 increments, and (b) coherence transfer via comparatively small long-range couplings was considered to suffer less from relaxation induced losses by setting up the experiment for observation of the nucleus with the sharper lines (i.e., the longer effective transversal relaxation time), and keeping the time of evolution of transversal magnetisation on the more rapidly relaxing tin nuclei as short as possible.

Advantages of HETCOR over HMQC type pulse sequences became evident in cases where indirect detection of the high-γ nucleus allows

acquisition of the correlation map with sufficient resolution in a minimum number of t_1 increments,[18,19] or for correlations between a spin-1/2 and a quadrupolar nucleus.[49] In the latter case, the preference for HETCOR-type experiments can be explained because they minimise the pulse repetition rate by excitation of the nucleus with the shorter T_1 relaxation time, and detects the nucleus with the sharper lines, thus improving the signal-to-noise ratio.

Accounts on gradient-enhanced X/Y HMQC experiments remain somewhat inconclusive. Although gradient-enhanced HMQC pulse schemes for ^{1}H/X correlation are well established[1] and some experiments combining X/Y-multiple quantum coherence transfer steps with PFG's for coherence selection have been communicated,[27,43] another report stated the failure of attempts to apply PFG-HMQC methods to obtain decent ^{19}F/^{13}C correlation spectra of certain fluoro-polymers, presumably as a consequence of problems with refocusing homonuclear $J_{F,F}$ couplings during t_1.[21] Whereas the latter finding owes much to the special structure of the nuclear spin-system involved, there are as well some further, more technical aspects about PFG-HMQC schemes that deserve consideration. Thus, a particular characteristic of the phase-cycled HMQC experiment is its insensitivity to pulse imperfections and off-resonance effects which is due to the absence of 180°-pulses on the indirectly observed nucleus.[1,11,50] As many common PFG-HMQC implementations involve insertion of the gradient pulse into a τ-180°(Y)-τ spin echo sequence,[1] this might thus lead to an unwanted reduction of the accessible spectral range in F_1 and contribute to a further degradation of the correlation spectra. Considering these effects leaves one with the choice of either to compensate for the limited excitation bandwidth by using composite refocusing pulses, or to acquire PFG-HMQC spectra in magnitude-mode which is feasible without the need to apply π-pulses in the indirect domain and has e.g., been used in a two-dimensional experiment involving relayed ^{1}H/(X)/Y coherence transfer,[43] or, finally, to keep using phase-cycling rather than PFG's for coherence selection. The latter is still routinely employed e.g., for the indirect detection of the metal NMR spectra of rhodium complexes (see below) where large chemical shift ranges have to be covered but, owing to the 100% natural abundance of the ^{103}Rh isotope, suppression of parent signals is no particularly important issue.

HSQC rather than HMQC-based transfer schemes have recently in particular been employed in various indirectly detected two- and three-dimensional ^{1}H/X/Y correlation experiments involving multi-step coherence-transfer in either direction.[38–40,43,44] The application of PFG's appears to be essential to obtain a sufficiently clean spectrum that is free of artefacts, and in many cases the pulse sequence shows only a satisfactory performance if composite pulses, with a larger excitation bandwidth than normal ones, are employed.[21,38,39,43] The pulse schemes yield generally phase-sensitive spectra with pure absorptive lines and do not suffer from splitting or broadening of the cross peaks as a consequence of the undesired evolution

of homonuclear couplings in the indirectly detected dimensions that is a common draw-back of HMQC-based experiments. Consequently, three-dimensional experiments of this type are best suited for the structural assignments of organoelement compounds with complicated structures or of product mixtures[47] where good spectral resolution in several dimensions is essential for the disentangling of overlapping signals and the solution of complicated assignment problems. Two-dimensional versions with relayed ^{1}H/(X)/Y coherence transfer[43,44] can be employed as a time-saving alternative to the long-lasting three-dimensional experiment in the analysis of medium-sized organometallics whose NMR spectra reveal a medium degree of complexity.

3. RECENT APPLICATIONS OF X/Y CORRELATIONS

The recent applications of heteronuclear X/Y correlation spectroscopy in inorganic and organometallic chemistry show a strong focus on two key issues, viz. the use of indirect detection techniques to measure the chemical shifts of scarcely accessible, insensitive nuclei and the utilisation of multi-dimensional correlation techniques to derive structural assignments in the heteroatom-containing backbones of organometallic (macro)molecules. The utilisation of inverse spectroscopy for sensitivity improvement is frequently of vital importance for metal NMR studies on inorganic and organometallic complexes with low-γ transition metals, while the analysis of coupling pathways and chemical bond patterns dominates the application of X/Y correlations for the structural elucidation of non-metallic organoelement compounds. For the sake of clarity, the remainder of this section is divided according to the chemical nature of the materials studied into two parts which put special emphasis on applications devoted to the analysis of transition metal complexes and of non-metallic organoelement compounds, respectively. It should be noted, however, that a strict separation according to the key issues addressed at the top of this paragraph is not feasible as the application of X/Y correlation methods serves often a combination of different objectives, and aspects of both issues will thus appear in either part.

3.1. Transition metal NMR studies of organometallic and inorganic coordination compounds

Transition metal NMR spectroscopy is not only a valuable source of structural information, but metal chemical shifts may also permit predictions of the reactivity and possibly even catalytic activity of a complex.[51] The key to such analyses is frequently the observation of correlations of metal chemical shifts

with reaction rates or other physical or chemical properties which can be traced back to a common electronic origin of the individual features. While a concise analysis is outside the scope of this article, a basic understanding of the underlying effects is feasible if one remembers that changes in metal chemical shifts are largely determined by the paramagnetic shielding term σ_p which is often approximated by the expression given in equation (2)[51] where ΔE denotes an average electronic excitation energy, $\langle r^{-3} \rangle$ a non-s-orbital expansion term, and P_u and D_u are p- and d-orbital population terms, respectively.

$$\sigma_p \propto -(\Delta E)^{-1} \cdot (\langle r^{-3} \rangle_{np} \cdot P_u + \langle r^{-3} \rangle_{md} \cdot D_u) \tag{2}$$

3.1.1. *Indirect measurement of metal NMR data*

Applicable techniques for the measurement of metal NMR spectra depend on the magnetic properties of the nuclide to be observed.[51] Indirect detection techniques have predominantly been used for the studies of spin-1/2 nuclides such as ^{57}Fe, ^{103}Rh, ^{109}Ag, ^{183}W and ^{187}Os which are hard to study in direct detection experiments because of their low gyromagnetic ratios and concomitant long relaxation times. The application of inverse spectroscopy has been applied to all of the nuclides mentioned,[11] but because of the relevance of rhodium complexes for many applications in homogeneous catalysis, recent spectroscopic studies exhibit a pronounced focus on complexes with this metal.

Many stable rhodium complexes that are of potential interest for catalytic applications contain phosphine or phosphite ligands, and inverse experiments with ^{31}P detection thus appear as a natural choice for the indirect observation of the ^{103}Rh NMR spectra and are in fact used by various research groups as a routine method for compound characterisation nowadays.[52–66] The theoretical sensitivity advantage of ^{1}H-detected inverse correlation experiments is often outweighed by the fact that ^{31}P/^{103}Rh coherence transfer via the appreciably large $^{1}J_{Rh,P}$ coupling is easily feasible even in cases where ^{1}H/^{103}Rh coherence transfer suffers from substantial losses due to relaxation or dynamic effects or is impossible in the absence of suitable long-range couplings,[56] and both methods are frequently used as complementary rather than competitive approaches.[56,65] As both ^{31}P and ^{103}Rh nuclei occur in 100% natural abundance, the application of pulsed field gradients to aid the selection of the wanted signals in the presence of large undesired parent signals is generally not considered necessary, and the basic phase-cycled HMQC pulse scheme appears to be the experiment of choice. The defocusing delays in the HMQC sequence are normally set to match the large $^{1}J_{Rh,P}$ couplings of 100–200 Hz, but modification of the delays to select coherence transfer via long-range couplings ($^{n}J_{Rh,P} \approx 3$–20 Hz) has also been applied.[54,63]

Indirect detection through a heteronucleus other than ^{31}P has been employed in the application of ^{13}C/^{103}Rh correlations to the spectroscopic study of substituted rhodium carbonyl clusters of composition $[Rh_6(CO)_{15}L]$,[33,55,67] $[Rh_6(CO)_{14}L_2]$,[55,67] $[Rh_6C(CO)_{14}]^{2-}$ [54] (L = various 2-electron donor ligands), and the mixed clusters $[Rh_2Pt_3(CO)_9(PPh_3)_3]$ and $[Rh_2Pt_2(CO)_7(PPh_3)_3]$,[66] respectively. Motivation of the investigation of these clusters was provided both by their relevance in catalysis and their interesting structural and dynamic properties, and ^{13}C/^{103}Rh correlation techniques were employed together with other NMR experiments for the verification of the structures and to obtain secure spectral assignments. A special technical aspect of these experiments has already been discussed in Section 2.2.1 and refers to the possibility of distinguishing between terminal and face-bridging coordination modes of carbonyl ligands by means of the observation of triple-quantum effects in the correlation spectra.[33]

The potential of inverse spectroscopy to the characterisation of rhodium complexes with unusual molecular structures was further demonstrated in the spectroscopic characterisation of complexes with cationic bis-(phosphonio)-benzophospholide ligands that bind to the metal via the lone-pairs of a two- and a three-coordinate phosphorus atom,[56] and of compounds featuring rhodium–hydrogen–tin three-centre bonds.[57–60] The rhodium chemical shifts of pentacoordinate acyl- and hydridorhodium complexes which are considered important intermediates in hydroformylation reactions were determined from both ^{31}P and ^{13}C detected HMQC spectra at high H_2/CO pressures in sapphire NMR tubes.[64,68] An unprecedented yet highly interesting approach to use rhodium NMR spectroscopy for the recognition of P-chiral phosphines was reported by Magiera et al.[63] who were able to discriminate the different diastereoisomers obtained from the reaction of racemic phosphines with a chiral dirhodium complex $[Rh_2(R*CO_2)_4]$ (see Fig. 14) by means of two-dimensional ^{31}P/^{103}Rh HMQC spectra. Even though the acquisition of metal NMR spectra is not obligatory for the determination of enantiomer ratios (which is easily feasible e.g., from the much more easily available ^{31}P NMR spectra), it proved of importance for a concise characterisation of the complexes and permitted the assignment of the two different rhodium environments, gave an exquisite demonstration of the J-coupling selectivity of the HMQC transfer, and allowed one to determine the coupling constant between the two metal nuclei from a passive splitting of the correlation signal along the F_1 axis.

Recent applications of X/Y correlation techniques to measure chemical shifts of low-γ, spin-1/2 transition metal nuclei other than rhodium focused mainly on the analysis of silver and tungsten complexes; in addition, the use of ^{13}C-relayed ^{1}H/^{195}Pt correlations for the stereochemical analysis of some platinum complexes was explored.[44] A report on the application of ^{31}P/^{51}V correlation spectroscopy demonstrated further the possibility of indirect detection of rapidly relaxing quadrupolar metal nuclei and the feasibility of the
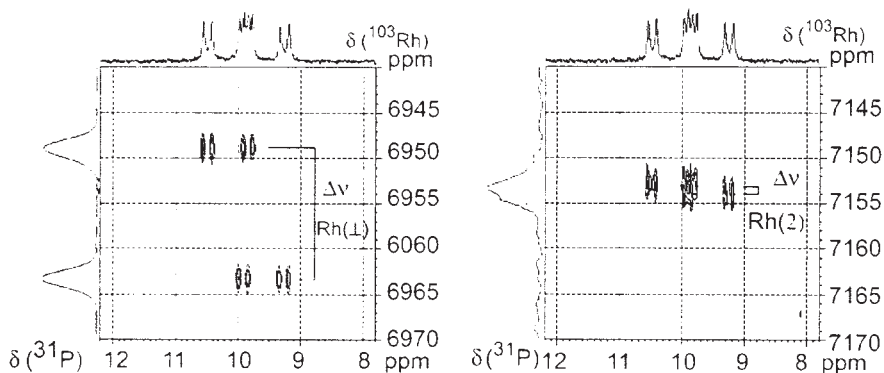
Fig. 14. $^{31}P/^{103}Rh\{^1H\}$ HMQC NMR spectra of the adduct of chiral $[Rh_2\{(R)\text{-mtpa}\}_4]$ ($(R)\text{-mtpa} = R$-1-methoxy-1-trifluoromethyl-phenylacetate, anion of Mosher's acid) with the racemic phosphane $PPh(Me)(NEt_2)$ obtained via a HMQC sequence tuned to observe correlation signals via $^1J_{Rh,P}$ (defocusing delay 4.5 ms, left) and $^2J_{Rh,P}$ (defocusing delay 19 ms, right) to give the chemical shifts of the directly bonded $Rh(\perp)$ and the remote $Rh(2)$ metal atoms in the dinuclear adduct. Each spectrum displays two well resolved sets of peaks indicating the presence of two diastereomers with different ^{31}P and ^{103}Rh chemical shifts with the chiral discrimination $(\delta\nu)$ being clearly larger for $Rh(\perp)$ than for $Rh(2)$. Reproduced from ref. [63] by permission of John Wiley & Sons.

two-dimensional method for the constitution analysis and signal assignments, even though from the point of sensitivity the indirect detection proved less advantageous as compared to direct observation of the highly sensitive metal nucleus.[49]

Studies of ^{31}P-detected $^{31}P/^{109}Ag$ HMQC of spectra silver complexes were conducted in the first place to aid in the concise spectroscopic characterisation of both stable and kinetically highly labile complexes which could only be identified from NMR spectroscopic studies at low temperatures.[69,70] Investigation of the ^{183}W NMR spectra of organometallic complexes were performed for tungsten carbyne and vinylidene complexes that carry phosphines as spectator ligands,[48,71] a series of phosphenium complexes featuring coordination of tungsten to a formally divalent cationic phosphorus atom,[72] and for some complexes of phosphorus-heterocycles with delocalised π-electron systems that bind to tungsten either via a lone-pair at phosphorus or another donor atom.[73,74] The spectra were recorded either via ^{31}P-detected $^{31}P/^{183}W$ HMQC without gradient assistance,[48,71–73] or as ^1H-detected, ^{31}P-relayed $^1H/(^{31}P)/^{183}W$ correlation with gradient selection,[74] and both direct ($^1J_{W,P} > 200$ Hz) and long-range couplings ($^nJ_{W,P}$ 3–15 Hz[73,74]) were used for coherence transfer. The relative performance of ^{31}P- and ^1H-based methods for the detection of ^{183}W is governed by similar factors as in the case of ^{103}Rh, and both methods are frequently used as complementary rather than competitive approaches.[48] The assignment of coupling pathways, relative
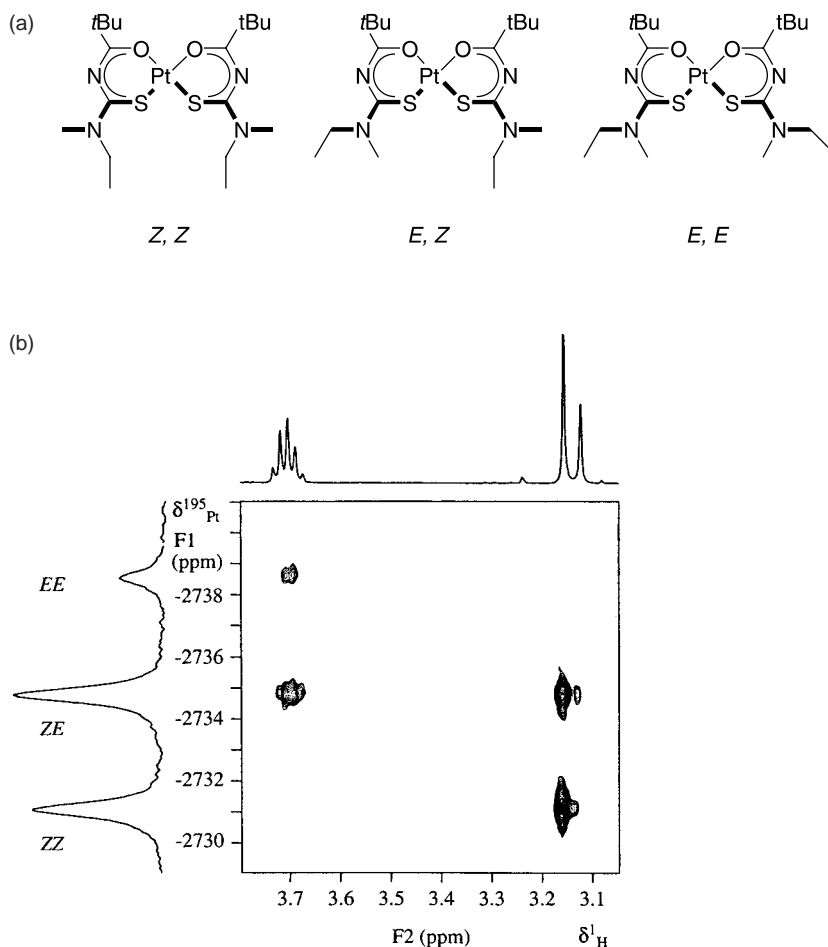
Fig. 15. The stereoisomeric thiourea-platinum complexes shown in (a) display large $^4J_{Pt,C}$ couplings for the α-carbon atom in that branch of the N,N-dialkyl substituent which is in a favourable 'W' configuration with respect to the metal atom (thick bonds). The assignment of the (fortuitously overlapping) ^1H and ^{195}Pt NMR signals of all three stereoisomers was feasible by means of indirect detection of these couplings from a ^1H detected $^1H/(^{13}C)/^{195}Pt$ correlation spectrum which is shown in (b) together with the one-dimensional ^1H and ^{195}Pt NMR projections. Reproduced from Ref. 44 by permission of John Wiley & Sons.

signs of coupling constants,[71,73] and last, but not least, the determination of ^{183}W chemical shifts, served both for the verification of structural assignments and the analysis of electronic influences on trends in metal chemical shifts (see below).

The application of $^1H/(^{13}C)/^{195}Pt$ relayed correlation spectroscopy for the characterisation of the thiourea-platinum complexes shown in Fig. 15[44] may

serve as an example to demonstrate the power of inverse two-dimensional spectroscopy even for metal nuclei of medium receptivity where direct acquisition of metal NMR spectra is easily feasible. The problem in this example is thus not the impossibility to acquire the ^{195}Pt NMR spectrum, but rather the assignment of the resonances of the three configurational isomers present as a mixture. A solution to this problem was found in the observation that couplings to the carbon atoms in the *N,N*-dialkyl substituent were in each isomer $^4J_{PtC}$ only evident for the branch which is in a favourable 'W' configuration with respect to the platinum atom. Consequently, the metal atoms in the *E,E*- and *Z,Z*-isomers exhibit a single ^{195}Pt/^{13}C correlation connecting the ^{195}Pt resonance with the ^{13}C signal of either a set of two identical CH_2 or CH_3 carbon atoms, respectively, while the metal atom in the *E,Z*-isomer simultaneously displays both correlations. The mapping of the different connectivities, and thus the signal assignment, becomes immediately evident from the displayed two-dimensional $^1H/(^{13}C)/^{195}$Pt correlation spectrum (Fig. 15) in which indirect detection of the ^{13}C signals through the directly attached hydrogen atoms was chosen for the reason of higher sensitivity.

3.1.2. *Interpretation of trends in metal chemical shifts*

Analysis of trends in transition metal chemical shifts was in most cases attempted by exploring statistical correlations with other observable spectroscopic quantities such as ligand atom chemical shifts or metal-ligand coupling constants,[57–60,72] with Hammett and Tolman parameters,[64] or by making qualitative assessments on the basis of steric or electronic effects (e.g., different σ-donor/π-acceptor capability) associated with the formal exchange of single ligands in a series of isostructural complexes.[48,56,65,71] For an interpretation of the established trends it was generally assumed that the variations in chemical shifts are determined by changes in the paramagnetic shielding contribution and can be described in the frame of the approximation given in equation (2). In most cases, the variation of the ΔE^{-1} or $\langle r^{-3} \rangle$ terms, respectively, was identified as the dominating factor that governs the variation of metal chemical shifts.[48,56–60,64,65,71]

Even though the outlined approach allowed the successful rationalisation of many experimentally observed shift/structure and shift/reactivity correlations, Leitner *et al.* have pointed out that such relations cannot be expected to be universally valid and require that structural variations are modest and avoid large simultaneous changes in parameters that may have opposite effects on metal chemical shifts.[61] To overcome these drawbacks and establish a more rational interpretation of chemical shift trends, they used a combination of experimental and computational efforts to assess the importance of different electronic and structural factors on the metal chemical shifts of a series of rhodium complexes with bidentate chelating bisphosphine ligands. The basis of their approach is first the validation of experimentally observed metal shifts by

the computational data derived from studies of the same compounds, and subsequent simulations of the influence of structural distortions by computing the variation of the metal chemical shifts upon variation of individually selected geometrical parameters. It appears that the major improvement of this approach is the possibility to separate not only the electronic and structural influences on the variation of metal shifts, but also to assess *quantitatively* the relative importance of the individual influences. Thus, the finding that sterically induced changes in the metal coordination sphere exert a strong influence on the rhodium shifts reproduces earlier findings of purely empirical studies.[11,64,65] In addition Leitner *et al*. were able to demonstrate that electronic effects on the metal shifts of complexes [{$R_2P(CH_2)_nPR_2$}Rh{hexafluoroacetylacetonate}] (R = *p*-substituted aryl) induce variations of rhodium shifts not exceeding 80 ppm and are transmitted via a direct inductive influence, whereas much larger shift differences of a total span of $\sim$ 800 ppm are mainly introduced by a parallel increase of Rh–P distances and P–Rh–P bond angles which accompany an increasing size of the chelate ring.[61]

3.2. Structure elucidation of heteroatom-containing backbones in organoelement compounds

The conceptual advantage of using two-dimensional X/Y or three-dimensional ^{1}H/X/Y correlations for the visualisation of coupling pathways and the direct mapping of heteroatom connectivities in the backbone of organoelement compounds has long been recognised,[11] and even if their general utilisation in the field of constitutional analysis lags behind that of multi-dimensional H/C or H/X correlations, these methods are highly valued as powerful analytical tools in special areas, e.g., the structural analysis of elementorganic polymers where both ^{1}H and ^{13}C NMR spectra show rather low signal dispersion, the structural analysis of fluoro-organics or inorganic species such as phosphazenes (or silicones) and lithium amides whose backbones are nearly devoid of proton (and carbon) atoms. Owing to the chemical nature of the substrates of interest, most applications of X/Y or ^{1}H/X/Y correlation methods involve at least one of the four elements ^{31}P, ^{19}F, ^{13}C, or ^{6}Li (which is better suited for correlation spectroscopy than the more abundant nuclide ^{7}Li because of its lower quadrupole moment), respectively. The interest in the analytical characterisation of organofluorine and organophosphorus compounds seems to be triggered both by the concern to characterise the properties of these important materials and the excellent receptivity of the ^{19}F and ^{31}P nuclei whereas ^{13}C is of interest as the most abundant constituent of the molecular frameworks of organometallic compounds in general.

Although the different applications discussed in this section are closely related and follow similar conceptions, we will discuss applications of two-dimensional X/Y and three-dimensional ^{1}H/X/Y correlations in two separate

parts. ^{1}H/(X)/Y correlations with relayed coherence transfer can for this purpose be considered a special case of X/Y correlations where one coupling partner is indirectly detected via protons, and will be dealt with appropriately.

3.2.1. *Application of two-dimensional X/Y and ^{1}H/(X)/Y correlation methods*

Two-dimensional X/Y correlation techniques are particularly well suited to elucidate the solution structures of organoelement molecules or kinetically labile aggregates of organolithium reagents of medium complexity. Of all conceivable combinations of heteroelements X and Y, those involving fluorine as one nucleus are considered unique as the high receptivity of ^{19}F offers an excellent opportunity for the indirect detection of scalar coupled heteronuclei (^{19}F-based inverse spectroscopy yields nearly 86% of the sensitivity enhancement of ^{1}H-based ^{1}H/X correlation experiments), and the two-dimensional technique facilitates unambiguous signal assignments in the case of many fluoro-organics whose one-dimensional NMR spectra are complicated by higher-order effects and intricate coupling patterns. In fact, both issues have stimulated recent investigations of the prospect of ^{19}F/Y correlations in the analysis of organoelement compounds and fluorine containing polymers.

The use of ^{19}F-detected inverse NMR spectroscopy for the detection of ^{15}N signals was demonstrated by the spectroscopic characterisation of some fluorinated pyridines.[27] The experiments were carried out by using an accordion-optimised IMPEACH-MBC pulse sequence which was designed for the simultaneous observation of correlation signals over a wide range of long-range couplings of different magnitude and has been discussed in some detail in Section 2.1. Determination of the relative signs of heteronuclear $^nJ_{F,H}/^nJ_{N,H}$ and $^nJ_{F,H}/^nJ_{F,C}$ coupling constants for 2,4-dinitrofluorobenzene has been the motivation to measure ^{19}F/^{15}N and ^{19}F/^{13}C long-range correlations of this compound,[75] and ^{19}F-detected ^{19}F/^{13}C HMQC or gradient-assisted HSQC spectra have been used as an indispensable aid in the process of deriving unequivocal assignments of both the ^{19}F and ^{13}C NMR spectra of various fluorinated halocarbons[76,77] and a difluoroethene-hexafluoropropene co-polymerisate.[21] Two further examples of ^{19}F-based correlation techniques involve the use of a ^{19}F/^{117}Sn HMQC correlation as the key experiment to verify a fluxional structure with dynamically equilibrating fluorine-tin dative bonds of a dimeric difluoro-tetra-tert.butyl-stannoxane in solution,[78] and the use of ^{19}F/^{77}Se HETCOR spectra to assign both the ^{19}F and ^{77}Se resonance signals of isomeric fluoro-phenylseleno-alkenes.[18]

Even though the NMR receptivity of ^{31}P is substantially lower than that of ^{19}F, ^{31}P-detected ^{31}P/^{15}N HMQC[79] and gradient enhanced HSQC correlation spectra[25] have successfully been applied to detect and assign the ^{15}N resonance signals of various acyclic and cyclic phosphazenes and their complexes. One-dimensional versions of the gradient-assisted HSQC experiment have
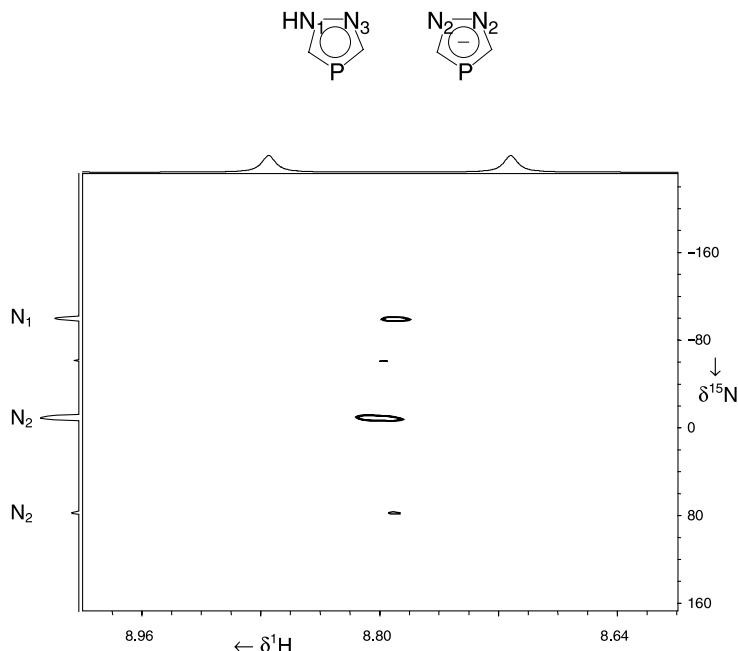
Fig. 16. ^{1}H/(^{31}P)/^{15}N correlation spectrum of a dynamically equilibrating mixture of 1,2,4-diazaphosphole and its conjugate base, 1,2,4-diazaphospholide, which was obtained by incomplete deprotonation of the former. The exchange is rapid on the ^{1}H (see projection on top) and ^{31}P chemical shift time scale, but still slow on the ^{15}N chemical shift time scale, making indirect observation of the ^{15}N NMR signals via relayed coherence transfer across the large large $^2J_{P,H}$ (≈ 40 Hz) and $^2J_{P,N}$ (≈ 20–30 Hz) couplings feasible. The spectrum was acquired by using the pulse sequence shown in Fig. 11a which was modified by employing composite $180°$ pulses on the ^{15}N channel (from ref. 80).

further served to accomplish precise measurements of the magnitude of $^nJ_{P,N}$ coupling constants.[25] A superior sensitivity gain than with ^{31}P detected correlation experiments was feasible by performing the indirect detection of ^{15}N resonances and $^nJ_{P,N}$ coupling constants from ^{1}H-detected ^{1}H/(^{31}P)/^{15}N triple resonance shift correlations with relayed magnetisation transfer or ^{1}H-detected $J_{P,N}$-resolved spectra, respectively.[43] Pulse sequences for these experiments which involve two consecutive INEPT-transfer steps have been discussed in detail in Section 2.2.2, and their application has been demonstrated by measuring ^{15}N chemical shifts and $J_{P,N}$ couplings in azidophosphines (cf. Fig. 13) and aromatic phosphorus heterocycles. A further illustration of the successful utilisation of a relayed ^{1}H/(^{31}P)/^{15}N coherence transfer scheme is given by the indirectly detected ^{15}N NMR spectrum of a sample of partially deprotonated 1,2,4-diazaphosphole shown in Fig. 16.[80] The observation of three correlation signals is explained by the

simultaneous presence of the 1,2,4-diazaphosphole and its conjugate base, respectively, and the occurrence of all three correlations at the same ^{31}P and ^{1}H chemical shifts is due to the presence of dynamic exchange which is moderately slow on the ^{15}N but fast on the ^{31}P and ^{1}H chemical shift time scales. Signal broadening effects associated with the exchange process impeded the observation of the ^{15}N signals in single pulse or INEPT as well as ^{1}H-based HMBC experiments via $^{n}J_{N,H}$ long-range couplings. In consideration of these findings, the success of the relayed $^{1}H/(^{31}P)/^{15}N$ experiment is presumably attributable to the fact that the relayed coherence transfer via large $^{2}J_{P,H}$ (≈ 40 Hz) and $^{2}J_{P,N}$ (≈ 20–30 Hz) couplings requires shorter times and is thus less susceptible to the adverse effects of relaxation and chemical exchange than INEPT or HMBC experiments via small $^{2}J_{N,H}$ couplings.

Similar relayed $^{1}H/(^{31}P)/X$ coherence transfer experiments, as discussed above for $X = {}^{15}N$, have also been utilised to resolve ambiguous assignments of ^{13}C NMR signals ($X = {}^{13}C$) of aromatic phosphorus heterocycles,[43,73] and ^{31}P-detected $^{31}P/^{119}Sn$ HMQC spectroscopy has been applied to obtain unequivocal assignments of the ^{31}P and ^{119}Sn NMR signals of diastereomeric dibutyltinphosphonate oligomers.[81]

The last topic to be discussed in this section refers to the application of Li/Y correlation techniques aimed at a concise structural characterisation of lithium organyls and lithium amides which are eminently important chemical reagents. The formation of individual reagents is often accomplished by metallation (Li–H or Li–X exchange) reactions, and it is well known that the chemical reactivity of the resulting species is strongly affected by aggregation and solvation processes. Lithium has two naturally occurring isotopes, and even if ^{7}Li exhibits better receptivity, both because of its higher natural abundance and its higher gyromagnetic ratio,^{6}Li is much better suited for correlation spectroscopy and behaves, because of its much smaller quadrupole moment, very much like a spin-1/2 nucleus.[82] In order to improve the NMR receptivity, experiments involving ^{6}Li are routinely performed with uniformly [^{6}Li] labelled ($>95\%$ isotopic abundance) or even [$^{6}Li,^{13}C$] or [$^{6}Li,^{15}N$] doubly labelled substrates. In order to slow down chemical exchange, recording the spectra at low temperatures down to $-120°C$ may be required.

Two-dimensional $^{6}Li/Y$ correlation spectra of organolithium reagents have been studied for some time and although in previous reports a variety of elements such as ^{31}P, ^{29}Si, and ^{7}Li[11,82] have been employed as the heteronucleus Y, recent studies focused essentially on the application of $^{6}Li/^{13}C$ and $^{6}Li/^{15}N$ correlations for the structural investigation of lithium amides and lithium organyls, respectively. Methods employed include predominantly $^{6}Li/^{13}C$[34,83–86] and $^{6}Li/^{15}N$ HMQC[84,87,88] correlations with coherence transfer via $^{1}J_{C,Li}$ or $^{1}J_{N,Li}$ for the determination of connectivity patterns, and $^{6}Li/^{13}C$ J-resolved spectroscopy[84–86] for the verification of the

number of coupling partners in individual aggregates. Coherence selection was generally accomplished by phase-cycling schemes rather than PFG's, but the optimisation of the pulse sequence to allow the efficient detection of XY_m spin systems with several indirectly detected spins has been given some consideration.[34]

In contrast to earlier investigations in this field,[11] which dealt mainly with the structure elucidation of aggregates of simple reagents, the focus of the more recent studies has turned more and more to the investigation of increasingly complex systems, including the structure elucidation of mixed lithium alkyl/lithium amide or lithium alkyl/lithium alkoxide aggregates,[83–86] the identification of complicated ladder structures of lithium amides,[87] studies of solvation effects at low ligand concentration,[88] and the aggregation of chiral reagents.[83,84,86] A common feature of all of these studies is that attempts to solve analytical problems of increasing complexity require an appropriate diversity of the experimental approach, and two-dimensional X/Y correlation experiments make up just a part in a series of various one- and two-dimensional experiments aiming at the characterisation of static molecular structures as well as the mechanism and kinetics of dynamic exchange effects.

3.2.2. *Application of three-dimensional $^1H/X/Y$ correlation methods*

Dispersion of NMR signals in three dimensions is normally chosen if the resolution of overlapping signals in both one- and two-dimensional spectra remains incomplete,[47] or if the assignment of correlations in two-dimensional spectra remains ambiguous, e.g., because of the presence of accidental (near) degeneracy of different $^nJ_{XY}$ coupling constants.[42] Applications where these aspects gain importance include the analysis of synthetic polymers composed of a sequence of chemically like repeat units, or of mixtures of isomers where the signals of several closely similar small or medium sized molecules may overlap in a way that unambiguous assignment of the spectral lines of the individual components and thus the elucidation of their constitution is no longer feasible. Owing to the chemical composition of the substrates studied, the three-dimensional correlation experiments performed so far relied generally on the element combination $^1H/^{13}C/Y$ where Y denotes heteroatoms such as ^{19}F, ^{29}Si, ^{31}P or ^{119}Sn that are either directly interspersed between the carbon atoms in the backbone of a polymer or molecule, or occur in substituents along the chain or as a marker for the chain end of a polymer, respectively.

Recent examples of the application of three-dimensional $^1H/^{13}C/Y$ correlation spectroscopy for the characterisation of polymers included studies of polystyrene samples obtained by diphenylphosphinyl radical initiated polymerisation of styrene (Y = ^{31}P),[38,39,86] and the characterisation of Sn-containing polybutadiene that was prepared by anionic polymerisation

and subsequent capping of the chain ends of the resulting living polymer with
$Bu_3SnCl.$[89] The heteroatoms serve in both cases as spin labels that mark
the chain ends, and most experiments rely on an 'out-and-back' coherence
transfer which employs $^1J_{C,H}$ and $^nJ_{C,Y}$ couplings to shuffle magnetisation
from a proton to the adjacent carbon atom and further to the heteronuclear
spin label, and vice versa (cf. Fig. 8).

The advantage of the application of three-dimensional NMR methods
to characterise the heteroatom-containing structures in a polymer is two-
fold. First, the characterisation of chain end structures containing ^{13}C and
possibly a second rare heteronucleus such as ^{119}Sn in natural isotopic
abundance is a highly challenging task as it requires the detection of
signals under complete and uniform suppression of up to 10^6 times stronger
signals of the remaining protons in the sample. The observation of the
desired correlations in the three-dimensional spectrum benefits in this respect
in particular from the fact that the combination of double isotope selection
via the coherence transfer pathway and PFG's removes not only the signals
of protons not coupled to a heteronucleus, but also the C–H correlations
originating from the main chain repeat units which dominate the two-
dimensional $^1H/^{13}C$ HMQC spectrum and obscure many of the desired
correlations from the chain end structures (Fig. 17).[89] Second, the 3D
experiment may allow one to distinguish between the signals of carbon
atoms that are separated by one, two or three bonds from the heteroatom and
thus provide valuable stereochemical information on chain-end structures up
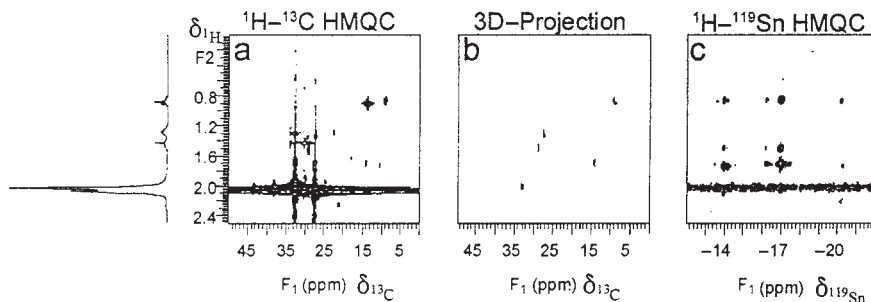
Fig. 17. Comparison of the $^1H/^{13}C$ HMQC spectrum (a), an indirectly observed $^{13}/^{119}Sn$
correlation obtained as the appropriate projection of a three-dimensional $^1H/^{13}C/^{119}Sn$
shift correlation experiment (b), and the $^1H/^{119}Sn$ HMQC spectrum of a tin-modified
polybutadiene sample which was prepared by capping the chain ends of a living anionic
polymer with Bu_3Sn-groups. The $^1H/^{13}C$ HMQC spectrum is dominated by strong
signals from the main polymer chain which obscure many of the resonances from the
chain ends. (c) The $^1H/^{119}Sn$ HMQC spectrum shows correlations between the tin
and aliphatic protons, but not to olefinic ones which would allow to distinguish
between structures having *cis*- and *trans*-configurated double bonds in 2,3-position with
respect to tin. Reproduced with permission from Ref. 44. Copyright 2000 American
Chemical Society.

to the tetrad level.[38,86,89] Two different approaches to accomplish the spectral editing have been used which utilise either the distribution of magnetisation transferred to the α-carbon atom adjacent to the heteroatom spin-label to the neighbouring carbon atoms in an isotopically labelled sample by means of a TOCSY mixing sequence (H(Xa)Y-XX-TOCSY experiment),[38,39] or exploited the existing differences in the magnitudes of $^{n}J_{C,Y}$ coupling constants over a different number of bonds that allow one to tune the defocusing delays in the pulse sequence in such a way so as to select only correlations via a defined number of bonds.[89]

   That 3D NMR techniques are not only useful for the analysis of macromolecules but may also be put to use for the characterisation of small and medium sized molecules was successfully demonstrated by studies of a mixture of isomeric organosilanes prepared by hydrosilylation of 4-vinyl-1-cyclohexene and some small first and second generation carbosilane dendrimers by using three-dimensional $^{1}H/^{13}C/^{29}Si$ correlation techniques.[42,47] Three-dimensional spectroscopy was in these cases unavoidable in order to derive secure resonance assignments and a definite structural proof, since both one- and two-dimensional techniques fail to completely resolve the strongly overlapping resonances originating from the different isomeric components or structurally similar repeat units in the same molecule. The techniques used were the same as in the studies on polymers discussed above, and as before the adaptation of defocusing delays to select coherence transfer pathways via $^{1}J_{Si,C}$ and $^{n}J_{Si,C}$ ($n = 2$, 3) couplings were feasible and provided crucial information that allowed one to distinguish between correlations arising from carbon atoms directly adjacent to the silicon atom and those from more remote ones, respectively.

4. CONCLUSIONS

Multi-dimensional X/Y correlation spectroscopy involving correlation between two different heteronuclei is not only widely used for the characterisation of bio-molecules, but has over the years found a gradually but steadily increasing acceptance in organometallic and organoelement chemistry. X/Y correlations are particularly valued in these areas due to their unique potential for the direct observation of heteroatom connectivities in molecular and supramolecular systems, and for the rapid indirect measurement of chemical shifts of low-γ nuclei. The information accessible by such experiments has not only a great impact on structure elucidation, but may further be utilised to gain insight into reaction mechanisms and help to understand chemical properties of inorganic and organometallic compounds. This is evidenced by the examples in this review which have demonstrated that the principal applications of these methods focus to date on the constitutional analysis of organoelement compounds with molecular structures of increasing complexity,

and on the evaluation of trends in transition metal NMR data. The latter are not only sensitive probes that allow one to monitor small changes in the electronic structure of metal complexes, but receive growing attention as a tool in establishing quantitative structure-activity relationships which may help in the rational understanding of the reactivity of metal complexes, or aid in the design of catalysts with higher efficiencies or selectivities.[51]

With the recent methodical improvements which involve, in particular, the incorporation of pulsed field gradients and the design of two- and three-dimensional experiments for the indirect detection of X/Y connectivities through observation of ^{1}H, the application of X/Y correlations in organo-metallic and organoelement chemistry has now arrived at the state-of-the-art level of modern NMR spectroscopy. The experimental methods have reached a certain state of maturity which should, together with the increasing availability of appropriately equipped NMR spectrometers, allow their future use as tools to solve analytical problems on a routine basis. In the light of these arguments, it appears that the largest challenge in the further development of the use of X/Y correlation techniques in organometallic and organoelement chemistry in the near future is not the further methodical improvement, but rather putting the methods to work and explore new fields of application. Considering the assets of X/Y correlation spectroscopy as an analytical tool, its use appears to be particularly promising in such currently rapidly developing areas as catalysis research, investigation of structures and dynamics of novel organometallic compounds with unprecedented bonding situations, or the structural characterisation of various kinds of (macro)molecular materials.

REFERENCES

1. For a current review on methods and applications of 2D-NMR methods, see: *Two Dimensional NMR Spectroscopy. Applications for Chemists and Biochemists*, 2nd edn, W. R. Croasmun, R. M. K. Carlson, eds., VCH Publishers, Weinheim, 1994.
2. R. R. Ernst, G. Bodenhausen and A. Wokaun, *Principles of Nuclear Magnetic Resonance in One and Two Dimensions*, Oxford University Press, Oxford, 1987.
3. R. Benn and A. Rufinska, *Angew. Chem.*, 1986, **98**, 851–871; *Angew. Chem. Int. Ed. Engl.*, 1986, **25**, 861.
4. B. E. Mann, *Annu. Rep. NMR Spectrosc.*, 1991, **24**, 141.
5. S. Berger, T. Fäcke and R. Wagner, *Magn. Reson. Chem.*, 1996, **34**, 4–13.
6. T. Fäcke, R. Wagner and S. Berger, *Concepts Magn. Reson.*, 1994, **6**, 293–306.
7. H. Günther, *Advanced Applications of NMR to Organometallic Chemistry*, M. Gielen, R. Willem, B. Wrackmeyer, eds., Wiley & Sons, New York, 1996, 247–290.
8. S. Berger, T. Fäcke, R. Wagner, 1996, in Ref. 7, 29–44.
9. F. López-Ortiz and R. J. Carbajo, *Curr. Org. Chem.*, 1988, **2**, 97–130.
10. W. McFarlane, A. M. Noble and J. M. Winfield, *J. Chem. Soc. A*, 1971, 948–953.
11. D. Gudat, *Annu. Rep. NMR Spectrosc.*, 1999, **38**, 139–202.
12. A. Mc Dermott, *Biol. Magn. Reson.*, 2003, **20**, 103–120.

13. D. D. Laws, H. L. Bitter and A. Jerschaw, *Angew. Chem. Int. Ed. Engl.*, 2002, **41**, 3096–3129.
14. C. Griesinger, H. Schwalbe, J. Schleucher, M. Sattler, 1994, in Ref. 1, 457–580.
15. N. M. Agh-Atabay, C. Bayat and U. Yazgic, *Rev. Inorg. Chem.*, 1998, **18**, 223–238.
16. S. Berger and F. Müller, *Chem. Ber.*, 1995, **128**, 799–802.
17. R. K. Harris, E. D. Becker, S. M. Cabral de Menezes, R. Goodfellow and P. Granger, *Pure Appl. Chem.*, 2001, **73**, 1795–1818.
18. H. Poleschner and K. Seppelt, *Magn. Reson. Chem.*, 2002, **40**, 777–780.
19. A. Lyčka, D. Micák, A. Holeček, M. Biesemans, J. C. Martins and R. Willem, *Organometallics*, 2000, **19**, 703–706.
20. J. Keeler, R. T. Clowes, A. L. Davis and E. D. Laue, *Methods Enzymol.*, 1994, **239**, 145–207.
21. O. Assemat and P. L. Rinaldi, *NMR Spectroscopy of Polymers in Solution and the Solid State*, ACS Symp. Ser., 2003, **834**, 29–42.
22. A. L. Davis, J. Keeler, E. D. Laue and D. Moskau, *J. Magn. Reson.*, 1992, **98**, 207.
23. O. W. Sørensen, G. W. Eich, M. H. Levitt, G. Bodenhausen and R. R. Ernst, *Progr. NMR Spectrosc.*, 1983, **16**, 183ff.
24. L. E. Kay, P. Keifer and T. Saarinen, *J. Am. Chem. Soc.*, 1992, **114**, 10663–10665.
25. R. J. Carbajo and F. López-Ortiz, *J. Magn. Reson.*, 2001, **148**, 165–168.
26. A. G. Palmer, III, J. Cavanagh, P. E. Wright and M. Rance, *J. Magn. Reson.*, 1991, **93**, 151–170.
27. D. E. Russell, C. E. Hadden, G. E. Martin and K. Krishnamurthy, *Magn. Reson. Chem.*, 2002, **40**, 207–210.
28. G. Bodenhausen and R. R. Ernst, *J. Am. Chem. Soc.*, 1982, **104**, 1304–1309.
29. R. Wagner and S. Berger, *Magn. Reson. Chem.*, 1998, **36**, S44–S46.
30. C. E. Hadden, G. E. Martin and V. V. Krishnamurthy, *J. Magn. Reson.*, 1999, **140**, 274–280.
31. D. Nanz and W. von Philipsborn, *J. Magn. Reson.*, 1991, **92**, 560–571.
32. D. Nanz and W. von Philipsborn, *J. Magn. Reson.*, 1992, **100**, 243–253.
33. B. T. Heaton, J. A. Iggo, I. S. Podkorytov, D. J. Smawfield, S. P. Tunik and R. Whyman, *J. Chem. Soc. Dalton Trans.*, 1999, 1917–1919.
34. B. Xiang, M. D. Winemiller, T. F. Briggs, D. J. Fuller and D. B. Collum, *Magn. Reson. Chem.*, 2001, **39**, 137–140.
35. H. Kessler, S. Mronga and G. Gemmecker, *Magn. Reson. Chem.*, 1991, **29**, 527.
36. T. Saito, R. E. Medsker, H. J. Harwood and P. L. Rinaldi, *J. Magn. Reson. Ser. A*, 1996, **120**, 125–128.
37. M. Chai, T. Saito, Z. Pi, C. Tessier and P. L. Rinaldi, *Macromol.*, 1997, **30**, 1240–1242.
38. T. Saito and P. L. Rinaldi, *J. Magn. Reson.*, 1998, **130**, 135–139.
39. T. Saito and P. L. Rinaldi, *J. Magn. Reson.*, 1998, **132**, 41–53.
40. J. P. Marino, H. Schwalbe, C. Anklin, W. Bermel, D. M. Crothers and C. Griesinger, *J. Am. Chem. Soc.*, 1994, **116**, 6472–6473.
41. M. Ikura, L. E. Kay and A. Bax, *Biochem.*, 1990, **29**, 4659.
42. M. Chai, Z. Pi, C. Tessier and P. L. Rinaldi, *J. Am. Chem. Soc.*, 1999, **121**, 273–279.
43. D. Gudat, *Magn. Reson. Chem.*, 2003, **41**, 253–259.
44. D. Argyropoulos, E. Hoffmann, S. Mtongana and K. R. Koch, *Magn. Reson. Chem.*, 2003, **41**, 102–106.
45. W. Koźmiński, D. Sperandio and D. Nanz, *Magn. Reson. Chem.*, 1996, **34**, 311.
46. W. C. Hutton, J. J. Likos, J. K. Gard and J. R. Garbow, *J. Labelled Compds. Radiopharmac.*, 1997, **41**, 87–95.
47. W. Liu, P. L. Rinaldi, L. Galya, J. E. Hansen and L. Wilczek, *Organometallics*, 2002, **21**, 3250–3257.
48. R. J. Carbajo, L. Zhang and F. López-Ortiz, *Magn. Reson. Chem.*, 1998, **36**, 807–814.
49. D. Gudat, U. Fischbeck, F. Tabellion, M. Billen and F. Preuss, *Magn. Reson. Chem.*, 2002, **40**, 139–146.
50. R. Benn, H. Brennecke, J. Heck and A. Rufinska, *Inorg. Chem.*, 1987, **26**, 2826–2829.

51. W. von Philipsborn, *Chem. Soc. Rev.*, 1999, **28**, 95–105.
52. M. Soleilhavoup, L. Viau, G. Commenges, C. Lepetit and R. Chauvin, *Eur. J. Inorg. Chem.*, 2003, 207–212.
53. N. Feiken, P. Pregosin and G. Trabesinger, *Organometallics*, 1998, **17**, 4510–4518.
54. J. S. Z. Sabunchai, B. T. Heaton, J. A. Iggo, C. Jacob and I. S. Podkorytov, *J. Clust. Sci.*, 2001, **12**, 339–348.
55. E. V. Grachova, B. T. Heaton, J. A. Iggo, I. S. Podkorytov, D. J. Smawfield, S. P. Tunik and R. Whyman, *J. Chem. Soc. Dalton Trans.*, 2001, 3303–3311.
56. S. Häp, M. Nieger, D. Gudat, M. Betke-Hornfeck and D. Schramm, *Organometallics*, 2001, **20**, 2679–2685.
57. V. Circu, M. A. Fernandes and L. Carlton, *Inorg. Chem.*, 2002, **41**, 3859–3865.
58. L. Carlton, *Inorg. Chem.*, 2000, **39**, 4510–4519.
59. L. Carlton, R. Weber and D. C. Levendis, *Inorg. Chem.*, 1998, **37**, 1264–1271.
60. L. Carlton, *Appl. Organomet. Chem.*, 2001, **15**, 157–160.
61. W. Leitner, M. Bühl, R. Fornika, C. Six, W. Baumann, E. Dinjus, M. Kessler, C. Krüger and A. Rufinska, *Organometallics*, 1999, **18**, 1196–1206.
62. M. Bühl, W. Baumann, R. Kadyrov and A. Borner, *Helv. Chim. Acta*, 1999, **82**, 811–820.
63. D. Magiera, W. Baumann, I. S. Podkorytov, J. Omelanczuk and D. Duddeck, *Eur. J. Inorg. Chem.*, 2002, 3253–3257.
64. F. R. Bregman, J. M. Ernsting, F. Müller, M. D. K. Boele, L. A. van der Veen and C. J. Elsevier, *J. Organomet. Chem.*, 1999, **592**, 306–311.
65. M. Aizenberg, J. Ott, C. J. Elsevier and D. Milstein, *J. Organomet. Chem.*, 1998, **551**, 81–92.
66. F. M. Dolgushin, E. V. Grachova, B. T. Heaton, J. A. Iggo, I. O. Koshevoy, I. S. Podkorytov, D. J. Smawfield, S. P. Tunik, R. Whyman, A. I. Yanovskii, *J. Chem. Soc. Dalton Trans.*, 1999, 1609–1614.
67. S. P. Tunik, I. S. Podkorytov, B. T. Heaton, J. A. Iggo and J. Sampanthar, *J. Organomet. Chem.*, 1998, **550**, 221–231.
68. S. C. van der Slot, P. C. J. Kramer, P.W.N.M. van Leeuwen, J. A. Iggo and B. T. Heaton, *Organometallics*, 2001, **20**, 430–441.
69. S. J. Berners-Price, R. J. Bowen, P. J. Harvey, P. C. Healey and G. A. Koutsantonis, *J. Chem. Soc. Dalton Trans.*, 1998, 1743–1750.
70. Z. Bajko, J. Daniels, D. Gudat, S. Häp and M. Nieger, *Organometallics*, 2002, **21**, 5182–5189.
71. L. Zhang, M. P. Gamasa, J. Gimeno, R. J. Carbajo, F. López-Ortiz, M. F. C. Guedes da Silva and A. J. L. Pombeiro, *Eur. J. Inorg. Chem.*, 2000, 341–350.
72. D. Gudat, A. Haghverdi and M. Nieger, *J. Organomet. Chem.*, 2001, **617**, 383–394.
73. A. Fuchs, D. Gudat, M. Nieger, O. Schmidt, M. Sebastian, L. Nyulaszi and E. Niecke, *Chem. Eur. J.*, 2002, **8**, 2188–2196.
74. L. Szarvas, Z. Bajko, S. Fusz, S. Burck, J. Daniels, M. Nieger and D. Gudat, *Z. Anorg. Allg. Chem.*, 2002, **628**, 2303–2310.
75. A. Ariza-Castolo, J. A. Guerrero-Alvarez and J. Peralta-Cruz, *Magn. Reson. Chem.* F, **41**, 49–52.
76. A. Foris, *Magn. Reson. Chem.*, 2001, **39**, 386–398.
77. A. A. Ribeiro and K. Umayahara, *Magn. Reson. Chem.*, 2003, **41**, 107–114.
78. J. Beckmann, M. Biesemans, K. Hassler, K. Jurkschat, J. C. Martins, M. Schürman and R. Willem, *Inorg. Chem.*, 1998, **37**, 4891–4897.
79. G. A. Carriedo, F. J. García Alonso, J. L. García, R. J. Carbajo and F. López-Ortiz, *Eur. J. Inorg. Chem.*, 1999, 1015–1020.
80. D. Gudat, unpublished results.
81. F. Ribot, C. Sanchez, M. Biesemans, F. A. G. Mercier, J. C. Martins, M. Gielen and R. Willem, *Organometallics*, 2001, **20**, 2593–2603.

82. H. Günther, *Advanced Applications of NMR to Organometallic Chemistry*, M. Gielen, R. Willem, and B. Wrackmeyer, eds., Wiley & Sons, New York, 1996, 247–290.
83. A. Thompson, E. G. Corley, M. F. Huntington, E. J. J. Grabowski, J. F. Remenar and D. B. Collum, *J. Am. Chem. Soc.*, 1998, **120**, 2028–2038.
84. R. L. Parsons, J. M. Fortunak, R. L. Doro, G. D. Harris, G. S. Kauffman, W. A. Nugent, M. D. Winemiller, T. F. Briggs, B. Xiang and D. B. Collum, *J. Am. Chem. Soc.*, 2001, **123**, 9135–9143.
85. X. Sun, M. D. Winemiller, B. Xiang and D. B. Collum, *J. Am. Chem. Soc.*, 2001, **123**, 8039–8043.
86. T. F. Briggs, M. D. Winemiller, B. Xiang and D. B. Collum, *J. Org. Chem.*, 2001, **66**, 6291–6298.
87. J. L. Rutherford and D. B. Collum, *J. Am. Chem. Soc.*, 1999, **121**, 10198–10202.
88. J. L. Rutherford and D. B. Collum, *J. Am. Chem. Soc.*, 2001, **123**, 199–202.
89. W. Liu, T. Saito, L. Li, P. L. Rinaldi, R. Hirst, A. F. Halasa and J. Wisintainer, *Macromolecules*, 2000, **33**, 2364–2369.

NMR Studies of Biomolecular Dynamics and Structural Plasticity Using Residual Dipolar Couplings

JOEL R. TOLMAN[1] and HASHIM M. AL-HASHIMI[2]

[1]*Department of Chemistry, Johns Hopkins University, 3400 N. Charles St., Baltimore, MD 21218, USA*
[2]*Department of Chemistry & Biophysics Research Division, University of Michigan, Ann Arbor, MI 48109-1055, USA*

Due to their exquisite sensitivity to bond vector orientations and distances, residual dipolar couplings are emerging as a powerful NMR methodology for probing the conformational dynamics of biomolecules. The global organization of multi-domain proteins and complexes can now be accurately established in solution, providing insights into distinguishing structural features under different solution environments or with respect to the solid state. Collective motions of domains or secondary structural elements occurring over sub-millisecond timescales, which have resisted characterization using

traditional techniques, can now be directly probed using suitable residual dipolar coupling-based techniques. Advances in methods for achieving molecular alignment and data interpretation are enabling characterization of motions with increasingly high resolution. There are now approaches for determining residual dipolar coupling-based generalized order parameters, which can complement their spin relaxation counterparts due to their broader timescale sensitivity. The existence of multiple conformations can now more easily be detected and the residual dipolar coupling data used to confirm or refute models for the conformational fluctuations. It can be expected that future biomolecular NMR studies will increasingly benefit from residual dipolar coupling applications which can recognize and account for molecular flexibility.

1. INTRODUCTION

The recent sequencing of genomes from various organisms, and the ensuing characterization of the cast of gene products participating in cell function, offers new opportunities for furthering our understanding of the complex processes underlying cell function and survival.[1,2] Among the several challenges in the post-genomic *era*, one will inevitably be the classification and articulation of a logical framework which unifies the vast amount of biological data within the constraints of both physical insight and predictive power. One aspect of this challenge is to achieve a molecular-level understanding of the fundamental events underlying biological function. This in turn requires knowledge of the structure of biomolecules, their fluctuations and interactions, and modulations thereof under the various cellular environments.

The determination of the three-dimensional structures of biomolecules using X-ray crystallography and NMR spectroscopy has become commonplace, although the determined structures remain subject to well-known experimental limitations. Crystal packing forces and the conditions needed to yield well diffracting crystals can lead to an all atomic description that may not always accurately reflect the situation under physiological solution conditions. While NMR enjoys applicability under solution conditions, insufficient structural constraints or non-linear averaging of structural constraints by molecular motions can lead to inaccuracies or distortions in the resulting structure. Although biomolecules often localize in diverse cellular compartments having distinct chemical environments, structures are more often determined under one set of conditions (i.e., ionic strength, pH, temperature, crowding), which typically afford favourable application of crystallographic or NMR spectroscopic methods. Nevertheless, knowledge of structure has allowed the articulation of biomolecular interactions at the molecular level in terms of surface complementarity, hydrogen

bonding, hydrophobic and electrostatic interactions. These structures have often confirmed previously suspected or conserved residues as functionally relevant due to their spatial disposition relative to catalytic sites and bindng interfaces. This close correspondence observed between structure and function forms the basis for much of the recent structural genomics activity.[2]

Although the accuracy with which atomic structures of biomolecules are determined has often allowed extraction of useful functional information, it has long been recognized that biomolecules are not rigid, and that changes in conformation, as a function of time, may also be important to function. Motions of residues can allow for optimal formation of contact during induced-fit complex formation, provide plasticity for modulating a bio-molecular structure in response to ligand binding, allow for organization of the rates of substrate entry and exit, and provide thermodynamic control of binding affinities through changes in configurational entropy.[3,4] However, due to the formidable experimental challenges associated with the study of dynamics, most of the evidence for a role of dynamics in function has come from recognition that structural information alone is inadequate to explain all observations. Myoglobin, the first protein to have its structure determined, is a case in point. Perutz and co-workers noted that, based on the three-dimensional positions of atoms, there was no passageway for ligand entry into the heme binding pocket and proposed that dynamics were necessary for its function.[5] After decades of further study, dynamics is still implicated in myoglobin function, although the exact details remain elusive.[6] Compelling lines of evidence for a role of dynamics in function has also come from studies on the temperature dependence of protein motions using a variety of biophysical techniques. These studies have revealed a dynamic transition that is manifested by a significant increase in the amplitudes, breadth of timescale, and anharmonicity of motions above a critical temperature referred to as the 'protein glass transition temperature' ($T_g \sim 180$–220 K).[7] The anharmonic motions are believed to be collective/diffusive in nature,[8] linking conformational sub-states.[9] Importantly, the onset of harmonic motions has been linked to protein activity, with the activity of several proteins being diminished at temperatures below T_g.[9,10,11]

NMR spectroscopy is an increasingly important tool for the elucidation of biomolecular dynamics and its role in biological function.[12–18] A variety of NMR techniques can be employed to provide site specific information on motions occurring over a wide range of biologically relevant timescales, as shown in Fig. 1. Fast motions such as bond librations and the motions of flexible loops and side-chains, can be probed using spin relaxation measurements; slower motions such as ring flips or conformational rearrangements occurring on microsecond–millisecond timescales can be probed using relaxation dispersion and cross-correlated relaxation experiments and even slower motions (>1 s) can be probed using magnetization transfer
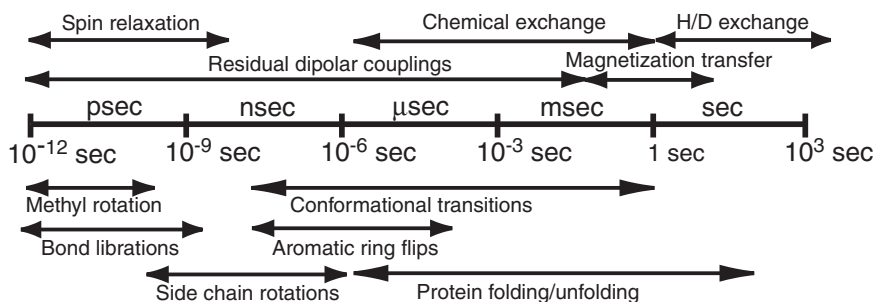
Fig. 1. Depiction of the motional timescale sensitivity of various NMR methods for studying dynamics. For comparison, the approximate motional regimes for various biological motions are also indicated.

and hydrogen/deuterium exchange experiments. As such, NMR studies have played an important role in implicating or confirming the role of mobility in functionally active residues during enzyme catalysis, ligand entry, allostery and entropic control.[3,4,12–18]

Yet our current understanding of biomolecules at a molecular level remains deficient. An all encompassing description of biomolecules would include the position of all atoms as a function of time and also the chemical environment. We are currently far from this picture. For example, the interpretation of spin relaxation experiments, sensitive to the picosecond–nanosecond motional timescales, can become complicated in the presence of significant anisotropy of rotational diffusion and internal motions. Relaxation dispersion experiments can probe the slower motions of nuclei that experience different chemical shielding environments, but direct interpretation in terms of a motional model remains difficult. But the common denominator to NMR studies of dynamics is the insufficient quantity of data. It is challenging to extrapolate from the NMR measurements to a structural description of the conformational changes occurring. What are the precise conformations that control ligand entry/egress from reactive centres, modulate catalytic behaviour and lead to allosteric control? How heterogeneous are reactions such as molecular recognition and catalysis? Answering such questions may prove to be important and this in turn will be predicated on continuing the development of techniques capable of probing processes as complex as dynamics.

The emergence of NMR methodology for the measurement of residual dipolar couplings (RDCs) as an additional NMR probe of dynamics, although far from resolving these issues, holds considerable promise for bringing us closer to the realization of these goals. The excitement about use of RDCs for probing biomolecular dynamics originates from a number of important points. First, RDCs are broadly sensitive to motions occurring on submillisecond timescales (see Fig. 1), including intermediate timescale

motions (nanosecond–microsecond) that have traditionally been difficult to probe with significant spatial resolution. Secondly, RDCs are intrinsically sensitive to both the amplitudes and asymmetries of motions, and thus contain structurally descript information regarding molecular fluctuations. Significantly, RDCs can be exploited to provide this information both quantitatively and in great abundance. Finally, the orientational constraints derived from RDCs are of an inherent precision and accuracy such that the quality of solution state NMR structures can in certain cases rival those determined using crystallographic methods. This has strengthened the ability to reliably identify subtle differences between structures determined in the solution and solid-state, providing insight into crystal packing forces and molecular plasticity.

This review focuses on developments in RDC methodology of particular relevance to the study of dynamics. There is inevitably considerable overlap with structural applications, and thus for completeness, we refer the reader to a number of thorough reviews on the subject.[19–29] The organization for our discussion will be as follows. In Section 2, we discuss the theoretical basis and the assumptions involved in the extraction of structural and dynamic information from RDCs. In Section 3, we review the experimental tools for achieving macromolecular alignment as well as some methods for the experimental determination and prediction of molecular alignment. In subsequent sections, we review recent applications demonstrating use of RDCs in probing dynamics in protein systems (Sections 4 and 5), nucleic acids (Section 6) and oligosaccharides (Section 7).

2. THEORETICAL BACKGROUND

The theoretical foundation for NMR spectroscopy of aligned systems has been developed in numerous forms over the years, extending from early field aligned and liquid crystal applications[30–40] to much more recent biomolecular applications.[19,20] Although for many of these applications the theoretical background is relatively straightforward, the use of different notations and conventions can complicate matters. In what follows, we first develop the underlying theoretical basis for typical RDC-based biomolecular structural refinement applications, with some attempt made to highlight notational differences. We then extend the theoretical framework to accommodate more recent developments in applying RDCs to the study of dynamics. The discussion is focused almost exclusively on RDCs, however the tools described are also applicable to residual chemical shift anisotropy and quadrupolar coupling interactions, with only some minor modifications to the equations.

2.1. The dipolar interaction

The nuclear dipole–dipole interaction arises due to the direct magnetic interaction between a pair of nuclear magnetic moments, in analogy to the interaction between a pair of bar magnets. For commonly studied magnetic nuclei, dipole interaction strengths reach energies in the kHz range. On the other hand, Zeeman interaction strengths typically fall well into the MHz range. This renders the non-secular terms of the dipolar Hamiltonian completely ineffective in influencing the eigenenergies of the system. Hence, we need only consider a truncated dipolar Hamiltonian.[41,42] When expressed in the laboratory frame (units in Hz), the dipolar interaction between two weakly coupled nuclei labelled i and j assumes a rather simple form,

$$H_{ij}^{D}(t) = -\left(\frac{\mu_0}{4\pi}\right) \frac{\gamma_i \gamma_j h}{2\pi^2 r_{ij}^3(t)} \, I_{iz} I_{jz} P_2(\cos\theta_{ij}(t)) \tag{1}$$

where r_{ij} is the internuclear distance between spins, γ_i and γ_j are the gyromagnetic ratios of spins i and j respectively, and the I_{kz} are spin angular momentum operators. The angular portion of the dipolar Hamiltonian is described using the second rank Legendre function, $P_2(\cos\theta_{ij}(t))$, which is a function of the angle θ_{ij} subtended by the magnetic field and the ijth internuclear vector.

   The time dependence of this dipolar Hamiltonian arises due to motions that change the distance between the nuclei or the angle, θ_{ij}, between the internuclear vector and the externally applied magnetic field. In the solution state, the angle θ_{ij} fluctuates due to both overall molecular reorientation and internal motions. RDCs can be measured when the time-averaged resultant of these processes does not vanish. This leads to a finite contribution to the static spin Hamiltonian, in turn influencing the eigenenergies of the system such that a contribution to the splittings of lines may be observed. The contribution to observed couplings, arising from the time-averaged dipolar Hamiltonian, is related to these eigenenergies according to,

$$D_{ij}^{res} = \left\langle \beta\beta \left| \overline{H}_{ij}^{D} \right| \beta\beta \right\rangle - \left\langle \beta\alpha \left| \overline{H}_{ij}^{D} \right| \beta\alpha \right\rangle - \left\langle \alpha\beta \left| \overline{H}_{ij}^{D} \right| \alpha\beta \right\rangle + \left\langle \alpha\alpha \left| \overline{H}_{ij}^{D} \right| \alpha\alpha \right\rangle \tag{2}$$

where $\overline{H}_{ij}^{D}$ refers to the time averaged dipolar Hamiltonian. This leads to the following expression,

$$D_{ij}^{res} = -\left(\frac{\mu_0}{4\pi}\right) \frac{\gamma_i \gamma_j h}{2\pi^2 r_{ij,eff}^3} \left\langle P_2(\cos\theta_{ij}(t)) \right\rangle \tag{3}$$

with the time averaging indicated by the angle brackets. Normally an effective internuclear distance, $r_{ij,eff}$, is introduced in order to remove the

explicit consideration of distance averaging and its correlation with angular averaging. The justification for this separation rests on the assumption that distance and angular averaging are likely to occur on very different time-scales and thus their averages can be computed independently.[43] For directly bonded nuclei, or those related through a rigid molecular framework, violations of this assumption are expected to be negligible upon proper choice of an effective internuclear distance.[44]

Most typically of interest is the average of the angular part in Eq. (3), which reflects the orientational distribution of the *ij*th internuclear vector relative to the magnetic field. Under an isotropic distribution of molecular orientations, this average will vanish, explaining why line splittings arising from dipole–dipole interactions are not typically observed in high resolution NMR spectra. Their observation requires an anisotropic (non-uniform) distribution of molecular orientations. The RDCs observed under these conditions will report on a convolution of the effects of overall molecular motion, internal motion, and structural characteristics. The challenge is to separate these different contributions to the observed couplings.

2.2. Rigid molecules

An appreciation of the relationship between experimentally observed RDCs and molecular structure is most easily gained by assuming complete rigidity of the molecule. This assumption also allows one to proceed with a minimum of data, and thus it is the predominant route for the majority of RDC-based structure refinement applications. While this assumption clearly will not hold generally, in many circumstances deviations from rigidity appear to be small enough to be safely neglected. The underlying theoretical develop-ment has appeared in numerous forms throughout the literature, but the foundation common to most is the order tensor formalism.[37,38,45] In what follows, this order tensor formalism will be introduced and presented in several of its different guises.

2.2.1. *The order tensor*

It was recognized that for a rigid molecule one can expand the angular aver-age contained in Eq. (3) into a sum of geometric terms describing the orientation of the internuclear vector within the molecule, and corresponding averages that describe the nature and extent of the ordering of the entire molecule.[37,38,45]

$$\langle P_2(\cos\theta_{ij})\rangle = \sum_{kl=xyz} S_{kl}\cos(\alpha_k^{ij})\cos(\alpha_l^{ij}) \tag{4}$$
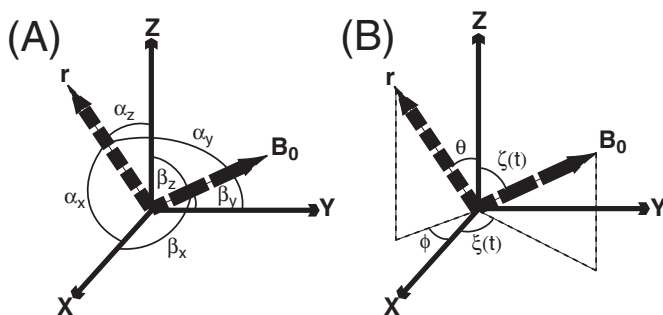
Fig. 2. The angular coordinates used to describe the orientation of the magnetic field, $\mathbf{B_0}$, and an internuclear vector, $\mathbf{r}$, relative to an arbitrarily chosen coordinate frame which is fixed to the molecule. Description in terms of (A) direction cosines and (B) polar angles.

The rigid molecular geometry is described using direction cosines, in which α_n^{ij} subtends the angle between the *ij*th internuclear vector and the *n*-axis within an arbitrarily placed set of Cartesian coordinate axes (Fig. 2A). The averages that describe the ordering of the molecule are represented by the terms S_{kl}, which form the elements of a Cartesian 3×3 tensor called the order tensor. The elements of the order tensor are formally defined in terms of time averages over functions describing the orientation of the magnetic field relative to some arbitrarily chosen molecule fixed coordinate system,

$$S_{kl} = \left\langle \frac{3}{2}\cos(\beta_k(t))\cos(\beta_l(t)) - \frac{1}{2}\delta_{kl} \right\rangle \tag{5}$$

where δ_{kl} represents the Kronecker delta function and the time dependent angles $\beta_n(t)$, shown in Fig. 2A, describe the instantaneous orientation of the magnetic field. From Eq. (5), it is apparent that the Saupe tensor is symmetric and traceless, and is thus composed of only five independent elements. It can thus always be diagonalized, with the magnitude and asymmetry of alignment contained in the eigenvalues, and the orientation of the principal axis system (PAS) of molecular alignment specified by the transformation matrix formed from the eigenvectors.

It is important to recognize that the Saupe order tensor does not provide a complete description of alignment. Rather it describes the details of molecular alignment only to the extent necessary to adequately account for the observation of the residuals of anisotropic NMR parameters such as chemical shift, dipolar couplings or quadrupolar couplings. Indeed, the Saupe order tensor parameters correspond only to the 2nd rank part of the orientational probability distribution function (OPDF) describing the orientation of the magnetic field relative to a coordinate frame fixed to the rigid molecular fragment. In general, the full orientational probability distribution

function, $P(\theta, \phi)$, for a vector (such as B_0) can be expressed in terms of infinite series of spherical harmonics,

$$P(\theta, \phi) = \frac{1}{4\pi} + \sum_{l=1}^{\infty} \sum_{m=-l}^{l} c_{lm} Y_{lm}^*(\theta, \phi) \tag{6}$$

where θ and ϕ are the polar angles describing the orientation of the vector relative to the molecule fixed set of coordinate axes, the Y's are the normalized spherical harmonics and the c's are scalar coefficients. Although this function can describe any possible OPDF, its experimental determination is not likely to be feasible due to the infinite number of parameters required to describe it. The description of NMR observables such as RDCs, however, only requires knowledge of a small part of this function, due to the simple geometrical dependence of RDCs on spatial coordinates. To see this, we utilize the spherical harmonic addition theorem,

$$\langle P_2(\cos\theta_{ij}) \rangle = \frac{4\pi}{5} \sum_{q=-2}^{2} Y_{2q}^*(\theta\phi) Y_{2q}(\zeta(t)\xi(t)) \tag{7}$$

to expand the 2nd rank Legendre function of Eq. (3), where $(\theta, \phi) = \Phi$ are polar angles describing the orientation of the internuclear vector within the arbitrary molecular frame and $(\zeta(t), \xi(t)) = \Omega(t)$ describe the orientation of the magnetic field relative to the same molecular frame. For a rigid molecule, only the angles $(\zeta(t), \xi(t))$ describing the magnetic field vector relative to the molecular reference frame are time dependent. This separation into variables internal and external to the molecule is analogous to the classic formulation of the Saupe order tensor (see Eq. (4)). This leads to the following expression for the dipolar contribution to the coupling observed between a pair of spins i and j,

$$D_{ij}^{res} = -\left(\frac{\mu_0}{4\pi}\right) \frac{\gamma_i \gamma_j h}{2\pi^2 r_{ij}^3} \frac{4\pi}{5} \sum_{q=-2}^{2} Y_{2q}^*(\Phi) \langle Y_{2q}(\Omega(t)) \rangle \tag{8}$$

With knowledge of the full OPDF in Eq. (6), the averages in Eq. (8) can be evaluated by integration with respect to the angles ζ and ξ, which is straightforward due to the orthogonality properties of the spherical harmonics.[46]

$$\langle Y_{2q}(\Omega(t)) \rangle = \int\int P(\zeta, \xi) Y_{2q}(\zeta, \xi) \sin\zeta \, d\zeta \, d\xi = c_{lm}\delta_{2l}\delta_{mq} = c_{2q} \tag{9}$$

As can be seen, only the 2nd rank part of the OPDF, described by the five coefficients c_{2q}, contributes to the observation of RDCs. These coefficients

are related to the elements of the Saupe order tensor by a linear transforma-tion.[37] The advantage of this rather simple situation is that only five parameters are necessary to completely describe the molecular alignment for purposes of analysis of RDCs. The disadvantage is that only a small portion of the full OPDF can be characterized by means of an analysis of measured RDCs.

   This limited sampling of the OPDF may, in many cases, be of small consequence when the objective is the description of molecular alignment relative to the magnetic field. Often the alignment of the molecule deviates only slightly from isotropy and can thus be described predominantly by lower order terms in Eq. (6). However, as will be discussed later, the description of the motion of an internuclear vector can also be described with an OPDF of this same form. But in contrast, a large number of terms (in Eq. (6)) are typically required to fully describe the dynamics of the internuclear vector due to the fact that its orientation will generally be highly localized. As a consequence, the *apparent* mean orientation of the internuclear vector, as derived from RDC analysis, can deviate considerably from reality if motions are both extensive and highly anisotropic in nature. This situation is somewhat analogous to the description of a complicated one-dimensional distribution function in terms of just the first and second moments.

2.2.2. *Description of molecular alignment*

The calculation or experimental determination of the five parameters that constitute the Saupe order tensor, commonly referred to as the alignment tensor, is often the first step in the analysis of RDC data. In general, the elements of the order tensor will be determined in some arbitrary frame, in which their physical interpretation is not readily apparent. A more intui-tive representation of the order tensor is achieved by diagonalization of the corresponding symmetric 3×3 matrix by means of a unitary transformation $\mathbf{S}' = \mathbf{TST}^{-1}$. The transformation $\mathbf{T}$ which diagonalizes the order tensor will transform the molecular coordinates from the arbitrary frame, in which the initial values of the angles α_n^{ij} are determined (Fig. 2), into the PAS of the order tensor. The corresponding eigenvalues of the order tensor describe the magnitude of alignment along each of the three orthogonal principal axes. Only two of the eigenvalues are independent as the three must sum to zero. Depicted in Fig. 3 are the principal axes of the order tensor superimposed on a ribbon diagram of a protein. For systems which tend to orient parallel to the magnetic field, the placement of the principal axes corresponds to a determination of the directions both most probably (the z-axis) and least probably (the y-axis) aligned parallel to the magnetic field, subject to maintenance of orthogonality of the three axes. The magnitudes of alignment can be expressed in many forms, but at minimum may be considered to describe the degree of ordering of the principal axis (usually z) and the difference in ordering along the x and y axes.
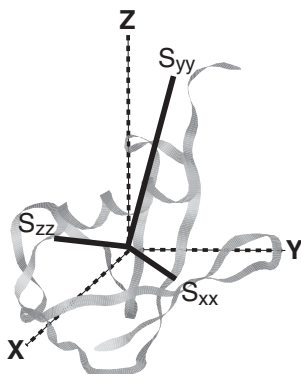
Fig. 3. The principal axis system of the order tensor corresponds to the specific positioning of a set of coordinate axes relative to the molecule, as indicated by the S_{xx}, S_{yy} and S_{zz} labelled axes. The rotation which diagonalizes the order tensor also carries the initial molecular coordinate frame, specified by the x, y and z labelled axes, into the PAS of the order tensor. This figure was prepared using the program Module.[193]

It is common to work with an expression for RDCs written in the PAS of alignment since this leads to simplification of Eq. (8), with the remaining nonzero elements $\langle Y_{2q}(\zeta(t), \xi(t)) \rangle$ related to the diagonalized Saupe order tensor elements (S_{zz} and ($S_{xx} - S_{yy}$)) which describe the magnitudes of alignment. When written in its PAS, Eq. (8) becomes,

$$D_{ij}^{res} = -\left(\frac{\mu_0}{4\pi}\right) \frac{\gamma_i \gamma_j h}{2\pi^2 r_{ij}^3} \left\{ S_{zz} Y_{20}(\theta, \phi) + \sqrt{\frac{2}{3}} (S_{xx} - S_{yy})(Y_{22}(\theta, \phi) + Y_{2-2}(\theta, \phi)) \right\}$$
(10)

The explicit expansion of the spherical harmonic functions describing the orientation of the *ij*th internuclear vector leads to the following expression,

$$D_{ij}^{res} = -\left(\frac{\mu_0}{4\pi}\right) \frac{\gamma_i \gamma_j h}{2\pi^2 r_{ij}^3} \left\{ S_{zz} \frac{1}{2}(3\cos^2\theta - 1) + \frac{1}{2}(S_{xx} - S_{yy})\sin^2\theta \cos2\phi \right\}$$
(11)

or alternatively

$$D_{ij}^{res} = -\left(\frac{\mu_0}{4\pi}\right) \frac{\gamma_i \gamma_j h}{2\pi^2 r_{ij}^3} S_{zz} \left\{ \frac{1}{2}(3\cos^2\theta - 1) + \frac{1}{2}\eta \sin^2\theta \cos2\phi \right\}$$
(12)

in which the asymmetry, η, is defined as $(S_{xx} - S_{yy})/S_{zz}$. Some confusion can arise due to differing conventions for the identification of the principal axes. Although there are exceptions, it is often specified that the PAS forms a

right-handed coordinate system with principal axes chosen according to $|S_{zz}| \geq |S_{yy}| \geq |S_{xx}|$. These conditions will constrain η to lie between values of 0 and 1. Frequently, the order tensor is expressed in terms of a magnitude D_a and rhombicity R,

$$D_{ij}^{res} = D_a^{ij}\left\{(3\cos^2\theta - 1) + \frac{3}{2}R\sin^2\theta\cos2\phi\right\} \tag{13}$$

where

$$D_a^{ij} = -\left(\frac{\mu_0}{4\pi}\right)\frac{\gamma_i\gamma_jh}{2\pi^2r_{ij}^3}\left(\frac{1}{2}S_{zz}\right); \qquad R = \frac{2}{3}\eta \tag{14}$$

For cases in which alignment is achieved due to interaction between the magnetic field and the anisotropic magnetic susceptibility (χ) of the molecule, expressions can be derived for the magnitude of alignment as a function of magnetic field strength, susceptibility anisotropy and temperature. One can relate the magnitudes of alignment to the magnetic susceptibility anisotropies (units in m^3) as follows[30,31,39,40]

$$S_{zz} = \Delta\chi\left[\frac{B^2}{15\mu_0kT}\right] \qquad S_{xx} - S_{yy} = \delta\chi\left[\frac{B^2}{10\mu_0kT}\right] \tag{15}$$

From the expression of RDCs in the PAS of alignment (whether Eq. (12) or Eq. (13)), it is clear that a given RDC measurement, D_{ij}^{res}, does not correspond to a unique orientation of the internuclear vector. In fact the
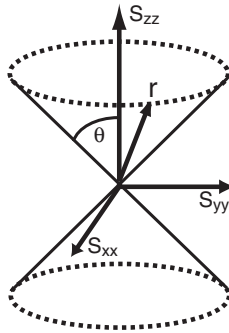
Fig. 4. For axially symmetric alignment, a single measured residual dipolar coupling is consistent with orientations of the corresponding internuclear vector, **r**, which deviate from the principal (z) axis of the order tensor by an angle θ, thus describing the surface of a cone, and its inverse. If alignment departs from axial symmetry, then the cone of permissible orientations will require further description in terms of an azimuth angle ϕ and exhibit some distortion along the x and y directions.

allowed orientations of the internuclear vector will lie on the surface of a cone as shown in Fig. 4. In general, the cone of Fig. 4 will be distorted along the x and y by an amount dependent on the asymmetry of alignment. This ambiguity poses some considerable complications for the interpretation of RDC data in terms of molecular structural and dynamic parameters.

2.3. Flexible molecules

All molecules are flexible to some extent and thus all of the theoretical development contained in the previous section relies on the assumption that the effects of flexibility can be safely neglected. Although this appears to be a valid approach in some cases, it is necessary in most cases because of a lack of sufficient information. Nevertheless, there are several reasons to consider the effects of flexibility on the observed RDCs and the subsequent implications for successful interpretation.[47] Among these is the need to understand better the implications that the neglect of mobility will have on structural interpretations of RDCs. In addition, the broad temporal sensitivity of RDCs to motion represents an opportunity to probe biomolecular dynamics. Although this would in general appear to be a very complicated task, there are several circumstances under which RDCs constitute a powerful probe of dynamics. We discuss below these circumstances and the corresponding nature of the information concerning dynamics which can be extracted from RDCs.

For purposes relevant to the analysis of RDCs, one might crudely partition the continuum of molecular dynamics into three broad categories, illustrated in Fig. 5. The first category (Fig. 5A) is that in which the molecule is characterized better in terms of its disorder rather than its structure. Although the molecule may periodically assume some structured conformations, the different conformations that it assumes are highly dissimilar. At present, this regime is inaccessible to detailed study at an atomic level of resolution. From the perspective of RDC-based analysis, each conformational sub-state would have its own associated order tensor and molecular geometry and the observed RDCs would be a population weighted average of contributions from each sub-state. Without fairly extensive prior information, the interpretation of RDCs measured for systems in this dynamic regime is fraught with difficulties and is largely restricted to qualitative analysis. The second category (Fig. 5B) corresponds to considerably simplified cases where there are local regions or domains which exhibit some persistent structural properties. Although the overall picture may be one of considerable mobility, in which a wide range of different conformers are populated, the presence of some separately structured domains allows their individual analysis using fairly standard analysis tools. This analysis can establish the global conformation as well as provide insights into
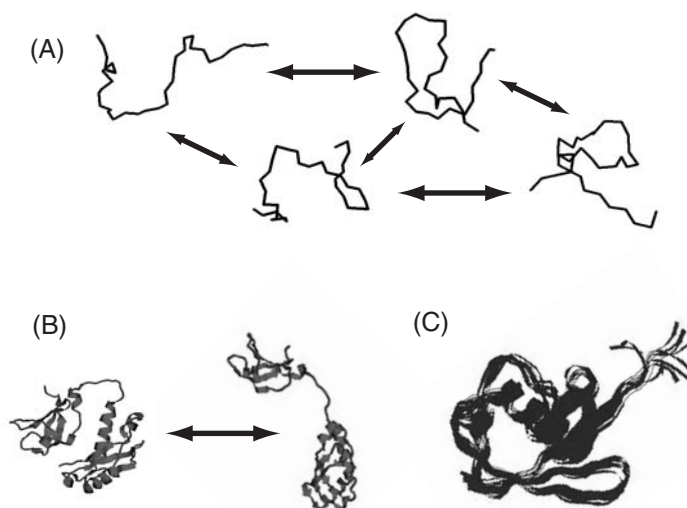
Fig. 5. The applicability of different approaches to the analysis of RDCs depends on the nature of the dynamics of the molecule. For this purpose, three different motional regimes may be specified. (A) Molecules which exist in several completely different conformations, thus precluding the determination of a single order tensor. (B) Some well structured regions exist, but may exhibit extensive motions relative to one another. (C) The molecule can be described in terms of a mean conformation about which motional excursions occur.

amplitudes and asymmetries of motions. Depending on the exact details of the system, some conclusions of a more quantitative nature may be obtained. The third category (Fig. 5C) is that of a well structured molecule, for which the concept of a mean structure would clearly be applicable and which, in large part, encompasses the majority of the successes of structural biology. In this regime, RDCs can not only inform on the mean conformation but they are also capable of providing information regarding the motional fluctuations about the mean conformation.

2.3.1. *Relative motion of rigid molecular subunits*

Due to the modular architecture of many biomolecules, there are often cases where certain segments of a molecule may reasonably be assumed to be rigid but that can otherwise undergo rigid-body motions. In these cases, inter-fragment orientations and dynamics can be characterized by solving for fragment-specific order tensors using at least five independent RDC measurements per fragment.[19,48,49] A first order degree of separation of structural and dynamical contributions to RDCs can be attained through

diagonalization of the order tensor, yielding a PAS frame and eigenvalues then contain the desired structural and dynamical information respectively. Superposition of fragment centred order tensor frames yields constraints on the average inter-fragment alignment (Fig. 6A) with an accuracy that is tolerant to errors arising due to moderate inter-fragment motional averaging ($<15°$), while comparison of fragment-specific principal order parameters (eigenvalues of the order tensor) can provide information about inter-fragment motions (Fig. 6B).[49] For fragments which remain rigid with respect to one another, one expects determination of identical principal order parameters, reflecting a common degree of molecular ordering, while motions can lead to differences dependent on both the amplitudes and asymmetry of the motion as well as the intrinsic alignment propensities of individual fragments. To simplify comparison of the magnitudes of alignment, a parameter called the generalized degree of order (GDO), symbolized by ϑ, has been introduced to provide a single scalar measure of the magnitude of alignment.[49]

$$\vartheta = \sqrt{\frac{2}{3} \sum_{ij} S_{ij}^2} \tag{16}$$

The GDO is related to the standard deviation of the distribution of RDCs according to,

$$\sigma_{D^{res}} = \sqrt{\frac{1}{5}} \left| \left(\frac{\mu_0}{4\pi}\right) \frac{\gamma_i \gamma_j h}{2\pi^2 r_{ij}^3} \right| \vartheta \tag{17}$$

As discussed later in the context of specific applications, comparison of the generalized degree of order (GDO) obtained for different fragments can provide a lower bound for the extent of motional averaging. For example, identical GDOs measured for different fragments indicates consistency with complete rigidity, although one cannot exclude motional effects which are identical for all fragments considered.

2.3.2. *Motional fluctuations about a mean conformation*

In extending our conceptualization of a molecule from one of rigidity to one which exhibits mobility, the smallest increment in mobility is to consider that the molecule exists in a mean conformation about which fluctuations of sufficiently small amplitude occur such that the molecule is not significantly distorted from its mean. This model may be particularly applicable for macromolecules, where large amplitude, highly correlated motions may be exceptional events due to their significant enthalpic cost and modest entropic gain. For situations which conform to this motional regime, it is possible to deploy RDC-based methods in order to study these motions, although some further theoretical development is required.
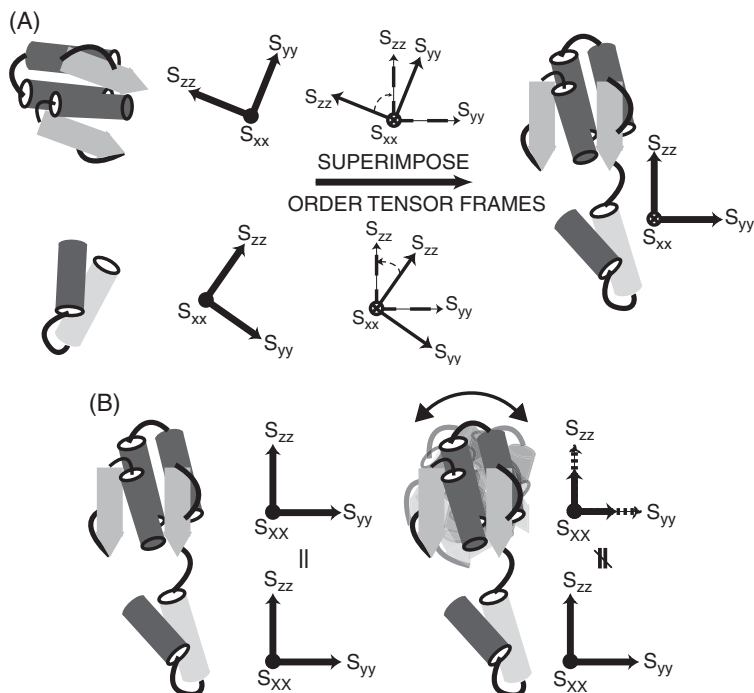
Fig. 6. Determining relative molecular fragment orientations and dynamics using order tensor analysis of RDCs. Molecular fragments are shown as protein domains but can also be other structural fragments derived from biomolecules (A) Relative fragment alignment can be determined by superimposing fragment specific order tensor frames describing average molecular alignment relative to the applied magnetic field. (B) For rigidly connected fragments, principal order parameters (S_{zz}, S_{yy}, S_{xx}) will be identical, while inter-sub-structure motions over a wide range of timescales ($<$ millisecond) can lead to variations dependent on both the amplitude and directions of motions. Shown is an example where motions of one fragment about the S_{xx} direction leads primarily to attenuations in the order parameters along the S_{zz} and S_{yy} directions while the order along the S_{xx} direction remains unchanged.

It proves convenient to represent the Saupe tensor, $\hat{S}$, in terms of just its five independent elements. These five independent tensorial elements are written as a vector, **s**, and are related as follows to the elements of the relevant 3×3 Saupe tensor described in Eq. (5).

$$\mathbf{s} = \left[S_{zz}, \frac{1}{\sqrt{3}}(S_{xx} - S_{yy}), \frac{2}{\sqrt{3}}S_{xz}, \frac{2}{\sqrt{3}}S_{yz}, \frac{2}{\sqrt{3}}S_{xy} \right] \tag{18}$$

The direction cosine functions, $\cos\alpha_n^{ij}$, used to describe the rigid molecular geometry can be rearranged into a tensor $\hat{R}^{ij}$ in analogy to the Saupe tensor $\hat{S}$

used to describe the alignment of the molecule. The corresponding relationships are summarized below,

$$\mathbf{r}^{ij} = \left[R_{zz}^{ij}, \frac{1}{\sqrt{3}} (R_{xx}^{ij} - R_{yy}^{ij}), \frac{2}{\sqrt{3}} R_{xz}^{ij}, \frac{2}{\sqrt{3}} R_{yz}^{ij}, \frac{2}{\sqrt{3}} R_{xy}^{ij} \right] \qquad (19)$$

with

$$R_{kl}^{ij} = \left\langle \frac{1}{2} (3\cos\alpha_k^{ij}\cos\alpha_l^{ij} - \delta_{kl}) \right\rangle \qquad (20)$$

in which δ_{kl} represents the Kronecker delta function and the angles α_n^{ij} describe the orientation of the ijth internuclear vector relative to the arbitrary reference frame (Fig. 2A). The angle brackets in Eq. (20) indicate that the elements of the tensor $\hat{R}^{ij}$ are time averaged due to *internal motions* of the ijth internuclear vector. This formulation of the problem in terms of the irreducible tensor elements of $\hat{S}$ and $\hat{R}^{ij}$ leads to yet another alternative form of the classic Saupe formulation [38,45] of Eq. (4).

$$\langle P_2(\cos\theta_{ij}) \rangle = \sum_k r_k^{ij} s_k = \frac{4\pi}{5} \sum_{q=-2}^{2} \left\langle Y_{2q}^*(\theta(t), \phi(t)) \right\rangle \left\langle Y_{2q}(\zeta(t), \xi(t)) \right\rangle \qquad (21)$$

The applicability of Eq. (21) rests on the validity of the assumption that the averages over internal and external variables are uncorrelated and thus can be calculated separately. Furthermore, the expression of Eq. (21) emphasizes the close similarity of the irreducible Cartesian representation to the expression of the problem in terms of polar angles and the normalized 2nd rank spherical harmonics Y (see Eq. (7)). The corresponding polar angles $(\theta(t), \phi(t))$ and $(\zeta(t), \xi(t))$, shown in Fig. 2B, describe the orientation of the internuclear vector and the magnetic field relative to the arbitrary reference frame, respectively. The different representations are related according to the following relationships.[37]

$$\frac{2}{\sqrt{3}} S_{xz} = \sqrt{\frac{1}{2}}\sqrt{\frac{4\pi}{5}} (\langle Y_{21}(\Omega(t)) \rangle - \langle Y_{2-1}(\Omega(t)) \rangle)$$

$$\frac{2}{\sqrt{3}} S_{yz} = i\sqrt{\frac{1}{2}}\sqrt{\frac{4\pi}{5}} (\langle Y_{2-1}(\Omega(t)) \rangle + \langle Y_{21}(\Omega(t)) \rangle)$$

$$\frac{2}{\sqrt{3}} S_{xy} = i\sqrt{\frac{1}{2}}\sqrt{\frac{4\pi}{5}} (\langle Y_{22}(\Omega(t)) \rangle - \langle Y_{2-2}(\Omega(t)) \rangle)$$

$$\frac{1}{\sqrt{3}} (S_{xx} - S_{yy}) = \sqrt{\frac{1}{2}}\sqrt{\frac{4\pi}{5}} (\langle Y_{22}(\Omega(t)) \rangle + \langle Y_{2-2}(\Omega(t)) \rangle)$$

$$S_{zz} = \sqrt{\frac{4\pi}{5}} \langle Y_{20}(\Omega(t)) \rangle \qquad (22)$$

Substituting the irreducible Cartesian expression of Eq. (21) into Eq. (3) leads to the following expression for RDCs between a pair of nuclei i and j.

$$D_{ij}^{res} = -\left(\frac{\mu_0}{4\pi}\right)\frac{\gamma_i\gamma_j h}{2\pi^2 r_{ij}^3} \sum_k r_k^{ij} s_k \tag{23}$$

The explicit separation of the effects of internal motion and overall alignment according to either Eq. (23) above, or a suitably modified version of Eq. (8), is desirable for two reasons. The first is that the expression corresponds to a linear algebraic system of equations which can be approached using well established mathematical methods. The second is that the collection of the internal geometrical terms into a tensor $\hat{R}^{ij}$, defined analogously to the order tensor, greatly facilitates the interpretation of the resulting tensorial elements in terms of physical properties of interest.

2.3.3. *Separation of mean orientation and dynamics*

The reliance of the interpretation of RDCs on the existence of some structured region within the molecule arises from the need to specify a molecule fixed frame, which guides the partitioning of the spatial degrees of freedom between overall molecular motion and internal motions and structural properties. Provided that such a partitioning is permissible (i.e., the use of Eq. (21) is valid), the subsequent interpretation of RDCs in terms of structural and dynamic properties becomes a matter of the physical interpretation of the individual tensors $\hat{R}^{ij}$, which describe the averaged angular functions for the *ij*th dipolar interaction. The key to this interpretation is to recognize the mathematical correspondence of $\hat{R}^{ij}$ to $\hat{S}$ and to recall their respective relationship to the OPDF describing the *ij*th internuclear vector and the magnetic field vector relative to the molecule fixed frame.[20,50] Therefore, we might expect that diagonalization of the 3×3 Cartesian matrix representation of $\hat{R}^{ij}$ will, as for the order tensor, provide the desired physical description. This separation into structural and dynamic characteristics is illustrated in Fig. 7. The unitary transformation which diagonalizes $\hat{R}^{ij}$ describes the rotation from the molecule fixed frame into the local PAS of the *ij*th interaction. When described in terms of Euler angles (α, β, γ), the angles α and β correspond to the polar angles specifying the mean orientation of the internuclear vector between spins i and j. The situation becomes ambiguous if the internuclear vector is highly mobile, in which case the 'orientation' is better described as corresponding to the direction of highest ordering of the vector. The eigenvalues of $\hat{R}^{ij}$ are order parameters which describe the amplitude of motion. If the *ij*th internuclear vector is rigid, then it follows that $R_{zz}^{ij} = 1$ and $R_{xx}^{ij} = R_{yy}^{ij} = -1/2$ in analogy with the order tensor. More generally, the element R_{zz}^{ij} corresponds to the axial order parameter and the difference $(R_{xx}^{ij} - R_{yy}^{ij})$
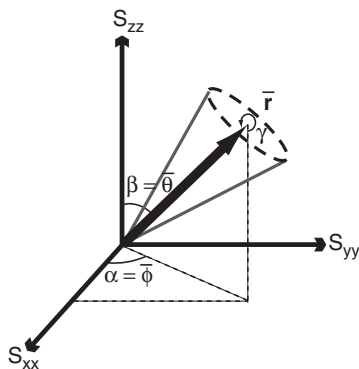
Fig. 7. The nature of information concerning the mean orientation and dynamics of an internuclear vector **r**, which can be obtained from RDC analysis. Upon diagonalization of the Cartesian dipolar interaction tensor $\hat{\mathbf{R}}^{ij}$, described in the text, the mean vector orientation, $\bar{\mathbf{r}}$, will be described by the Euler angles α and β. The eigenvalues will correspond to the axial and rhombic order parameters which describe the amplitude of motion. If the motion is asymmetric, as reflected in a nonzero rhombic order parameter, then the principal direction of asymmetry is described by the Euler angle γ.

reflect the asymmetry of motion. In the case that motion is asymmetric, the direction of motion is described by the third Euler angle, γ. The dipolar generalized order parameter S_{rdc} is defined as a function of both the radial and axial ordering, according to,

$$S_{ij,rdc}^2 = \left[\hat{R}_{zz}^{ij} \right]^2 + \frac{1}{3} \left[\hat{R}_{xx}^{ij} - \hat{R}_{yy}^{ij} \right]^2 \qquad (24)$$

This definition is analogous to that of the more common spin relaxation generalized order parameter, although the sensitivity to motional timescales is very different. As will be discussed later, a further distinguishing characteristic is that RDC analysis can in principle allow the explicit separation and determination of the direction and extent of the motional asymmetry.

3. MOLECULAR ALIGNMENT

The anisotropic nature of the dipolar, quadrupolar and chemical shift anisotropy interactions requires that the isotropy of molecular orientation relative to the applied magnetic field be broken in order to allow their direct observation in terms of shifts in the frequencies of resonances.[20,32,38–40] For high resolution NMR studies this has meant, thus far, that some degree of alignment of the molecule needs to be established. Almost all molecules will align to a small extent due to the anisotropy of their magnetic

susceptibility (χ) and the interaction between the resulting induced magnetic dipole and the magnetic field.[19,32,39,40,51] However, with the exception of paramagnetic or diamagnetic systems with considerable aromatic content, the degree of biomolecular alignment is often too minute (approximately 1 part in 10,000) at current magnetic field strengths (<20 T) to allow measurement of RDCs with a useful level of accuracy and precision.[19] It is therefore typical that some sort of ordered alignment medium is utilized in order to induce a sufficiently large and controllable degree of molecular alignment.[52] This approach relies on interactions between the solute molecule and the highly ordered medium, which mediate the transfer of a small degree of order to the solute molecule. Optimally, the transferred order is large enough to make RDCs or other tensorial interactions readily measurable (on the order of 10 Hz), while remaining weak enough to preserve the high spectral resolution characteristic of solution NMR, allowing use of the extensive repertoire of high resolution NMR experiments. The physical nature of the induced molecular alignment, described by the order tensor, and its spatial relationship to the dipolar interaction vectors will dictate what is observed in the NMR experiment. Thus an understanding of the mechanisms underlying molecular alignment is important for the structural and dynamical analysis of RDC. In this section, we review the variety of alignment media now demonstrated to be compatible with biomolecular studies, as well as methods for the experimental estimation and theoretical prediction of order tensors.
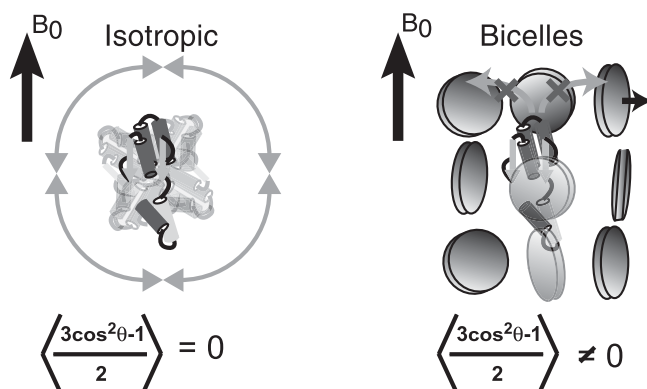
3.1. Alignment media

There is now an impressive repertoire of anisotropic ordering media which can be employed for the purpose of establishing a weak degree of molecular alignment, most of which have already been reviewed.[20,21,23,24,53,54] This provides the biomolecular NMR spectroscopist with numerous options for achieving the desired degree of alignment under a variety of pH, ionic strength, detergent and temperature conditions. The result is that most biomolecules can now be successfully aligned and subjected to RDC-based analysis. Aside from concerns about finding a medium which is compatible with the biomolecule of interest, there is increasing interest in employing several different media for modulating solute alignment and obtaining complementary sets of RDC data,[55,56] which can enhance the amount of retrievable information concerning structure and dynamics.[50,57–59] This ability to modulate the alignment of a molecule stems from the complexity of interactions between the solute molecule and the medium. At a fundamental level, the molecule interacts with the medium either through steric or electrostatic interactions, which may involve specific binding of the solute molecule to the medium, or more non-specific steric obstruction

interactions. In addition, the morphology of the medium itself can affect alignment due to differences in the nature of interaction or differences in the disposition of the medium relative to the magnetic field. The end result is that the observed alignment for the molecule is the ensemble average over all possible interactions with the medium. While there have been some strong correlations observed between sets of RDCs measured in two different media, for proteins at least it seems that the prospects are good for achieving different alignment conditions. Indeed, there are now reports detailing the measurement of at least five independent sets of RDCs.[58,59] We provide below an overview of the media which have to date been demonstrated to be acceptable for use in biomolecular NMR studies.

With modern magnetic field strengths approaching 20 T, it is possible in certain cases to achieve sufficient molecular alignment for molecules possessing large magnetic susceptibility anisotropies.[19,40] Net alignment in these cases is achieved due to the interaction between the magnetic field and the induced magnetic dipole, which varies according to the orientation of the molecule relative to the magnetic field. Magnetic field induced alignment was first demonstrated more than 20 years ago by means of observed residual quadrupolar couplings,[39] followed by the observation of field induced RDCs,[32] and furthermore was the method employed for first demonstrating that RDCs could be observed in macromolecules.[51] Although for many applications, the use of an external medium is desirable because of the stronger degree of molecular alignment which can be achieved, field induced alignment will remain a useful tool because it does not pose any potentially perturbative influence on the macromolecule and because the physical basis for alignment is relatively easily understood. Furthermore, because field-induced and ordering media induced alignment have different physical bases, they can provide complementary information, as demonstrated by some recent applications.[60–62]

The first demonstration of the alignment of a protein by means of an external medium was carried out by Tjandra and Bax for the protein ubiquitin dissolved in a dilute solution (5% by weight) of 1,2-di-tetradecanoyl-*sn*-glycero-3-phosphocoline (DMPC) and 1,2-di-hexanoyl-*sn*-glycero-3-phospho-coline (DHPC) in a molar ratio of 2.9:1.[52] This binary mixture forms putative discoidal micelles (although this model is now in question)[63] which originally were utilized as a bilayer mimetic.[64,65] It undergoes a phase transition at ~30°C from an isotropic phase to an anisotropic phase. This medium, along with a number of variations, is commonly referred to as 'bicelles',[66] and is depicted in Fig. 8. An advantage of the medium is that isotropic and anisotropic conditions can be selected by changing the temperature, but some disadvantages accrue as well, in that it is difficult to recover the biomolecule from the bicelle preparation and the lipids are prone to hydrolysis. The DMPC/DHPC bicelles often exhibit phase separation after only short periods.[67] The stability can be improved by adding small amounts of charged

Fig. 8. Partial alignment of biomolecules using field oriented ordering media such as discoidal 'bicelles' allows direct measurement of residual dipolar interactions under solution NMR conditions.

detergents (SDS or CTAB) to help prevent aggregation.[68] When added in larger amounts, the alignment can often be significantly modified due to electrostatic interactions with the solute.[55] There are now ether-based bicelles which do not hydrolyze[69,70] and also bicelles composed of a mixture of DLPC and CHAPSO.[71] Although these developments have introduced much more flexibility with respect to sample conditions, they produce a very similar alignment of the biomolecule in the absence of added charge.[58]

Shortly after the introduction of bicelles as an alignment medium, it was shown that suspensions of rod-like viruses could be used to induce alignment.[53,72,73] Several different viruses have been shown to be suitable including bacteriophage Pf1,[53,72] bacteriophage fd and tobacco mosaic virus.[73] The most commonly employed virus is Pf1,[53] which has favourable properties due in part to its lower nematic threshold concentration.[74] All of these media carry a strong negative charge at neutral pH and align parallel to the magnetic field. It has been shown for Pf1 that alignment can be modulated by addition of NaCl, which diminishes the electrostatic component to alignment relative to the steric component.[74] Suspensions of purple membrane fragments at relatively low concentrations have also been shown to be effective, and produce alignment through largely electrostatic interactions due to their strong negative charge.[75,76] Although virus-based and purple-membrane-based media require a separate isotropic sample in order to measure scalar couplings, a significant advantage is that the macromolecule can readily be recovered from these media by means of centrifugation. Cellulose crystallites, which are much more weakly charged, form an anisotropic chiral nematic phase at sufficient concentrations.[77] The crystallites orient perpendicular to the magnetic field with a helical arrangement along the direction of magnetic field with a pitch on the order of tens of microns.

The classical ternary liquid crystalline phase composed of cetyl pyridinium halide, *n*-hexanol and brine have also been demonstrated to be acceptable as alignment media, using both Cl⁻ and Br⁻ as anions.[78,79] The bromide form will assume the desired anisotropic phase at much lower ionic strengths (25–30 mM) than the chloride form (100s of mM).[80] Both present a strong positive charge in contrast to virus and PM phases. Alternatively, a nonionic phase can be formed by use of alkyl-polyethylene glycol and *n*-hexanol.[81] This is an attractive general purpose phase because of its robustness to wide variations in pH, its stability across an approximately 30°C temperature range, and its purely steric mechanism of alignment, which does not induce additional line broadening in the NMR spectrum of the biomolecule, as is normally the case for charged media.

The media discussed thus far all orient relative to the applied magnetic field. Although they may form locally ordered domains, the external magnetic field is necessary in order to enforce the necessary macroscopic ordering of the medium. There are now a number of media which are ordered mechanically (i.e., independently of the magnetic field). The basis for most of these media is the use of polyacrylamide gels. As shown by Sass *et al.*[82] and Tycko and co-workers,[83,84] stretching or compressing a polyacrylamide gel will produce a net anisotropic environment as experienced by a biomolecule which has diffused into the gel. The magnitude of the alignment can be controlled by adjusting the amount of strain or by modifying the gel density. A disadvantage is that any inhomogeneities in the degree of strain will exhibit as additional line broadening. Strained polyacrylamide gels produce alignment through a steric mechanism, but recently it has been shown that polymerization in the presence of acrylic acid can produce a negatively charged gel.[85] In some further developments, it has been shown that PM fragments[86] or bacteriophage Pf1[87] can be immobilized within the gel matrix, allowing the direction of order of the medium to be manipulated independently of the magnetic field. A similar result has been achieved using the triblock copolymer Pluronic F-127 to immobilize Pf1 particles.[88] Interestingly, the immobilization of Pf1 can be made reversible by means of adjustment of the temperature.

3.2. Experimental determination of the order tensor

In Section 2 it was established theoretically that, relative to some molecule-fixed reference axes, a molecular order (alignment) tensor with five independent parameters was sufficient to describe the molecular orientation upon which the observed dipolar couplings depend. Based on knowledge of the order tensor and the molecular structure, it is possible to predict the corresponding RDCs. From this relationship, one might anticipate that

knowledge of the molecular structure and a set of RDC measurements should be sufficient to allow determination of the order tensor. In fact, this is straightforward provided that a sufficient number (i.e., five) of independent measurements are available. Recall that the axial and rhombic magnitudes of alignment and the polar angles of the internuclear vector, expressed in the PAS of alignment, are related to the expected values of the RDCs according to Eq. (12) or Eq. (13). From a set of RDCs and a known molecular structure, it is clear that one could perform a grid search or utilize a non-linear least squares fitting routine in order to find the five values of the order tensor (comprised of two magnitudes and three Euler angles) which optimize agreement between experimental and predicted dipolar couplings. However, recognition that the problem becomes linear when expressed in terms of irreducible order tensor elements (Eqs. (8) and (23)) allows the efficient determination of the order tensor by means of singular value decomposition.[89]

3.2.1. Determination of the order tensor by SVD

The determination of the order tensor corresponds to the solution of a linear algebraic problem of standard $Ax = b$ form. To see this, consider that Eq. (23) may be expressed in the following form,

$$\tilde{D}_{ij}^{res} = \frac{D_{ij}^{res}}{K} = [\mathbf{r}^{ij}]^{tr}\mathbf{s}; \qquad K = -\left(\frac{\mu_0}{4\pi}\right)\frac{\gamma_i\gamma_j h}{2\pi^2 r_{ij}^3} \qquad (25)$$

in which the interaction constant K has been factored out for convenience. The column vector $\mathbf{s}$ contains the elements of the order (alignment) tensor and $[\mathbf{r}^{ij}]^{tr}$ denotes the transposed (i.e., row) vector containing the specific geometrical information pertaining to the ijth dipolar interaction. If multiple RDC measurements are available, then additional row-vectors $[\mathbf{r}^{ij}]^{tr}$ and their corresponding measurements D_{ij} can be organized into the following set of linear equations,

$$\tilde{\mathbf{d}} = \mathbf{Rs} \qquad (26)$$

where $\mathbf{d}$ is a column vector containing the experimental RDC data and $\mathbf{R}$ is a matrix containing the individual $\mathbf{r}^{ij}$ vectors along its rows. The order tensor $\mathbf{s}$ is the unknown five dimensional vector to be solved for. If five independent measurements are available then one can solve for the five unknowns. In this case, the solution to this linear system of equations can be written as,

$$\mathbf{s} = \mathbf{R}^+\tilde{\mathbf{d}} \qquad (27)$$

where the matrix $\mathbf{R}^{+}$ denotes the Moore–Penrose generalized inverse of the matrix $\mathbf{R}$.[90,91] The Moore–Penrose (M–P) generalized inverse of a matrix $\mathbf{T}$ can be defined as the matrix $\mathbf{M}$ which satisfies all four of the following conditions,

(i) $\mathbf{MTM} = \mathbf{M}$

(ii) $\mathbf{TMT} = \mathbf{T}$

(iii) $\mathbf{MT}$ is symmetric

(iv) $\mathbf{TM}$ is symmetric   (28)

Although the M–P inverse is only one of many different generalized inverses, it is desirable here in that it will produce the least squares solution and its definition is unique.

The utility of singular value decomposition (SVD) for the determination of the order tensor stems from the formation of the M–P inverse, which is straightforward based on the SVD of a matrix. All matrices can be factored into a product of three matrices via SVD,[92]

$$[\mathbf{M}(k \times l)] = [\mathbf{U}_M(k \times r)][\mathbf{W}_M(r \times r)][\mathbf{V}_M^{tr}(r \times l)] \tag{29}$$

where $\mathbf{U}$ and $\mathbf{V}$ are orthogonal matrices and $\mathbf{W}$ is diagonal and comprised of the singular values. The Moore–Penrose inverse of a matrix is readily formed based on the SVD of the matrix.[90,91]

$$\mathbf{M}^{+} = \mathbf{V}_B \begin{pmatrix} 1/w_1 & & & & \\ & 1/w_2 & & & \\ & & 1/w_3 & & \\ & & & \ddots & \\ & & & & 1/w_n \end{pmatrix} \mathbf{U}_B^{tr} \tag{30}$$

An advantage of using linear algebraic methods based on the M–P inverse is that the independence of the measurements is readily diagnosed.[90–92] Even in cases where the data is insufficiently independent, there are well defined procedures for establishing the set of valid solutions. This is a strong advantage relative to non-linear least squares minimization or grid search approaches to the determination of the order tensor. While these methods will find the same global minimum as the SVD approach, in underdetermined situations they can be misleading if not employed with caution. A simple measure for the degree to which the measurements are independent is the condition number.[90–92] It is defined as the ratio of the largest to smallest singular values, (w_1/w_n). A value of 1 is the ideal case in which the measurements are perfectly independent, while on the other hand large condition numbers indicate an increasingly non-uniform sampling of the necessary

orientations, as may often be the case in RDC analysis. A large condition number will reflect the presence of relatively large uncertainties in estimation of the order tensor. This is especially true when the number of measurements is limited to approximately less than 20 or there is reason to suspect that the orientations of internuclear vectors are not well distributed. The condition number should therefore always be checked during determination of the order tensor. The level at which the condition number is deemed to be unacceptable depends somewhat on the precision of the measurements themselves, however a value of 10 or less is normally desirable.

There are situations when it can be difficult to obtain a sufficiently independent set of RDC measurements, such as in small molecules or in cases when poor chemical shift resolution limits the number of data points. As pointed out by Losonzci *et al.*,[89] in these cases it is still possible to restrict the possible solutions for the order tensor, with remaining ambiguities possibly lifted using additional experimental means or physical considerations. The procedure for dealing with this underdetermined case is to generate a unique solution for the existing data and then supplement this solution with vectors drawn randomly from the so-called null space. All solutions constructed in this manner are equally valid. The full set of solutions for the best fit order tensor in this underdetermined case is written,[50]

$$\mathbf{s} = \mathbf{R}^+\tilde{\mathbf{d}} + (\mathbf{1} - \mathbf{R}^+\mathbf{R})\mathbf{z} \tag{31}$$

where $\mathbf{z}$ is any vector of dimension five and $\mathbf{1}$ refers to the identity matrix.

3.2.2. *Inversion symmetry of the order tensor*

Provided that the data are sufficiently independent, a unique solution for the irreducible elements of the order tensor is obtained according to Eq. (27). As discussed in Section 2.3.3, the order tensor parameters can be recast into a more physically intuitive form by formation of the 3×3 order tensor followed by diagonalization. The magnitude of alignment is described by the eigenvalues while the orientation of the PAS is contained in the eigenvectors, often described using Euler angles. Some potential for confusion exists with regard to the Euler angles due to the invariance of the order tensor under inversion. As a consequence, there will be four different sets of Euler angles which carry the system into the PAS of molecular alignment. This is solely due to the fact that the z-axis of alignment is not distinguishable from the –z-axis and likewise for the x and y-axes. Given a set of Euler angles (α, β, γ), the other three valid sets are,

$$(\alpha, \beta, \gamma + 180), \quad (\alpha, 180 - \beta, \gamma), \quad (\alpha, 180 - \beta, \gamma + 180) \tag{32}$$

For the description of the order tensor of an isolated molecule or domain, this ambiguity has no practical significance. However, it becomes an important consideration when establishing the orientation of two or more domains, as will be discussed in Section 4. This degeneracy can be lifted by considering a small number of NOE derived constraints, stereo chemical considerations, or through acquisition of RDCs in an additional independent aligning medium.[55,56]

## 3.3. Prediction of molecular alignment

The determination of the five elements of the order tensor play a fundamental role in the interpretation of RDCs in terms of molecular structure and dynamics. Although the elements of the order tensor describing the alignment of a molecule are typically estimated from the measured RDCs, the same information can in principle be derived from knowledge of the solute properties (e.g., molecular structure) and consideration of the forces leading to alignment. In addition to providing useful structural constraints, the ability to predict alignment based on structure can provide a powerful tool for the characterization of dynamics, as this can provide an independent reference measure of the expected solute alignment based on a rigid molecular shape. It also provides further physical insight into the nature of the fundamental intermolecular interactions governing the transfer of alignment from media to solute molecule.

The earliest examples of structure-based order tensor prediction for macromolecules stem from field alignment studies. In these studies, the total magnetic susceptibility tensor (χ) governing alignment can be estimated by means of summation over all functional groups having significant individual magnetic anisotropies ($\Delta\chi$), such as aromatic groups or the peptide bonds in proteins.[51] In the early work on field aligned myoglobin,[51] independent calculations of the diamagnetic χ-tensor based on the knowledge of the molecular structure was critical for independently defining the total χ-tensor (which included paramagnetic and diamagnetic contributions). Deviations between experimental RDCs and values predicted based on the calculated susceptibility tensor provided the basis for the interpretation of RDCs in terms of dynamics.[47,93] Shortly thereafter, a study on a field aligned DNA-protein complex utilized structure-based χ-tensor calculations for the DNA component in order to aid refinement of the protein structure based on field induced RDCs.[94] Further applications utilizing structure-based predictions of the χ-tensor have also appeared recently in applications involving nucleic acids.[62,95,96]

Although the operative forces underlying field alignment are physically well understood, a key question that followed the introduction of bicelles as an

ordering medium was the mechanism of alignment for biomolecules.[52,97,98] This has been a persistent area of inquiry since the emergence of liquid crystalline solvents for NMR spectroscopy.[99] Early on in the applications to macromolecules, Bax and co-workers noted that alignment in neutral bicelles is dependent on molecular shape, as the order tensor PAS for ubiquitin determined using RDCs closely coincided with its corresponding diffusion tensor determined using spin relaxation.[52,97,98] Drawing from previous developments in the liquid crystal literature,[99] it was suggested that protein solute orientations are differentially obstructed due to the proximity of ordered particles, leading to a net alignment of the solute that was dependent on the concentration of the ordering media. Soon after, it was demonstrated that doping bicelles with positively or negatively charged detergents leads to modulations in the alignment of charged proteins.[55] This suggested that electrostatic interactions can also play an important role in inducing biomolecular alignment.

Progress to date in the development of protocols for predicting the alignment of biomolecules in ordering media based on their structure has been confined to cases where steric obstruction is the dominant mechanism of alignment. Zweckstetter and Bax introduced the first example applicable to high-resolution NMR of biomolecules.[100] In this 'simulation of sterically induced alignment' (SSIA) approach, all orientations of the solute molecule are examined for steric obstruction with the ordering particle as a function of the solute–particle distance. Orientations that cause steric obstruction are then excluded from a tensorial average over coordinates relating the molecule to the magnetic field. Using this simple model, the authors demonstrated that the elements of the order tensor for proteins dissolved in bicelles and their corresponding RDCs could be calculated at a high level of accuracy. Shown in Fig. 9 is a comparison of experimental and SSIA-predicted order tensor PAS frames for an RNA molecule.[101] In contrast, the alignment of the positively charged Ig binding domain from the *Streptococcal* protein G could not be accurately predicted when in the presence of negatively charged phage particles. This observation was attributed to the neglect of attractive electrostatic interactions between the ordering medium and the protein solute. The authors noted that the ability to predict steric alignment can be a useful tool for establishing the oligomerization state in solution or even for establishing the presence of dynamics. In particular, the experimentally determined alignment for the protein cyanovirin-N was found to be in better agreement with values calculated based on the structure of its monomeric form characterized by NMR rather that its domain-swapped dimeric form observed in the crystalline state. In contrast, the experimental order tensor for the apo-S100B protein was in better agreement with predictions based on a dimeric rather than monomeric form.[100]
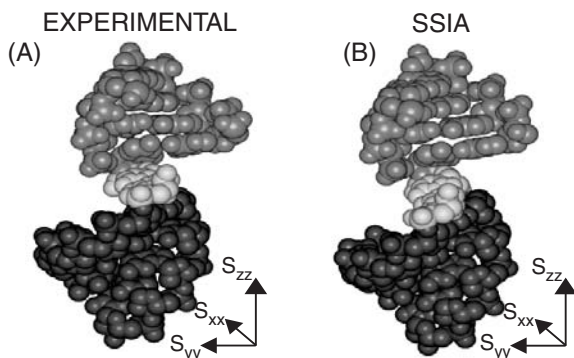
Fig. 9. Comparison of the principal axis systems of alignment for the TAR RNA in bacteriophage Pf1 as (A) experimentally determined and (B) predicted using the program SSIA.[100]

The SSIA approach utilizes an all-atom representation of the macro-molecule for the subsequent sampling and averaging over all orientations and translations. A number of approaches have been introduced since then which aim to significantly simplify the prediction of alignment. The primary advantage of these approaches is that they are much more efficient, lending themselves to inclusion in a structural refinement protocol or for studies of dynamics in which large ensembles of different conformers may be considered. The first of these approaches, reported by Azurmendi and Bush, utilized a procedure termed 'tracking alignment from the moment of inertia tensor' (TRAMITE).[102] In TRAMITE, four of the elements of the order tensor describing its orientation and asymmetry are expressed in terms of the eigenvalues of the solute's inertia tensor, leaving the absolute degree of alignment (a scaling factor) as the only adjustable parameter. Equipped with the ability to calculate RDCs for a given structural model, the authors examined agreement between measured RDCs and values calculated by TRAMITE for 1000 models generated for a rigid trisaccharide Lewis[X] using Monte Carlo simulations. The structural model yielding best agreement exhibited glycosidic angles in agreement with those previously reported using a more traditional and time-consuming structure refinement against RDCs. Another interesting application involved the analysis of ensemble averaged molecular conformations generated using Monte Carlo simulations of the pentasaccharide LNF-2. Here, RDCs were calculated using TRAMITE for a sub-set of conformations and the averaged values were compared to their experimental counterparts. Relative to the case in which a single structure was assumed, by accounting for extensive mobility of the disaccharide tail they were able to achieve better correlation between measured and calculated RDCs.

Fernandes *et al.* have reported analytical expressions for the orientation of hard rigid particles by planar obstacles.[103] Their detailed theoretical treatment models the macromolecule as an axially symmetric ellipsoidal particle, with semi-axes in correspondence with the gyration tensor of the molecule. The analytical solutions were tested using eight different proteins in the PDB which were accompanied by RDC containing constraint files. In spite of the fact that their model assumes an axially symmetric prolate ellipsoid for the solute, good agreement was found for all eight cases, as gauged by the correlation between predicted and measured RDCs.

Almond and Axelson have introduced an approach of some resemblance to TRAMITE, but based on the molecule's gyration tensor, which more closely reflects molecular shape and thus provides higher accuracy for molecules of highly anisotropic shape.[104] They propose that the eigenvalues of the order tensor can be predicted to an accuracy which nearly matches SSIA, according to the simple relationship,

$$(S_{11}, S_{22}, S_{33}) \propto \left(1 - \frac{1}{2}\,\delta, \delta - \frac{1}{2}, \ -\frac{1}{2} - \frac{1}{2}\,\delta \right) \tag{33}$$

where δ is a shape factor related to the square roots of the eigenvalues (ρ_1, ρ_2, ρ_3 with $\rho_1 > \rho_2 > \rho_3$) of the gyration tensor,

$$\delta = \frac{(\rho_2 - \rho_3)}{(\rho_1 - \rho_3)} \tag{34}$$

They tested the predictive power of the method on the same datasets as were utilized by Fernandes *et al.*[103] The correlations between their predictions based on Eqs. (33) and (34) and the experimental RDCs were higher than those obtained using the analytical expressions of Fernandes *et al.*, but very similar to the results obtained using TRAMITE.

4. APPLICATIONS TO PROTEIN DOMAINS

Proteins are often composed of multiple domains rather than their single domain counterparts, with up to two-thirds of proteins in prokaryotes[105] and four-fifths in eukaryotes[106] believed to be multi-domain systems. Domains typically possess structural autonomy and their coding sequences are subject to duplication and recombination. As such, domains constitute evolutionary units that have been shuffled by nature to give rise to the structural complexity needed in mediating a variety of biological events, including signal transduction, transcriptional activation and enzyme action.[107,108] Distinct functionality can be encoded in individual domains, or domains can act collectively to perform a single task, with functionally active residues residing

at the interfaces lining the domains. In all of these cases, the three-dimensional spatial organization of domains is a critical aspect of function.

For a long time, NMR spectroscopy has had limited success in the accurate characterization of inter-domain ordering and dynamics. Aside from the potentially high molecular weights of multi-domain systems, long flexible linkers frequently connect domains. This has rendered the observation and interpretation of inter-domain NOEs and hence determination of relative domain alignment, and/or rearrangement in response to changes in the chemical environment, very challenging by NMR. Progress has been made in the use of spin relaxation measurements for determining inter-domain orientation,[109,110] but these applications require that the protein molecule possess a sufficiently anisotropic diffusion profile. The difficulty in determining domain-alignment under solution conditions has in turn made it more difficult to evaluate the accuracy of multi-domain protein structures determined using X-ray crystallography. This is an important issue, because in the absence of inter-domain contacts and presence of flexible linker residues, inter-domain orientations can become highly vulnerable to crystal packing forces.

There have also been challenges in probing inter-domain dynamics by NMR. While insight into the local flexibility of residues linking domains can be attained using NMR spin relaxation methods, the consequence of these localized motions on inter-domain orientations can be more difficult to characterize. As a result, it has been difficult to elucidate not only the higher order organization of multiple domains, but also their dynamics at equilibrium and their potential role in ligand-induced inter-domain reorganization, a phenomena that is probably more the norm than the exception in multi-domain protein systems.

Over the last few years, RDC-based approaches have provided a new avenue for probing inter-domain alignment and dynamics using NMR. Indeed, these applications probably represent the greatest impact of RDC methodology to date. The vast majority of these studies have focused on using RDCs for deriving information about domain organization, frequently exploiting already available X-ray or NMR structures of individual domains. Several studies now report differences between the principal order parameters (i.e., the eigenvalues of the order tensor) derived for individual domains using RDCs, providing a direct measure of relative inter-domain mobility and often revealing motions of large amplitude. In other studies, RDCs have provided decisive structural constraints on domain–domain alignment in solution, in some cases pointing to discrepancies between solution and solid state structures of multi-domain systems, and providing new insight into plasticity and/or potential effects of the physicochemical environment. Several reviews have now appeared describing how RDCs can improve the precision and accuracy with which inter-domain alignment can be determined by NMR.[20,23,24,111] We discuss a subset of studies involving RDC investigations of multi-domain proteins

with an emphasis on studies that revealed new aspects about inter-domain dynamics.

4.1. Direct evidence for inter-domain dynamics in multi-domain proteins

Ever since the early studies on the protein cyanometmyglobin, it was recognized that RDCs could provide a powerful approach for measuring the amplitudes and directions of motions involving collective movements of intact structural elements.[47] Such collective dynamics have historically been difficult to probe because they often occur on timescales inaccessible to techniques such as molecular dynamics simulations and NMR spin relaxation. In the case of cyanometmyglobin, motions did not involve intact domains, but rather individual secondary structural elements. The RDCs measured in field-aligned cyanometmyglobin were found to disagree with predictions based on the static X-ray structure of the protein and an independent determination of the molecular susceptibility tensor. Remarkably, far better agreement could be attained when allowing individual α-helices to move collectively under 'cone' or 'arc' type trajectories. This dynamic picture of cyanometmyglobin was consistent with a large body of work demonstrating the need for a dynamic component in order to explain myoglobin ligand binding.[6]

Following the introduction of liquid crystals and other media for achieving the alignment of biomolecules, a number of applications appeared harnessing RDCs in the determination of relative domain orientations. An early example was a study by Fischer et al. which investigated the utility of RDCs in defining the structure and dynamics of a two domain fragment composed of the B and C domains of the barely lectin protein (BLBC).[112] Each domain binds specific carbohydrate ligands, with the relative orientation of the two domains assuming particular importance due to its role in the amplification of binding affinity, which is otherwise weak for individual domains. A structure of this protein had been previously determined using traditional NOE-based methods, but the relative positioning of the two domains was poorly defined due to the scarcity of observed inter-domain NOEs.[113] Using an X-ray structure from the closely homologous protein wheat germ agglutinin (WGA) as a model for the two domains, and RDCs measured using a bicelle alignment medium, order tensors were determined for the individual domains. The reassembly of domains based on the superposition of domain-fixed order tensor frames resulted in structures that remained consistent with the previously determined NOE constraints. However, inter-domain alignment deviated from that observed in the WGA X-ray structure, possibly due to real differences between the BLBC and WGA proteins and the study of a smaller fragment in the NMR study. Significantly, the magnitudes of the order tensors determined for the two domains differed

by a factor of ~ 3, and this difference was attenuated in a different bicelle preparation doped with a larger amount of the positively charged detergent, CTAB. The authors attributed the observed large differences in order tensor magnitudes to partial association of one of the domains with the bicelle particles. The preferential association of one of the domains with the bicelle medium provided the means whereby the existence of extensive inter-domain motions of amplitude $\sim \pm 40°$ could be established.

In a more recent study, Clore and co-workers used RDCs to probe inter-domain motions in two multidomain systems.[114,115] One system involves a ~ 30 kDa complex between KH3 and KH4 domains of the FUSE binding protein (FBP) with a 29mer single-stranded DNA.[115] In the NMR structure of the complex, the KH3 and KH4 domain, which are separated by a glycine rich 30 residue flexible linker, do not interact with one another and their respective interaction sites with the DNA strand are separated by five bases that do not make contacts with either domain. Significantly, the magnitudes of the principal order parameters estimated for the KH3 and KH4 domains from a normalized histogram distribution of measured RDCs differ markedly, with the values for KH3 being attenuated by $\sim 50\%$ relative to KH4. These results indicated the presence of substantial inter-domain motions in the complex which, based on analysis of spin relaxation, could be characterized as independent wobbling of the domains within cones having semi-angles of $\sim 30°$. The basis for differential alignment of the two domains was attributed to the association of a different number of DNA bases and hence negative phosphate charges to each of the two domains. The authors proposed that inter-domain motions are likely to be important for FBP function, as this results in a series of single stranded hinge points in the DNA which can facilitate interactions with other, sometimes more mobile components of the transcription machinery. The authors also applied a similar procedure to probe motions in the constant region of the nuclear envelope protein LAP2, which is comprised of two so-called LEM domains separated by a 60 residue flexible linker.[114] Again, the measured magnitudes of the order tensors (i.e., principal order parameters) for the two domains differed markedly; with ordering of the N-terminal domain attenuated by $\sim 64\%$ and of *opposite sign* relative to the C-terminal domain. The authors interpreted these results as independent reorientation of the two domains. Interestingly, the observation of order tensor magnitudes of opposite sign for the two domains is indicative of direction of principal ordering which is, respectively, parallel and perpendicular to the magnetic field.

Fesik and co-workers have reported a study on the conserved two-domain protein SP14.3 from *S. pneumoniae*.[116] Although the function of this protein was not known, it was believed to be essential for *S. pneumoniae* and thus represented a target for development of therapeutics. Intriguingly, although the NMR structure indicated that the C- and N-terminal domains are separated by only a three-residue linker, a single order tensor could not be determined

during structure refinement that satisfied all measured RDCs. Independent determination of order tensors for individual domains yielded far better agreement with measured RDCs, yet with different principal order parameters determined for each domain. The magnitude of ordering for the N-terminal domain was attenuated by $\sim 25\%$ relative to the C-terminal domain, consistent with the presence of inter-domain motions. Differential ordering of the two domains in bacteriophage Pf1 could be attributed to differences in electrostatic charge, with the slightly positive charge on the C-terminal domain favouring association with Pf1 and the negative change on the N-terminal domain favouring repulsion.

4.2. Structural dynamics of multi-domain proteins

A series of studies by Kay and co-workers on the maltodextrin binding protein (MBP) illustrated the potential for determining domain–domain alignment using RDCs under different ligation conditions and decisively revealed differences between inter-domain alignments determined under solution and solid-state conditions.[111] MBP is a 370-residue protein which consists of two domains of comparable size that are separated by two β-strands and an α-helix stretch. Previous X-ray studies have demonstrated variable inter-domain disposition for MBP with only very minor changes observed within individual domain conformations. In particular, binding of maltose to MBP induces a transition from an 'open' to a 'closed' conformation that subsequently facilitates binding to a number of chemoreceptors. Using an extensive set of RDCs and four previous X-ray structures as input coordinates for the two domains, the relative domain alignment in MBP bound to β-cyclodextrin was determined.[117] Significantly, the average solution conformation determined using RDCs differed from its X-ray counterpart by $\sim 11°$ in closure angle. The solution conformation was more 'closed' relative to the X-ray counterpart, resulting in closer association between the ligand and N-terminal domain, with a concomitant decrease in the solvent accessible area in the binding cleft. The authors attributed this difference to crystal packing forces, and demonstrated that the conformation determined for MBP accurately reflects an average conformation in solution even if there were inter-domain motions. The authors subsequently corroborated their RDC-based domain–domain results with an independent analysis of the relative domain orientations using diffusion anisotropy measurements,[109,110] conducted in the absence of ordering media.[118] These findings were significant because they indicated that, at least in the case of MBP, the ordering media appears to have little effect on its average inter-domain conformation. Intriguingly, and in contrast to the β-cyclodextrin bound state, a similar RDC study on MBP in the *apo* and maltotriose-bound forms revealed solution inter-domain conformations that are far more similar

to their X-ray counterparts.[119] Collectively, these studies not only shed light into inter-domain plasticity and effects of crystal packing forces, but also demonstrated the feasibility of using RDCs in investigating inter-domain alignment under different physiologically relevant conditions.

Bax and co-workers reported an RDC study of the protein calmodulin (CaM).[120] CaM plays numerous roles in Ca^{2+}-dependent signalling pathways and is comprised of N-terminal and C-terminal domains that have 46% sequence identity. The two domains are separated by a 27 residue α-helical linker and are each comprised of two EF hand-type Ca^{2+} binding helix–loop–helix motifs. CaM requires Ca^{2+} for its function. Structurally, Ca^{2+} induces flexibility in the centre of the inter-domain linker which is otherwise α-helical in *apo*CaM, enabling the two domains to clamp onto their target molecules and bind with high affinity. It also leads to reorientation of the two helices in the EF motifs such as to adopt a more 'open' conformation that exposes hydrophobic residues needed for binding to molecular targets. Using previous X-ray structural coordinates of CaM as models for individual domain conformations in the RDC analysis, the authors demonstrated not only that the inter-domain orientation fluctuates apparently randomly in solution, but that there are substantial differences between the solution conformation of the EF motif in the N-terminal domain and its X-ray structure counterpart. In particular, the inter-helical angle determined in solution differed by as much as $25°$ relative to other X-ray structures, adopting a far more 'closed' conformation. The authors attributed this difference to crystal packing forces and potentially to dynamical changes in the EF conformation.

Kay and co-workers also reported a study on Bacteriophage T4 lysozyme,[119] which is an enzyme that catalyzes hydrolysis of the $\beta(1 \rightarrow 4)$ glycosidic linkage in peptidoglycan substrates. The substrate binds in the cleft formed by an N- and C-terminal domain. An X-ray structure of free T4 lysozyme shows a closed conformation for the domains which resembles that observed in the substrate bound state, eliciting questions regarding how such a large substrate could bind the enzyme. It was postulated that a more 'open' form must partly exist in solution. Using RDCs measured on a C54T/C97A T4 lysozyme mutant under four different aligning conditions, along with model structures for the N- and C-terminal domains from previous X-ray and NMR structures, the average inter-domain orientation was determined. Very good agreement in inter-domain orientations was determined when using RDCs measured under different conditions, confirming again that despite weak inter-domain interactions characteristic of multi-domain systems, the aligning medium has a very small influence on average inter-domain conformation. However, the solution state inter-domain alignment determined using RDCs was significantly more 'open' relative to its X-ray structure counterpart by $-15°$ to $-19°$ and $-7°$ to $-18°$ in 'closure' and 'twist' angles respectively. The solution conformation could be described as

an equal population weighted average of 'open' and 'closed' conformations, though the nature of this dynamical equilibrium could not be confirmed based on the measured RDCs.

The quaternary structure of human normal adult haemoglobin (HbCO A) in solution has now been determined using RDCs.[121] Hb A is a dimeric allosteric protein that consists of two α-chains and two β-chains. Oxygenation of Hb A is cooperative, and in its simplest description, mediated by putative conformational changes induced through relaxation of a low affinity tense state (T) to a high affinity relaxed state (R) upon O_2 binding. A more recent X-ray structure of Hb A has revealed another distinct state (designated R2), which is more similar to the R state than to the T state. The primary difference between the R and R2 states is not the relative alignment of the α and β chains in the monomeric units, but rather their relative quaternary alignment or the orientation of the C2 axis of symmetry relative to the monomeric $\alpha\beta$ unit. Using previous X-ray structures of Hb A as starting coordinates for individual $\alpha\beta$ chains, the quaternary conformation and principal axis-centred C2 axis of symmetry was determined using RDCs. Interestingly, the analysis yielded an orientation for the C2 axis of symmetry that is halfway between that observed for the R and R2 states. Although RDCs were not used to assess if this conformation represents a dynamical average, ^{15}N relaxation measurements pointed to the presence of significant conformational exchange contributions at contact sites between the $\alpha1\beta1$ and $\alpha2\beta2$ dimers. Based on these findings, the authors proposed that HbCO exists in dynamic equilibrium between the R and R2 conformational states.

There have been other studies in which there was agreement between domain–domain alignment determined using RDCs in solution and X-ray crystallography in the solid state. A recent example by Prestegard and co-workers on a trimeric mannose binding protein (MBP) is illustrative.[122] Here, the relative orientation of monomeric units was determined through calculation of a monomer-centred order tensor frame using RDCs measured on the protein and a previous X-ray structure as input coordinates for the monomer conformation. For a trimeric protein, the principal S_{zz} direction must coincide with the C3 rotational axis of symmetry, and the order tensor should exhibit axial symmetry.[123] The authors demonstrated that the experimentally derived order tensor was indeed axially symmetric, and that the determined orientation of the C3 axis of symmetry relative to the monomeric unit, and hence the orientation of monomeric units in the trimer, were in excellent agreement with the X-ray structure.

An account has now appeared in which the domain–domain alignment determined using RDCs exhibits potential discrepancies with the alignment determined using NMR rotational diffusion measurements. In a study on polyubiquitin chains, Fushman and co-workers found small differences in the relative alignment of two ubiquitin units in Ub_2 determined using RDCs and rotational diffusion measurements.[124] The NMR study

had indicated that the two ubiquitin domains undergo conformational exchange between a predominant 'closed' conformation and a weakly populated 'open' conformation. When one of the domains was aligned, rotation of the other domain by 18° around the z-axis and 10° and 4° around the other orthogonal axes was necessary to bring agreement between the RDC and rotational diffusion derived structures. The authors noted that while this difference is within the experimental uncertainty, it could also be the result of differences in the motional averages probed by RDCs and spin relaxation measurements. Comparison of results derived from RDCs and rotational diffusion will likely be a promising area of future development, as the latter two techniques have distinct sensitivities to motional timescales.

5. PROTEIN DYNAMICS AT THE LOCAL LEVEL

The utility of RDCs for probing conformational dynamics is not limited to applications involving domain–domain alignment. There are approaches that can allow the fluctuations involving backbone and side-chain groups to be examined in more detail, although these applications have been slower to appear because of the need for accompanying methodological development. Indeed, some of the earlier applications centred around the determination of order tensors for sub-molecular fragments using standard techniques. This approach can provide insight into the dynamics of small molecular sub-fragments according to the observed variations in ordering between different fragments. Furthermore, methods have been introduced and tailored to provide site-specific probes of side-chain dynamics in protein systems. Recently, some approaches have also been introduced which utilize complementary sets of RDCs measured under a wide variety of alignment conditions, bypassing the requirement for the locally rigid fragments needed for determination of order tensors. These applications can provide atomic resolution in that they allow direct characterization of generalized order parameters, potentially including a description of the motional asymmetry, corresponding to motions of single bond vectors. Furthermore, these multi-alignment approaches show promise for the identification of minute changes in the biomolecular structure and dynamics occurring due to change in environment (i.e., change in orienting media) and have exciting implications for describing functional states of biomolecules that are higher in energy than the ground state typically measured.

5.1. Segmental fluctuations along the protein backbone

RDC methods used to probe the structural dynamics between relatively large molecular fragments such as domains in multi-domain proteins can be

just as well applied to molecular fragments much smaller in size, such as individual peptide units. This carries advantages but also new difficulties. The advantages are that it can allow detection of more localized motional fluctuations in proteins, while relaxing requirements for prior structural knowledge of intact elements; potentially to an extent such that only local geometrical relationships need be known. The minimum size for the fragment is determined by the requirement that at least five independent RDC measurements be available per fragment. The price for this 'divide and conquer' approach is that the fewer available data points per fragment will lead to decreases in precision and greater susceptibilities to errors arising from inaccurate fragment geometries. Zweckstetter and Bax[125] have characterized the decreases in precision of order parameters upon reduction of the number of data points, which highlights the need to carefully explore the precision of determined order tensor parameters and the subsequent impact on conclusions. Upper limits for the imprecision of determined order parameters were not presented, but can be established according to the observed agreement between experimental and predicted RDCs. The collection of data in additional media represents a route for overcoming unacceptable levels of precision.

Tolman and co-workers reported the first such application of the order tensor formalism to small backbone fragments of the protein ubiquitin.[49] In order to provide some basis for the interpretation of the experiments, the authors explored by simulation the effects of internal motions on the subsequent interpretation of fragment specific order tensors in terms of structural and dynamic parameters. They found that orientational (i.e., structural) information is unperturbed provided that the internal motions are isotropic in character. However, the presence of anisotropic motions can lead to distortions in the orientational parameters as well as additional complications in the interpretation of motions themselves. The application to ubiquitin utilized an extensive set of RDCs, including $^1D_{N–HN}$, $^1D_{C'–N}$, $^1D_{C'–C\alpha}$, $^2D_{C'–HN}$, $^1D_{C\alpha–H\alpha}$, $^1D_{C\alpha–C\beta}$ and $^2D_{C'–H\alpha}$ couplings, which were measured using bicelles as an alignment medium. Unfortunately, the data were still insufficient in number to examine only rigid peptide bond units and so their 'rigid' fragments included the following C^α group, which thus encompassed one torsional degree of freedom (the backbone dihedral angle ϕ). The results were consistent with larger variations in motional amplitudes between sites than expected based on spin relaxation order parameters, but on the other hand were not of sufficient precision to conclusively exclude explanations involving less mobility. A further observation was the inability to adequately explain the RDC data, even after extensive explorations of alternative values for the relevant dihedral ϕ, for approximately 30% of fragments, predominantly localized in two loop regions. These results underscore the incomplete picture provided by a structural model alone.

Another study by Zuiderweg and co-workers on the enzyme ribonuclease binase nicely illustrates how RDCs may be combined with other NMR probes of dynamics to get a more comprehensive picture of motions.[126] Using a previous X-ray structure of the protein as input for analysis, Wang *et al.* determined order tensors for groups of five sequential N–H vectors along the backbone of the protein. The window encompassing the five N–H vectors was 'scanned' along the entire polypeptide allowing determination of order tensors at a quintet basis. Regions exhibiting departures from the X-ray structure, manifested as differences in order tensor principal axis frames and/or principal order parameters, correlated well with regions identified as having slow conformational exchange as probed using ^{15}N R_2 relaxation rates in the presence and absence of a Carr-Purcell-Meiboom-Gill (CPMG) multiple-pulse refocusing sequence, with most of these residues belonging to the active site. An exception was a region encompassing two β-strands which, while exhibiting slow conformational exchange based on relaxation measurements, appeared otherwise well structured based on RDCs and deuterium/proton exchange rates. The authors suggested that the conformational exchange broadening is probably not due to motions of these residues, but rather, due to motions of dynamic loops that hover directly above the sheet. Interpretation of exchange broadening is often subject to such anomalies, and the measurement of RDCs was shown as one possibility for identifying these cases.

5.2. Structural dynamics of side-chains

Conformational plasticity of surface side-chains is often critical for proper formation of intermolecular contacts between proteins and their cognate targets. Side-chain dynamics can allow proteins to employ the same inter-action surface to recognize a wide variety of molecules. The importance of side-chains in protein function also renders their conformational dynamics of considerable interest in the rational design of therapeutics.[127,128] NMR methods for probing side-chain dynamics include measurement and analysis of ^{3}J coupling constants, intraresidue NOEs, ^{13}C and ^{2}H spin relaxation, and dipole–dipole cross-correlation rates.[12,13,15,129] While the above methods provide complementary information regarding side-chain dynamics, additional probes of dynamics are useful. Recent applications have appeared in which RDCs have been shown to be useful probes of side-chain conformation or dynamics. We discuss a sub-set of these applications of relevance to studies of dynamics, noting that other works have also appeared which deal with measurements of RDCs involving side-chain nuclei and their use in structure determination.[61,130,131]

The analysis of side-chain RDCs is potentially complicated due to the possibility of extensive internal motions coupled with concomitant uncertain-ties of overall molecular alignment. Thus an attractive target for RDC-based

studies has been the β-carbon, which benefits from the relative rigidity of the protein backbone. The analysis of C^β–H^β RDCs can therefore be considered to comprise fairly direct probes of the χ_1 rotameric distribution. Chou and Bax have reported a straightforward approach for probing the χ_1 rotameric state based on measurements of C^β–H^β, C^α–H^α and C^α–C' RDCs.[132] By recognizing that C^β–H^β bonds in staggered conformations are parallel to either C^α–H^α, C^α–N or C^α–C' bonds, it is possible in many cases to identify χ_1 rotamers simply by comparison of the appropriately scaled RDCs. No knowledge of the order tensor or molecular structure is necessary. In a demonstration utilizing the protein calmodulin, results were consistent with 50% of non-Gly/Ala side-chain existing solely in ideal staggered rotameric conformers. The majority of these residues were located in regular secondary structural elements or in regions shielded from the solvent. For other residues, the measured RDCs were inconsistent with a single rotameric state, indicating either a rotameric state skewed from ideality or the existence of averaging among different rotamers.

Mittermaier and Kay have carried out a detailed RDC-based study of χ_1 rotamer distributions for the B1 domain of peptostreptococcal protein L.[133] Using two sets of backbone RDC data, collected in bacteriophage Pf1 and bicelle media, they obtained order tensor parameters using a set of crystallographic coordinates for the structural model. This allowed the refinement of C^α–C^β bond orientations, which then provided the basis for their quantitative interpretation of C^β–H^β RDCs for 38 out of a possible 49 residues in the context of three different models. The three models were: (A) a static χ_1 rotameric state (B) gaussian fluctuations about a mean χ_1 torsion and (C) the population of multiple rotameric states. They found that nearly 75% of χ_1 torsions examined could be adequately accounted for by a static model. By contrast, the data for 11 residues were much better fit when jumps between rotamers were permitted (model C). The authors note that relatively small harmonic fluctuations (model B) about the mean rotameric state produces only small effects on measured RDCs. This is supported by their observation that, except for one case, the static model reproduced the data as well as the gaussian fluctuation model.

In a recent paper by Sprangers et al.,[134] a simple but effective approach for the analysis of aromatic ring dynamics has been proposed. The work describes the structure determination of the SMN (survival of motor neuron) Tudor domain, using both crystallographic and NMR methods. The structures are largely in agreement, except for differences observed for some conserved aromatic residues which form part of the sDMA (symmetrically dimethylated arginine) binding pocket. The authors demonstrate that it is possible to account for aromatic ring dynamics and thus recover the underlying mean structural information. The presence of Phe or Tyr ring dynamics is normally suspected upon observation of degeneracy of δ and ε chemical shifts, although the possibility of identical shielding environments cannot be

excluded. It is shown that measurement of $^{13}C^{\beta}$–$^{13}C^{\gamma}$ and aromatic ^{13}C–^1H RDCs in the ring can confirm, and furthermore distinguish a ring flip model from models of higher symmetry (i.e., 3-fold and higher). This is because higher symmetry will average all of the ring δ and ε C–H RDCs to a value of -0.125 $D_{C\beta-C\gamma}$. On the other hand, a ring flip model will produce an average of the RDCs corresponding to the two distinct C–H orientations. In their analysis of the SMN Tudor domain, they found that the RDC data supported a ring flip model in all cases, and that the motionally corrected RDC values agreed with the NMR structural results. The authors proposed that the observation of a different conformation in the crystallographic study demonstrates a degree of conformational plasticity which may be an important factor for binding.

5.3. Generalized order parameters from RDCs

As discussed in previous sections, RDCs offer extended sensitivity to motional timescales, ranging from picoseconds to milliseconds, relative to spin relaxation-based approaches. Nevertheless, the two share a close mathematical relationship in that their sensitivity to motion can be described by means of an order parameter S, with RDCs depending on motional amplitudes according to S, and spin relaxation exhibiting a dependence according to S^2.[135] This correspondence suggests that some rough timescale resolution might be achieved by comparison of the spin relaxation vs. dipolar order parameters. However, it is only very recently that the necessary theoretical and experimental advances have been made to allow the determination of generalized order parameters from RDC data. This stems from the difficulties in separating the effects due to structure, internal motion and overall alignment. The separation of these effects therefore relies on extensive RDC measurements, employing many different complementary alignment media. Nevertheless, these multi-alignment approaches are now feasible given the substantial repertoire of alignment media which are now available.

   The success of these new multi-alignment approaches for the extraction of generalized order parameters from RDCs relies on a couple of fundamental assumptions. The first of these, as described in Section 2, is that the molecule is structured enough that the internal dynamics remain uncorrelated with the overall alignment. This corresponds to the assumption that the separation of averaging in Eq. (21) remains valid. If this does not hold, then overall alignment and internal motion will be convoluted in some nonlinear manner. The second assumption is that the structure and dynamics of the molecule is not influenced by change of medium. Provided that both of these assumptions are permissible, the acquisition of sufficient

RDC data can allow the five averages (i.e., the elements of $\mathbf{r}^{ij}$ in Eq. (23)) describing each dipolar interaction tensor to be determined, and subsequently interpreted in terms of mean internuclear vector orientations and an associated description of dynamics. To date, there are a couple of different approaches which have been introduced for the analysis and interpretation of RDCs acquired in multiple alignment media.

5.3.1. *The model free approach*

Griesinger and co-workers have recently introduced an approach,[57,58] with the aim of extracting generalized order parameters from RDCs, which they call the model free approach in analogy to the method of Lipari and Szabo for the analysis of spin relaxation data.[135] The 'model free' label indicates that the description of motion is couched in terms of generalized order parameters, accompanied by an explicit description of the magnitude and direction of the motional asymmetry, in accordance with the illustration of Fig. 7. Some insight into the procedure may be gained by reconsideration of Fig. 4, which illustrates the cone of solutions corresponding to the permissible internuclear vector orientations consistent with a single measured dipolar coupling. The use of a second and different alignment medium reduces this continuum of possibilities to just a few discrete orientations which lie at the intersection of the two corresponding cones[55] (Fig. 10). If additional tensors (and thus cones) are added it becomes clear that the solution for the (presumed static) vector orientation will become over-determined. The model free approach to the analysis of RDCs attributes this disagreement to motions of the specific internuclear vector.

The formal procedure for extracting these motions stems from the recognition that just as five independent RDC measurements (supplemented by knowledge of the molecular structure) are sufficient to allow determination of the order tensor, at least five independent *sets* of RDCs measured in different alignment media, and accompanied by knowledge of their associated order tensors, can allow the five *averaged* functions constituting the individual tensors $\hat{R}^{ij}$ to be determined. We recall that these tensors $\hat{R}^{ij}$ describe the spatial part of the *ij*th dipolar interaction, and upon diagonalization will provide a description of the mean orientation and dynamics of the vector. Mathematically, the problem amounts to the solution of the linear algebraic system of five equations represented by

$$\tilde{d}^{ij} = \mathbf{A}\mathbf{r}^{ij} \tag{35}$$

in which the matrix $\mathbf{A}$ contains the individual order tensors along its rows, the vector $\mathbf{d}^{ij}$ contains the corresponding measurements for the *ij*th interaction in each medium, and $\mathbf{r}^{ij}$ is the desired vector to be solved for, and contains
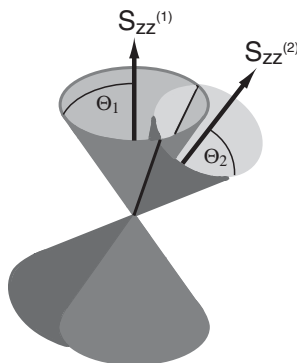
Fig. 10. Measurement of RDCs in a second, different alignment medium can significantly reduce the possible corresponding internuclear vector orientations. Permissible orientations will correspond to the intersection of cones, which are placed according to the respective principal axis systems of ordering.

the irreducible components of the Cartesian tensor $\hat{R}^{ij}$. As the order tensors must be known beforehand, it is necessary to have prior knowledge of the molecular structure in order to solve for r^{ij}.

The first step in the model free approach[57,58] is to determine the corresponding order tensors for each separate RDC dataset, based on a set of structural coordinates. The irreducible tensorial descriptions of each of these order tensors are arranged into the so-called **F** matrix. This matrix is of dimension $5 \times M$ in which M is the total number of distinct RDC datasets acquired using different alignment media. The following formulation appears in the work of Peti et al.,[58]

$$\frac{D_i^{\text{exp}}}{D_{i,zz}} = \sum_{M=-2}^{2} F_{i,M}\langle Y_{2,M}(\theta^{mol}, \phi^{mol})\rangle \tag{36}$$

where D_i^{exp} refers to an experimental dipolar coupling measured in the ith alignment medium, the Y's refer to the five averaged spherical harmonics describing the internuclear vector and expressed in a molecule fixed frame, and $D_{i,zz}$ refers to the principal magnitude of the ith order tensor. Aside from some notational differences, Eqs. (35) and (36) are essentially identical. Formation of the Moore–Penrose inverse of the **F** matrix allows solution of the linear system of equations for each of the five averages $\langle Y_{2m}(\theta^{mol}, \phi^{mol})\rangle$, for each of the individual internuclear vectors. The success of this approach relies on the measurement of sets of RDCs in at least five *different* alignment media, which if fulfilled, will manifest in the non-singularity of the matrix **F**. Peti et al. advise that the condition number

obtained should be less than ten in order to assure adequate precision of the results.[58]

The model free approach to the analysis of RDCs has been demonstrated with an application to the protein ubiquitin.[58] In this study, eleven different alignment media were employed for the measurement of one-bond amide N–H RDCs. Their results, for 32 N–H sites along the protein backbone, indicate fairly large variations in the dipolar generalized order parameters (S_{rdc}^2). Relative values obtained for S_{rdc}^2 ranged between 0.5 and 1.0, with the most rigid region of the protein corresponding to the single α-helix formed by residues 24–34. The authors discuss in considerable detail different approaches for estimating the absolute scaling factor for the S_{rdc}^2, which is difficult to ascertain from the RDC data alone. Unlike the situation for ^{15}N spin relaxation studies, knowledge of the properly averaged bond length is not sufficient to allow the absolute magnitude of the RDC-derived order parameters to be established. This is due to the fact that it is not generally possible to determine to what extent the overall magnitude of the order tensor has absorbed contributions from internal flexibility. In general, this will lead to an underestimation of the magnitude of alignment to an extent related to the amount of internal motion present. In an effort to estimate the value of this overall scaling factor, $^1H^N$–$^1H^\alpha$ RDCs were measured, which were expected to be less sensitive to internal motions than the amide ^{15}N–^{1}H RDCs. By comparison of the two, they concluded that the magnitude of the order tensor, determined using ^{15}N–^{1}H RDCs, was underestimated by a least a factor of 0.78.

More recently, a more detailed account has appeared, using the same RDC data as for the initial demonstration of the model free approach but focusing on the single α-helix in ubiquitin.[136] For the six residues within the helix that could be investigated, the averaged spherical harmonics obtained (see Eq. (36)) are all consistent with highly anisotropic motional averaging, and furthermore exhibit a striking coincidence in the principal direction of anisotropy between these amide N–H sites. Although an analysis of RDCs of this sort cannot directly establish correlation of motion between different interactions, the authors inferred the existence of correlated helical motion based on the similarity of motional parameters between sites. Using molecular mechanical calculations, they determined that the collective, asymmetric helix motion consistent with their RDC analysis ($\pm 22.5^\circ$) could be accommodated without violating any of the NOE constraints for ubiquitin by more than 0.2 Å. This work emphasizes the ability of RDC methods to detect subtle motions not previously detectable from consideration of NOEs.

In a recent work by Tolman,[50] a refinement approach similar to the model free approach was described which extends the realm of applicability to cases in which RDC datasets acquired in five different alignment media are not available. The theoretical development proceeds from recognition that, in general, the RDC data in its entirety can be represented by a single

matrix equation,

$$\mathbf{D} = K\mathbf{BA}; \qquad K = -\left(\frac{\mu_0}{4\pi}\right)\frac{\gamma_I\gamma_S h}{2\pi^2 r_{IS}^3} \qquad (37)$$

In this case, the $N \times M$ matrix $\mathbf{D}$ contains the actual RDC measurements row-indexed by site and column-indexed according to the specific alignment medium. The matrix $\mathbf{B}$, which is of dimension $N \times 5$, contains the irreducible tensorial components (i.e., the $\mathbf{r}^{ij}$ of Eq. (19)) describing each of the N individual dipolar interactions, and the matrix $\mathbf{A}$ contains the corresponding irreducible tensorial descriptions of the order tensors. This corresponds simply to a consolidation of all such vectors $\mathbf{r}^{ij}$ and $\mathbf{s}$ appearing in Eq. (23). Also note the similarity in form to Eq. (36), although the $\mathbf{A}$ matrix differs from the $\mathbf{F}$ matrix in scaling according to the principal magnitude of order and the interaction constant K.

Starting from the matrix formulation of the problem in Eq. (37), the following analytical expression can be derived for the best-fit solution, $\mathbf{B}_{ref}$, which describes both the mean orientations and corresponding descriptions of the dynamics for each internuclear vector.[50]

$$\mathbf{B}_{ref} = \mathbf{B}_{md} + \mathbf{D}(\mathbf{B}_{md}^+\mathbf{D})^+ - \mathbf{B}_{md}\mathbf{B}_{md}^+\mathbf{D}(\mathbf{B}_{md}^+\mathbf{D})^+ \qquad (38)$$

The superscript $+$ denotes the Moore–Penrose inverse of the relevant matrix. This formula requires as input both the RDC data contained in $\mathbf{D}$ and an initial set of internuclear vector orientations, taken from a set of structural coordinates and expressed in terms of the matrix $\mathbf{B}_{md}$. Since the best fit solution is not unique, Equation (38) provides the solution closest to the initial structure $\mathbf{B}_{md}$. Equation (38) is in principle applicable regardless of the amount of data available, but encounters practical limitations associated with the simultaneous refinement of structure and dynamics starting from a rigid structure. Hence, the resulting order parameters strongly depend on the quality of both the data and the initial model structure. An advantage of the procedure is that it can be applied blindly to all residues, regardless of the extent of mobility, and offers a potentially useful route for obtaining structural information which is partially corrected for the effects of dynamics. In the event that five independent alignments have been achieved, Eq. (38) reduces to,

$$\mathbf{B}_{ref} = \mathbf{D}\mathbf{A}^+ \qquad (39)$$

which is closely related to the model free approach.[57,58]

5.3.2. Direct interpretation of dipolar couplings

Tolman has shown that prior knowledge of a structure is not necessary when RDCs can be measured in at least five different alignment media.[50] This

procedure for the *de novo* extraction of both structural and dynamic information from the RDCs is referred to as Direct Interpretation of Dipolar Couplings (DIDC). The DIDC method proceeds based on recognition that the ranges of the matrices **D** and **B** in Eq. (37) are identical when five independent alignment media have been employed for the measurement of RDCs. This allows the desired matrix **B**, which contains the tensorial description of each of the individual dipolar interactions, to be described almost entirely in terms of the raw RDC data, contained in the matrix **D**, according to,

$$\mathbf{B} = \mathbf{U_D}\mathbf{\Lambda} \tag{40}$$

where $\mathbf{U_D}$ is the $N \times 5$ column-orthogonal matrix specifying a basis which spans the range of **D**. The matrix $\mathbf{U_D}$ is readily obtained from the singular value decomposition of the matrix **D** (which produces $\mathbf{D} = \mathbf{U_D}\mathbf{W_D}\mathbf{V_D^{tr}}$; see Section 3). The matrix $\mathbf{\Lambda}$ is the 5×5 matrix which embodies the remaining unknown parameters which cannot be determined from the RDC data alone. Tolman proposes that, for biomolecules, this matrix $\mathbf{\Lambda}$ can be estimated with good precision and accuracy by selecting the solution which produces the minimum variation in the resulting generalized order parameters.[50] This is carried out by the following minimization,

$$||Diag\{\mathbf{U_D}\mathbf{\Lambda}\mathbf{\Lambda}^{tr}\mathbf{U_D^{tr}}\} - 1^{(N)}||_{\min} \tag{41}$$

with **1** corresponding to the identity matrix. The matrix $\mathbf{\Lambda}$ determined in this fashion will produce the solution with the minimum amount of motion necessary to explain the data *exactly*. Some additional features of the DIDC approach is that it provides for the signal averaging between RDC datasets acquired in different alignment media, and can allow an assessment to be made as to whether the assumption of uniform structure and dynamics across media has been maintained.

The DIDC method has been demonstrated very recently in an experimental application to the amide N–H bonds of ubiquitin.[59] In contrast to previous refinement-based approaches to the estimation of dipolar generalized order parameters, the resulting order parameters (Fig. 11) show considerably less site-to-site variability and exhibit a correlation ($r = 0.63$) with ^{15}N spin relaxation order parameters for ubiquitin.[137] These results support a conclusion that the conformational space occupied by ubiquitin is predominantly sampled on the picosecond motional timescale. The DIDC approach can also determine bond orientations with high fidelity, with mean N–H bond orientations for ubiquitin, determined by DIDC, exhibiting an agreement with the RDC-refined orientations (starting from either NMR or X-ray structural coordinates) essentially to within the estimated experimental precision of $2°$. The ability to obtain both N–H bond orientations
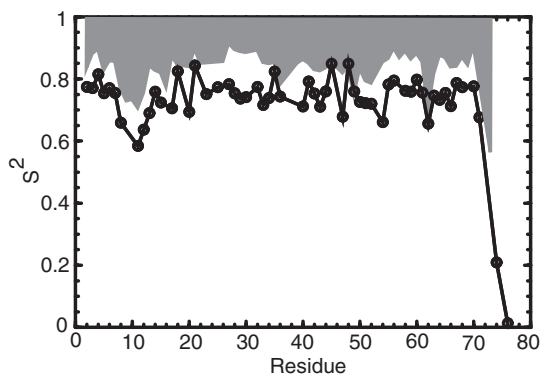
Fig. 11. Dipolar generalized order parameters squared (S^2_{rdc}) determined using the DIDC approach for the protein ubiquitin (solid lines and circles). The shaded region represents the generalized order parameters squared determined using ^{15}N spin relaxation methods.[137] Due to the extended timescale sensitivity of RDCs, the overall scaling for the dipolar order parameters was chosen such that S^2_{rdc} values were equal to or less than the corresponding spin relaxation order parameters.

and generalized order parameters *de novo* based solely on RDCs could represent a route to the TROSY-based[138] structure determination of larger proteins.

5.3.3. *Conformational heterogeneity across alignment media*

Although multiple-alignment based approaches hold great promise for the study of the structure and dynamics of biomolecules, the straightforward use of these approaches depends on the assumed invariance of the structural and dynamic properties of the biomolecule to changes in the alignment medium. Brushweiler and co-workers have introduced a method called SECONDA (Self-Consistency of Dipolar Couplings Analysis) which can assess whether the conformational properties of the biomolecule are heterogeneous or homogeneous across media.[139,140] Their approach relies on the measurement of RDCs in at least six different alignment media. Since only five RDC datasets can be linearly independent if the biomolecule is invariant, the existence of additional independent datasets can be attributed to changes in the structure and dynamics of the macromolecule under study. In an experimental application of SECONDA, they concluded that the protein ubiquitin is generally homogeneous across different alignment media. This is in agreement with the results from the DIDC analysis of ubiquitin, which can assess heterogeneity by similar means and which found no evidence at all for variations between media.[59] These observations are also in agreement with results, obtained on multi-domain proteins and discussed in Section 4 which

show no indication of alignment media induced perturbations. It is likely that media-induced perturbations of biomolecular structure and dynamics will be observed for some systems. Although this would complicate their analysis, the DIDC and SECONDA approaches may provide a route to the characterization of these environmentally induced perturbations.

6. APPLICATIONS TO RNA

Like multi-domain protein systems, RNA structures are modular, with secondary structures often forming independently of tertiary contacts. Tertiary contacts in RNA are rare, and often mediated by divalent and monovalent ions. As such, RNA global conformation may commonly encompass rigid body motions of well defined secondary structural elements such as helices about flexible 'hinge' points formed by flexible residues within bulge and junction motifs. The growing repertoire of RNA structures determined both in the free state and in complex with cognate protein targets all display striking changes in RNA global conformation upon recognition.[141,142] Mounting evidence also implicates similar rearrangements of intact secondary structural domains during RNA catalysis.[143–145] These studies indicate that the conformational dynamics of both the hinge residues and the domains that they link may be important to RNA function.

Challenges of a similar nature to those encountered in studies of extended multi-domain proteins, have largely precluded the accurate characterization of conformational dynamics in nucleic acids. As is the case for multi-domain proteins, the accuracy of nucleic acid global conformations determined using X-ray crystallography may be compromised by crystal packing forces[146] and by requirements for high ionic strengths (higher than physiological conditions) in order to quench repulsive electrostatic forces and allow favourable crystal packing. As is the case for multi-domain proteins, heavy reliance on short-range NOE-derived distance constraints often leads to substantial imprecision in the determination of the global conformation of nucleic acids; with severe spectral overlap and low proton densities further compounding these limitations. These hinderences have made it difficult to identify differences between nucleic acid conformations determined in the solution and solid state. Local fluctuations of hinge residues in nucleic acids can be probed using spin relaxation,[147,148] although the presence of substantial scalar couplings network and anisotropic diffusion profiles can make these studies more challenging for nucleic acids compared to proteins. However, the direct characterization of domain–domain dynamics in nucleic acids has been inaccessible to conventional NMR methods. RDC methods have helped to alleviate some of these difficulties, by improving the quality of nucleic acid structures determined by NMR and by providing a

new probe of both local and global conformational dynamics. Discrepancies and similarities between conformations determined in the solution and solid-state have began to emerge and sometimes understood, while new insight has been gained into both global and local motions.

The application of RDC-based methods to the study of nucleic acid structure and dynamics can be more challenging than for protein systems. In general, RNA adopts far more regular structures compared to proteins. This, along with often more severe spectral overlap, renders measurement of RDCs between independently oriented interaction vectors more difficult, which in turn can handicap the interpretation of RDCs in terms of structure and dynamics. Some methodological developments have been described which offer protocols that can help overcome some of these limitations.[22,101,149–151] There are also several reports now demonstrating the favourable impact of RDCs on NMR structure determination of nucleic acids and their protein complexes.[62,94,96,152–158] As many of these studies have been reviewed previously,[24,159–161] we focus primarily on recent work targeting RNA, with emphasis on studies that shed light on local and global dynamics.

Blackledge and co-workers employed RDCs in an examination of the alignment and dynamics of two stems in the theophylline-binding RNA.[150] Structure refinement was undertaken in a series of steps starting with independent refinement of the local conformation of the two stems regions against NOEs, J-coupling constraints and RDCs, followed by refinement of the entire structure against all NMR constraints. Although the derived principal order parameters were very similar for the two stems, they obtained indications for the presence of dynamics in a bulge nucleotide C27 that links the two stems. The RDC values measured in this nucleotide anomalously differed from its neighbouring residues, and previous NOE and rotating frame ^{13}C relaxation measurements indicated that this nucleotide is flexible in solution. The authors proposed that some degree of conformational averaging of the residue could account for the observations, although with less motional flexibility than indicated in a high-temperature (550 K) restrained molecular dynamics simulation.

Warren *et al.* have investigated the structure of the Sacricin–Ricin loop RNA using RDCs.[162] The inclusion of RDC orientational constraints in addition to traditional NOE and J-coupling derived constraints resulted in significant improvements in the definition of the overall topology of the molecule. These results pointed to differences in global conformation between the NMR and X-ray structures of the Sacricin–Ricin loop, with the solution structure exhibiting a greater degree of bending relative to the solid state structure. In contrast, the inclusion of RDC constraints resulted in a refined conformation for a G-U-A base triple which was much more similar to the conformation observed in the X-ray structure, and unlike that observed in a previous NMR structure determined in the absence of RDCs.

At present, only one RDC study has provided direct evidence for domain–domain dynamics in RNA. Al-Hashimi *et al.* used RDCs to investigate the structure and dynamics of two stems in the stem-loop transactivation response element (TAR) RNA (Fig. 12A).[101] Previous NOE-based structures of TAR showed that while TAR adopts a bent average conformation in the free state (inter-helical angle of $\sim 45°$), binding of TAR to peptides derived from its cognate transactivator protein target *Tat* leads to a conformation in which the two helical domains are far more coaxially aligned. Using an order tensor analysis of RDCs and idealized A-form geometries as models for the two stems, the average inter-helical angle determined using RDCs was well defined, ranging between 44–54°, and in agreement with previous electric birefringence studies.[163] However, the two helices in TAR exhibited markedly different principal order parameters, indicating the presence of substantial inter-helical motions (Fig. 12B). Interpretation of the order parameters using a cone motional model[47] yielded rigid-body inter-helical motions with amplitudes of $46 \pm 4°$. These results were interpreted as evidence for a tertiary capture mode of TAR recognition, in which a transiently populated 'linear' conformational sub-state that is distinct from the average 'bent' state is poised for protein recognition.

The inter-helical bending observed in the conformations of free TAR[164,163] had long been in disagreement with the coaxially aligned X-ray structure
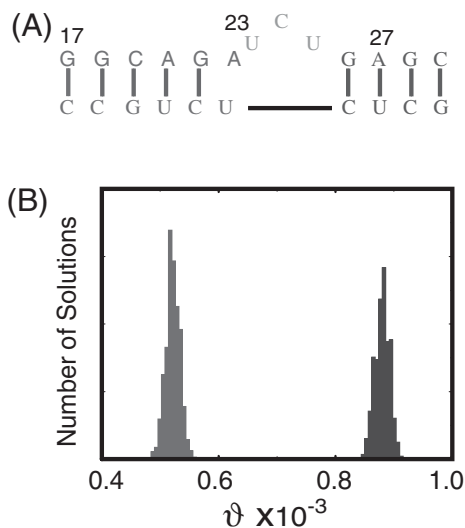
Fig. 12. (A) Secondary structure of a TAR RNA analogue where the six residue hairpin loop in wt-TAR (CUGGGA) has been replaced with the stable tetraloop (UUCG). (B) Histogram plots of the generalized degree of order (ϑ) describing the degree of molecular alignment for the two helices. The large difference in alignment indicates the presence of inter-helical motions.

of TAR determined in the presence of a high concentration of divalent cations.[165] A more recent RDC study[166] has now established that binding of Mg^{2+} ions to TAR not only leads to complete quenching of the inter-helical motions in free TAR (Fig. 13B), but also to a coaxially aligned conformation for the two stems that is more similar to that observed in the solid-state X-ray structure (Fig. 13A). It appears that divalent ions, which are likely needed for stabilization and crystallization of the TAR conformation, and not crystal packing forces *per se*, are responsible for the previously observed differences between the solution and solid state structures of TAR. Interestingly, the average inter-domain alignment determined for TAR in the presence of Mg^{2+} is within the envelope of conformations that appear, based on RDCs, dynamically accessible in the free state.

Pardi and co-workers have recently reported an RDC study examining the conformation of the hammerhead ribozyme.[167] Previous high-resolution X-ray structures of the hammerhead ribozyme determined under high salt conditions do not correlate well with mutational/modification data, and conformational changes have been proposed that carry the X-ray structure to a catalytically active conformation.[168–170] Interestingly, the measured RDCs correlated poorly with best-fit values predicted using coordinates from the X-ray structure. Subsequent determination of the global RNA conformation using RDCs indicated a more extended conformation relative to the X-ray structure, also in better agreement with previous fluorescence resonance energy transfer (FRET) studies.[171,172] Specifically, the inter-helical angles between stems I-II, II-III and I-III were for the NMR structure (absence of Mg^{2+})/X-ray structure (presence of Mg^{2+}) were 153°/152°, 100°/169°, 77°/152° respectively. The derived principal order parameters for the three stems were very similar, consistent with a rigid RNA global conformation.

Pardi and co-workers have also investigated the conformational dynamics of the iron-responsive element (IRE) RNA using RDCs.[151] As in the case of TAR, IRE consists of two helical stems, except that they are separated by only a single bulge residue. A number of protocols were explored for refinement of the structure against RDCs, including independent refinement of the local conformation of individual domains followed by refinement of the global structure and vice versa. In the RDC-refined structures, the two helices adopt a bent inter-helical angle of $\sim 35°$. The RDC-based principal order parameters derived for the two helices were very similar, suggesting that the global conformation of IRE is stable. Nevertheless, signatures of local fluctuations were found. In particular, bulge residue C7, which was previously shown to be disordered based on NOE and ^{13}C $T_{1\rho}$ relaxation data, adopts a number of different conformations with distinct glycosidic dihedral angles (χ) in the ensemble of structures. The inclusion of RDC data for three residues in the hairpin loop (G15, U16 and C18), which lack base-pairing interactions, resulted in higher energy penalties, indicating that a single conformation for these residues cannot
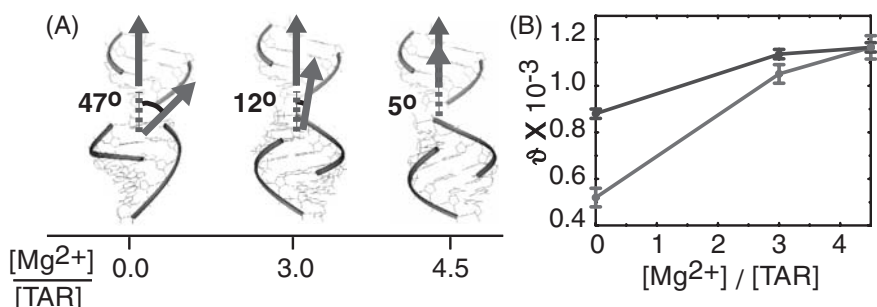
Fig. 13. Structural dynamics of TAR RNA in response to increasing Mg^{2+} concentrations. (A) The TAR inter-helical conformation as a function of [Mg]:[TAR] stoichiometry. Ribbon representation of the relative orientation of stem I (bottom) and II (top) determined by superimposing stem-specific principal axes. The helix axis of stem II is superimposed for all three conformations along the molecular 'z' direction. (B) The generalized degree of order (ϑ) for stem I (lower line) and II (upper line), as a function of [Mg]:[TAR] stoichiometry. Addition of Mg^{2+} leads to attenuations in the difference between helix-specific ϑ values indicating quenching of inter-helical motions.

be found that satisfies measured RDCs and hence the presence of conformational averaging.

It is noteworthy that the ability to probe inter-domain motions using RDCs is predicated on the domains possessing different alignment properties within the specific ordering medium. For two identical domains linked by a flexible linker, the degree of alignment and domain-specific principal order parameters will always be identical, regardless of the degree of inter-domain motions. Hence, as eluded to earlier in Section 2, the measurement of similar principal order parameters for two or more domains is not conclusive evidence that the domains are rigid with respect to one another. This becomes an important issue when domains have similar molecular properties, as can often occur in small RNA molecules targeted by NMR studies. These considerations all relate back to the problem of how to effect a separation of overall alignment effects from internal motional effects.

A recent study by Al-Hashimi and co-workers attempted to address some of the above concerns by employing measurements of RDCs in field aligned RNA molecules, with specific application to the TAR RNA molecule discussed above.[173] This approach relies on comparing χ-tensors determined experimentally using measured field induced RDCs with values estimated based on a rigid average structure. The χ-tensor can be calculated for an RNA conformation through tensor summation of contributions from individual base group susceptibilities. The $\Delta\chi$ values calculated for individual domains in TAR were almost identical, indicating that the situation alluded to above, wherein the two domains have similar alignment propensities, would apply. For a rigid structure, one expects the total measured and calculated χ-tensors to agree within experimental uncertainty. The

existence of motions, however, can lead to discrepancies. The experimental application to TAR found that the magnitude of alignment was attenuated by $\sim 55\%$ relative to expectations based on values calculated using a static structure. Using a framework for analyzing cone motions between domains which accounts for correlations between motions and alignment, the results were interpreted as additional evidence for substantial directionally unbiased motions between the two domains in Mg^{2+}-free TAR.

7. APPLICATIONS TO OLIGOSACCHARIDES

Oligosaccharides, aside from their role in energy storage and as structural elements in bacterial and plant cell walls, are emerging as an important component in cell–cell recognition and intracellular signalling.[174,175] An increasing number of proteins are being discovered to undergo post-translational glycosylation. Relative to proteins and nucleic acids, oligosaccharides can assume enormously diverse forms, and arguably have a greater degree of conformational flexibility, which appears ideal for their role in recognition and signalling, but presents challenges for their structural and dynamic characterization. NMR structure determination of oligosaccharides has traditionally been difficult due to problems associated with the acquisition of sufficient short-range constraints to define an extended topology.[176] This is exacerbated by motions, which in oligosaccharides often involve combinations of oscillations about well defined conformations as well as jumps between distinct conformational sub-states.[177] Interpretation of NOE data is complicated by often extensive flexibility and unfavourable correlation times, which can render NOEs a complicated function of local mobility and diffusional anisotropy. Although rotating frame measurements, and more complete spin relaxation analysis can help, the shortage of constraints is a persistent problem. Residual dipolar couplings can play a significant role in studies of oligosaccharide conformational dynamics because they provide long range constraints in abundance, and are well suited to situations in which semi-rigid fragments, such as sugar rings, are present.

While the use of RDCs for the characterization of oligosaccharide structure and dynamics dates back to 1989,[178] applications have only flourished following the inception of ordering media for aligning macromolecules. For a fuller account of RDC applications to the study of oligosaccharides, the reader is encouraged to explore some of the accounts not discussed here.[179–187] One of the early applications of RDCs was reported by Homans and co-workers, in a study of a ^{13}C-enriched trisaccharide moiety from the ganglioside Gm3 (Gm3-OS, Neu5Acα2-3Galβ1-4Glc).[188] RDCs measured for this trisaccharide, dissolved in a dilute bicelle solution, were incorporated into a simulated annealing protocol, and two families of structures were

generated that exhibited consistency with the measured RDCs. The conformations generated were in agreement with suggestions from a previous study of this trisaccharide and were also populated during a 5 nanosecond molecular dynamics simulation.

A study by Prestegard and co-workers on a trisaccharide molecule, methyl 3,6-di-O-(α-D-mannopyranosyl)-α-D-mannopyranoside revealed the potential for characterizing both conformation and dynamics using RDCs.[189] As for protein and nucleic acid applications, oligosaccharides can also be divided into constituent fragments for which the molecular geometry can be assumed to be known, which in this case were the individual pyranose rings. Determination of the individual order tensors, based on RDCs measured in both bicelle and phage Pf1 ordering media, was followed by superposition of ring-centred order tensor PAS frames. Similar inter-ring orientations were found for rings I and III in both media, but different relative orientations were obtained for ring II, which is linked to ring III. This observation alone points to 'distortions', due to motions, in the apparent RDC derived conformations. Further support for motion was provided by the principal order parameters. For rings I and III, very similar principal order parameters were obtained for order tensors determined in both bicelle and phage media, but much more attenuated principal order parameters (by 40 %) were observed for ring II in both media. The picture that emerged was a well-defined I-III linkage and a significant mobile II-III linkage, consistent with previous studies and expectations based on the extra degree of freedom in the 1-6 glycosidic linkage.

Duus and co-workers[190] utilized molecular dynamics simulations to aid in the interpretation of RDCs measured for the same trisaccharide mentioned above. An important question that was considered was the effect of the existence of multiple conformations for the trisaccharide, which may exhibit different molecular shapes and thus different order tensor parameters. A 50 nanosecond molecular dynamics trajectory of the trisaccharide in water was used in conjunction with back-calculation of order tensors, based on a steric obstruction model for alignment, in order to predict RDCs. Focusing on the flexible $\alpha(1 \rightarrow 6)$ linkage between rings II and III, the authors used the molecular dynamics simulations to predict the averaged order tensors resulting from the two conformers (gg and gt) that were populated during the simulations. Fitting the populations of the two conformers against measured RDC yielded a 55% gg and 45% gt conformational mix. These results were in agreement with previous studies of the trisaccharide, including the study by Prestegard and co-workers.[189]

In another study, Freedberg employed RDCs to investigate the conformational dynamics of the fructofuranosyl ring of sucrose.[191] Twenty structures for the fructose ring, sampling different pucker geometries, were interrogated for agreement with measured RDCs. The four best-fit structures were found to be in the NE quadrant of the pseudorotational wheel (18°, 36°,

54° and 72°). The observation that multiple conformers agreed with the RDCs was interpreted as evidence for having limited but nevertheless multiple and dynamically interconverting sugar pucker conformations.

Stevensson *et al.* reported an interesting approach for the characterization of the conformational distribution of the dissacharide α-L-Rha*p*-(1 $\rightarrow$ 2)-α-L-Rha*p*-OMe using RDCs.[192] Their APME approach utilizes a combination of additive potential (AP) models and maximum entropy (ME) methods. Their study proceeded by determination of the order tensors for individual rings using intra-residue RDCs, followed by characterization of the glycosidic conformational distribution function, $P(\phi, \psi)$, using inter-residue RDCs, J-couplings and NOEs. The preliminary order tensor analysis of intra-residue RDCs showed that the principal order parameters derived for the two rings differed by a factor 1.2, indicating the presence of inter-ring motions. A conformational distribution function was thus derived using the APME method, which provides the least biased and flattest distribution consistent with measured data. The results demonstrated how RDC-based evidence for motion between rings could be further characterized in terms of a specific conformational distribution function describing the intervening torsional degrees of freedom.

8. CONCLUSIONS AND FUTURE PERSPECTIVES

Residual dipolar couplings have been recognized primarily as a rich source of long-range orientational constraints, complementary to traditional short-range NOE and J-coupling derived constraints. The use of RDCs has already led to increases in the accuracy and precision of biomolecular structures determined by NMR. In this review, we have emphasized the multi-faceted role that RDCs can play in the elucidation of dynamics or structural plasticity. On one hand, improvements in our ability to characterize the structure of flexible and often extended biomolecules with the use of RDCs has allowed for the characterization of subtle differences between solution and solid state structures; differences that might otherwise be lost within the uncertainties of the solution state coordinates. These studies have provided some insights into molecular plasticity and the situations in which crystal packing forces may be problematic. But on the other hand, crystallographic structures of globular domains can be productively combined with RDC-based analysis to establish the quaternary organization and dynamics of multi-domain biomolecules or complexes in solution. More than ever before, X-ray crystallography and NMR spectroscopy are being employed in tandem.

There are also tremendous possibilities for using RDCs as a direct probe of conformational dynamics. Recalcitrant problems such as the characterization of intermediate timescale motions (microsecond–nanosecond), both for

fluctuations involving intact domains or individual bond vectors, are no longer out of reach. The future challenge will be to better establish the relationship between time averaged RDCs and molecular conformation, through combination with other NMR probes of molecular dynamics or by means of more extensive RDC measurements made utilizing multiple alignment media.

We can draw a number of general conclusions from the RDC studies reported thus far on biomolecular dynamics. Modular biomolecules, such as multi-domain proteins, RNA and oligosaccharides, often exhibit limited contacts between structurally well-defined domains, and are accompanied by substantial inter-domain motions. In light of the fact that domain rearrangements are often critical for biological activity, such motions are likely to be important for function. Whether these motions are arbitrary in nature or more structurally defined and constrained, remains to be determined. The examination of moieties linking domains may shed further light on this question. It is also clear that, for extended molecules such as multi-domain proteins and nucleic acids, discrepancies can arise between structures determined in the solid and solution state. While the X-ray structures may be an artifact of crystal packing forces, they may also reflect energetically stable sub-states that are populated in solution. Another explanation for discrepencies between solution and solid-state structures may be attributed to differences in conditions used in deriving the structural information.

For the foreseeable future, the number of motional parameters that can be characterized using NMR will lag considerably behind the number of parameters needed to completely specify a dynamic biomolecule. There are several routes which may help to close this gap. The combined use of biophysical techniques, such as neutron diffraction, X-ray crystallography, molecular dynamics simulations and fluorescence resonance energy transfer may aid data interpretation considerably. The complexity of the motions may be simplified using computer generated models that encompass information regarding motional amplitudes, asymmetries and correlations across different timescales. Finally, one must wonder if, as observed in biomolecular structures, motions are not infinite in their complexity, but rather fall into discrete classes with similar characteristics. In this regard, the structural genomics effort, and opportunities in the systematic study of biomolecular dynamics as function of amino-acid sequence and structure may prove to be equally important. The measurements of RDCs will likely play an important role in these future investigations.

ACKNOWLEDGEMENTS

provided by Johns Hopkins University (JRT) and the University of Michigan (HMA).

REFERENCES

1. J. Skolnick and J. S. Fetrow, *Trends Biotechnol.*, 2000, **18**, 34–39.
2. A. Sali, *Nat. Struct. Biol.*, 1998, **5**, 1029–1032.
3. O. Jardetzky and J. F. Lefevre, *FEBS Lett.*, 1994, **338**, 246–250.
4. O. Jardetzky, *Prog. Biophys. Mol. Biol.*, 1996, **65**, 171.
5. M. F. Perutz and F. S. Mathews, *J. Mol. Biol.*, 1966, **21**, 199.
6. M. Brunori, *Biophys. Chem.*, 2000, **86**, 221–230.
7. I. E. Iben, D. Braunstein, W. Doster, H. Frauenfelder, M. K. Hong, J. B. Johnson, S. Luck, P. Ormos, A. Schulte, P. J. Steinbach, A. H. Xie and R. D. Young, *Phys. Rev. Lett.*, 1989, **62**, 1916–1919.
8. P. J. Steinbach and B. R. Brooks, *Proc. Natl. Acad. Sci. USA*, 1996, **93**, 55–59.
9. H. Frauenfelder, S. G. Sligar and P. G. Wolynes, *Science*, 1991, **254**, 1598–1603.
10. M. Ferrand, A. J. Dianoux, W. Petry and G. Zaccai, *Proc. Natl. Acad. Sci. USA*, 1993, **90**, 9668–9672.
11. B. F. Rasmussen, A. M. Stock, D. Ringe and G. A. Petsko, *Nature*, 1992, **357**, 423–424.
12. L. E. Kay, *Nat. Struct. Biol.*, 1998, **5**, 513–517.
13. R. Ishima and D. A. Torchia, *Nat. Struct. Biol.*, 2000, **7**, 740–743.
14. A. G., 3rd, Palmer, C. D. Kroenke and J. P. Loria, *Methods Enzymol.*, 2001, **339**, 204–238.
15. A. J. Wand, *Nat. Struct. Biol.*, 2001, **8**, 926–931.
16. M. Akke, *Curr. Opin. Struct. Biol.*, 2002, **12**, 642–647.
17. D. A. Case, *Acc. Chem. Res.*, 2002, **35**, 325–331.
18. R. Bruschweiler, *Curr. Opin. Struct. Biol.*, 2003, **13**, 175–183.
19. J. H. Prestegard, J. R. Tolman, H. M. Al-Hashimi and M. Andrec, *Biological Magnetic Resonance*, Vol. 17, N. R. Krishna and L. J. Berliner, eds., Plenum, New York, 1999, 311–355.
20. J. H. Prestegard, H. M. Al-Hashimi and J. R. Tolman, *Q. Rev. Biophys.*, 2000, **33**, 371–424.
21. N. Tjandra, *Struct. Fold. Des.*, 1999, **7**, R205–R211.
22. E. T. Mollova, M. R. Hansen and A. Pardi, *J. Am. Chem. Soc.*, 2000, **122**, 11561–11562.
23. A. Bax, G. Kontaxis and N. Tjandra, *Methods Enzymol.*, 2001, **339**, 127–174.
24. J. R. Tolman, *Curr. Opin. Struct. Biol.*, 2001, **11**, 532–539.
25. H. M. Al-Hashimi and D. J. Patel, *J. Biomol. NMR*, 2002, **22**, 1–8.
26. B. Simon and M. Sattler, *Angew. Chem. Int. Ed. Engl.*, 2002, **41**, 437–440.
27. A. M. Gronenborn, *CR Biol.*, 2002, **325**, 957–966.
28. G. M. Clore and C. D. Schwieters, *Curr. Opin. Struct. Biol.*, 2002, **12**, 146–153.
29. A. Bax, *Protein Sci.*, 2003, **12**, 1–16.
30. E. W. Bastiaan, C. Maclean, P. C. M. Van Zilj and A. A. Bothner-by, *Ann. Rep. NMR Spec.*, 1987, **19**, 35–77.
31. E. W. Bastiaan and C. MacLean, *NMR-Basic Princ. Prog.*, 1990, **25**, 17–43.
32. C. Gayathri, A. A. Bothner-By, P. C. M. van Zijl and C. MacLean, *Chem. Phys. Lett.*, 1982, **87**, 192–196.
33. P. C. M. van Zijl, B. H. Ruessink, J. Bulthuis and C. MacLean, *Acc. Chem. Res.*, 1984, **17**, 172–180.
34. I. W. Emsley and J. C. Lindon, *NMR Spectroscopy Using Liquid Crystal Solvents*, Pergamon Press, Oxford, 1975.
35. P. Diehl and C. L. Khetrapal, *NMR: Basic Principles and Progress*, Vol. 1, Springer-Verlag, New York, 1969.
36. C. L. Khetrapal, A. C. Kunwar, A. G. Tracey and P. Diehl, eds., Springer-Verlag, Berlin, 1975.

37. L. C. Snyder, *J. Chem. Phys.*, 1965, **43**, 4041–4050.
38. A. Saupe, *Angew. Chem. Int. Ed. Engl.*, 1968, **7**, 97–112.
39. J. A. B. Lohman and C. MacLean, *Chem. Phys.*, 1978, **35**, 269–274.
40. A. A. Bothner-By, *Encyclopedia of Nuclear Magnetic Resonance*, D. M. Grant and R. K. Harris, eds., Wiley, Chichester, 1995, 2932–2938.
41. A. Abragam, *Principles of Nuclear Magnetism*, Clarendon Press, Oxford, 1961.
42. R. R. Ernst, G. Bodenhausen and A. Wokaun, *Principles of Nuclear Magnetic Resonance in One and Two Dimensions*, Clarendon Press, Oxford, 1987.
43. D. A. Case, *J. Biomol. NMR*, 1999, **15**, 95–102.
44. M. Ottiger and A. Bax, *J. Am. Chem. Soc.*, 1998, **120**, 12334–12341.
45. A. Saupe, *Z. Naturforsh.*, 1964, **19a**, 161.
46. A. R. Edmonds, *Angular momentum in quantum mechanics*, Princeton Univ. Press, Princeton, New Jersey, 1968.
47. J. R. Tolman, J. M. Flanagan, M. A. Kennedy and J. H. Prestegard, *Nat. Struct. Biol.*, 1997, **4**, 292–297.
48. J. A. Losonczi and J. H. Prestegard, *Biochemistry*, 1998, **37**, 706–716.
49. J. R. Tolman, H. M. Al-Hashimi, L. E. Kay and J. H. Prestegard, *J. Am. Chem. Soc.*, 2001, **123**, 1416–1424.
50. J. R. Tolman, *J. Am. Chem. Soc.*, 2002, **124**, 12020–12030.
51. J. R. Tolman, J. M. Flanagan, M. A. Kennedy and J. H. Prestegard, *Proc. Natl. Acad. Sci. USA*, 1995, **92**, 9279–9283.
52. N. Tjandra and A. Bax, *Science*, 1997, **278**, 1111–1114.
53. M. R. Hansen, P. Hanson and A. Pardi, *Method Enzymol.*, 2000, **317**, 220–240.
54. J. H. Prestegard and A. I. Kishore, *Curr. Opin. Chem. Biol.*, 2001, **5**, 584–590.
55. B. E. Ramirez and A. Bax, *J. Am. Chem. Soc.*, 1998, **120**, 9106–9107.
56. H. M. Al-Hashimi, H. Valafar, M. Terrell, E. R. Zartler, M. K. Eidsness and J. H. Prestegard, *J. Magn. Reson.*, 2000, **143**, 402–406.
57. J. Meiler, J. J. Prompers, W. Peti, C. Griesinger and R. Bruschweiler, *J. Am. Chem. Soc.*, 2001, **123**, 6098–6107.
58. W. Peti, J. Meiler, R. Bruschweiler and C. Griesinger, *J. Am. Chem. Soc.*, 2002, **124**, 5822–5833.
59. K. Briggman and J. R. Tolman, *J. Am. Chem. Soc.*, 2003, **125**, 10164–10165.
60. I. Bertini, M. B. L. Janik, L. Gaohua, C. Luchinat and A. Rosato, *Biochemistry*, 2000, submitted.
61. I. Bertini, I. C. Felli and C. Luchinat, *J. Biomol. NMR*, 2000, **18**, 347–355.
62. H. M. Al-Hashimi, A. Majumdar, A. Gorin, A. Kettani, E. Skripkin and D. J. Patel, *J. Am. Chem. Soc.*, 2001, **123**, 633–640.
63. S. Gaemers and A. Bax, *J. Am. Chem. Soc.*, 2001, **123**, 12343–12352.
64. P. Ram and J. H. Prestegard, *Biochim. Biophys. Acta*, 1988, **940**, 289–294.
65. C. R. Sanders, B. J. Hare, K. P. Howard and J. H. Prestegard, *Prog. Nucl. Magn. Reson. Spectrosc.*, 1994, **26**, 421–444.
66. C. R. Sanders and R. S. Prosser, *Struct. Fold. Des.*, 1998, **6**, 1227–1234.
67. M. Ottiger and A. Bax, *J. Biomol. NMR*, 1998, **12**, 361–372.
68. J. A. Losonczi and J. H. Prestegard, *J. Biomol. NMR*, 1998, **12**, 447–451.
69. M. Ottiger and A. Bax, *J. Biomol. NMR*, 1999, **13**, 187–191.
70. S. Cavagnero, H. J. Dyson and P. E. Wright, *J. Biomol. NMR*, 1999, **13**, 387–391.
71. H. Wang, M. Eberstadt, E. T. Olejniczak, R. P. Meadows and S. W. Fesik, *J. Biomol. NMR*, 1998, **12**, 443–446.
72. M. R. Hansen, L. Mueller and A. Pardi, *Nat. Struct. Biol.*, 1998, **5**, 1065–1074.
73. G. M. Clore, M. R. Starich and A. M. Gronenborn, *J. Am. Chem. Soc.*, 1998, **120**, 10571–10572.
74. M. Zweckstetter and A. Bax, *J. Biomol. NMR*, 2001, **20**, 365–377.

75. J. Sass, F. Cordier, A. Hoffmann, A. Cousin, J. G. Omichinski, H. Lowen and S. Grzesiek, *J. Am. Chem. Soc.*, 1999, **121**, 2047–2055.

76. B. W. Koenig, J. S. Hu, M. Ottiger, S. Bose, R. W. Hendler and A. Bax, *J. Am. Chem. Soc.*, 1999, **121**, 1385–1386.

77. K. Fleming, D. Gray, S. Prasannan and S. Matthews, *J. Am. Chem. Soc.*, 2000, **122**, 5224–5225.

78. R. S. Prosser, J. A. Losonczi and I. V. Shiyanovskaya, *J. Am. Chem. Soc.*, 1998, **120**, 11010–11011.

79. L. G. Barrientos, C. Dolan and A. M. Gronenborn, *J. Biomol. NMR*, 2000, **16**, 329–337.

80. L. G. Barrientos, K. Gawrisch, N. Cheng, A. C. Steven and A. M. Gronenborn, *Langmuir*, 2002, **18**, 3773–3779.

81. M. Ruckert and G. Otting, *J. Am. Chem. Soc.*, 2000, **122**, 7793–7797.

82. H. J. Sass, G. Musco, S. J. Stahl, P. T. Wingfield and S. Grzesiek, *J. Biomol. NMR*, 2000, **18**, 303–309.

83. R. Tycko, F. J. Blanco and Y. Ishii, *J. Am. Chem. Soc.*, 2000, **122**, 9340–9341.

84. Y. Ishii, M. A. Markus and R. Tycko, *J. Biomol. NMR*, 2001, **21**, 141–151.

85. S. Meier, D. Haussinger and S. Grzesiek, *J. Biomol. NMR*, 2002, **24**, 351–356.

86. H.-J. Sass, G. Musco, S. J. Stahl, P. T. Wingfield and S. Grzesiek, *J. Biomol. NMR*, 2000, **18**, 303–309.

87. J. F. Trempe, F. G. Morin, Z. C. Xia, R. H. Marchessault and K. Gehring, *J. Biomol. NMR*, 2002, **22**, 83–87.

88. S. A. Riley, J. R. Giuliani and M. P. Augustine, *J. Magn. Reson.*, 2002, **159**, 82–86.

89. J. A. Losonczi, M. Andrec, M. W. F. Fischer and J. H. Prestegard, *J. Magn. Reson.*, 1999, **138**, 334–342.

90. A. Albert, *Regression and the Moore-Penrose Pseudoinverse*, Academic Press, New York, 1972.

91. A. Ben-Israel and T. N. E. Greville, *Generalized Inverses: Theory and Applications*, John Wiley & Sons, New York, 1974.

92. W. H. Press, S. A. Teukolsky, W. T. Vetterling and B. P. Flannery, *Numerical Recepies in C*, Cambridge University Press, Cambridge, 1992.

93. N. Tjandra, S. Grzesiek and A. Bax, *J. Am. Chem. Soc.*, 1996, **118**, 6264–6272.

94. N. Tjandra, J. G. Omichinski, A. M. Gronenborn, G. M. Clore and A. Bax, *Nat. Struct. Biol.*, 1997, **4**, 732–738.

95. H. M. Al-Hashimi, J. R. Tolman, A. Majumdar, A. Gorin and D. J. Patel, *J. Am. Chem. Soc.*, 2001, **123**, 5806–5807.

96. H. M. Al-Hashimi, A. Gorin, A. Majumdar and D. J. Patel, *J. Am. Chem. Soc.*, 2001, **123**, 3179–3180.

97. A. Bax and N. Tjandra, *J. Biomol. NMR*, 1997, **10**, 289–292.

98. A. Bax and S. E. Ealick, *Curr. Opin. Struct. Biol.*, 1997, **7**, 669–671.

99. E. E. Burnell and C. A. de Lange, *Chem. Rev.*, 1998, **98**, 2359–2387.

100. M. Zweckstetter and A. Bax, *J. Am. Chem. Soc.*, 2000, **122**, 3791–3792.

101. H. M. Al-Hashimi, Y. Gosser, A. Gorin, W. Hu, A. Majumdar and D. J. Patel, *J. Mol. Biol.*, 2002, **315**, 95–102.

102. H. F. Azurmendi and C. A. Bush, *J. Am. Chem. Soc.*, 2002, **124**, 2426–2427.

103. M. X. Fernandes, P. Bernado, M. Pons and J. Garcia de la Torre, *J. Am. Chem. Soc.*, 2001, **123**, 12037–12047.

104. A. Almond and J. B. Axelsen, *J. Am. Chem. Soc.*, 2002, **124**, 9986–9987.

105. S. A. Teichmann, J. Park and C. Chothia, *Proc. Natl. Acad. Sci. USA*, 1998, **95**, 14658–14663.

106. E. V. Koonin, L. Aravind and A. S. Kondrashov, *Cell*, 2000, **101**, 573–576.

107. C. Chothia, J. Gough, C. Vogel and S. A. Teichmann, *Science*, 2003, **300**, 1701–1703.

108. C. Khosla and P. B. Harbury, *Nature*, 2001, **409**, 247–252.

109. N. Tjandra, D. S. Garrett, A. M. Gronenborn, A. Bax and G. M. Clore, *Nat. Struct. Biol.*, 1997, **4**, 443–449.
110. D. Fushman, R. Xu and D. Cowburn, *Biochemistry*, 1999, **38**, 10225–10230.
111. L. E. Kay, *Nuclear Magnetic Resonance of Biological Macromolecules*, *Pt B*, Vol. 339, 2001, pp. 174–203.
112. M. W. F. Fischer, J. A. Losonczi, J. L. Weaver and J. H. Prestegard, *Biochemistry*, 1999, **38**, 9013–9022.
113. J. L. Weaver and J. H. Prestegard, *Biochemistry*, 1998, **37**, 116–128.
114. D. T. Braddock, M. Cai, J. L. Baber, Y. Huang and G. M. Clore, *J. Am. Chem. Soc.*, 2001, **123**, 8634–8635.
115. D. T. Braddock, J. M. Louis, J. L. Baber, D. Levens and G. M. Clore, *Nature*, 2002, **415**, 1051–1056.
116. L. Yu, A. H. Gunasekera, J. Mack, E. T. Olejniczak, L. E. Chovan, X. Ruan, D. L. Towne, C. G. Lerner and S. W. Fesik, *J. Mol. Biol.*, 2001, **311**, 593–604.
117. N. R. Skrynnikov, N. K. Goto, D. Yang, W. Y. Choy, J. R. Tolman, G. A. Mueller and L. E. Kay, *J. Mol. Biol.*, 2000, **295**, 1265–1273.
118. P. M. Hwang, N. R. Skrynnikov and L. E. Kay, *J. Biomol. NMR*, 2001, **20**, 83–88.
119. J. Evenas, V. Tugarinov, N. R. Skrynnikov, N. K. Goto, R. Muhandiram and L. E. Kay, *J. Mol. Biol.*, 2001, **309**, 961–974.
120. J. J. Chou, S. Li, C. B. Klee and A. Bax, *Nat. Struct. Biol.*, 2001, **8**, 990–997.
121. J. A. Lukin, G. Kontaxis, V. Simplaceanu, Y. Yuan, A. Bax and C. Ho, *Proc. Natl. Acad. Sci. USA*, 2003, **100**, 517–520.
122. N. U. Jain, S. Noble and J. H. Prestegard, *J. Mol. Biol.*, 2003, **328**, 451–462.
123. H. M. Al-Hashimi, P. J. Bolon and J. H. Prestegard, *J. Magn. Reson.*, 2000, **142**, 153–158.
124. R. Varadan, O. Walker, C. Pickart and D. Fushman, *J. Mol. Biol.*, 2002, **324**, 637–647.
125. M. Zweckstetter and A. Bax, *J. Biomol. NMR*, 2002, **23**, 127–137.
126. L. C. Wang, Y. X. Pang, T. Holder, J. R. Brender, A. V. Kurochkin and E. R. P. Zuiderweg, *Proc. Natl. Acad. Sci. USA*, 2001, **98**, 7684–7689.
127. H. A. Carlson, *Curr. Opin. Chem. Biol.*, 2002, **6**, 447–452.
128. H. A. Carlson, *Curr. Pharm. Des.*, 2002, **8**, 1571–1578.
129. B. Reif, M. Hennig and C. Griesinger, *Science*, 1997, **276**, 1230–1233.
130. M. L. Cai, Y. Huang and G. M. Clore, *J. Am. Chem. Soc.*, 2001, **123**, 8642–8643.
131. N. Sibille, B. Bersch, J. Coves, M. Blackledge and B. Brutscher, *J. Am. Chem. Soc.*, 2002, **124**, 14616–14625.
132. J. J. Chou and A. Bax, *J. Am. Chem. Soc.*, 2001, **123**, 3844–3845.
133. A. Mittermaier and L. E. Kay, *J. Am. Chem. Soc.*, 2001, **123**, 6892–6903.
134. R. Sprangers, M. R. Groves, I. Sinning and M. Sattler, *J. Mol. Biol.*, 2003, **327**, 507–520.
135. G. Lipari and A. Szabo, *J. Am. Chem. Soc.*, 1982, **104**, 4546–4559.
136. J. Meiler, W. Peti and C. Griesinger, *J. Am. Chem. Soc.*, 2003, **125**, 8072–8073.
137. N. Tjandra, S. E. Feller, R. W. Pastor and A. Bax, *J. Am. Chem. Soc.*, 1995, **117**, 12562–12566.
138. K. Wuthrich, K. Pervushin, R. Riek, M. Salzmann and G. Wider, *Abstr. Pap. Am. Chem. Soc.*, 2000, 219, 11-PHYS.
139. J. C. Hus and R. Bruschweiler, *J. Biomol. NMR*, 2002, **24**, 123–132.
140. J. C. Hus, W. Peti, C. Griesinger and R. Bruschweiler, *J. Am. Chem. Soc.*, 2003, **125**, 5596–5597.
141. J. R. Williamson, *Nat. Struct. Biol.*, 2000, **7**, 834–837.
142. N. Leulliot and G. Varani, *Biochemistry*, 2001, **40**, 7947–7956.
143. X. Zhuang, H. Kim, M. J. Pereira, H. P. Babcock, N. G. Walter and S. Chu, *Science*, 2002, **296**, 1473–1476.

144. N. G. Walter, P. A. Chan, K. J. Hampel, D. P. Millar and J. M. Burke, *Biochemistry*, 2001, **40**, 2580–2587.
145. M. Menger, F. Eckstein and D. Porschke, *Nucleic Acids Res.*, 2000, **28**, 4428–4434.
146. R. E. Dickerson, D. S. Goodsell, M. L. Kopka and P. E. Pjura, *J. Biomol. Struct. Dyn.*, 1987, **5**, 557–579.
147. C. G. Hoogstraten, J. R. Wank and A. Pardi, *Biochemistry*, 2000, **39**, 9951–9958.
148. M. Akke, R. Fiala, F. Jiang, D. Patel and A. G. Palmer, *RNA-Publ. RNA Soc.*, 1997, **3**, 702–709.
149. J. J. Warren and P. B. Moore, *J. Magn. Reson.*, 2001, **149**, 271–275.
150. N. Sibille, A. Pardi, J. P. Simorre and M. Blackledge, *J. Am. Chem. Soc.*, 2001, **123**, 12135–12146.
151. S. A. McCallum and A. Pardi, *J. Mol. Biol.*, 2003, **326**, 1037–1050.
152. P. Bayer, L. Varani and G. Varani, *J. Biomol. NMR*, 1999, **14**, 149–155.
153. N. Tjandra, S. Tate, A. Ono, M. Kainosho and A. Bax, *J. Am. Chem. Soc.*, 2000, **122**, 6190–6200.
154. A. Vermeulen, H. J. Zhou and A. Pardi, *J. Am. Chem. Soc.*, 2000, **122**, 9638–9647.
155. L. Trantirek, M. Urbasek, R. Stefl, J. Feigon and V. Sklenar, *J. Am. Chem. Soc.*, 2000, **122**, 10454–10455.
156. D. MacDonald, K. Herbert, X. L. Zhang, T. Polgruto and P. Lu, *J. Mol. Biol.*, 2001, **306**, 1081–1098.
157. P. Padrta, R. Stefl, L. Kralik, L. Zidek and V. Sklenar, *J. Biomol. NMR*, 2002, **24**, 1–14.
158. T. Sprules, N. Green, M. Featherstone and K. Gehring, *J. Biol. Chem.*, 2003, **278**, 1053–1058.
159. E. T. Mollova and A. Pardi, *Curr. Opin. Struct. Biol.*, 2000, **10**, 298–302.
160. L. Zidek, R. Stefl and V. Sklenar, *Curr. Opin. Struct. Biol.*, 2001, **11**, 275–281.
161. D. MacDonald and P. Lu, *Curr. Opin. Struct. Biol.*, 2002, **12**, 337–343.
162. J. J. Warren and P. B. Moore, *J. Biomol. NMR*, 2001, **20**, 311–323.
163. M. Zacharias and P. J. Hagerman, *Proc. Natl. Acad. Sci. USA*, 1995, **92**, 6052–6056.
164. F. Aboul-ela, J. Karn and G. Varani, *Nucleic Acids Res.*, 1996, **24**, 3974–3981.
165. J. A. Ippolito and T. A. Steitz, *Proc. Natl. Acad. Sci. USA*, 1998, **95**, 9819–9824.
166. H. M. Al-Hashimi, S. W. Pitt, A. Majumdar, W. Xu and D. J. Patel, *J. Mol. Biol.*, 2003, **329**, 867–873.
167. K. Bondensgaard, E. T. Mollova and A. Pardi, *Biochemistry*, 2002, **41**, 11532–11542.
168. H. W. Pley, K. M. Flaherty and D. B. McKay, *Nature*, 1994, **372**, 68–74.
169. W. G. Scott, J. T. Finch and A. Klug, *Cell*, 1995, **81**, 991–1002.
170. W. G. Scott, J. B. Murray, J. R. Arnold, B. L. Stoddard and A. Klug, *Science*, 1996, **274**, 2065–2069.
171. G. S. Bassi, N. E. Mollegaard, A. I. Murchie, E. von Kitzing and D. M. Lilley, *Nat. Struct. Biol.*, 1995, **2**, 45–55.
172. G. S. Bassi, A. I. Murchie, F. Walter, R. M. Clegg and D. M. Lilley, *EMBO J.*, 1997, **16**, 7481–7489.
173. Q. Zhang, R. Throolin, S. Pitt, A. Serganov and H. M. Al-Hashimi, *J. Am. Chem. Soc.*, 2003, submitted.
174. S. Roseman, *J. Biol. Chem.*, 2001, **276**, 41527–41542.
175. C. Schaffer and P. Messner, *Biochimie*, 2001, **83**, 591–599.
176. C. A. Bush, M. Martin-Pastor and A. Imberty, *Annu. Rev. Biophys. Biomol. Struct.*, 1999, **28**, 269–293.
177. R. J. Woods, *Glycoconj. J.*, 1998, **15**, 209–216.
178. P. Ram, L. Mazzola and J. H. Prestegard, *J. Am. Chem. Soc.*, 1989, **111**, 3176–3182.
179. M. Martin-Pastor and C. A. Bush, *Carbohydr. Res.*, 2000, **323**, 147–155.
180. M. Martin-Pastor and C. A. Bush, *Biochemistry*, 2000, **39**, 4674–4683.

181. M. Martin-Pastor, A. Canales-Mayordomo and J. Jimenez-Barbero, *J. Biomol. NMR*, 2003, **26**, 345–353.
182. T. N. Pham, T. Liptaj, K. Bromek and D. Uhrin, *J. Magn. Reson.*, 2002, **157**, 200–209.
183. A. Almond, J. Bunkenborg, T. Franch, C. H. Gotfredsen and J. O. Duus, *J. Am. Chem. Soc.*, 2001, **123**, 4792–4802.
184. B. Stevensson, A. V. Komolkin, D. Sandstrom and A. Maliniak, *J. Chem. Phys.*, 2001, **114**, 2332–2339.
185. A. Kjellberg and S. W. Homans, *J. Magn. Reson.*, 2001, **151**, 90–93.
186. H. F. Azurmendi, M. Martin-Pastor and C. A. Bush, *Biopolymers*, 2002, **63**, 89–98.
187. H. F. Azurmendi and C. A. Bush, *Carbohydr. Res.*, 2002, **337**, 905–915.
188. G. R. Kiddle and S. W. Homans, *FEBS Lett.*, 1998, **436**, 128–130.
189. F. Tian, H. M. Al-Hashimi, J. L. Craighead and J. H. Prestegard, *J. Am. Chem. Soc.*, 2001, **123**, 485–492.
190. A. Almond and J. O. Duus, *J. Biomol. NMR*, 2001, **20**, 351–363.
191. D. I. Freedberg, *J. Am. Chem. Soc.*, 2002, **124**, 2358–2362.
192. B. Stevensson, C. Landersjo, G. Widmalm and A. Maliniak, *J. Am. Chem. Soc.*, 2002, **124**, 5946–5947.
193. P. Dosset, J. C. Hus, D. Marion and M. Blackledge, *J. Biomol. NMR*, 2001, **20**, 223–231.

Advances in Theoretical and Physical Aspects of Spin–Spin Coupling Constants

RUBÉN H. CONTRERAS[1], VERÓNICA BARONE[1],
JULIO C. FACELLI[2] and JUAN E. PERALTA[3]

[1]*Physics Department, School of Sciences, University of Buenos Aires and CONICET, Ciudad Universitaria, P. 1, (1428) Buenos Aires, Argentina*
[2]*Center for High Performance Computing, University of Utah, 155 South 1452 East RM 405 Salt Lake City, UT 84112-0190, USA*
[3]*Department of Chemistry, Rice University, Houston, TX 77005-1892, USA*

In this work a selection of papers dealing with NMR indirect spin–spin coupling constants published between 1999 and May 2003 are reviewed. Care is taken to avoid overlap between this work and several important review articles published during this period. A general introduction is followed by two main sections. In the first section, the most relevant advances in theoretical approaches to calculate and analyze these spectral parameters are discussed. The relevant role played by both non-relativistic and relativistic DFT-based approaches is highlighted. In the second section, calculations, analyses and measurements of couplings in molecular systems providing an interesting insight into how intra- and intermolecular interactions affect spin–spin couplings are discussed. Special attention is given to couplings transmitted through a hydrogen-bond, a phenomenon that proved to be very important for studying important aspects of structural molecular biology. Other interactions are also discussed, such as the through-space transmission, proximity effects, factors that define the stereo-specific behaviour of several types of couplings,

medium effects and nuclear motion effects. Instead of aiming at an exhaustive analysis of the current bibliography, priority is given to comments that convey both the idea of the enormous potential that indirect spin–spin couplings have for studying molecular processes as well as their usefulness as probes to study subtle aspects of electronic molecular structure.

Abbreviations: ADF, Amsterdam density functional; AIM, atoms in molecules; AO, atomic orbital; CAS, complete active space; CC, coupled clusters; CCSD, coupled cluster singles and doubles; CHF, coupled Hartree–Fock; CI, configuration interaction; CLOPPA, contributions from localized orbitals within the PP approach; CP, coupled perturbed; DFT, density functional theory; DNA, deoxyribonucleic acid; DSO, diamagnetic spin orbital; EOM, equation of motion; FC, Fermi contact; FPT, finite perturbation theory; GGA, generalized gradient approximation; HF, Hartree–Fock; INDO, intermediate neglect of differential overlap; JOC-PSP, Decomposition of J into orbital contributions using partial spin polarization; KS, Kohn and Sham; LMO, localized molecular orbital; MCSCF, multiconfigurational SCF; MO, molecular orbital; MP, Møler–Plesset; NBO, natural bond orbital; NCTI, neglect of charge transfer interactions; NJC, natural J coupling; NLMO, natural localized molecular orbital; NMR, nuclear magnetic resonance; NNBI, neglect of non-bonded interactions; NO, natural orbital; PCM, polarizable continuum model; PSO, paramagnetic spin orbital; RAS, restricted active space; RHF, restricted Hartree–Fock; RNA, ribonucleic acid; RPA, random phase approximation; RSPT, Rayleigh–Schrödinger perturbation theory; SCF, self consistent field; SCPT, self consistent perturbation theory; SD, spin dipolar; SOPPA, second order polarization propagator approximation; SOS, sum over states; TS, through-space; ZORA, zeroth-order regular approximation

1. INTRODUCTION

This work is an update of the previous two which appeared under the same title in this periodical series[1,2] and its main aims are similar to those of the previous two. The material covered in this work intends to be useful for both theoretically and experimentally oriented scientists. It covers selected papers published until the first days of May, 2003; if some important works were omitted the authors wish to apologize for that. In order to simplify the notation, whenever a spin–spin coupling constant, J(X, Y), is quoted without explicitly showing the isotopic species for the X and Y nuclei, it will be understood that they correspond to the respective spin-1/2 species with the largest natural abundance.

During the last five years there was an important renewed interest in spin–spin coupling constants as probes to study fine details of molecular electronic structures, especially in biological macromolecules.[3,4] One of the main reasons for this has been the notable improvement in experimental techniques that took place during the review period,[5–10] allowing experimentalists to accurately measure very small coupling constants in large compounds, specially those transmitted through a hydrogen-bond.[11–13] Also, during this period there has been an important increase in works reporting collaborations between experimentally and theoretically oriented scientists. The theoretical analysis of coupling constants has also received a renewed interest,[14] although many of the currently used approaches were presented previously; most of them were described in detail in the recent reviews by Helgaker *et al.*[15] and by Fukui.[16] These reviews contain detailed accounts of the fundamentals and applications of *ab initio* high level post-Hartree–Fock approaches used during this period. In this work care is taken to keep to a minimum the overlap with any of them as well as with the material presented in the series, Specialist Periodical Reports in NMR, published annually by the Royal Society of Chemistry.[17]

A point that must be highlighted is the significant increase in published papers where coupling constants are studied within the framework of the Density Functional Theory, DFT. Many results presented during this period using this approach are quite promising since medium-sized compounds can be studied with reasonable accuracy, even without resorting to special computing facilities. A further advantage of the recently reported DFT-based methods is that they include new methods to dissect coupling constants in bond contributions: two versions are the natural J coupling, NJC, approach[18,19] and the decomposition of J into orbital contributions using partial polarization, JOC-PSP.[20] These types of analyses can provide interesting physicochemical insight on how spin–spin couplings are affected by different types of interactions and, therefore, increase the usefulness of these parameters to study molecular problems. It also must be noted that Ziegler and co-workers have presented, during this review period, a relativistic DFT approach[21,22] to calculate spin–spin couplings and, therefore, the scope of DFT has broadened to include heavy atom containing molecules.

Non-relativistic calculation of spin–spin couplings are based on the four interactions between magnetic nuclei and electrons described by Ramsey, eqs. (1a–b)

$$H_{\text{DSO}} = \frac{\mu_0^2 e\hbar\mu_B}{(4\pi)^2} \sum_{A,B} \gamma_A\gamma_B \sum_k \frac{[(\mathbf{I}_A \cdot \mathbf{I}_B)(\mathbf{r}_{kA} \cdot \mathbf{r}_{kB}) - (\mathbf{I}_A \cdot \mathbf{r}_{kB})(\mathbf{I}_B \cdot \mathbf{r}_{kA})]}{r_{kA}^3 r_{kB}^3} \quad (1a)$$

$$H_{\text{PSO}} = \frac{\mu_0\hbar\mu_B}{2\pi i} \sum_A \gamma_A\mathbf{I}_A \cdot \sum_k \frac{(\mathbf{r}_{kA} \times \nabla_k)}{r_{kA}^3} \quad (1b)$$

$$H_{\text{SD}} = \frac{\mu_0 \hbar \mu_B}{2\pi} \sum_A \gamma_A \sum_k \left[\frac{3(\mathbf{S}_k \cdot \mathbf{r}_{kA})(\mathbf{I}_A \cdot \mathbf{r}_{kA})}{r_{kA}^5} - \frac{(\mathbf{S}_k \cdot \mathbf{I}_A)}{r_{kA}^3} \right] \tag{1c}$$

$$H_{\text{FC}} = \frac{4\mu_0 \hbar \mu_B}{3} \sum_A \gamma_A \sum_k \delta(\mathbf{r}_{kA}) \frac{(\mathbf{S}_k \cdot \mathbf{I}_A)}{r_{kA}^3} \tag{1d}$$

where, subscripts to H stand, respectively, for DSO: diamagnetic spin orbit; PSO: paramagnetic spin orbit; SD: spin dipolar; and FC: Fermi contact interactions.

It is interesting to note that recently Pyykkö published a short paper entitled 'Perspective on Norman Ramsey's theories of NMR chemical shifts and nuclear spin–spin couplings', where a concise and interesting account of the early development of the theory of high resolution NMR parameters is given.[23]

When the NMR measurements are carried out in an isotropic phase, the four (1a–1d) interactions define four isotropic contributions to the scalar coupling constant,

$$J_{M,N} = \left(\frac{1}{3}\right) Tr \mathbf{J}_{M,N} = J^{\text{DSO}}(M, N) + J^{\text{PSO}}(M, N) + J^{\text{SD}}(M, N) + J^{\text{FC}}(M, N) \tag{2}$$

while when measurements are carried out in an anisotropic phase, then interactions (1a–1d) also provide four contributions to the **J** second rank tensor,

$$\mathbf{J}_{M,N} = \mathbf{J}^{\text{DSO}}(M, N) + \mathbf{J}^{\text{PSO}}(M, N) + \mathbf{J}^{\text{SD}}(M, N) + \mathbf{J}^{\text{FC/SD}}(M, N). \tag{3}$$

Vaara *et al.*[24] have published a very important and exhaustive review on spin–spin coupling tensors determined either experimentally or by quantum chemical calculations. Among several other topics, comparisons of anisotropic contributions calculated with different approaches are given in this review.

All terms contributing to either $J_{M,N}$ or $\mathbf{J}_{M,N}$ are proportional to the magnetogyric ratio of both coupled nuclei, M and N. Since this is a nuclear property not associated with the molecular electronic structure, the reduced coupling constants, $K_{M,N}$ or $\mathbf{K}_{M,N}$ are often quoted instead of $J_{M,N}$ or $\mathbf{J}_{M,N}$, respectively. They are related by

$$K_{M,N} = 4\pi^2 \frac{J_{M,N}}{h\gamma_M \gamma_N} \tag{4}$$

High level calculations of the four terms of $J_{M,N}$ couplings generally provide in-depth insight into many aspects of the electronic molecular structure of the

compound under study. However, sometimes the enormous potential of spin–spin couplings to provide insight into subtle aspects of molecular electronic structures can be used more efficiently resorting to either partitions of calculated couplings or reasonably simplified approaches. This methodology has been widely employed within semi-empirical approaches[1] that even nowadays can provide useful insight to rationalize experimental results in polyatomic compounds where, at present, high level *ab initio* calculations are prohibitively expensive. Following this line of thought, Barfield *et al.*[25] complemented their DFT–FPT calculations of the FC term of *trans*-hydrogen bond couplings, $^{2h}J(N, N)$, $^{1h}J(N, H)$ and $^{1}J(N, H)$ in Hoogsteen–Watson–Crick T.A–T and C^{+}.G–C triplets with estimates from the well known delocalized MO model of Pople and Santry.[26,27] A similar analysis was also reported by Barfield *et al.*[28] when studying $J(H, H)$ couplings mainly transmitted through-space and when studying $^{4}J(H, H)$ couplings in propanic and allylic systems.[29]

   Proton–proton quantum exchange couplings. About 15 years ago a different mechanism for the indirect spin–spin coupling interaction was detected. A detailed account of this coupling mechanism was given in a review by Sabo–Etienne and Chaudret.[30] In order to keep the length of the present work within reasonable limits this subject will not be further considered since these couplings are important only in certain types of hydride complexes. Therefore, only a few references to interesting works on this topic, reported during this review period, are given here.[31] Limbach *et al.*[32] used the valence bond order concept to establish a correlation between the dihydrogen distance in dihydrogen/dihydride complexes and the $J(H, H)/J(D, H)/J(T, H)$ coupling constants in isotopomers of several complexes. Limbach and other co-authors[33] used similar concepts to study low barrier hydrogen bonds. Quantum exchange couplings in unsymmetrical trihydride osmium compounds were studied by Esteruelas *et al.*[34]

2. CALCULATION AND ANALYSIS OF SPIN–SPIN COUPLING CONSTANTS

2.1. HF and post-Hartree–Fock based methods

There has been only limited progress in this area. Hartree–Fock instabilities remain the largest obstacle for HF calculations of J couplings, forcing the use of electron correlated methods to obtain reliable results in most cases. Besides, it is now well known that electron correlation effects are very important when looking for quantitative agreement between calculated and experimental couplings. The need for electron-correlated methods greatly limits the size of molecules for which these calculations can be achieved successfully. Fortunately a great deal of progress has been made, using both

the non-relativistic and relativistic approaches of DFT-based methods. A more comprehensive discussion of the DFT calculations of J couplings is given in Section 2.2.

2.1.1. *Non-relativistic approaches*

Fukui has published one of the most comprehensive treatises[16] on the theory of nuclear spin–spin couplings. While the article presents a limited number of examples of calculated J couplings, it provides a comprehensive derivation of the Hartree–Fock theory of J couplings and several approaches to include electron correlation effects in the calculations. Fukui's review presents formulae to calculate J couplings using the MCSF, Møller–Plesset and Coupled Cluster methods. Interested readers should consult this work for finding the necessary theoretical background for the calculations of J couplings using high level *ab initio* methods that include electron correlation effects.

   Although *Hartree–Fock* instabilities have been very well known for many years, in the current literature there are references to this problem that, if not clarified, could be somewhat misleading. High resolution NMR spectroscopy is applied mostly to study closed-shell molecular systems since in most molecular systems containing an odd number of electrons the electronic magnetization masks the macroscopic nuclear magnetization whose changes are detected by NMR spectroscopy. For this reason, although not explicitly stated, it is assumed that the molecular system under study has a singlet ground state and therefore the wave function for the ground state is calculated imposing this restriction. However, to be able to apply the Rayleigh–Schrödinger perturbation theory, RSPT, to calculate any molecular property, the energy of the ground state must correspond to a minimum with respect to any 'variable' involved in the perturbative Hamiltonian. If this condition is not fulfilled it is theoretically unsound to apply RSPT, and the results provided by such a calculation are devoid of any physical meaning. It is well known that in many unsaturated compounds the *ab initio* Hartree–Fock approximation yields a singlet ground state whose energy is not a minimum if the closed-shell restriction is relaxed. When this condition holds it is said that such a molecular system presents 'Hartree–Fock instability of the non-singlet type'. Such a condition is important when calculating both the FC and SD terms since their perturbative Hamiltonians include the electron spin operator, eqs. (1c,1d). In general the calculated FC term seems to be proportionally more sensitive to such a condition than does the SD one. It is important to emphasize that in such a situation to apply RSPT using any of their equivalent implementations (finite perturbation theory, FPT,[35] either with a single[35,36] or a double perturbation,[37] coupled-perturbed Hartree–Fock, CPHF also called SCPT,[38] and random phase approximation, RPA[39]) may yield unreliable results. It is important to note that it is common usage in the

current literature to refer to these approximations as SCF (self consistent field) ones.

Frequently, in unsaturated compounds the Hartree–Fock non-singlet instability problem originates in the π-electronic system and in such a situation the calculated FC contribution transmitted through this electronic system shows a reversed sign, and in some instances, a very large absolute value. Closely related to a non-singlet instability condition is that dubbed as a 'quasi-instability condition';[40] in this case, if the quasi-instability condition originates in the π-electronic system, extremely large values of the calculated FC term transmitted through that system are predicted although their sign is correctly reproduced. Some years ago[41] there were attempts to get at least a semi-quantitative criterion to determine when the quasi-instability condition is present. It was based on the polarization propagator approach calculated at the RPA level.[39] In unsaturated compounds when one of the polarization propagator eigenvalues is close to zero but positive, then the ground state wave function presents a non-singlet quasi-unstable condition. The closer to zero such an eigenvalue is, the more overvalued the FC π-transmitted component is. If one of the polarization propagator eigenvalues is negative, then the corresponding wave function presents a non-singlet unstable condition and the resulting FC π-transmitted component is also calculated with the wrong sign. If the negative eigenvalue is close to zero, then the absolute value of the FC π-component is also notably overvalued. Very recently a paper was published where a brief account is given of difficulties associated with the spin–spin coupling calculation when a non-singlet instability condition is present.[42] It is important to recall that DFT calculations of spin–spin couplings represent a significant improvement on restricted Hartree–Fock theory in the sense that no non-singlet instability problems have been found in DFT.[43]

As a consequence of the HF instabilities discussed above, the largest body of non-relativistic calculations of J couplings published in recent years has used electron correlated methods. In particular the EOM–CCSD[44] and LR–MCSCF[15] methods, the former as it is implemented in the ACES II program[45] and the latter as it is implemented in the Dalton program[46] have become the most common tools to calculate J couplings using *ab initio* methods. It is noteworthy to mention the use of the former in the extensive work reported by Del Bene *et al.* in the study of coupling constants transmitted through hydrogen bonds, and the latter for the study of analogous problems by Pecul *et al.*, and by Wasylishen *et al.* to study the **J** coupling tensor. Such applications are described elsewhere in this review.

Several studies have been published reporting the convergence properties of J coupling calculations involving different approaches.[47–51] The convergence properties, with both the basis set and the number and type of configurations included in the calculations, have been extensively reported for MCSCF J coupling calculations. Lantto and Vaara[52] studied the effects of the core

valence correlations on the $^1J(X, H)$ and $^2J(H, H)$ couplings of first and second row hydrides, finding that including core orbitals in the calculations is important for $^1J(X, H)$, but play a minor role for $^2J(H, H)$. Jaszuński and Ruud[53] provided extensive results on the convergence properties of the J couplings in acetylene with both the basis set and the CI expansion. The very large basis sets used in this study ensure that the results are near the basis-set limit. The same research group continued their study of spin–spin couplings carrying out MCSCF calculations in hydrogen fluoride,[54] water[55] and ethylene.[56] For H_2O they also calculated rovibrational corrections from a spin–spin coupling surface fitted up to quartic order. In all cases these authors report excellent agreement between their calculated and the respective experimental values, but only for HF the calculated values are within the experimental error of the measurements. In all these papers they also presented an interesting comparison between their calculated coupling constants and other values, taken from the literature, and calculated with different approaches. Gauss *et al.*[57] performed full configuration interaction calculations of $^1J(^{11}B, H)$ in BH and they demonstrated that unrelaxed Coupled Cluster, CC, calculations provide excellent results specially when triple excitation effects are included via the full CCSDT. The theoretical estimate given by Gauss *et al.* for $^1J(^{11}B, H)$ is $+50.67$ Hz. The effect of triple excitations in CC calculation of couplings was also discussed by Auer and Gauss.[58]

2.1.2. *Relativistic approaches*

The largest number of J coupling calculations including relativistic effects has been done using DFT within the ZORA approximation,[59] these calculations are discussed in Section 2.2.2. The complete four component theory for J couplings has been published several years ago by Aucar and Oddershede,[60] but its implementation has been somehow slow. There have been only a few applications of this theory in recent years. Visscher *et al.* have used this formulation to calculate the anisotropy of **J** coupling tensors and the respective isotropic J couplings in hydrogen halides[61] and Enevoldsen *et al.*[62] reported calculations in MH_4 (M=C, Si, Ge, Sn, Pb) and $Pb(CH_3)_3H$. In both cases the calculations were carried out at the RPA level using the Dirac–Coulomb Hamiltonian. Kirpekar and Sauer[63] performed non-relativistic calculations of all terms of scalar couplings in PbH_4 and included the one-electron part of the spin–orbit correction, FC–PSO. Calculations of the non-relativistic terms were performed at different levels, i.e, RPA, multi-configurational linear response, SOPPA and SPPA(CCSD). The spin–orbit corrections were calculated at the RPA level. The $^1J(Pb, H)$ coupling is dominated by the FC term and the inclusion of electron correlation effects does not alter this trend, but it is interesting to quote that the inclusion of such effects causes the SD term to change its sign. At the RPA level the one-electron

FC–PSO cross term amounts to about 10% of the FC term. In the same paper the effects of nuclear motion were investigated by calculating the coupling constants as a function of the totally symmetric stretching coordinate. Vaara *et al.*[64] performed calculations of spin–orbit interaction effects on spin–spin couplings where the FC–PSO and FC–SD contributions and one- and two-electron terms were considered. They studied the $^1\mathbf{J}(X, H)$ and $^2\mathbf{J}(H, H)$ coupling tensors in XH_2 (X=O, S, Se, Te) and XH (X=F, Cl, Br, I). The non-relativistic values were calculated both within the SCF and MCSCF approaches. For the $^2\mathbf{J}(H, H)$ tensors in XH_2 Vaara *et al.* also calculated contributions originating in second order induced contributions owing to the magnetic field dependence of the spin–orbit Hamiltonian.

Romero and Aucar[65] have presented a Quantum Electro Dynamics, QED, theory of J couplings, this new theory reduces to the relativistic and classical formulations when appropriate limits are taken, but because the authors did not perform any calculations using this new formulation, it is difficult to assess the impact that it may have in practical applications.

2.2. DFT-based methods

2.2.1. *Non-relativistic approaches*

One of the most important, pioneering works for calculating spin–spin coupling constants within the DFT framework was published by Malkin, Malkina *et al.*[66–69] Their approach is frequently employed in the current literature to calculate coupling constants in medium sized molecules obtaining a reasonable accuracy.[70–73] Malkin's method takes into account only three of the four terms that contribute to the isotropic couplings, namely the FC, the PSO and DSO contributions, while the SD contribution is neglected.

The PSO term is calculated in this approach using the SOS formalism. In the zero order SOS approximation of Malkina *et al.*, the difference between the ground state energy and the excited state energy in the SOS expression is approximated by the one-electron orbital energy difference between the highest occupied MO and the lowest virtual MO. This approximation can be improved by including an additional exchange correction; this procedure is dubbed the Loc.1 approximation in the current bibliography. As a result, in both frameworks SOS and SOS Loc.1, they obtain a set of uncoupled equations where the electron–electron response is either neglected or only partially included. These approximations are adequate when performing calculations of the PSO term using non-hybrid exchange correlation functionals because the PSO operator involves only a change in the electronic current density induced by the nuclear magnetic moments. However, in the case of hybrid

functionals (like the popular B3LYP) the electron–electron response includes an amount of the HF exchange response, and then the SOS approximation does not yield the linear response of the electronic system. In this way, as also happens within the Hartree–Fock methodology,[74] the SOS formalism constitutes a lower level of approximation than the Coupled Perturbed–Kohn Sham, CP–KS, one.

In most DFT coupling calculations the FC contribution is calculated using the finite perturbation theory, FPT, using either a single[36] or a double perturbation[75,76] scheme, although in some instances[77] it is calculated using the sum-over-states, SOS, formalism. During the last few years the CP–KS methodology became the most frequently used to calculate the FC term.[43,78,79] In the last of these papers the computational efficiency of the single FPT and CP–KS approaches are compared in a set of coupling constants.

The fundamentals of the CP–KS approach to evaluate spin–spin couplings were clearly delineated in a recent paper by Sychrovský *et al.*[78] where an interesting comparison of PSO terms calculated in some small molecules within the SOS and CP–DFT approximations is presented. On the other hand, they also presented CP–KS calculations of the FC and SD terms. Thus, these authors[78] for the first time presented the calculations of all four terms of scalar couplings within the DFT framework. Shortly afterwards Helgaker *et al.*[43] also reported calculations of the four terms of scalar couplings (FC, SD and PSO calculated within the CP–KS approach) using a modified version of the Dalton program,[46] and recently, Helgaker with other co-authors[80] reported the DFT calculations of all anisotropic terms of spin–spin couplings and compared the results thus obtained with high level *ab initio* calculations at the LR–MCSCF level. Barone *et al.*[79] reported DFT calculations of all four isotropic terms of spin–spin couplings using an *ad hoc* modified version of the Gaussian98 program.[81] Within this method the FC term can be calculated either within the single FPT or the CP–KS approaches; results obtained within both perturbative approaches are compared and for all practical purposes both yield the same numerical values.[79] The SD term is calculated within the FPT approach and the PSO term is calculated within the CP–KS perturbation scheme. This *ad hoc* modified version of the Gaussian98 suite of programs can be used to decompose either the FC[18] or the PSO[82] terms into bond contributions. For the FC term this partition can be carried out either within the FPT or the CP–KP schemes. These partitions were dubbed the 'natural J coupling dissection', NJC. This dissection of the FC term was also combined with the 'deletion procedure' of the NBO method[83] to study, in an approximate way, the influence of some electron delocalization interactions on the different NJC contributions.[84] This procedure was dubbed 'neglect of charge transfer interactions', NCTI, since it somewhat resembles Barfield's 'neglect of non-bonded interactions', NNBI approach.[85]

In Peralta *et al*.'s[18,82] method the NJC decomposition into localized molecular orbitals procedure is as follows. Given a perturbative Hamiltonian A, A being either the FC or PSO operators, the corresponding J coupling term can be obtained as

$$J_{NM}^{A} = \gamma_N \gamma_M \frac{\hbar}{2\pi} \frac{1}{3} \mathrm{Tr}\left(\mathbf{P}_N^{1,A} \mathbf{h}_M^A\right) \tag{5}$$

where $\mathbf{P}_N^{1,A}$ stands for the first order density matrix obtained through the CP (or either the FPT scheme for the FC term) procedure after the perturbation A is introduced. Since the matrix representation of the perturbative Hamiltonian is usually expressed in terms of atomic orbitals (AO), it is common to perform this calculation in the AO base. However, when intending to separate the J couplings into localized molecular orbital contributions, a transformation from the AO base to the LMO base is necessary. Utilizing an alternative expression for the trace of the $\mathbf{P}_N^{1,\,A} \mathbf{h}_M^A$ product, the following equation is obtained

$$J_{NM}^{\mathrm{PSO}} = \gamma_N \gamma_M \frac{\hbar}{2\pi} \frac{1}{3} \sum_{ij} a_{ij} = \gamma_N \gamma_M \frac{\hbar}{2\pi} \frac{1}{3} \left\{ \sum_{i\,occ} \left(\sum_{j\,occ} a_{ij} + 2 \sum_{j\,vac} a_{ij} \right) + \sum_{\substack{i\,vacj \\ j\,vac}} a_{ij} \right\} \tag{6}$$

where $a_{ij} = (\tilde{\mathbf{P}}_N^{1,A})_{ij} (\tilde{\mathbf{h}}_M^A)_{ij}$, i.e., the product of the transformed first order density matrix and the transformed perturbative Hamiltonian. Eq. (6) represents Peralta *et al*.'s NJC decomposition and is usually presented in the NLMO base, with integer occupation numbers for each LMO. Weinhold *et al*.[19] reported a similar dissection for the FC term calculated within the FPT scheme. This decomposition is given both in terms of the NLMOs (in the same way as it was given by Peralta *et al*.) and also in terms of the NBOs. This last approach aims at distinguishing between contributions originating from a formal Lewis localized structure and from non-lewis contributions. Cremer *et al*.[20] has recently presented a new approach to decompose all four terms of scalar couplings into localized orbitals, JOC–PSP. They made a detailed comparison between both NJC approaches and that of the JOC–PSP.

Since the Tomassi *et al*.[86,87] Polarizable Continuum Model, PCM, to describe dielectric solvent effects is implemented within the Gaussian98[81] suite of programs, Peralta and Barone's modified version of the Gaussian98 suite of programs can be used to calculate solvent effects on the FC, SD and DSO terms (however for the FC term the perturbative FPT approach should be used if solvent effects are to be calculated).

Some authors claim that DFT based methods to calculate coupling constants are not adequate to deal with NMR couplings involving a lone-pair

Table 1.   Comparison between calculated MCSCF[a], DFT[b] and experimental[a] J(C, F), J(H, F) and J(F, F) couplings (in Hz) in *para*-difluorobenzene[c]

$^nJ(X,Y)$	Method	FC	SD	PSO	DSO	Total	Exp.
$^1J(C, F)$	MCSCF	−210.7	11.3	13.8	0.9	−184.7	−242.61
	DFT	−321.5	5.9	−4.3	0.9	−319.0	
$^2J(C, F)$	MCSCF	50.1	3.8	−11.3	−0.1	42.5	24.29
	DFT	32.51	3.7	−14.8	−0.1	21.3	
$^3J(C, F)$	MCSCF	6.6	−2.3	−0.5	−0.3	3.5	8.18
	DFT	8.4	−1.9	0.0	−0.3	6.2	
$^4J(C, F)$	MCSCF	4.6	4.2	−1.2	−0.2	7.4	2.67
	DFT	0.9	5.2	−1.7	−0.2	4.2	
$^3J(H, F)$	MCSCF	3.3	−0.9	−1.3	−0.1	1.0	7.905
	DFT	11.2	−0.9	−2.3	−0.1	7.9	
$^4J(H, F)$	MCSCF	7.0	−0.1	1.2	−1.3	6.8	4.122
	DFT	4.3	−0.2	1.1	−1.3	3.9	
$^5J(F, F)$	MCSCF	11.2	10.8	0.7	−1.0	22.7	17.445
	DFT	8.3	15.0	−1.1	−1.1	21.1	

[a] Taken from Ref. 89.
[b] Ref. 175 calculated at the DFT-B3LYP/aug-cc-pVTZ-J level.
[c] All values are in Hz.

bearing atom.[69] However, a perusal of the current literature suggests that this assertion should be taken with some caution since in several works DFT calculated couplings involving at least one lone-pair bearing atom were reported and their general agreement with the experimental values is very satisfactory.[88] As an example, in Table 1 the J(C, F), J(H, F) and J(F, F) couplings in *para*-difluorobenzene calculated[89] with an MCSCF[46] approach are compared with those calculated with the hybrid B3LYP[90–92] functional, which appears to be the best one to calculate NMR coupling constants.[43,78,93] Recently, other J(F, F) couplings calculated within the DFT approach were reported in a few aromatic compounds and very good agreement with experimental values was also achieved.[79,94] There are also several works where couplings transmitted through a hydrogen bond are studied using approaches based on DFT and their results are quite promising.[25,88,95] Nonetheless, there are some difficult cases for the DFT calculation of coupling constants but they seem to be not typical of the pair of coupled nuclei but of certain configurations of the coupling pathway. For instance, difficult cases for the DFT calculation are $^{1h}J(F, H)$ and $^{2h}J(F, F)$ couplings in complexes $[F(HF)_n]^-$;[96] $^1J(F, H)$ in FH, $^1J(F, C)$ in for instance, FCH_3, and $^2J(F, F)$ when both fluorine atoms are bonded to an sp^2 carbon atom.[82] But, the calculation of some of these couplings seems to be a challenging task even for high level *ab initio* approaches.[82] The $^2J(F, F)$ couplings where the F atoms are bonded to an sp^3 hybridized carbon atom seem to work somewhat better (see Table 2).

Table 2. Comparison between calculated $^2J(F, F)$ couplings in $CH_2F_2{}^a$, $CHF_3{}^a$ and $CHF_2OH{}^a$. An electronegative atom placed α to C_i causes a very large decrease in $^2J(F, F)$ which originates mainly in the PSO and SD terms

Molecule	DSO	PSO	SD	FC	Total
$CH_2F_2{}^b$	−1.1	132.7	74.5	140.0	346.1
$CH_2F_2{}^c$	−1.1	134.4	73.7	111.4	318.4
$CH_2F_2{}^d$	−1.1	134.6	89.2	113.4	336.1
$CHF_3{}^b$	−0.8	−13.4	40.6	125.9	152.3
$CHF_3{}^c$	−0.9	−13.1	41.6	96.6	124.2
$CHF_3{}^d$	−0.9	−22.4	47.6	33.9	58.2
$CHF_2OH{}^c$	−0.8	−16.6	45.5	113.4	141.5
$CHF_2OH{}^d$	−0.7	−23.7	52.6	53.6	81.8

[a] Geometry optimizations obtained at the MP2/cc-pVTZ level.
[b] Taken from Ref. 374.
[c] SOPPA / aug-ccPVTZ-J.
[d] DFT-B3LYP/ aug-ccPVTZ-J.

Patchkovskii et al.[97] analyzed the effect of the self-interaction correction on the calculation of spin–spin couplings in the DFT framework. When introducing such a correction, they observed an overall worsening of the total calculated coupling due to an exaggerated change in the FC term. However, the PSO contribution seems to achieve an important improvement, suggesting that self-interaction corrections could be important in molecules where this last contribution is dominant.

Recently, Pecul and Helgaker[98] carried out a comparison between DFT, MCSCF and CCSD calculated and experimental couplings for benchmarking the performance of DFT as compared with high level *ab initio* methods. Ethane, methanol and methylamine were chosen as model systems to carry out this comparison, which includes one-bond $J(C, H)$, $J(C, C)$, $J(N, H)$, $J(CN)$, $J(O, H)$ and $J(C, O)$, two-bond $J(H, H)$ and $J(C, H)$ and three-bond $J(H, H)$ couplings. In this last case, the dihedral angle dependence as given by these three methods and experimental values are also compared. In all these calculations the four isotropic contributions were included, being the DFT results obtained with the Helgaker et al.[43] implementation.

2.2.2. Relativistic approaches

As commented above, DFT has proven to be a powerful tool to predict NMR spin–spin couplings in medium and large molecules containing light atoms.[24] This fact motivated Autschbach and Ziegler[21,22] to implement the calculation of NMR spin–spin couplings using the zeroth-order regular approximation (ZORA) formalism. Within this framework, the perturbed

Hamiltonians that are needed to deal with coupling constants are: the ZORA–DSO,

$$h_{ij}^{\text{ZDSO}}(A, B) = \frac{K}{c^4} \frac{\delta_{ij}(\mathbf{r}_A \cdot \mathbf{r}_B) - r_{Ai}r_{Bj}}{r_A^3 r_B^3}, \tag{7}$$

corresponding to the relativistic analogue of the DSO Hamiltonian; the ZORA–PSO,

$$h_j^{\text{ZPSO}}(A) = \frac{K}{2ic^2 r_A^3}(\mathbf{r}_A \times \nabla)_j + (\mathbf{r}_A \times \nabla)_j \frac{K}{2ic^2 r_A^3}, \tag{8}$$

which, in the non-relativistic limit, gives place to the PSO operator, and the ZORA–SO,

$$h_j^{\text{ZSO}}(A) = \frac{4\pi K}{3c^2}\sigma_j\delta(\mathbf{r}_A) + \frac{K}{2c^2}\left(\frac{2(\boldsymbol{\sigma} \cdot \mathbf{r}_A)r_{Aj}}{r_{Aj}^5} - \frac{\sigma_j}{r_{Aj}^3}\right)$$
$$+ \frac{1}{2c^2 r_A^3}\big[\{(\nabla K) \cdot \mathbf{r}_A\}\sigma_j - (\nabla_j K)(\boldsymbol{\sigma} \cdot \mathbf{r}_A)\big]. \tag{9}$$

This last operator yields, in the non-relativistic limit, the FC and SD perturbative Hamiltonians. In Eqs. (7)–(9), $K = 2c^2(2c^2 - V)^{-1}$ is the kinematic factor arising from the ZORA formalism and $\boldsymbol{\sigma}$ are the Pauli matrices. The implementation of this method was done in the Amsterdam density functional (ADF) package[99] using Slater-type functions as a basis set. The linear response of the Kohn–Sham equations is calculated by means of first-order coupled (or uncoupled, in the case of the ZPSO Hamiltonian) perturbed Kohn–Sham equations. Scalar relativistic spin–spin couplings reported in Ref. 21 omit the contributions to eq. (9) that arise from the mixing of orbitals of different spins. This simplification is supported by the fact that in the non-relativistic case, the SD term usually yields to a very small contribution to the total isotropic coupling. But, as has been pointed out for difluorobenzenes,[100] and for J(F, F) couplings involving other configurations of the coupling pathways[79,82] this is not the general case. Several examples of scalar ZORA spin–spin couplings corresponding to one-bond Hg–C are shown in Table 3, where the improvements from the relativistic corrections are apparent.

In a subsequent work[22] Autschbach and Ziegler incorporated the ZORA SD and the SO contributions in a two-component fashion, allowing the mixing of spin and orbital magnetic perturbations. As a consequence, two new contributions to the total scalar coupling take place, namely, the ZSD and the cross terms ZFC+ZSD and ZPSO. It is interesting to compare the performance of the GGA computations employing non-relativistic, scalar relativistic and

Table 3. Non-relativistic and Scalar ZORA Hg-C spin–spin couplings (in Hz) calculated at the GGA level.[a] Experimental values are also shown, taken from the same paper

Molecule	Non-relat.	Scalar ZORA	Exp.
$HgMe_2$	331	450	700
HgMeCl	689	1063	1430
HgMeBr	702	1075	1393
HgMeI	681	993	1301
$Hg(CN)_2$	1232	2396	3141
$[Hg(CN)_4]^{2-}$	590	1571	1540

[a] Taken from Ref. 21.

Table 4. Non-relativistic, scalar and spin–orbit ZORA calculated in Tl–X (X = F, Cl, Br and I). Spin–spin couplings (in Hz) calculated at the GGA level.[a] Experimental values are also shown.

	TlF	TlCl	TlBr	TlI
Non-relat.	−798	−92	−415	−409
Scalar ZORA	−921	−89	−251	−163
SO ZORA	−1349	−151	−602	−542
Exp.[b]	−1340	−155	−689	−673

[a] Ref. 22.
[b] Ref. 112.

spin–orbit relativistic approximations. Values obtained using these approaches for the TlX (X = F, Cl, Br and I) compounds, where strong spin–orbit effects are expected, are displayed in Table 4. Along this series of thallium halides, the SO–ZORA method correctly reproduces the experimental trend, but only a fair agreement is obtained for the heaviest two members of the series.

It should be remarked that this is the first practical implementation of the calculation of spin–spin couplings involving heavy atoms applicable to medium sized molecular systems. Formerly, Khandogin and Ziegler[101] developed a frozen core scalar relativistic approach in combination with the non-relativistic FC and PSO operators, but the quality of results thus obtained is poorer than those obtained with ZORA.

Bryce and Wasylishen[102] calculated the reduced coupling tensors of fluorine-, chlorine-, bromine-, iodine- and xenon-containing molecules representing a wide variety of geometrical bonding arrangements. They found periodic trends in the one-bond reduced isotropic couplings for isovalent and isostructural molecules. They also found an excellent agreement with experimental values, ascribed mainly to the use of reliable molecular structures and the inclusion of both scalar and spin–orbit effects in their

calculations. Interestingly, Bryce and Wasylishen[102] found that the isotropic ZPSO contribution correlates with the number of electron lone pairs on the central heavy atom. Also, the contribution of the ZORA FC+SD term was found to increase linearly with the separation between the central heavy atom and the fluorine involved in the coupling for a given series of compounds.

Bagno and Saielli[103] reported spin–spin coupling constants J(Xe, F), J(Xe, N), J(Xe, O), J(Xe, Cl) and J(Xe, Xe) in covalent compounds and weakly bound complexes employing the DFT spin–orbit ZORA method. Autschbach and Ziegler[104] investigated solvent effects on heavy atom spin–spin coupling constants of the type $^1J(Hg, C)$ and $^1J(Pt, P)$ by taking explicitly into account the coordination of the heavy atom with solvent molecules. Their findings in HgX (X = Me$_2$, MeCl, MeBr, MeI, (CN)$_2$), and *cis-* and *trans-*PtX$_2$Y$_2$ (X = PMe; Y = H, Cl) show that the most important corrections to the non-relativistic, unsolvated calculations correspond to the change of the FC term due to scalar relativistic and solvent effects, whereas spin–orbit effects and the influence of the ZORA SD term are fairly small. Another interesting application using the same approach to take solvent effects into account within the SO–ZORA formalism was presented in the calculation of the spin–spin couplings in [(NC)$_5$Pt–Tl(CN)]$^-$.[105]

An extensive study of spin–spin coupling tensors in a series of diatomic halogen molecules has been carried out by Bryce and co-workers[106] using the ZORA–DFT approach. The same method was applied by Bryce and Wasylishen[107] to analyze $^1J(Ag, C)$ in silver cyanide in the solid phase. An explanation of the large difference between $^1J(Pt, Pt)$ in [Pt$_2$(CO)$_6$]$^{2+}$ and [Pt$_2$(CO)$_2$Cl$_4$]$^{2-}$ in terms of contributions from localized orbitals is given by Autschbach *et al.*[108] The same authors[109] also analyzed the large $^1J(Hg, Hg)$ spin–spin coupling observed in Hg$_2^{2+}$ and Hg$_3^{2+}$, including (explicitly in the ZORA calculation) the surrounding ligands, solvent molecules and counter ions. They found that calculations on the bare ion Hg$_2^{2+}$ can amount to ~900 kHz, while the effect of the medium decreases this value, suggesting that a system based on Hg$_2^{2+}$ could potentially present $^1J(Hg, Hg)$ couplings of about 500 kHz or higher.

2.3. The Spin–Spin Coupling Tensor

Jokisaari's group have continued their work on anisotropies of **J** couplings using both experimental and theoretical approaches. The experiments have been done using liquid crystals as solvents and the calculations were carried out using the MCSCF method implemented in the DALTON program system.[46] Studies were reported in *p*-difluoro benzene, fluoromethanes and methylsilane.[89] The combined use of theory and experiment resolves many of the experimental ambiguities found in NMR when using liquid crystals as solvents.

These calculations using highly correlated *ab initio* methods are important because they show that several of the coupling mechanisms can make significant contributions to the anisotropy of **J** couplings.

Several new developments leading to an understanding of the anisotropy of **J** coupling tensors have been reported by Wasylishen's group. In one of the papers of this series[110] they reported the first complete calculation of the symmetric and antisymmetric components of the **J** tensor using *ab initio* methods. Taking ClF_3 and OF_2 as the model compounds and using the MCSCF method implemented in the DALTON program[46] the authors show that the calculated **J** tensors in these compounds follow the symmetry rules given by Buckingham,[111] relating local symmetry with the number of unique **J** tensor elements. Unfortunately, there is no experimental evidence to compare the calculated antisymmetric components with their experimental counterparts.

Another important piece of work from this group[112] presents a comprehensive study of the anisotropy of the **J** couplings in a series of diatomic molecules. These authors also made use of the relationship between hyperfine constants, C_3, and the anisotropy of the **J** tensor in LiH, LiF, KF, Na_2 and ClF to demonstrate that their calculations can reproduce the full **J** tensor well. This justifies applying such an approach to a larger set of diatomic molecules. It is noteworthy to mention that this relationship between the C_3 coefficient in the hyperfine constant and the anisotropy of the **J** tensor has not been used routinely when studying the anisotropy of the **J** tensor. Perhaps this is due to the need to perform a careful rovibrational analysis to extract the anisotropy of the **J** tensor from the C_3 coefficient. While the results reported in this paper are significant, they are limited to molecules with light elements, because of the difficulties in applying MCSCF methods to molecules containing heavy atoms, for which very large basis sets and relativistic corrections are needed. These problems have been overcome by the same research group using the ZORA–DFT approach,[21,22] quoted above, to calculate the anisotropies of the interhalogen **J** couplings in halogenated compounds[106] and Xenon and group 17 fluorides.[102] These are the first studies that provide any information on the behaviour of the anisotropy of the **J** couplings along the periodic table. Not unexpectedly, the authors found that the anisotropy of the reduced coupling $\Delta \mathbf{K}$, which is negative in these compounds, linearly increases in magnitude with the product of the atomic numbers of the coupled nuclei. It is remarkable that the linear coefficient for $\Delta \mathbf{K}$, -0.3674×10^{20} N Å^{-2} m^{-3} is almost the same, in magnitude, as the coefficient for the reduced constant K, 0.3669×10^{20} N Å^{-2} m^{-3}. In tetramethyldiphosphine disulphide Wasylishen *et al.*[113] determined an experimental upper limit for $\Delta^1 \mathbf{J}(P, P)$ of about 450 Hz. For a detailed account of experimental and theoretical calculations of the anisotropy of the **J** tensor readers are referred to the recent Vaara *et al.*[24] review paper.

3. COUPLING MECHANISMS AND FACTORS
AFFECTING THEM

Experimentally in an isotropic phase and without any partial orientation of the solute molecules, it is only possible to observe the average value or trace of the second rank **J** tensor. In the current literature this quantity is commonly referred to as 'the scalar coupling', which is a somewhat misleading expression. Obviously, it would be more correct to call it 'the isotropic coupling' as can be seen in several papers; however to follow the common usage in this work these expressions will be used indistinctly.

Although the scalar couplings have contributions from the four Ramsey interactions, PSO, DSO, SD and FC, experimentally only the total value is amenable to measurement. The relative importance of each of these four terms cannot be verified directly by experiment. If the role played by each of these terms in building up any coupling constant could be assessed, then the potential of these couplings for studying molecular problems could be notably broadened. With the rapid increase in reliably of the calculated couplings that took place in recent years, some trends emerge when a comprehensive evaluation of data accessible in the current literature is made. However, some caution should be taken to extrapolate such trends ascribing to them an unjustified generality.

Sometimes it is assumed that the FC term is by far the dominating contribution to any coupling constant, at least in cases involving light atoms, up to the B to Ne row in the Periodical Table. For couplings involving H, C and/or N nuclei in saturated compounds this assertion seems generally to hold although there could be important exceptions, e.g., $^1J(N, N)$ in N_2. For couplings involving two fluorine atoms both the PSO and SD terms can be notably more important than the FC term even in saturated compounds e.g., $^2J(F, F)$ couplings.[79]

Frequently it is found in the literature that in couplings involving H and C or N nuclei contibutions from the DSO and PSO terms almost cancel each other. Although there are many examples where this assertion holds, it is by no means a general property. There are many examples where it is known that both the PSO and DSO terms are of the same sign; a few examples are quoted below. The main features of the coupling pathway for the DSO term are, after the FC one, the best understood. This is so much so, that just by inspection it can be easily predicted if, for a given configuration of the coupled nuclei, its contribution should be important or not and if it is expected to be positive or negative. Such an estimation can be obtained remembering that the space spanned by electrons in a molecule can be partitioned into two regions.[114] For two coupled nuclei, A and B, a sphere of diameter A–B can be defined. The electrons inside such a sphere yield a negative contribution to $K^{DSO}(A, B)$, while the electrons outside the sphere yield a positive contribution. For instance in cubane a negative DSO

term dominates the $^4J(C, H)$ and $^5J(H, H)$ couplings;[115] in acetylene the calculated DSO contribution to $^3J(H, H)$ is -3.59 Hz;[53] in ethane for the 180° dihedral angle conformation, the DSO term of $^3J(H, H)$ was calculated as -3.13 Hz.[116] In bicyclo[1.1.1]pentane the DSO contribution to $^4J(H, H)$ coupling, -2.40 Hz, was taken some time ago as an example of this trend.[117] Recently, Krivdin,[118] using *ab initio* ground state wave functions, calculated J(H,H) couplings between bridgehead protons and found that along the series bicyclo[1.1.1]pentane, bicyclo[2.1.1]hexane, bicyclo[2.2.1]heptane and bicyclo[2.2.2]octane, the respective DSO contributions to such couplings are -2.68; -2.35; -2.12 and -1.98 Hz. This trend also reflects the expected decrease when increasing the inter-nuclear distance of the DSO interaction. It should also be recalled that the DSO term is notably insensitive to the basis set employed in its calculation.[119] Two examples of couplings where the DSO and PSO terms are of like sign are $^1J(N, H)$ and $^2J(N, H)$ in methanimine and related compounds.[42]

It is often assumed that the stereochemical dependence of all coupling constants is defined by the behaviour of the FC term. However, now it is known that, for instance, for $^3J(F, F)$ couplings through an ethanic fragment, F–C–C–F, all four Ramsey terms strongly depend on the dihedral angle defined by the coupling pathway.[120] Although the relative importance of the DSO term is much smaller than those of the PSO, SD and FC terms. Other known examples where the stereochemical dependence of non-contact terms define the experimental trend is the $^4J(F, F)$ coupling in bridge-fluorinated bicyclo[1.1.1]pentanedicarbolylates.[121]

In unsaturated compounds J(C, C) couplings could have significant PSO and SD contributions, although the FC is still the most important one. A case in point is the comparison of the different contributions to the $^1J(C_4, C_5)$ coupling for 2-OH-pyridine when calculations are carried out using the 2-OH-pyridine and 1H,2-pyridone optimized structures,[122] Table 5. For the first tautomer the $C_4 = C_5$ bond corresponds to an aromatic bond, while for the second, it corresponds to a formal single bond, although it undergoes a strong conjugative interaction. While changes in the SD and PSO term are

Table 5. Influence of the double bond character on the FC and PSO terms (in Hz) of the $^1J(C_4,C_5)$ coupling in 2-OH-pyridine and in 1H,2-pyridone[a]

	FC	PSO	SD	DSO	Total	Exp.
$^1J(C_4,C_5)^b$	63.9	−6.9	0.9	0.2	58.3	51.7
$^1J(C_4,C_5)^c$	54.3	−4.6	0.6	0.3	50.6	

[a] Calculated and Experimental values taken from Ref.122.
[b] Calculated values using the 2-OH-pyridine optimized structure.
[c] Calculated values using the 1H,2-pyridone optimized structure.

in percentage terms important, they are too small to affect the total coupling. It is observed that the PSO term is negative and its absolute value decreases when decreasing the $C_4=C_5$ double bond character. As expected, the FC term decreases markedly when decreasing the $C_4=C_5$ double bond character. Although both effects tend to cancel each other, the FC trend is more important than that of the PSO term. The better agreement between the calculated and the experimental value obtained when using the pyridone structure for the calculation is consistent with the well known fact that in solution the tautomeric equilibrium favours the -one structure.[123]

Soncini and Lazzeretti[124,125] succeeded in providing important insight into the transmission mechanisms of the FC, SD and PSO+DSO terms. To this end, they studied molecular response properties via perturbed density functions, i.e., a given property is defined as a three-dimensional integral involving these density functions to first-order. In the case of the four Ramsey terms of spin–spin couplings they are taken as three-dimensional integrals involving the first-order current densities induced by nuclear magnetic moments.[126] Among the main conclusions of Soncini and Lazzeretti's studies are those about the transmission mechanisms of spin–spin couplings. The FC term is transmitted through the Fermi correlation interactions; a similar assertion seems to hold for the SD term, while the main feature of the transmission mechanism of the PSO term is the conservation of the electronic angular momentum. Bader *et al.*[127] have arrived at similar conclusions, i.e., the delocalization of the Fermi hole between the coupled nuclei is the mechanism whereby the spin perturbation caused by the magnetic interaction of an electron with one of the coupled nuclei is transmitted to the second one. Such observations about the FC transmission mechanism are further evidence that *trans*-hydrogen bond couplings cannot be taken as evidence of any degree of covalence for that bond (see below).

New perspectives are visualised for notably enhancing the possibility of understanding relationships between coupling constants and subtle aspects of molecular electronic structures. In fact, at the end of this review period, Cremer *et al.*[20] presented a new approach to deconvolute each term of the isotropic couplings in localized molecular orbital contributions. The three second order terms of such couplings are calculated within the CP–KS perturbative formalism and it can be applied in a restricted manner in such a way that only a sub-set of LMOs are allowed to be perturbed by the presence of a nuclear magnetic moment. This method is dubbed JOC–PSP (decomposition of J into orbital contributions using partial spin polarization) and the first applications to study transmission mechanisms of couplings will soon be published.[128] Another interesting application of the JOC–PSP method published by Wu and Cremer[129] is the analysis of multipath transmission of scalar couplings in cyclic compounds.

3.1. Intra- and intermolecular interaction effects on spin–spin coupling constants

3.1.1. *Proximity effects*

There is no general agreement among different authors about how to designate couplings between nuclei belonging to two different moieties which are proximate in space but they are separated by a considerable number of formal bonds.[130] As mentioned in other sections, notations used in this work intend to follow the common usage found frequently in the current literature. When two molecular fragments are close in space, the spin information associated to a given coupling can be transmitted between them.[131] In particular, it has been known for several years that spin–spin couplings can be efficiently transmitted through a hydrogen bond.[1,2] These couplings, which are now dubbed '*trans*-hydrogen bond couplings', are designated either as $^{nh}J(X, Y)$ or $^{hn}J(X, Y)$, where X and Y are the coupled nuclei which are n bonds apart, one of them being the hydrogen bond.[4] It is known that even long-range couplings, i.e., $n > 3$, can have part of their coupling pathway determined by a hydrogen bond.[132] An important point that should be recalled is that a transmission pathway defined by a hydrogen bond is essentially similar whether the two molecular fragments are two moieties of the same molecule or they are part of two molecules forming a complex. Although often in the former case it can be safely assumed, on physicochemical grounds, that a given coupling is transmitted through-space, there could be some instances where it is not easy to discriminate if part of the coupling information is transmitted through the bonds connecting the coupled nuclei. Also, the geometry of an intramolecular hydrogen bond can be affected by steric requirements which are not present in molecular complexes.

At present, there is much interest in studying *trans*-hydrogen bond couplings in biological systems[3] where many such complexes are often held together by more than one hydrogen bond and then co-operative effects could be important making such hydrogen bonds very strong.[133] During the last decade there has been a large increase in NMR experimental techniques, and now many $^{nh}J(X, Y)$ couplings are amenable to measurement even in very large compounds or when the absolute values of such couplings are very small; references for some of these experimental methods are Refs. 7, 9–11, 88 and 134–138. Taking into account the notable importance of this topic for structural molecular biology, papers dealing with $^{nh}J(X, Y)$ are reviewed in Section 3.1.1.1. The other two sub-sections, Section 3.1.1.2 and Section 3.1.1.3 deal, respectively, with couplings mainly transmitted through-space, and with the proximity effect on couplings between nuclei belonging to one of the two proximate molecular fragments or, in molecular complexes, the effects upon complex formation on intra-monomer couplings.

There is a certain degree of arbitrariness in the choice of papers reviewed in Sections 3.1.1.1 and 3.1.1.2. As in all this work, the main criterion chosen here to discuss some topics in either of these two subsections is the common usage of the different terms found in the current literature. A case in point is that of J(F, H) and J(F, C) couplings transmitted by spatial proximity, i.e., through interactions of the type F–H–C, which are discussed in 3.1.1.2. However, a recent paper by Mele *et al.*[139] discussed a proximity interaction of this type in 2′,3′-dideoxy-4′-(fluoromethyl)nucleosides, which corresponds to an attractive interaction that can be considered a hydrogen bond of the type $C(sp^3)$–F–H–$C(sp^3)$, i.e., this paper could be discussed as well in Section 3.1.1.1. On the other hand, some papers dealing with intermolecular interactions could also be included in Section 3.3 where papers dealing with medium effects on couplings are commented on.

3.1.1.1. Spin–spin coupling constants transmitted through a hydrogen bond X–H–Y, $^{nh}J(X, Y)$
During this review period there was an explosive increase in the number of $^{nh}J(X, Y)$ couplings reported and discussed in the literature. Interesting review articles on this subject have been published recently.[4,134,140,141] One of the intriguing aspects of *trans*-hydrogen-bond couplings is that, for a Z–H–Y moiety, $^{2h}J(Z, Y)$ in many cases is larger than $^{1h}J(Y, H)$, a trend which is ascribed to the presence of a negative contribution to the latter.[33,142] In a recent paper, Weinhold *et al.*[143] performed the dissection into NBO contributions of the FC terms of $^{2h}J(N, N)$ and $^{1h}J(N, H)$ couplings in a DNA A–T base pair. The FC contribution to both couplings is largely determined by three terms, two corresponding to Lewis-type contributions coming from the nitrogen non-bonding electron pair, n(N), of adenine and the thymine N–H bond and one from pair-wise delocalization of spin density, n(N) → (NH)*. For $^{2h}J(N, N)$ these three terms are positive while for $^{1h}J(N, H)$ the former two are positive while the latter is negative resulting in a smaller positive coupling.

According to some authors the existence of a *trans*-hydrogen bond coupling must be taken as evidence of the partial covalent character of that hydrogen bond. A similar concept can also be found in the current literature about through-space transmitted couplings which are considered to be evidence of the existence of a weak bond connecting the coupled nuclei. This is a controversial point which was addressed recently in several papers using different approaches and where the main conclusion is that a *trans*-hydrogen bond coupling cannot be used as evidence for a covalent bonding. Similarly, the existence of a through-space coupling between proximate moieties cannot be taken as evidence either of an attractive or a repulsive interaction between the moieties. Since many years, interactions involved in a hydrogen bond were separated into several types of contributions[144] most of them being attractive and at least one of them being repulsive. A well known theoretical approach to obtain such a partition is that of Morokuma *et al.*[145] although at present

topological analyses based on the Bader's Atoms in Molecules, AIM, approach[146] are preferred to analyze hydrogen bonds since they do not require the introduction of further approximations into the ground state wave function. In short, it is accepted that the main attractive terms for HB interactions are charge transfer, electrostatic, polarization and dispersion interactions. It is well known that charge transfer interactions, which can be associated with the interaction defining a certain degree of covalent character of a hydrogen bond,[83,143] constitute an efficient pathway to transmit the FC term of spin–spin couplings.[19,143,147–150] However, this is not the only interaction present in a hydrogen bond that could define an efficient pathway for transmitting the spin information associated with the FC term. For instance, during this review period intermolecular couplings in van der Waals complexes were calculated and sizeable values were obtained. The main aim of such works is to show that van der Waals interactions also define an FC coupling pathway, although in some cases, not a very efficient one, like in the xenon dimer, Xe_2, where $J(^{129}Xe, ^{131}Xe)$ was calculated as a few mHz.[151] Bagno *et al.*[152,153] used a DFT-based approach to study the transmission of intermolecular couplings in complexes methane–benzene [**1a**] and benzene–benzene [**1b**].

[1a]   [1b]
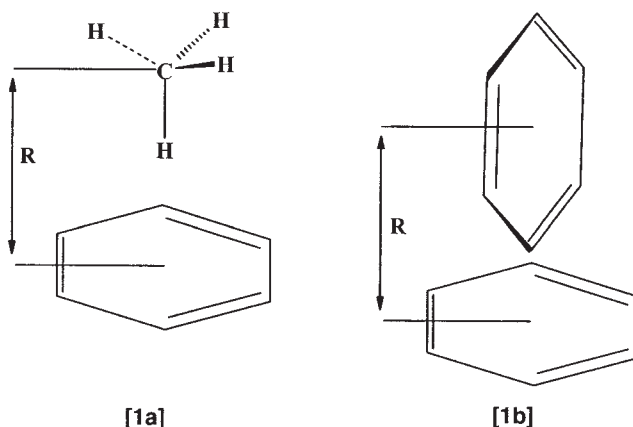
Pecul calculated the $^1J(^3He, ^3He)$ coupling in He_2,[154] i.e., one of the weakest bonded van der Waals complexes, using full CI[46] and EOM–CCSD methods.[44,155–158] She found that in this complex the FC term of such coupling decreases exponentially with the d(He–He) distance; being $^1J(^3He, ^3He) \cong 22$ Hz, for d(He–He) = 4 au and falling below 0.1 Hz for d(He–He) = 7 au. Pecul concluded that the main FC coupling pathway is the overlap between the electronic clouds of both helium atoms and that its efficiency does not depend on whether this corresponds to an attractive or repulsive interaction. Similarly, Pecul *et al.*[159] carried out calculations based on

an MCSCF wave function approach to study intermolecular $J(F, H)$ couplings in FH, FHF⁻, $(FH)_2$ and in a weak van der Waals complex, i.e., $[CH_4–HF]$. In this way, Pecul *et al.*[159] studied four systems with various strengths of bonding between the F and H atoms. They shown that the absolute value of $^{1h}J(F, H)$ in all of these systems decreases along this series, and that its sign is positive for $(FH)_2$, while it is negative for all of the other three compounds. When comparing $^{1h}K(F, H)$ and $^{2h}K(F, F)$ in $(FH)_2$ with the corresponding reduced couplings in $(OH_2)_2$ Pecul *et al.* concluded that intermolecular reduced couplings are not a measure of the hydrogen bond strength when they correspond to different types of nuclei. They argued that the presence of $^{1h}J(F, H)$ in the weak van der Waals complex refutes the hypothesis that *trans*-hydrogen-bond couplings are indicative of the covalent character of a hydrogen bond.

Electrostatic interactions, although they affect notably intra-molecular couplings[147,160–162] do not constitute a pathway for transmitting any term of spin–spin couplings.

It has been known for many years that the 'closed shell' interaction, which corresponds to spin exchange interactions (Pauli's exclusion principle or Fermi's correlation effect) defines a very efficient FC coupling pathway.[35] One of the classical examples is that the spin information associated with the FC term of $J(H, H)$ couplings can be transmitted through the π-electronic system in unsaturated compounds.[163] Electrons of such symmetry cannot participate directly in an FC interaction with a magnetic nucleus due to the node of the π-orbitals at the nuclear sites. However, exchange interactions between σ- and π-electrons define the spin polarization of the latter.[74,163,164] As commented above, Bader *et al.*[127] and Soncini and Lazzeretti[124,125] have presented very interesting papers where, in elegant ways, they show that the main transmission mechanism of the FC and the SD terms is the Fermi correlation interaction.

Arnold and Oldfield[165] using the Bader AIM approach[146] showed that a strong (and repulsive) closed shell interaction between two overlapping proximate moieties can define an efficient pathway for transmitting the spin information associated with the FC interaction. Bryce and Wasylishen[166] arrived at a similar conclusion by studying intermolecular couplings in the $[CH_4–HF]$ and $[CFH_3–HF]$ complexes. Therefore, in agreement with other works commented on above, these results indicate that if a spin–spin coupling is observed between two atoms belonging to proximate moieties, such coupling cannot be used as a probe to determine the existence of either a weak bond or a covalent hydrogen-bond between them. In short, the FC term can be transmitted between two moieties as long as there is an overlap of their electronic clouds, it is irrelevant whether such an interaction is repulsive or attractive.

Recently,[94,166,167] it was reported that the through-space $^{TS}J(F, F)$ coupling between proximate F atoms can have a substantial contribution from the PSO term. It is important to stress that comments made above about interactions

defining a coupling pathway refer only to the transmission of the FC term. Features of coupling pathways corresponding to the through-space transmission of the PSO term are quite different and there can be such a transmission even if the respective electronic clouds do not significantly overlap. This point is further discussed in the 3.1.1.2 subsection. In several instances it was found that *trans*-hydrogen bond long-range couplings are dominated by the DSO and PSO contributions,[168] where the DSO contribution follows the trends shown for this coupling contribution in any other molecular system[114] (see above).

Limbach *et al.*[169] observed *trans*-hydrogen bond couplings in hydrogen-bonded ionic clusters of the type $[F(HF)_n]^-$ ($n = 1$–4). Perera and Bartlett,[96] using the EOM–CCSD approach[45] calculated the *trans*-hydrogen-bond couplings in such clusters after optimizing their respective geometries at the CCSD(T)/aug-cc-pVDZ level. Such optimized geometries exhibit $D_{\infty h}$, C_{2v}, D_{3h} and T_d symmetries for $n = 1$, 2, 3 and 4, respectively. In Table 6 Perera and Bartlett's calculated $^{1h}J(F, H)$, $^1J(F, H)$ and $^{2h}J(F, F)$ couplings are compared with the corresponding experimental values, showing a good agreement with them. It is interesting to note that these values follow the sign trend observed for the corresponding *trans*-hydrogen-bond couplings in the N–H–N system (see below). Shenderovich *et al.*[170] measured H/D isotope effects on the low temperature $J(F, H)$ and $J(F, F)$ scalar couplings in different isotopomers of $(FH)_2F$- and $(FH)_3F$- dissolved in the Freon mixture CDF_3/CDF_2Cl.

During the last few years several works were aimed at understanding how *trans*-hydrogen bond couplings can be adequate parameters to study the main aspects of the so called 'low barrier hydrogen bonds'.[33,142,171] Limbach *et al.*[172] measured the NMR spectra, at low temperature, of homoconjugated ions tetrabutylammonium(TBA)-hydrogen-difluoride, TBA- maleate, TBA-bis-acetate and bis-collidimium-tetrafluoroborate. In the first of these complexes they measured at 130 K, $^1J(F, H) = 124$ Hz, while in the latter they measured

Table 6. Comparison between calculated and experimental $^1J(F, H)$, $^{1h}J(F, H)$ and $^{2h}J(F, F)$ couplings (in Hz) in hydrogen-bond ionic clusters of the $[F(HF)_n]^-$ ($n = 1$ to 4) type. All values in Hz

	$^1J(F, H)$		$^{1h}J(F, H)$		$^{2h}J(F, F)$	
n	Calc.[a]	Exp.[b]	Calc.[a]	Exp.[b]	Calc.[a]	Exp.[b]
1	100	124 ± 3	100	124 ± 3	225	–
2	388	354 ± 3	−45	-24 ± 3	179	146 ± 4
3	426	430 ± 4	−57	-41 ± 3	101	92 ± 5
4	492	480 ± 5	−57	< 10	11	< 15

[a] Calculated values are taken from Ref. 96.
[b] Experimental values from Ref. 169.

^{1}J(N, H) $= 40$ Hz at 150 K. Limbach *et al.*[171] measured at temperatures ranging from 112 K to 200 K the NMR spectra of the complex between FH and ^{15}N-enriched 2,4,6-trimethylpyridine [2].

CH₃... (structure)

[2]
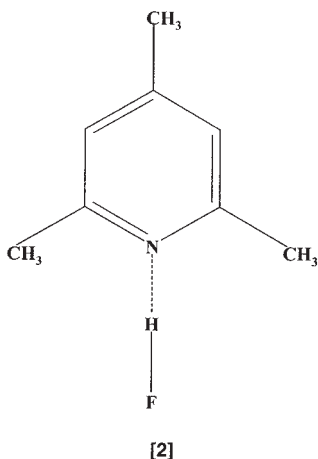
In order to study the effect of a polar solvent on the F–H–N hydrogen bond they prepared samples using a mixture of CDF_3 and CDF_2Cl whose dielectric constant increases drastically when lowering the temperature ($\varepsilon = 40$ at about 100 K). They observed that, when lowering the temperature, the absolute value of ^{1h}J(N, H) increases, while ^{1}J(F, H) decreases and ^{2h}J(F, N) remains constant within the margin of error. The largest ^{1h}J(N, H) value that they measured is ^{1h}J(N, H) $= 54$ Hz at 112 K. On the other hand, they also measured a very large ^{2h}J(F, N,) $= 96$ Hz. This value contrasts with those that they measured in more asymmetric complexes, such as for instance, [2,4,6-trimethylpyridine]HFH[2,4,6-trimethylpyridine]$^+$; [2,4,6-trimethylpyridine]$(HF)_2$ and [2,4,6-trimethylpyridine]$(HF)_3$. Such results led Golubev *et al.*[171] to take substantial ^{2h}J(F, N) values as a probe to detect the formation of a low-barrier F–H–N hydrogen bond.

Limbach *et al.*[33] performed DFT calculations on ^{1}J(N, H) and ^{2h}J(N, N) couplings in the anion $[C \equiv N–L–N \equiv C]^-$ (L $=$ H, D) and in the cyclic bonded formamide dimer $(HCNHNH_2)_2$ to study how such couplings depend on the geometry of the hydrogen bond. To describe such a relationship they employed the valence bond order model and compared the NHN and FHF- hydrogen bonded systems.

Del Bene *et al.*[173] used the EOM–CCSD method[45] to study how *trans*-hydrogen bond couplings, ^{2h}J(X, Y), can be used as fingerprints for identifying different types of hydrogen bonds. To this end, they took a set of 10 complexes involving neutral, cationic and anionic species stabilized by X–H–Y hydrogen bonds. These results led the authors to classify hydrogen bonds in three different categories, i.e., 'traditional', 'proton-shared' and 'ion-pair'.

Del Bene and Jordan[174] studied how structural data on hydrogen bonds obtained through vibrational and NMR spectroscopies are related to each other. They reported, for X–H–Y hydrogen bonds, relationships among the X–Y distance, the anharmonic proton-stretching frequency, the ^{1}H chemical shift and ^{2h}J(X, Y) coupling constant. A common pattern found in several papers for calculated *trans*-hydrogen-bond couplings, ^{nh}J(X, Y), using either post-Hartree–Fock or DFT approaches is that, unless they are long-range couplings ($n > 2$), they are largely dominated by the FC term, although there are some exceptions to this trend. In fact, calculations for the ^{1h}J(F, H) coupling in *o*-fluoro-N-methylbenzamide [**3**], show that it is dominated by the PSO contribution.[175]
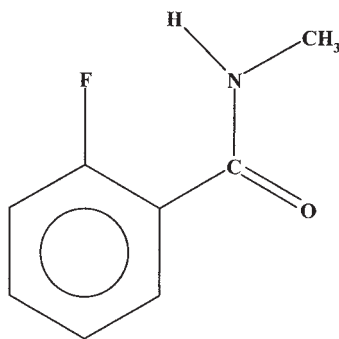
[**3**]

In this compound *trans*-hydrogen bond couplings were studied several years ago although ^{1h}J(F, H) could not be observed due to rapid chemical exchange. Calculations of ^{1h}J(F, H) in 1-fluoro-8-methyl-naphthalene for the methyl group conformation that defines the closest approach between the F and H atoms, showed also that this is dominated by the PSO contribution.[175] In the former compound the long-range ^{4h}J(F, H) couplings are found to also have a substantial PSO contribution. Similar results were reported by Pecul *et al.*[168] when using the MCSCF linear response, LR–MCSCF, method[15] to calculate long-range ^{nh}J(X, Y) couplings transmitted through an XH–O hydrogen bond in complexes of a few simple organic molecules. Del Bene *et al.*[176] studied, using the EOM–CCSD method, the transmission of scalar couplings through dihydrogen interactions of the type X–H–H–M in complexes where C–H, N–H and O–H are playing the role of proton donor groups while that of proton acceptor groups are played by ^{7}Li–H and ^{23}N–H moieties. Del Bene *et al.*[176] called couplings thus transmitted as ndJ(A, B), where A and B are the coupled nuclei and *n* is the number of bonds separating them. ^{1d}J(H, H) couplings are found to have non-negligible PSO and DSO contributions, although they tend to cancel each other. These authors discussed several structural and geometric trends for ^{1d}J(H, H) and ^{3d}J(X, M).

Dingley and Grzesiek[177] have reported for the first time the measurement of $^{2h}J(N, N)$ couplings in Watson–Crick base pairs [**4-a,b**] of a ^{15}N-labelled 69-nucleotide RNA domain.

[4a]

[4b]
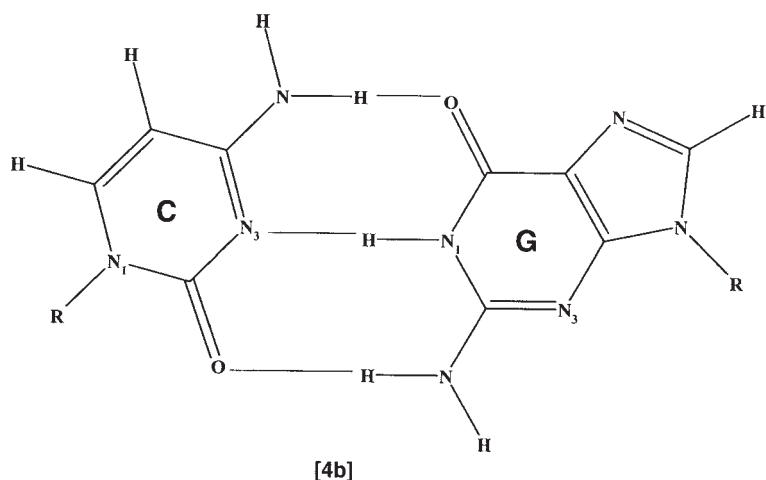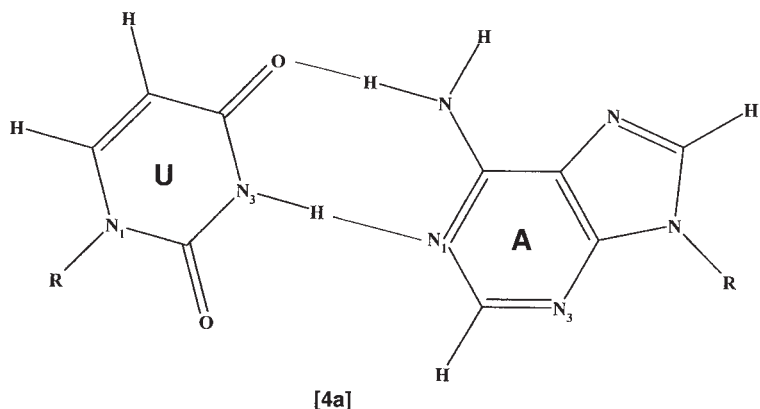
This was shortly followed by the works of Pervushin *et al.*[6] who observed such couplings in a 14 base-pair ^{15}N-labelled DNA duplex. Pervushin *et al.*[6] could also observe in such a DNA duplex the corresponding $^{1h}J(N, H)$ coupling which was undetectable in the pioneering work by Dingley and Grzesiek.[177] These two papers started a long series of works where several types of $^{nh}J(X, Y)$ couplings were observed in bio-macromolecules, where special experimental techniques are required to determine them.[5–7,10–12,137,178] In a subsequent paper, Dingley, Grzesiek, Barfield *et al.*[88] reported the measurement of $^{2h}J(N, N)$ and the corresponding $^{1h}J(N, H)$ and $^{1}J(N, H)$ couplings for Hoogsteen–Watson–Crick T • A–T and C+ • G–C triplexes [**5-a,b**].
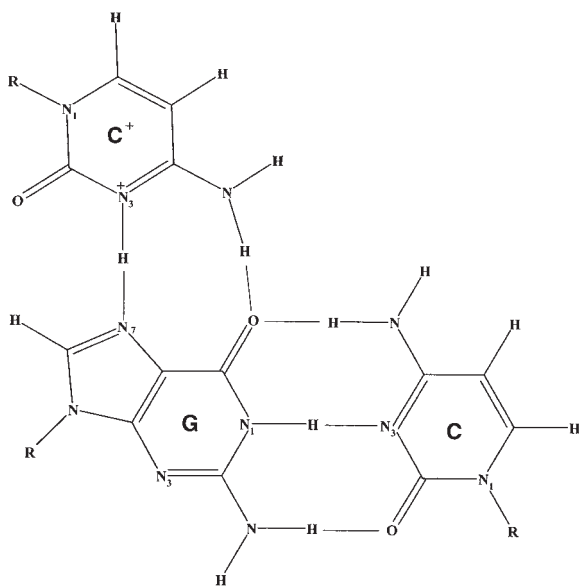
[5a]
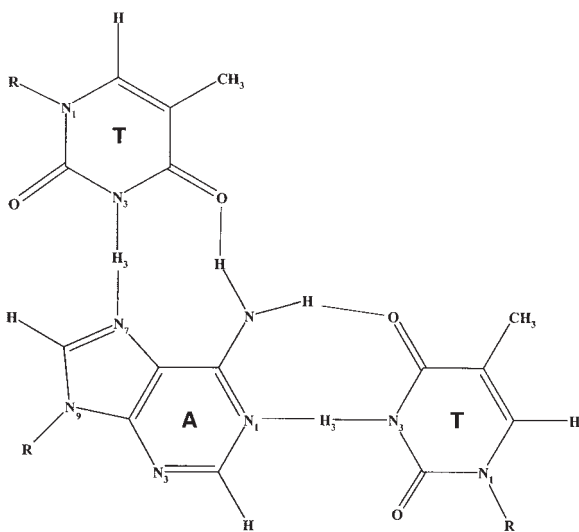
[5b]

They observed that, when decreasing the R(N–N) distance, the absolute value of $^1J(N, H)$ decreases. Weisz *et al.* used the absolute value of $^1J(N, H)$ as a probe to compare the strength of the N–H–N hydrogen bond between adenosine and 4-thiouridine in a Watson–Crick and a Hoogsteen hydrogen

bond.[179] Such a ^{1}J(N, H) coupling was also used as a probe to study how substituent effects affect the strength of the N–H–N hydrogen bond in a Watson–Crick pair.[180] Now it is known that a decrease in the absolute value of ^{1}J(N, H) is accompanied by a concomitant increase in the absolute value of ^{1h}J(N, H).[143] These trends are consistent with an increase of the n(N) → (N–H)* charge transfer interaction,[2,143] which also yields an increase in the covalent character of such a hydrogen bond.[143] Barfield *et al.*[88] presented a theoretical study of such couplings using the FPT–DFT approach to calculate the FC term in the 16-atom model system [6] which corresponds to a fragment
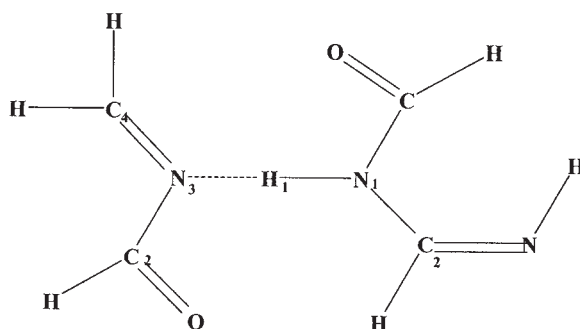
[6]

clipped out from the X-ray structure of a Watson–Crick G–C base pair; the other three terms of the scalar couplings, PSO, SD and DSO, were neglected. They also found that the calculated ^{2h}J(N, N) couplings are positive and that they increase when decreasing the R(N–N) distance, which is in agreement with experimental values reported in the same paper. Both calculated ^{2h}J(N, N) and ^{1}J(N, H) couplings correlate with the calculated chemical shift of the proton involved in the hydrogen bond, δ(H), in agreement with experimental values, i.e.,

$$^{2h}J(N, N)_{calc} = 1.17\delta(H) - 9.4 (r = 0.9999); \tag{10}$$

$$^{1}J(N, H)_{calc} = 1.01\delta(H) - 91.9 (r = 0.9844) \tag{11}$$

and

$$^{2h}J(N, N)_{exp} = 1.27\delta(H) - 9.6 (r = 0.861); \tag{12}$$

$$^{1}J(N, H)_{exp} = 1.02\delta(H) - 100.6 (r = 0.864) \tag{13}$$

where the couplings are in Hz and chemical shifts in ppm. ^{1h}J(N, H) couplings are calculated to be positive ($\gamma(^{15}N) < 0$), in agreement with

the values of $^{1h}J(N, H)$ couplings reported by Pervushin *et al.*[6] i.e., $^{1h}K(N, H)$ is negative paralleling the behaviour of through-space $^{1h}J(F, H)$ couplings reported previously for proximate F and H atoms[181] (see Section 3.1.1.2).

Scheurer and Brüschweiler[71] calculated $^{2h}J(N, N)$ couplings in three nucleic acid base pairs, namely, Watson–Crick uracil–adenine (U–A) [4a] and cytosine–guanine (C–G) base pairs [4b] and in the Hoogsteen adenine–thymine (A–T) base pair [7].
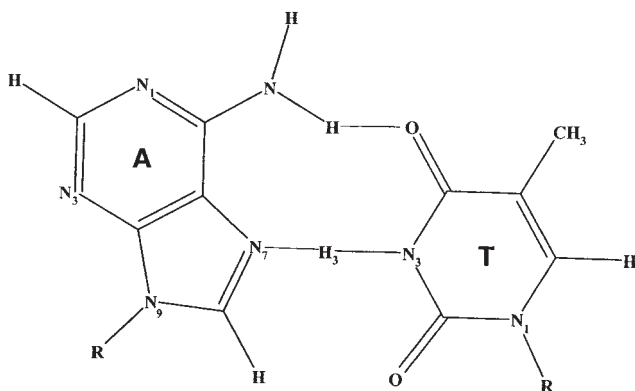
[7]

For the former two they used geometries taken from the Dickerson–Drew dodecamer.[182,183] Scheurer and Brüschweiler's calculations of $^{2h}J(N, N)$ couplings were performed using the Loc.1 SOS–DFT approximation of Malkin *et al.* as implemented in the deMon program.[66–69,184–186] In the three cases, they found that the FC term is by far the dominant one, in comparison with the PSO and DSO terms (the SD term was not included in their calculation). Calculated values for the couplings in the three base pairs quoted above are 7.65 Hz, 5.36 Hz and 6.45 Hz, i.e., they are very close to the corresponding experimental values.[6,177] In the same paper Scheurer and Brüschweiler[71] also reported calculations of $^{3h}J(N, C')$ couplings through polypeptide N–H–O=C hydrogen bonds. Protein backbone hydrogen bonds were modeled by these authors using two N-methylacetamide molecules suitably arranged. $^{3h}J(N, C')$ values were calculated as a function of the hydrogen bond length, R(N–O) and of the out-of-plane tilt angle $\theta(OH^NN)$. For all ranges of the geometrical parameters considered, negative $^{3h}J(N, C')$ couplings were found in agreement with experimental values. The authors related the R(N–O) distance to the size of $^{3h}J(N, C')$ and to the amide proton chemical shift. Majumdar *et al.*[187,188] detected $^{2h}J(N, N)$ couplings in N–H–N hydrogen bonds where the H proton signal is broadened to extinction. Marino *et al.*[137] detected $^{2h}J(N, N)$ couplings in A–U base pairs in the dynamic region of RNA structure where the exchangeable proton involved in

the N–H–N hydrogen bond is unobservable by NMR. Barfield *et al.*[25] calculated, within the DFT framework, the FC contributions to $^{2h}J(N, N)$, $^1J(N, H)$ and $^{1h}J(N, H)$ for the imino hydrogen bonding region of Hoogsteen– Watson–Crick T • A–T and C$^+$ • G–C triplets. Calculations were carried out for different interresidue separations for the four types of base pairs. Barfield *et al.*[25] observed that NMR parameters for the hydrogen bond region of the T • A, A–T and G–C base pairs exhibit very similar dependencies on the d(N–N) distance. In order to obtain a qualitative analysis of couplings in the hydrogen bond region the FC term was analyzed via a simple LCAO–MO SOS model. Calculated couplings were found to be consistent with the corresponding experimental values measured in the complex spectra of these nucleic acid associations.

Del Bene and Bartlett[189] investigated how sensitive $^{2h}J(N, N)$ couplings are to the type of covalent bonding at the nitrogen atoms. For this purpose, they calculated the $^{2h}J(N, N)$ coupling for several complexes of the type CNH–X (X = pyridine, NCLi, NH$_3$, NCH) and the complex pyrrole– NCH. The coupling constants were calculated using the EOM–CCSD[45] approach and some features of their calculated values are consistent with those found by Scheurer and Brüschweiler,[71] for instance, for $^{2h}J(N, N)$ couplings the non contact terms are negligible in comparison with the FC term. Del Bene and Bartlett[189] also concluded that the $^{2h}J(N, N)$ dependence on the d(N–N) distance is not very sensitive to the bonding at the nitrogen atoms, although such bondings determine the equilibrium N–N distance, which in turn, determines the value of the corresponding $^{2h}J(N, N)$ coupling. Such conclusions led Del Bene and Bartlett to consider the CNH–NCH molecular complex an adequate model to study $^{2h}J(N, N)$ couplings in Watson–Crick base pairs. In the CNH–NCH complex they calculated $^{2h}J(N, N) = 7.2$ Hz for an N–N distance of 2.90 Å, which is in good agreement with the experimentally measured couplings in the A–U and G–C Watson–Crick base pairs [**4-a,b**] reported by Dingley and Grzesiek.[177] Afterwards, Del Bene *et al.*[190] studied vibrational effects on the $^{2h}J(N, N)$ coupling in the same complex, CNH–NCH, calculating the expectation value of such a coupling obtained from a two-dimensional surface calculated using the EOM–CCSD method.[45] Pecul *et al.*[191] took the molecular complexes formamide–formamide and formamide–formamidine as model systems to study several features of $^{1h}J(N, H)$ and $^{2h}J(N, N)$ couplings. Both types of couplings decrease rapidly when increasing the hydrogen bond length, a trend which was not observed for the long-range J(H, H) intermolecular couplings in the same complex. Pecul *et al.*[191] also discussed the possibility of using several intra-molecular couplings to analyze hydrogen bonds. A case in point is the $^2J(N, H)$ coupling across the carbonyl moiety, which is very sensitive to intermolecular interactions due to the strong negative hyperconjugations of type n(p) → (C–N)* and n(p) → (C–H)* (see Section 3.3).

Del Bene *et al.*,[192] using the EOM–CCSD approach,[45] have studied what parameters determine $^{2h}J(N, N)$ and $^{2h}J(^{17}O, ^{17}O)$ couplings across an X–H$^+$–X moiety (X = N, O). They found that $|^{1h}J(X, H)| > |^{2h}J(X, X)|$ in complexes with symmetric hydrogen bonds, but for non-symmetric ones it holds that $|^{1}J(N, H)| > |^{2h}J(N, N)| > |^{1h}J(N, H)|$. How the transmission of $^{2h}J(N, N)$ for cationic complexes, N–H$^+$–N compare with N–H–N in neutral complexes was also studied by Del Bene *et al.*[193] in two series of complexes comprising both types of molecular systems. A similar study where $^{2h}J(F, N)$ couplings for cationic complexes, N–H$^+$–F, are compared with similar couplings in neutral complexes, F–H–N,[194] was also reported by Del Bene *et al.*[195] In both cases proton donors include sp, sp^2 and sp^3 hybridized N atoms and the couplings are calculated using the EOM–CCSD approach.[45] In the neutral complexes they found that $^{2h}J(F, N)$ in F–H–N hydrogen bonds are more sensitive to the N hybridization than $^{2h}J(N, N)$ in complexes stabilized either by N–H–N or N–H$^+$–N hydrogen bonds. In both neutral and cationic complexes electronic features of the corresponding hydrogen bonds were analyzed using the AIM theory.[146] Del Bene *et al.* found that in both types of complexes such couplings are by far dominated by the FC term, which, in both cases, is strongly dependent on the d(F–N) distance, but only slightly dependent on small variations of the hydrogen bond linearity.

Bryce and Wasylishen[196] have presented *ab initio* calculations of $^{2h}J(N, N)$ couplings using a MCSCF wave function taking the methyleneimine dimer [8] as a model system.

[8]
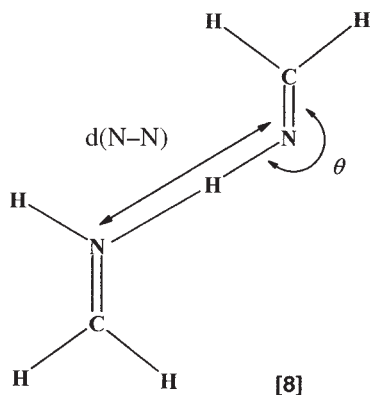
These authors not only consider the isotropic value of such a coupling but also study its tensor character, $^{2h}J(N, N)$, where all four anisotropic terms were considered, i.e., FC/SD, PSO, SD and DSO. They studied systematically the dependence of the $^{2h}J(N, N)$ coupling with the hydrogen bond length, d(N–N), and bond angle, θ. For the latter fixed at $\theta = 180°$, they find that the isotropic part of $^{2h}J(N, N)$, $^{2h}J_{iso}(N, N)$, decays exponentially when increasing

d(N–N). For values of d(N–N) larger than 2.25 Å such a dependence was fitted to Eq. (14)

$$^{2h}J_{iso}(N, N)(Hz) = 9640 \exp[-2.73d(N-N)]; \ (R^2 = 0.9959) \quad (14)$$

or, equivalently, to

$$d(N-N)(\overset{\circ}{A}) = -0.37 \ln[^{2h}J_{iso}(N, N)] + 3.36 \quad (15)$$

In agreement with works cited above,[71,189] Bryce and Wasylishen[196] also conclude that $^{2h}J_{iso}(N,N)$ is dominated by the FC term. On the other hand, they report that the anisotropy of that tensor, $\Delta[^{2h}J(N, N)]$, is dominated by the FC/SD term and that it is not insignificant when compared to $^{2h}J_{iso}(N, N)$. Bryce and Wasylishen[196] also highlight the dependence of $^{2h}J(N, N)$ on θ, the hydrogen bond angle [**8**].

Experimental evidence of the important dependence of $^{2h}J(N, N)$ on both the d(N–N) distance and the angle θ is provided, among others, by Majumdar *et al.*[197] who measured such couplings in non Watson–Crick base pairs in unusual nucleic acids. For instance, they measured $^{2h}J(N_6, N_7) = 2.45 \pm 0.03$ Hz in an **A–A** mismatch segment of the DNA d(GGAGGAT)$_2$, which is smaller than those measured, at ~ 7 Hz, for Watson–Crick base pairs.[177] Majumdar *et al.*[197] consider that such smaller couplings could indicate weaker hydrogen bonding for a mismatched alignment. Majumdar *et al.*[11] have presented a suite of NMR pulse sequences for studying multi-stranded DNA architectures containing intricate hydrogen-bonded networks mediated primarily through mismatched base pairing. Bytchenkoff *et al.*[198] have studied the temperature dependence between 280 and 310 K of internucleotide $^{2h}J(N, N)$ couplings in (A–U) [**4a**] and (C–G) [**4b**] base pairs of a 22 nucleotide RNA oligomer. In all cases they observe that such $^{2h}J(N, N)$ couplings decrease monotonically with increasing temperature and that such dependence is more pronounced in the former than in the latter base pair. Liu *et al.*[10] have measured $^{4h}J(N, N) = 0.136 \pm 0.021$ Hz transmitted through an N_{1i}–H_{1i}–O_{6j}=C_{6j}–N_{1j} segment of a $G \bullet G \bullet G \bullet G$ tetrad.

Pervushin *et al.*[199] have measured both $^{2h}J(N, N)$ and $^{1h}J(N, H)$ couplings for a DNA–protein complex and compared such values with those measured in the 14-mer DNA duplex. They observe that the corresponding $^{2h}J(N, N)$ couplings in the DNA–protein complex are very similar to those measured for the DNA free in solution, which was rationalized as being indicative that very small conformational changes take place in this DNA duplex upon binding to the protein. However, the corresponding $^{1h}J(N, H)$ couplings seem to be more sensitive to small conformational changes since significant differences are observed upon the DNA–protein complex formation. In order to study hydrogen bonding between the amide backbone of Arg7 and the remote

imidazole side chain of His106 in the 44 kDa trimeric enzyme chorismate mutase from Bacillus subtilis, Pervushin et al.[200] chose the complex between acetylethylamine and imidazol as a model system. They calculated $^{2h}J(N, N)$ and $^{1h}J(N, H)$ couplings using the SOS–DFT approach for a wide range of mutual orientations; the former is found to depend strongly on the cone angle aligned with the amide group involved in such a hydrogen bond. The latter is found to be relatively insensitive to the same angle. Majumdar et al.[188] have detected $^{2h}J(N, N)$ in the human T-cell leukemia virus-1 rex peptide–RNA aptamer complex.

$^{2h}J(N, C)$ couplings transmitted through a hydrogen bond of the type C–H–N were studied, from a theoretical point of view, by Del Bene et al.[201] Coupling constants were calculated using the EOM–CCSD method[45] and 17 neutral, 3 cationic and 3 anionic complexes were considered as model systems. In all cases the $^{2h}J(N, C)$ couplings are dominated by the FC term, and they exhibit some dependence on the nature of the hybridization and the nature of the bonding at the C atom of the proton-donor C–H bond. Complexes with $C–H^+–N$, $N–H^+–C$ and $C–H–N^-$ hydrogen bonds have shorter C–N distances and, concomitantly, larger $^{2h}J(N, C)$ couplings than for the neutral cases. $^{1h}J(O, H)$ and $^{2h}J(O, C)$ couplings through hydrogen bonds of the type C–H–O were studied by Ruiz de Azúa et al.[202] $NCH : H_2O$ and $CH_4 : H_2O$ were taken as model systems and coupling calculations were carried out at the RPA and SOPPA levels. Orbital contributions to such couplings were studied using the CLOPPA approach[203] at the RPA level.

Observations of inter-residue $^{3h}J(N, C')$ couplings through an N–H–O=C pathway in proteins were first reported by Cordier and Grzesiek,[7] Bax et al.[12,204] and Wang et al.[205] Using a quantitative-J correlation technique they determined values of $^{3h}J(N_i, C'_j)$ couplings ranging from 0.25 to 0.9 Hz, the largest values correspond to β-sheet conformations (average value 0.65 ± 0.14 Hz) whereas such couplings are smaller in α-helical structures (average value 0.38 ± 0.12 Hz). Cordier, Grzesiek and co-authors[206] succeeded in measuring $^{2h}J(C', H)$ in ubiquitin and found that $^{2h}J(C', H) = (0.94 \pm 0.02)^{3h}J(N, C')$, i.e., the absolute value of the two-bond coupling is only slightly smaller than the three-bond coupling, although it is much more difficult to be observed than the latter. Cornilescu, Hu and Bax[12] detected in the protein ubiquitin $^{3h}J(N, C')$ couplings between the donating ^{15}N atom and the accepting carbonyl/carboxyl ^{13}C. Bax et al.[204] determined that in proteins $^{3h}J(N, C')$ couplings are negative, and their absolute values are indicative of the strength of the hydrogen bond. They found the correlation given by equation (16)

$$^{3h}J(N, C') = [-59000 \ \exp(-4R_{NO}) \pm 0.09] \ \text{Hz}, \tag{16}$$

or equivalently,

$$R_{NO} = [2.75 - 0.25 \ \ln(-^{3h}J(N, C')) \pm 0.06] \overset{\circ}{A} \tag{17}$$

which is valid over the small range of N–O hydrogen bond lengths, i.e., 2.8–3.3 Å. Bax et al.[204] reported the measurement of $^{3h}J(N, C')$ connectivities across hydrogen bonds in a 30 kDa protein. Hydrogen bonding in cold-shock protein A of Escherichia coli was studied by NMR spectroscopy by Alxandrescu et al.[207] Liu et al.[208,209] have detected $^{3h}J(NCO_{2\delta})$ couplings transmitted through a weak side chain–main chain hydrogen bond between the backbone amide and the glutamate carboxylate moieties of distinct residues in a 12 kDa protein. These couplings are smaller than those transmitted through hydrogen bonds involving backbone atoms, $^{3h}J(N, C')$. Barfield[210] has performed a detailed FPT–DFT study of the FC term of $^{3h}J(N, C')$ inter-residue couplings in proteins using as a model system a formamide dimer generated from the crystallographic structure of the immunoglobulin binding domain of strepto-coccal protein G. Such experimental structures were used to build up the pathway for such couplings in N–H–O=C, where the proton position was determined by optimizing its energy while keeping all of the other geometrical parameters fixed. Barfield found that three geometrical parameters are very important for defining the $^{3h}J(N, C')$ values, namely, the d(H–O) distance; the H–O=C angle, θ, and the dihedral N–H–O=C angle, ρ, this dependence can be reduced to:

$$^{3h}J(N, C') = \{-1.35\cos^2\theta + [0.57\cos^2\rho + 0.14\cos\rho]\sin^2\theta\}$$
$$\times \exp[-3.2\Delta\delta(H-O)] + 0.01\,Hz \tag{18}$$

Markwick et al.[211] have included in the FTP-DFT analysis of $^{3h}J(N, C')$ couplings in proteins, the effects of the conformation motion; such effects were introduced using molecular dynamics simulations.

Grzesiek et al.[212] have presented a pulse scheme which allows the observation and quantification of *trans*-hydrogen bond $^{3h}J(N, C')$ couplings in nucleic acid base pairs between the imino nitrogen and the carbonyl-carbon nuclei in guanine quartets of the Oxy-1.5 DNA quadruplex. These authors determined that the absolute values of such couplings are close to 0.2 Hz, i.e., smaller than the analogous $^{3h}J(N, C')$ couplings in proteins. Cremer et al.[213] have studied *trans*-hydrogen bond couplings in ubiquitin using the CP–DFT approach which is implemented in the Cologne program,[214] including all four terms of the isotropic couplings.

Pecul et al.[191] chose the formamide dimer as a model system to study different features of $^{3h}J(N, C)$ transmitted through an N–H–O=C hydrogen bond. A similar study was carried out by Bagno[215] but considering only the FC term calculated within the FPT–DFT approach. As a model system Bagno studied first the formamide dimer varying, among other geometrical parameters, the hydrogen bond angle. $^{2h}J(N, C)$ and $^{3h}J(N, C)$ couplings in ubiquitin were also studied by Bagno[215] using as input geometry the X-ray structure of ubiquitin, trimming all amino acids, except the one of interest,

and replacing the two adjacent ones by acetyl groups. Using the AIM[146] approach Oldfield *et al.*[165] showed that $^{3h}J((N, C'))$ couplings observed between the peptide groups in proteins are mediated mainly by a closed shell, non-covalent interaction between the donor hydrogen atom and the acceptor oxygen atom.

In protonated 1,8-bis(dimethylamino)-naphthalene [9a] $^{2h}J(N'_1, N'_8) = + 8.7$ Hz, which is mediated by the proton since in the unprotonated compound [9b] the corresponding $J(N'_1, N'_8)$ coupling was not detected. In [9a] the (N–H–N)+ interaction corresponds to a classical low-barrier hydrogen bond with a symmetric configuration.

[9a]   [9b]
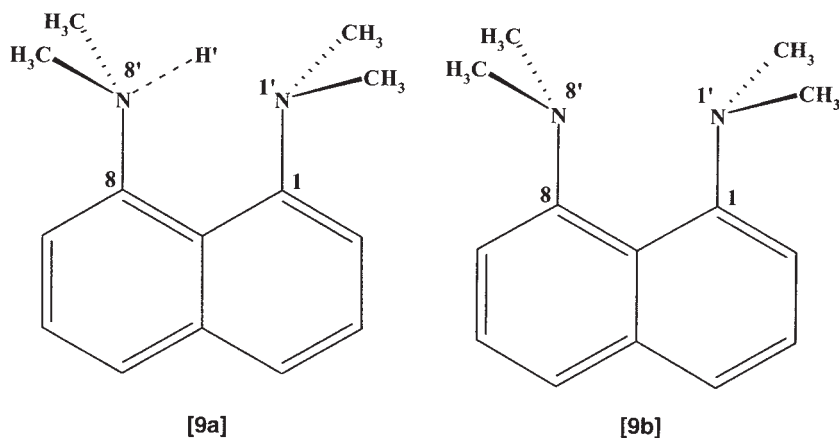
The value measured for $^{1h}J(N, H)$ is 30.4 Hz, and, when analyzing the different couplings involving side-chain atoms, it was assumed that this coupling is negative, $^1J(N_1, H') = {}^1J(N_8, H') = -30.4$ Hz. It is interesting to compare this trend with that found experimentally[169] in the small clusters $[F(HF)_n]^-$, which were also studied from a theoretical point of view by Bartlett *et al.*[96] A few of these values are shown in Table 6.

In the solid state Emsley *et al.*[216] have measured, $^{2h}J(N, N)$ couplings in [10] obtaining $^{2h}J(N, N) = 8 \pm 1$ Hz, which is quite close to the corresponding value measured in solution, 8.6 Hz.[217,218] It should be noted that the same assertion holds for $^1J(N_9, N_1')$ whose respective measured values are 12 ± 1 Hz and 11.8 Hz. These authors[219] have also measured the analogous couplings in [11] where they obtained $^{2h}J(N, N) = 10.6$ Hz, $^{1h}J(N, H) = + 4.4$ Hz and $^1J(N, H) = -88.6$ Hz. The last two values can be compared with $^1J(N, H) = -40.8$ Hz for both couplings in [10],[219] where this last value was taken as a confirmation that in [10] there is a rapid tautomerism. $^{1h}J(N, H)$ couplings involving 2'-hydroxyl protons in a frameshifting mRNA pseudoknot were recently reported by Giedroc *et al.*[220]

[10]   [11]
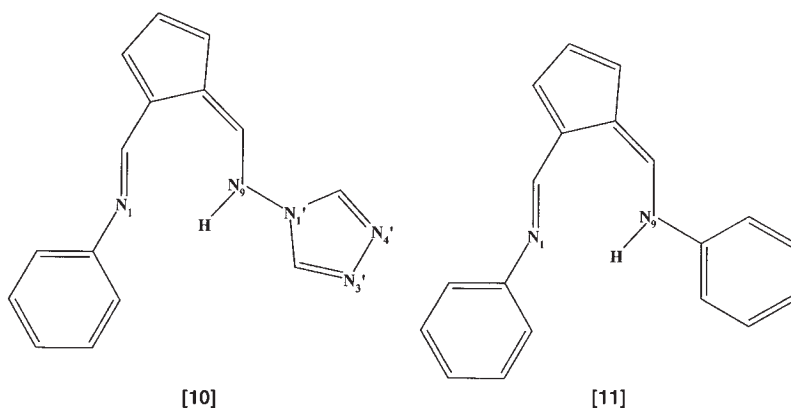
Del Bene *et al.* have studied, from a theoretical point of view, the effect of an isotropic external electric field on complexes with either HCl or HBr playing the role of proton donors and NH_3, $N(CH_3)_3$[221,222] or pyridine[223] as proton acceptors. Such an isotropic electric field corresponds to a simple model to emulate matrix effects. The nature of the corresponding hydrogen bond depends on the electric field strength in such a way that when increasing its strength the hydrogen bond changes from traditional to proton-shared to ion-pair according to the hydrogen bond classification made by Del Bene *et al.*[173,221,224,225] Del Bene *et al.*[223] have calculated, using the EOM–CCSD approach,[45] the $^{2h}J(^{35}Cl, {}^{15}N)$ coupling constant in the HCl/pyridine complex as a function of the equilibrium geometry corresponding to each electric field strength but with this field turned off when calculating $^{2h}J(^{35}Cl, N)$. They observed that the magnitude of such a coupling increases as the electric field strength increases, exhibiting a maximum at a field of 0.0040 au, and then decreases with increasing the field strength.

The temperature dependence of protein hydrogen bond properties was studied by Cordier and Grzesiek.[138] They observed that, when increasing the temperature, $^{3h}J(N, C)$ couplings weaken, the amide protons resonances show low frequency shifts, and the sequential $^1J(N, C')$ couplings decrease. It is worth noting that when increasing the N–H–O distance, the hydrogen bond inhibition of the $n_p(O) \rightarrow (C'–N)^*$ negative hyperconjugation decreases and therefore a concomitant decrease in the corresponding $^1J(N, C')$ couplings is observed.

Experimental $^{3h}J(P, N)$ couplings across N–H–O–P and $^{2h}J(P, H)$ across both N–H–O–P and O–H–O–P hydrogen bonds in protein–nucleotide complexes were first reported independently by Rüterjans *et al.*[135] and by Mishima *et al.*[136] For instance, these authors measured the absolute values of $^{3h}J(P, N) = 4.44 \pm 0.06$ and $^{2h}J(P, H) = 3.9 \pm 0.8$ Hz between Ala18 and the α-phosphate in wild-type Ras.GDP. Observations made by Mishima *et al.*[136] led them to suggest that $^{3h}J(P, N)$ couplings are sensitive to the linear

arrangement of the N–H–O–P hydrogen bond, and that they could only be observed for almost a linear configuration. Del Bene et al.[226], using the EOM–CCSD approach,[45] performed a detailed study of this type of *trans*-hydrogen bond couplings in model cationic and anionic complexes. Their calculations show that, for a P(V) coordinated atom in the cationic NH_4^+–OPH3 complex the results are in agreement with Mishima et al.'s assumption. For a linear or nearly linear N–H–O–P arrangement the predicted $^{3h}J(P, N)$ coupling is of sufficient magnitude to be measured experimentally. Czernek and Brüschweiler[227] performed DFT calculations on such couplings in different amino acid residues using the deMon-NMR program of Malkin et al.[66–69] In such calculations only the FC, PSO and DSO terms were taken into account. They truncated each residue at its N-terminus with an acetyl group and at its C-terminus with a N-methylamino group. Calculated $^{3h}J(P, N)$ and $^{2h}J(P, N)$ values for the acceptor of GDP and amidic nuclei of Gly13, Gly 15, Lys 16 and Ser17 do not exceed 0.37 and −0.90 Hz, respectively. However, for Ala18 $^{3h}J(P, N)$ and $^{2h}J(P, N)$ the calculated values are −4.00 and −3.36 Hz, respectively, which are close to the measured values, although experimentally it is only known that they are of like signs.[136] The authors plotted $^{3h}J(P, N)$ in the model of Ala18 as a function of the d(N–O) distance and the P–O–H angle, and correlated both $^{2h}J(P, N)$ and $^{3h}J(P, N)$ with such geometrical parameters. With these correlations they expected to obtain useful constraints for the determination of the structures of protein–nucleotide complexes in solution.

Del Bene et al.[228] have studied, from a theoretical viewpoint, the $^{4h}J(P, P)$ value in [12] intending to mimic the similar coupling in the cationic system [13], which was measured some years ago.[229] To this end, they employed the EOM–CCSD approach implemented in the ACESII program.[45] Del Bene et al.[228] also calculated $^{4h}J(P, P)$ in [12] as a function of the d(N–N) distance, keeping all other structural parameters fixed at their optimized values. For the optimized structure the N–H–N angle is close to 170° and $^{4h}J(P, P)$ ranges from 14.3 Hz for d(N–N) = 2.53 Å, to 3.0 Hz for d(N–N) 3.53 Å. The $^{4h}J(P, P)$ coupling in [13] could not be measured accurately and it is estimated that the calculated values are in good agreement with the experimental trend. Recently Elguero et al.[230] have measured in the bromide of a protonated iminophosphorane substituted proton sponge [14] $^{4h}J(P, P) = 1.6$ Hz.
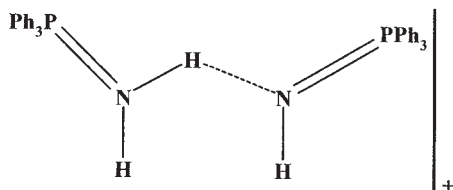
[12]
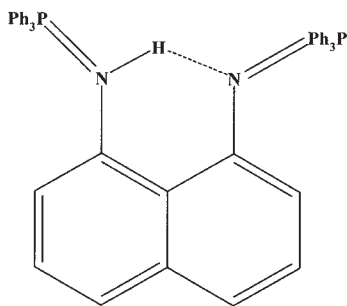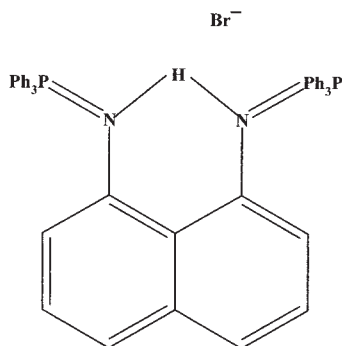
[13]   [14]

In several papers Pecul *et al.* have applied the LR–MCSCF method to study a variety of $^{nh}J(X, Y)$ couplings. For instance, they studied[159] $J(F, H)$ couplings transmitted through a hydrogen bond in FHF^- and $(HF)_2$ complexes and in a weak van der Waals complex $[CH_4–HF]$. In the same paper they analyzed how the $^1J(F, H)$ coupling transmitted through a covalent bond (in FH) is affected upon complex formation. In the X–H–O hydrogen-bonded complexes $CH_2O–H_2O$, $C_2H_2–H_2O$, $CH_3OH–H_2O$ and $(HCOOH)_2$ Pecul *et al.*[168] have studied several *trans*-hydrogen-bond couplings.

Intramolecular $^{1h}J(N, H)$ couplings were measured in the range of 195 to 302 K in order to study the proton transfer equilibrium in a series of N-(R-salicylidene)-alkylamines.[231]

3.1.1.2. Spin–spin couplings transmitted through-space

J(H, H) couplings. J(H, H) scalar couplings through a hydrogen bond between hydroxyl groups were studied by Barfield *et al.*[95] in 1,3- and 1,4-diols from both theoretical and experimental approaches. Calculated couplings include only the FC term which was calculated using the FPT-DFT approach. Subsequently, Barfield *et al.*[28] studied *trans*-annular J(H, H) couplings in half-cage alcohols and rigid 1,3- and 1,4-diols. Such couplings involve C–H–O–H, O–H–O–H and C–H–H–C coupling pathways. These authors performed calculations of the FC term of such couplings using the FPT–DFT approach and observed in the first type of compounds how they depend on the OH orientation. These authors in the same paper discuss the possible utility of J(H, H) involving two proximate OH groups for structural studies of carbohydrates. In an alkaloid, *tiliacorinine*, a seven-bond J(H, H) of 0.4 Hz was observed between the resonances of two aromatic protons located on two different benzene rings.[232] Through-space J(H, H) and J(C, H) couplings in C–H/π bonded complexes were studied by Bagno *et al.*[233] For most calculations they used the DFT framework as implemented in the deMon

program,[66–69] and for smaller van der Waals dimers they used the SOPPA approach as implemented in the Dalton package.[46]

J(F, H) and J(F, C) couplings. J(F, H) couplings mainly transmitted through-space, ^{TS}J(F, H), were studied in considerable detail during the last two decades and several systematic trends have been established.[1,2,234–236] One of its peculiar features is that, for a configuration like [15] the sign of the ^{TS}J(F, H) coupling depends on the α angle. At this point it is important to recall three interesting papers where J(F, H) couplings mainly transmitted through space were studied. In 8,13-dichloro-1,2,3,4-tetrafluoro-9-methyltripticene [16] Yamamoto *et al.*[237] reported J(F$_1$, H$_{sc}$) = +6.1 Hz and J(F$_1$, H$_{ap}$) = +8.7 Hz; in 8-fluoro-1-methylnaphthalene, [17a] Adcock *et al.*[238] reported |J(F, H$_{Me}$)| = 7.5 Hz and in the 8-fluoro-N-metylquinolinium salt [17b] Barfield *et al.*[239] reported J(F, H$_{Me}$) = +8.8 Hz.
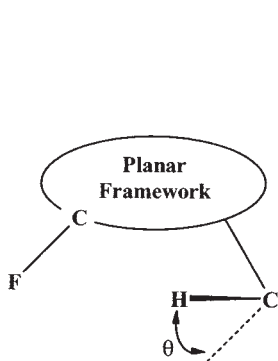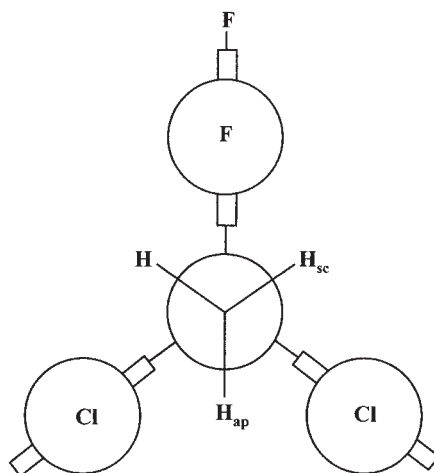
[15]   [16]
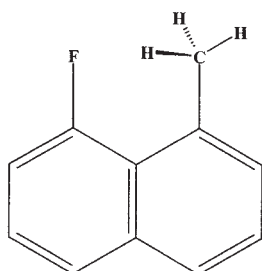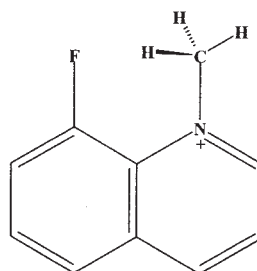
[17a]   [17b]

The role played by the C–H bond in transmitting the corresponding $^{TS}J(F, C)$ coupling, i.e., transmitted through the F–H–C pathway, was also discussed many years ago.[236,240] Since this is frequently the coupling pathway for a $^{TS}J(F, C)$ coupling it seems convenient to discuss this together with the $^{TS}J(F, C)$ and $^{TS}J(F, H)$ couplings since for such a configuration they are closely related. Bryce and Wasylishen[166] studied $^{TS}J(F, H)$ and $^{TS}J(F, C)$ couplings in systems [18-a,b,c] which show different configurations for the coupled nuclei than that shown in [15]. In the model complexes [18a], [18b] and [18c] considered by Bryce and Wasylishen,[166] $^{TS}J(F, C)$ increases exponentially when decreasing the d(F–C) distance. They find that both $^{TS}J(F, H_a)$ and $^{TS}J(F, H_{b,c,d})$ are positive and increase exponentially when decreasing the d(F–C) distance. However, both the absolute value and the exponential decay are smaller for $^{TS}J(F, H_{b,c,d})$ than for $^{TS}J(F, H_a)$. Configuration (a) resembles somewhat the configuration between the F atom and the methyl protons in 8,13-dichloro-1,2,3,4-tetrafluoro-9-methyltripticene [16] where Yamamoto *et al.*[237] reported that all three $^{TS}J(F, H)$ couplings are positive, the largest absolute value of the three is that of the 180° conformation. In both cases it is postulated that the coupling pathway is determined by the LMOs localized on fluorine and the rear lobe of the LMO that corresponds to the C–H$_a$ bond.[235,241,242] In 3,3-bis(2,5-difluorophenyl)-3H-isobenzofuran-1-one Szczecinski[243] reported J(F, C) and J(F, H) couplings with substantial through-space transmitted components. In several trifluoromethylated functional dienoates, aryldienoates and triethylnoates Palmas *et al.*[244] have reported several J(F, H) couplings mainly transmitted through-space.

[18a]   [18b]

[18c]
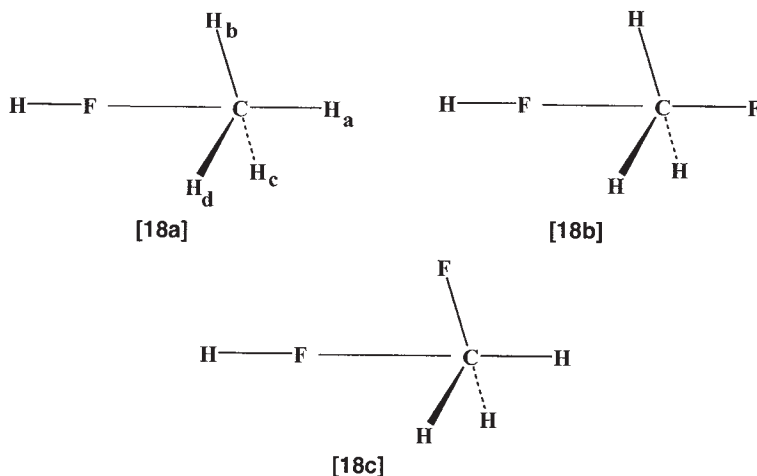
Although through-space pathways for J(F, C) couplings such as, for instance, the proximate π-electronic systems in cyclophenes [19] are known,[245] most commonly $^{TS}J(F, C)$ couplings correspond to configurations where they

are transmitted through an intermediate C–H bond[240] and most of these couplings are known to be of unlike sign with respect to $^{TS}J(F, H)$ coupling when α is close to 0° [15] i.e., $^{TS}J(F, C) > 0;$[181] and their absolute values mostly depend on the d(F–H) distance. Such a difference in sign contrasts with the results observed for inter-ring couplings in cyclophenes where $^{TS}J(F, H)$ and $^{TS}J(F, C)$ are found to be of the same sign.[245]
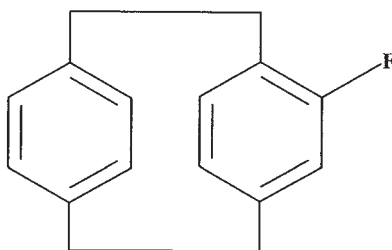
[19]

In a series of 4,5-disubstituted 1-acetyl-8-fluoronaphthalenes [20] Jaime-Figueroa et al.[246] studied the $^{TS}J(F, C)$ couplings considered to be transmitted through a C–H bond. Jaime-Figueroa et al. found that in the series [20](Y = H) both the $^5J(F, C)$ and $^6J(F, H)$ couplings are sensitive to the nature of a substituent placed at C_4.
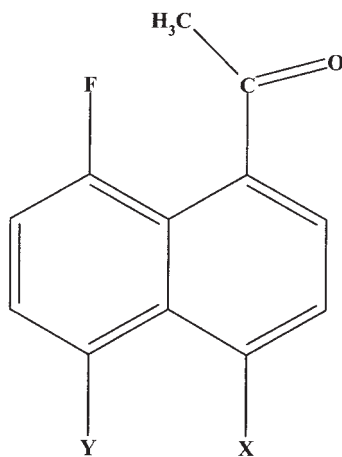
[20]

For such compounds there is a resonance interaction between the acetyl group and substituents of opposite electronic properties that causes θ [21] to be smaller than for X = H, making the distance between F_8 and the CH_3 group also smaller. It should be recalled that the observed couplings correspond to

the average value of those corresponding to each C–H methyl bond. Jaime-Figueroa *et al.*[246] reported values of $^5J(F, C)$ ranging from 10.97 Hz ($X = -N = PPh_3$) to 8.28 Hz ($X = SOCH_3$) while the corresponding $^6J(F, H)$ couplings range from 4.82 to 3.15 Hz. For $X = F$, $^5J(F, C)$ and $^6J(F,H)$ couplings depend on the solvent dielectric constant, ε, both couplings decrease with an increasing ε, which is consistent with a larger θ angle when solutions are prepared in a more polar solvent; they find linear correlations between $^5J(F, C)$ and $^6J(F, H)$ and ε.
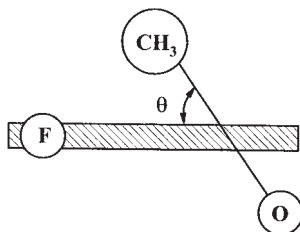
[21]

Melle *et al.*[139] have studied $^{TS}J(F, H)$ and $^{TS}J(F, C)$ couplings in several 5′-*O*-benzyl-2′,3′-dideoxy-4′-(fluoromethyl)-nucleosides (containing either purinic or pyrimidinic nucleobases), corresponding to $^7J(F, H_6)$ and $^6J(F, C_6)$ in the latter and to $^7J(F, H_8)$ and $^6J(F, C_8)$ in the former. These couplings were only observed in the alfa anomers and they depend strongly on solvent. In one of the compounds (with a pyrimidinic nucleobase with an NO_2 group at ring position 5) they measured such couplings in several solvents and they obtained good linear correlations between both measured couplings and the Kamlet-Taft solvatochromic beta parameter, which is taken as an empirical hydrogen bond acceptor scale.[247] They obtained $^7J(F, H_6)$ couplings ranging from 3.10 Hz to 1.61 Hz and $^6J(F, C_6)$ couplings ranging from 9.10 Hz to 4.70 Hz for chloroform and hexamethylphosphoric triamide solutions, respectively. Through-space $^5J(F, H)$ were also observed in 2′-deoxy-2′-fluoro-D-arabinose nucleic acid duplex[248] between the H6/H8 protons and fluorine atoms. Similar couplings were also observed in free nucleotides.[249]

As commented above, for a configuration such as [15] both the sign and absolute value of the corresponding $^{TS}J(F, H)$ coupling depends on α. For $\alpha < \alpha_0$, $^{TS}J(F, H) < 0$, while $^{TS}J(F ,H) > 0$ for $\alpha > \alpha_0$, where α_0 was estimated as $39° \geq \alpha_0 \geq 30°$.[181] One of the interesting features of these two types of couplings, $^{TS}J(F,C)$ and $^{TS}J(F,H)$, is that, although the latter may be close to 0 Hz, i.e., for α close to α_0, the former could show an important value well amenable to measurement. Very interesting examples of such $^{TS}J(F,C_p)$ couplings (11.0, 11.2 and 5.2 Hz, for $X = OMe$, $Y = CH_2CH_2$; $X = H$, $Y = CH_2CH_2$; and $X = H$, $Y = S$, respectively) were reported by

Burgess *et al.*[250] in compounds [**22**] where the corresponding $^{TS}J(F, H)$ couplings could not be observed, i.e., probably, the respective α angles are close to α_0. The seven fused-rings define a non-planar structure. It is interesting to note that the proximity between the F and H atoms yields on the former a de-shielding effect of *ca.* 13 ppm, which resembles the methyl proximity effect on the F chemical shift reported several years ago.[251] The corresponding effect on the H chemical shift is a de-shielding effect of about 0.50 ppm.
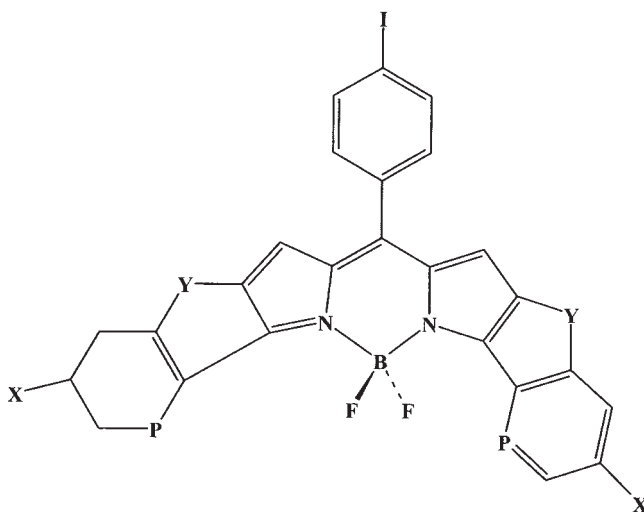
[**22**]

The use of through-space transmitted $J(F, H)$ and $J(F, C)$ couplings to determine the configurational assignments in trifluoromethylvinyl compounds was discussed by Matsubara *et al.*[252] The importance of a C–H bond for mediating the latter coupling was highlighted. $^{TS}J(F, C)$ couplings were reported in dicyanomethylene fluoroarenes in which the F atom is proximate to one of the cyano groups, i.e., these are $^{TS}J(F, C_{sp})$ couplings.

In iridium and rhodium complexes containing fluorinated phenyl ligands like IrCp*(C6F5)Pme3)I and RhCp*(C6F5)Pme3)I important through-space $J(F, H)$ and $J(P, F)$ couplings were reported by Hughes *et al.*[253]

J(F, F) couplings. $J(F, F)$ couplings mainly transmitted through space have continued to be of much interest during the last few years. An interesting review has been published by Gakh *et al.*[254] where the use of fluorine as an NMR probe for structural studies of chemical and biological systems is discussed. They quote various long-range $J(F, F)$ couplings with unusual transmission pathways, some of them taken from the literature and others measured by these authors as part of their work. Among the latter it is worth

while to note the $^5J(F, F) \approx 39$ Hz in 1,4-difluorocubane [**23**]($X = F$) where the $d(C_1\text{–}C_4)$ distance is 2.57 Å and the electronic distribution both within the cubane cage and in the cubane faces cannot explain, according to Gakh *et al.*,[254] the existence either of a through-space or a through-bond transmission. Apparently,[254] a similar mechanism should be operating for $^7J(F, F) = 2.8$ Hz in difluorodiadamantane [**24**]. Gakh *et al.*[254] have also reported the $^nJ(F, C)$ couplings $(n = 1, 2, 3, 4)$ in three 4-derivatives of 1-flourocubane and highlighted the large values measured for $n = 4$ when $X = F$, Cl, I, which were rationalized as transmitted through a similar mechanism as $^5J(F, F)$ ($X = F$). However, it is noted that similar very large halogen substituent effects were reported and studied[255,256] in $^3J(C_1, H_3)$ couplings in X-bicyclo[1.1.1]-pentanes and such large values were rationalized as originating in the multipath additivity for the transmission of the FC interaction. Therefore, it would not be surprising if those large values for $^4J(F, C_4)$ and $^5J(F, F)$ in 1,4-difluorocubane originate in a multiple-path connecting the coupled nuclei.

[23]   [24]
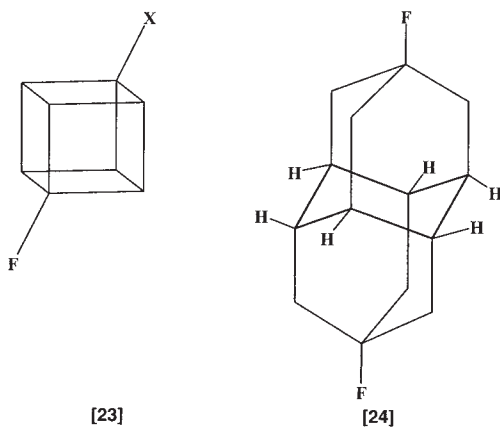
Previously Ernst *et al.* studied $J(F, F)$ couplings transmitted through-space in several fluorinated derivatives of cyclophanes[257–261] and correlated them with the corresponding $d(F\text{–}F)$ distance, obtaining

$$^{TS}J(F, F) = 275,000\exp[-0.0321d(F\text{–}F)] \qquad (19)$$

where $^{TS}J(F, F)$ is in Hz and $d(F\text{–}F)$ is in pm. The main features of the $^{TS}J(F, F)$ in difluorinated cyclophanes were discussed in a review article by Ernst,[245] for instance, in compound [**25**] the sign of $^{TS}J(F, F)$ was determined to be positive (+42.1 Hz). Besides, Eq. (19) depends much more strongly on $d(F\text{–}F)$ than a similar equation obtained by Hilton and Sutcliffe[262] many years before,
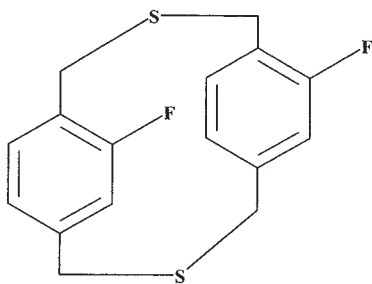
[25]

$$^{TS}J(F, F) = 6800\exp[-0.0199d(F–F)] \tag{20}$$

Continuing that study, Ernst and Sakhaii[263] measured J(F, F) couplings in a series of 1-(x-fluorophenyl)-8-(y-fluorophenyl)naphthalenes (x, y = 2, 3, 4). [26]. They observed inter-ring J(F, F) couplings which are supposed to be transmitted through space. Interring J(F, F) couplings were also reported by Espinet et al.[264] in cis-Bis(bromotetrafluorophenyl)palladium(II) complexes. Espinet with other co-authors[265] have measured strong $^{TS}J(F, F)$ couplings between endo ortho fluorine atoms in dinuclear azolato-bridged complexes of the nickel group with haloaryl ligands. In complexes of ruthenium II, Ru(dppe)(CO)$_2$(OSO$_2$CF$_3$)$_2$ and Ru(dppe)(CO)(H$_2$O)(OSO$_2$CF$_3$)$_2$, $^{TS}J(F, F)$ couplings were reported by Mahon et al.[266]
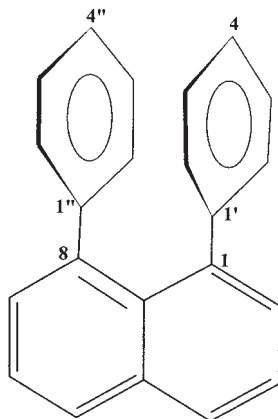
[26]

Mallory et al.[134] have reported peri-J(F, F) couplings in a set of eighteen compounds related structurally to 1,8-difluoronaphthalene [27]. They correlated these peri-J(F, F) couplings with the distance between both coupled nuclei, d(F–F), obtaining
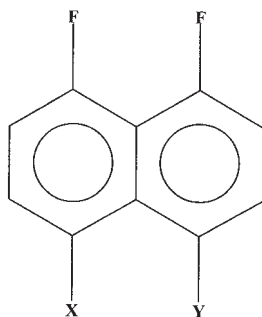
[27]

$$J(F, F) = (1.703 \times 10^7) \exp[-4.960 d(F\text{–}F)] \tag{21}$$

and, although many experimental points fall well within such a curve, it is also conspicuous that a few compounds are outliers, e.g., [27] with X and Y: –CPh=CPh–; –CH=CH–; –C(=NOH)–C(=NOH)– and –(2,3-quinoxaline)–, respectively. Oldfield *et al.*[167] have studied $^{TS}J(F, F)$ couplings within the DFT framework using the deMon-NMR program.[66–69] They take into account the FC (evaluated within the FPT approach), the PSO (evaluated at the SOS approach) and the DSO terms. As a test case, Oldfield *et al.*[167] took *cis* and *trans* conformers [28-a,b] of perfluoropropenone where experimental values are known for $^4J(F_1, F_2)$, i.e., 84.5 Hz and 2 Hz, respectively;[267] their calculated values are, respectively, 83.0 Hz and −0.7 Hz in very good agreement with the experimental values. In order to eliminate all through-bond contributions, Oldfield *et al.*[167] prepared three different model systems with the same d(F–F) distance like in [28a] and with the corresponding F–X vectors having the same direction [29-a,b,c,d].

[28a]   **[28b]**
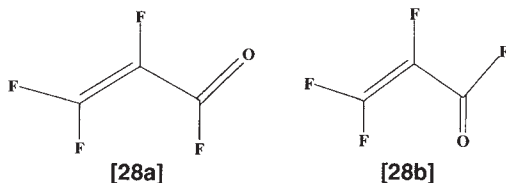
It is interesting to note that the respective values calculated in their (a), (b) and (c) models are $^{TS}J(F, F) = 33.2$ Hz, 55.2 Hz and 71.5 Hz, respectively, i.e., the TS component for the same d(F–F) and the same directions of the F–X vectors, markedly depends on the moieties bonded to each fluorine atom. They also studied the $^{TS}J(F, F)$ component for several *peri* J(F, F) couplings in several of Mallory *et al.*'s[130] compounds using models (b) and (c), and total couplings were studied using 2,4-difluoro-1,3-pentadiene, (d), as a model compound. In all cases the geometries used are the local geometries of Mallory *et al.*'s

compounds optimized at the HF/6-31G(d,p) level. Oldfield *et al.*[167] obtained negative PSO terms for models that take into account only the TS component, but calculations with the (d) model, which includes a possible TB contribution, yield a positive PSO term. However, a different rationalization of such a trend can be found (see below). These results are very interesting since this is the first time that a significant calculated PSO term transmitted through space was reported, although its existence was postulated many years before.[268] Similar results were afterwards reported by Peralta *et al.*[94] and Bryce and Wasylishen.[166] The latter authors performed MCSCF calculations in [CH$_4$–HF] and [CFH$_3$–HF] complexes taken as model systems and considering the configurations (a), (b) and (c) shown in [18-a,b,c]. For conformations (b) and (c) Bryce and Wasylishen find that $^{TS}J(F, F)$ couplings decrease exponentially with the d(F–C) distance, but the respective coefficients differ notably. This suggests that the exponential coefficients are very sensitive to the configurations of both F atoms. Bryce and Wasylishen also report the relative contributions of the FC, DSO, PSO and SD terms; they observe that such relative contributions are very different for configurations (b) and (c). They also discuss the fact that a $^{TS}J(F, F)$ coupling between two proximate moieties cannot be taken as indicative of any covalent bonding between both F atoms. Peralta *et al.*[94] performed DFT calculations in a few of Mallory *et al.*'s[130] compounds taking into account all four isotropic terms within the DFT framework (the FC and SD terms were calculated using the FPT approach and the PSO term was calculated at the CP-KS level) in the actual compounds as well as in the [29-a] model system.

[29]
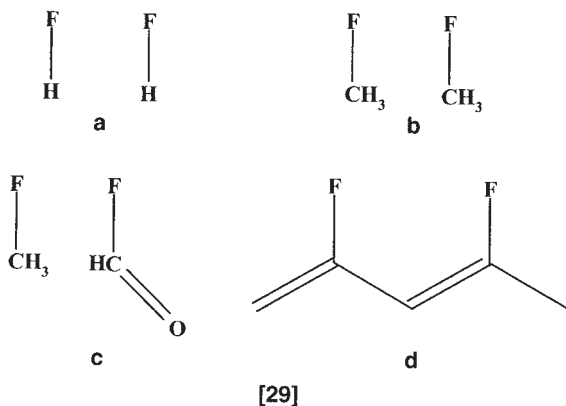
Taking into account all of these data gathered from the current literature an attempt can be made to get some insight on the through space transmission mechanisms of both the FC and the PSO terms of J(F, F) couplings. The former mechanism is discussed in Refs. 12 and 88, using an analysis based on the NJC dissection of the total FC term. A qualitative analysis[82] of the
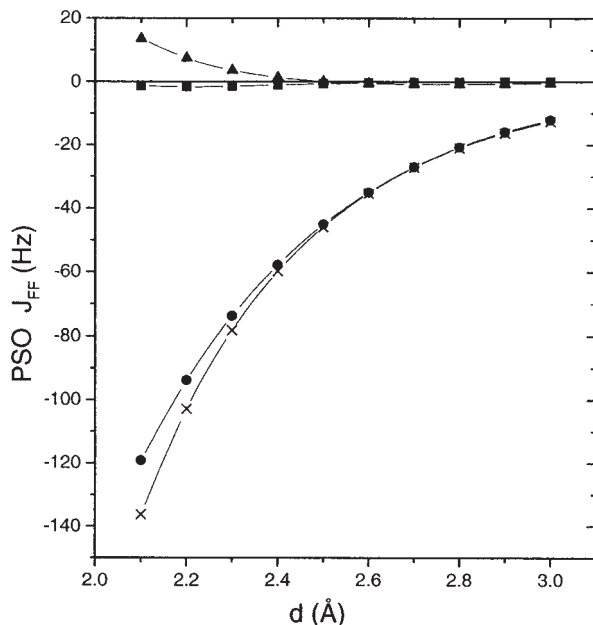
Fig. 1. Dissection of $^{TS}J(F, F)$ PSO term into NLMOs contributions in the HF dimer at the DFT-B3LYP level. :–■– : LP1, –▲– : LP2, – × –: LP3, –●–: Total.

behaviour of the $^{TS}J_{PSO}$ term can be obtained by observing some features of the H_{PSO} perturbative Hamiltonian, Eq. (1b) and considering that J_{PSO} is obtained through second-order perturbation theory. Within the RPA approximation, J_{PSO} can be split into a sum of terms, each depending on two occupied and two vacant LMOs.[1] Besides, since the H_{PSO} operator, Eq. (1b), involves the rotation operator, $(\mathbf{r}_{kA} \times \nabla_k)$, such terms will be significant when there is substantial overlap between an occupied LMO rotated by 90° and a vacant LMO at the site of a chemical bond. This is the case, for instance, of F lone pairs with significant p character and the corresponding (F–X)* antibond. The energy gap, $\Delta\varepsilon$, between these two LMOs is also very important for defining the magnitude of such contributions; such an energy gap depends markedly on the X atom and on its hybridization. Therefore, observing the through-space $J(F, F)_{PSO}$ couplings calculated by Oldfield *et al.*,[167] together with some *ad hoc* calculations,[175] Fig. 1, and the Soncini and Lazzeretti's recent results[124,126] an intuitive description of the through-space transmission of the PSO term for $J(F, F)$ couplings is obtained. According to Soncini and Lazzeretti[126] the analysis of the transmission mechanism for the PSO term should be based on the conservation of the electronic angular momentum induced in the whole molecule due to the nuclear magnetic moments of the coupled nuclei. As quoted above, Oldfield *et al.*[167] used a few model systems, [**29-a,b,c**], to study the through-space component of $^4J(F, F)$ couplings in perfluoropropenone and

in a few of the *peri*-difluoronaphthalene analogs studied by Mallory *et al.*[130] It is important to note that in these models the arrangement of the coupled nuclei is similar, defining a configuration that can be dubbed of type **U** although in some cases commented on below it does not correspond to a planar one. In model [**29-a**] *ad hoc* CP-KS calculations[175] of the PSO contribution to the J(F, F) coupling were carried out for different d(F–F) distances and the results thus found are plotted in Fig. 1 where the corresponding NJC contributions are also shown. It should be noted that in this model system both fluorines are symmetric; for this reason, each NJC contribution is the sum of the equivalent terms of each monomer. It is observed that, although $^{TS}J(F, F)_{PSO}$ decreases with the d(F–F) distance, this decay is at a much lower rate than that of the corresponding $^{TS}J(F, F)_{FC}$, which decreases exponentially. For d(F–F) = 3.0 Å, $^{TS}J(F, F)_{PSO} = -12.1$ Hz and by far the main NJC contribution originates in the LP(3) non-bonding electron pairs of both fluorine atoms, which correspond to the NBO orbitals of higher energy. It can be expected that, for a fixed d(F–F) distance, $^{TS}J(F,F)_{PSO}$ should depend on the energy gap, $\Delta\varepsilon$, between the (F–H)* antibonding and the fluorine LP(3) orbital. It is worth noting that when increasing the d(F–F) distance, the s% character of the F–H bond at the F atom also increases and thus the energy gap between the LP(3) lone pair and the (F–H)* antibonding orbital becomes larger. A couple of values for the [**29-a**] model are as follows: for d(F–F) = 2.1 Å, $\Delta\varepsilon = 0.8242$ a.u. and for d(F–F) = 3.0 Å, $\Delta\varepsilon = 0.8415$ a.u. It is interesting to compare Oldfield *et al.*'s $^{TS}J_{PSO}$ results for the perfluoropropenone models [**29-a,b,c**], i.e., considering the same d(F–F) distance and the same orientation of the F–X vector as given in these author's work. These $^{TS}J_{PSO}$ values are, for model (c), -11.0 Hz, for model (b), -33.7 Hz and for model (a), -46.5 Hz. It should be noted that the electronegativity of the atom bonded to F decreases along this series. This is consistent with the trend quoted above for the $\Delta\varepsilon$ gap behaviour, i.e., when increasing $\Delta\varepsilon$ the corresponding $^{TS}J_{PSO}$ becomes more positive. Therefore, it can be expected that for a larger gap (larger X electronegativity) and a similar **U** configuration of the F–X bonds, $^{TS}J_{PSO}$ could be positive. An arrangement similar to that called **U** here, is called the 'proximate arrangement' by Shtarev *et al.*[121]

Barone *et al.*'s[94] calculations of all four Ramsey terms of $^4J(F, F)$ couplings in a few of Mallory *et al.*'s[130] compounds can also complement this rationalization. When analyzing the through space transmission of J(F, F) couplings it is of particular interest to compare the behaviour of the different Ramsey terms for compounds [**27**](X = Y = H) and [**27**](X and Y: –CH=CH–). It is recalled that the latter is the most conspicuous 'outlier' in Mallory *et al.*'s correlation between $^4J(F, F)$ couplings and the d(F–F) distance, Eq. (21) According to Barone *et al.*[94] the 'outlier' condition of [**27**](X and Y: –CH=CH–) is due mainly to the trend of the PSO term. For this reason it is interesting to compare the difference between the major NJC contributions to the PSO term of $^4J(F, F)$ in [**27**](X = Y = H) and [**27**](X and Y: –CH=CH–),

Table 7.   Comparison of the NJC contributions to the PSO term of $^4J(F,F)$ couplings in Mallory's [19]($X=Y=H$) and [19]($X,Y=-C\equiv C-$) compounds at the DFT/B3LYP level

$X,Y=$	H	$-C\equiv C-$
LP1	1.45	2.08
LP2	3.14	9.64
LP3	−2.90	2.08
LP(F) tot	1.69	13.79
Cr(F)	0.01	0.02
Cr(C)	−0.18	−0.17
C–F	2.29	2.71
C–C	0.82	2.14
C–H	0.03	0.01
Total	4.66	18.51

Table 7. Since in both compounds the fluorine atoms are chemically equivalent, each NJC contribution is the sum of equivalent contributions in the left-hand side and right-hand side rings. Fluorine non-bonding electron pairs are numbered as in the NBO approach, i.e., orbitals from lowest to highest energies, or, equivalently, from highest to lowest s% character of the corresponding lone pair. LP(3) corresponds to the two π-type lone pairs, one on each F atom. It is observed that the largest difference in the NJC components comes from the LP(2) contributions, being the next in importance to those of LP(3). Therefore, these contributions must correspond, according to second order perturbation theory, to virtual transitions involving the LP(2) or LP(3) lone pairs and the vacant LMO localized on the corresponding C–F bond. These, according to the qualitative description given above, can be considered approximately equal to the NBO (C–F)* antibonding orbital. This suggests that NJC-PSO contributions involving those from LP(2) and LP(3) correspond to through-space contributions and therefore, the main difference between the PSO terms in [27]($X=Y=H$) and [27](X and Y: –CH=CH–) comes from the difference in the through-space transmission of the PSO terms. Where do these differences come from? All three LP contributions to $^{TS}J_{PSO}(F,F)$ become more positive when going from [27]($X=Y=H$) and [27](X and Y: –CH=CH–). This suggests that the geometry distortion around the C–F bonds in [27](X and Y: –CH=CH–) when compared with the [27]($X=Y=H$) geometry, increases the corresponding $\Delta\varepsilon$ values between the fluorine lone pair orbitals and the (C–F)* antibonding orbitals. It should be recalled that the d(F–F) distance in [27](X and Y: –CH=CH–) is notably larger than in [27]($X=Y=H$). There is also about 2 Hz difference between the C–C contributions. Probably, this difference comes from the difference in aromaticity between these two compounds; in fact while [27]($X=Y=H$) is an aromatic compound, [27](X and Y: –CH=CH–) is an antiaromatic compound. This seems to indicate that the 'outlier' condition of [27]

(X and Y: –CH=CH–) for Mallory *et al.*'s correlation arises mainly from the behaviour of the through space transmitted component of the PSO term. The same paper by Barone *et al.*[94] reported the NJC analysis of the FC term of $^4J(F, F)$ couplings in these compounds analogous to 1,8-difluoro-napthalene. These results are similar to those discussed by Peralta *et al.*[18] when these authors presented the NJC dissection of the FC term within the FPT-DFT calculation of the FC term. Pecul *et al.*[159] have reported MCSCF calculations of $^{TS}J(F, F)$ couplings in the $(FH)_2$ dimer where that coupling is dominated by the PSO term.

Chupakhin *et al.*[269] have reported in several ethyl-1-(2-NR^{1}R^2-3, 3,3-trifluoropropyl)-6,7,8-trifluoro-4-oxoquinoline-3-carboxylates $^{TS}J(F, F)$ couplings between the aromatic F_8 atom and the fluorine atoms at the trifluoromethyl group. In fused fluoroquinolones Charushin *et al.*[270] have reported the experimental absolute values of several interesting $^{TS}J(H, H)$, $^{TS}J(F, H)$ and $^{TS}J(F, F)$ couplings. The latter seem to be transmitted through an unusual coupling pathway since values of $^7J(F_1, F_{11})$ ranging from 3.5 to 4.0 Hz in compounds of the type [30] are observed, while $^6J(F_1, H_{12})$ couplings ranging from 3.3 to 4.0 Hz have also been measured, suggesting for the former a coupling pathway of the type F_1–H_{12}–C_{12}–C_{11}–F_{11}. It must be noted that $^{TS}J(F, F)$ values transmitted through other unusual coupling pathways were reported previously.[1,254,271]

[30]
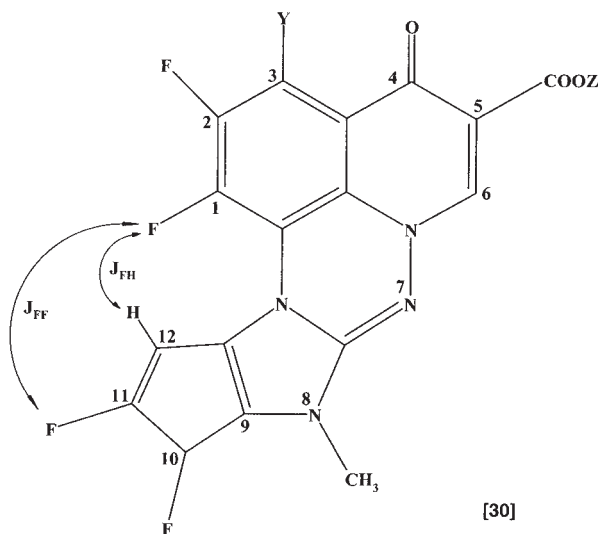
Shtarev *et al.*[121,272] have measured $^4J(F, F)$ proximate couplings, i.e., in a non-planar **U** configuration, in a series of bridge-fluorinated dimethyl bicylo[1.1.1]pentane-1,3-dicarboxylates, [31-a,b], where they obtained values of such couplings ranging from 48.9 to 97.9 Hz (in absolute value). They linearly correlated these couplings with the calculated d(F–F) distance

(optimized at the MP2/6-31G* level) in analogous compounds but where the two bridge-head COOCH$_3$ groups were trimmed and replaced by H atoms. Such a correlation has a negative slope,

[31a]   [31b]
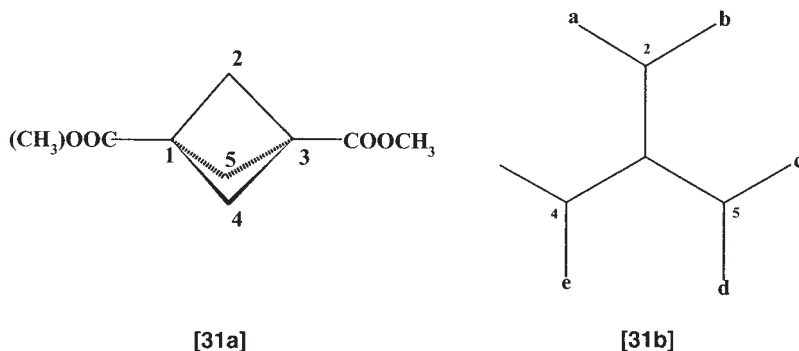
$$|^4J(F, F)(prox)| = -3.20d(F - F) + 872.5, \qquad (22)$$

where d(F–F) is in pm, J in Hz, and the correlation coefficient is 0.978. This linear decrease of the |J(F, F)| coupling with the increase of the d(F–F) distance separating both coupled nuclei suggests that they are dominated by a through space transmission of the PSO term and not by the FC contribution. The PSO term is significantly affected when increasing the number of F atoms bonded to the carbon bridge atoms, which in turn, increases the strain at the bicyclo cage. The larger the strain at the cage substrate, the larger is the carbon s character of the C–F bonds which define the **U** pathway. Such changes in the C–F bond hybridization would affect the corresponding energy gaps between the F lone-pairs and the (C–F)* antibonding orbital. It is very interesting to compare Shtarev *et al.*'s[121] proximate couplings predicted by Eq. (22) with the experimental value of the analogous coupling for the *cis* rotamer of *per*-fluoropropanone [28a], $^4J(F, F) = 84.5$ Hz.[267] According to the [28a] optimized geometry at the B3LYP/6-31G(d,p) level the F–F distance is 2.634 Å.[273] For this F–F distance Eq. (22) yields $^4J(F, F) \approx ca.$ 45 Hz, which is notably smaller than the experimental value. Since in Shtarev *et al.*'s compounds two similar coupling pathways connect the coupled F atoms for the 'proximate' configuration, it suggests that, like the FC term, the PSO contribution would also show an approximate dual-path additivity.

Miscellaneous $^{TS}J(X, Y)$ *couplings.* In 2-OEt,3-CH$_3$-pyrazine [32] $|^3J(N_4, H_{Me})| = 3.11$ Hz and $|^3J(N_1, H_5)| = 1.75$ Hz were reported,[274] the former is notably larger than the latter in spite of being N$_1$ and H$_5$ placed in a *trans* arrangement. This suggests that the $^3J(N_4, H_{Me})$ coupling has an important TS contribution. Howard *et al.*[275] have reported a large through-space $^{TS}J(^{203,205}Tl, H)$ coupling in a dithallium(I) cryptate. Tomoda *et al.* have reported $^{TS}J(Se, F)$ couplings in compounds [33] and [34][276,277] where they find an attractive Se–F interaction. From an experimental point of view they

evaluate weak Se–F interactions by studying the temperature dependence of the $^{TS}J(Se, F)$ coupling and the stabilization mechanisms are analyzed on the basis of the observed solvent effect on that coupling.
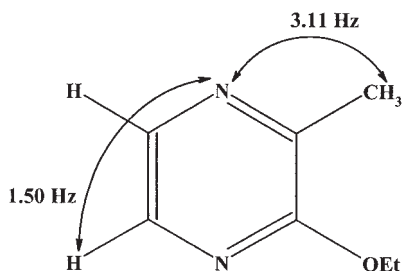
[32]

An NBO[83] analysis shows that the main stabilizing mechanism is the charge delocalization $n(F) \rightarrow (Se-X_{\alpha})^*$ interaction.[276] They report strong solvent effects on $^{TS}J(Se, F)$ couplings, for instance, $^{TS}J(Se, F)$ ranges from 81.8 Hz (C_6D_6) to 39.0 Hz $(DMSO_{d=6})$ in [33](X=CN) and from 23.0 Hz (C_6D_6) to 32.6 Hz $(DMSO_{d=6})$ in [33](X=SeAr), i.e., they show opposite trends. On the other hand, $^{TS}J(Se, F)$ depends strongly on temperature and in [33](X=CN) and in [33](X=SeAr), when using the same solvent, they follow similar trends. Similar Se–N non-bonded interactions were reported previously by the same authors[278] in 2-selenobenzylamine derivatives where they measured J(Se, N) couplings transmitted through the non bonded Se–N interaction as large as 59.3 Hz. Yamaguchi et al.[279] have reported $^{TS}J(C, H)$ couplings transmitted through an intramolecular Sb–N nonbonded interaction in 2-(N,N-dimethyl-aminomethyl)phenyl bis(4-methylphenyl)stibine. Such couplings are assumed to be transmitted through the rather unusual H–C–N–Sb–C pathway. This N–Sb non-bonded interaction yields a high frequency shift of the ^{15}N signal. It is interesting to note that Tomoda et al.[276] also observed a high frequency shift of the F signal in compounds [33] due to the F–Se non-bonded interaction (with the exception of the compound containing the Se–Br moiety, which could be due to a heavy atom effect transmitted through-space).
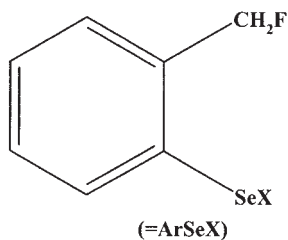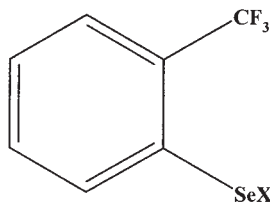
[33]   **[34]**

McFarlane and McFarlane[280] measured $^3J(P, P)$ couplings in a series of *polykis*(diphenylphosphino)benzanes, $(Ph_2P)_nC_6H_{6-n}$. They found that for P^{III} coordinated atoms such couplings are large and vary considerably with steric factors. These authors discussed previously[281] the role played by electron lone-pair relative orientations in defining such couplings. Works dealing with the $^{TS}J(P, P)$ component transmitted through the overlap of lone pairs of both P atoms in similar couplings were discussed previously[147] and no further comment is given here. Schmutzler *et al.*[282] have reported $^{TS}J(P, P)$ couplings in monoxidized sulfur and selenium derivatives of 1,8-bis(diphenylphosphino)-naphthalene (43 and 53 Hz, respectively). In the selenium derivative they also observed the corresponding $^{TS}J(Se, P)$ coupling, 54 Hz. In the crystal structure of the last compound these authors measured for the d(P–P) distance 324.8 pm and for the d(P–Se) distance, 341.1 pm, both of these distances are smaller than the sum of the corresponding van der Waals radii, 380 and 390 pm, respectively. Pétraud, Ratier *et al.*[283] have observed $^{TS}J(P, P)$ couplings in phosphitylated mono- and disaccharide compounds originating from donor–acceptor chelating interactions between phosphorus and oxygen atoms in spatially close dioxaphospholare rings. They report, among others, $^8J(P, P) = 0.4$ Hz and $^6J(P, P)$ couplings ranging from 2.5 to 3.1 Hz.

3.1.1.3. Effects of a proximate moiety on coupling constants

If two molecular fragments are close in space (or two molecules form a complex), coupling constants within each unit may also be affected by the interaction with the second one. When this happens, and enough insight can be obtained into how these couplings are changed, such couplings become interesting probes for the study of conformations and configurations. For instance, it is known[147,160,162,202] that the electrostatic part of the proximity interaction X–H–Y in most cases yields an increase on the corresponding $^1J(Y, H)$ coupling, while a charge transfer interaction of the type $n(X) \rightarrow (Y–H)^*$ yields a decrease on the corresponding $^1J(Y, H)$ coupling. In ordinary hydrogen bonds the latter effect in general predominates, while in weak hydrogen bonds, i.e., contacts where the proton donor, Y, is a carbon atom, X–H–C, in general the electrostatic effect defines the effect on $^1J(C, H)$ couplings.

Afonin *et al.*[284] have carried out a detailed study where it is shown how an adequate knowledge of proximity effects on $^1J(C, H)$ and $^2J(H, H)$ couplings, and of stereospecific effects of lone-pairs on $^1J(C, C)$ couplings are of great help when determining the configurational and comformational preferences of O-vinyl ketoximes [35]. A systematic increase of the $^1J(C, H_f)$ coupling with the sample concentration in CCl_4 was observed by Ribeiro-Claro *et al.*[285] in 4-ethoxybenzaldehyde (where H_f stands for the formyl proton). These authors interpret such a trend as indicative of the increase in $^1J(C, H_f)$ upon dimer formation when increasing the sample concentration. One-, two- and three-bond $J(C, H)$ and $J(C, C)$ couplings in platinum

(IV)-carbohydrate complexes were employed by Steinborn *et al.*[286] to provide new insights into the effect of structure and conformation of saccharides on the magnitudes of such couplings. The effects on the $^1J(N, H)$ couplings of the uridine imino group upon complex formation with adenosine to form either Watson–Crick or Hoogsteen pairs were measured by Weisz *et al.*[287] The effect of complex formation on several intramolecular couplings upon formation of Watson–Crick G–C pairs and of a mismatched base pair G–A of a DNA hairpin was studied experimentally and theoretically by Cremer *et al.*[288] All four isotropic terms of the couplings were evaluated within the DFT-B3LYP framework, where the three second-order terms calculated within the CP-KS formalism.

[35]
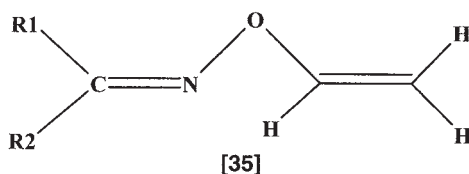
  Pecul and Sadlej[289] have carried out, using a MCSCF wave function, a detailed theoretical study of how spin–spin couplings in the water molecule are affected upon dimer formation. Calculations were performed for the water monomer, the water dimer and each of these two systems surrounded by a dielectric medium. Using the same approach a similar study was carried out in the $(FH)_2$ dimer.[159] Pecul and Sadlej[290] also carried out an LR-MCSCF study of how intramolecular couplings in the ammonia dimer are affected upon dimerization. They studied three different configurations for this dimer, and found that proximity effects on $^1J(N, H)$ couplings in all of these cases correlate with the strength of the corresponding hydrogen bond. They compared such a result with those that they obtained previously for the $(FH)_2$ and $(OH_2)_2$ dimers finding similar trends. Pecul *et al.*[168] carried out a very detailed study of how intramolecular couplings are affected upon complex formation in the model systems $CH_2O–H_2O$, $C_2H_2–OH_2$, $CH_3OH–H_2O$ and $(HCOOH)_2$. In this latter paper they used the same MCSCF method as in the three cited above, and they compared the results thus found taking into account different restricted active spaces with those obtained at the CHF level. For the $CH_2O–H_2O$ molecular complex, the CHF results are completely unreliable which obviously indicates the presence of a HF instability of the non-singlet type in the ground state of formaldehyde, CH_2O, which is very likely to originate in its π-electronic system. It is interesting to note that Pecul *et al.*'s MCSCF results for the absolute value of $^1J(^{17}O, ^1H)$ couplings, corresponding to an O–H bond undergoing an interaction of the type O–H–O, are increased in comparison with the corresponding monomer value. This trend contrasts with the experimental values reported by Chandrasekaran and Boykin[291] in cyclopen-tanol and related compounds where the $^1J(^{17}O, ^1H)$ coupling is found to be

concentration and temperature dependent. This behaviour was rationalized as originating in self-associations due to hydrogen-bond interactions of type O–H–O, in such a way that, with an increase in such interactions, the absolute value of $^1J(^{17}O, {}^1H)$ decreases.

The use of $^1J(C, H)$ couplings as probes to study the binding of imidazole ring ligands to metals was analyzed by Marzilli *et al.*[292,293] An agostic interaction on an aromatic C–H bond was detected by Chaudret *et al.*[294] observing a reduction in the corresponding $^1J(C, H)$ coupling. One bond couplings in rhodium–hydrogen–tin three-centre bonds in compounds of the type [Rh(Cl)(H)(SnPh3)(PPh3)(py)] were studied by Carlton.[295]

In previous papers Juranić *et al.*[296,297] have reported that in a protein main chain $^1J(N, C')$ couplings are sensitive to hydrogen bond formation between peptide groups. Using the present knowledge of $^{3h}J(N, C')$ couplings transmitted through the hydrogen bond network of human ubiquitin, Juranić *et al.*[298] have correlated $^1J(N, C')$ with both $^{3h}J(N, C')$ couplings involving the adjacent peptide groups, [36], and have obtained

$$^1J(N, C')(k, k-1) + 2.74 \, {}^{3h}J(N, C')(k, n-1)$$
$$- 0.88 \, {}^{3h}J(N, C')(m, k-1) - 15.6 = 0 \qquad (23)$$

[36]
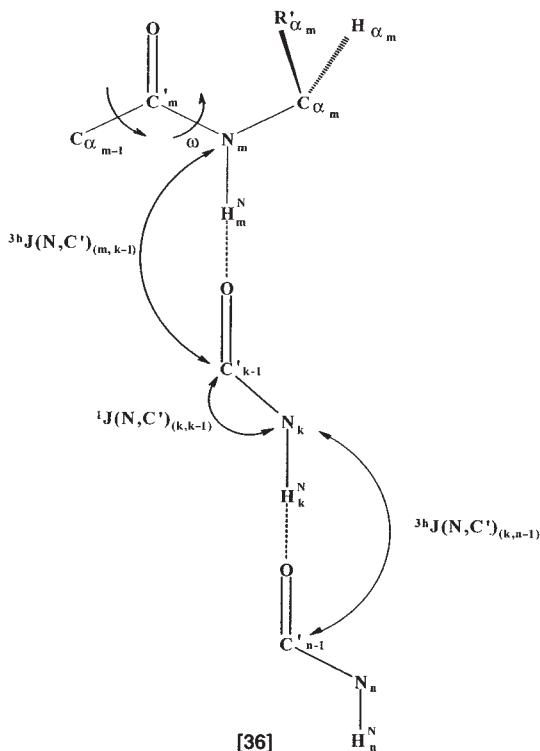
This correlation indicates that variations in the peptide bond electronic structure could affect the value of $^{3h}J(N, C')$ independently of the local hydrogen-bond geometry. This problem was further studied by Juranić et al.[299] in a subsequent paper. They created a comprehensive database of $^{3h}J(N, C')$ and $^1J(N, C')$ couplings by measuring such couplings in ubiquitin (αβ-fold), intestinal fatty acid binding protein (β-barrel) and carp parvalbumin (α-helical). These authors also studied the correlation between $^{3h}J(N, C')(m,k-1)$ and $^{3h}J(N, C')(k,n-1)$ couplings and its positive slope was used as an indication that hydrogen bonds in the network enhance each other, which was taken as experimental evidence for positive hydrogen bond co-operative effects across the peptide groups.[298]

It was observed in alkali metal complexes of a hexafluoro macrocyclic cage compound that the C–F–cation interaction yields a reduction of the absolute value of the corresponding $^1J(F, C)$ coupling. In the case of Cs$^+$ a through-space $^1J(^{133}Cs, F) = 35.1$ Hz was also observed.[300]

3.2. Stereospecific and geometric aspects and substituent effects

Several stereospecific effects on coupling constants were recently reviewed[147] and substantial overlap with this work is avoided. Continuing their extensive study on the anomeric effect Cuevas, Juaristi et al.[70,301] (and references cited therein) have performed DFT calculations of the FC, DSO and PSO terms of $^1J(C, H)$ couplings in cyclohexane, oxygen-, sulfur-, and/or nitrogen-containing six-membered heterocycles and in derivatives of cyclohexanone using the deMon program.[66–69] Such calculations were accompanied with NBO analyses of the hyperconjugative charge transfer interactions that in these compounds can affect such a type of coupling constant. Many of the papers that were published during the review period dealing with conformational and structural aspects of biological compounds include DFT calculations of couplings. This approach allows one to study the angular dependence of many couplings in rather large molecules, increasing the potential of NMR spectroscopy to study different aspects of molecular structures. Malkin et al.[302] used the deMon program[66–69] to study the angular dependence of $^1J(C, H)$ and $^3J(C, H)$ couplings in methyl-β-D-xylopyranoside. In a subsequent paper Malkin et al.[303] studied the stereochemical dependence of $^1J(C_1, H_1)$ and $^3J(C_{Me}, H_1)$ couplings in the α anomer of that carbohydrate. In the same paper they reported measurements of $J(H, H)$ and $J(C, H)$ couplings and observed a good agreement between the calculated and measured values. Comparison between the angular dependences of $^3J(C_{Me}, H_1)$ in both anomers yields a very interesting rationalization of the influence of the anomeric effect on these vicinal couplings. Such a trend is consistent with that observed previously for this type of three-bond coupling.[147] Tähtinen et al.[304] performed FPT-DFT/ B3LYP calculations of the FC term of $^3J(H_4, H_5)$ couplings in cis-fused

7a(8a)-methyl octa(hexa)hydrocyclopenta[d][1, 3]oxazines and [3, 1]benzoxa-zines; the results thus found are compared with experimental values previously measured by Tähtinen with other co-authors.[305]

Several DFT calculations of the structures of carbohydrates and their influence on a variety of spin–spin couplings were published; just a selection of them is quoted here. Serianni, Carmichael *et al.*[76] have studied the behaviour of $J(C, H)$ and $J(C, C)$ couplings in aldofuranosyl rings. These couplings were calculated within the DFT/B3LYP framework, including only the FC term and using the FPT double perturbation approach. These authors have previously calculated the same couplings, using the same perturbative approach, but using the Hartree–Fock approximation as well as other post Hartree–Fock approaches that take into account electron correlation effects. Stereochemical trends of $J(C, H)$ and $J(C, C)$ couplings are quite similar to those they reported previously.[306] The DFT derived Karplus curve for $^3J(C, C)$ couplings they obtained in this paper is quite similar to that calculated previously which was derived from experimental values.[93] In saccharides Serianni, Carmichael *et al.*[307] applied theoretical and experimental approaches to correlate $^2J(H, H)$, $^3J(H, H)$ and $^1J(C, H)$ couplings within the exocyclic hydroxymethyl groups with some molecular parameters. Theoretical calcula-tions of coupling constants including only the FC term, were carried out at the DFT/B3LYP level and equations expressing such correlations for $^2J(H, H)$ and $^3J(H, H)$ were derived. Serianni, Carmichael *et al.*[308] have applied the same approach to study the angular dependence of *trans*-O-glycosidic $^3J(COCH)$ and $^3J(COCC)$ couplings in four model disaccharides. These authors,[309] using the same approach, have studied the stereochemical dependence of two-bond $J(COC)$ couplings across glycosidic linkages. They also applied such an approach to a study of 2-deoxy-β-D-*erythro*-pentofuranose the hydromethyl group conformation and the substituent effects on molecular structure calculating one-, two- and three-bond $J(C, H)$ and $J(C, C)$ couplings. Carmichael, Serianni *et al.*[310] have used the same approach to study how one-, two- and three-bond $J(C, H)$ and $J(C, C)$ couplings are affected by the $O \rightarrow N$ substitution and by N-protonation. To this end, they studied the effect of an amino group substitution at the C_1 position in aldofuranosyl rings and in 2-deoxy-β-D-*erythro*-pentofuranylamine both in its unprotonated and proto-nated forms. The conformational flexibility of a disaccharide was studied by Widmalm *et al.*[311] using experimental *trans*-glycosidic couplings and molecular dynamics simulations.

The study of pseudorotating ring molecules has received much attention during the last part of this review period.[312–315] Cremer *et al.*[312] formulated a new Karplus equation for a pseudorotating five membered ring. CP-DFT calculated couplings are expanded as a function of the puckering amplitude q and the pseudorotation angle ϕ. This approach was applied to cyclopen-tane,[312] and tetrahydrofuran.[315] Shortly afterwards, Wu and Cremer[314] presented a new approach for determining the conformational features of

pseudorotating rings. This approach was dubbed DORCO, determination of ring conformations, and it can be used to determine the most stable conformations of puckered rings by comparing measured with calculated CP-DFT couplings. Chertkov *et al*. performed a complete analysis of the proton spectra of *trans*-1,2-dibromocyclopentane and *trans*-1,2-dichlorocyclopentane.[315]

A DNA decamer was studied by measuring the relevant J(H, H) couplings.[316] J(H, H) couplings for α-anomers of C_5-substituted 2′-deoxyuridines were measured by Remin *et al*.[317] and they were compared with the corresponding values in their β-anomers.

Static and dynamic effects on three-bond couplings in proteins and peptides were studied by Case, Scheurer and Brüschweiler[318] using as model systems Ace-Ala-NMe and Ala-Ala-NH_2. Couplings were calculated using the SOS-DFT approach as implemented in the deMon program[66–69] which includes only the FC, PSO and DSO terms. To take into account dynamic effects DFT calculations were performed on snapshots taken from a molecular dynamics simulation of ubiquitin at room temperature and considering water as solvent. Zetta *et al*.[319] observed $^1J(^{14}N, ^1H)$ couplings when performing a conformational study of a collagen peptide using ^1H NMR spectroscopy. Bouř *et al*.[320] calculated J(H, H) couplings to study the conformation of the dipeptide cyclo(L-Pro-L-Pro). SOS-DFT and CP-DFT values for different conformations were compared with experimental values measured as part of the same work. The largest differences observed for the two theoretical approaches were found for *geminal* couplings. They observed that the DFT-calculated couplings are a convenient and more universal alternative to the use of conventional empirical techniques based on the Karplus equations.

Plots of $J(C_3, OH)$ vs. $J(C_1, OH)$ were used in [37] as probes to monitor tautomerism.[321] $^1J(N, H)$ and $^3J(H_N, H)$ couplings were used to study the proton transfer equilibrium in Schiff bases derived from 2-hydroxy-1-naphthaldehyde and 1-hydro-2-acetonaphthone.[322] An example of how to apply the *J-based configuration analysis*[323] for the stereochemical determination of acyclic structures was given by Murata *et al*.,[324] who also presented a method for elucidating the relative configuration of acyclic organic compounds based on two- and three-bond J(C, H) and $^3J(H, H)$ couplings.[325]

[37]
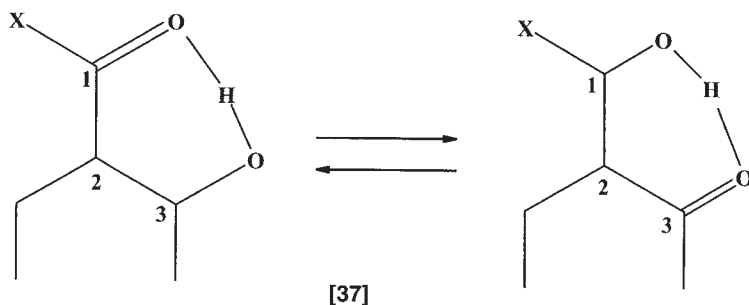
The intramolecular surfaces of all ethane couplings were calculated by Pecul *et al.*[326] using the MCSCF method. In this way, they modified the Karplus equation for the $^3J(H, H)$ coupling by including the influence of the C–C and C–H bond lengths and the CCH angle. The sensitivity of all other ethane couplings to changes in geometrical parameters was also discussed. They observed that 80% of the changes in $^1J(C, C)$ induced by the internal rotation arises from changes in the PSO term, while changes in the FC term are less than 1% of the total effect. Karplus equation coefficients and their components using self-consistent field and second-order polarization propagator methods, SOPPA[47,327] and SOPPA(CCSD),[47,328] were calculated by Grayson and Sauer.[116] These coefficients were compared with those obtained by other *ab initio* calculations and with those derived from experimental data. Among the former, should be quoted those obtained with the MCSCF approach by Pecul *et al.*[326] and by Guilleme *et al.*[329]

During the last few years several types of coupling constants were used frequently as probes to study stereochemical aspects. Variations of $^1J(C_\alpha, C_\beta)$ couplings in polypeptides were found by Case *et al.*[72] to correlate with the backbone conformation. These authors found that deviations of this coupling from those measured in the corresponding free amino acid can be correlated to the backbone conformation through

$$\Delta[^1J(C_\alpha, C_\beta)] = 1.3 + 0.6\cos(\psi - 61°) + 2.2\cos[2(\psi - 61°)]$$
$$- 0.9\cos[2(\phi + 20°)] \pm 0.5\,\text{Hz} \qquad (24)$$

where ϕ and ψ are the intra-residue polypeptide backbone torsion angles. DFT calculations performed[72] on the peptide analogue Ace-Ala-NMe for both $^1J(C_\alpha, C_\beta)$ and $^1J(C_\alpha, H_\alpha)$ as a function of ψ for some fixed ϕ values are in good agreement with experimental couplings, although their absolute values are too small, by about 3 Hz for the former and about 10 Hz for the latter.

$^3J(X, Y)$ couplings have continued to be the ones most commonly used in stereochemical analyses, especially in biological compounds like proteins, nucleosides and carbohydrates. The best known stereospecific relationship for coupling constants continues to be the Karplus equation,[330–332] which relates *vicinal* $J(X, Y)$ couplings transmitted through a saturated fragment X–Z_1–Z_2–Y with the corresponding torsion angle around the Z_1–Z_2 bond. Several modifications have been introduced in order to take into account different effects; some of them were decribed previously[147,333] and others are commented on in this section.

For a coupling pathway through a peptide bond, a new Karplus equation has been reparameterized[334] for $^3J(H_N, H_\alpha)$ couplings,

$$^3J(H_N, H_\alpha) = 7.90\cos^2(\phi - 60°) - 1.05\cos(\phi - 60°) + 0.65\,(\text{in Hz}) \qquad (25)$$

and its performance compared[335] with that parameterized by Hu and Bax[336] where the respective coefficients are 7.09, -1.42 and 1.55 Hz. Löhr et al.[337] presented a method to improve the measurement of $^3J(H_i^\alpha, N_{i+1})$ couplings in H_2O dissolved proteins and, with values thus measured, they parameterized a Karplus-type curve in terms of the backbone torsion angle ψ,

$$^3J(H_i^\alpha, N_{i+1}) = -1.00\cos^2(\psi - 120°) + 0.65\cos(\psi - 120°) - 0.15 \,(\text{in Hz}) \quad (26)$$

Perera and Bartlett[338] used N-methylacetamide as a model peptide fragment and considered its *cis*- and *trans*-conformations [**38**] to calculate $^3J(H_N, H_\alpha)$ as a function of the torsion angle around the N–Me bond, ϕ.

cis   *trans*
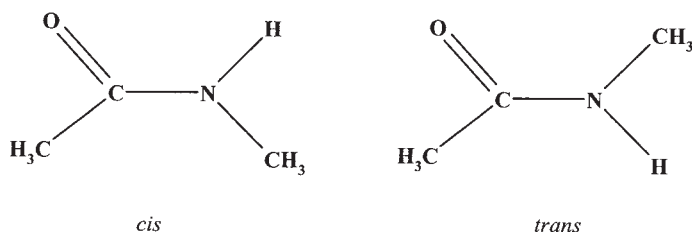
[**38**]

Fitting the calculated values with a Karplus-like equation, they obtained:

$$^3J(H_N, H_\alpha) = (8.09 \pm 0.42)\cos^2\varphi - (1.17 \pm 0.16)\cos\varphi + (0.70 \pm 0.31) \quad (27)$$

$$^3J(H_N, H_\alpha) = (9.27 \pm 0.20)\cos^2\varphi - (1.19 \pm 0.08)\cos\varphi + (0.69 \pm 0.15) \quad (28)$$

for the *trans* and *cis* rotamers, respectively. Coupling constants were calculated with the EOM-CC(SD) method.[45] Perera and Bartlett compared the coefficients thus found with those reported in the literature.[339–344]

Sugar-base $^3J(C, H)$ couplings were studied[345] by considering purine and pyrimidine nucleosides. The authors performed SOS DFT calculations using the deMon code[66–69] for different values of the glycosidic torsion angle χ ranging from 0° to 360° (χ is defined as the O_4–C_1'–N_1–C_2 torsion in pyrimidine and O_4–C_1'–N_9–C_4 torsion in purine nucleosides). They fitted calculated values with Karplus curves which show different trends for purine and pyrimidine nucleosides. For the former, a 'normal' $^3J(C_6, H_1')_{cis} < {}^3J(C_6, H_1')_{trans}$ relationship was obtained while for the latter this relation is reversed, i.e., $^3J(C_8, H_1')_{cis} > {}^3J(C_8, H_1')_{trans}$. This last result is in agreement with experimental values measured by Sklenář et al.[346] In a subsequent paper Munzarová and Sklenář[347] studied, using the deMon code,[66–69] the relationship between the $^3J(C_{2/4}, H_1')$, $^3J(C_{6/8}, H_1')$ and $^1J(C_1', H_1')$ couplings with the torsion angle χ in deoxyribonucleosides and several bicyclo ribonucleosides. All calculated

couplings are in very good agreement with the available experimental data. Munzarová and Sklenář fitted such calculated couplings to Karplus-like equations and discussed the influence of the sugar ring pucker and the hydroxymethyl conformation on such couplings. They also observed that for three-bond couplings Karplus parameters depend strongly on the nucleic acid base involved.

The Karplus relationship for $^3J(C, H)$ couplings was calibrated using experimental data measured in a tethered disaccharide trapped as its *anti* conformer[348] where the ψ glycosidic torsional angle is close to 160°. The observed coupling exceeds the corresponding values calculated using empirically determined Karplus parameters[349–351] but it is smaller than the value obtained by the theoretically determined relationship found by Carmichael *et al.*[308] Houseknecht *et al.*[352] observed discrepancies between couplings obtained with the Carmichael *et al.*[308] Karplus equation and experimental values for torsion angles close to 0° and 180° and prepared a modified version of that equation in order to take into account both the anomeric and electronegative effects on it. They performed DFT calculations using the deMon code[66–69] in model rigid compounds. Houseknecht *et al.* have also scaled DFT calculated values by a factor of 0.833 to improve the agreement with experimental values. This scaling factor is consistent with that obtained previously by Houseknecht *et al.*[353] The resulting equation thus obtained is

$$^3J(C_1, H_4) = 8.14\cos^2\theta - 0.61\cos\theta - 0.15 + G[0.71 - 1.46\{\cos^2(\theta(\xi) + 42G)\}]$$
$$+ H[0.71 - 1.46\{\cos^2(-\theta(\xi) + 42H)\}] \quad (29)$$

where, G and H are the electronegativities of the substituents at C_1 and $\xi = +1$ for α-glycosides and $\xi = -1$ for β-glycosides.

Widmalm *et al.*[354] reported the measurement of $^3J(C, H)$ couplings through glycosidic linkages in β-linked disaccharides and also for vicinally disubstituted trisaccharides. Widmalm with other co-authors[355] reported the measurement of trans-glycosidic $^3J(C, H)$ couplings in the trisaccharide 2′-fucosyllactose.

In proteins, it is reported that $^3J(C_\alpha, H_N)$ and $^3J(C_\alpha, C_\alpha)$ not only depend on ω but also on the ψ torsion angle, behaviour which is referred to as 'non-Karplus-type dependence'[356,357] (see [39]). An empirical Karplus equation was obtained by Bax *et al.*[358] for $^3J(C', C_\beta)$ in ubiquitin using experimental couplings and backbone ϕ angles taken from its crystal structure,

$$^3J(C', C_\beta) = 1.59\cos^2(\phi - 120°) - 0.67\cos(\phi - 120°) + 0.27 \, \text{Hz}. \quad (30)$$

$^3J(C, C)$ couplings through a C–O–C–C pathway were studied, both experimentally and theoretically, in carbohydrates [93] and a Karplus-like relationship

was developed. Calculations were carried out within the DFT framework where only the FC term was taken into account and it was calculated using the perturbative FPT approach using the double perturbation method. The authors found that there are other factors, besides the dihedral angle, that affect the magnitude of such couplings, the main one is the position of terminal electronegative substituents. Apparently, in-pathway oxygens and oxygens appended to internal carbons do not exert a significant influence on the magnitude of $^3J(C,C)$ couplings. These authors propose a simple Karplus equation for *trans*-O-glycoside $^3J(C,C)$ couplings and they discussed the utility of the *trans*-O-glycosidic *geminal* $J(C,C)$ couplings to provide structural information.

A Karplus-like equation for $^3J(F,H)$ couplings was empirically determined by Thibaudeau *et al.*[359] and it was applied[360] to a study of conformations in fluorinated compounds.

Stereospecific trends of $J(F,F)$ couplings are, in general, less well known than those of other couplings involving first-row atoms. Experimental trends of $J(F,F)$ couplings in fluorinated carbohydrate compounds were reviewed by Michalik *et al.*[361] Until recently, it was assumed that $^3J(F,F)$ couplings do not follow a smooth dependence with the F–C–C–F torsion angle, ϕ, in contrast to known trends in several other types of vicinal couplings. It is assumed that such a peculiar behaviour is due to dominating substituent effects. So far there are very few high level *ab initio* calculations of $J(F,F)$ couplings reported in the literature. However, it seems that both in saturated[121] as well as in unsaturated compounds,[82] non-contact mechanisms dominate such couplings. Based on DFT/B3LYP calculations of the FC, SD, PSO and DSO terms in 1,2-difluoroethane, a Karplus-like equation was presented[120] for $^3J(F,F)$ couplings. All four Ramsey terms of the $^3J(F,F)$ couplings depend strongly on the torsion angle (see Fig. 2), each term follows a smooth ϕ dependence but their sum follows an unusual trend. All four terms become very small (in absolute value) for ϕ values close to $90°$. The peculiar behaviour of the total $^3J(F,F)$ coupling is found to be due to the significant non-contact contributions calculated for a torsion angle ranging from 120 to $180°$. However, there is also another interesting feature for this range of torsional angles, namely, the FC contribution is negative. For comparative purposes the Karplus curve for $^3J(H,H)$ in butane, calculated at the same level of theory as in Fig. 2, is presented in Fig. 3. The dissection of the FC term of $^3J(F,F)$ into NJC contributions shows that such a negative value originates in the in-plane lone pair contribution. It is also remarkable that the SD contribution follows a kind of Karplus-type dependence being positive for the *cis* and *trans* conformations of the F atoms, where SD(*cis*) < SD(*trans*).

A Karplus like dependence with the torsion angle for $^3J(P,C)$ couplings has been used for nucleotides.[362] Polak and Plavec[363] have used the Karplus-like dependence of $^3J(H,H)$, $^3J(P,H)$ and $^3J(P,C)$ couplings to determine the
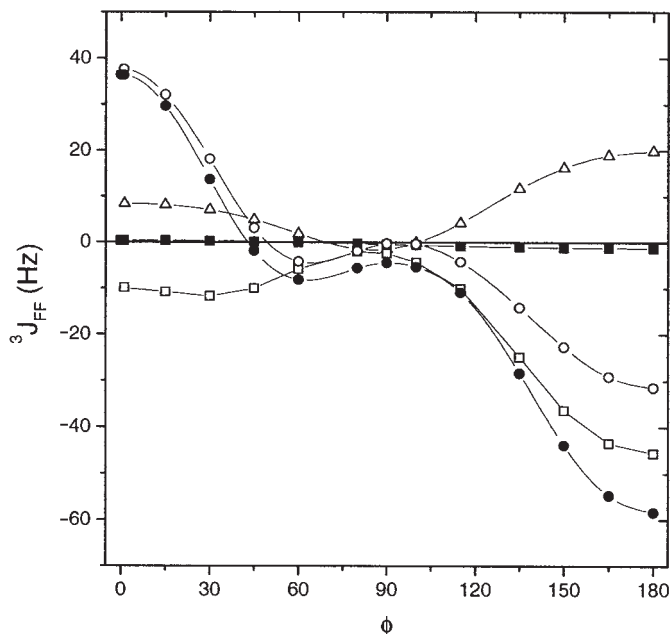
Fig. 2. $^3J(F, F)$ Karplus curve for difluoroethane at the DFT-B3LYP/6-311G** level. –●–: Total, –○– : FC, –△–: SD, –□–: PSO, –■–: DSO.

conformations of 2′-deoxyguanosine 5′-methylmonophosphate, 2′-deoxyguanosine 3′-methylmonophosphate and their interactions with Mg^{2+}, Zn^{2+} and Hg^{2+}. It is known that $^3J(Se, C)$ across $C=N$ double bonds[364] and $^3J(Se, Se)$ couplings of diselenoolefines and tetraselenafulvalenes[365] satisfy the relationship $^3J(cis) > ^3J(trans)$, which is ascribed to a through-space contribution.[147] Poleschner *et al.*[366] have measured *vicinal cis* and *trans* $J(Se, F)$ couplings in 1,1-difluorovinylphenyl selenide, $F_2=CHSePh$, obtaining values of 3.2 and 40.8 Hz, respectively, i.e., they satisfy the 'normal' relationship, $^3J_{cis} < ^3J_{trans}$. These authors have also observed that *trans*-$^3J(Se, F)$ values across a $C=C$ double bond are sensitive to structural aspects since measured values for this type of coupling range from < 1 to 68.5 Hz.

Sproviero and Burton[367] have studied the contribution of stereoelectronic interactions to $^3J(H, H)$ and $^4J(H, H)$ couplings using RPA calculations and NBO analyses. As model compounds they chose ethane, propane, propene and methylcyclopropane.

Structural dependences of $^4J(H, H)$ in propanic and allylic systems were recently studied by Barfield[29] calculating, within the FPT-DFT approach, the FC term of such couplings. In propane Barfield carried out calculations for different values of the dihedral angles about the C_1–C_2 and C_2–C_3 bonds and for different values of the C_1–C_2–C_3 internal angle. Using these calculated values he established a four-term trigonometric expression, which was then
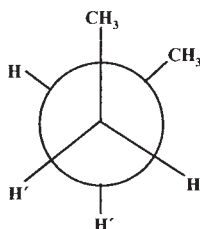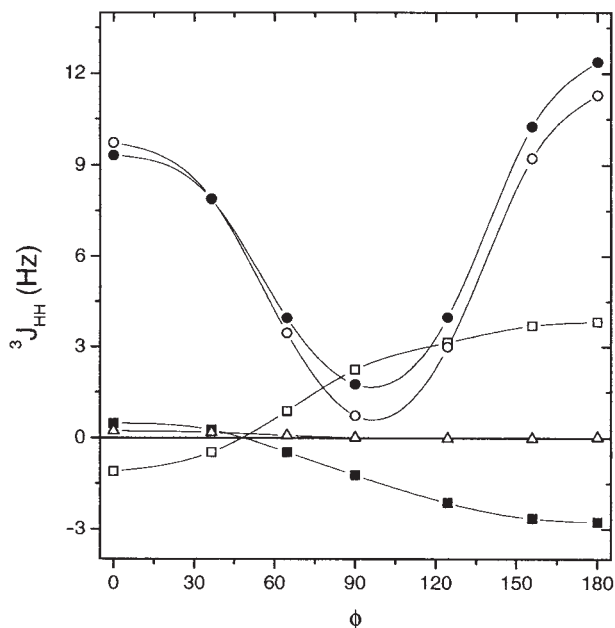
Fig. 3. ^{3}J(H, H) Karplus curve for butane at the DFT-B3LYP/6-311G** level. –●–: Total, –○– : FC, –△–: SD, –□–: PSO, –■–: DSO.

applied to bicycloalkanes, observing that for non-W arrangements of the coupled protons such an expression gives predicted couplings often with signs opposite to those experimentally determined.

Shtarev et al.[121] have measured J(F, F) couplings in a series of bridge-fluorinated dimethyl bicyclo[1.1.1]pentane-1,3-dicarboxylates, [31a], which involve ^{2}J(F, F) and ^{4}J(F, F) couplings. The latter correspond to three different coupling pathways, namely, W, 'sickle' and 'proximate', [31b], (F_a, F_d), (F_a, F_c) and (F_b, F_c), respectively; the last one is discussed above when dealing with ^{TS}J(F, F) couplings. The measured ^{2}J(F, F), ^{4}J(F, F)(W) and ^{4}J(F, F)(sickle) couplings range from 141.5 to 162.0 Hz, 9.7 to 33.5 Hz and 0 to 8.6 Hz, respectively. These geminal couplings are somewhat smaller than those known in other aliphatic CF_2 groups where in general they range from 200 to

350 Hz.[361] However, an interesting set of $^2J(F, F)$ values for aliphatic CF_2 moieties was recently reported[368] in a series of exo-3,3-difluoro-tricyclo[3.2.1.0^{2,4}]octyl drivatives, they range from 145.5 to 163.3 Hz. Such values suggest that $^2J(F, F)$ for aliphatic CF_2 moieties are very sensitive to the strain at the C atom. Apparently, such a strain effect seems to work as an electronegative substituent placed α to the C atom (see next subsection). Shtarev *et al.*[121] also performed EOM-CCSD[45] calculations of $J(F, F)$ in the trimmed difluorinated compound where both F atoms are connected by a **W** pathway, i.e., the bridge-head $COOCH_3$ groups are replaced by H atoms. They calculated $^4J^W(PSO) = -40.7$, $^4J^W(DSO) = -1.3$, $^4J^W(SD) = 3.6$ and $^4J^W(FC) = 1.6$ Hz, i.e., $^4J^{Tot}(F, F) = -36.8$ Hz (experimental value: 29.8 Hz); the whole trend is by far dominated by the PSO term, which is negative in sign.

The structures of highly distorted cage compounds were determined by measuring short- and long-range spin–spin couplings.[369]

Exceptionally small $^1J(C_2, C_3)$ coupling constants were reported by Kamienska-Trela *et al.*[370] in 2-lithiothiophene, 2-lithio-N-methylpyrrol and 2-lithiofuran. These peculiar couplings are accompanied by very large and positive $^2J(C_2, H_3)$ couplings. For instance, in 2-lithiothiophene, $^1J(C_2, C_3) = 27.6$ Hz and $^2J(C_2, H_3) = +21.8$ Hz. Similar effects on $^1J(C_2, C_3)$ in 2-lithiopyridine N-oxide were reported previously,[371] and recently a similar trend was also observed in 1-lithiodiacetylene[372] and in 2-lithiopyridine.[373] In this last work DFT calculations of the FC, PSO and DSO contributions to $^1J(C_2, C_3)$ in several 2-X-pyridine N-oxide and 2-X-pyridines were presented. Unfortunately, the SD term was not considered in this interesting paper since in unsaturated compounds it could have a non-negligible influence. It is interesting to note that the large sensitivity of $^1J(C_2, C_3)$ to the X electronegativity comes through the FC term, being, for instance, $^1J(C_2, C_3)_{PSO} = -6.17$ Hz (2-fluoropyridine); -7.10 Hz (pyridine) and -7.15 Hz (2-lithiopydirine). Such results contrast with calculated values reported (SOPPA, SOPPA(CCSD) and DFT) for $^2J(F, F)$, Table 2, and $^3J(F, F)$ couplings where the respective PSO term is by far the most sensitive of the four Ramsey terms to the electronegativity of the substituent.[82] They also contrast with trends of fluorine substituent effects on calculated $^1J(F, C)$ in CH_3F and CH_2F_2,[374] see Table 8.

Substituent effects on different types of couplings were studied by Aucar *et al.*[42] performing SOPPA (CCSD)[47] calculations in methanimine, ethanimine, methanaloxime and ethanaloxime using the aug-cc-pVTZ-J basis set which was specially designed by the same authors to calculate spin–spin couplings. All four isotropic terms are taken into account, and substituent effects on the orientational nitrogen lone pair effect on one- and two-bond $J(C, H)$, $J(C, C)$ couplings are discussed.

Substituent effects on intermolecular $J(H, H)$ and $J(C, H)$ couplings in van der Waals dimers were studied by Scorrano *et al.*[375] by performing both

Table 8. Fluorine substituent effects on the $^1J(F, C)$ coupling in fluorinated derivatives of methane[a]

	CH_3F	ΔF	CH_2F_2	$\Delta F'$	CHF_3
DSO	+0.42	+0.34	+0.76	+0.43	+1.19
PSO	+35.20	−40.02	−4.82	−20.53	−25.35
SD	+20.21	−7.85	+12.36	−4.69	+7.67
FC	−212.39	−16.62	−229.01	+3.43	−225.58
Total	−156.56	−64.15	−220.71	−21.36	−242.07
Exp.	−163.00	−70.91	−233.91	−38.27	−272.18

[a] Calculated and experimental values taken from Ref. 374.

ab initio (RAS-SCF and SOPPA) and DFT calculations on a few molecular complexes taken as model systems. None of the attempted substitutions, either in the donor π system or in the acceptor C–H bond have affected the through-space spin–spin couplings. Orientation of oxygen substituent effects on $^2J(C, H)$ and $^3J(C, H)$ couplings were studied by Podányi *et al.*[376] measuring such couplings in 12 iridoid glucosides. They introduced corrections to the $^3J(C, H)$ Karplus equation[377] by including additional terms describing the O-substitutions at the α-position and with a simple term describing the O-substitution at β- and γ-carbon atoms.

$^2J(F, F)$ couplings are known to be very sensitive to several factors. For instance, for a coupling pathway of the type F–C_i–F, they depend strongly on the hybridization at the carbon atom, ranging from 10 to 100 Hz for an sp^2 hybridized C_i carbon atom, and from 200 to 350 Hz for an sp^3 hybridization.[361] During this review period very interesting $^2J(F, F)$ couplings were reported in a series of fluorinated oxetanes [40] by Brey and Brey.[378]

[39]
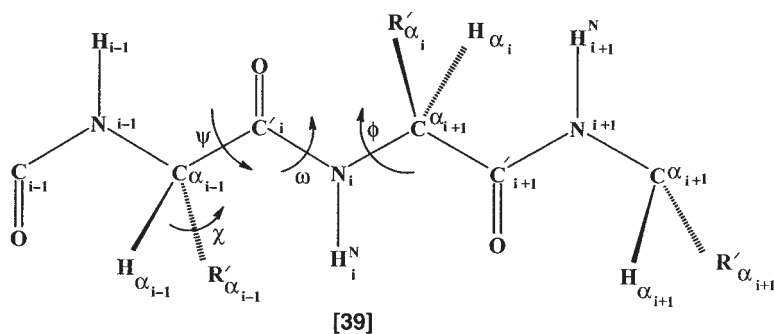
In particular, those with the oxygen atom placed α to C_i show a very large substituent effect. For instance, $^2J(F, F) = 221$ Hz in [40](2CF$_3$)$_2$,3F$_2$,4FH and $^2J(F, F) = 96$ Hz in [40](2CF$_3$)$_2$,3FH,4F$_2$ where it is observed that the α-oxygen atom in the latter causes a reduction of $^2J(F, F)$ to a value smaller than one

half. Similar effects, corresponding to an OH group and to an F atom bonded to C_i, were calculated using both the SOPPA and DFT/B3LYP methods for $^2J(F, F)$ couplings in CHF_2OH and in CHF_3.[82] In this last compound results obtained with the MCSCF method are also known from the literature.[374] From these calculations the large substituent effects can be rationalized as originating in the PSO and SD terms, as they are displayed in Table 2.
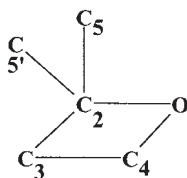
[40]

Sauer et al.[379] studied halogen substituent effects on $^3J(H, H)$ couplings in compounds CH_3CH_2X (X = F, Cl, Br, I) performing calculations of all of the four terms of the scalar couplings, being the FC, PSO and SD terms calculated using the SOPPA method (the DSO as usual is calculated as a first order quantity). They discuss in detail the use of locally dense basis sets in order to optimize the computational time. Comparison between calculated and experimental values is poorer for the heavier halogens. According to calculations carried out in this laboratory[256] this trend could be improved if heavy halogen substituent effects are calculated using electronic core potentials that include some relativistic effects instead of performing all electron calculations.

The effect of the orientation of the lone pairs is in general well known and the main trends were described and classified in detail by Gil and Philipsborn[380] several years ago. Some examples were recently discussed[147] where the FC term for several types of coupling were calculated for different relative orientations between the coupling pathway and the lone pair under consideration (calculations were carried out within the single FPT-DFT/B3LYP framework). A particular case of a lone pair orientation effect on $^1J(C, H)$ couplings is the so called 'anomeric' effect although Reed and Schleyer[381] prefer to call it a 'negative hyperconjugative interaction'. During the last few years this subject has received a good deal of attention and many papers have appeared either discussing special features or using the known trends for stereochemical analyses. The importance of the anomeric effect in carbohydrate structural determination was stressed in a review by Bock et al.[382] and by a long series of works by Juaristi et al. (see cites given in Ref. 301).

The orientational effect of a lone-pair on a proximate C–H bond was discussed some years ago from both experimental[383–385] and theoretical[386]

points of view. During this review period Carmichael *et al.*[310] have discussed a similar lone-pair effect on a C–H bond in 2-deoxy-β-D-ribofuranosylamine. In the same paper these authors discuss the sterochemical dependence of $^1J(C, H)$, $^2J(C, H)$, $^1J(C, C)$ and $^2J(C, C)$ couplings. They carried out calculations of the respective FC term of such couplings using the double-perturbation FPT-DFT/B3LYP approach. Among other topics they discussed changes in the stereochemical dependence of such couplings upon protonation of the NH_2 group. They validated previous suggestions[271] that a different projection rule[387] is required for the interpretation of $^2J(C_2, H_1)$ in nucleosides. Schraml[388] has presented interesting examples of silylated derivatives of hydroxamic acids where the orientation of the N lone pair affects the magnitude of the $^1J(C, C)$ couplings. Aucar *et al.*[50] carried out SOPPA and SOPPA(CCSD) calculations of the four isotropic contributions to scalar couplings in C_2H_4, CH_2NH, CH_2O and CH_2S in order to investigate both the role played by the heteroatom lone-pairs and the electronegativity of the CH_2, NH, O and S moieties. Results thus obtained for C_2H_4 are compared with EOM-CCSD and RAS-SCF values taken from the literature. Small but optimized Gaussian basis sets for calculating scalar couplings are also presented in this paper. The aug-cc-pVTZ-J basis set thus obtained is at present quite promising since good quality scalar coupling calculations can be carried out at a much lower computational cost than using very extended basis sets. This assertion seems to hold not only for post-Hartree–Fock but also for DFT/B3LYP calculations.[51]

For a configuration such as [41a] the lone pair causes an important reduction in the corresponding *vicinal* $^3J(H, H)$. This effect is similar to the known reduction of $^3J(H, H)$ couplings at anomeric carbons.[389]

[41a]   [41b]
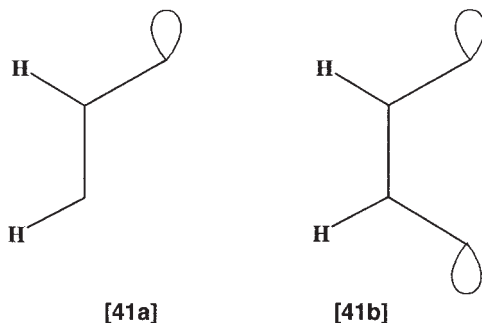
In some furanose rings H_1 and H_2 are virtually eclipsed and the corresponding measured $^3J(H_1, H_2)$ is 3.6 Hz, which is significantly lower than expected (≈ 5.5 Hz) for the 18° torsion angle measured by crystallography.[286] Interesting examples of $^3J(H, H)_{cis}$ couplings are reported by Sommer *et al.*[274] where such a lone-pair effect is notably increased since there are two N non-bonding electron pairs in a similar configuration, [41b]. In fact, in 2-R-pyrazines, [42], they

report $^3J(H_5, H_6)$ values ranging from 2.49 (R = O=CCH$_3$) to 2.83 Hz (R=OCH$_3$). Apparently, this effect originates in a strong negative hypercon-jugation into the three-bond coupling pathway.[147] This rationalization is supported by the small value reported for the *cis*-J(H, H) coupling in formamide [43].
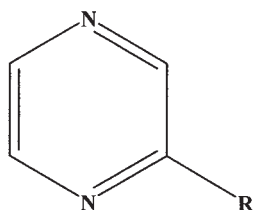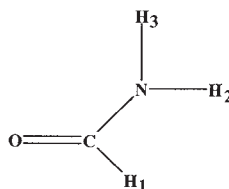
[42]   [43]

In fact, Vaara *et al.*[390] measured 2.25 Hz for *cis*-$^3J(H, H)$ and 13.90 Hz for the *trans*-$^3J(H, H)$ couplings. This last coupling recently was also measured by Farrar *et al.*[391] in a dilute solution of CCl$_4$ and a value of $^3J(H_1, H_3)=+13.7$ Hz is reported. These authors consider that for such solutions, couplings would practically be the same as those corresponding to an isolated formamide molecule. For these two vicinal J(H, H) couplings in [43] there are two strong negative hyperconjugative interactions. They correspond to the $n(p) \rightarrow (C_c–N)^*$ and $n(p) \rightarrow (C_c–H_f)^*$ electron delocalizations, where n(p) stands for the in-plane oxygen lone pair with pure p character. It is interesting to note that, according to the parameterization given by Hu and Bax,[2] for the $^3J(H–N–C–H)$ Karplus-type relationship *cis*-$^3J(H–N–C–H)$ couplings should be 7.22 Hz and *trans*-$^3J(H–N–C–H)$ couplings should be 10.06 Hz. This seems to indicate that the [41a] lone pair effect should correspond to an important reduction of the *cis*-$^3J(H–N–C–H)$ coupling while it should correspond to a proportionally smaller increase for the *trans*-$^3J(H–N–C–H)$ coupling. Probably, these assertions hold for other *vicinal* couplings dominated by the FC interaction.

$^3J(HNCH)$ in methylamine and $^3J(HOCH)$ in methanol were calculated as a function of the respective dihedral angle[392] from a MCSCF wave function. It is observed that, when other geometry parameters are allowed to relax during the internal rotation, these couplings do not change their trends much.

3.3. Medium effects

Since medium effects alter intra-molecular hyperconjugative interac-tions,[147,393,394] which, in turn affect many spin–spin couplings, it can be expected that couplings that are defined by hyperconjugative interactions will

also be sensitive to intermolecular interactions. For this reason an assertion sometimes found in the current literature that medium effects are only sizeable in one-bond couplings should be taken with caution. A case in point is $^2J(N, H)$ in formamide [**43**], where a very large solvent effect was measured recently[395] (see below).

Pecul and Sadlej[396] have studied the influence of electrostatic and dispersion interactions on the spin–spin couplings in acetylene using as model systems the C_2H_2–H^+ and C_2H_2–He complexes. Calculations of the different couplings were carried out at the CAS SCF level and taken as functions of the intermolecular geometry. Changes in all couplings upon complex formation are of opposite signs for complex formations with H^+ and He and are dominated by the FC term. The former complex was taken as a model to study electrostatic and induction effects, while the latter was taken as a model to study the dispersion effects. Shortly afterwards, Jackowski et al.[397,398] measured $^1J(C, C)$, $^1J(C, H)$, $^2J(C, H)$ and $^3J(H, H)$ couplings in 1,2-^{13}C-acetylene at low density in binary mixtures of xenon and carbon dioxide gases, and in some liquid solvents. In this way they determined all couplings in 1,2-^{13}C-acetylene as a function of xenon and of carbon dioxide density, and extrapolating such plots to zero density they could determine all couplings independent of the gaseous solvent. Afterwards, such values were corrected for acetylene–acetylene intermolecular interactions obtaining reliable couplings for an isolated $^{13}C_2H_2$ molecule. They are $^1J(C, C) = 174.78 \pm 0.02$, $^1J(C, H) = 247.56 \pm 0.05$, $^2J(C, H) = 50.14 \pm 0.05$ and $^3J(H, H) = 9.62 \pm 0.05$ Hz. When measuring these parameters using several liquid solvents Jackowski et al. observed that the most sensitive of these couplings is $^1J(C, C)$. When using acetone as solvent they measured $^1J(C, C) = 165.8$ Hz. Shortly afterwards, Jaszuński and Ruud[53] performed very accurate high level ab initio calculations using large CI expansions and very large basis sets for all scalar couplings in acetylene. They compared values thus found with other calculations and with experimental values taken from the literature.[397,399,400] Jaszuński and Ruud[53] also calculated the anisotropy of the corresponding coupling tensors obtaining $\Delta^1J(C, C) = 47.73$, $\Delta^1J(C, H) = -62.61$, $\Delta^2J(C, H) = 30.38$ and $\Delta^3J(H, H) = 3.49$ Hz. Oddershede, Raynes et al.[400] performed detailed SOPPA (CCSD)[47,328] calculations of correlated surfaces for $^1J(C, H)$, $^1J(C, C)$, $^2J(C, H)$ and $^3J(H,H)$ in acetylene [see Section 3.4].

Pecul and Sadlej[96] have studied geometry and solvent effects on the different couplings of methanol and methylamine using a MCSCF wave function. As it could be expected based on known stereochemical dependences of $^1J(C, H)$, $^2J(O, H)$ and $^2J(N, H)$ couplings,[147] it is found that in these two compounds such couplings depend notably on the internal rotation. The changes of these couplings induced by variations in geometry are dominated by the FC term. However, this assertion does not hold for $^1J(O, C)$ in methanol, $^1J(N, C)$ in methylamine and $^1J(C, C)$ in ethane where the geometry-induced changes are dominated by the PSO term.

The reaction field theory is used[96] to simulate the effect of the water environment; the results on how couplings are affected by this medium effect are compatible with the known inhibition of the anomeric effect due to solvent dielectric influence. In this way, it is calculated that in methanol and methylamine only one-bond and $^2J(H, H)$ and $^2J(N, H)$ couplings are affected by the water environment. Changes in such couplings are dominated by the FC term.

Jacowski *et al.*[401] have measured spin–spin couplings in 1-^{13}C-^{15}N-enriched acetonitrile in gaseous mixtures of SF_6 and CO_2 and reported values for couplings free from intermolecular interactions as $^1J(C, N) = -16.20 \pm 0.01$, $^2J(C, H) = -10.18 \pm 0.02$ and $^3J(N, H) = -1.34 \pm 0.02$ Hz. They also measured all $CH_3{}^{13}C^{15}N$ coupling constants in three different liquid solvents, i.e., cyclohexane, acetone and neat acetonitrile. All these values are compared with those calculated by Bartlett *et al.*[402] using the EOM-CCSD approach.[45] Jacowski *et al.*[403] in a subsequent paper completed the measurement of the remaining couplings in gaseous acetonitrile, using as solvents the same gases, i.e., sulfur hexafluoride and carbon dioxide. For a binary mixture of gases Jacowski *et al.*[403] use

$$J(X, Y) = J_0(X, Y) + J_{AA}(X, Y)_{\rho A} + J_{AB}(X, Y)_{\rho B} + \ldots \qquad (31)$$

where, $J_0(X, Y)$ is the coupling between the X and Y nuclei at the zero density limit, and $J_{AA}(X, Y)$ and $J_{AB}(X, Y)$ are solely due to intermolecular effects in the binary collisions A–A and A–B molecules, respectively. They measured for acetonitrile, $^1J_0(C, C) = 60.12 \pm 0.05$ Hz and $^1J_0(C, H) = 134.03 \pm 0.01$ Hz, observing a very good agreement, within the experimental error, for values obtained using both solvents quoted above. They also reported values for the $^1J_{AB}(C, C)$ and $^1J_{AB}(C, H)$ coefficients. Jackowski's team[404] have also measured couplings in gaseous fluoromethane-d$_3$ and determined the first two coefficients in Eq. (31) for $^1J(F, C)$, $^1J(C, D)$ and $^2J(F, D)$. For the respective J_0 coefficients they obtained – 160.75 ± 0.05 Hz, 22.45 ± 0.05 Hz and 7.20 ± 0.05 Hz, which correspond to couplings for an isolated molecule. Jackowski[405] has reviewed the recent results of couplings measured in the gas phase and discussed them in relation to *ab initio* calculations.

Helgaker *et al.*[406] have presented high-level calculations of spin–spin couplings in SeH_2 in vacuum and in different solvents, which were modelled using a continuous dielectric medium. The introduction of the dielectric medium improves the agreement between the calculated $^2J(H, H)$ coupling with experiment. If relativistic effects are taken into account on $^1J(Se, H)$ coupling, which are very large, *ca.* 50 Hz, Helgaker *et al.*'s results compare very favourably with the experimental value. On the other hand, relativistic effects on *geminal* J(H, H) in SeH_2 are found to be of marginal importance. Helgaker *et al.*[407] studied, from a theoretical point of view, solvent effects on spin–spin couplings in SH_2 and HCN. To this end, dielectric solvent effects are taken into

account by a dielectric medium and the couplings are calculated using both Hartree–Fock and MCSCF wave functions. For these two compounds dielectric effects on couplings are found to be substantial, being of a similar magnitude to the rovibrational and electron correlation effects. This continuous model cannot take into account the influence of specific interactions that could take place between solute and solvent.

There is experimental evidence indicating that the anomeric effect is somewhat inhibited when increasing the solvent dielectric constant.[408,409] At this point it is recalled that Schleyer et al.[381] designate the anomeric effect as a negative hyperconjugation interaction n → (X–Y)*, where n is a non-bonding electron pair and (X–Y)* is an antibonding orbital and the magnitude of such an interaction depends, among other factors, on their stereospecific orientation. Since it is known how the anomeric effect affects the FC term of ^{1}J(C, H),[70,301,410] ^{2}J(H, H) and ^{3}J(H, H) couplings,[147] it can be expected that such couplings depend on the solvent dielectric constant. This problem for ^{1}J(C, H) couplings was addressed recently by Zaccari et al.[393] using the PCM model[86,87] to take into account the dielectric solvent effect on the FC, SD and DSO terms of ^{1}J(C, H) couplings, which were calculated within the DFT framework using the hybrid B3LYP functional, and the FPT perturbative approach for the former two terms. Calculations were carried out on compound [44] where experimental ^{1}J(C, H$_s$) and ^{1}J(C, H$_a$) couplings are known.[411,412]
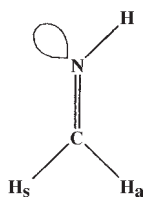
[44]

It is observed that only the latter, ^{1}J(C, H$_a$), is affected by the dielectric solvent effect, while ^{1}J(C, H$_s$) is notably insensitive to such an effect. The former increases monotonically when increasing ε, i.e., the inhibition of the anomeric effect yields an increase in ^{1}J(C, H$_a$); however, a saturation effect is observed for ε close to 10. In the same paper specific interactions between solute and solvent effects were taken into account considering one-to-one complexes for solute and DMSO and one- and two-to-one for solute and water. Dielectric solvent contributions to proximity effects on ^{1}J(C, H) were also considered; it is observed that the dielectric solvent yields a decrease in any of the proximity effects considered in the paper. In a subsequent paper, Zaccari et al.[394] studied medium effects on ^{1}J(C, H) and ^{2}J(C, H) couplings in acetaldehyde, [45], a topic previously studied by Ando et al.[413]
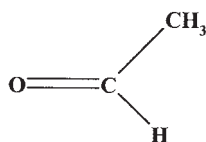
[45]

In Ref. 394 they consider the following effects: the 'direct' solvent dielectric constant on such couplings; the 'indirect' solvent effect due to geometrical changes induced by the solvent dielectric effect, and specific interactions in two different one-to-one solute-DMSO complexes. Geometry changes induced by solvent effects on these last interactions were also considered. It is interesting to note that the absolute value of the experimental solvent effects for these $^1J(C, H)$ and $^2J(C, H)$ are very similar; whence the relative solvent-induced changes are much more important on the $^2J(C, H)$ than on the $^1J(C, H)$ coupling in acetaldehyde. The large solvent effect on this $^2J(C, H)$ coupling is compatible with the solvent dielectric inhibition of the strong negative hyperconjugation that takes place in this compound.

In formamide, [43], Farrar *et al.*[391] reported $^1J(N, H)$ couplings measured in a CCl$_4$ dilute solution, i.e., $^1J(N, H_3) = -87.4$ Hz and $^1J(N, H_2) = -88.3$ Hz. When comparing these values with those reported many years ago in water solution, i.e., $^1J(N, H_3) = -86.93$ Hz and $^1J(N, H_2) = -91.30$ Hz, it suggests that the latter is notably more sensitive to medium effects than the former.

It is emphasized that many spin–spin couplings are very sensitive to negative hyperconjugative interactions.[147] Therefore, it can be expected that such couplings are notably affected by the solvent dielectric constant. The spectrum of ^{15}N-formamide [43], was recently measured by Taha and True[395] in the gas phase at fast exchange rates, in water (5 mol%), tetrachloroethane-d$_2$ (1 mol%), DMSO (1 mol%), and as a neat solution. It is found that $^2J(N, H_f)$ strongly depends on solvent, decreasing its absolute value when increasing the solvent dielectric constant, e.g., in gas phase, $|^2J(N, H_f)| = 20.14$ Hz and in the DMSO solution, 15.30 Hz, i.e., ΔDMSO $= -4.84$ Hz. This coupling was measured in water solution many years ago, and a value of -14.47 Hz was reported.[414] Vaara *et al.*[390] have measured this same coupling in the gas phase and obtain $|^2J(N, H_f)| = 21.5$ Hz at 483 K. It should be recalled that this coupling is a typical *geminal* coupling, $^2J(X, Y)$, through a carbonyl carbon atom, and these are, in general, of an uncommonly large absolute value, being positive provided the magnetogyric ratios of both coupled nuclei are of the same sign, i.e., $^2K(X, Y) > 0$.[415] Such solvent effect on $^2J(N, H_f)$ is similar to that reported years ago by Ando *et al.*[412] in acetaldehyde [45] where, they measured $^2J(C_{Me}, H_f) = 29.54$ and 26.25 Hz in the gas phase and in DMSO, respectively, i.e., ΔDMSO $= -3.29$ Hz. This difference should be compared with that in formamide, taking into account the respective magnetogyric ratios,

i.e., $4.84|\gamma(^{13}C)/\gamma(^{15}N)| = 12.00$ Hz, therefore, $^2J(N, H_f)$ in formamide seems to be more than three times more sensitive to solvent dielectric effects than $^2J(C_{Me}, H_f)$ in acetaldehyde. Apparently, this behaviour can easily be rationalized considering that *geminal* couplings through a carbonyl carbon atom, $^2J(X, Y)$, are greatly increased by *intra*-group $n_p(O) \rightarrow (Cc–X, Y)^*$ negative hyperconjugative interactions[147] and any effect that affects such interactions should alter the corresponding $^2J(X, Y)$ couplings. In particular, when increasing the solvent dielectric constant such negative hyperconjugations should be inhibited causing a reduction of the absolute values of such *geminal* couplings. On the other hand, in formamide the negative hyperconjugation $n_p(O) \rightarrow (Cc–N)^*$ should be notably stronger than the corresponding $n_p(O) \rightarrow (Cc–C)^*$ interaction in acetaldehyde since the $(Cc–N)^*$ antibonding orbital in the former is notably a better electron acceptor than $(Cc–C)^*$ in the latter.[83]

Sychrovský *et al.*[416] have studied solvent effects on one-bond $^1J(X, H)$, $^1J(C, X)$ and two-bond $^2J(X, H)$ (X = X, N) couplings in G•C and G•A nucleic acid base pairs using both the PCM model as implemented by Tomasi *et al.*[417] and an explicit model including both nucleic acids and base pairs solvated by water molecules. Couplings were calculated within the CP-DFT/B3LYP as it is implemented in the COLOGNE 99 program.[214] Calculated couplings are in a significantly better agreement with experimental couplings when solvent effects are taken into account. The largest solvent induced shift is observed for $^1J(C_8, H_8)$ in adenine and guanine.

A new code for calculating solvent effects on scalar couplings evaluated either at HF, MCSCF or DFT levels has been presented by Ruud *et al.*[418] Solvent effects are taken into account using the PCM[86, 419–421] and Ruud *et al.* calculated solvent effects on scalar couplings in benzene within the DFT framework. The results thus obtained are compared with the experimental values.

3.4. Intramolecular dynamics effects

During the last few years nuclear motion effects on coupling constants was studied in several papers[190,422] MCSCF calculations of the rovibrationally averaged spin–spin coupling for the FH molecule were presented by Helgaker *et al.*[423] The four Ramsey contributions of $^1J(F, H)$ were compared for different sizes of the multiconfigurational self-consistent field wave functions. Electron correlation effects are estimated for three second-order Ramsey terms. Rovibrational corrections were obained in a simple manner, employing just one Gaussian function for the vibrational wave function. These authors consider that the precision they obtain is higher than that of the experiment.

Vibrational effects on the $^{2h}J(F, F)$ coupling in FHF^- and FDF^- were studied by Del Bene *et al.*[424] using the EOM-CCSD approach[45] to generate the

^{2h}J(F, F) surface. One interesting feature of these calculations is that the ^{2h}J(F, F) coupling, unlike ^{2h}J(X, Y) (X, Y = N, O, Cl) through hydrogen bonds of the type N–H–N, N–H–O, O–H–O and Cl–H–N, has important PSO and SD contributions. For the equilibrium geometry they obtain ^{2h}J(F, F) = 254.4 Hz, and its expectation value for the ground vibrational state, decreases to 212.7 Hz, which is consistent with the estimated experimental value, 220 Hz. Vibrational averaging of ^{2h}J(N, N) couplings were studied[190] using as a model system, the CNH : NCH complex. The authors presented expectation values for ^{2h}J(N, N) obtained from a two-dimensional EOM-CCSD/(qzp, qz2p) surface. A calculated thermally averaged value of ^{2h}J(N, N) = 6.75 Hz at 298 K is reported. The influence of vibrational and isotopic effects of *trans*-hydrogen bond ^{2h}J(^{35}Cl, ^{15}N) couplings were also studied by Del Bene *et al.*[425] in model complexes of Cl and NH_3. Calculations were also carried out using the EOM-CCSD approach.[45] In order to model different types of hydrogen bonds, i.e., traditional, proton-shared and ion-pair,[173] they perform their study considering external electric fields of 0.0000, 0.0055 and 0.0150 AU, respectively.

Sauer *et al.*[400,426] have calculated, using the SOPPA(CCSD) method, in acetylene, the coordinate and internal valence coordinate coefficients for each of the four coupling surfaces. For this linear compound they give the calculated dependence for all four coupling constants on the different bond lengths and bond angles; all four couplings are found to be sensitive to geometrical parameters. In a similar way as they have reported previously for some couplings in other compounds,[427] (CH_4),[428,237] $(BH_4^-;$ $NH_4^+,$ $SiH_4)$[326] and (C_2H_6) they find an 'unexpected differential sensitivity' for ^{1}J(C, H), which is more sensitive to the $C \equiv C$ bond stretching than to the stretching of the corresponding C–H bond. Calculated couplings at the equilibrium geometry, are compared with other values taken from the current literature. Sauer with other co-authors[429] use the same approach to calculate in the silane molecule the symmetry and internal valence coordinate coefficients for the ^{1}J(Si, H) and ^{2}J(H, H) coupling surfaces. These two couplings are found to be more sensitive to geometry than the analogous couplings in methane. In the same paper these authors report: experimental values for ^{1}J(Si, H) in the silane isotopomers $^{29}SiH_4$, -201.3 ± 0.4 Hz, and $^{29}SiHD_3$, -199.9 ± 0.4 Hz, and for ^{2}J(H, H) in the silane isotopomers $^{29}SiH_3D$, $^{29}SiH_2D_2$ and $^{29}SiHD_3$. The calculated couplings are in excellent agreement with the experimental couplings.

Ruud *et al.*[418] have presented a new estimation for the gas phase ^{1}J(C, H) coupling in benzene for a vibrating molecule at 300 K of 157.46 Hz. Helgaker *et al.*[430] have presented a DFT/B3LYP study of the vibrational corrections to coupling constants. First, they have applied their approach to a set of small molecules where they compare the zero-point-vibration corrections, using different basis sets, to several types of couplings. A similar comparison is made for the same couplings for harmonic and anharmonic

vibrational contributions. Helgaker *et al.*[430] have also generated a list of empirical equilibrium couplings subtracting the vibrational correction from the corresponding experimental values. They also apply their approach to calculate all scalar couplings in benzene as well as their respective empirical equilibrium values.

3.5. Miscellaneous effects and studies

The magnitude of $^1J(^6Li, ^{15}N)$ couplings is very dependent upon the coordination number at the lithium rather than the aggregation state.[431–433] One- and two-bond $J(^{13}C, ^6Li)$, one-bond $J(^{15}N, ^6Li)$ and $^2J(^6Li, ^6Li)$ couplings have been studied.[434] Geometric structures were calculated within the DFT framework and solvent effects were taken into account when determining the organolithium compounds conformation. Calculations were carried out at the HF and MP2 levels and all four terms were included for isotropic contributions. Agreement between calculated and experimental couplings is found provided the aggregation and/or the solvation of such compounds is considered.

The ^1H NMR spectra of several organic compounds were predicted by Bagno[435] by calculating all $J(H, H)$ couplings and proton chemical shifts in each compound. In general, very good agreement with experimental spectra is obtained without resorting to any previous knowledge of the involved parameters. Coupling constants were calculated using the DFT approach of Malkin *et al.*,[66–69] where only the FC, PSO and DSO terms are taken into account. In all cases considered by Bagno,[435] the PSO and DSO terms practically cancel each other; therefore, for the $J(H, H)$ couplings involved in such spectra only the FC term plays a significant role.

When studying the conversion of site-specific deuterated *closo*-1,2-$C_2B_{10}H_{12}$ to deuerated *nido*-7,8-$[C_2B_9H_{12}]^-$ ion Onak *et al.*[436] performed FPT-INDO calculations on this ion. Onak, Jaballas and Barfield[437] calculated, using the FPT-DFT/B3LYP approach, the FC contribution to $^1J(^{11}B, ^1H)$ couplings in polyhedral carboranes and boron hydrides. They obtain a reasonable agreement with experimental couplings, which suggests that this FPT-DFT/B3LYP approach could be of great help for identifying NMR spectra in this type of compound. A few features of $^1J(^{11}B, ^1H)$ couplings in boranes were discussed by Heřmánek in a review paper mainly devoted to boron chemical shifts.[438] Wrackmeyer *et al.*[439] have reported $^1J(^{31}P, ^{11}B)$ and $^1J(^{31}P, ^{31}P)$ couplings in halogenated polyhedral phosphaboranes.

The influence of strain on $^1J(C, C)$ couplings has received some attention during the review period, and few examples are given here. Galasso and Carmichael[440] have performed DFT calculations (only the FC term) for $^1J(C, C)$ couplings corresponding to ultra-short and overlong C–C single bonds

and for compounds with the shortest C–C non-bonding distance, where both coupled C atoms are tetravalent. They obtain very good agreement between calculated and experimental values. Berger *et al.*[441] have measured $^1J(C,C)$, $^1J(C,H)$, $^2J(C,H)$ and $^3J(H,H)$ couplings in four strained alkenes and, surprisingly, they find that the $^1J(C,C)$ couplings through the double-bond are practically not affected. The dihedral C–C=C–C angle in the most strained compound is calculated as 130.7°. They complement such measurements with the DFT calculation of the $^1J(C,C)$ coupling through the double bond. To this end, they employ the Malkin *et al.* approach[66–69] which only takes into account the FC, PSO and DSO terms (it should be noted that, erroneously, in this paper it is quoted that the SD term was calculated). The small differences observed in the calculated couplings originates only in the FC term, although in this case the behaviour of the SD term could be important. In a series of papers Krivdin has carried out calculations of J(C,C) couplings in several strained compounds. In the first paper of this series, Krivdin *et al.*[442] calculated $^1J(C,C)$ couplings in cyclopropane, aziridine and oxirane. For several basis sets calculations were carried out using the SOPPA approach[47,327] and compared with those obtained within the DFT/B3LYP level, using in both approaches the same basis sets. For these three compounds $^1J(C,C)$ couplings of similar quality (compared with experimental values) are obtained when they are calculated with the aug-cc-pVTZ-J[50] basis set. In these three cases the three non-contact contributions are notably smaller than the FC term. It is conspicuous that the convergence of calculated couplings can be appreciated in the SOPPA but not in the B3LYP values reported by Krivdin *et al.*[442] The problem of J coupling DFT calculation convergence with the size of the basis set was recently addressed in detail by Peralta *et al.*[51] In the second paper of this series, Krivdin[443] calculated J(C,C) couplings in bicyclobutane, propellane and spiropentane at the SOPPA level. Particularly interesting are $^1J(C,C)$ couplings involving both bridgehead carbon atoms for the first two compounds. For bicyclobutane Krivdin compares SOPPA results obtained with different basis sets with those obtained at the DFT/B3LYP level and with the experimental value measured in 2,2,4,4-tetramethylbicyclo[1.1.0]butane, −14.39, −17.22 and −17.49 Hz, respectively. In propellane the best SOPPA calculation is +20.67. For this last coupling Pecul *et al.*[444] obtained a value of 21.84 Hz using the CCSD approach as implemented in the Aces II program.[45] In the third paper of this series,[445] Krivdin carried out calculations in tetrahedrane, prismane and cubane obtaining J(C,C) couplings in good agreement with the available experimental values. All these three compounds show a decreased s-characters of their C–C bonds, which is the result of their remarkable steric strain. In these compounds the observed structural trends are governed by the FC term; however, non-contact contributions are far from being negligible. In the fourth member of this series of papers Krivdin presents SOPPA calculations on bicycloalkanes[118] where one-bond and long-range J(C,C), J(C,H) and J(H,H) values are considered giving special emphasis to

the coupling transmission mechanisms at bridgeheads. Geometric input parameters and electron correlation effects on calculated couplings are discussed. Krivdin also derived additive coupling increments for $J(C, C)$, $J(C, H)$ and $J(H, H)$ based on the calculated values of couplings in the model bicycloalkanes. Such increments are in reasonably good agreement with the known values obtained earlier on purely empirical grounds. Non-additive contributions are found to be particularly important for $J(C, C)$ and $J(H, H)$ couplings in bicyclo[1.1.1]pentane. Pecul *et al.*[444] have also calculate all $J(C, C)$, $J(C, H)$ and $J(H, H)$ in bicyclo[1.1.1]pentane. Kamienska-Trela *et al.*[446] have recently reported the measurement of $^1J(C, C)$ couplings in alkylsubstituted cyclopropanes and cyclopropenes, and complemented such measurements with DFT/B3LYP calculated values, which were obtained with the deMon program.[66–69] In the latter compounds they experimentally observed that a $SiPh_3$ group bonded to the sp^2 carbon atom yields an important reduction in the adjacent $^1J(C, C)$ through a formal single bond. Theoretical results reproduce very well this trend where the $SiPh_3$ group is replaced by the silyl one. Jaszuński *et al.*[447] have calculated couplings in bicyclobutane using a series of MCSCF functions and CCSD wave function and values thus obtained are compared with each other. The calculated values are close to the experimental couplings with the exception of $^2J(H, H)$ where the best calculated value is -5.00 Hz, while the experimental value is notably more positive. It is important to recall that this experimental value is consistent with trends discussed elsewhere[147] for *geminal* couplings dominated by the FC term.

Several interesting $J(F, H)$, $J(F, C)$ and $J(F, F)$ couplings in two-carbon chlorofluorocarbons are reported by Béguin *et al.*[448] $J(Si, H)$ couplings in non-classical M–H–Si–X interligand hypervalent interactions are studied in Ref. 449, Wrackmeyer *et al.*[450–453] have observed how the magnitude and sign of $^1J(P, C)$ and $^1J(P, N)$ are dominated by the phosphorus lone pair. In compounds of type $(Me_3Sn)_4M$ (M $= ^{13}C$, ^{29}Si, ^{73}Ge, ^{119}Sn) the signs for reduced one- and two-bond couplings involving M are reported by Wrackmeyer *et al.*[451] These authors find $^1K(Sn, M) > 0$ for all four M nuclei quoted above, on the other hand, they find that $^2K(Sn, M, ^{13}C) > 0$ for M $= ^{13}C$, ^{29}Si, ^{73}Ge but it is negtive for M $= ^{119}Sn$. For *vicinal* couplings of type $^3K(Sn–M–Sn–^{13}C)$ Wrackmeyer *et al.*[121] determine that they are positive for the four kind of atoms quoted above. The same authors[452] have also determined that $^1J(^{119}Sn, ^{73}Ge) = +37$ Hz in $Ge(SnMe_3)_4$. In mononuclear half-sandwich rhodium complexes couplings between the ^{103}Rh nucleus and nuclei belonging to the pentamethylcyclopentadienyl moiety are observed and various relative scalar coupling signs determined.[453] In cyanogold(I) complexes of the type $R_3PAu^{13}C^{15}N$, $^2J(P, C)$ and $^3J(PN)$ couplings through the Au atom are reported by Hussain *et al.*[454] McDermott *et al.*[455] have reported the detection of a scalar $^3J(P, H)$ coupling in a microtesla magnetic field.

Peringer *et al.*[456] have reported values of $^1J(Hg, Hg)$ couplings as large as 284,000 Hz in complexes of $[Hg–Hg]^{2+}$ with crown ethers. In solid state minium, Pb_3O_4, the $Pb^{4+}–Pb^{2+}$ isotropic coupling, $J(Pb, Pb)$, of 2.3 ± 0.1 kHz is reported.[457] The existence of this coupling is suggested to be a result of relativistically enhanced 6s–6p promotion that seems to take place in heavy elements, which results in decreased hybridization efficiency and increased stability of lower oxidation states. It seems that such effects are to be expected for other relativistically bound molecular ions like $[Hg_2]^{2+}$.

The dependence of long-range $^nJ(P, H)$ ($n = 3$, 6, 7) couplings on the bond order between phosphorus and its substituents was discussed for several phosphoramidates.[458]

ACKNOWLEDGEMENTS

REFERENCES

1. R. H. Contreras and J. C. Facelli, *Ann. Rep. NMR Spectrosc.*, 1993, **27**, 255.
2. R. H. Contreras, J. E. Peralta, C. G. Giribet, M. C. Ruiz de Azúa and J. C. Facelli, *Ann. Rep. NMR Spectrosc.*, 2000, **41**, 55.
3. D. A. Case, *Curr. Opin. Struct. Biol.*, 2000, **10**, 197.
4. A. J. Dingley, F. Cordier and S. Grzesiek, *Concepts Magn. Reson.*, 2001, **13**, 103.
5. L. Žídek, R. Štefl and V. Sklenář, *Curr. Opin. Struct. Biol.*, 2001, **11**, 275.
6. K. Pervushin, A. Ono, C. Fernández, M. Kainosho and K. Wöthrich, *Proc. Natl. Acad. Sci., USA*, 1998, **95**, 14147.
7. F. Cordier and S. Grzesiek, *J. Am. Chem. Soc.*, 1999, **121**, 1601.
8. Y. Xia, K. H. Sze and G. Zhu, *J. Biomol. NMR*, 2000, **18**, 261.
9. X. Yan, X. Kong, Y. Xia, K. H. Sae and G. Zhu, *J. Magn. Reson.*, 2000, **147**, 357.
10. A. Liu, A. Majumdar, W. Hu, A. Kettani, E. Skripkin and D. J. Patel, *J. Am. Chem. Soc.*, 2000, **122**, 3206.
11. A. Majumdar and D. J. Patel, *Acc. Chem. Res.*, 2002, **35**, 1.
12. G. Cornilescu, J.-S. Hu and A. Bax, *J. Am. Chem. Soc.*, 1999, **121**, 2949.
13. A. Majumdar, *Magn. Reson. Chem.*, 2001, **39**, S166.
14. S. P. A. Sauer and M. J. Packer, The Ab Initio Calculation of Molecular Properties other than the Potential Energy Surface, *Computational Molecular Spectroscopy*, P. R. Bunker and P. Jensen, eds., Wiley, London, 2000, Chapter 7, pp. 221.
15. T. Helgaker, M. Jaszuński and K. Ruud, *Chem. Rev.*, 1999, **99**, 293.
16. H. Fukui, *Prog. NMR Spectrosc.*, 1999, **35**, 267.

17. G. A. Webb, ed., *Specialist Periodical Reports, Nuclear Magnetic Resonance*, Vols. 28–31, Chapters on applications of spin–spin couplings, The Royal Society of Chemistry, Cambridge, UK, 1999–2002.

18. J. E. Peralta, R. H. Contreras and J. P. Snyder, *J. Chem. Soc. Chem. Commun.*, 2000, , 2025.

19. S. J. Wilkens, W. M. Westler, J. L. Markley and F. Weinhold, *J. Am. Chem. Soc.*, 2001, **123**, 12026.

20. A. Wu and D. Cremer, *J. Am. Chem. Soc.* (in press).

21. J. Autschbach and T. Ziegler, *J. Chem. Phys.*, 2000, **113**, 936.

22. J. Autschbach and T. Ziegler, *J. Chem. Phys.*, 2000, **113**, 9410.

23. P. Pyykkö, *Theor. Chem. Acc.*, 2000, **103**, 214.

24. J. Vaara, J. Jokisaari, R. E. Wasylishen and D. L. Bryce, *Prog. NMR Spectrosc.*, 2002, **41**, 233.

25. M. Barfield, A. J. Dingley, J. Feigon and S. Grzesiek, *J. Am. Chem. Soc.*, 2001, **123**, 4014.

26. J. A. Pople and D. P. Santry, *Mol. Phys.*, 1964, **7**, 269.

27. J. A. Pople and D. P. Santry, *Mol. Phys.*, 1964, **8**, 1.

28. M. Barfield, J. M. Bergset and D. J. O'Leary, *Magn. Reson. Chem.*, 2001, **39**, S115.

29. M. Barfield, *Magn. Reson. Chem.*, 2003, **41**, 344.

30. S. Sabo-Etienne and B. Chaudret, *Chem. Rev.*, 1998, **98**, 2077.

31. D. V. Yandulov, D. Huang, J. C. Huffman and K. Caulton, *Inorg. Chem.*, 2000, **39**, 1919.

32. S. Gründemann, H.-H. Limbach, G. Buntkowsky, S. Sabo-Etienne and B. Chaudret, *J. Phys. Chem. A*, 1999, **103**, 4752.

33. H. Benedict, I. G. Shenderovich, O. L. Malkina, V. G. Malkin, G. S. Denisov, N. S. Golubev and H.-H. Limbach, *J. Am. Chem. Soc.*, 2000, **122**, 1979.

34. A. Castillo, G. Barea, M. A. Esteruelas, F. J. Lahoz, A. LLedós, F. Maseras, J. Modrego, E. Oñate, L. A. Oro, N. Ruiz, E. Solá, *Inorg. Chem.*, 1999, **38**, 1814.

35. J. A. Pople and D. L. Beveridge, *Approximate Molecular Orbital Theory*, McGraw-Hill, New York, 1970.

36. J. A. Pople, J. J. W. McIver and N. S. Ostlund, *J. Chem. Phys.*, 1968, **49**, 2960 and 2965.

37. A. Laaksonen and J. Kowalewski, *J. Am. Chem. Soc.*, 1981, **53**, 5277.

38. A. C. Blizzard and D. P. Santry, *J. Chem. Phys.*, 1971, **55**, 959.

39. J. Oddershede, *Adv. Quantum. Chem.*, 1978, **11**, 275.

40. G. E. Scuseria, A. R. Engelmann and R. H. Contreras, *Theoret. Chim. Acta*, 1982, **61**, 49.

41. R. M. Lobayan and G. A. Aucar, *J. Mol. Struct. (Theochem.)*, 1998, **452**, 13.

42. P. F. Provasi, G. A. Aucar and S. P. A. Sauer, *Int. J. Mol. Sci.*, 2003, **4**, 231.

43. T. Helgaker, M. Watson and N. C. Handy, *J. Chem. Phys.*, 2000, **113**, 9402.

44. S. A. Perera, H. Sekino and R. J. Bartlett, *J. Chem. Phys.*, 1994, **101**, 2186.

45. ACES II program, J. F. Stanton, J. Gauss, J. D. Watts, M. Nooijen, N. Oliphant, S. A. Perera, P. G. Szalay, W. J. Lauderdale, S. R. Gwaltney, S. Beck, A. Balkova, D. E. Bernholdt, K.-K. Baeck, P. Tozyczko, H. Sekino, C. Huber, and R. J. Bartlett. University of Florida, http://www.qtp.ufl.edu/Aces2/.

46. T. Helgaker, H. J. Aa. Jensen, P. Jørgensen, J. Olsen, K. Ruud, H. Ågren, T. Andersen, K. L. Bak, V. Bakken, O. Christiansen, P. Dahle, E. K. Dalskov, T. Enevoldsen, B. Fernandez, H. Heiberg, H. Hettema, D. Jonsson, S. Kirpekar, R. Kobayashi, H. Koch, K. V. Mikkelsen, P. Norman, M. J. Packer, T. Saue, P. R. Taylor and O. Vahtras, DALTON, an electronic structure program. http://www.sdsc.edu/dalton/manual/.

47. T. Enevoldsen, J. Oddershede and S. P. A. Sauer, *Theor. Chem. Acc.*, 1998, **100**, 275.

48. J. Guilleme and J. San Fabián, *J. Chem. Phys.*, 1998, **109**, 8168.

49. T. Helgaker, M. Jaszuński, K. Ruud and A. Górska, *Theor. Chem. Acc.*, 1998, **99**, 175.

50. P. F. Provasi, G. A. Aucar and S. P. A. Sauer, *J. Chem. Phys.*, 2001, **115**, 1324.

51. J. E. Peralta, G. E. Scuseria, J. R. Cheeseman and M. J. Frisch, *Chem. Phys. Lett.*, 2003, **375**, 452.

52. P. Lantto and J. Vaara, *J. Chem. Phys.*, 2001, **114**, 5482.

53. M. Jaszuński and K. Ruud, *Chem. Phys. Lett.*, 2001, **336**, 473.

54. J. San Fabián, J. Casanueva, E. San Fabián and J. Guilleme, *J. Chem. Phys.*, 2000, **112**, 4143.
55. J. Casanueva, J. San Fabián, E. Díez and A. L. Esteban, *J. Mol. Struct.*, 2001, **565–566**, 449.
56. J. San Fabián, J. Casanueva, E. Díez and A. L. Esteban, *Chem. Phys. Lett.*, 2002, **361**, 159.
57. A. A. Auer, J. Gauss and M. Pecul, *Chem. Phys. Lett.*, 2003, **368**, 172.
58. A. A. Auer and J. Gauss, *J. Chem. Phys.*, 2001, **115**, 1619.
59. J. Autschbach and T. Ziegler, *Encyclopedia of NMR*, D. M Grant and R. K. Harris, eds., Supplementary Volume, John Wiley & Sons, Ltd, London, 2002, 306.
60. G. A. Aucar and J. Oddershede, *Int. J. Quantum. Chem.*, 1993, **47**, 425.
61. L. Visscher, T. Enevoldsen, T. Saue, H. J. A. Jensen and J. Oddershede, *J. Comp. Chem.*, 1999, **20**, 1262.
62. L. Enevoldsen, T. Visscher, T. Saue, H. J. Aa. Jensen and J. Oddershede, *J. Chem. Phys.*, 2000, **112**, 3493.
63. S. Kirpekar and S. P. A. Sauer, *Theor. Chem. Acc.*, 1999, **103**, 146.
64. J. Vaara, K. Ruud and O. Vahtras, *J. Comp. Chem.*, 1999, **20**, 1314.
65. R. Romero and G. A. Aucar, *Phys. Rev.*, 2002, **65**, 53411.
66. V. G. Malkin, O. L. Malkina, M. E. Casida and D. R. Salahub, *J. Am. Chem. Soc.*, 1994, **116**, 5898.
67. V. G. Malkin, O. L. Malkina, L. A. Eriksson and D. R. Salahub, *Theoretical and Computational Chemistry*, Vol. 1, *Density Functional Calculations*, P. Politzer and J. M. Seminario, eds., Elsevier, Amsterdam, 1994.
68. G. Malkin, O. L. Malkina, L. A. Eriksson and D. R. Salahub, *Theoretical and Computational chemistry,* Vol. 2, J. M. Seminario and P. Politzer, eds., Elsevier, Amsterdam, 1995, 273.
69. O. L. Malkina, D. R. Salahub and V. G. Malkin, *J. Chem. Phys.*, 1996, **105**, 8793.
70. G. Cuevas, E. Juaristi and A. Vela, *J. Phys. Chem.* A, 1999, **103**, 932.
71. C. Scheurer and R. Brüschweiler, *J. Am. Chem. Soc.*, 1999, **121**, 8661.
72. G. Cornilescu, A. Bax and D. A. Case, *J. Am. Chem. Soc.*, 2000, **122**, 2168.
73. J. Czernek, J. Lang and V. Sklenár, *J. Phys. Chem.* A, 2000, **104**, 2788.
74. J. Kowalewski, *Prog. NMR Spectrosc.*, 1977, **11**, 1.
75. J. Kowalewski, A. Laaksonen, B. Roos and P. Siegbahn, *J. Chem. Phys.*, 1979, **71**, 2896.
76. F. Cloran, I. Carmichael and A. S. Serianni, *J. Phys. Chem.* A, 1999, **103**, 3783.
77. P. Bouř and M. Budesinsky, *J. Chem. Phys.*, 1999, **110**, 2836.
78. V. Sychrovský, J. Gräfenstein and D. Cremer, *J. Chem. Phys.*, 2000, **113**, 3530.
79. V. Barone, J. E. Peralta, R. H. Contreras and J. P. Snyder, *J. Phys. Chem. A*, 2002, **106**, 5607.
80. P. Lantto, J. Vaara and T. Helgaker, *J. Chem. Phys.*, 2002, **117**, 5998.
81. Gaussian 98, Revision A.7; Gaussian, Inc.: Pittsburgh, PA, 1998. M. J. Frisch, G. W. Trucks, H. B. Schlegel, G. E. Scuseria, M. A. Robb, J. R. Cheeseman, V. G. Zakrzewski, J. A. Montgomery Jr., R. E. Stratmann, J. C. Burant, S. Dapprich, J. M. Millam, A. D. Daniels, K. N. Kudin, M. C. Strain, O. Farkas, J. Tomasi, V. Barone, M. Cossi, R. Cammi, B. Mennucci, C. Pomelli, C. Adamo, S. Clifford, J. Ochterski, G. A. Petersson, P. Y. Ayala, Q. Cui, K. Morokuma, D. K. Malick, A. D. Rabuck, K. Raghavachari, J. B. Foresman, J. Cioslowski, J. V. Ortiz, A. G. Baboul, B. B. Stefanov, G. Liu, A. Liashenko, P. Piskorz, I. Komaromi, R. Gomperts, R. L. Martin, D. J. Fox, T. Keith, M. A. Al-Laham, C. Y. Peng, A. Nanayakkara, C. Gonzalez, M. Challacombe, P. M. W. Gill, B. Johnson, W. Chen, M. W. Wong, J. L. Andres, C. Gonzalez, M. Head-Gordon, E. S. Replogle, J. A. Pople.
82. V. Barone, P. F. Provasi, J. E. Peralta, J. P. Snyder, S. P. A. Sauer and R. H. Contreras, *J. Phys. Chem.* A, 2003, **107**, 4748.
83. A. E. Reed, L. A. Curtis and F. Weinhold, *Chem. Rev.*, 1988, **88**, 899.
84. V. Barone, J. E. Peralta, R. H. Contreras, A. V. Sosnin and L. B. Krivdin, *Magn. Reson. Chem. Chem.*, 2001, **39**, 600.
85. M. Barfield, *J. Am. Chem. Soc.*, 1980, **102**, 1.
86. S. Miertuš, E. Scrocco and J. Tomasi, *Chem. Phys.*, 1981, **55**, 117.
87. S. Miertuš and J. Tomasi, *Chem. Phys.*, 1982, **65**, 239.

88. A. J. Dingley, J. E. Masse, R. D. Peterson, M. Barfield, J. Feigon and S. Grzesiek, *J. Am. Chem. Soc.*, 1999, **121**, 6019.

89. J. Vaara, J. Kaski and J. Jokisaari, *J. Phys. Chem.* A, 1999, **103**, 5675.

90. A. D. Becke, *Phys. Rev.*, 1988, **A38**, 3098.

91. C. Lee, W. Yang and R. G. Parr, *Phys. Rev.*, 1988, **B37**, 785.

92. A. D. Becke, *J. Chem. Phys.*, 1993, **98**, 5648.

93. B. Bose, S. Zhao, R. Stenutz, F. Cloran, P. B. Bondo, G. Bondo, B. Hertz, I. Charmichael and A. S. Serianni, *J. Am. Chem. Soc.*, 1998, **120**, 11158.

94. J. E. Peralta, V. Barone, R. H. Contreras, D. G. Zaccari and J. P. Snyder, *J. Am. Chem. Soc.*, 2001, **123**, 9162.

95. M. Fierman, A. Nelson, S. I. Khan, M. Barfield and D. L. O'Leary, *Org. Letts.*, 2000, **2**, 2077.

96. S. A. Perera and R. J. Bartlett, *J. Am. Chem. Soc.*, 2000, **122**, 1231.

97. S. Patchkovskii, J. Autschbach and T. Ziegler, *J. Chem. Phys.*, 2001, **115**, 26.

98. M. Pecul and T. Helgaker, *Int. J. Mol. Sci.*, 2003, **4**, 143.

99. ADF 1999.02, Theoretical Chemistry, Vrije Universiteit, Amsterdam, http://www.scm.com.

100. J. E. Peralta, V. Barone, M. C. Ruiz de Azúa and R. H. Contreras, *Mol. Phys.*, 2001, **99**, 655.

101. J. Khandogin and T. Ziegler, *J. Phys. Chem.* A, 2000, **104**, 113.

102. D. L. Bryce and R. E. Wasylishen, *Inorg. Chem.*, 2002, **41**, 3091.

103. A. Bagno and G. Saielli, *Chem. Eur. J.*, 2003, **9**, 1486.

104. J. Autschbach and T. Ziegler, *J. Am. Chem. Soc.*, 2001, **123**, 3341.

105. J. Autschbach and T. Ziegler, *J. Am. Chem. Soc.*, 2001, **123**, 5320.

106. D. L. Bryce, R. E. Wasylishen, J. Autschbach and T. Ziegler, *J. Am. Chem. Soc.*, 2002, **124**, 4894.

107. D. L. Bryce and R. E. Wasylishen, *Inorg. Chem.*, 2002, **41**, 4131.

108. J. Autschbach, C. D. Igna and T. Ziegler, *J. Am. Chem. Soc.*, 2003, **125**, 1028.

109. J. Autschbach, C. D. Igna and T. Ziegler, *J. Am. Chem. Soc.*, 2003, **125**, 4937.

110. D. L. Bryce and R. E. Wasylishen, *J. Am. Chem. Soc.*, 2000, **122**, 11236.

111. A. D. Buckingham and I. Love, *J. Magn. Reson.*, 1970, **2**, 338.

112. D. L. Bryce and R. E. Wasylishen, *J. Am. Chem. Soc.*, 2000, **122**, 3197.

113. M. Gee, R. E. Wasylishen, K. Eichele and J. F. Britten, *J. Phys. Chem.* A, 2000, **104**, 4598.

114. J. E. Pérez, F. S. Ortíz, R. H. Contreras, C. G. Giribet and M. C. Ruiz de Azúa, *J. Mol. Struct. (Theochem)*, 1990, **210**, 193.

115. V. Galasso, *Chem. Phys.*, 1994, **184**, 107.

116. M. Grayson and S. P. A. Sauer, *Mol. Phys.*, 2000, **98**, 1981.

117. P. Lazzeretti, M. Malagoli, R. Zanasi, E. W. Della, I. J. Lochert, C. G. Giribet, M. C. Ruiz de Azúa and R. H. Contreras, *J. Chem. Soc. Faraday Trans.*, 1995, **91**, 4031.

118. L. B. Krivdin, *Magn. Reson. Chem.*, 2003, **41**, 417.

119. G. E. Scuseria, *Chem. Phys.*, 1986, **107**, 417.

120. S. Kurtkaya, V. Barone, J. E. Peralta, R. H. Contreras and J. P. Snyder, *J. Am. Chem. Soc.*, 2002, **124**, 9702.

121. A. B. Shtarev, E. Pinkhassik, M. D. Levin, I. Stibor and J. Michl, *J. Am. Chem. Soc.*, 2001, **123**, 3484.

122. D. G. de Kowalewski, V. J. Kowalewski, G. Eskuche and R. H. Contreras, to be published.

123. J. C. Facelli, A. M. Orendt, R. H. Contreras, M. F. Tufró and D. G. de Kowalewski, *J. Phys. Chem.*, 1992, **96**, 7895.

124. A. Soncini and P. Lazzeretti, *J. Chem. Phys.*, 2003, **118**, 7165.

125. A. Soncini and P. Lazzeretti, *J. Chem. Phys.*, 2003, **118**, 7165.

126. A. Soncini and P. Lazzeretti, *J. Chem. Phys.*, 2003, **119**, 1343.

127. C. F. Matta, J. Hernández-Trujillo and R. F. W. Bader, *J. Phys. Chem.* A, 2002, **106**, 7369.

128. A. Wu, J. Gräfenstein and D. Cremer, *J. Phys. Chem.* A, submitted for publication.

129. A. Wu and D. Cremer, *Phys. Chem. Chem. Phys.*, 2003, **107**, 7043.

130. F. B. Mallory, C. W. Mallory, K. E. Butler, M. B. Lewis, A. Q. Xia, E. D., Fredenburgh, Jr., L. E. Luzik, M. M. Ramanjulu, Q. N. Va, M. M. Francl, D. A. Freed, C. C. Wray, C. Hann, M. Nerz-Stormes, P. J. Carroll and L. E. Chirlian, *J. Am. Chem. Soc.*, 2000, **122**, 4108.

131. L. Petrakis and C. H. Sederholm, *J. Chem. Phys.*, 1961, **35**, 1243.

132. I. D. Rae, J. A. Weigold, R. H. Contreras and R. R. Biekofsky, *Magn. Reson. Chem.*, 1993, **31**, 836.

133. N. Kobko, L. Paraskevas, E. del Río and J. J. Dannenberg, *J. Am. Chem. Soc.*, 2001, **123**, 4348.

134. I. Alkorta and J. Elguero, *Int. J. Mol. Sci.*, 2003, **4**, 64.

135. F. Löhr, S. G. Mayhew and H. Rüterjans, *J. Am. Chem. Soc.*, 2000, **122**, 9289.

136. M. Mishima, M. Hatanaka, S. Yokoyama, T. Ikegami, M. Walchli, Y. Ito and M. Shirakawa, *J. Am. Chem. Soc.*, 2000, **122**, 5883.

137. B. Luy and J. P. Marino, *J. Am. Chem. Soc.*, 2000, **122**, 8095.

138. F. Cordier and S. Grzesiek, *J. Mol. Biol.*, 2002, **715**, 739.

139. A. Mele, B. Vergani, F. Viani, S. V. Meille, A. Farina and P. Bravo, *Eur. J. Org. Chem.*, 1999, 187.

140. S. Grzesiek, F. Codier and A. J. Dingley, *Methods Enzymol.*, 2001, **338**, 111.

141. E. T. Mollova and A. Pardi, *Curr. Opin. Struct. Biol.*, 2000, **10**, 298.

142. M. Pietrzak, J. Wehling, H.-H. Limbach, N. S. Golubev, C. López, R. M. Claramunt and J. Elguero, *J. Am. Chem. Soc.*, 2001, **123**, 4338.

143. S. J. Wilkens, W. M. Westler, F. Weinhold and J. L. Markley, *J. Am. Chem. Soc.*, 2002, **124**, 1190.

144. G. Náray-Szabó, *Molecular Interactions. From an der Waals to Strongly Bound Complexes*, S. Scheiner, ed., Wiley, New York, 1997, Chapter 10.

145. K. Morokuma, *J. Chem. Phys.*, 1971, **55**, 1236.

146. R. F. W. Bader, *Atoms in Molecules—A Quantum Theory*, Clarendon Press, Oxford, 1990.

147. R. H. Contreras and J. E. Peralta, *Prog. NMR Spectrosc.*, 2000, **37**, 321.

148. A. S. Edison, J. L. Markley and F. Weinhold, *J. Phys. Chem.*, 1993, **97**, 11657.

149. A. S. Edison, J. L. Markley and F. Weinhold, *J. Biomolec. NMR*, 1994, **4**, 519.

150. A. S. Edison, F. Weinhold, W. M. Westler and J. K. Markley, *J. Biomol. NMR*, 1994, **4**, 543.

151. F. R. Salsbury and R. A. Harris, *Mol. Phys.*, 1998, **94**, 307.

152. A. Bagno, G. Saielli and G. Scorrano, *Angew. Chem.*, 2001, **113**, 2600.

153. A. Bagno, G. Saielli and G. Scorrano, *Angew. Chem. Int. Ed.*, 2001, **4**, 2532.

154. M. Pecul, *J. Chem. Phys.*, 2000, **113**, 10835.

155. J. F. Stanton and R. J. Bartlett, *J. Chem. Phys.*, 1993, **98**, 7029.

156. S. A. Perera, M. Nooijen and R. J. Bartlett, *J. Chem. Phys.*, 1996, **104**, 3290.

157. S. A. Perera and R. J. Bartlett, *J. Am. Chem. Soc.*, 1995, **117**, 8476.

158. S. A. Perera and R. J. Bartlett, *J. Am. Chem. Soc.*, 1996, **118**, 7849.

159. M. Pecul, J. Sadlej and J. Leszczynski, *J. Chem. Phys.*, 2001, **115**, 5498.

160. C. G. Giribet, C. V. Vizioli, M. C. Ruiz de Azúa, R. H. Contreras, J. J. Dannenberg and A. Masunov, *J. Chem. Soc. Faraday Trans.*, 1996, **92**, 3029.

161. C. Vizioli, M. C. Ruiz de Azúa, C. G. Giribet, R. H. Contreras, L. Turi, J. J. Dannenberg, I. D. Rae, J. A. Weigold, M. Malagoli, R. Zanasi and P. Lazzeretti, *J. Phys. Chem.*, 1994, **98**, 8858.

162. A. V. Afonin, C. V. Vizioli, M. Ruiz de Azúa and R. H. Contreras, *Bull. Acad. Sci. Russia, Div. Chem. Sci.*, 1996, **45**, 1362.

163. Th. Steiger, S. Gey and R. Radeglia, *Mol. Phys.*, 1975, **30**, 1727.

164. J. Kowalewski, *Annu. Rep. NMR Spectrosc.*, 1982, **12**, 81.

165. W. D. Arnold and E. Oldfield, *J. Am. Chem. Soc.*, 2000, **122**, 12835.

166. D. L. Bryce and R. E. Wasylishen, *J. Mol. Struct.*, 2002, **602–603**, 463.

167. W. D. Arnold, J. Mao, H. Sun and E. Oldfield, *J. Am. Chem. Soc.*, 2000, **122**, 12164.

168. M. Pecul, J. Leszczynski and J. Sadlej, *J. Chem. Phys.*, 2000, **112**, 7930.
169. I. G. Shenderovich, S. N. Smirnov, G. S. Denisov, V. A. Gindin, N. S. Golubev, A. Dunger, R. Reibke, S. Kirpekar, S. Malkina, H. Limbach, *Ver. Bunsen-Ges. Phys. Chem.*, 1998, **102**, 422.
170. I. G. Shenderovich, H.-H. Limbach, S. N. Smirnov, P. M. Tolstoy, G. S. Denisov and N. S. Golubev, *Phys. Chem. Chem. Phys.*, 2002, **4**, 5488.
171. N. S. Golubev, I. G. Shenderovich, S. N. Smirnov, G. S. Denisov and H.-H. Limbach, *Chem. Eur. J.*, 1999, **5**, 492.
172. P. Schah-Mohammedi, I. G. Shenderovich, C. Detering, H.-H. Limbach, P. M. Tolstoy, S. N. Smirnov, G. S. Denisov and N. S. Golubev, *J. Am. Chem. Soc.*, 2000, **122**, 12878.
173. J. E. Del Bene, S. A. Perera and R. J. Bartlett, *J. Am. Chem. Soc.*, 2000, **122**, 3560.
174. J. E. Del Bene and M. J. T. Jordan, *J. Am. Chem. Soc.*, 2000, **122**, 4794.
175. Unpublished results of this laboratory.
176. J. E. Del Bene, S. A. Perera, R. J. Bartlett, I. Alkorta, J. Elguero, O. Mó and M. Yáñez, *J. Phys. Chem.* A, 2002, **106**, 9331.
177. A. J. Dingley and S. Grzesiek, *J. Am. Chem. Soc.*, 1998, **120**, 8293.
178. A. Liu, W. Hu, S. Qamar and A. Majumdar, *J. Biomol. NMR*, 2000, **17**, 55.
179. E. M. B. Janke, A. Dunger, H.-H. Limbach and K. Weisz, *Magn. Reson. Chem.*, 2001, **39**, S177.
180. R. Ishikawa, C. Kojima, A. Ono and M. Kainosho, *Magn. Reson. Chem.*, 2001, **39**, S159.
181. I. D. Rae, J. A. Weigold, R. H. Contreras and G. Yamamoto, *Magn. Reson. Chem.*, 1992, **30**, 1047.
182. R. Wing, T. Takano, K. Itakura and R. E. Dickerson, *Nature*, 1980, **287**, 755.
183. V. Tereshko, G. Minasov and M. Egli, *J. Am. Chem. Soc.*, 1999, **121**, 470.
184. A. St-Amant and D. R. Salahub, *Chem. Phys. Lett.*, 1990, **169**, 387.
185. D. R. Salahub, R. Fournier, P. Mlynarski, I. Papai, A. St-Amant and J. Ushio, *Density Functional Methods in Chemistry*, J. Labanowski and J. Andzelm, eds., Springer, New York, 1991.
186. V. G. Malkin, O. L. Malkina and D. R. Salahub, *Chem. Phys. Lett.*, 1994, **221**, 91.
187. A. Majumdar, A. Kettani, E. Stripkin and D. J. Patel, *J. Biomol. NMR*, 1999, **15**, 207.
188. A. Liu, A. Majumdar, F. Jiang, N. Chernichenko, E. Skripkin and D. J. Patel, *J. Am. Chem. Soc.*, 2000, **122**, 11226.
189. J. E. Del Bene and R. J. Bartlett, *J. Am. Chem. Soc.*, 2000, **122**, 10480.
190. M. J. T. Jordan, J. S.-S. Toh and J. E. Del Bene, *Chem. Phys. Lett.*, 2001, **346**, 288.
191. M. Pecul, J. Leszczynski and J. Sadlej, *J. Phys. Chem.* A, 2000, **104**, 8105.
192. J. E. Del Bene, S. A. Perera and R. J. Bartlett, *J. Phys. Chem.* A, 2001, **105**, 930.
193. J. E. Del Bene, S. A. Perera and R. Bartlett, *Magn. Reson. Chem.*, 2001, **39**, S109.
194. J. E. Del Bene, S. A. Perera, R. L. Bartlett, M. Yañez, O. Mó, J. Elguero and I. Alkorta, *J. Phys. Chem.* A, 2003, **107**, 3121.
195. J. E. Del Bene, S. A. Perera, R. L. Bartlett, M. Yañez, O. Mó, J. Elguero and I. Alkorta, *J. Phys. Chem.* A, 2003, **107**, 3126.
196. D. L. Bryce and R. E. Wasylishen, *J. Biomol. NMR*, 2001, **19**, 371.
197. A. Majumdar, A. Kettani and E. Stripkin, *J. Biomol. NMR*, 1999, **14**, 67.
198. D. Bytchenkoff, E. Chiarparin, D. Fruh, S. Rudisser and G. Bodenhausen, *Magn. Reson. Chem.*, 2002, **40**, 377.
199. K. Pervushin, C. Fernández, R. Riek, A. Ono, M. Kainosho and K. Wüthrich, *J. Biomol. NMR*, 2000, **16**, 39.
200. T. Heinz, O. Moreira and K. Pervushin, *Helv. Chim. Acta*, 2002, **85**, 3984.
201. J. E. Del Bene, S. A. Perera, R. L. Bartlett, M. Yañez, O. Mó, J. Elguero and I. Alkorta, *J. Phys. Chem.* A, 2003, **107**, 3222.
202. C. G. Giribet, M. C. Ruiz de Azúa, C. V. Vizioli and C. N. Cavasotto, *Int. J. Mol. Sci.*, 2003, **4**, 203.

203. A. C. Diz, C. G. Giribet, C. C. Ruiz de Azúa and R. H. Contreras, *Int. J. Quantum Chem.*, 1990, **37**, 663.
204. G. Cornilescu, B. E. Ramirez, M. K. Frank, G. M. Clore, A. M. Gronenborn and A. Bax, *J. Am. Chem. Soc.*, 1999, **121**, 6275.
205. Y.-X. Wang, J. Jacob, F. Cordier, P. Wingfield, S. J. Stahl, S. Lee-huang, D. Torchia and S. Grzesiek, *J. Biomol. NMR*, 1999, **14**, 181.
206. F. Cordier, M. Rogowski, S. Grzesiek and A. Bax, *J. Magn. Reson.*, 1999, **140**, 510.
207. A. T. Alexandrescu, D. R. Snyder and F. Abildgaard, *Protein Sci.*, 2001, **10**, 1856.
208. A. Liu, W. Hu, A. Majumdar, M. K. Rosen and D. J. Patel, *J. Biomol. NMR*, 2000, **17**, 79.
209. A. Liu, W. Hu, A. Majumdar, M. K. Rosen and D. J. Patel, *J. Biomol. NMR*, 2000, **17**, 305.
210. M. Barfield, *J. Am. Chem. Soc.*, 2002, **124**, 4158.
211. P. R. L. Markwick, R. Sprangers and M. Sattler, *J. Am. Chem. Soc.*, 2003, **125**, 644.
212. A. J. Dingley, J. E. Masse, J. Feigon and S. Grzesiek, *J. Biomol. NMR*, 2000, **16**, 279.
213. T. Tuttle, A. Wu, E. Kraka and D. Cremer, *J. Am. Chem. Soc.*, submitted for publication.
214. E. Kraka, J. Grafenstein, J. Gauss, F. Reichel, L. Olsson, Z. Konkoli and D. Cremer, *Program package COLOGNE 99*, Goteborg University, Geteborg, 1999.
215. A. Bagno, *Chem. Eur. J.*, 2000, **6**, 2925.
216. S. P. Brown, M. Pérez-Torralba, D. Sanz, R. S. Claramunt and L. Emsley, *J. Am. Chem. Soc.*, 2002, **124**, 1152.
217. R. M. Claramunt, D. Sanz, S. H. Alarcón, M. Pérez-Torralba, J. Elguero, C. Foces-Foces, M. Pietrzsak, U. Langer and H.-H. Limbach, *Angew. Chem. Int. Ed.*, 2001, **40**, 420.
218. M. Pietrzsak, H.-H. Limbach, M. Pérez-Torralba, D. Sanz, R. M. Claramunt and J. Elguero, *J. Org. Chem.*, 2002, **67**, 1462.
219. M. Pietrzak, H.-H. Limbach, M. Pérez-Torralba, D. Sanz, R. M. Claramunt and J. Elguero, *Magn. Reson. Chem.*, 2001, **39**, S100.
220. D. P. Giedroc, P. E. V. Cornish and M. Hennig, *J. Am. Chem. Soc.*, 2003, **125**, 4676.
221. M. J. T. Jordan and J. E. Del Bene, *J. Am. Chem. Soc.*, 2000, **122**, 2101.
222. J. Bevitt, K. Chapman, D. Crittenden, M. J. T. Jordan and J. E. Del Bene, *J. Phys. Chem.,* A, 2001, **105**, 3371.
223. K. Chapman, D. Crittenden, J. Bevitt, M. J. T. Jordan and J. E. Del Bene, *J. Phys. Chem.* A, 2001, **105**, 5442.
224. K. Szczepaniek, P. Chabrier, W. B. Person and J. E. Del Bene, *J. Mol. Struct.*, 2000, **520**, 1.
225. J. E. Del Bene and M. J. T. Jordan, *Theochem*, 2001, **573**, 11.
226. J. E. Del Bene, S. A. Perera, R. J. Bartlett, J. Elguero, I. Alkorta, C. López-Leonardo and M. Alajarin, *J. Am. Chem. Soc.*, 2002, **124**, 6393.
227. J. Czernek and R. Brüschweiler, *J. Am. Chem. Soc.*, 2001, **123**, 11079.
228. J. E. Del Bene, S. A. Perera, R. J. Bartlett, I. Alkorta and J. Elguero, *J. Phys. Chem.* A, 2000, **104**, 7165.
229. J. Laynez, M. Menéndez, J. L. S. Velasco, A. L. Llamas-Saiz, C. Foces-Foce, J. Elguero, P. Molina and M. Alajarín, *J. Chem. Soc. Perkin Trans.*, 1993, **2**, 709.
230. J. Elguero, A. Fruchier, M. L. Jimeno and P. Molina, *J. Chem. Res. Synop.*, 2002, 34.
231. W. Schilf, B. Kamieński, T. Dziembowska, Z. Rozwadowski and Szady-Chelmíenecka, *J. Mol. Struct.*, 2000, **552**, 33.
232. N. S. Bhacca, G. P. Juneau, D. C. Lankin, B. Mukherjee, T. Seal, J. O. Escobedo and R. M. Strongin, *Org. Letts.*, 2000, **2**, 3813.
233. A. Bagno, G. Casella, G. Saielliand and G. Scorrano, *Int. J. Mol. Sci.*, 2003, **4**, 193.
234. R. H. Contreras, M. A. Natiello and G. E. Scuseria, *Magn. Reson. Rev.*, 1985, **9**, 239.
235. R. E. Waylishen and M. Barfield, *J. Am. Chem. Soc.*, 1975, **97**, 4545.
236. R. H. Contreras, C. G. Giribet, M. A. Natiello, J. Perez, I. D. Rae and J. A. Weigold, *Aust. J. Chem.*, 1985, **38**, 1779.
237. G. Yamamoto and M. Oki, *Tet. Lett.*, 1985, **26**, 457.
238. W. Adcock and S. Q. A. Rizvi, *Aust. J. Chem.*, 1973, **26**, 2659.

239. M. Barfield, S. R. Walter, K. A. Clark, G. W. Gribble, K. W. Haden, W. J.- Kelly and C. S. LeHoullier, *Org. Magn. Reson.*, 1982, **20**, 92.

240. M. A. Natiello and R. H. Contreras, *Chem. Phys. Lett.*, 1984, **104**, 568.

241. J. Weinwald and A. Lewis, *J. Am. Chem. Soc.*, 1961, **83**, 2769.

242. M. Barfield, A. M. Dean, C. J. Fallick, R. J. Spear, S. Sternhell and P. W. Westerman, *J. Am. Chem. Soc.*, 1975, **97**, 1482.

243. P. Szczecinski, *Bull. Polish Acad. Sci.*, 1999, **47**, 25.

244. P. Palmas, J. Thibonnet, J.-L. Parrain, M. Abarbri, F. David-Quillot and A. Duchene, *Magn. Reson. Chem.*, 2000, **40**, 537.

245. L. Ernst, *Prog. NMR Spectrosc.*, 2000, **37**, 47.

246. S. Jaime-Figueroa, L. J. Kurz, Y. Liu and R. Cruz, *Spectrochim. Acta*, 2000, **A56**, 1167.

247. R. W. Taft and M. J. Kamlet, *Magn. Reson. Chem.*, 1980, **14**, 485.

248. J.-F. Trempe, C. J. Wilds, A.Yu. Denisov, R. T. Pon, M. J. Damba and K. Gehring, *J. Am. Chem. Soc.*, 2001, **123**, 4896.

249. C. J. Wilds and M. J. Damha, *Nucleic Acids Res.*, 2000, **28**, 3625.

250. J. Chen, J. Reibenspies, A. Derecskei-Kovacs and K. Burgess, *J. Chem. Soc. Chem. Comm.*, 1999, 2501.

251. G. W. Gribble, D. J. Keavy, E. R. Olson, I. D. Rae, A. Staffa, T. E. Herr, M. B. Ferraro and R. H. Contreras, *Magn. Reson. Chem.*, 1991, **29**, 422.

252. K. Matsubara, A. Oba and Y. Usui, *Magn. Reson. Chem.*, 1998, **36**, 761.

253. R. P. Hughes, R. B. Laritchev, A. Willimason, C. D. Incarvito, L. N. Zakharov and A. L. Rheingold, *Organometallics*, 2002, **21**, 4873.

254. Y. G. Gakh, A. A. Gakh and A. M. Gronenborn, *Magn. Reson. Chem.*, 2000, **38**, 551.

255. E. W. Della, I. J. Lochert, N. M. Peruchena, G. A. Aucar and R. H. Contreras, *J. Phys. Org. Chem.*, 1996, **9**, 168.

256. V. Barone, J. E. Peralta and R. H. Contreras, *J. Comput. Chem.*, 2001, **22**, 1615.

257. L. Ernst and K. Ibrom, *Angew. Chem. Int. Ed.*, 1995, **34**, 1881.

258. L. Ernst, K. Ibrom, K. Marat, R. H. Mitchell, G. J. Bodwell and G. W. Bushnell, *Chem. Ber.*, 1994, **127**, 1119.

259. L. Ernst and K. Ibrom, *Magn. Reson. Chem.*, 1998, **36**, S71.

260. L. Ernst and K. Ibrom, *Magn. Reson. Chem.*, 1997, **35**, 868.

261. L. Ernst and K. Ibrom, *Magn. Reson. Chem.*, 1999, **37**, 441.

262. J. Hilton and L. H. Sutcliffe, *Spectrochim. Acta, A*, 1976, **32**, 201.

263. L. Ernst and P. Sakhaii, *Magn. Reson. Chem.*, 2000, **38**, 559.

264. A. C. Albéniz, A. L. Casado and P. Espinet, *Organometallics*, 1997, **16**, 5416.

265. P. Espinet, A. M. Gallego, J. M. Martinez-Ilarduya and E. Pastor, *Inorg. Chem.*, 2000, **39**, 975.

266. M. F. Mahon, M. K. Whittlesey and P. T. Wood, *Organometallics*, 1999, **18**, 4068.

267. W. S. Bray and K. C. Ramy, *J. Chem. Phys.*, 1963, **39**, 844.

268. V. I. Bakhmutov, M. V. Galakhov and E. I. Fedin, *Magn. Reson. Chem.*, 1985, **23**, 971.

269. A. Ya. Aizikovich, M. V. Nikonov, M. I. Kodess, V. Yu. Korotaev, V. N. Charushin and O. N. Chupakhin, *Tetrahedron*, 2000, **56**, 1923.

270. V. N. Charushin, E. V. Nosova, G. N. Lipunova and M. I. Kodess, *J. Fluor. Chem.*, 2001, **110**, 25.

271. T. Bandyopadhyay, J. Wu, W. A. Stripe, I. Carmichael and A. S. Serianni, *J. Am. Chem. Soc.*, 1997, **119**, 1737.

272. M. D. Levin, S. J. Hamrock, P. Kaszynski, A. B. Shtarev, G. A. Levina, B. C. Noll, M. E. Ashley, R. Newmark, G. G. I. Moore and J. Michl, *J. Am. Chem. Soc.*, 1997, **119**, 12750.

273. Unpublished results from these Laboratories.

274. H. Sommer, H.-J. Bertram, G. E. Krammer, C. O. Schmidt, W. Stumpe, P. Werkhoff and M. Zviely, *Magn. Reson. Chem.*, 2000, **38**, 907.

275. O. W. Howarth, J. Nelson and V. McKee, *J. Chem. Soc., Chem. Comm.*, 2000, 21.

276. M. Iwaoka, H. Komatsu, T. Katsuda and S. Tomoda, *J. Am. Chem. Soc.*, 2002, **124**, 1902.

277. M. Iwaoka, H. Komatsu and S. Tomoda, *Chem. Lett.*, 1998, 969.

278. M. Iwaoka and S. Tomoda, *J. Am. Chem. Soc.*, 1996, **118**, 8077.

279. T. Tokunaga, H. Seki, S. Yasuike, M. Ikoma, J. Kurita and K. Yamaguchi, *Tet. Lett.*, 2000, **41**, 1031.

280. H. C. E. McFarlane and W. McFarlane, *Polyhedron*, 1999, **18**, 2117.

281. H. C. E. McFarlane and W. McFarlane, *Polyhedron*, 1988, **7**, 1875.

282. A. Karaçar, M. Freytag, H. Thönnessen, J. Omelanczuk, P. G. Jones, R. Bartsch and R. Schmutzler, *Z. Anorg. Allg. Chem.*, 2000, **626**, 2361.

283. L. Pouységu, B. De Jéso, J. C. Lartigue, M. Pétraud and M. Ratier, *Magn. Reson. Chem.*, 2000, **38**, 668.

284. A. V. Afonin, I. A. Ushakov, S. V. Zinchenko, O. A. Tarasova and B. A. Trofimov, *Magn. Reson. Chem.*, 2000, **38**, 994.

285. M. P. M. Marques, A. M. Amorin da Costa and P. J. A. Ribeiro-Claro, *J. Phys. Chem. A*, 2001, **105**, 5292.

286. H. Junicke, A. S. Serianni and D. Steinborn, *J. Org. Chem.*, 2000, **65**, 4153.

287. A. Dunger, H.-H. Limbach and K. Weisz, *J. Am. Chem. Soc.*, 2000, **122**, 10109.

288. V. Sychrovský, J. Vacek, P. Hobza, L. Žídek, V. Sklenář and D. Cremer, *J. Phys. Chem. B*, 2002, **106**, 10242.

289. M. Pecul and J. Sadlej, *Chem. Phys. Lett.*, 1999, **308**, 486.

290. M. Pecul and J. Sadlej, *Chem. Phys. Lett.*, 2002, **360**, 272.

291. S. Chandrasekaran and D. W. Boykin, *Heteroatom. Chem.*, 1992, **3**, 63.

292. S. J. Moore, M. Iwamoto and L. Marzilli, *Inorg. Chem.*, 1998, **37**, 1169.

293. S. J. Moore, R. J. Lachicotte, S. T. Sullivan and L. G. Marzilli, *Inorg. Chem.*, 1999, **38**, 383.

294. A. J. Toner, S. Gründemann, E. Clot, H.-H. Limbach, B. Donnadieu, S. Sabo-Etienne and B. Chaudret, *J. Am. Chem. Soc.*, 2000, **122**, 6777.

295. L. Carlton, *Inorg. Chem.*, 2000, **39**, 4510.

296. N. Juranić, K. P. Ilich and S. Macura, *J. Am. Chem. Soc.*, 1995, **117**, 405.

297. N. Juranić, V. A. Likić, F. G. Prendergast and S. Macura, *J. Am. Chem. Soc.*, 1996, **118**, 7859.

298. N. Juranić and S. Macura, *J. Am. Chem. Soc.*, 2001, **123**, 4099.

299. N. Juranić, M. C. Moncrieffe, V. A. Likić, F. G. Prendergast and S. Macura, *J. Am. Chem. Soc.*, 2000, **124**, 14221.

300. H. Takemura, S. Nakashima, N. Kon and T. Inazu, *Tet. Lett.*, 2000, **41**, 6105.

301. G. Cuevas and E. Juaristi, *J. Am. Chem. Soc.*, 2002, **124**, 13088.

302. M. Hricovíni, O. L. Malkina, F. Bízik, L. T. Nagy and V. G. Malkin, *J. Phys. Chem. A*, 1997, **101**, 9756.

303. O. L. Malkina, M. Hricovíni, F. Bízik and V. G. Malkin, *J. Phys. Chem. A*, 2001, **105**, 9188.

304. P. Tähtinen, A. Bagno, K. D. Klika and K. Pihlaja, *J. Am. Chem. Soc.*, 2003, **125**, 4609.

305. P. Tähtinen, J. Sinkkonen, K. D. Klika, V. Nieminen, G. Stájer, Z. Szakonyi, F. Füllöp and K. Pihlaja, *Chirality*, 2002, **14**, 187.

306. T. J. Church, I. Carmichael and A. S. Serianni, *J. Am. Chem. Soc.*, 1997, **119**, 8946.

307. R. Stenutz, I. Carmichael, G. Widmalm and A. S. Serianni, *J. Org. Chem.*, 2002, **67**, 949.

308. F. Cloran, I. Carmichael and A. S. Serianni, *J. Am. Chem. Soc.*, 1999, **121**, 9843.

309. F. Cloran, I. Carmichael and A. S. Serianni, *J. Am. Chem. Soc.*, 2001, **123**, 4781.

310. F. Cloran, Y. Zhu, J. Osborn, I. Carmichael and A. S. Serianni, *J. Am. Chem. Soc.*, 2000, **122**, 6435.

311. C. Höög and G. Widmalm, *J. Phys. Chem. A*, 2000, **104**, 9443.

312. A. Wu, D. Cremer, A. A. Auer and J. Gauss, *J. Phys. Chem. A*, 2002, **106**, 657.

313. A. Wu and D. Cremer, *Int. J. Mol. Sci.*, 2003, **4**, 158.

314. A. Wu and D. Cremer, *J. Phys. Chem. A*, 2003, **107**, 1797.

315. S. V. Zubkov and V. A. Chertkov, *Int. J. Mol. Sci.*, 2003, **4**, 107.

316. C. Kojima, E. Kawashima, T. Sekine, Y. Ishido, A. Ono, M. Kainosho and Y. Kyogoku, *J. Biomol. NMR*, 2001, **19**, 19.

317. J. Poznanski, K. Felczak, M. Bretner, T. Kulikowski and M. Remin, *Biochem. Biophys. Res. Commun.*, 2001, **283**, 1142.
318. D. A. Case, C. Scheurer and R. Brüschweiler, *J. Am. Chem. Soc.*, 2000, **122**, 10390.
319. R. Consonni, L. Santomo, R. Tenni, R. Longhi and L. Zetta, *FEBS Lett.*, 1998, **436**, 243.
320. P. Bouř, V. Sychrovský, P. Maloň, J. Hanzlíková, V. Baumruk, J. Pospíš and M. Buděínský, *J. Phys. Chem. A*, 2002, **106**, 7321.
321. E. V. Borisov, W. Zhang, S. Bolvig and P. E. Hansen, *Magn. Reson. Chem.*, 1998, **36**, S104.
322. T. Dziembowska, Z. Rozwadowski, A. Filarowski and P. E. Hansen, *Magn. Reson. Chem.*, 2001, **39**, S67.
323. N. Matsumori, D. Kaneno, M. Murata, H. Nakamura and K. Tachibana, *J. Org. Chem.*, 1999, **64**, 866.
324. M. Murata, S. Matsuoka, N. Matsumori, G. K. Paul and K. Tachibana, *J. Am. Chem. Soc.*, 1999, **121**, 870.
325. N. Matsumori, D. Kaneno, M. Murata, H. Nakamura and K. Tachibana, *J. Org. Chem.*, 1999, **64**, 866.
326. M. Pecul, M. Jaszuński and J. Sadlej, *Chem. Phys. Lett.*, 1999, **305**, 139.
327. E. S. Nielsen, P. Jorgensen and J. Oddershede, *J. Chem. Phys.*, 1980, **73**, 6238.
328. S. P. A. Sauer, *J. Phys. B. At. Mol. Opt. Phys.*, 1997, **59**, 3773.
329. J. Guilleme, J. San-Fabián, J. Casanueva and E. Díez, *Chem. Phys. Lett.*, 1999, **314**, 168.
330. M. Karplus, *J. Chem. Phys.*, 1959, **30**, 11.
331. M. Karplus, *J. Am. Chem. Soc.*, 1963, **85**, 2870.
332. M. Barfield and M. Karplus, *J. Am. Chem. Soc.*, 1969, **91**, 1.
333. W. A. Thomas, *Prog. NMR Spectrosc.*, 1997, **30**, 183.
334. J. M. Schmidt, M. Blümel, F. Löhr and H. Rüterjans, *J. Biomol. NMR*, 1999, **14**, 1.
335. F. Löhr, J. M. Schmidt and H. Rüterjans, *J. Am. Chem. Soc.*, 1999, **121**, 11821.
336. S.-J. Hu and A. Bax, *J. Am. Chem. Soc.*, 1997, **119**, 6360.
337. F. Löhr, J. M. Schmidt, S. Maurer and H. Rüterjans, *J. Magn. Reson.*, 2001, **153**, 75.
338. S. A. Perera and R. J. Bartlett, *Magn. Reson. Chem.*, 2001, **39**, S183.
339. M. Barfield and H. L. Gearhart, *J. Am. Chem. Soc.*, 1973, **95**, 641.
340. J. Nél, *Pure Appl. Chem.*, 1972, **31**, 201.
341. M. T. Cung, M. Marruad and J. Néel, *Ann. Chim. (Paris)*, 1972, **7**, 183.
342. M. T. Cung, M. Marruad and J. Néel, *Macromolecules*, 1974, **7**, 606.
343. G. N. Ramachandran and R. Chandrasekaran, *Biopolymers*, 1971, **10**, 935.
344. V. F. Bystrov, V. T. Ivanov, S. L. Portnova, T. A. Balashova and Y. A. Ovchinnikov, *Tetrahedron*, 1973, **29**, 873.
345. M. L. Munzarová and V. Sklenář, *J. Am. Chem. Soc.*, 2002, **124**, 10666.
346. L. Tantírek, R. Štefrl, J. E. Masse, J. Feigon and V. Sklenář, *J. Biomol. NMR*, 2002, **23**, 1.
347. M. L. Munzarová and V. Sklenář, *J. Am. Chem. Soc.*, 2003, **125**, 3649.
348. S. A. Wacowich-Sgarbi, C. C. Ling, A. Otter and D. R. Bundle, *J. Am. Chem. Soc.*, 2001, **123**, 4362.
349. B. Mulloy, T. A. Frenkiel and D. B. Davies, *Carbohydr. Res.*, 1988, **184**, 39.
350. I. Tvaroska, M. Hricovini and E. Petrakova, *Carbohydr. Res.*, 1989, **189**, 359.
351. I. Tvaroska and F. Taravel, *Adv. Carbohydr. Chem. Biochem.*, 1995, **51**, 15.
352. J. B. Houseknecht, T. L. Lowary and C. M. Hadad, *J. Phys. Chem. A*, 2003, **107**, 372.
353. J. B. Houseknecht, P. R. McCarren, T. L. Lowary and C. M. Hadad, *J. Am. Chem. Soc.*, 2001, **123**, 8811.
354. T. Rundlöf, A. Kjellberg, C. Damberg, T. Nishida and G. Widmalm, *Magn. Reson. Chem.*, 1998, **36**, 839.
355. T. Rundlöf and G. Widmalm, *Magn. Reson. Chem.*, 2001, **39**, 381.
356. M. Hennig, W. Bermel, H. Schwalbe and C. Griesinger, *J. Am. Chem. Soc.*, 2000, **122**, 6268.
357. W. Peti, M. Hennig, L. J. Smith and H. Schwalbe, *J. Am. Chem. Soc.*, 2000, **122**, 12017.
358. J.-S. Hu and A. Bax, *J. Am. Chem. Soc.*, 1997, **119**, 6360.

359. C. Thibaudeau, J. Plavec and J. Chattopadhyya, *J. Org. Chem.*, 1998, **63**, 4967.
360. P. G. Goekjian, G.-Z. Wu, S. Chen, L. Zhou, M. R. Jirousek, J. R. Gillig, L. M. Ballas and J. T. Dixon, *J. Org. Chem.*, 1999, **64**, 4238.
361. M. Michalik, M. Hein and M. Frank, *Carbohydr. Res.*, 2000, **327**, 185.
362. E. Gács-Baitz, L. A. Wozniak and M. Kajtár-Peredy, *Chirality*, 2000, **12**, 675.
363. M. Polak and J. Plavec, *Eur. J. Inorg. Chem.*, 1999, 547.
364. C. O. Meese and W. Walter, *Magn. Reson. Chem.*, 1985, **23**, 327.
365. I. Johannseen and H. Eggert, *J. Am. Chem. Soc.*, 1984, **106**, 1240.
366. H. Poleschner, M. Heydenreich and R. Radeglia, *Magn. Reson. Chem.*, 1999, **37**, 333.
367. E. M. Sproviero and G. Burton, *J. Phys. Chem.* A, 2002, **106**, 7834.
368. M. A. Battiste and R. G. Posey, *J. Fluor. Chem.*, 2000, **102**, 285.
369. T. Hasegawa, *CACS Forum*, 1999, **19**, 29.
370. A. Dabrowski, K. Kamienska-Trela and J. Wójcik, *Spectrochim. Acta* A, 1999, **56**, 91.
371. K. Kamineska-Trela, *Isotopes in physical and Biological Sciences 2*, E. Buncel and J. R. Jones, eds., Elsevier, Amsterdam, 1991, 297.
372. K. Kamienska-Trela, L. Kania, W. Schilf and I. Balova, *Spectrochim. Acta* A, 1999, **55**, 817.
373. K. Kamienska-Trela, L. Kania, P. Bernatowicz, M. Bechcicka, L. Kaczmarek and J. Wójcik, *Spectrochim. Acta* A, 2000, **56**, 2079.
374. P. Lantto, J. Kaski, J. Vaara and J. Jokisaari, *Chem. Eur. J.*, 2000, **6**, 1395.
375. A. Bagno, G. Saielli and G. Scorrano, *ARKIVOC*, 2002, **IV**, 38.
376. M. Morvai, T. Nagy, A. Kocsis, L. F. Szabó and B. Podányi, *Magn. Reson. Chem.*, 2000, **38**, 343.
377. R. Aydin and H. Günther, *Magn. Reson. Chem.*, 1990, **28**, 448.
378. W. S. Brey and M. L. Brey, *J. Fluor. Chem.*, 2000, **102**, 219.
379. P. F. Provasi, G. A. Aucar and S. P. A. Sauer, *J. Chem. Phys.*, 2000, **112**, 6201.
380. M. S. Gil and W. von Philipsborn, *Magn. Reson. Chem.*, 1989, **27**, 409.
381. A. E. Reed and P. V. R. Schleyer, *J. Am. Chem. Soc.*, 1990, **112**, 1434.
382. J. Ø. Duus, C. H. Gotfredsen and K. Bock, *Chem. Rev.*, 2000, **100**, 4589.
383. A. V. Afonin and M. A. Andriyankov, *Zh. Org. Chem.*, 1988, **24**, 1034.
384. A. V. Afonin, M. V. Sigalov, S. E. Korustova, I. A. Aliev, A. V. Vashchenko and B. A. Trofimov, *Magn. Reson. Chem.*, 1990, **28**, 580.
385. H. Satonaka, K. Abe and M. Hirota, *Bull. Chem. Soc. Jpn.*, 1988, **61**, 2031.
386. C. Vizioli, M. C. Ruiz de Azúa, C. G. Giribet, R. H. Contreras, L. Turi, J. J. Dannenberg, I. D. Rae, J. A. Weigold, M. Malagoli, R. Zanasi and P. Lazzeretti, *J. Phys. Chem.*, 1994, **98**, 8858.
387. K. Bock and C. Pedersen, *Acta Chem. Scand.*, 1977, **B31**, 354.
388. J. Schraml, *App. Organomet. Chem.*, 2000, **14**, 604.
389. K. Bock and H. Thøgersen, *Ann. Rep. NMR Spectrosc.*, 1982, **13**, 1.
390. J. Vaara, J. Kaski, J. Jokisaari and P. Diehl, *J. Phys. Chem.* A, 1997, **101**, 5069.
391. M. J. Hansen, M. A. Wendt, F. Weinhold and T. C. Farrar, *Mol. Phys.*, 2002, **100**, 2807.
392. M. Pecul and J. Sadlej, *Chem. Phys.*, 2000, **255**, 137.
393. D. G. Zaccari, J. P. Snyder, J. E. Peralta, O. E. Taurian, R. H. Contreras and V. Barone, *Mol. Phys.*, 2002, **100**, 705.
394. D. G. Zaccari, V. Barone, J. E. Peralta, R. H. Contreras, O. E. Taurian, E. Díez and A. Esteban, *Int. J. Mol. Sci.*, 2003, **4**, 93.
395. A. N. Taha and N. S. True, *J. Phys. Chem.* A, 2000, **104**, 2985.
396. M. Pecul and J. Sadlej, *Chem. Phys.*, 1999, **248**, 27.
397. K. Jackowski, M. Wilczek, M. Pecul and J. Sadlej, *J. Phys. Chem.* A, 2000, **104**, 5955.
398. K. Jackowski, M. Wilczek, M. Pecul and J. Sadlej, *J. Phys. Chem.* A, 2000, **104**, 9806.
399. J. Kaski, P. Lantto, J. Vaara and J. Jokisaari, *J. Am. Chem. Soc.*, 1998, **120**, 3993.
400. R. D. Wigglesworth, W. T. Raynes, S. Kirpekar, J. Oddershede and S. P. A. Sauer, *J. Chem. Phys.*, 2000, **112**, 3735.

401. M. Wilczek, W. Koźmiński and K. Jackowski, *Chem. Phys. Lett.*, 2000, **358**, 263.
402. S. A. Perera, M. Nooijen and R. J. Bartlett, *J. Chem. Phys.*, 1996, **104**, 3290.
403. K. Jackowski and M. Wilczek, *J. Mol. Struct.*, 2003, **651-653**, 259.
404. K. Jackowski, M. Kubiszewsk and W. Makulski, *J. Mol. Struct.*, 2002, **614**, 267.
405. K. Jackowski, *Int. J. Mol. Sci.*, 2003, **4**, 135.
406. P.-O. Åstrand, K. Ruud, K. V. Mikkelsen and T. Helgaker, *J. Chem. Phys.*, 1998, **108**, 2528.
407. K. V. Mikkelsen, K. Ruud and T. Helgaker, *J. Comput. Chem.*, 1999, **20**, 1281.
408. E. L. Eliel and G. A. Giza, *J. Org. Chem.*, 1968, **33**, 3754.
409. R. U. Lemieux, A. A. Pavia, J. C. Marti and K. A. Watanabe, *Can. J. Chem.*, 1969, **47**, 4427.
410. I. V. Alabugin, *J. Org. Chem.*, 2000, **65**, 3910.
411. N. de Kimpe, R. Verhe, L. De Buyck and N. Schamp, *Can. J. Chem.*, 1984, **62**, 1812.
412. B. Braillon, M. C. Lasne, J. L. Rippoli and J. M. Denis, *Nouv. J. Chim.*, 1982, **6**, 121.
413. I. Ando, Y. Inoue, S. Watanabe, Y. Sakamoto and G. A. Webb, *J. Mol. Liquids*, 1984, **27**, 179.
414. R. J. Chuck, D. G. Gilles and E. W. Randall, *Mol. Phys.*, 1969, **16**, 121.
415. P. E. Hansen, *The Chemistry of Double-bonded Functional Groups*, S. Patai, ed., Wiley, New York, 1989, Chapter 3.
416. V. Sychrovský, B. Schneider, P. Hobza, L. Židek and V. Sklenár, *Phys. Chem. Chem. Phys.*, 2003, **5**, 734.
417. V. Barone, M. Cossi and J. Tomasi, *J. Comput. Chem.*, 1998, **19**, 404.
418. K. Ruud, L. Frediani, R. Cammi and B. Mennucci, *Int. J. Mol. Sci.*, 2003, **4**, 119.
419. R. Cammi and J. Tomasi, *J. Comput. Chem.*, 1995, **16**, 1449.
420. B. Mennucci, E. Cancés and J. Tomasi, *J. Phys. Chem. B*, 1997, **101**, 10506.
421. R. Cammi, L. Frediani, B. Mennucci, J. Tomasi, K. Ruud and K. V. Mikkelsen, *J. Chem. Phys.*, 2002, **117**, 13.
422. S. P. A. Sauer, C. Kyhn Møller, H. Koch, I. Paidarová and V. Špirko, *Chem. Phys.*, 1998, **238**, 385.
423. P.-O. Åstrand, K. Ruud, K. V. Mikkelsen and T. Helgaker, *J. Chem. Phys.*, 1999, **110**, 9463.
424. J. E. Del Bene, M. J. T. Jordan, S. A. Perera and R. J. Bartlett, *J. Phys. Chem. A*, 2001, **105**, 8399.
425. J. E. Del Bene and M. J. T. Jordan, *J. Phys. Chem. A*, 2002, **106**, 5385.
426. R. D. Wigglesworth, W. T. Raynes, S. Kirpekar, J. Oddershede and S. P. A. Sauer, *J. Chem. Phys.*, 2001, **114**, 9192.
427. W. T. Raynes, J. Geertsen and J. Oddershede, *Chem. Phys. Lett.*, 1992, **197**, 516.
428. S. P. A. Sauer and W. T. Raynes, *J. Chem. Phys.*, 2000, **115**, 3121.
429. S. P. A. Sauer, W. T. Raynes and R. A. Nicholls, *J. Chem. Phys.*, 2001, **115**, 5994.
430. T. A. Ruden, O. B. Lutnæs and T. Helgaker, *J. Chem. Phys.*, 2003, **118**, 9572.
431. J. Eriksson, P. I. Arvidsson and Ö. Davidsson, *J. Am. Chem. Soc.*, 2000, **122**, 9310.
432. T. Koizumi, K. Morihashi and O. Kikuchi, *Bull. Chem. Soc. Jpn.*, 1996, **69**, 305.
433. K. B. Aubrecht, B. L. Lucht and D. B. Collum, *Organometallics*, 1999, **18**, 2981.
434. O. Parisel, C. Fressigné, J. Maddaluno and C. Giessner-Prettre, *J. Org. Chem.*, 2003, **68**, 1290.
435. A. Bagno, *Chem. Eur. J.*, 2001, **7**, 1652.
436. H. Lee, T. Onak, J. Jaballas, U. Tran, T. U. Truong and H. T. To, *Inorg. Chim. Acta*, 1999, **289**, 11.
437. T. Onak, J. Jaballas and M. Barfield, *J. Am. Chem. Soc.*, 1999, **121**, 2850.
438. S. Heřmánek, *Inorg. Chim. Acta*, 1999, **289**, 20.
439. W. Keller, W. Haubold and B. Wrackmeyer, *Magn. Reson. Chem.*, 1999, **37**, 545.
440. V. Galasso and I. Carmichael, *J. Phys. Chem. A*, 2000, **104**, 6271.
441. S. Berger, A. Krebs, B. Thölke and H.-U. Siehl, *Magn. Reson. Chem.*, 2000, **38**, 566.
442. L. B. Krivdin, S. P. A. Sauer, J. E. Peralta and R. H. Contreras, *Magn. Reson. Chem.*, 2002, **40**, 187.
443. L. B. Krivdin, *Magn. Reson. Chem.*, 2003, **41**, 91.

444. M. Pecul, H. Dodziuk, M. Jaszuńki, O. Lukin and J. Leszczyński, *Phys. Chem. Chem. Phys.*, 2001, **3**, 1986.

445. L. Krivdin, *Magn. Reson. Chem.*, 2003, **41**, 157.

446. K. Kamieńska-Trela, B. Bernatowicz, W. Lüttke, R. Machinek and M. Trætteborg, *Magn. Reson. Chem.*, 2002, **40**, 640.

447. M. Jaszuński, G. Dolgonos and H. Dodziuk, *Theor. Chem. Acc.*, 2002, **108**, 240.

448. M. Tordeux, C. Wakselman, O. Jarjayes and C. G. Béguin, *Magn. Reson. Chem.*, 2001, **39**, 301.

449. S. R. Dubberley, S. K. Ignatov, N. H. Rees and A. G. Razuvaev, *J. Am. Chem. Soc.*, 2003, **125**, 642.

450. R. Contreras, J. M. Grevy, Z. García-Hernández, M. Güizado-Rodriguez and B. Wrackmeyer, *Heteroatom Chem.*, 2001, **12**, 542.

451. B. Wrackmeyer and P. Bernatowicz, *J. Organomet. Chem.*, 1999, **579**, 133.

452. B. Wrackmeyer and P. Bernatowicz, *Magn. Reson. Chem.*, 1999, **37**, 418.

453. M. Herberhold, T. Daniel, D. Daschner, W. Milius and B. Wrackmeyer, *J. Organomet. Chem.*, 1999, **585**, 234.

454. A. A. Isab, M. S. Hussain, M. N. Akhtar, M. I. M. Wazeer and A. R. Al-Arfaj, *Polyhedron*, 1999, **18**, 1401.

455. R. McDermott, A. H. Trabesinger, M. Mück, E. L. Hahn, A. Pines and J. Clarke, *Science*, 2002, **295**, 2247.

456. R. Malleier, H. Kopacka, W. Schuh, K. Wurst and P. Peringer, *J. Chem. Soc., Chem. Comm.*, 2001, 51.

457. S. P. Gabuda, S. G. Kozlova, V. V. Terskikh, C. Dybowski, G. Neue and D. L. Perry, *Solid State NMR*, 1999, **15**, 103.

458. K. Gholivand, S. Ghadimi, H. Nadimanesh and A. Forouzanfar, *Magn. Reson. Chem.*, 2001, **39**, 684.

High Resolution Magic Angle Spinning – Applications to Solid Phase Synthetic Systems and Other Semi-Solids

WILLIAM P. POWER

Department of Chemistry, University of Waterloo, Waterloo, ON N2L 3G1, Canada

High resolution magic angle spinning, or HRMAS, is the combined application of high resolution NMR experiments with dipolar- and susceptibility-reducing sample rotation to viscous or gel-like samples. This technique has generated a great deal of activity into applications of NMR to questions of structure in systems ranging from solid phase synthesis to materials, whole cells and tissues. This review introduces the principles of this technique, outlines the specialized NMR experiments it has made possible, then describes applications arising from it over the last ten years, with particular emphasis on the last five years.

1. INTRODUCTION

Through the 1990s, there was an explosion of interest in the application of solid-phase synthetic strategies with particular emphasis towards combinatorial chemistry.[1] These solid-phase reactions aimed to create vast libraries of compounds using automated synthesizers, which were then subjected to high-throughput screening in order to identify potential drug candidates. As interest increased in the use of polymer supports for such syntheses, it became apparent that there was a need for a reliable, familiar and amenable technique to permit the identification of products, intermediates and reaction progress. While products could be rapidly and readily identified using mass

spectrometry of products liberated from the solid support,[2] identification of intermediates and monitoring of reaction progress proved more difficult, due to the desire to perform an *in situ* analysis, rather than an *ex situ* approach following cleavage. NMR spectroscopy has been one technique that has attempted to address this need, and has been the one most applied to such problems. It has a long history of application to solution and solid samples, and there is an ample background of studies of so-called 'semi-solids', such as membranes[3–5] and gels.[6,7] Together with instrumental developments centred on the area of *high resolution magic angle spinning* or HRMAS, there has been a significant increase in the breadth of NMR research that includes the use of magic angle spinning. This experimental technique, once solely relegated to the study of pure solids,[8] is now commonly used in traditional high-resolution experiments (hence the name HRMAS) aimed at structure elucidation of organic or biological molecules present in a semi-solid milieu, due to its beneficial reductions in line width arising from removal of dipolar and susceptibility broadening. These applications are the focus of this review.

Solid-phase synthesis has been around much longer than the recent explosion of interest. First developed in the early 1960s by Merrifield (for which he was awarded the 1984 Nobel Prize in Chemistry),[9] it has been a core technique in peptide synthesis since that time.[10] The basic idea of solid-phase synthesis is straightforward – it uses a polymer support to which are tethered the reactants of interest. Addition of reagents in large excess can be used to drive reactions to completion, since purification is completed simply by filtering and washing the polymer support with product still attached. Once the desired product has been formed in the appropriate yield, that product is liberated from the polymer by cleaving the bond between them, providing a pure compound that requires no further manipulation. This approach was readily automated[11] and the resulting synthesizers are standard tools within many bio-organic research labs today.

The polymers that are used are varied, but the most common have been weakly cross-linked microporous polystyrene resins, that have the desirable attribute that they readily swell in organic solvents, providing access to the polymer by the solvent, or whatever reagent may be dissolved in it. The resins themselves are most commonly made by polymerizing styrene in the presence of 1–2% 1,4-divinylbenzene (as the crosslinking agent), then functionalizing the resulting resin by attaching chemically accessible 'linkers' to some number of phenyl groups along the polymer chain, usually at coverages ranging from 0.1 to 1.0 mmol of linker sites/g resin. This means that a typical support used in a solid-phase reaction would have anywhere from 1 to 10% of the backbone 'functionalized' for possible reactions. The structure of one such linker in a particularly common support called Wang resin[12] is depicted in Fig. 1. More recently, more flexible resins, particularly those based on polyethyleneglycol, have found favour for some specialized reactions, or, as noted later, specifically, for improved spectral properties.
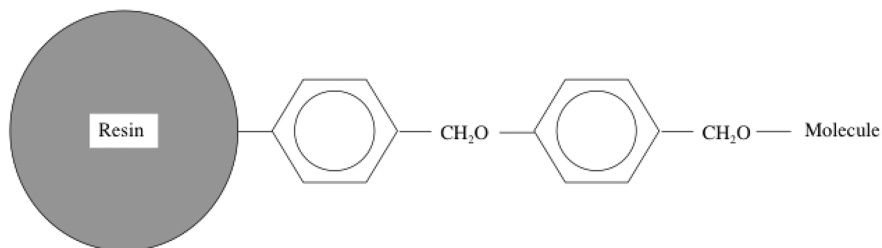
Fig. 1. Chemical structure of Wang resin, where the resin is 1–2% crosslinked polystyrene and the 'molecule' is the species synthesized and ultimately liberated from the resin.

Herein lies the difficulty for an *in situ* analytical technique – up to 99% of the sample represents the matrix or background, as the polymer resin. The chemically interesting part, that which needs to be identified and elucidated, can be 1% or less of the total sample, yet cannot be separated physically from the background. Traditional techniques such as IR and Raman spectroscopy have been applied with some success to these systems, but the overwhelming signals arising from the polymer support complicate the analyses. NMR spectroscopy, with its inherent nuclear site resolution, has provided an important, and constantly improving, tool in the analyses of such samples. These difficulties are not unique to solid-phase synthesis, hence HRMAS has been applied to an ever-widening range of samples. These other applications are noted as well in this review.

The reader should note that several other reviews on areas spanning parts of this topic (among others) have been published in the past, particularly by two pioneers in this area, Keifer[13–15] and Shapiro.[16–20]

2. NATURE OF THE SAMPLES

The flexible structure of a swollen polymer support, in reality a polymer gel, imposes novel properties on the samples as they are analysed using NMR. The restricted motion of the polymer backbone ensures that the dipolar coupling between the protons in the sample are not completely removed, even upon the addition of organic solvent and concomitant swelling of the matrix. In addition, though often less considered in NMR experiments of single-phase samples, the magnetic susceptibility of the samples changes at the interfaces between polymer (solid) and solvent (solution). As there are many such interfaces within the polymer gel, these susceptibility differences cause broadening of the resulting NMR signals. As a consequence, the NMR spectrum of such a polymer gel obtained under conditions typical for high-resolution NMR of solution samples provides extremely low resolution, as evident in Fig. 2 for Wang resin.
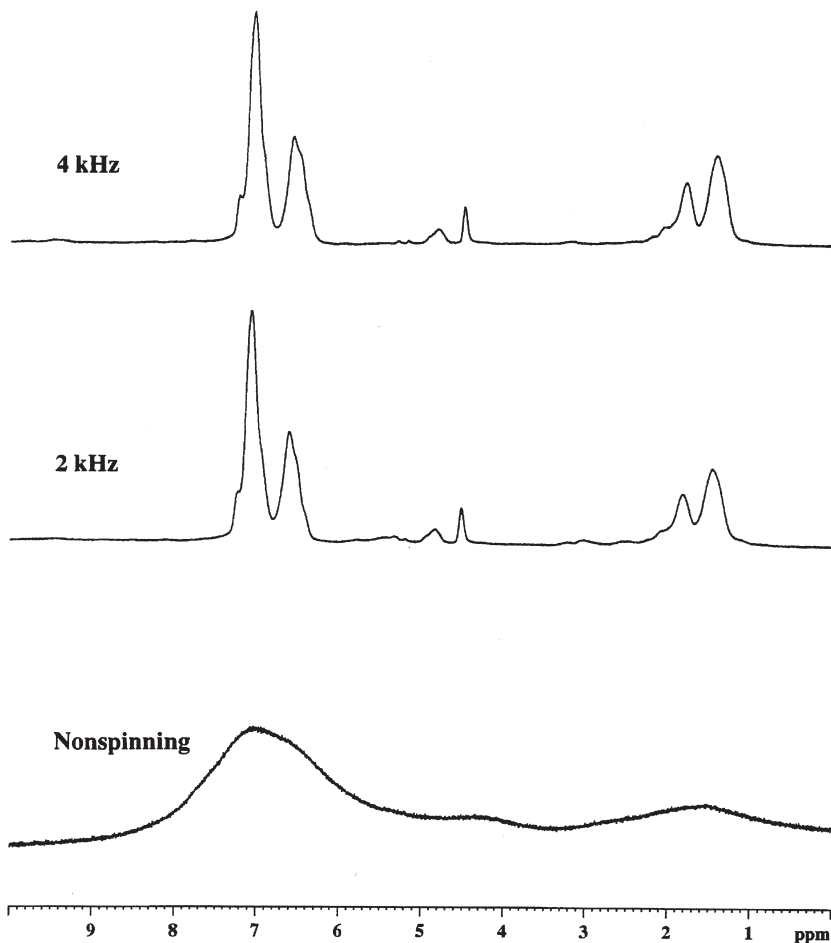
Fig. 2. 500 MHz ^{1}H NMR spectra of Wang resin swollen in CD_2Cl_2 with magic angle spinning at 0, 2 and 4 kHz.

Early on, attempts to deal with these broad lines focussed on the use of heteronuclei as the probes of choices. Carbon-13, in particular, was used in gel samples prepared in standard NMR tubes and observed in experiments identical to those applied to solution samples.[21] Other heteronuclei, such as ^{31}P[22] and ^{19}F,[23] have been used because of their favourable relaxation characteristics and dilute nature in the samples investigated. This approach suffers from the increased experiment time compared to ^{1}H NMR, and from the sometimes sparse nature of the information available from dilute sites within the samples.

Dipolar broadening constitutes a routinely-overcome barrier in high-resolution NMR of solids, and the consequences are readily removed in the

solid state by a combination of high power decoupling and magic angle spinning.[8] The flexibility of the polymer backbone in gels is sufficient to reduce the broadening to degrees that obviate the application of high-power decoupling; combined with this is the ultimate desire to use the protons as the nuclei of observation, rather than the normal target of decoupling. These two considerations reduce the required approach to magic angle spinning alone, which uses the geometric dependence of the dipolar interaction to remove the broadening provided a suitably fast time-average due to sample spinning can be created. The magic angle, so called due to its seemingly magic ability to remove broadening from solid-state NMR spectra, results from the dependence of the dipolar interaction (as well as others, including chemical shift anisotropy) on the second-order Legendre polynomial, $P_2(\cos\theta) = (1/2)(3\cos^2\theta - 1)$. This function has a value of 0 when the angle θ, which represents the angle between the dipolar vector between two coupled nuclei and the vector representing the direction of the applied magnetic field, adopts a value of $\cos^{-1}(1/\sqrt{3})$ or 54.74°. In a suitably simple and structured single crystal, it is possible to align the crystal such that all dipolar vectors point in one direction (actually, an equivalent cone of directions) with this angle about the magnetic field; in a randomly distributed sample, such as a polycrystalline powder or a polymer gel, such simultaneous alignment is impossible. However, as long as a sample is reoriented at this angle at a rate that is faster than the interaction which is causing the broadening, the time average is sufficient as well to remove the broadening. This time average utilizes the property that a Legendre polynomial can be decomposed into products of other Legendre polynomials. If one factor in the product can be made equal to zero, e.g., by choosing the spinning axis to lie at 54.74° with respect to the field, the product must be zero as well, hence the broadening is removed. This is illustrated in Fig. 3 – the 'dashed' dipolar vector in the rotor on the left of the figure has had its orientation dependence detailed to the right. By choosing to rotate it about an axis oriented at 54.74°, the time average of its orientation dependence with respect to the magnetic field, B_o, denoted by the angle χ, becomes zero, due to the first term in the product becoming zero. This occurs for *all* vectors regardless of their orientations in the rotor, denoted by the angle β, as long as the rate of rotation is greater than the strength of the interaction expressed in Hz. At sample spinning rates less than the strength of the interaction, it is possible to achieve line narrowing as well, provided the broadening is *inhomogeneous* in nature. The considerable albeit restricted internal motion of the polymer in the polymer gel is sufficient to ensure that the line broadening behaves inhomogeneously at all times. Details on the differences in the types on line broadening is discussed in detail elsewhere.[24,25]

An equally troublesome and perhaps less common and less appreciated difficulty in the high resolution NMR of these gels is the occurrence of susceptibility broadening.[26] Magnetic susceptibility, symbolized by χ, occurs
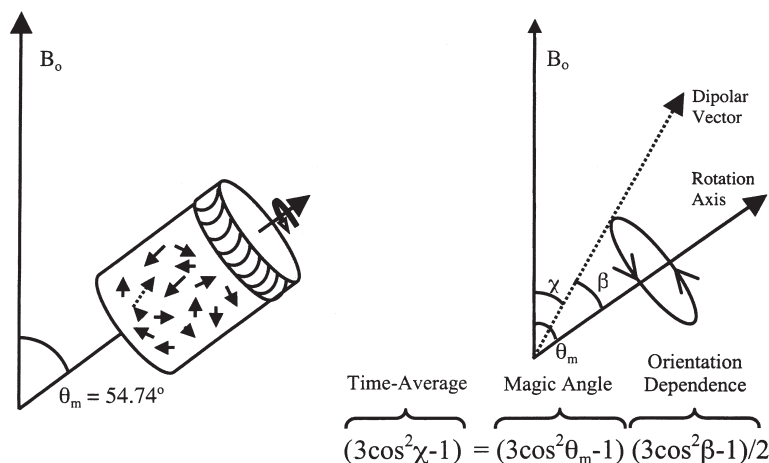
Fig. 3. Magic angle spinning and its effect on anisotropic interactions. The dashed vector, denoting one particular dipolar interaction, or some other measure of molecular orientation, is shown on the right in terms of the geometry of sample spinning. By rotating the sample rapidly about an appropriate axis, the anisotropy or broadening experienced by the nucleus can be reduced to zero.

in all samples; it is the factor by which magnetic field strength, H_0, becomes magnetic flux, B_0, as

$$H_0(1 + \chi) = B_0 \qquad (1)$$

Susceptibility *differences*, $\Delta\chi$, act as field inhomogeneities, since

$$H_0(1 + \Delta\chi) = \Delta B_0. \qquad (2)$$

These inhomogeneities, since they arise from the sample itself, cannot be removed by improved shimming, nor by common approaches based on sample geometry (spherical chambers, infinite cylinders, etc.). They do, however, depend geometrically on the magnetic field direction according to $P_2(\cos\theta)$, hence are also removed by magic angle spinning.

   In each case, the amount of line broadening introduced is sufficiently small to require relatively modest rates of sample spinning (from 2 to 5 kHz), but large enough to completely overwhelm any attempt to extract useful spectra obtained without magic angle spinning. These aspects are evident in the ^{1}H NMR spectra of Wang resin displayed in Fig. 2. Fortunately, hardware facilitating magic angle spinning under the modest conditions required for these samples is relatively common, and readily added to existing equipment if unavailable. Both Varian and Bruker have developed their own approaches to high-resolution magic-angle spinning, depending on the needs of the users, and 'third-party' solutions exist as well. All include the necessary

probe and spinning controller providing ready access to the techniques required for acquisition of useful spectra; each approach may suit some labs better than others. A detailed survey of the different experimental approaches has been completed.[27]

The first product ideally suited to these applications was the NanoProbe from Varian, Inc. (Palo Alto, CA, USA), which was originally developed to deal with very small sample quantities.[28] Magic angle spinning of the very small samples in thin glass tubes was used to limit the susceptibility problems that arise in such cases. Their solution proved ideal for gel-phase samples,[29] as the sample cells were inexpensive, easy to load and use, and readily handled and inspected for aspects such as the absences of bubbles. Sample spinning of the glass tubes was accomplished through fitting of a tapered fluted collar that fit within the stator of the probe. Since the original application involved solution phase samples, the probe construction from the design stage on was amenable to high resolution by proper choice of materials and geometry used.

Bruker Biospin, Inc. (Karlsruhe, Germany), had extensive experience in solid-state NMR where magic angle spinning has been a requirement for decades, and their standard MAS probes could be applied to gel-phase samples with little problem.[30] Standard MAS rotors used for solid-state NMR have been adapted for use with lipid dispersions and similarly viscous samples using spherical glass inserts.[31] Demands for susceptibility matching of probe materials and long-term stability afforded by a lock circuit led Bruker to introduce more specialized HRMAS probes within the last five years. Again, the technical demands were relatively modest, but the need for both high resolution and MAS abilities necessitated some design changes to marry the elements required by both criteria.

Doty Scientific, Inc. (Columbia, SC, USA) has been relatively successful in incorporating high resolution capabilities into their more standard solid-state MAS probes,[32] where, in a traditional application, the extra care may not ever be noticed, but it provides the ability to use one MAS probe for both solid and gel-phase samples. They have introduced a sample insert that permits ready preparation of a number of samples that can be inserted into a MAS rotor for spectral acquisition, then preserved (or discarded) without requiring the dedication of a more expensive rotor.

There are a wide variety of samples that have been investigated in this way, even within the field of solid phase synthesis, due to the wide range of resins and solvent conditions employed. While the first report used a particularly flexible resin, TantaGel,[33] its low loading capacity led Wehler and Westman[34] to investigate other resins, including the common Merrifield resin based on cross-linked polystyrene. Keifer has compiled survey of the effects of combinations of nine commercially-available resins with seven common solvents on spectral quality.[35] In general, the more soluble and mobile the resin, the narrower the lines obtained in HRMAS NMR spectra of such samples – however, there are often chemical or cost factors that dictate the choice

of resin beyond the NMR characteristics. More recent work has indicated the anisotropic bulk magnetic susceptibility differences, for example, from local aromatic groups, contributes significantly to the residual linewidth in HRMAS NMR,[36] since these effects are not removed by MAS. The authors encouraged the use of non-aromatic polymers. This was confirmed in their later study[37] where they also accounted for polymer dynamics as a contributor to line widths for a tetrapeptide attached to three different resins, some of which were free of aromatics.

3. SPECIALIZED NMR TECHNIQUES

In spite of the dramatic line-narrowing afforded by the application of MAS techniques, significant broad lines are still encountered that arise from the polymer support, particularly for the common polystyrene-based resins like Wang, comprising some 99+% of the overall sample. Different approaches have been taken to reduce or remove these 'background' signals that span broad regions of the ^{1}H NMR spectrum, from 1.0 to 2.2 ppm (arising from polymer aliphatic), 4.8 to 5.2 ppm (linker) and 6.4 to 7.2 ppm (aromatic) (see Fig. 2). The earliest investigations utilized C–H correlations to provide enhanced resolution through the ^{13}C spectral range, either directly[38] (taking approximately 20 h) or indirectly[39] (with acquisition times totalling 3–6 h). The indirect HMQC result is particularly significant for its application to a sample comprised of a *single* bead of resin, although acquisition was limited to the 99% ^{13}C enriched methoxy groups in [3,5-dimethoxy-^{13}C]benzoic acid bound to Wang resin. Single-bead detection has been reported also using ^{1}H HRMAS NMR,[40] and the requirements for undertaking such analyses on combinatorial libraries have been described recently.[41] Improvements with the addition of gradients along the magic angle spinning axis,[42] incorporating both HMQC and HMBC variants of indirect heteronuclear correlation, demonstrated significant promise for gradients in high-resolution MAS applications (see Fig. 4). These authors noted that HR MAS applications are particularly amenable to the improvements introduced by the addition of gradients, due to the heterogeneous nature of the samples and the modulation due to rapid sample spinning. The technical aspects of including gradients in MAS probes have been explored.[43,44]

Direct ^{1}H observation should be much more direct and straightforward for rapid use in structure elucidation, preferably in a 1D spectrum, and most subsequent attempts focussed on maintaining that speed and utility. Spin-echoes were applied first,[34,45] utilizing the differences in transverse relaxation rates between the cross-linked polymer and relatively more mobile resin-bound molecule of interest. Wehler and Westman also had some success applying pre-saturation to the resin signals.[34] While some attenuation is afforded, it is at the expense of some spectral intensity from the resin-bound molecule
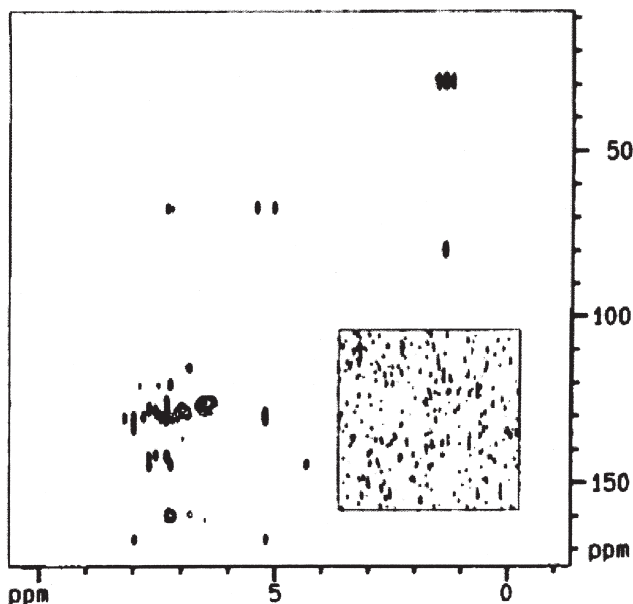
Fig. 4. 400 MHz gradient HRMAS ^{1}H–^{13}C HMBC spectrum of N-FMOC-N-Boc-L-Lysine on Wang resin swollen in CDCl$_3$ and spun at 5 kHz. The inset shows the low artifact level of the spectrum. Reproduced with permission from Ref. 42. Copyright 1996 American Chemical Society.

and loss of quantification. There is also a need to adjust the delay in the spin-echo sequence to optimize the conditions for each sample, and possible loss of isochronous signals when pre-saturation is applied. These two early reports, however, also showed the ease with which standard high resolution sequences COSY and TOCSY could be applied to these samples with great success.

Another approach resulting in suppression of the polymer, but with the added benefit of enhanced resolution, was either E.COSY[46] or 2D J-resolved experiments.[47] In E.COSY,[46] chemical shifts were scaled during the evolution time to reduce them to the order of the J coupling – this has the added benefit of reducing the inhomogeneous contribution to the line broadening in the resulting 2D spectra. Coupling constants were then extracted from the multiplet cross-peaks. The 2D J-resolved experiment as applied resulted in a spectrum that was projected *untilted* to a 1D spectrum, preserving the coupling information.[47] Entending this approach by incorporating the 2D SECSY (spin-echo-correlated) experiment resulted in enhanced resolution together with connectivity information normally obtained through COSY and TOCSY experiments.[48] The addition of gradients substantially reduced the artifacts present in the SECSY spectra.

The addition of gradients adds another possible discrimination mechanism to the NMR spectroscopy of these systems – the possibility of using differences in diffusion rates to distinguish between the various components of the heterogeneous polymer-solvent gel. First applied to reduce residual solvent resonances,[49] it permitted the use of minimal amounts of deuterated solvents, in concentrations only necessary for locking of the sample. The advantage of reducing this requirement is the ability to monitor reactions underway without purifying the polymer from the reaction (protonated) solvent and replacing it with the deuterated equivalent. Instead, addition of a drop of deuterated solvent for lock purposes was all that was required. This 'diffusion-filtered' technique has been used also to distinguish species attached to the resin from impurities trapped within the polymer matrix, but not covalently bound (see Fig. 5).[50] This technique has been used in conjuction with COSY,[50,51] and TOCSY,[49,52], as well as NOESY.[53] In each case, differences in the mobility of the pendant molecule and polymeric backbone resulted
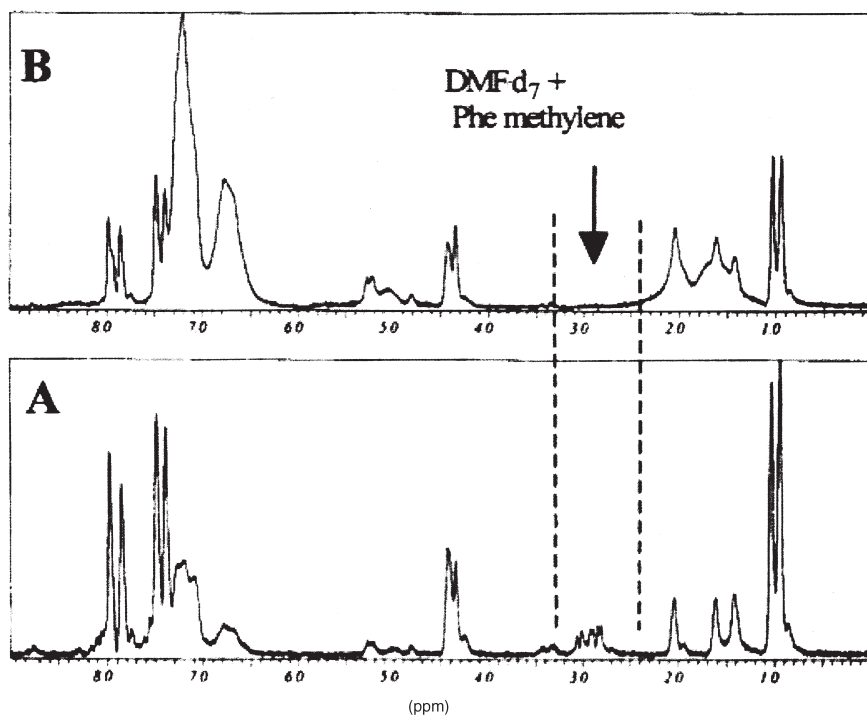
Fig. 5. 500 MHz HRMAS ^{1}H NMR spectra of FMOC-isoleucine on Wang resin swollen in DMF-d_7 and spun at 4 kHz. Spectrum **A** shows the presence of dissolved phenylalanine peaks, particularly around 3.0 ppm from its methylene protons, and residual protons of the solvent. Application of a diffusion filter using gradients selectively removes these signals in spectrum **B**. Reproduced with permission from Ref. 50. Copyright 1999 Elsevier.

in some attenuation of the polymer matrix signals, under suitable experimental conditions, in both 1D and 2D spectra.

Another approach permitting acquisition of 1D ^{1}H NMR spectra without interference from the underlying polymer has been the use of a 1D variant of TOCSY.[54] With the appropriate conditions, that appeared robust on the range of samples investigated, significant reduction of the polymer matrix signals were achieved, while maintaining the quantitative nature of the remaining signals arising from the resin-bound molecule. An example of a ^{1}H HRMAS NMR spectrum obtained for a three-residue peptide attached to Wang resin using this sequence is provided in Fig. 6. It was noted that more recent isotropic mixing sequences, like DIPSI-2 and FLOPSY-8, performed better than older sequences based on homonuclear decoupling, like MLEV, and that all the TOCSY-based approaches were both better in quality and easier to apply than spin-echo based experiments.

Several groups have investigated the detailed application of TOCSY in this non-standard format – where the magnetization is subjected to modulation
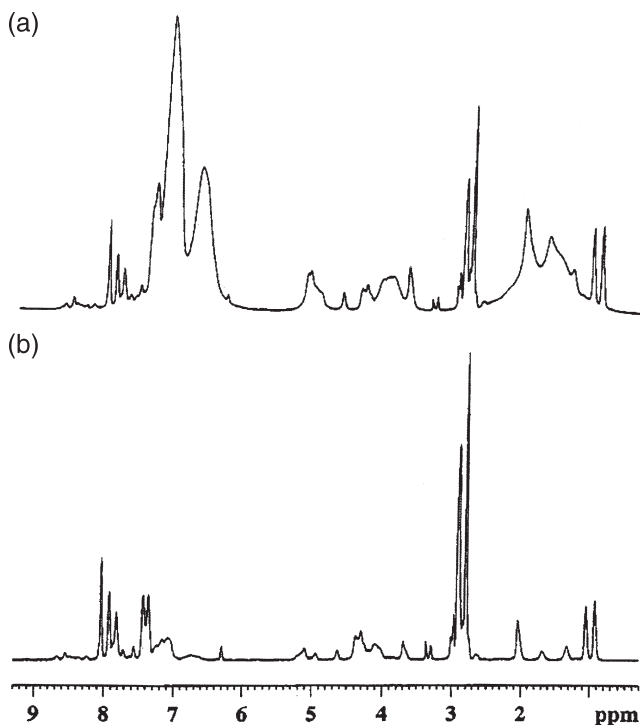
Fig. 6. 500 MHz ^{1}H HRMAS NMR spectra of FMOC-Ala-Ile-Asp-Wang swollen with DMF-d_7 and spun at 5 kHz. Spectra were obtained without (a) and with (b) using a 1D TOCSY variant[54] to reduce polymer signals. Note the substantially reduced signals arising from polystyrene in the aromatic (6.5–7.5 ppm) and aliphatic (1.5–2.5 ppm) regions.

from the rapid rotation of the sample under MAS. Early work on membranes[55] indicated coherence transfer under INEPT (for heteronuclei) and TOCSY (for homonuclei) sequences could be used without modification or interference from the sample spinning. In liquids spun at the magic angle, pronounced improvement in the quality of H–H TOCSY spectra could be obtained by replacing the DIPSI-2 sequence with an adiabatic mixing sequence, WURST-2.[56] In polymer-supported peptides, an apparent rotational resonance effect, whereby magnetization is destroyed when rf field strengths match integer multiples of the spinning rate, has been demonstrated under both MLEV and DIPSI-2 versions of TOCSY,[57] as well as clean-TOCSY.[58] This effect was ascribed to the presence of radial B_1 inhomogeneities. Interestingly, the adiabatic sequence mentioned above performs best under rotational resonance conditions. Clearly, care must be taken when applying TOCSY experiments to liquid or semi-solid samples under MAS, particularly with regard to the mixing sequence and the rf field strengths applied.

Solution-type NMR experiments are not the only ones that can be applied to these heterogeneous swollen polymer gels. Experiments based on solid-state NMR have been applied to characterize through-space correlations utilizing dipolar recoupling techniques.[59] Rather than relying on incoherent relaxation-derived exchange, as NOESY does, the recoupling schemes use coherent polarization transfer via dipolar or J coupling – in fact, the dipolar and J coupling evolutions could be separated, providing very useful structural information. It should be noted that this approach provides more direct information on distances than that typically available from NOE measurements.

4. APPLICATIONS TO POLYMER-SUPPORTED SPECIES

4.1. Solid phase organic synthesis

NMR spectroscopy has long been a method of choice for organic chemists to monitor the progress and evaluate the success of reactions. The availability of new tools such as HRMAS has enhanced their ability to develop and apply solid phase reactions, particularly for combinatorial chemistry, since the chemistry can be investigated *in situ* and under reaction conditions. The first application to the monitoring of a reaction in progress was that of a three-step synthesis involving the Heck reaction on a solid support,[60] an important carbon–carbon bond-forming procedure important in solid phase organic chemistry. TOCSY, NOESY and HMQC spectra were obtained to elucidate the structures of intermediates throughout the reaction. The authors tested a variety of solvents and cautioned that the optimal solvent choice (for swelling of the resin) may change during a reaction sequence as the product grows and changes in character.

The addition of an amino acid and subsequent conversion to the hydantoin were monitored on single beads using both one-dimensional ^{1}H and COSY NMR.[40] With beads of 400–750 μm holding ∼ 10–65 nmol of amino acid per bead, acquisition time of 3 min for 1D and 40 min for COSY were sufficient when 1–4 beads were placed in the MAS rotor.

Overlap from resin signals, mentioned previously, can be overcome in several ways, and is particularly important when following reactions involving aromatic groups attached to polystyrene based resins. Spin echo MAS NMR was applied to follow the progress of a reduction of a resin-bound methyl benzoate to the alcohol.[45] One-dimensional ^{1}H as well as COSY and TOCSY spectra were used to elucidate the reaction products, although transformations were readily apparent in the 1D spectra alone.

Multipin crowns are a useful synthetic tool when synthesizing large libraries of related compounds. However, the geometry of these pins makes them difficult to analyze directly. Chin et al.[61] have demonstrated that the pins can be placed in HRMAS probes, have their NMR spectra taken, then replaced in the pin assembly without any loss in reactivity. A resin-bound aldehyde was first characterized by ^{1}H NMR, then subjected to a Wittig reaction, the success of which was confirmed by a subsequent NMR spectrum of the same crown showing the expected olefin peak and no aldehyde signal. Spin echoes were used to overcome the large and broad background signals from the polymer in the resin and the crown. Subsequent work by Sefler and Gerritz[62] has shown that similar results can be obtained with NanoProbes, by shaving off small slices of the crowns for NMR analysis at various stages of the reactions. A dependence on solvent with different crowns was noted, and a variety of one- and two-dimensional ^{1}H and ^{13}C NMR spectra were obtained.

The Sharpless asymmetric dehydroxylation of resin-bound olefins was monitored using ^{1}H, ^{13}C and HMQC HRMAS NMR.[63] The authors found ^{13}C HRMAS NMR to be particularly suited to evaluating the progress of this reaction and permitted the enantiomeric excesses of the products to be determined before they were cleaved from the support. Most importantly, they were able to evaluate the types of substrates amenable to this reaction on solid supports, showing the ability of HRMAS NMR to contribute to synthetic questions. Transformation of the unnatural amino acid Lys(NH_2) on a poly (ethylene glycol)-dimethylacrylamide (PEGA) resin to 6-hydroxynorleucine was confirmed by application of TOCSY HRMAS experiments.[64]

An evaluation of different methods for monitoring reaction progress in solid phase organic chemistry has been carried out, using a five-step reaction sequence for the synthesis of tri-substituted amines.[65] While FTIR is noted for its sensitivity, permitting rapid analysis of a single bead alone cannot provide subtle details on the progress of the reaction. The authors rank the conclusiveness of several experiments (single bead FTIR, ^{1}H HRMAS, COSY HRMAS, HMQC HRMAS and ^{13}C HRMAS) to provide reaction details

at each step – of these, HMQC HRMAS ranks best in every step, although its experiment time of 140 min makes it a relatively time-consuming experiment. FTIR, in combination with ^{1}H HRMAS, was proposed as the most efficient and least demanding combination of methods to evaluate reaction progress, with resort to HMQC for particular details when necessary; although the authors concede FTIR provided little help in the last three of the five steps of the reaction. A combined analytical approach using both FTIR and ^{1}H HRMAS NMR[66] has been used successfully to follow the synthesis of β-aminosubstituted piperidinols through ring-opening of an 3,4-epoxypiperidine, and the clues afforded by a combination of these available *in situ* techniques are extremely valuable in describing the outcomes of new chemical procedures, as reported in the solid-phase synthesis of bicyclo[2,2,2]octanones.[67]

A novel selenium-based traceless linker for combinatorial chemistry using a solid support was demonstrated using gradient HRMAS NMR to evaluate and follow the reactions.[68] The acceleration of spectral acquisition using gradients was profound, with COSY-45, HSQC and HMBC spectra available in less than six min. As mentioned by Maas *et al.*,[42] the advantages of gradient technology to HRMAS applications is even more striking than its advantages to solution state NMR. Recently, a silylated linker has been used for palladium cross-coupling reactions with complete conversion as indicated by ^{1}H HRMAS NMR.[69]

In any solid-phase synthesis, the characteristics of the resin, and the elucidation of its role via spectroscopic methods, are crucial, both to the success of the reaction(s) and to the understanding of the chemistry.[70,71] Several resins have been evaluated with particular emphasis on the application of HRMAS NMR to understand their properties, including a graft co-polymer resin incorporating styrene and oxyethylene[72] and polyethylene glycol cross-linked vs. grafted resins.[73] The effect of using different resins was evident both in the reaction product ratios and the HRMAS spectral quality in the multistep synthesis of 2,5-diketopiperazines.[74] A non-aromatic resin based on polyoxyethylene-polyoxypropylene provided enough spectral resolution to permit full assignment of products including their quantitative yields while still attached to the resin.

Three different approaches to sample preparation for reaction monitoring were investigated by Warrass and Lippens.[75] The progress of a Horner-Emmons reaction, where a phosphonodiester is converted to a monoaldehyde under an excess of terephthalaldehyde, was followed, first, in a reaction carried out in a MAS rotor in a deuterated solvent; second, by removing an aliquot from a reaction, then purifying it (by washing, drying and reswelling in a pure solvent) before placing it in a MAS rotor for analysis; and third, by directly placing an aliquot from an ongoing reaction into a MAS rotor without any purification or other manipulation. All three methods provided useful information on the progress of the reaction – for the third
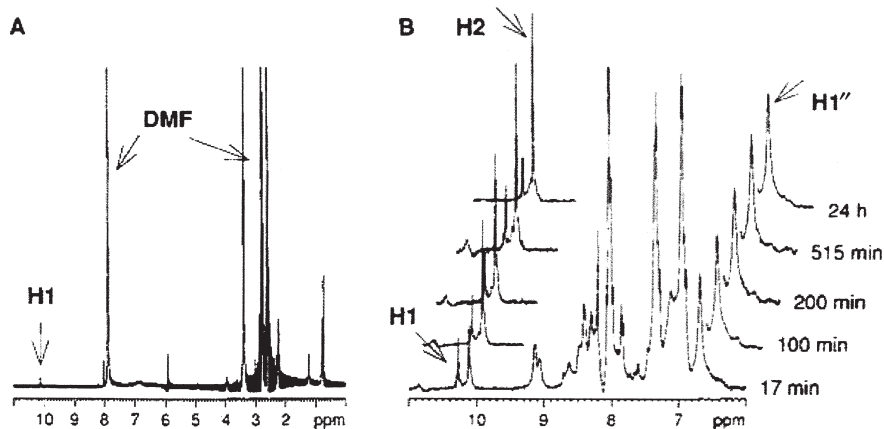
Fig. 7. 300 MHz ^{1}H HRMAS NMR spectra of a resin suspension swollen with DMF-d_7 from a reaction mixture and spun at 4 kHz. The spectrum (A) was obtained with a single-pulse sequence. The spectra in (B), liberated from the reaction vessel at the times indicated, were obtained using a diffusion filter to reduce the signals from non-bound species. Note the excellent suppression of the solvent DMF peak at 8 ppm. Reproduced with permission from Ref. 75. Copyright 2000 American Chemical Society.

sample, application of a gradient-based diffusion filter noted previously[49] was necessary to remove the signals arising from protonated solvent and excess reagents in the reaction mixture – this procedure provided excellent results, evident in the spectra presented in Fig. 7. This method represents the most useful approach for routine reaction monitoring, as it requires no special sample preparation and can be used with normal solid-phase reaction conditions (no need for deuterated solvents or special resins). Recently, Fruchart and co-workers[76] have applied this approach to solid-phase enolate chemistry, with interesting observations on the immobilization of the reagent in the polymer matrix, a feature that would be missed without direct analysis of the crude reaction mixture and application of the diffusion filter.

This diffusion-filtered approach has been extended in application to macroscopic supports, specifically a Synphase lantern.[77] The advantage of the diffusion-filtered experiment was extended to suppression of the macroscopic support signals, not just those of the protonated solvents. Although, the lanterns required some modification to fit in the MAS rotors, it is proposed that manufacturers account for this size restriction in future formats of these supports.

While much of the application of HRMAS to solid-phase organic chemistry has been via ^{1}H NMR, ^{13}C HRMAS NMR has been used to determine resin loading.[78] Two methods were applied, using both internal standards added to the resin in known amounts, or using features of the resin structure itself as a standard for calibration of the spectral intensities. The first method

was available only in resins that swell to a significant extent; solubilization of the added standards became an issue for resins that do not swell as much as 4 mL/g. The significant experiment time (2–3 h/sample) was cited as a barrier to the routine use of this method, and the need for efficient ^{1}H decoupling was noted, since the ^{13}C linewidths should be as narrow as possible for accurate intensity comparisons.

4.2. Solid phase peptide synthesis

The first applications of solid phase synthesis were to peptides, hence it is no surprise that there have been several reports of HRMAS studies of peptide systems attached to a support. One of the earliest reports of HRMAS in a supported sample was that of Wang-bound lysine, whose structure was determined by TOCSY and HMQC HRMAS NMR.[38] More recently, HRMAS NMR has been used to identify several peptidomimetic inhibitors of hepatitis C virus NS3 protease while on the resin.[79] However, it is perhaps a bit surprising that more has not been made of HRMAS in attacking problems of relevance to peptide synthesis, although most recent interest is moving that way. Combinatorial chemistry and solid phase organic chemistry has been a much more active area using HRMAS techniques.

Traditional protein NMR spectroscopy of smaller proteins relies of ^{15}N-filtered experiments, due to the relatively low expense of introducing ^{15}N labels into proteins (compared to ^{13}C) and the concomitant ability to use heteronuclear filtering to improve resolution in the ^{1}H NMR dimension. Jelinek *et al.* were the first to demonstrate the ability to transfer this approach to peptides on TantaGel.[80] They also showed the ability to detect pronounced peptide structure through the appearance of strong NOE correlations in ^{1}H NOESY HRMAS spectra as shown in Fig. 8. This had important implications for the search of biological activity in peptides attached to supports, as the structure on the support may be different or more pronounced than in solution, if present at all in solution in peptides of this small size.

In situ identification of peptide conformation is particularly important in understanding the origins of 'difficult couplings', where peptide coupling becomes incomplete at stages of peptide chain growth in the solid-phase synthesis of a variety of sequences. Attempts to apply NMR to the identification of its causes have been reported in the past, with general reduction in mobility and concomitant increase in observed line width observed at the expected junctures in a given synthesis, but with little direct evidence as to the causes.[81,82] Applications of HRMAS have been limited by the absence of long-range NOE's, indicating an extended structure.[83] Application of Chemical Shift Index methods[84,85] confirmed this structural motif, and aggregation of the chains has been concluded to be the origin of reaction
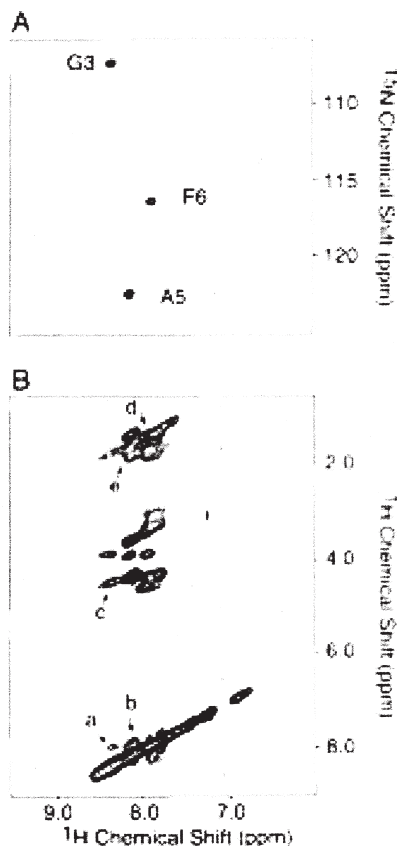
Fig. 8. 750 MHz ^{1}H-^{15}N HMQC (A) and ^{1}H NOESY (B) HRMAS NMR spectra of Gly-Pro-Gly-Arg-Ala-Phe on TantaGel resin swollen with DMSO-d_6. Spectrum A shows the excellent sensitivity obtained when selective labeling of peptide residues 3, 5 and 6 of this sequence is used. Spectrum B shows the substantial NOE i,i+1 cross-peaks (indicated by the letters a–e) obtained with a NOE mixing time of 200 ms, indicating substantial structure in this short sequence under these conditions. Reproduced with permission from Ref. 80. Copyright 1998 Elsevier.

difficulties. Addition of DMSO was shown to increase peptide mobility and reaction efficiency, with significant decrease in spectral line width and improved spectral quality also apparent. Subsequent work on poly-alanine chains[86], again using the Chemical Shift Index approach, showed that a discharge of the resin (reduction of the number of peptide sites from 0.754 mmol/g to 10, 2 and 1% of that) reduced the aggregation and hence improved coupling efficiency. In the non-aggregated state, the (Ala)$_{12}$ chains on 0.015 mmol/g (2%) resin demonstrated an α-helical structure, according to the Chemical Shift Index data. Sensitivity was too low for traditional NOESY analysis.

Any secondary structure present in a polymer-supported peptide chain will be influenced by the nature of the support – this was evident in a recent study of the conformations adopted by a 19-residue fragment of the capsid viral protein VP1 of foot-and-mouth disease virus on three different supports.[87] In two of the supports, based in one case on polystyrene and another one on polyethylene glycol-acrylamide, the structure was ill-characterized other than being relatively 'condensed' with significant spectral overlap and missing (likely broadened) peaks. The third support, a polyoxyethylene-polyoxypropylene polymer, indicated a helical conformation adopted by the peptide in DMF-d_7 solution. Homonuclear ^{1}H COSY TOCSY and NOESY and heteronuclear ^{1}H–^{15}N HSQC and ^{1}H–^{13}C HSQC-TOCSY spectra were acquired. ROESY spectra are indicated in the supporting materials but not depicted in the article. Secondary structure was elucidated using both NOE connectivities and the Chemical Shift Index. While this report shows the ability of HRMAS NMR to elucidate structure, it also shows strong caution must be exercised in assessing the relevance of any structure ultimately found. Changes in support or solvents can cause significant changes in the nature and extent of any secondary structure, hence conclusions concerning structure should be drawn from conditions most relevant to the conditions in which structure might be important.

Localized water clusters have been identified in the ^{1}H HRMAS NMR spectra of charged peptides at intermediate steps of the Boc-based coupling strategy.[88] The deprotected tripeptide Gly-Phe-Ala-NH$_3^+$ formed an ion pair with trifluoroacetate and caused a splitting of the residual water signal in DMF solution, a bulk water signal at 3.60 ppm and a broader 'solvated' signal at 3.77 ppm. EXSY experiments, results of one of which are shown in Fig. 9, as well as ROESY spectra confirmed the presence of an exchange process involving the terminal NH$_3^+$ group and each of the water signals. Dilution of the peptide, and indeed the residual water, within the protected environment of a DMF-swollen polystyrene resin, coupled with characterization by HRMAS NMR spectroscopy, provided a significant new insight to the structure of these bound water molecules.

Proteins of a much larger scale have also been immobilized on solid supports, permitting investigations of their interactions with small molecules via HRMAS NMR spectroscopy. Using controlled pore glass as a support, Klein et al.[89] attached the 36 kDa protein wheat germ agglutinin and applied saturation transfer difference (STD) NMR spectroscopy to detect binding, if any, between the protein and any of seven oligosaccharides in a mixture. Since the STD technique removes any unchanged signals from the resulting difference spectra, only changes that are associated with specific binding to the protein are evident. This one-dimensional technique can be applied with large excess of small-molecule binding candidates, making sensitivity and experiment time demands very reasonable. This technique has been proposed for high-throughput screening of compound libraries.
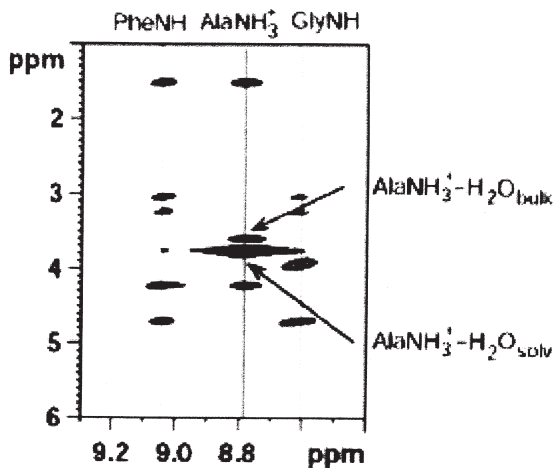
Fig. 9. 600 MHz ^{1}H EXSY spectrum showing the exchange of magnetization between ammonium protons and two distinct water components in a peptidyl-water cluster bound to p-aminomethyl polystyrene resin swollen in DMF-d_7. Reproduced with permission from Ref. 88. Copyright 2001 American Chemical Society.

Despite the importance of carbohydrates and glycopeptides in biological functions such as cell signalling and recognition, the difficulty of this chemistry[90] has meant there have been very few attempts to apply HRMAS to such synthetic systems. Early work by Seeberger and co-workers[91] demonstrated that glycal formation via solid-phase synthesis (on a Merrifield resin) could be followed and characterized using 1D ^{1}H–^{13}C and 2D ^{1}H–^{13}C HMQC HRMAS NMR spectroscopy. Most importantly, the anomeric carbons could be clearly identified and monitored. A novel 4,5-dibromooctane-1,8-diol linker for solid-phase oligosaccharide synthesis has been evaluated using HRMAS NMR spectroscopy.[92] Direct glycosylation of peptide side chains while attached to a resin have also been monitored and characterized using DQF-COSY and NOESY HRMAS experiments.[93] It seems likely that application of HRMAS techniques to problematic reactions will aid in the development of this difficult chemistry.

5. APPLICATIONS TO POLYMERS, WHOLE CELLS AND TISSUES

While both solution and solid-state NMR has been routinely applied to polymers for many years, there have been a few recent applications of HRMAS to polymer systems, analyzing polymerization mechanisms and characterizing the resulting polymers in the swollen state. The vulcanization of butadiene rubber by cyclic disulfides was shown to follow two different mechanisms with two different classes of sulfur compounds – cross-linking progressed

through addition of the cyclic disulfides such as 1,2-dithiacyclooctane,[94] and through α substitution for *N*-cyclohexyl-2-benzothiazole sulfenamide and tetramethylthiuram disulfide,[95] to the olefinic bonds. A variety of HRMAS techniques were applied with great success in these studies, including COSY, TOCSY, NOESY, HETCOR and ^{13}C DEPT with compelling examples of improved resolution provided by application of MAS to swollen polymer samples, compared to conventional solid-state MAS of dry powders. This feature of improved information content in suitably prepared swollen polymers was further emphasized by Bachmann *et al.*[96] in an investigation of polyalkylvinyl ether phases. In contrast to solid-phase organic or peptide chemistry, polymer chemistry does not have the luxury of simply treating the polymer backbone as a background – indeed, demands for resolution are increased to be able to distinguish subtle variations in the polymer chain. HRMAS of swollen polymer systems is beginning to be used routinely as an important new tool for polymer chemistry alongside traditional solid-state MAS, as in the above examples. Other examples of this approach include the sol-gel synthesis of inorganic-organic silicate hybrids,[97] where the mobility of the resulting xerogels was characterized through relaxation measurements. A sorbent system based on β-cyclodextrin polymers was also characterized through the combined application of solid-state MAS of dry polymer and HRMAS of the swollen sorbent system in the presence of various guest molecules.[98] It is also being applied together with solution NMR studies, such as in recent work on hydrophobically modified water-soluble polyacrylamides,[99] or in the characterization of etherification side reactions in hyperbranched polycondensation reactions of 2,2-bis(hydroxy)-methylpropionic acid.[100] In each case, the ability of HRMAS to provide 'solution-like' spectra in viscous or gel samples provides important complementary insights into the polymer structure that would not otherwise have been accessible, by either traditional NMR or by mass spectrometric or IR analyses.

More complex systems involving interactions between different components or phases has been the focus of some recent applications of HRMAS, specifically because of the ability of this technique to remove the susceptibility broadening that results in featureless spectra in routine solution NMR experiments. Polymers functionalized with pyridyl ligands form non-covalent complexes with metalloporphyrins, and the specific interactions and geometries comprising these complexes have been elucidated from the chemical shift changes that occur upon complexation.[101] Without the high resolution afforded by HRMAS, these subtle shifts would not have been observed. A similar yet more striking demonstration of the information available when these shifts can be well defined is evident in the recent report of 'threading', both reversibly and irreversibly, of a macrocycle onto polyethyleneglycol chains.[102] The macrocycle, depicted in Fig. 10 as a simple 'ring', causes splitting of the polyethyleneglycol proton signals upon its
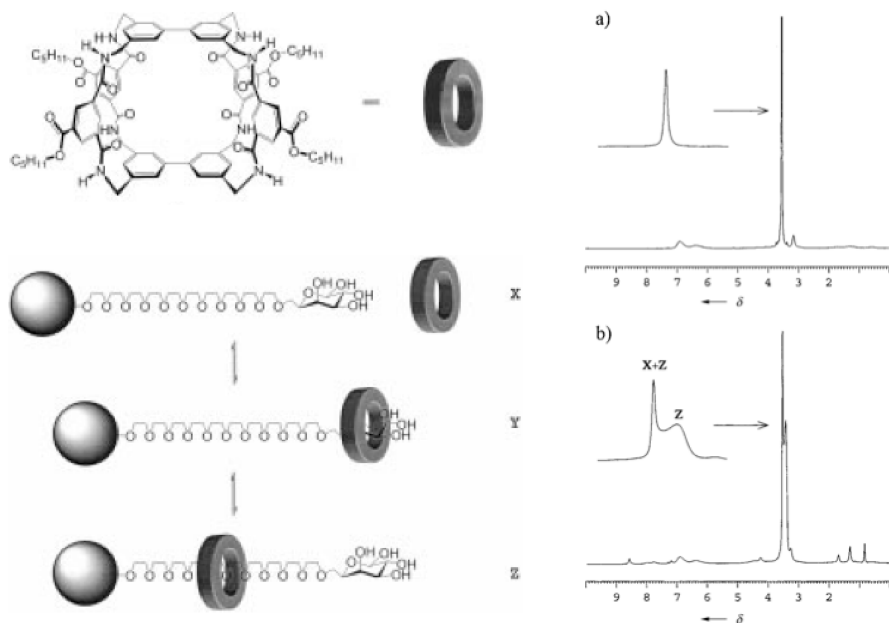
Fig. 10. 400 MHz ^{1}H HRMAS NMR spectra of ArgoGel resin swollen with 92% CDCl$_3$/8% CD$_3$OD. The macrocycle, stylized as a ring, reversibly 'threads' onto the polyethyleneglycol chain in a scheme depicted on the left. This is evident in the spectra to the right, where the upper unsplit spectrum was obtained in the absence of the macrocycle, and the lower was obtained after addition of the macrocycle. Reproduced with permission from Ref. 102. Copyright 2001 Wiley-VCH.

addition to the resin, which could then be reversed with the addition of another sugar for which the macrocycle had higher affinity.

Encapsulation of herbicides within anionic clays was readily identified by the loss of ^{1}H HRMAS NMR signal associated with immobilization of the molecules between clay layers.[103] The application of HRMAS to soil samples has been shown to provide important results on the interaction of herbicide and other organic components with the soil matrix, using 1D ^{1}H HRMAS, selective TOCSY and 2D TOCSY experiments.[104] Significant advantages to the HRMAS approach are its reduced samples preparation needs, with no extraction, pre-treatment or purification required.

Membranes have been an active focus of NMR research for some time, using techniques appropriate to both solution and oriented samples to determine dynamics and structure. Readers are encouraged to consult several excellent recent reviews on this broad area,[4,5,105] as only highlights directly related to HRMAS will be included here. While MAS has been applied for some time at modest rotation rates typical of HRMAS,[7] recent applications at high spinning speeds (> 10 kHz) provided high resolution ^{1}H NMR

spectra of peptides in membranes in one and two dimensions, often in per-deuterated membranes,[106–108] though not exclusively.[109] The spectra were of suitable quality that conformational information about the peptide was obtained, providing otherwise inaccessible structural details concerning membrane peptides. Dynamics play an important role, both in the function of membrane peptides, and on the application of HRMAS.[4,110]

One excellent example was the recent demonstration that three ubiquinone molecules bind as co-factors to the mitochondrial membrane protein complex cytochrome bc_1.[111] Two-dimensional ^1H–^{13}C HSQC NMR of ^{13}C-labelled ubiquinone with calibrated reference standards (^{13}C-labelled acetate) were used to quantify the amount of free ubiquinone – bound ubiquinone was unobservable due to its loss of rotational mobility and subsequent signal broadening. Particular reasons for using HRMAS as opposed to solid-state NMR on oriented or frozen samples were summarized by the authors in the experimental description. Specifically, they cited the need for only a single label in the HRMAS approach and its higher sensitivity.

Concerning the membrane itself, phospholipid hydration was characterized in terms of the types of water, bound and bulk, and their exchange rates, as well as direct observation of the intermolecular contacts between the phosphate headgroup and bound water via HRMAS HOESY and between lipids in mixed membranes via HRMAS NOESY.[112] Significantly, Zhou and co-workers found little dehydration of the membranes even when rotation rates as high as 9 kHz were used, providing some comfort that the centripetal forces of sample rotation are not changing the structure of the membrane.

Some of the most interesting applications of HRMAS have been to samples composed of living cells.[113] Cell surfaces, in particular, are important in cell recognition, important in identifying, e.g., pathogens or tumors. The lipopolysaccharides found on cell surfaces of several bacteria, *Yokonella regensburgei*,[114] *Hafnia alvei*[115] and *Plesiomonas shigelloides*,[116] have been structurally characterized on intact bacteria cells, as well as in isolated form. In combination with other techniques, such as MALDI-TOF mass spectrometry, gel electrophoresis and GC-MS, precise details of the polysaccharide structure were determined, in large part due to the chemical specificity of the NMR spectra, which included 1D ^1H, TOCSY, NOESY, HMQC and HSQC-DEPT experiments. Identities of the repeating units of the sugars, and their substitution patterns, were readily discerned from the NMR results, and the preservation of the structure from intact cells to isolated polysaccharide was confirmed. Spin-echo experiments were used to reduce the spectral contribution of broad background signals for studies involving the intact bacterial cells.

The application of both solution and HRMAS NMR to the study of osmoregulated periplasmic glucans in cells of the bacterium *Ralsonia solanacearum* showed important differences in the reproducibility of the spectral results, with HRMAS NMR providing consistent and better quality

spectra.[117] Incorporation of ^{13}C-labelled glucose into the glucans was used to increase the sensitivity and aid in assignment. One-dimensional ^{1}H–^{13}C and 2D HSQC spectra were collected, and the application of a diffusion filter via gradients (*see above*) reduced, but did not eliminate, the aqueous solvent peak. The remainder, ascribed to intracellular water, was removed with the addition of a weak presaturation pulse. 'Spiking' of the cell samples with a solution of ^{13}C$_1$-enriched glucan followed by an HSQC experiment incorporating a diffusion filter, the results of which are depicted in Fig. 11, confirmed that only glucans present in the cells contributed to the resulting spectrum – extracellular glucans were diffusing too rapidly to survive the gradient filter. In parallel to the phospholipid hydration results described above, rotation of the sample at 6 kHz was shown not to disturb the structure of the cell, as no lysis was detected in the NMR spectra, making this a robust and highly useful analytical tool for *in vivo* cellular investigations.

Beyond bacteria, mammalian cells undergoing membrane rupture due to transfection with plasmid DNA have been shown to exhibit increased levels of phosphocholine by ^{1}H HRMAS NMR.[118] In general, this new area of research, which has been coined 'in-cell' NMR spectroscopy, is not limited to HRMAS studies,[119] but clearly there is an important role for HRMAS in the study of these heterogeneous living systems.

Direct analysis of tissue samples by HRMAS NMR provides important simplifications in their analyses, as chemical extraction or other treatment is no longer required. Rather, the tissue sample may be analyzed directly following placement of a small portion within a MAS rotor or sample cell.[120] Consequently, there has been a great deal of activity in identifying the markers of cancer in cells as well as other diagnostic issues with a view to substantially simplifying, hence speeding, the testing of tissues. Specific applications to human tissues have included detection of changing neurochemical levels in brains afflicted with Pick disease;[121] identification of tumor metabolic markers in cancers of human breast ducts;[122] detection of increased lipid levels in renal cell carcinoma tumours, accompanied by much more rapid diagnostic results;[123] establishment of differences in metabolic markers between liposarcoma (a soft tissue cancer) and lipoma that otherwise would require cell cultures[124,125]; and the non-destructive quantitation of spermine, a possible inhibitor to tumor growth, in human prostate tissue by HRMAS which correlated well with traditional histopathology methods.[126] A comparison between the results of *in vivo* ^{1}H MRS of brain tumors with ^{1}H HRMAS NMR of biopsy samples of the same tumors indicated much better spectral quality in the HRMAS results, and good qualitative agreement between the two methods.[127,128] The improved spectral quality compared to MRS is clearly evident in Fig. 12, although the increased field strength used for the HRMAS spectra is one obvious (and perhaps unfair) advantage. In combination with MRS, the authors believe HRMAS of biopsy tissue provides greater biochemical detail of the *in vivo* results.[128]
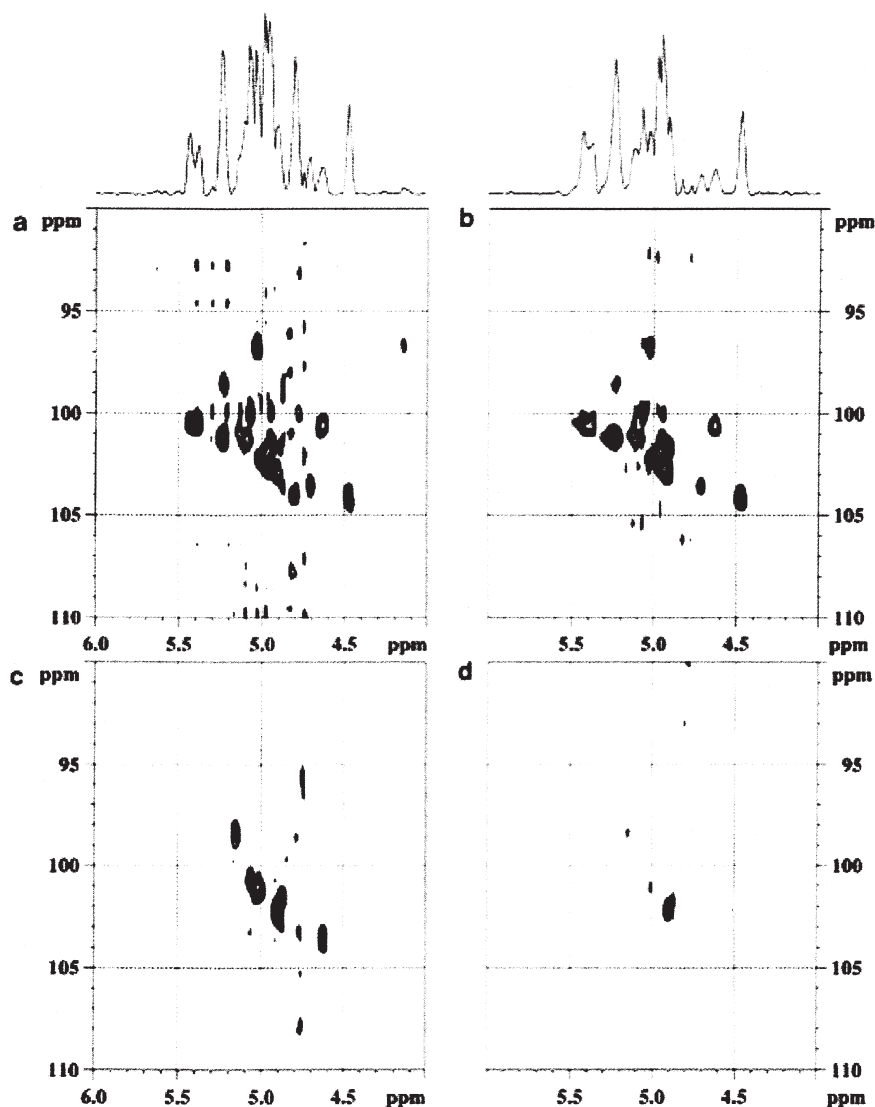
Fig. 11. 600 MHz ^{1}H-^{13}C HSQC HRMAS NMR spectra of *Ralsonia solanacearum* obtained without (a, c) and with (b, d) a diffusion filter. The (a, d) arise from cells grown on ^{13}C$_1$-glucose, and their ^{1}H projections for this region is shown; the (c, d) lower spectra arise from natural-abundance samples which have had a 2 mM solution of ^{13}C$_1$-labelled glucans added. Note that once the diffusion filter is applied, only glucans within the cell are evident in the spectrum at (d), compared to the number of peaks in the (c) spectrum. This confirms the integrity of the cells under sample spinning. The cells grown on enriched media show a much higher number of peaks, as expected. Reproduced with permission from Ref. 117. Copyright 2001 Elsevier.
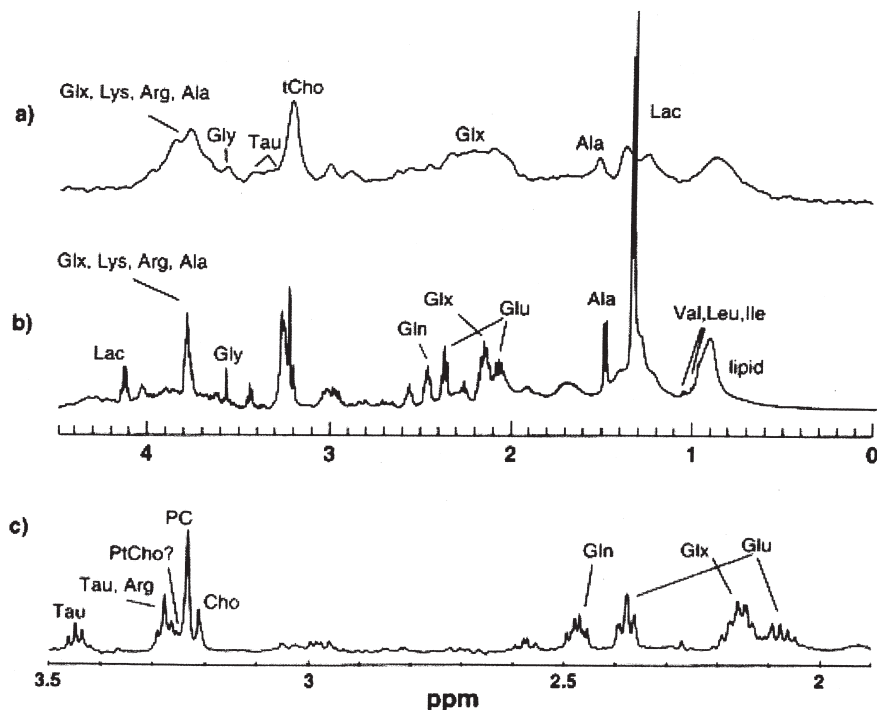
Fig. 12. (a) 64 MHz ^{1}H STEAM MRS spectrum of a brain tumor *in vivo*, and 500 MHz ^{1}H HRMAS NMR spectrum of a biopsied sample of the same tumour using (b) presaturation, and (c) a spin echo sequence. Metabolites are identified directly on the spectra. For HRMAS, the samples were rotated at 4 kHz. Reproduced with permission from Ref. 128. Copyright 1999 Elsevier.

Temperature control, and cooling of the tissue samples (to 2° C, typically, during experiments), has been cited as an extremely important experimental parameter in limiting tissue degradation during the HRMAS analyses.[121] In addition, total experiment times are kept as short as possible, with 1D ^{1}H experiments completed in several minutes at most. Consequently, in most cases, concentration and marker measurements have not included more time-consuming 2D experiments (although use of gradient MAS probes may reduce this time constraint considerably). In no case was any disruption of the tissue integrity due to the rapid rotation of the sample noted, ensuring the robustness and relevance of the HRMAS results. A study of procedures for sample preparation for HRMAS has been completed,[129] as has an example of temperature calibration in HRMAS for tissue samples,[130] for interested readers to take note.

Many tissue studies rely on animal models, rats and mice in particular, hence there have been several reports of HRMAS studies of animal tissues. As in human tissues, the primary goal has been to establish biochemical

profiles for different tissues, either as a marker of disease, or, in one novel application, to determine differences between wild and laboratory species.[131] Analysis of rat kidney tissue showed, under rapid rates of rotation (12 kHz MAS) different signals arising from the lipid profiles of cortex and papillary extracts, with the visible triglyceride signal in the cortex arising from more constrained environments.[132] This difference was undetectable at routine rotation rates of 4.2 kHz. A number of low-molecular-weight compounds were detected directly in cancerous lymph nodes in rats;[133] in rat liver samples using 1D and 2D ^{1}H–^{13}C HRMAS;[134] correlated by 1D ^{1}H NMR between rat liver tissue (using HRMAS) and urine and plasma samples (using solution NMR) in rats suffering from hepatitis;[135] and in rat testis using 1D, 2D and diffusion-filtered ^{1}H HRMAS.[136] The biochemical effects of a toxic agent (2-bromoethanamine hydrobromide) on rats, in liver and kidney tissues, has also been investigated using 1D and 2D ^{1}H HRMAS NMR of intact tissue.[137] The changes in phospholipid metabolism accompanying treatment of melanoma tumors in mice with cystemustine were monitored using 1D and 2D ^{1}H HRMAS of the tumor tissue.[138] The metabolic composition of heart muscle tissue in *mdx* mice, an animal model for Duchenne muscular dystrophy, was determined using a combination of 1D ^{1}H, 2D COSY and ^{1}H–^{13}C HSQC HRMAS NMR. Again, advantages of HRMAS cited in these reports were the increased resolution compared to *in vivo* MRS, the lack of any sample pre-treatment, the ability to monitor changes within the tissue itself, and the limited amount of sample required compared to analyses of tissue extracts. In most cases, a T_2 filter (spin echo) was also used to remove broad unresolved components of the spectra.

Finally, low-molecular-weight compounds have been identified *in situ* in plant tissues, including red algae,[139,140] mango,[141,142] and wheat gluten.[143] Comparison of the HRMAS results with those of FAB mass spectrometry and GC-MS showed excellent correlation, vindicating the quantitative analysis provided by NMR.[139,140] The biochemical changes associated with ripening of mango were followed by HRMAS of mango pulp, with almost 40 metabolites identified, and levels of the different sugars (fructose, glucose and sucrose) were measured.[141,142] The resolution enhancement afforded by HRMAS permitted multi-dimensional NMR experiments to be performed, which allowed, for the first time, determination of significant structural elements of the high-M_r subunits of the wheat gluten storage proteins in hydrated form.[143]

6. SUMMARY AND PROSPECTS

The applications of HRMAS have been quite diverse, revealing the abilities of NMR to probe structure and dynamics in the previously troublesome area of semi-solids that could not be investigated by solid-state or solution

NMR methods alone. The marriage of high resolution techniques with magic angle spinning has been an area of active development over the last decade, with much better equipment, particularly specialized probes, available now. It seems quite clear that HRMAS probes benefit from the same care in probe geometry and construction materials that have characterized traditional solution NMR probes, and great benefits in improved lineshapes and sensitivity have been realized. In terms of applicability, there have been no reports of any adverse effects of rapid sample spinning on the integrity of any of the systems reviewed here. Also, it has been demonstrated that the addition of gradients not only improves the capabilities of HRMAS by reducing experiment times of multidimensional experiments, it also permits the characterization of and, more significantly, discrimination by diffusion differences between 'free' and 'bound' species in these systems. This has been of particular benefit in studying reaction mixtures, obviating the need for deuterated solvents, and whole cells, permitting the differentiation of intra- and extra-cellular species.

By now, HRMAS has matured into a relatively routine technique. Magic angle spinning equipment is added relatively easily to existing high resolution NMR spectrometers, and the experiments used are no more complicated or difcult to set up than solution NMR experiments already familiar to many non-specialists in NMR. Care should be taken that the magic angle spinning equipment available suits the application desired – some equipment is quite well suited to a high throughput of samples rapidly prepared, but with a relatively low, though often sufficient, upper limit on spinning rates. Other equipment provides higher attainable spinning rates, but requires either greater time in sample preparation or greater expense in MAS rotors for routine applications. Researchers interested in applying these techniques should consider and evaluate their experimental needs.

REFERENCES

1. L. A. Thompson and J. A. Ellman, Synthesis and applications of small molecule libraries, *Chem. Rev.*, 1996, **96**, 555–600.
2. B. J. Egner and M. Bradley, Analytical techniques for solid-phase organic and combinatorial synthesis, *Drug Discovery Today*, 1997, **2**, 102–109.
3. J. H. Davis, Deuterium magnetic resonance study of the gel and liquid crystalline phases of dipalmitoyl phosphatidylcholine, *Biophys. J.*, 1979, **27**, 339–358.
4. D. E. Warschawski, J. D. Gross and R. G. Griffin, Effects of membrane peptide dynamics on high-resolution magic-angle spinning NMR, *J. Chim.-Phys. Phys. Biol.*, 1998, **95**, 460–466.
5. C. Glaubitz, An introduction to MAS NMR spectroscopy on oriented membrane proteins, *Concepts in Magnetic Resonance*, 2000, **12**, 137–151.
6. S. I. Manatt, S. F. Amsden, C. A. Bettison, W. T. Frazer, J. T. Gudman, B. E. Lenk, J. F. Lubetich, E. A. McNelly, S. C. Smith, D. J. Templeton, R. P. Pinnell, A fluorine-19

NMR approach for studying Merrifield solid-phase peptide synthesis, *Tet. Lett.*, 1980, **21**, 1397–1400.

7. J. Forbes, C. Husted and E. Oldfield, High-field, high-resolution "magic-angle" sample-spinning nuclear magnetic resonance spectroscopic studies of gel and liquid crystalline lipid bilayers and the effects of cholesterol, *J. Am. Chem. Soc.*, 1988, **110**, 1059–1065.

8. E. R. Andrew, A. Bradbury and R. G. Eades, Nuclear magnetic resonance spectra from a crystal rotated at high speed, *Nature*, 1958, **182**, 1659.

9. R. B. Merrifield, Solid phase peptide synthesis. I. The synthesis of a tetrapeptide, *J. Am. Chem. Soc.*, 1963, **85**, 2149–2154.

10. E. Bayer, Towards the chemical synthesis of proteins, *Angew. Chem., Int. Ed. Engl.*, 1991, **30**, 113–216.

11. R. B. Merrifield, Automated synthesis of peptides, *Science*, 1965, **156**, 178–185.

12. S.-S. Wang, *p*-Alkoxybenzyl alcohol resin and *p*-alkoxybenzyloxycarbonylhydrazide resin for solid phase synthesis of protected peptide fragments, *J. Am. Chem. Soc.*, 1973, **95**, 1328–1333.

13. P. A. Keifer, New methods for obtaining high-resolution NMR spectra of solid-phase synthesis resins, natural products, and solution-state combinatorial chemistry libraries, *Drugs of the Future*, 1998, **23**, 301–317.

14. P. A. Keifer, NMR tools for biotechnology, *Curr. Opin. Biotechnol.*, 1999, **10**, 34–41.

15. P.A. Keifer, The NMR "toolkit" for compound characterization, *Integrated Drug Discovery Technologies*, 485–541, 2002.

16. M. J. Shapiro and J. R. Wareing, NMR methods in combinatorial chemistry, *Curr. Opin. Chem. Biol.*, 1998, **2**, 372–375.

17. M. J. Shapiro and J. S. Gounarides, NMR methods utilized in combinatorial chemistry research, *Progress in Nuclear Magnetic Resonance Spectroscopy*, 1999, **35**, 153–200.

18. M. J. Shapiro, NMR methods, *Analytical Techniques in Combinatorial Chemistry*, 2000, 77–111.

19. M. J. Shapiro and J. S. Gounarides, High resolution MAS-NMR in combinatorial chemistry, *Biotechnol. Bioeng.*, 2000, **71**, 130–148.

20. G. C. Look, C. P. Holmes, J. P. Chinn and M. A. Gallop, Methods for combinatorial organic synthesis: The use of fast ^{13}C nmr analysis for gel phase reaction monitoring, *J. Org. Chem.*, 1994, **59**, 7588–7590.

21. F. Bardella, R. Eritja, E. Pedroso and E. Giralt, Gel-phase P-31-NMR-a new analytical tool to evaluate solid-phase oligonucleotide synthesis, *Bioorg. Med. Chem. Lett.*, 1993, **3**, 2793–2796.

22. D. Stones, D. J. Miller, M. W. Beaton, T. J. Rutherford and D. Gani, A method for the quantification of resin loading using ^{19}F gel phase NMR spectroscopy and a new method for benzyl ether linker cleavage in solid phase chemistry, *Tet. Lett*, 1998, **39**, 4875–4878.

23. M. Mehring. *Principles of High Resolution NMR in Solids*, volume 11 of *NMR-Basic Principles and Progress*. Springer-Verlag, Berlin, second, revised and enlarged edition, 1983.

24. K. Schmidt-Rohr and H. W. Spiess,   *Multidimensional Solid-State NMR and Polymers*, Academic Press, London, 1994.

25. D. L. VanderHart, Magnetic susceptibility and high resolution NMR of liquids and solids, D. M. Grant and R. K. Harris, eds., *Encyclopedia of Nuclear Magnetic Resonance*, Wiley, New York, 1996, 2938–2946.

26. P. A. Keifer, L. Baltusis, D. M. Rice, A. A. Tymiak and J. N. Shoolery, A comparison of NMR spectra obtained for solid-phase-synthesis resins using conventional high-resolution, magic-angle-spinning, and high-resolution magic-angle-spinning probes, *J. Magn. Reson., Series A*, 1996, **119**, 65–75.

27. T. M. Barbara, Cylindrical demagnetization fields and microprobe design in highresolution NMR, *J. Magn. Reson., Series A*, 1994, **109**, 265–269.

28. W. L. Fitch, G. Detre, C. L. Homes, J. N. Shoolery and P. A. Keifer, High-resolution ^{1}H NMR in solid-phase organic synthesis, *J. Org. Chem.*, 1994, **59**, 7955–7956.

29. R. C. Anderson, M. A. Jarema, M. J. Shapiro, J. P. Stokes and M. Ziliox, Analytical techniques in combinatorial chemistry: MAS CH correlation in solvent-swollen resin, *J. Org. Chem.*, 1995, **60**, 2650–2651.

30. Z. Zhou, B. G. Sayer, R. E. Stark and R. M. Epand, High-resolution magic-angle spinning ^{1}H nuclear magnetic resonance studies of lipid dispersions using spherical glass ampoules, *Chem. Phys. Lipids*, 1997, **90**, 45–53.

31. F. D. Doty, G. Entzminger and Y. A. Yang, Magnetism in high-resolution NMR probe design. II: HR MAS, *Concepts in Magnetic Resonance*, 1998, **10**, 239–260.

32. E. Bayer, K. Albert, H. Wikkisch, W. Rapp and B. Hemmasi, Carbon-13 nmr relaxation times of a tripeptide methyl ester and its polymer-bound analogs, *Macromolecules*, 1990, **23**, 1937–1940.

33. T. Wehler and J. Westman, Magic angle spinning NMR: A valuable tool for monitoring the progress of reactions in solid phase synthesis, *Tet. Lett.*, 1996, **37**, 4771–4774.

34. P. A. Keifer, Influence of resin structure, tether length, and solvent upon the high-resolution ^{1}H NMR spectra of solid-phase-synthesis resins, *J. Org. Chem.*, 1996, **61**, 1558–1559.

35. K. Elbayed, M. Bourdonneau, J. Furrer, T. Richert, J. Raya, J. Hirschinger and M. Piotto, Origin of the residual NMR linewidth of a peptide bound to a resin under magic angle spinning, *J. Magn. Reson.*, 1999, **136**, 127–129.

36. J. Furrer, K. Elbayed, M. Bourdonneau, J. Raya, D. Limal, A. Bianco and M. Piotto, Dynamic and magnetic susceptibility effects on the MAS NMR linewidth of a tetrapeptide bound to different resins, *Magn. Reson. Chem.*, 2002, **40**, 123–132.

37. R. C. Anderson, J. P. Stokes and M. J. Shapiro, Structure determination in combinatorial chemistry: Utilization of magic angle spinning HMQC and TOCSY NMR spectra in the structure determination of Wang-bound lysine, *Tet. Lett.*, 1995, **36**, 5311–5314.

38. S. K. Sarkar, R. S. Garigipati, J. L. Adams and P. A. Keifer, An NMR method to identify nondestructively chemical compounds bound to a single solid-phase-synthesis bead for combinatorial chemistry applications, *J. Am. Chem. Soc.*, 1996, **118**, 2305–2306.

39. M. Pursch, G. Schlotterbeck, L.-H. Tseng, K. Albert and W. Rapp, Monitoring the reaction progress in combinatorial chemistry: ^{1}H MAS NMR investigations on single macro beads in the suspended state, *Angew. Chem., Int. Ed. Engl.*, 1996, **35**, 2867–2869.

40. C. H. Gotfredsen, M. Grotli, M. Willert, M. Meldal and J. O. Duus, Single-bead structure elucidation. Requirements for analysis of combinatorial solid-phase libraries by Nanoprobe MAS-NMR spectroscopy, *J. Chem. Soc. Perkin*, 2000, **1**, 1167–1171.

41. W. E. Maas, F. H. Laukien and D. G. Cory, Gradient, high resolution, magic angle spinning NMR, *J. Am. Chem. Soc.*, 1996, **118**, 13085–13086.

42. R. Bowtell and A. Peters, Magic angle gradient coil design, *J. Magn. Reson., Series A*, 1994, **115**, 55–59.

43. T. M. Barbara and C. E. Bronnimann, Target field design for magic angle gradient coils, *J. Magn. Reson.*, 1999, **140**, 285–288.

44. R. S. Garigipati, B. Adams, J. L. Adams and S. K. Sarkar, Use of spin echo magic angle spinning ^{1}H NMR in reaction monitoring in combinatorial organic synthesis, *J. Org. Chem.*, 1996, **61**, 2911–2914.

45. A. Meissner, P. Bloch, E. Humpfer, M. Spraul and O. W. Sørensen, Reduction of inhomogeneous line broadening in two-dimensional high-resolution MAS NMR spectra of molecules attached to swelled resins in solid-phase synthesis, *J. Am. Chem. Soc.*, 1997, **119**, 1787–1788.

46. M. J. Shapiro, J. Chin, R. E. Marti and M. A. Jarosinski, Enhanced resolution in MAS NMR for combinatorial chemistry, *Tet. Lett.*, 1997, **38**, 1333–1336.

47. J. Chin, B. Fell, S. Pochapsky, M. J. Shapiro and J. R. Wareing, 2D SECSY NMR for combinatorial chemistry. High resolution MAS spectra for resin-bound molecules, *J. Org. Chem.*, 1998, **63**, 1309–1311.

48. R. Warrass, J. M. Wieruszeski and G. Lippens, Efficient suppression of solvent resonances in HR-MAS of resin-supported molecules, *J. Am. Chem. Soc.*, 1999, **121**, 3787–3788.

49. M. J. Shapiro, J. Chin, A. Chen, J. R. Wareing, Q. Tang, R. A. Tommasi and H. R. Marepalli, Covalent or trapped? PFG diffusion MAS NMR for combinatorial chemistry, *Tet. Lett.*, 1999, **40**, 6141–6143.

50. J. Chin, A. Chen and M. J. Shapiro, Improved high-resolution diffusion filtered ^{1}H MAS NMR, *Magn. Reson. Chem.*, 2000, **38**, 782–784.

51. P. Rousselot-Pailley, D. Maux, J. M. Wieruszeski, J. L. Aubagnac, J. Martinez and G. Lippens, Impurity detection in solid-phase organic chemistry: Scope and limits of HR MAS NMR, *Tetrahedron*, 2000, **56**, 5163–5167.

52. J. A. Chin, A. Chen and M. J. Shapiro, SPEEDY: Spin-echo enhanced diffusion filtered spectroscopy. A new tool for high resolution MAS NMR, *J. Comb. Chem.*, 2000, **2**, 293–296.

53. M. J. T. Ditty, H. N. Hunter, R. M. E. Mainville and W. P. Power, NMR applications for solid-phase synthesis: Part I. suppression of residual polymer signals in 1D ^{1}H NMR spectroscopy of polymer-supported species, *Magn. Reson. Chem.*, 2001, **39**, 241–248.

54. J. D. Gross, P. R. Costa, J. P. Dubacq, D. E. Warschawski, P. N. Lirsac, P. F. Devaux and R. G. Griffin, Multidimensional NMR in lipid systems. Coherence transfer through J couplings under MAS., *J. Magn. Reson.*, *Series B*, 1995, **106**, 187–190.

55. Ē. Kupče, P.A. Keifer and M. Delepierre, Adiabatic TOCSY MAS in liquids, *J. Magn. Reson.*, 2001, **148**, 115–120.

56. M. Piotto, M. Bourdonneau, J. Furrer, A. Bianco, J. Raya and K. Elbayed, Destruction of magnetization during TOCSY experiments performed under magic angle spinning: Effect of radial B_1 inhomogeneities, *J. Magn. Reson.*, 2001, **149**, 114–118.

57. J. M. Wieruszeski, G. Montagne, G. Chessari, P. Rousselot-Pailley and G. Lippens, Rotor synchronization of radiofrequency and gradient pulses in high-resolution magic angle spinning NMR, *J. Magn. Reson.*, 2001, **152**, 95–102.

58. K. Thieme, G. Zech, H. Kunz, H. W. Spiess and I. Schnell, Dipolar recoupling in NOESY-type ^{1}H–^{1}H NMR experiments under HRMAS conditions, *Org. Lett.*, 2002, **4**, 1559–1562.

59. I. E. Pop, C. F. Dhalluin, B. Déprez, P. C. Melnyk, G. M. Lippens and A. Tartar, Monitoring of a three-step solid phase synthesis involving a heck reaction using magic angle spinning NMR spectroscopy, *Tetrahedron*, 1996, **52**, 12209–12222.

60. J. Chin, B. Fell, M. J. Shapiro, J. Tomesch, J. R. Wareing and A. M. Bray, Magic angle spinning NMR for reaction monitoring and structure determination of molecules attached to multipin crowns, *J. Org. Chem.*, 1997, **62**, 538–539.

61. A. M. Sefler and S. S. Gerritz, Using one- and two-dimensional NMR techniques to characterize reaction products bound to Chiron SynPhase crowns, *J. Comb. Chem.*, 2000, **2**, 127–133.

62. R. Riedl, R. Tappe and A. Berkessel, Probing the scope of the asymmetric dihydroxylation of polymer-bound olefins. Monitoring by HRMAS NMR allows for reaction control and on-bead measurement of enantiomeric excess, *J. Am. Chem. Soc.*, 1998, **120**, 8994–9000.

63. D. Bonnet, C. Rommens, H. Gras-Masse and O. Melnyk, A novel and mild solid phase hydroperoxydeamination reaction, *Tet. Lett.*, 1999, **40**, 7315–7318.

64. Y. Kuo, X. Ouyang, R. W. Armstrong and M. M. Murphy, A case study of employing spectroscopic tools for monitoring reactions in the developmental stage of a combinatorial chemistry library, *J. Org. Chem.*, 1998, **63**, 8719–8722.

65. G. Rosse, F. Ouertani and H. Schroeder, Efficient solid-phase synthesis of β-amino-substituted piperidinols, *J. Comb. Chem.*, 1999, **1**, 397–401.

66. P. Grice, A. G. Leach, S. V. Ley, A. Massi and D. M. Mynett, Combined application of analytical techniques for the characterization of polymer supported species, *J. Comb. Chem.*, 2000, **2**, 491–495.

67. T. Ruhland, K. Andersen and H. Pedersen, Selenium-linking strategy for traceless solid-phase synthesis: Direct loading, aliphatic C–H bond formation upon cleavage and reaction monitoring by gradient MAS NMR spectroscopy, *J. Org. Chem.*, 1998, **63**, 9204–9211.

68. R. Duboc, M. Savignac and J. P. Genet, Palladium cross-coupling reactions on solid support using a new silylated linker, *J. Organomet. Chem.*, 2002, **643**, 512–515.

69. A. R. Vaino and K. D. Janda, Solid-phase organic synthesis: A critical understanding of the resin, *J. Comb. Chem.*, 2000, **2**, 579–596.

70. S. W. Gerritz, Quantitative techniques for the comparison of solid supports, *Curr. Opin. Chem. Biol.*, 2001, **5**, 264–268.

71. O. W. Gooding, S. Baudart, T. L. Deegan, K. Heisler, J. W. Labadie, W. S. Newcomb, J. A. Porco and P. van Eikeren, On the development of new poly(styrene-oxyethylene) graft copolymer resin supports for solid-phase organic synthesis, *J. Comb. Chem.*, 1999, **1**, 113–122.

72. M. Grøtli, C. H. Gotfredsen, J. Rademann, J. Buchardt, A. J. Clark, J. O. Duus and M. Meldal, Physical properties of poly(ethylene glycol) (PEG)-based resins for combinatorial solid phase organic chemistry: A comparison of PEG-cross-linked and PEG-grafted resins, *J. Comb. Chem.*, 2000, **2**, 108–119.

73. A. Bianco, J. Furrer, D. Limal, G. Guichard, K. Elbayed, J. Raya, M. Piotto and J. P. Briand, Multistep synthesis of 2,5-diketopiperazines on different solid supports monitored by high resolution magic angle spinning NMR spectroscopy, *J. Comb. Chem.*, 2000, **2**, 681–690.

74. R. Warrass and G. Lippens, Quantitative monitoring of solid phase organic reactions by high-resolution magic angle spinning NMR spectroscopy, *J. Org. Chem.*, 2000, **65**, 2946–2950.

75. J. S. Fruchart, G. Lippens, C. Kuhn, H. Gras-Masse and O. Melnyk, Solid-phase enolate chemistry investigated using HR-MAS NMR spectroscopy, *J. Org. Chem.*, 2002, **67**, 526–532.

76. P. Rousselot-Pailley, N. J. Ede and G. Lippens, Monitoring of solid-phase organic synthesis on macroscopic supports by high-resolution magic angle spinning NMR, *J. Comb. Chem.*, 2001, **3**, 559–563.

77. R. Hany, D. Rentsch, B. Dhanapal and D. Obrecht, Quantitative determination of resin loading in solid-phase organic synthesis using C-13 MAS NMR, *J. Comb. Chem.*, 2001, **3**, 85–89.

78. M. A. Poupart, D. R. Cameron, C. Chabot, E. Ghiro, N. Goudreau, S. Goulet, M. Poirier and Y. S. Tsantrizos, Solid-phase synthesis of peptidomimetic inhibitors for the hepatitis C virus NS3 protease, *J. Org. Chem.*, 2001, **66**, 4743–4751.

79. R. Jelinek, A. P. Valente, K. G. Valentine and S. J. Opella, Two-dimensional NMR spectroscopy of peptides on beads, *J. Magn. Reson.*, 1997, **125**, 185–187.

80. A. G. Ludwick, L. W. Jelinski, D. Live, A. Kintanar and J. J. Dumais, Association of peptide chains during merrifield solid-phase peptide synthesis. a deuterium NMR study, *J. Am. Chem. Soc.*, 1986, **108**, 6493–6496.

81. C. M. Deber, M. K. Lutek, E. P. Heimer and A. M. Felix, Conformational origin of a difficult coupling in a human growth hormone releasing factor analog, *Peptide Res.*, 1989, **2**, 184–188.

82. C. Dhalluin, C. Boutillon, A. Tartar and G. Lippens, Magic angle spinning nuclear magnetic resonance in solid-phase peptide synthesis, *J. Am. Chem. Soc.*, 1997, **119**, 10494–10500.

83. D. S. Wishart, B. D. Sykes and F. M. Richards, The chemical shift index: A fast and simple method for the assignment of protein secondary structure through NMR spectroscopy, *Biochemistry*, 1992, **31**, 1647–1651.

84. J. S. Fruchart, G. Lippens, R. Warrass, C. Seetharaman, C. Dhalluin and C. Boutillon, The chemical shift index method applied to resin-bound peptides, *J. Pept. Res.*, 2000, **56**, 346–351.

85. R. Warrass, J.-M. Wieruszeski, C. Boutillon and G. Lippens, High-resolution magic angle spinning NMR study of resin-bound polyalanine peptides, *J. Am. Chem. Soc.*, 2000, **122**, 1789–1795.

86. J. Furrer, M. Piotto, M. Bourdonneau, D. Limal, G. Guichard, K. Elbayed, J. Raya, J. P. Briand and A. Bianco, Evidence of secondary structure by high-resolution magic

angle spinning NMR spectroscopy of a bioactive peptide bound to different solid supports, *J. Am. Chem. Soc.*, 2001, **123**, 4130–4138.

87. G. Chessari, J. M. Wieruszeski and G. Lippens, Detection of localized water clusters in a charged peptidyl resin, *J. Am. Chem. Soc.*, 2001, **123**, 12103–12104.

88. J. Klein, R. Meinecke, M. Mayer and B. Meyer, Detecting binding affinity to immobilized receptor proteins in compound libraries by HR-MAS STD NMR, *J. Am. Chem. Soc.*, 1999, **121**, 5336–5337.

89. P. M. St Hilaire and M. Meldal, Glycopeptide and oligosaccharide libraries, *Angew. Chem., Int. Ed. Engl.*, 2000, **39**, 1162–1179.

90. P. H. Seeberger, X. Beebe, G. D. Sukenick, S. Pochapsky and S. J. Danishefsky, Monitoring the progress of solid-phase oligosaccharide synthesis by high-resolution magic angle spinning NMR: observations of enhanced selectivity for β-glycoside formation from α-1,2-anhydro sugar donors in solid-phase couplings, *Angew. Chem., Int. Ed. Engl.*, 1997, **36**, 491–493.

91. L. G. Melean, W. C. Haase and P. H. Seeberger, A novel 4,5-dibromooctane-1,8-diol linker for solid-phase oligosaccharide synthesis, *Tet. Lett.*, 2000, **41**, 4329–4333.

92. K. M. Halkes, C. H. Gotfredsen, M. Grotli, L. P. Miranda, J. O. Duus and M. Meldal, Solid-phase glycosylation of peptide templates and on-bead MAS-NMR analysis: Perspectives for glycopeptide libraries, *Chemistry-A European Journal*, 2001, **7**, 3584–3591.

93. R. Hulst, R. M. Seyger, J. P. M. van Duynhoven, L. van der Does, J. W. M. Noordermeer and A. Bantjes, Vulcanization of butadiene rubber by means of cyclic disulfides. 2. A 2D solid state HRMAS NMR study on cross-link structures in BR vulcanizates, *Macromolecules*, 1999, **32**, 7509–7520.

94. R. Hulst, R. M. Seyger, J. P. M. van Duynhoven, L. van der Does, J. W. M. Noordermeer and A. Bantjes, Vulcanization of butadiene rubber by means of cyclic disulfides. 3. A 2D solid state HRMAS NMR study on accelerated sulfur vulcanizates of BR rubber, *Macromolecules*, 1999, **32**, 7521–7529.

95. S. Bachmann, C. Hellriegel, J. Wegmann, H. Handel and K. Albert, Characterization of polyalkylvinyl ether phases by solid-state and suspended-state nuclear magnetic resonance investigations, *Solid State Nucl. Magn. Reson.*, 2000, **17**, 39–51.

96. E. Lindner, S. Brugger, S. Steinbrecher, E. Plies and H. A. Mayer, Investigations on the mobility of novel sol-gel processed inorganic-organic hybrid materials, *J. Mater. Chem.*, 2001, **11**, 1393–1401.

97. G. Crini, M. Bourdonneau, B. Martel, M. Piotto, M. Morcellet, T. Richert, J. Vebrel, G. Torri and N. Morin, Solid-state NMR characterization of cyclomaltoheptaose (β-cyclodextrin) polymers using high-resolution magic angle spinning with gradients, *J. Appl. Polym. Sci.*, 2000, **75**, 1288–1295.

98. Y. Feng, L. Billon, B. Grassl, A. Khoukh and J. Francois, Hydrophobically associating polyacrylamides and their partially hydrolyzed derivatives prepared by post-modification. 1. Synthesis and characterization, *Polymer*, 2002, **43**, 2055–2064.

99. H. Komber, A. Ziemer and B. Voit, Etherification as side reaction in the hyperbranched poly-condensation of 2,2-bis(hydroxymethyl)propionic acid, *Macromolecules*, 2002, **35**, 3514–3519.

100. Y. R. de Miguel, N. Bampos, K. M. N. de Silva, S. A. Richards and J. K. M. Sanders, Gel phase MAS H-1 NMR as a probe for supramolecular interactions at the solid-liquid interface, *Chem. Commun.*, 1998, 2267–2268.

101. Y. F. Ng, J. C. Meillon, T. Ryan, A. P. Dominey, A. P. Davis and J. K. M. Sanders, Gel-phase MAS NMR spectroscopy of a polymer-supported pseudorotaxane and rotaxane: Receptor binding to an ''inert'' polyethylene glycol spacer, *Angewandte Chemie-International Edition*, 2001, **40**, 1757–1760.

102. B. Combourieu, J. Inacio, A. M. Delort and C. Forano, Differentiation of mobile and immobile pesticides on anionic clays by 1H HR MAS NMR spectroscopy, *Chemical Communications*, 2001, 2214–2215.

103. A. J. Simpson, W. L. Kingery, D. R. Shaw, M. Spraul, E. Humpfer and P. Dvortsak, The application of ^{1}H HR-MAS NMR spectroscopy for the study of structures and associations of organic components at the solid-aqueous interface of a whole soil, *Environ. Sci. Tech.*, 2001, **35**, 3321–3325.

104. D. E. Warschawski, M. Traikia, P. F. Devaux and G. Bodenhausen, Solid-state NMR for the study of membrane systems: The use of anisotropic interactions, *Biochimie*, 1998, **80**, 437–450.

105. J. H. Davis, M. Auger and R. S. Hodges, High resolution ^{1}H nuclear magnetic resonance of a transmembrane peptide, *Biophys. J.*, 1995, **69**, 1917–1932.

106. M. Bouchard, J. H. Davis and M. Auger, High-speed magic angle spinning solid-state ^{1}H nuclear magnetic resonance study of the conformation of gramicidin A in lipid bilayers, *Biophys. J.*, 1995, **69**, 1933–1938.

107. D. Huster, K. Kuhn, D. Kadereit, H. Waldmann and K. Arnold, ^{1}H high-resolution magic angle spinning NMR spectroscopy for the investigation of a Ras lipopeptide in a lipid membrane, *Angew. Chem., Int. Ed. Engl.*, 2001, **40**, 1056–1058.

108. C. Le Guerneve and M. Seigneuret, High-resolution mono- and multidimensional magic angle spinning ^{1}H nuclear magnetic resonance of membrane peptides in nondeuterated lipid membranes and H_2O, *Biophys. J.*, 1996, **71**, 2633–2644.

109. S. Bartoschek, M. Johansson, B. H. Geierstanger, J. G. Okun, C. R. D. Lancaster, E. Humpfer, L. Yu, C. A. Yu, C. Griesinger, U. Brandt, Three molecules of ubiquinone bind specifically to mitochondrial cytochrome bc_1 complex, *J. Biol. Chem.*, 2001, **276**, 35231–35234.

110. Z. Zhou, B. G. Sayer, D. W. Hughes, R. E. Stark and R. M. Epand, Studies of phospholipid hydration by high-resolution magic-angle spinning nuclear magnetic resonance, *Biophys. J.*, 1999, **76**,387–399.

111. P. Weybright, K. Millis, N. Campbell, D. G. Cory and S. Singer, Gradient, high-resolution, magic angle spinning ^{1}H nuclear magnetic resonance spectroscopy of intact cells, *Magn. Reson. Med.*, 1998, **39**, 337–344.

112. W. Jachymek, T. Niedziela, C. Petersson, C. Lugowski, J. Czaja and L. Kenne, Structures of the O-specific polysaccharides from *Yokenella regensburgei (Koserella trabulsii)* strains PCM 2476, 2477, 2478, and 2494: High-resolution magic-angle spinning NMR investigation of the O-specific polysaccharides in native lipopolysaccharides and directly on the surface of living bacteria, *Biochemistry*, 1999, **38**, 11788–11795.

113. W. Jachymek, J. Czaja, T. Niedziela, C. Lugowski and L. Kenne, Structural studies of the O-specific polysaccharide of *Hafnia alvei* strain PCM 1207 lipopolysaccharide, *Eur. J. Biochem.*, 1999, **266**, 53–61.

114. J. Czaja, W. Jachymek, T. Niedziela, C. Lugowski, E. Aldova and L. Kenne, Structural studies of the O-specific polysaccharide from *Plesiomonas shigelloides* strain CNCTC 113/92, *Eur. J. Biochem.*, 2000, **267**, 1672–1679.

115. J. M. Wieruszeski, A. Bohin, J. P. Bohin and G. Lippens, In vivo detection of the cyclic osmoregulated periplasmic glucan of *Ralstonia solanacearum* by high-resolution magic angle spinning NMR, *J. Magn. Reson.*, 2001, **151**, 118–123.

116. J. L. Griffin, C. J. Mann, J. Scott, C. C. Shoulders and J. K. Nicholson, Choline containing metabolites during cell transfection: an insight into magnetic resonance spectroscopy detectable changes, *FEBS Lett.*, 2001, **509**, 263–266.

117. Z. Serber and V. Dotsch, In-cell NMR spectroscopy, *Biochemistry*, 2001, **40**, 14317–14323.

118. K. K. Millis, W. E. Maas, D. G. Cory and S. Singer, Gradient, high-resolution, magic-angle spinning nuclear magnetic resonance spectroscopy of human adipocyte tissue, *Magn. Reson. Med.*, 1997, **38**, 399–403.

119. L. L. Cheng, M. J. Ma, L. Becerra, T. Ptak, I. Tracey, A. Lackner and R. G. Gonzalez, Quantitative neuropathology by high resolution magic angle spinning proton magnetic resonance spectroscopy, *Proc. Natl. Acad. Sci. USA*, 1997, **94**, 6408–6413.

120. L. L. Cheng, I. W. Chang, B. L. Smith and R. G. Gonzalez, Evaluating human breast ductal carcinomas with high-resolution magic-angle spinning proton magnetic resonance spectroscopy, *J. Magn. Reson.*, 1998, **135**, 194–202.

121. D. Moka, R. Vorreuther, H. Schicha, M. Spraul, E. Humpfer, M. Lipinski, P. J. D. Foxall, J. K. Nicholson and J. C. Lindon, Biochemical classification of kidney carcinoma biopsy samples using magic-angle-spinning ^{1}H nuclear magnetic resonance spectroscopy, *J. Pharm. Biomed. Anal.*, 1998, **17**, 125–132.

122. K. Millis, P. Weybright, N. Campbell, J. A. Fletcher, C. D. Fletcher, D. G. Cory and S. Singer, Classification of human liposarcoma and lipoma using *ex vivo* proton NMR spectroscopy, *Magn. Reson. Med.*, 1999, **41**, 257–267.

123. J.-H. Chen, B. M. Enloe, C. D. Fletcher, D. G. Cory and S. Singer, Biochemical analysis using high-resolution magic angle spinning NMR spectroscopy distinguishes lipoma-like well-differentiated liposarcoma from normal fat, *J. Am. Chem. Soc.*, 2001, **123**, 9200–9201.

124. L. L. Cheng, C. L. Wu, M. R. Smith and R. G. Gonzalez, Non-destructive quantitation of spermine in human prostate tissue samples using HRMAS ^{1}H NMR spectroscopy at 9.4 T, *FEBS Lett.*, 2001, **494**, 112–116.

125. L. L. Cheng, I. W. Chang, D. N. Louis and R. G. Gonzalez, Correlation of high-resolution magic angle spinning proton magnetic resonance spectroscopy with histopathology of intact human brain tumor specimens, *Cancer Res.*, 1998, **58**, 1825–1832.

126. S. J. Barton, F. A. Howe, A. M. Tomlins, S. A. Cudlip, J. K. Nicholson, B. A. Bell and J. R. Griffiths, Comparison of *in vivo* ^{1}H MRS of human brain tumors with ^{1}H HR-MAS spectroscopy of intact biopsy samples *in vitro*, *Magnetic Resonance Materials in Physics, Biology and Medicine*, 1999, **8**, 121–128.

127. N. J. Waters, S. Garrod, R. D. Farrant, J. N. Haselden, S. C. Connor, J. Connelly, J. C. Lindon, E. Holmes and J. K. Nicholson, High-resolution magic angle spinning H-1 NMR spectroscopy of intact liver and kidney: Optimization of sample preparation procedures and biochemical stability of tissue during spectral acquisition, *Anal. Biochem.*, 2000, **282**, 16–23.

128. A. W. Nicholls and R. J. Mortishire-Smith, Temperature calibration of a high-resolution magic-angle spinning NMR probe for analysis of tissue samples, *Magn. Reson. Chem.*, 2001, **39**, 773–776.

129. J. L. Griffin, L. A. Walker, S. Garrod, E. Holmes, R. F. Shore and J. K. Nicholson, NMR spectroscopy based metabonomic studies on the comparative biochemistry of the kidney and urine of the bank vole *(clethrionomys glareolus)*, wood mouse *(Apodemus sylvaticus)*, white toothed shrew *(Crocidura suaveolens)* and the laboratory rat, *Comparative Biochemistry and Physiology. Part B, Biochemistry and Molecular Biology*, 2000, **127**, 357–367.

130. S. Garrod, E. Humpfer, M. Spraul, S. C. Connor, S. Polley, J. Connelly, J. C. Lindon, J. K. Nicholson and E. Holmes, High-resolution magic angle spinning ^{1}H NMR spectroscopic studies on intact rat renal cortex and medulla, *Magn. Reson. Med.*, 1999, **41**, 1108–1118.

131. L. L. Cheng, C. L. Lean, A. Bogdanova, S. C. Wright, Jr., J. L. Ackerman, T. J. Brady and L. Garrido, Enhanced resolution of proton NMR spectra of malignant lymph nodes using magic-angle spinning, *Magn. Reson. Med.*, 1996, **36**, 653–658.

132. M. E. Bollard, S. Garrod, E. Holmes, J. C. Lincoln, E. Humpfer, M. Spraul and J. K. Nicholson, High-resolution ^{1}H and ^{1}H-C-13 magic angle spinning NMR spectroscopy of rat liver, *Magn. Reson. Med.*, 2000, **44**, 201–207.

133. N. J. Waters, E. Holmes, A. Williams, C. J. Waterfield, R. D. Farrant and J. K. Nicholson, NMR and pattern recognition studies on the time-related metabolic effects of α-naphthylisothiocyanate on liver, urine and plasma in the rat: an integrative metabonomic approach, *Chem. Res. Toxicol.*, 2001 **14**, 1401–1412.

134. J. L. Griffin, J. Troke, L. A. Walker, R. F. Shore, J. C. Lindon and J. K. Nicholson, The biochemical profile of rat testicular tissue as measured by magic angle spinning ^{1}H NMR spectroscopy, *FEBS Lett.*, 2000, **486**, 225–229.

135. S. Garrod, E. Humpher, S. C. Connor, J. C. Connelly, M. Spraul, J. K. Nicholson and E. Holmes, High-resolution ^{1}H NMR and magic angle spinning NMR spectroscopic investigation of the biochemical effects of 2-bromoethanamine in intact renal and hepatic tissue, *Magn. Reson. Med.*, 2001, **45**, 781–790.

136. D. Morvan, A. Demidem, J. Papon, M. De Latour and J. C. Madelmont, Melanoma tumors acquire a new phospholipid metabolism phenotype under cystemustine as revealed by high-resolution magic angle spinning proton nuclear magnetic resonance spectroscopy of intact tumor samples, *Cancer Res.*, 2002, **62**, 1890–1897.

137. A. Broberg, L. Kenne and M. Pedersen, *In situ* identification of major metabolites in the red alga *Gracilariopsis lemaneiformis* using high-resolution magic angle spinning nuclear magnetic resonance spectroscopy, *Planta*, 1998, **206**, 300–307.

138. A. Broberg and L. Kenne, Use of high-resolution magic angle spinning nuclear magnetic resonance spectroscopy for *in situ* studies of low-molecular-mass compounds in red algae, *Anal. Biochem.*, 2000, **284**, 367–374.

139. A. M. Gil, I. F. Duarte, I. Delgadillo, I. J. Colquhoun, F. Casuscelli, E. Humpfer and M. Spraul, Study of the compositional changes of mango during ripening by use of nuclear magnetic resonance spectroscopy, *J. Agric. Food Chem.*, 2000, **48**, 1524–1536.

140. I. F. Duarte, I. Delgadillo, M. Spraul, E. Humpfer and A. M. Gil, An NMR study of the biochemistry of mango: The effects of ripening, processing and microbial growth, *Special Publication Royal Society of Chemistry*, 2001, **262**(Magnetic Resonance in Food Science), 259–266.

141. E. Alberti, E. Humpfer, M. Spraul, S. M. Gilbert, A. S. Tatham, P. R. Shewry and A. M. Gil, A high resolution ^{1}H magic angle spinning NMR study of a high-M$_r$ subunit of wheat glutenin, *Biopolymers*, 2001, **58**, 33–45.

Index

Note – Page numbers in *italic* type refer to figures and tables.